

Innovation and Discovery in Russian Science and Engineering

Valentina Svalova *Editor*

Heat-Mass Transfer and Geodynamics of the Lithosphere

 Springer

Innovation and Discovery in Russian Science and Engineering

Series Editors

Stavros Syngellakis, *Ashurst Lodge, Wessex Institute of Technology,
Southampton, Hampshire, UK*

Jerome J. Connor, *Department of Civil & Environmental Engineering,
Massachusetts Institute of Technology, Cambridge, MA, USA*

This Series provides rapid dissemination of the most recent and advanced work in engineering, science, and technology originating within the foremost Russian Institutions, including the new Federal District Universities. It publishes outstanding, high-level pure and applied fields of science and all disciplines of engineering. All volumes in the Series are published in English and available to the international community. Whereas research into scientific problems and engineering challenges within Russia has, historically, developed along different lines than in Europe and North America. It has yielded similarly remarkable achievements utilizing different tools and methodologies than those used in the West. Availability of these contributions in English opens new research perspectives to members of the scientific and engineering community across the world and promotes dialogue at an international level around the important work of the Russian colleagues. The broad range of topics examined in the Series represent highly original research contributions and important technologic best practices developed in Russia and rigorously reviewed by peers across the international scientific community.

More information about this series at <http://www.springer.com/series/15790>

Valentina Svalova

Editor

Heat-Mass Transfer and Geodynamics of the Lithosphere

 Springer

Editor
Valentina Svalova
Russian Academy of Sciences
Moscow, Russia

ISSN 2520-8047 ISSN 2520-8055 (electronic)
Innovation and Discovery in Russian Science and Engineering
ISBN 978-3-030-63570-1 ISBN 978-3-030-63571-8 (eBook)
<https://doi.org/10.1007/978-3-030-63571-8>

© The Editor(s) (if applicable) and The Author(s), under exclusive license to Springer Nature Switzerland AG 2021

This work is subject to copyright. All rights are reserved by the Publisher, whether the whole or part of the material is concerned, specifically the rights of translation, reprinting, reuse of illustrations, recitation, broadcasting, reproduction on microfilms or in any other physical way, and transmission or information storage and retrieval, electronic adaptation, computer software, or by similar or dissimilar methodology now known or hereafter developed.

The use of general descriptive names, registered names, trademarks, service marks, etc. in this publication does not imply, even in the absence of a specific statement, that such names are exempt from the relevant protective laws and regulations and therefore free for general use.

The publisher, the authors, and the editors are safe to assume that the advice and information in this book are believed to be true and accurate at the date of publication. Neither the publisher nor the authors or the editors give a warranty, expressed or implied, with respect to the material contained herein or for any errors or omissions that may have been made. The publisher remains neutral with regard to jurisdictional claims in published maps and institutional affiliations.

This Springer imprint is published by the registered company Springer Nature Switzerland AG
The registered company address is: Gewerbestrasse 11, 6330 Cham, Switzerland

Preface

This book is devoted to research on the formation and evolution of geological structures, heat and mass transfer processes in the lithosphere, and their connection with deep-Earth geodynamics. It is concerned with a wide range of geological and geophysical phenomena arising in the Earth's lithosphere. It also explains how such phenomena can be investigated under the umbrella of a common approach to modelling heat-mass transfer processes.

All aspects of heat-mass transfer processes at different scales – global, regional, and local – and from various origins – natural and man-made ones – are investigated. The link of such phenomena with the properties and natural laws governing the behavior of the lithosphere is demonstrated. Particular reference is made to the geophysical properties of rocks, geothermal resources, geothermics, fluid dynamics, the stress-state of the lithosphere, deep geodynamics, plate tectonics, and seismicity, among others. The adopted research methodology includes the application of modeling, seismic tomography, geological field works, geological-geophysical methods, and in situ measurements through instrumentation.

Heat-mass transfer processes exist in all aspects of human and natural activity. They control and determine processes in the lithosphere and asthenosphere, the deep mantle, and through the whole Earth, as far as Earth's upper surface, in sedimentary cover and upper crust. They determine hydrogeological processes as well as geothermal energy use and utilization, and are connected very closely with the geological-geophysical properties of rocks and soils.

Moreover, the formation and evolution of geological structures could be a clue for understanding and modelling of deep mantle geodynamics including mantle plumes, mantle diapirs, and the geothermal regime of the lithosphere.

As the title suggests, the book consists of two main parts: (a) heat-mass transfer associated with natural and technogenic processes in the upper lithosphere and (b) geodynamics and seismicity of the lithosphere. Its material was written by more than 60 prominent Russian academic investigators working at a highly innovative and advanced scientific level.

The book can be of interest to professional scientists as well as students and non-professional readers. It can thus be used for research as well as educational purposes.

Its readers can get an insight on the state of a problem with widely different aspects. They can acquire new knowledge and understand which new aspects of the problem could be developed. This is especially important for researchers who look for new applications of the outcomes of their investigations.

Moscow, Russian Federation

Valentina Svalova

Contents

Part I Heat-Mass Transfer

The Processes of Heat and Mass Transfer in the Earth's Mantle.	3
Valeriy P. Trubitsyn, Alexander P. Trubitsyn, Mikhail N. Evseev, and Alexander N. Evseev	
Thermo-Gravity Model for Sedimentary Basins	25
Valentina B. Svalova	
Prospects for Identifying and Applied Use of Hydro and Petrothermal Energy Sources in Geodynamically Active Structures of the Eastern Segment of the Central Caucasus	35
V. B. Zaalishvili, Kh. O. Chotchaev, O. G. Burdzieva, D. A. Melkov, A. K. Dzhgamadze, V. B. Svalova, and A. V. Nikolaev	
Models of Geothermal Areas: New Insights from Electromagnetic Geothermometry.	65
Viacheslav V. Spichak and Olga K. Zakharova	
Explosive Processes in Permafrost Areas – New Type of Geocryological Hazard.	83
A. N. Khimenkov, D. O. Sergeev, A. N. Vlasov, D. B. Volkov-Bogorodsky, G. S. Tipenko, V. P. Merzlyakov, and Y. V. Stanilovskaya	
Borehole Temperature Measurements Under Free Thermal Convection.	101
Dmitry Yu Demezhko, Bogdan D. Khatskevich, and Mansur G. Mindubaev	
Geothermal Regime of Groundwater in Moscow Under Anthropogenic Impact	115
Gleb I. Batrak	

Part II Heat Transfer

- Geothermy of the Continental Margins of Eastern Russia** 123
Pavel Gornov
- On Geothermal Problems of the Marginal Seas** 139
Alexander Muravyev
- Heat Flow Asymmetry on the Mid-Oceanic Ridges
of Northern and Southern Earth Hemispheres** 159
M. D. Khutorskoy and E. A. Teveleva
- The Correlation Between Earth Heat Flow and Oil
and Gas Potential – Fundamental Pattern of Western Siberia** 179
Margarita F. Galieva, Daniil S. Krutenko, and Galina A. Lobova

Part III Fluid Transfer

- Influence of Hydrodynamic Conditions on the Mass
Transfer of Pollutants in the Areas of Liquidated Mines** 191
Gleb Batrak
- Factor Modeling of Mass Transfer of Pollutants in
the Areas of Hydrogeological Windows** 199
Irina Galitskaya and Lubov Gomanuk
- Hydraulic Fracture Problem for Poroelastic
Medium with Double Porosity** 219
Andrej Karakin
- Incompletely Coupled Equations of Hydraulic
Fracturing in Poroelastic Medium** 233
Andrey V. Karakin and Mukamay M. Ramazanov
- Geomechanical Model for Large Scale Hydraulic
Fracture Dynamics** 259
E. B. Savenkov and V. E. Borisov

Part IV Fluid – Thermal Properties

- Thermodynamic Properties of Geothermal Fluids from
South Russia: Kayakent and Kizlyar Hot Sources** 275
Ilmutdin M. Abdulgatov, Lala A. Akhmedova-Azizova, Rasul M. Aliev,
and Gasan B. Badavov
- Thermodynamic Properties of Geothermal Fluids
from South Russia: Izberbash and Ternair Hot Sources** 303
Ilmutdin M. Abdulgatov, Gasan B. Badavov,
Lala A. Akhmedova-Azizova, and Rasul M. Aliev

Part V Geophysics and Geodynamics

ROSA Database and GIS Project: Accumulation of the World Largest Oil and Gas Deposits in Geological History 337
 A. A. Odintsova, A. I. Rybkina, J. I. Nikolova, and A. A. Korolkova

Lithosphere of the West Transbaikalian Sector of the Central Asian Fold Belt According to Electromagnetic Studies 351
 Elena Pospeeva, Albert Duchkov, Vladimir Potapov, and Ludmila Sokolova

Caucasian-Arabian Segment of Alpine-Himalayan Convergence: An Example of Continental Collision Above Mantle Plume 381
 Evgenii V. Sharkov and Vladimir A. Lebedev

Geothermics and Seismicity of the Caucasus Region and the Inverse Problem of Geodynamics 391
 Valentina Svalova

Geothermics and Geodynamics of the Back-Arc Basins of the Alpine and Pacific Belts 401
 Valentina Svalova

Structure and Dynamics of the Lithosphere for the Eurasia-Pacific Transition Zone 411
 Ludmila P. Zabarinskaya, Nataliya A. Sergeyeva, Vladimir A. Rashidov, Mikhail V. Nisilevich, and Tamara A. Krylova

Structural Geodynamic Zoning of Eastern European Platform – The Basis for Creating of Geothermal Model 429
 Vladimir Makeev, Natalia Makarova, Valentina Svalova, and Tatyana Sukhanova

Part VI Seismicity

Recognition of Strong Earthquake-Prone Areas with a Single Learning Class. Caucasus, $M \geq 6.0$ 441
 Boris Dzeboev, Boris Dzeranov, and Maxim Pasishnichenko

Assessment of the Effect of Resonance Properties of Soils during Seismic Microzoning 455
 M. D. Kaurkin, V. V. Romanov, and D. O. Andreev

Seismotectonic Model of the Western Margin of the South American Plate 469
 Vladislav Morozov, Viktor Tatarinov, and Alexander Kagan

Permeability of the Continental Crust –Possible High Values from Laboratory Measurements and Seismological Data 481
 Mikhail V. Rodkin and Andrey V. Zharikov

Endogenous and Exogenous Manifestations of Geodynamic Activity in the Central Caucasus 499
V. B. Zaalishvili, Kh. O. Chotchaev, M. G. Berger, O. G. Burdzieva,
B. V. Dzeranov, D. A. Melkov, A. S. Kanukov, V. B. Svalova,
and A. V. Nikolaev

Index 533

Part I
Heat-Mass Transfer

The Processes of Heat and Mass Transfer in the Earth's Mantle



Valeriy P. Trubitsyn, Alexander P. Trubitsyn, Mikhail N. Evseev,
and Alexander N. Evseev

1 Introduction

The Earth is a heat engine in which the heat of decay of radioactive isotopes and the primordial heat of gravitational differentiation is converted into the energy of convective flows in the core and mantle. In the liquid outer core quasi-turbulent convection occurs with the velocities of about 0.05 cm/s or 15 km/year [1], while the convection in the high-viscosity mantle is in the plume mode with the velocities of about 10 cm/year. Convective currents in the mantle determine the global geodynamics of the Earth and are manifested in its relief, surface movements, volcanism and earthquakes.

According to the data of measurements [2] the total surface heat loss of the Earth is equal to $Q_t = 47 \text{ TW} \pm 2 \text{ TW}$. Accordingly, the average density of the surface heat flux is $q = 92 \text{ mW/m}^2$. The heat coming out through the continents equals 15 TW with a heat flux density of 71 mW/m^2 . The heat coming out through the oceans equals 32 TW with a density of 105 mW/m^2 .

The sources of the Earth's heat are the decay of radioactive elements and the primordial heat. In the process of evolution and cooling of the Earth both sources are reduced. The relationship between them for the modern Earth is not yet known. According to [3] various estimates give 15 to 41 TW for radiogenic heat and 12 to 30 TW for primordial heat.

In this paper we consider the processes of heat transfer only for the mantle of the modern Earth. The temperature difference across the mantle is supported by the heat

V. P. Trubitsyn (✉)
IPE RAS, IEPT RAS, Moscow, Russia
e-mail: trub@ifz.ru

A. P. Trubitsyn · M. N. Evseev · A. N. Evseev
IPE RAS, Moscow, Russia

© The Author(s), under exclusive license to Springer Nature
Switzerland AG 2021

V. Svalova (ed.), *Heat-Mass Transfer and Geodynamics of the Lithosphere*,
Innovation and Discovery in Russian Science and Engineering,
https://doi.org/10.1007/978-3-030-63571-8_1

flux coming from the core, the heat of decay of mantle radioactive isotopes and the residual primordial heat. Denote the radiogenic heat flux generated in the continental crust by Q_{rc} . In the model of the Earth's composition [4] this flux equals $Q_{rc} = 7$ TW [5–7]. It is 15% of the total heat flux of the Earth Q_t . Thus the mantle heat flux (minus the radioactive heat of the crust) will be equal to $Q_m = Q_t - Q_{rc} = 47 - 7 = 40$ TW = $0.85Q_t$ with a heat flux density of 77 mW/m². This flux is created by flow from the core Q_{cor} , heat of radioactive decay in the mantle Q_{rm} and the heat flow due to secular cooling of the mantle Q_{coolm} .

The silicate mantle and the crust (after segregation of the core, but without separation of the continental crust) produce a heat flux up to 20 TW [8] or 42% of Q_t . Subtracting the radioactive heat of the crust, we find the power of the radioactive heat of the mantle, equal to $Q_{rm} = 13$ TW or $0.275Q_t$.

The secular cooling rate of the mantle is estimated within a large range, from 50–70 K/Ga to 100 K/Ga [9]. With the mass of the Earth's mantle $M = 4 \cdot 10^{24}$ kg and heat capacity of $c_p = 1.2 \cdot 10^3$ J/(kgK) and $dT/dt = 90$ K/Gyr the heat flux due to secular cooling of mantle is equal $Q_{coolm} = c_p M dT/dt = 14$ TW.

Subtracting the cooling heat and the radioactive heat of the mantle from the mantle heat flux, we find the heat flux from the core equal to $Q_{cor} = Q_m - Q_{coolm} - Q_{rm} = 40 - 14 - 13 = 13$ TW. This value of heat flux from the core is in accordance with available estimations as 27.5% of Q_t [10, 11] (Fig. 1).

Thermal convection in the mantle occurs due to the temperature gradient, which is supported by its heating from below due to the heat flow from the core $Q_{cor} = 13$ TW, and by the total internal heating of the mantle (radiogenic heating and the heat

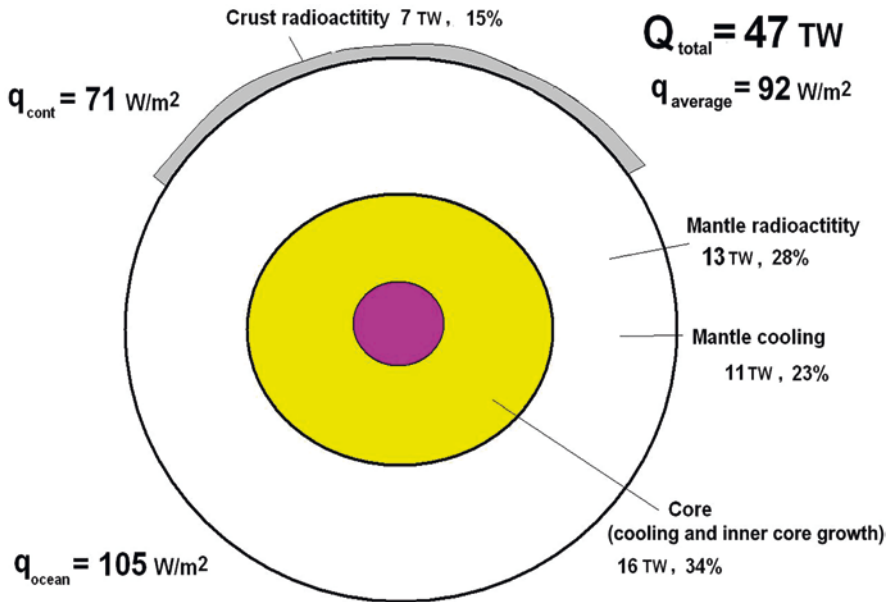


Fig. 1 The thermal balance of the Earth's mantle

released during secular cooling), i.e. by effective internal heat sources with a power of $Q_{\text{int}} = Q_{\text{rm}} + Q_{\text{cool}} = 27$ TW. Thus the mantle heating from inside Q_{int} is about 1.8 times more than the bottom heating Q_{cor} . So the mantle is heated as 70% from inside and 30% from below. This is consistent with the results of numerical models [10, 11] which demonstrated that the internal heating rate of the Earth's mantle is constrained to be $\approx 70\%$ by inferred plume heat flux and plume excess temperature.

Due to sphericity of the mantle, the heat flux density in the mantle decreases with radius about $(r/R)^2 = 3.4$ times. However, due to the internal heat sources, the density of the heat flux in the mantle should increase with radius. It is equal to $q_{\text{cor}} = Q_{\text{cor}}/(4\pi r^2) = 85$ mWT/m² at the core-mantle boundary and $q_{\text{m}} = Q_{\text{m}}/(4\pi R^2) = 78$ mWT/m² at the upper mantle surface (under the crust). As a result, despite of internal heating the heat flux density in the mantle does not significantly changes with the radius.

The temperature on the Earth's surface is approximately $T = 300$ K, and at the core-mantle boundary it is less than the melting temperature of silicates and more than the melting temperature of iron being estimated at about 4000 K [12].

For mantle thickness $D = 3000$ km the average temperature gradient $\text{grad}T$ is equal to 23 K/km. With $q = 90$ mW/m² and $k = 4$ Wm⁻¹ K⁻¹ the temperature at the core-mantle boundary would be equal to $T = 70,000$ K if the removal of heat from the Earth's interior occurred only due to thermal conductivity $q = k \text{ grad}T$. However, due to the fact that the hot silicate material of the mantle can flow, thermal convection occurs in the mantle which accelerates the removal of heat, and as a result the temperature at the core-mantle boundary becomes equal to 4000 K.

The feature of mantle convection is that the parameters of the mantle vary over a large range. Due to the compressibility of the material it is necessary to take into account the effects of adiabatic heating and cooling. The mantle viscosity changes with depth by 4 to 6 orders of magnitude. In this case, near the cold surface there is a strong lithospheric layer with a viscosity of up to 10^{26} Pa s.

However, the long-acting shear stresses create zones of micro-destruction in the lithosphere. In these local zones there is a brittle plastic flow with reduced effective viscosity. As a result, the lithosphere splits into separate plates. Plates with continents float on the convecting mantle, and oceanic plates without continents take part in the convective circulation of material throughout the mantle. As a result, the Earth's lithosphere inhibits convection and prevents heat from escaping the mantle much less than if it were continuous.

Solid-state phase transformations have a significant effect on mantle convection. In addition to convective mixing of multicomponent material, its differentiation takes place in the mantle. Due to the difference between the components in density and viscosity, the changing distribution of the components affects the convective flows. As effects of chemical reactions can be neglected, convection in the mantle can be called thermo-compositional rather than thermo-chemical one.

2 Equations of Mantle Convection

Convection is described by the equations of mass, momentum and energy transfer. Currently, the extended Boussinesq approximation (EBA) is widely used in the numerical models of mantle convection. With hydrostatic reference state the density of the mantle material is taken in the form.

$$\rho = \rho_0 \left[1 - \alpha T + (\delta\rho_p / \rho_0) \Gamma + (\delta\rho_a / \rho_0) C \right] \quad (1)$$

where ρ_0 is the average density of the mantle, T is the absolute temperature, α is the coefficient of thermal expansion, $\delta\rho_p$ is the density jump at the phase transition boundary, Γ is the phase function that takes a value of 0 or 1 for different phases, C is the concentration of the chemical component, $\delta\rho_c$ is the difference in the density of the chemical component.

To nondimensionalize the equations for spherical models we use the following scaling factors with characteristic values of the corresponding parameters: the Earth's radius R for length, $V_0 = \kappa_0/R$ for velocity, $t_0 = R^2/\kappa_0$ for time, ΔT for temperature, η_0 for viscosity, k_0 for thermal conductivity, $\kappa_0 = k_0/(\rho_0 c_p)$ for thermal diffusivity, α_0 for the thermal expansivity, $q_0 = k_0 T_0/R$ for heat flux, $\sigma_0 = \eta_0 \kappa_0/R^2$ for dynamic pressure and stress, $p_0 = \rho_0 g R$ for static pressure, $H_0 = c_p \kappa_0 \Delta T/R^2$ for the density of heat sources.

In the considered EBA approximation [13, 14] the mass transfer equation is written in a simplified form as a continuity equation.

$$\partial V_j / \partial x_j = 0. \quad (2)$$

In the Stokes momentum transfer equation the inertial terms are neglected:

$$0 = -\partial p / \partial x_i + \partial \tau_{ij} / \partial x_j + \left[\text{Ra}_R (\alpha T - \beta C) - \text{Rb} \Gamma \right] \delta_{ir} \quad (3)$$

The heat transfer equation takes into account conductive transfer, adiabatic heating and cooling, dissipative heating, heat release at phase transitions and heat release from internal sources.

$$\begin{aligned} DT / Dt = & \partial (\kappa \partial T / \partial x_j) / \partial x_j - \text{Di}_R \alpha (T + T_s) V_r + (\text{Di} / \text{Ra}) \tau_{ij} \partial V_i / \partial x_j \\ & + \gamma_k (\text{Rb} / \text{Ra}) \text{Di}_R \alpha (d\Gamma / d\pi) (T + T_s) V_r + H, \end{aligned} \quad (4)$$

where $H = Q_{\text{int}}/M_m$ is the density of internal heat sources (radiogenic heating and the heat released during secular cooling), M_m is the mass of the mantle.

The transport equation of a chemical component is written as a continuity condition for the impurity component.

$$\partial C / \partial t + V_j \partial C / \partial x_j = 0, \quad (5)$$

where $\tau_{ij} = 2\eta e_{ij} = \eta (\partial V_i / \partial x_j + \partial V_j / \partial x_i)$ is the tensor of viscous stresses.

The parameters of the material and the model are included in the Eqs. (2–4) in the form of dimensionless combinations. Here $\beta = (\delta\rho/\rho_0)/\alpha_0\Delta T$, $\Gamma = 0.5[1 + \tanh(\pi/w)]$ is the phase function, $\pi = (r-r_p) - \gamma(T-T_p) = -(h-h_p) - \gamma(T-T_p)$, $d\Gamma/d\pi = (2/w)(\Gamma - \Gamma^2)$, w is the half-width of the phase transition, $\gamma = dh/dT = (1/\rho g)dP/dT$ is the slope of the curve of phase equilibrium, $Ra_R = (R/D)^3 Ra$, where $Ra = (\rho_0\alpha_0 g \Delta T D^3)/(\kappa_0\eta_0)$ is the Rayleigh number, $Rb_R = (R/D)^3 Rb$, where $Rb = (\delta\rho g D^3)/(\kappa_0\eta_0)$ is the phase Rayleigh number, $Di_R = (R/D)Di$, where $Di = \alpha_0 g D / C_p$ is the dissipative number, $H_R = (R/D)^2 H$, where H is thermometric density of heat sources, $\Delta T = T_{\text{cmb}} - T_s$, $T_s = 273 \text{ K}$ is the surface temperature.

3 The Parameters of the Earth's Mantle

The characteristic values of parameters of the Earth's mantle [12] are the following: $D = 2890 \text{ km}$, $M_m = 4.0 \cdot 10^{24} \text{ kg}$, $\rho_0 = 4.5 \cdot 10^3 \text{ kg m}^{-3}$, $c_p = 1.25 \cdot 10^3 \text{ J/(kg K)}$, $\eta_0 = 10^{21} \text{ Pa s}$, the mean value of the thermal diffusivity $\kappa_0 = 10^{-6} \text{ m}^2/\text{s}$, the coefficient of thermal expansion $\alpha_0 = 2 \cdot 10^{-5} \text{ K}^{-1}$, the temperature difference $\Delta T = 3700 \text{ K}$. As noted above, the effective internal heating of the mantle equals 24 TW, so the density of mantle heat sources will be $6 \cdot 10^{-12} \text{ W/kg}$.

At these values of parameters for the compressible mantle, the scaling factors for velocity and time will be $\kappa_0/D = 1.1 \cdot 10^{-3} \text{ cm/yr.}$, $D^2/\kappa_0 = 2.6 \cdot 10^{11} \text{ y}$, and for the density of radioactive heat sources will be $0.55 \cdot 10^{-12} \text{ W/kg}$. The dimensionless parameters included in the convection equations are $Ra = 4.5 \cdot 10^7$, $Di = \alpha_0 D g / c_p = 0.45$, $H = H_{r+cool} = 11$.

The parameters of the mantle, the viscosity η , the thermal expansion coefficients α and the thermal diffusivity κ , included in the convection equations in the form of coefficients should be set as functions of depth and temperature.

The dependences of the dimensional coefficient of thermal expansion α and thermal conductivity k (as well as the thermal diffusivity κ) on the dimensionless depth $x = 1-z$ given in [15], can be approximated as (see Fig. 2).

$$\begin{aligned} \alpha &= 42 \cdot 10^{-5} (2.3 + x)^{-3} \text{ K}^{-1}, & k &= 3 \cdot [1 + 3.3x] \text{ W/mK}, \\ \kappa &= k / (\rho c_p) = 1.8 \cdot [1 + 3.3x] 10^{-6} \text{ m}^2 \text{ c}^{-1}. \end{aligned} \quad (6)$$

The most important parameter of the mantle is its viscosity. Viscosity is determined by the competition of diffusion and dislocation creep processes in the mantle and brittle plastic deformation in the lithosphere. Parameters included in the dependence of viscosity on temperature and pressure are found according to laboratory measurements and extrapolated to the mantle conditions. Such extrapolation leads

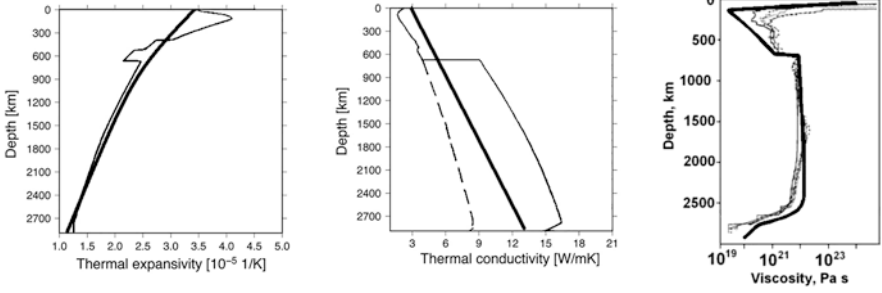


Fig. 2 Depth dependence for the coefficient of thermal expansion α and thermal conductivity k with two variants for the lower mantle [15]. Their simplified dependences approximated as (6) are shown by thick lines. The right panel shows the depth distribution of viscosity obtained from post-glacial rebound data [17], and the distribution calculated according to (1–6) (thick line)

to very high viscosity for lower mantle. Therefore, in this paper, we use the effective dependence of viscosity on temperature and pressure [16]. It was chosen as a common formula for diffusion creep with effective parameters which were selected from the condition of optimal agreement with the data of laboratory measurements and the results of solving the inverse problem for post-glacial uplifts [17].

$$\eta(p, T) = A \exp\left[\frac{(E_0 + pV_0)}{(T + T_s)}\right], \quad (7)$$

where E_0 is the activation energy, and V_0 is the volume of activation.

The activation energy value for the entire mantle is taken from the data for olivine $E_0 = 350$ kJ/mol. The piecewise constant coefficient A for the lower mantle was found from the condition of normalization to the viscosity $\eta(p, T) = A = 3 \cdot 10^{21}$ Pa s at a depth of 700 km. The coefficient A for the upper mantle was found from the condition of viscosity jump by the factor 30 on the phase boundary 660 km. The value of the activation volume for the upper mantle $V_0 = 4$ cm³/mol was taken according to the measurements for olivine, and the corresponding value for the lower mantle was taken two times smaller, $V_0 = 2$ cm³/mol.

To obtain the spatial distribution of viscosity in the mantle $\eta(x, y, z)$, we need to substitute the pressure and temperature of the mantle as a function of coordinates in the expression (7). Since the pressure can be considered hydrostatic, the dependence on the radius r will have the form $p = \rho_0 g(D - r)$. The temperature distribution in the mantle is not known in advance and can be founded only after solving the equations of convection (1–4) with the equation for viscosity $\eta(p, T)$ in the form (7).

Figure 2 (right) shows the calculated laterally averaged depth viscosity distribution along with the viscosity distribution obtained from of the post-glacial uplift data [17].

The dependence (7) describes only the Newtonian viscosity η_d for diffusion creep, which occurs in the lower mantle. In the upper mantle at depths of less than 200 km, the material can also flow through the dislocation creep mechanism, in

which the viscosity also depends on the strain rates in the form of a power function. The calculation of convection at the top of the upper mantle in an area where viscosity is determined by dislocation creep and has large variations requires considerable computing time. Therefore, the dislocation viscosity is often neglected, and the viscosity dependence (7) is considered as effective.

In the lithosphere at depths of less than 20 km and at temperatures below 600 K, the diffusion viscosity η_d (7), as well as the dislocation viscosity, are very high. However, in very slow processes brittle-plastic flow takes place with effective viscosity.

$$\eta_y = \tau_y / 2\varepsilon, \tau_y = \tau_0 + \mu P, \eta_y > \eta_{\max} \quad (8)$$

where $P = \rho gz$ is the lithostatic pressure, C_0 is the cohesive strength, μ is the friction coefficient, ρ is the density, z is the depth. For the mantle the parameters C_0 and μ depend little on the kind of material and have values of the order $C_0 \approx 10$ MPa and $\mu = 0.7$ [18].

The distribution of the effective viscosity in the entire mantle, taking into account the processes of high-temperature diffusion and brittle microfractures, under the condition of the additivity of the strain rates $\varepsilon = \varepsilon_d + \varepsilon_y$ can be described by a single formula.

$$\eta = 1 / (1 / \eta_d + 1 / \eta_y). \quad (9)$$

With rise of pressure and temperature the mantle material undergoes the phase transformations with jumps in density. The main ones are the olivine-wadsleyite transition at a depth of 420 km, with the slope of the curve of phase equilibrium $\gamma_{410} = 3$ Pa/K (Clapeyron slope) and the density jump $\delta\rho_{410} = 0.96\rho$, the ringwoodite-perovskite transition at a depth of 660 km with the Clapeyron slope $\gamma_{660} = -2.5$ Pa/K and the density jump $\delta\rho_{660} = 0.08\rho$, and the perovskite-postperovskite transition at a depth of 2750 km with the Clapeyron slope $\gamma_{2750} = 13$ Pa/K and the density jump $\delta\rho_{2750} = 0.015\rho$. With a positive slope γ a phase transition slightly accelerates convection, and with a negative slope γ it slows down convection.

4 Numerical Models of Vigorous Thermal Convection in the Regime of Pulsating Mantle Plumes

The structure of thermal convection depends fundamentally on its vigor, which in turn is determined by the values of the parameters of the mantle material and the conditions of its heating. With the parameters corresponding to the material and conditions in the modern Earth's mantle mentioned above, the Rayleigh number Ra characterizing the convection vigor is approximately 10^7 . With its secular evolution, the Earth cools down. Since the viscosity depends exponentially on the temperature,

the Rayleigh number for the mantle of the early Earth was probably an order of magnitude greater, and for the future Earth it will be several orders of magnitude smaller.

The character of mantle convective flows is usually considered in models that do not take into account the lithosphere. The viscosity in the upper cold lithospheric layer is also described by the effective viscosity, replacing in (7) the surface temperature T_s by its average mantle value [19]. Figure 3 shows the calculated structure of convection for Rayleigh numbers equal to 10^5 and 10^6 . Such Rayleigh numbers correspond to the future colder Earth, which has an average viscosity about 100 and 10 times greater than the present one. At $Ra = 10^5$ thermal convection with the viscosity depending on pressure and temperature (7) still remains almost stationary with regular cells.

With increasing Rayleigh number, ascending and descending convective flows become narrower. At $Ra = 10^6$ convection becomes unsteady and its structure begins to rearrange in shape and the number of flows. New ascending flows emerging at the bottom of the mantle gradually take a mushroom shape with a head and a tail and are called plumes. When plumes reach and breakthrough the surface they create large igneous provinces on continents and basalt plateaus at the bottom of the oceans.

The hot stream of a plume tail continues to rise and burns the moving lithosphere. At $Ra = 10^6$ the hot material of a plume tail rises uninterruptedly. So in this model a continuous ridge of volcanoes would appear on the surface of the moving lithospheric plate. It is shown [20] that life time of each plume is several hundred million years. The plumes die by pairwise association.

Figure 4 shows the calculated convection structure at higher vigor for Rayleigh numbers $Ra = 10^7$ and $Ra = 10^8$. Such Rayleigh numbers can correspond to the modern and early hotter Earth.

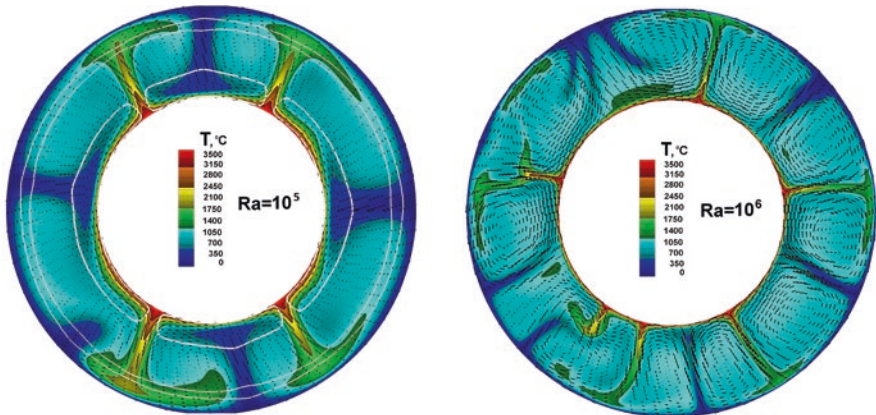


Fig. 3 Calculated thermal structure in a mantle with variable viscosity at low convective vigor for the cooling future Earth. The temperature is shown in gray scale; the flow velocities are shown by arrows. The deformed phase boundaries at depths 420 km, 660 km and 2750 km are shown with white lines

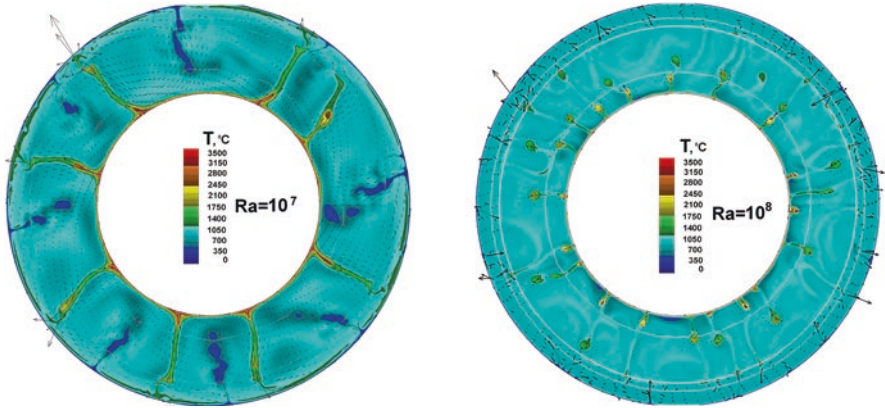


Fig. 4 Calculated thermal structure in a mantle with variable viscosity at high convective vigor for the modern and early hotter Earth. The temperature is shown in gray scale, the flow velocities are shown by arrows

As seen in Fig. 4, at $Ra = 10^7$ the mantle plumes become unstable. The heads of plumes are more pronounced, and most importantly, inside the plume tails, the hot material from the bottom of the mantle begins to rise not continuously, but in separate portions. Therefore, thermal mantle plumes should generate on the surface of a moving plate not a continuous ridge of volcanoes, but a chain of individual volcanoes. At the bottom of the ocean, each portion of hot material of thermal plumes generates a separate large island. This phenomenon for mantle plumes can be called pulsations. It should be noted that in the literature, the pulsations of plumes are often called not the pulsating rise of hot material in the tile of each individual plume, but a simple periodic disappearance and birth of new plumes.

The physical meaning of such pulsation of mantle plumes can be understood by comparing the structure of thermal convection at the Rayleigh number $Ra = 10^7$ and at even greater vigor. As seen in Fig. 4, at $Ra = 10^8$, the tails of the mantle plumes are broken, and a conveyor of rising portions of the hot material along the direction of the former plume is formed. Thus, it is necessary to distinct the modes of thermal convection with quasi-stationary plumes, with pulsating plume tails and with conveyors of rising portions of the hot material called thermals. Convection calculations at even higher Rayleigh numbers show that the ascending portions of hot material (thermals) become increasingly independent, and convection goes into a turbulent regime.

The above model of convection without taking into account the lithosphere can explain only the main dominant period of eruption in hot spots of the order of 10 million years. However, the intervals between volcanic eruptions in hot spots constitute a large spectrum (for example, the Hawaiian chain in the Pacific or a chain of volcanoes ending with a Yellowstone volcano). The whole range of hot spot chain eruptions is explained by the fact that the hot material supplied by the plume first accumulates under a moving lithospheric plate in the form of a sublithospheric hot

anomaly. In this hot anomaly, small-scale convection occurs during partial melting of the material. As a result, magma breaks from this anomaly to the surface occur periodically, forming chains of volcanoes [21].

5 Models of Thermal Convection that Include Plates

The process of splitting the Earth's lithosphere into separate plates was understood and began to be modeled after it was found that, with slow processes, shear stresses generate microcracks that can be healed in dynamic equilibrium. As a result, the process of long-term shear deformation can be mathematically written as a flow with effective viscosity depending not only on temperature and pressure, but also on shear stress [12]. In last decade, the problem of plate tectonics has been principally solved and the models show how plates can naturally and self-consistently form during thermal convection in a viscous fluid with the properties of the Earth's mantle [22].

Numerical experiments make it possible to show how the lithosphere is divided into separate rigid plates, see for example [18]. A heated fluid layer with temperature and pressure dependent diffusion viscosity that corresponds to silicate material of the mantle was considered. By the formula (7) the viscosity of the upper colder layer turns out very high, about 10^{26} Ps. As a result, a continuous layer of the lithosphere occurs at the surface of the mantle, and mantle convection occurs only under the lithosphere. Next, effective plasticity of the real Earth's material (allowing for microcracks and water content) was taken into account, when the viscosity depends not only on temperature and pressure, but also on stresses. This leads to the fact that in area of maximal shear stress the concentration of microcracks increase, and the effective viscosity drops sharply. The greatest stresses at convection arise over the descending convective flows. As a result, the rigid lithosphere is divided into separate rigid plates. These plates immerse to the mantle in the subduction zones, and a new material comes instead from the mantle to the surface in the mid-ocean ridges. Then it moves horizontally and cools. Accordingly, the plates thicken as they move away from the ridges. The simulation automatically reproduces the whole process.

Figure 5 shows that the horizontal velocities of all points inside each plate are identical and change abruptly at the joints of the plates in the ridges and subduction zones. Each plate moves at its own speed, thickens as it moves away from the ridge and sinks into the mantle in subduction zones. At the 660 km phase boundary the plates are bent and partially torn. The calculated fields of temperatures, viscosity, convective velocities, plate velocities and ocean floor relief with deep depressions in subduction zones and mid-ocean ridges correspond to the observed manifestations of lithospheric plate tectonics on the Earth.

Figure 6 shows the evolution of oceanic lithospheric plates. Plates participate in the convective circulation of the mantle material and immerse to the mantle in sub-

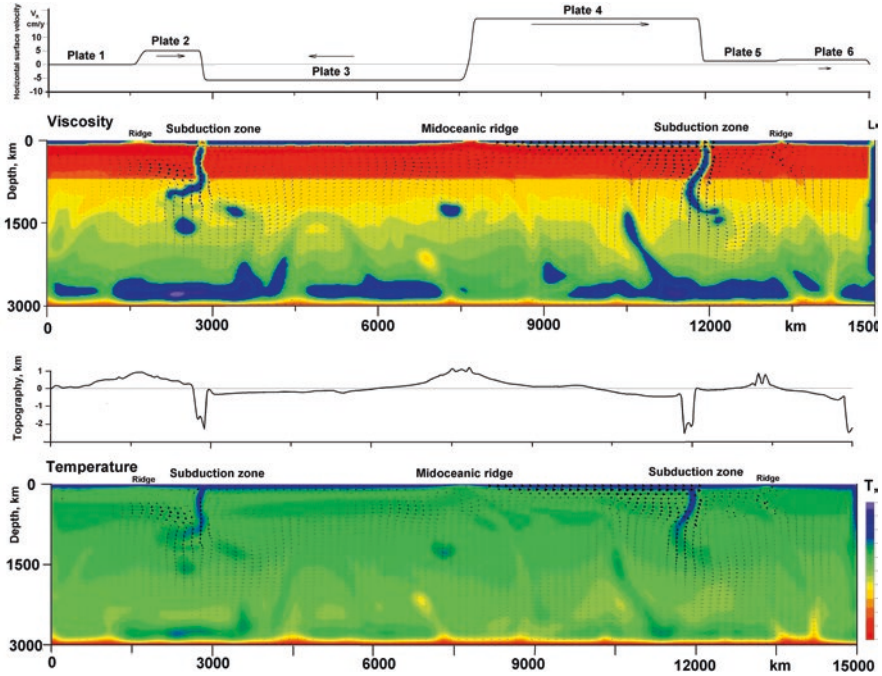


Fig. 5 The numerical model of convection in a heated layer with a viscoplastic rheology corresponding to the material of the Earth's mantle. The viscosity distribution is shown by the color scale (on the right). Flow velocities are indicated by arrows with a maximum value of 15 cm/year. Above are the distribution of the horizontal velocities of the resulting plates and the calculated relief of the ocean floor

duction zones. The ringwood-perovskite phase transition at a depth of 660 km slows down plates. They bend and partially break. The configurations of submerged plates near the 660 km boundary for different sites observed by tomography data can correspond to different stages of the calculated evolution of convection [22].

Despite the fact that the problem of splitting into separate plates has now been solved in principle, and this process can be reproduced in mathematical models, there are still problems of a more detailed study of the interaction of plates, in particular at the junctions of two oceanic plates in the subduction zone. According to observations, the subduction is usually one-sided, in which only one oceanic plate is submerged into the subduction zone. However, Fig. 5 shows that in the considered model of convection with a non-deformable upper boundary there is a two-sided subduction. Cramer et al. [26] showed that it is necessary to use more real boundary conditions. Under the oceans the lithosphere is covered with a layer of water. In this case, the upper boundary of the lithosphere can be deformed. Under such conditions, if one of the plates begins to bend and sink into the mantle at the junction, it will be below the other plate. As a result, only one of the plates begins to sink into the mantle, and the subduction becomes one-sided.

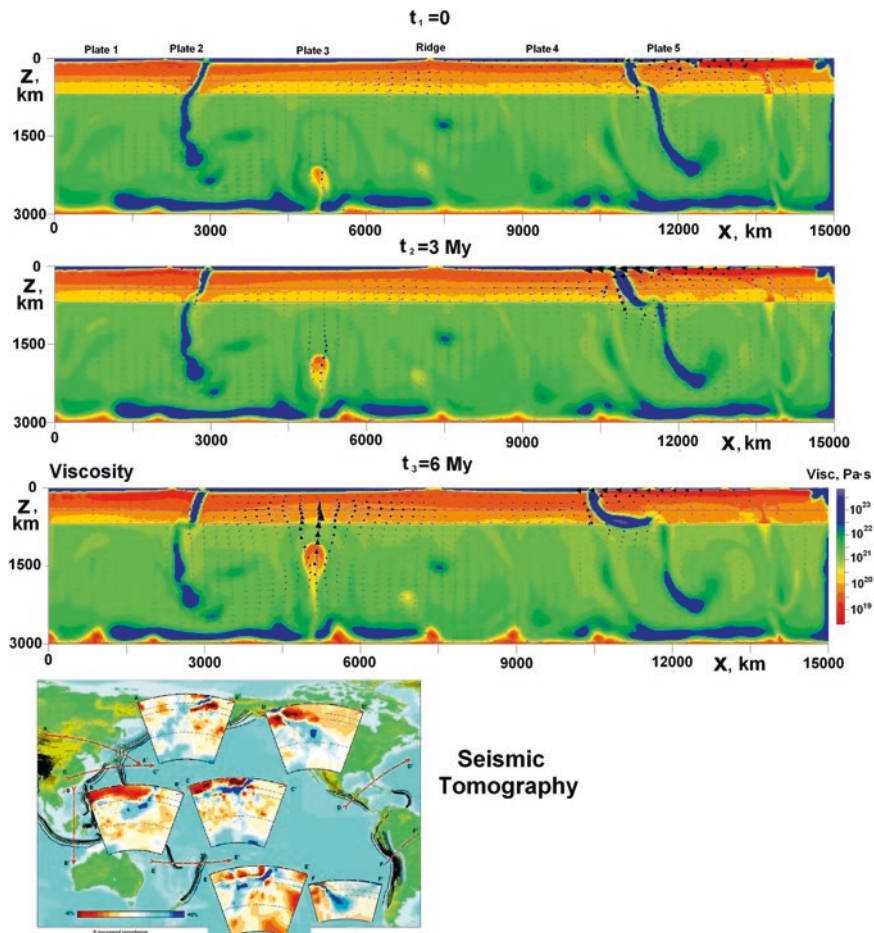


Fig. 6 The calculated evolution of configurations of submerged plates over time, with an interval of 3 my. Below, for comparison, the tomography data are shown [23–25], where low seismic velocities correspond to cold plates (blue)

To complement the theory of lithospheric plate tectonics, it is necessary to construct three-dimensional spherical convection models that take into account the self-consistent interaction of many plates.

6 Mantle Convection with Floating Continents

The oceans cover only about three-quarters of the Earth’s surface are separated by continents that can drift on a viscous mantle and change the configuration of the oceans. Numerical simulations of tectonics of floating continents were studied intensively in IFZ RAS in the 2000s, e.g [27–29]. To describe the interaction of convective flows with continents and to identify the characteristic features of continental drift, we solved a system of convection equations in a fluid along with Euler’s equations of motion of solids.

A numerical experiment makes it possible to understand the basic physical processes manifested in the interaction of convective flows with floating continents [28]. A layer of viscous heated fluid was considered, on which two continents in the form of light rigid plates were superimposed (see Fig. 7). Thermal convection occurs in the fluid with several convective cells. Convective currents drive the superimposed plates. Since the plates inhibit heat removal from the mantle, they change

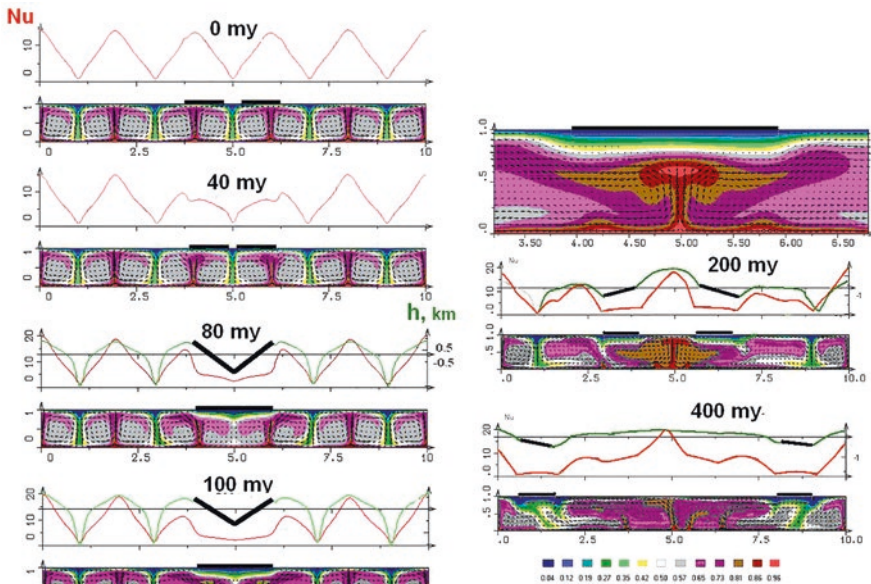


Fig. 7 Calculated evolution of thermal convection in a fluid layer with two floating plates (black color). The dimensionless temperature is indicated by the color scale. The red line is the dimensionless heat flux Nu , green line is the elevation h in km. The time is in million years

the temperature distribution in the mantle and cause changes in the entire structure of the mantle flows. The plates (continents) first combine over a downward convective flow and assemble into a supercontinent. Due to thermal blanket effect the mantle under the supercontinent gradually heats up, the supercontinent rises and breaks up. The entire cycle takes about 0.5 billion years.

The results of this numerical experiment on the simplest model confirm and illustrate the laws of continental drift discovered by A. Wegener and then developed by T. Wilson and reveal a number of new details.

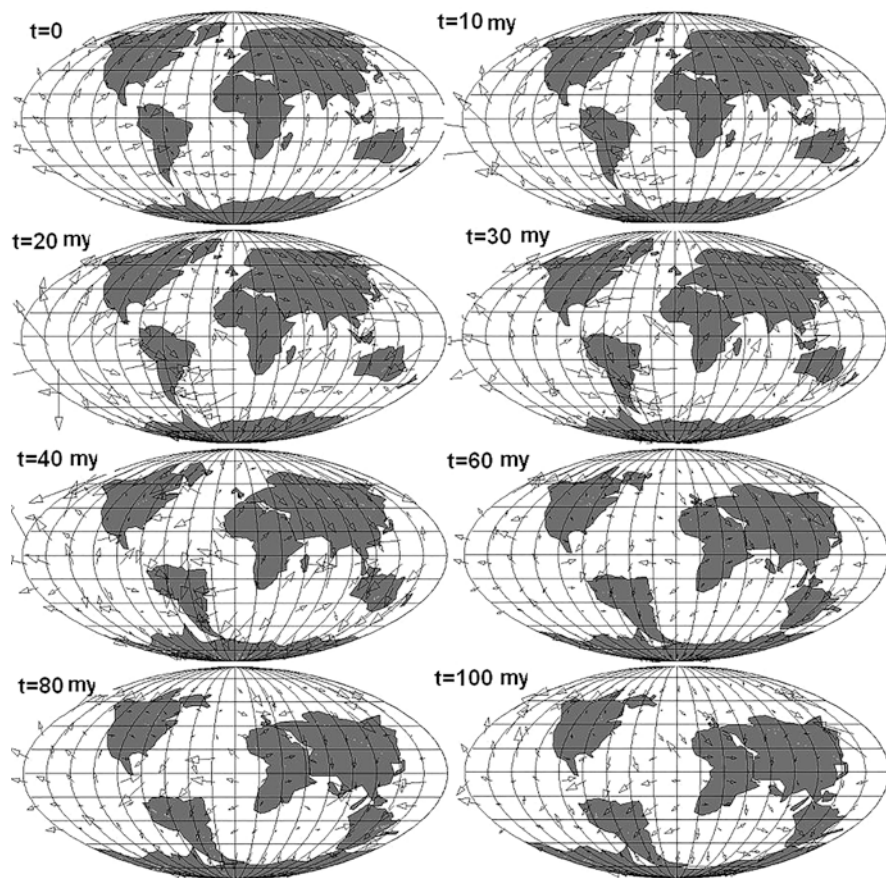


Fig. 8 A numerical model of the future of the continental drift. The time is shown in million years, the maximum length of the arrow corresponds to the speed of 12 cm/year. The contours show the calculated positions of continents and islands, and the arrows show the velocity of mantle flows in successive time intervals into the future for 100 my. According to the model, America will move to Antarctica, and Eurasia, Australia and Africa will assemble into a supercontinent

To simulate the future drift of continents, a spherical convection model was considered, which was as close as possible to the modern mantle [29]. Seismic tomography gives the spatial distribution of seismic wave velocities in the mantle. It is known how these velocities depend on temperature. The spatial distribution of temperature in the real modern Earth was found by recalculation. This temperature distribution was taken as the initial state. So in this case we deal with the convective model that corresponds to the real modern Earth. Six heat-conducting rigid floating plates were superimposed on the fluid surface, corresponding by form to modern continents, with eight smaller plates, corresponding by form to large islands, taken from geographical maps (see Fig. 8). Further, a nonlinear system of thermal convection equations was numerically solved together with a system of Euler equations for the movement and rotation of continents under the action of viscous coupling forces with mantle flows, taking into account the inverse thermal and mechanical influence of continents on convection. The cold zones of the initial mantle temperature field began to descent, and the hot ones began to rise. As a result, thermal convection developed in the mantle. Due to mechanical coupling the convective currents set in motion all the continents and islands. However, due to the thermal interaction, the continents constantly influence the temperature field in the mantle. Since the model is constructed taking into account mechanical and thermal interactions of the viscous mantle and solid continents and also the parameters of the material corresponding to the real modern Earth, it allowed to calculate the possible future drift of the continents.

This numerical model shows the evolution of mantle convection taking into account its real interaction with six continents and large islands. Already in the 2000s, there were opportunities to calculate models of thermal convection with floating continents. However, most researchers were engaged in the construction of the theory of tectonics of oceanic plates, since it was more relevant and it was clear that rigid plates can arise self-consistently within thermal convection with viscoplastic rheology. Recently, interest in modeling the interaction of continents with convection has increased [30–32]. At the same time, the main attention is currently paid to the refinement of the properties of the mantle material and the initial temperature distribution, while modeling the shapes of continents as simple squares.

7 Global Thermo-Chemical Model of the Earth with Accumulation of Heavy Components at the Bottom of the Mantle

Important for understanding structure of the Earth and global geodynamics in the last decade was the discovery of giant piles of heavy material at the bottom of the mantle. According to seismic tomography, there are two anomalous regions at the

bottom of the mantle under Africa with an average height of up to 1500 km and under the South Pacific with a height of up to 1000 km. In these regions the shear seismic velocities are reduced by 2% to 3% [33].

These piles are called Large Low Shear Velocity Provinces (LLSVP). The pile under Africa is called Tuzo in honor of T. Wilson, and the pile under the Pacific is called Jason in honor of J. Morgan. It is assumed that previously the mantle primary material enriched with iron and containing He_3 descended to the bottom of the mantle. Hereafter the oceanic crust began to go down into the mantle together with plates. At depths of about 80 km the basalt crust turns into eclogite, which is heavier than the mantle material. This eclogite accumulated as a heavy layer at the bottom of the mantle. Mantle currents have raked this material into two large piles.

This process can be illustrated by a simplified model of thermo-compositional convection in a heated spherical region (spherical axisymmetric annulus) at the Rayleigh number $\text{Ra} = 2 \cdot 10^7$ [34]. The even layer of a chemically different material with an increased density of 3% was placed at the bottom of the mantle. The calculations have shown that in the absence of continents and oceanic plates the descending mantle flows deform the layer of heavy material, and it decomposes into several small evenly spaced clusters.

Then the continent (as a region with the increased viscosity by four orders of magnitude) was incorporated in the model. Accumulation of heat under the continent leads to the rebuilding of convection pattern, and a large pile arises at the bottom of the mantle. Further two plates moving in different directions were added to the model. They were simulated by the prescribed surface velocity. As a result, the second large pile arises at the mantle bottom. Figure 9 shows the steady-state structure of mantle flows and temperature distribution for this case. It also demonstrates that all the heavy material at the bottom of the mantle was grouped into two large piles. The location of these piles is in good agreement with the tomography data [33].

This arrangement of piles is explained by the fact that the descending mantle currents drag the heavy material to the bottom of the mantle in different directions under the fixed continent (Africa) and under the large oceanic plate (Pacific).

At high pressures the mantle material turns into the postperovskite phase. In the absence of convection, the phase boundary of the perovskite-postperovskite transition is at a depth of 2750 km. In convection, lateral variations of the depth of this boundary occur, and their value is proportional to the Clapeyron slope of the phase change. The slope for the perovskite-postperovskite transition is very large. Therefore, in hot regions the equilibrium pressure of the phase transition increases so much (above the pressure at the bottom of the mantle) that the phase boundary falls outside the mantle. As a result, the phase of postperovskite in the mantle is not in a layer lying below the border of 2750 km, but, similar to the piles of heavy material, is located in two areas at the bottom of the mantle, where cold downward flows come. Figure 9 delineates these areas by a white line. It is noteworthy that the postperovskite regions are located at the bottom of the mantle just between eclogite piles.

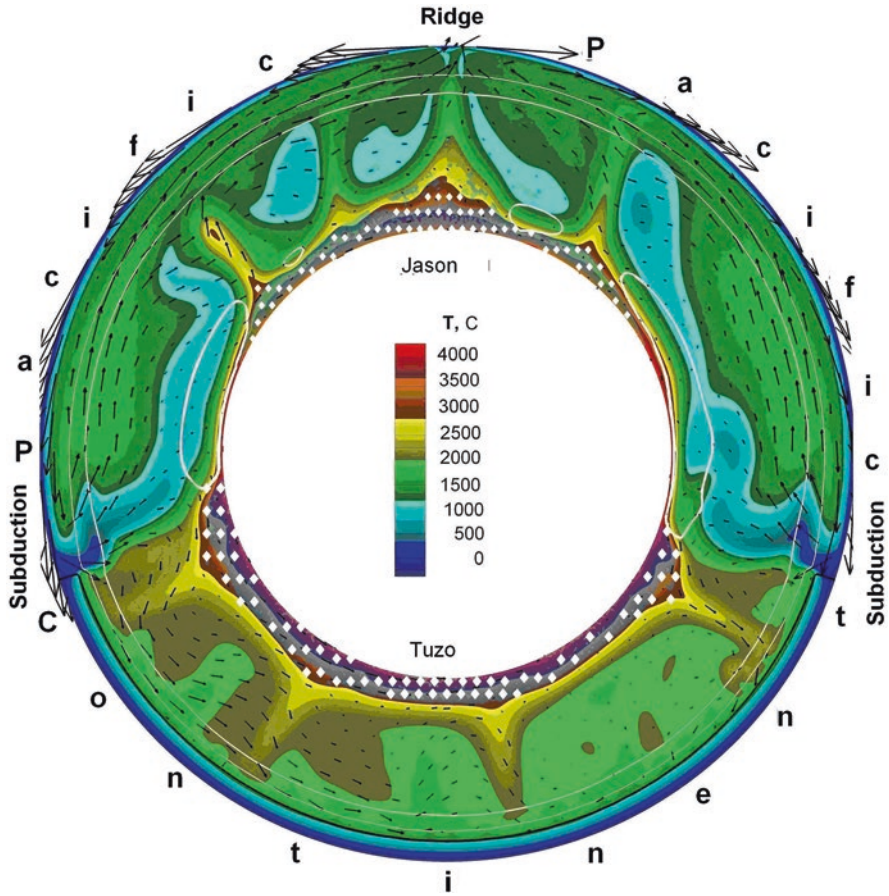


Fig. 9 Numerical model of thermal convection in the mantle taking into account the large fixed continent (Africa) and oceanic plates of the Pacific type. The temperature distribution is shown by color scale; the velocities of the mantle flows are shown by arrows. The diamonds indicate two piles under the Pacific (Tuzo) and under the Africa (Jason). White lines in the form of deformed circles show the phase boundaries at the average depths of 420 km and 660 km. The postperovskite phase is inside the lenses at the bottom of the mantle

As partially seen in Fig. 9 and as other more detailed models show, the mantle plumes of hot spots originate predominantly at the edges of heavy piles at the bottom of the mantle. Figure 9 also shows that the piles resting on the hot iron core are not only heavy, but also abnormally hot.

8 Conclusion

To date, the theory of global tectonics of the Earth is basically built. In its creation, the data of geophysical, geological and geochemical observations, data of laboratory studies of materials, as well as numerical modeling of heat and mass transfer processes were used.

Now it is clear why convection is possible in the mantle at a temperature below solidus, why cold “stone” plates with a thickness of more than 50 km can bend and not break when sink into the mantle. It turned out that this is due to the long duration of the processes in which diffusion has time to give the solids locally effective viscous properties.

On the long road to theory of Earth’s global tectonics there were periods of acceptance of erroneous hypotheses. For example, long time it was believed that convection in the mantle can be two-layer, and plumes rise independently of the thermal convection due to light chemical impurities.

The plumes are ascending convection jets that can occur both during thermal and thermochemical convection. At low vigor convection is laminar, at very large vigor it is turbulent, and in the intermediate case convection is in transition plume mode. The vigor of convection is determined by lateral variations in density, depending on the degree of heating and chemical impurities, as well as by the viscosity and thickness of the layer.

Deep mantle plumes cause catastrophic eruptions, and give rise to Large Igneous Provinces and hot spots on the Earth’s surface. By analogy with thermochemical subduction plumes, which arise due to chemical impurities, it was initially believed that the deep mantle plumes of hot spots also have a chemical nature. However, it turned out that they have a thermal nature. The high vigor of convection required for plumes is provided not by chemical impurities, but by a large temperature difference and low viscosity. These plumes originate at the boundary with a liquid, highly heat-conducting iron core, which constantly compensates for the removal of heat carried away by plumes from the place of their formation. Chemical impurities can only to change a little the properties of these plumes. Mantle plumes originate at the bottom of the mantle mainly at the edges of piles of heavy material, which is partially captured and reduces the buoyancy of plumes.

Due to the phase transition at a depth of 660 km, cold descending convective flows are inhibited, but convection remains a whole mantle one. The cold high-viscosity slabs descending to the bottom of the mantle (and somewhat the hot narrow plumes rising to the surface) set all the mantle material in circulation motion and interact with each other.

Figure 10 shows a schematic of the global thermochemical model of heat and mass transfer in a modern world.

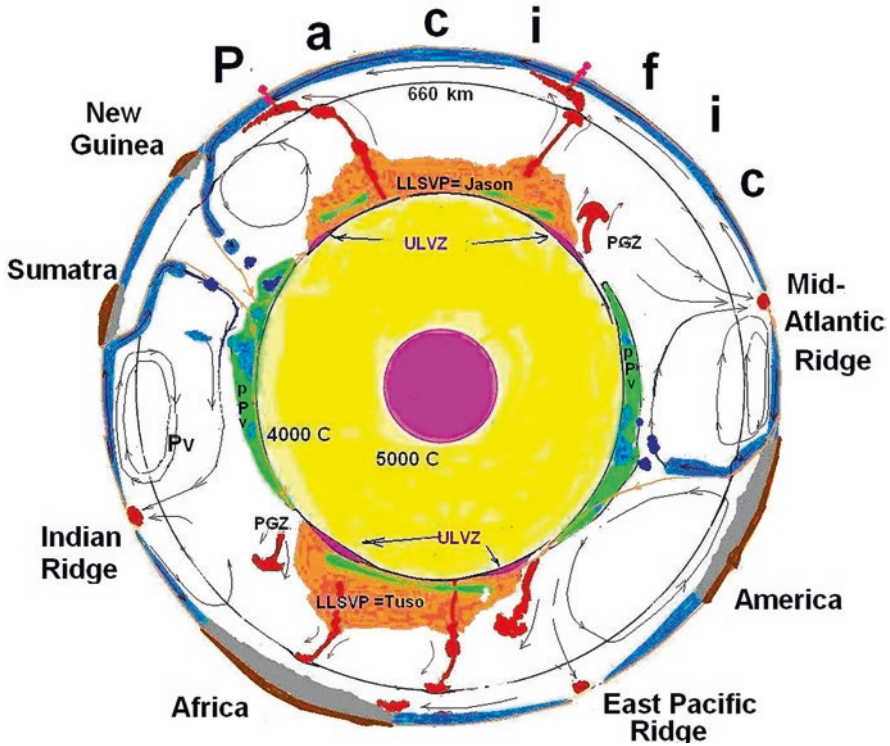


Fig. 10 Schematic thermochemical geodynamic model of the modern Earth in the equatorial section, supplemented by [35]. Continents are shown in dark brown, oceanic plates are in blue, the postperovskite (ppv) phase on the mantle bottom is in green, hot piles (Tuzo and Jason) are in brown, mantle plumes are in red, convective flows are lines with arrows, PGZ are zones of preferential plume generation, ULVZ are zones of ultra-low velocities, interpreted as zones with high iron content at a high degree of partial melting

This scheme of global thermochemical convection is still simplified. It shows the basic fundamental structures formed in the process of heat and mass transfer. The whole pattern of all currents is not yet known. In reality, due to convective mixing and separation, there are many geochemical reservoirs in the mantle. In this scheme, the formation of only the two most important ones is considered.

The construction of a complete three-dimensional picture of convective flows in the mantle, explaining the evolution of the distribution of chemical isotopes in the mantle, is the next problem of global geodynamics.

References

1. Jones CA (2007) Thermal and compositional convection in the outer core. In: Schubert G (ed) *Treatise on geophysics*, vol 8. Elsevier, Amsterdam, pp 133–181
2. Davies JH, Davies DR (2010) Earth's surface heat flux. *Solid Earth* 1:5–24. www.solid-earth.net/1/5/2010/
3. Dye ST (2012) Geoneutrinos and the radioactive power of the Earth. *Rev Geophys* 5(arXiv:1111.6099):0. <https://doi.org/10.1029/2012RG000400>
4. Rudnick RL, Gao S (2003) The composition of the continental crust. In: Holland H, Turekian KK (eds) *Treatise on geochemistry*, vol 3. Elsevier, Amsterdam, pp 1–64
5. Rudnick R, Fountain D (1995) Nature and composition of the continental crust: a lower crustal perspective. *Rev Geophys* 33:267–309
6. Jaupart C, Labrosse S, Mareschal JC (2007) Temperatures, heat and energy in the mantle of the Earth. In: Schubert G (ed) *Treatise on geophysics*, vol 7. Elsevier, Amsterdam, pp 253–303
7. Arevalo R Jr, McDonough WF, Luong M (2009) The K/U ratio of the silicate Earth: insights into mantle composition, structure and thermal evolution. *Earth Plan Sci Lett* 278:361–369
8. McDonough WF, Sun SS (1995) The composition of the Earth. *Chem Geol* 120:223–253
9. Berry AJ, Danyushevsky LV, O'Neill HC, Newville M, Sutton SR (2008) Oxidation state of iron in komatiitic melt inclusions indicates hot Archaean mantle. *Nature* 455:960–963
10. Leng W, Zhong S (2008) Controls on plume heat flux and plume excess temperature. *J Geophys Res* 113:B04408. <https://doi.org/10.1029/2007JB005155>
11. Zhang N, Zhong S (2011) Heat fluxes at the Earth's surface and core–mantle boundary since Pangea formation and their implications for the geomagnetic superchrons. *Earth Planet Sci Lett* 306:205–216
12. Schubert G, Turcotte DL, Olson P (2001) *Mantle convection in the Earth and planets*. Cambridge University Press, 940 pp
13. Trubitsyn VP, Trubitsyn AP (2015) Effects of compressibility in the mantle convection equations. *Izv Phys Solid Earth* 51:801–813. <https://doi.org/10.1134/s1069351315060129>
14. Yoshida M (2017) On approximations of the basic equations of terrestrial mantle convection used in published literature. *Phys Earth Planet Int* 268:11–17
15. Tosi N, Yuen DA (2011) Bent-shaped plumes and horizontal channel flow beneath the 660 km discontinuity. *Earth Planet Sci Lett* 312:348–359
16. Trubitsyn VP, Trubitsyn AP (2014) Numerical model for the generation of the ensemble of lithospheric plates and their penetration through the 660-km boundary. *Izv Phys Solid Earth* 50:853–864. <https://doi.org/10.1134/S106935131406010X>
17. Paulson A, Zhong S, Wahr J (2005) Modelling post-glacial rebound with lateral viscosity variations. *Geophys J Int* 163:357–371
18. Trubitsyn VP (2012) Rheology of the mantle and tectonics of the oceanic lithospheric plates. *Izv Phys Solid Earth* 48:467–485. <https://doi.org/10.1134/S1069351312060079>
19. Nakagawa T, Tackley PJ (2005) Deep mantle heat flow and thermal evolution of the Earth's core in thermochemical multiphase models of mantle convection. *Geochem Geophys Geosyst* 6:Q08003. <https://doi.org/10.1029/2005GC000967>
20. Trubitsyn VP, Evseev MN (2016) Pulsation of mantle plumes. *Russ J Earth Sci* 16:ES3005. <https://doi.org/10.2205/2016ES000569>
21. Ballmer MD, Ito G, van Hunen J, Ito G, Bianco TA, Tackley PJ (2009) Intraplate volcanism with complex age–distance patterns: a case for small-scale sublithospheric convection. *Geochem Geophys Geosyst* 10(6):1–22. <https://doi.org/10.1029/2009GC002386>
22. Bercovici D (2007) Mantle dynamics past, present, and future: an introduction and overview. In: Schubert G (ed) *Treatise on geophysics*, vol 7. Elsevier, Amsterdam, pp 1–22
23. Karason H, van der Hilst RD (2000) Constraints on mantle convection from seismic tomography. In: Richards MR, Gordon R, van der Hilst RD (eds) *The history and dynamics of global plate motion*, *Geophysical Monograph Series*, vol 121. American Geophysical Union, Washington, DC, pp 277–288

24. Albarede F, van der Hilst RD (2002) Zoned mantle convection. *Philos Trans Roy Soc London A* 360:2569–2592
25. Li C, van der Hilst RD, Engdahl ER, Burdick S (2008) A new global model for p wave speed variations in Earth's mantle. *Geochem Geophys Geosyst* 9(5):Q05018. <https://doi.org/10.1029/2007GC001806>
26. Cramer F, Tackley PJ, Meilick I, Gerya TV, Kaus BJP (2012) A free plate surface and weak oceanic crust produce single-sided subduction on Earth. *Geophys Res Lett* 39:L03306. <https://doi.org/10.1029/2011GL050046>
27. Trubitsyn VP (2000) Principles of the tectonics of floating continents. *Izv Phys Solid Earth* 36:708–741
28. Trubitsyn VP (2005) The tectonics of floating continents. *Herald Russ Acad Sci* 1:7–18
29. Trubitsyn VP (2008) Seismic tomography and continental drift. *Izv Phys Solid Earth* 44:857–872
30. Yoshida M (2010) Preliminary three-dimensional model of mantle convection with deformable, mobile continental lithosphere. *Earth Planet Sci Lett* 295:205–218
31. Yoshida M (2012) Dynamic role of the rheological contrast between cratonic and oceanic lithospheres in the longevity of cratonic lithosphere: a three dimensional numerical study. *Tectonophysics* 532(535):156–166
32. Yoshida M, Santosh M (2011) Supercontinents, mantle dynamics and plate tectonics: a perspective based on conceptual vs numerical models. *Earth Sci Rev* 105:1–24
33. Ritsema J, Deuss A, van Heijst HJ, Woodhouse JH (2011) S40RTS: a degree-40 shear-velocity model for the mantle from new Rayleigh wave dispersion, teleseismic traveltimes and normal-mode splitting function measurements. *Geophys J Int* 184:1223–1236
34. Evseev MN, Trubitsyn VP (2017) Pulsations and breaks of tails of thermal mantle plumes. *Dokl. Earth Sci* 476:1193–1194
35. Tronnes RG (2010) Structure, mineralogy and dynamics of the lowermost mantle. *Mineral Petrol* 99:243–261. <https://doi.org/10.1007/s00710-009-0068-z>

Thermo-Gravity Model for Sedimentary Basins



Valentina B. Svalova

1 Description of the Model

Numerous geological structures are characterized by rather gentle occurrence of layers and significant elevation of horizontal regional scale L over the vertical scale h of the typical thickness [2, 5, 12–14]. This allows to introduce a small parameter h/L into the analysis of the problem. The second small parameter of the problem F/R , F – the Frude number, R – the Reynolds number, arises while analysing the rheological behaviour of matter in the layers.

Slow lithospheric deformation will be simulated by models of viscous flow in a multilayered, incompressible, high viscosity Newtonian fluid, using the Navier-Stocks equations [7–11, 15].

Let us consider the rheological behaviour of a multilayered continuous medium, whose parameters (viscosity, density and thermal conductivity) vary from layer to layer. The movement in each layer is defined by the Navier-Stocks equation and the equation of continuity.

By expanding the velocities U , V , W , pressure P and boundary equation in series of powers of small parameter we can obtain the equations of layers boundaries in the zero approximation depending on the boundary morphology of the layers foot and its velocity field [7–10, 15].

Let us consider the evolution of the geological structures related to the approach of the mantle diapir to the layers lower boundary. In this case from the analysis of the obtained relationships, we may infer existence of a critical depth of the asthenosphere uplift defining the morphology of the basement surface [7–11, 15].

If the diapir is not deep or the velocity of diapir rise is large, then day surface is convex and reflects the morphology of the diapir.

V. B. Svalova (✉)
IEG RAS, Moscow, Russia

If the diapir is deep and upwelling is slow a depression is formed at the Earth's surface. And it is possible that stretching in layers is not large.

In case of restriction existing for the lateral extension above the ascending diapir it follows from the detailed analysis of the boundary morphology that there exist two critical depths of the mantle diapir that control the reconstruction of the movements above it. When the lithosphere is thin the boundary is convex at the center, i.e. it repeats the diapir morphology, while its marginal parts are concave which is caused by the convergence of lateral boundaries. For thick lithosphere the centre of structure is downwarped while its marginal parts are uplifted. This regime is conceivably responsible for the sedimentary basin formation. An intermediate regime is characterized by surficial movement reconstruction [7–11, 15]).

The surface elevation above the diapir depends on its velocity and depth. The regional geodynamics is controlled by the rheology of layers and depends on whether the layers have time for diffuence above the mantle or the velocity of the uprise prevails over the diffuence. This analysis of the dynamics of a layered lithosphere above a rising mantle diapir shows that if the diapir is deep and its velocity is low, a depression is formed on the Earth surface. If the velocity of rising diapir is high or the diapir is not deep a surface bulge can be formed. The comparison of the theoretical sections with geological reconstruction for Alpine belt sedimentary basins shows good conformity [7–11, 15].

It is possible to connect all stages of evolution of the Pre-Caspian Depression with upwelling of mantle diapir [6].

The Pre-Caspian Depression is a unique structure of ancient platforms with sedimentary cover near 24 km. The existence of mantle diapir could be confirmed by geophysical data, that fix two gravity maximum (Hobdinsky and Aralsorsky), the complex of higher electroconductivity at the depth of 70–100 km and higher deep heat flow in the center of structure.

The morphology of basement and Moho is characteristic for upwelling movements from deep mantle (Fig. 1, [4]), (Fig. 2, [1]).

The upwelling of mantle diapir in early riphej could be the reason of triangle rift in basement – Pachelmsky, Novoalekseevsky and Sappinsky – on the stage of swell formation. The stage of deep syncline formation in Pre-Caspian Depression is connected with regime of slow upwelling. More detailed information about sedimentary cover structure gives possibility to reconstruct more complicated picture of the structure evolution.

2 Geothermics of Sedimentary Basins

In the history of the Earth's evolution we have rather quick episodes (3–4 MY) of development of the geological structures and long periods (30–40 MY) of stable development. For short space of time in this sense the velocities of matter found from mechanical equations are substituted to the heat conductivity equation. Temperature and heat flow are continuous at the boundaries, $T = 0$ °C at the day

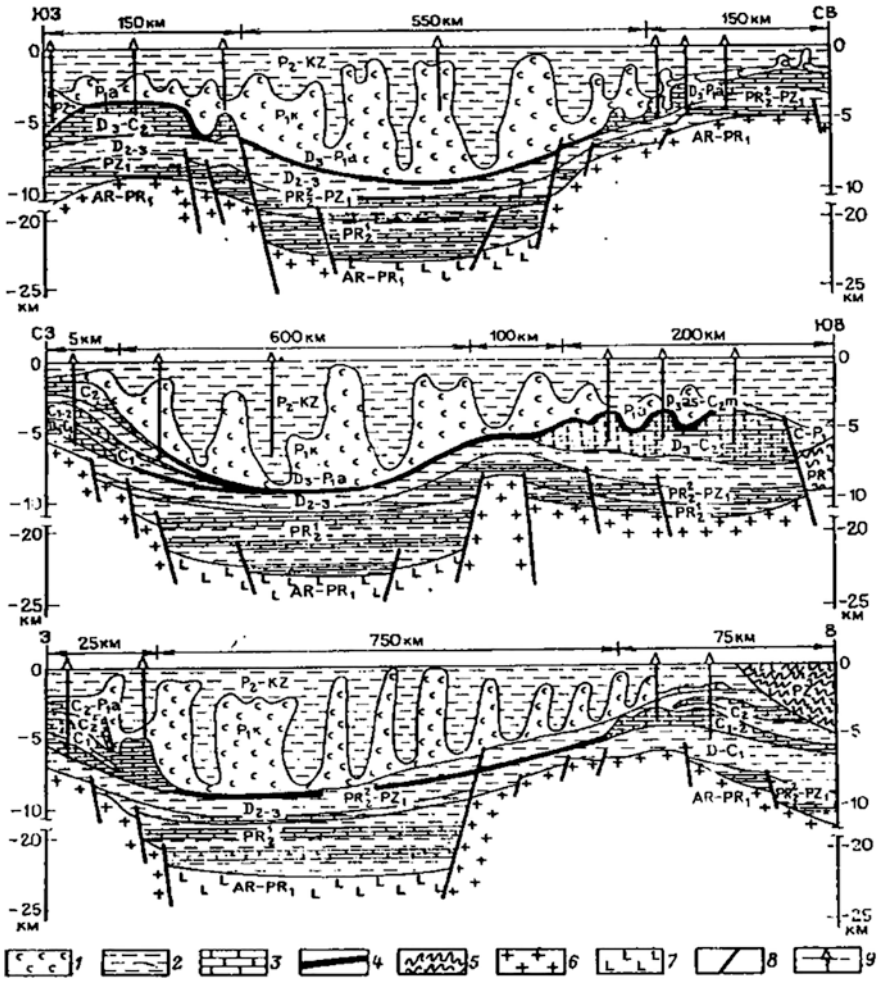


Fig. 1 Geological section of the Pre-Caspian Depression
 rocks: 1 – salts, 2 – terrigenous, 3 – carbonates, 4 – clays, 5 – condensated, complexes: 6 – granitic, 7 – basalts; 8 – faults, 9 – deep boreholes

surface, $T = 1200\text{ }^{\circ}\text{C}$ at the lithosphere – asthenosphere boundary. Analysis of results shows that surface grad T depends on the history of evolution and thickness of sedimentary cover [7–11, 15].

The temperature of basement surface depends on thickness of sedimentary cover and it is not isotherm. The analysis shows that for deep sedimentary basins the shape of possible oil-gas generation zones is concave in upper part of the basin and it is convex in deep part if deposits exist. In deep basins the possible zones of oil-gas generation are situated in peritherical parts of structure. In nondeep basins the deposits zones are formed in central part, that gives good agreement with geological

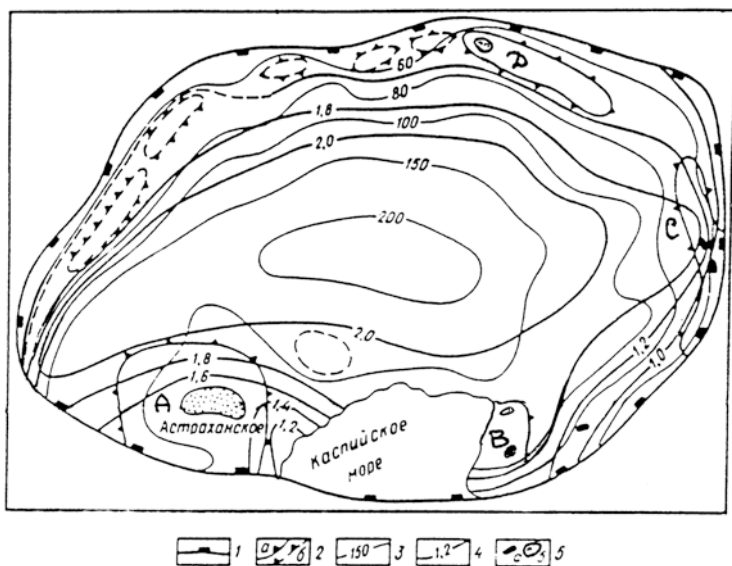


Fig. 2 Scheme of the thermal-pressure conditions of subsalt deposits of the Pre-Caspian Depression

Boundaries: 1 – of the Pre-Caspian oil-gas potential province, 2 – of the oil-gas potential zones (a – known, b – forecasted); 3 – the geoisotherms on the subsalt deposits surface, C; 4 – the isolines of anomalous layer pressure coefficients; 5 – oil /a/ and gas /b/ deposits. Main oil-gas deposits: A – Astrahan, B – Tengiz, C – Kenkijak, D – Karachaganak.

data. During the basin evolution the deposits zones arise in the central part, spread to the boundaries, destroy in the centre and stay in peripheral parts of the basin only. It could be a case of Pre-Caspian Depression [7–11, 15].

Convective movements help to temperature changing in the lithosphere. Sinking of the matter above the rising diapir on the stage of the deep depression formation can explain the low surface heat flow in Black sea and South Caspian Depression at the same time with high thickness of sedimentary cover.

Let us analyse some features of the geothermal field of the Pre-Caspian Depression. The regional geothermal background is normal. Heat-flow density increases from North to south and from East to West. Surface heat flow is 25–33 mW/m² in the North-East part and 50 mW/m² near the Caspian sea (Fig. 3, [3, 16]), Table 1.

Reconstruction of paleotemperatures by vitrinite reflectance for Eastern part of depression shows that the temperatures was 110–125 °C at the depth of 3.7–4.5 km, that is 40–50 °C higher than modern temperatures.

For the analysis of the geothermal field changings let us consider temperature distribution for stable stage of evolution.

Analysis of results shows that the smaller lithosphere thickness the larger surface heat flow. Maximum surface heat flow will be in the centre of depression above the mantle diapir. The geothermal data confirm it very well. Increase of sedimentary

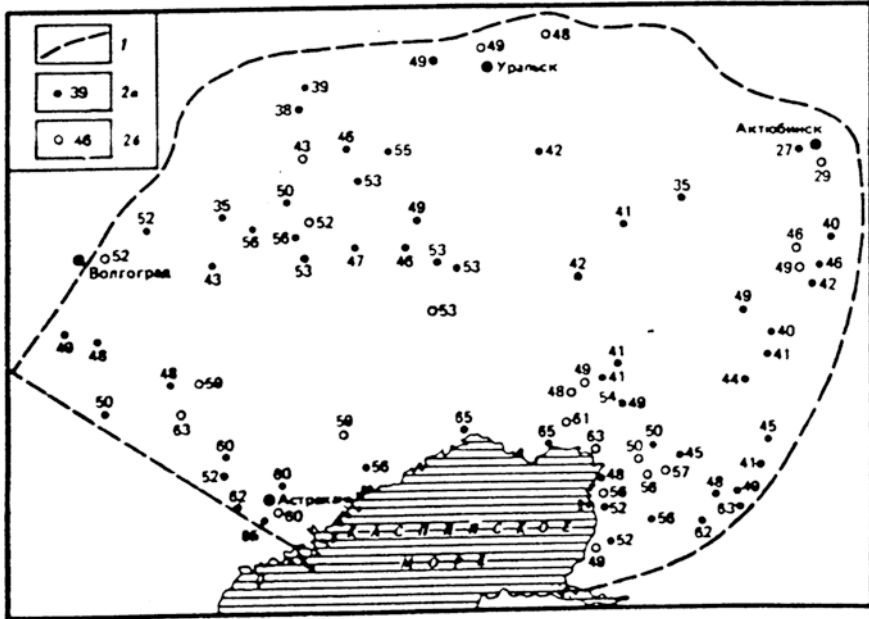


Fig. 3 Heat flow for the Pre-Caspian Depression, mW/m²
 1 – boundaries of the Pre-Caspian Depression, 2 – points of heat flow determination:
 a – separate, b – groups

Table 1 The main geothermal zones of the Pre-Caspian Depression

ZONE (Fig. 2)	T oC 5 km depth	∇ T °C /100 m
KENKIYAK	76–90	1,7–2,0
CASPIAN	162–186	2,8–3,1
TENGIZ	160–167	2,8–3,2
ASTRAHAN	124–156	3,0–3,6

cover thickness h influences on decrease of surface heat flow q very much. It explains again the low heat flow of Black sea and South Caspian Depression.

Every new stage of the diapir upwelling is characterized by smaller lithosphere thickness, but larger sedimentary cover thickness. It means that temperatures of oil-gas generation are achieved on smaller depth. The migration of oil window up the section takes place with any new episode of sink and sedimentation. New layers of sedimentary cover are involved to the process of oil-gas generation [7–11, 15].

Very important factor of temperature calculating for many sedimentary basins is the existence of salt layer. Investigation of subsalt complex for Pre-Caspian Depression is especially important as for gigantic oil and gas deposits there.

Let us consider three-layer sedimentary cover consisting of above-salt complex, salt complex and sub-salt complex with basement temperature $T(X, Y, t)$. Then we

Table 2 Temperature distribution for 500–1000 m depths in salt domes structures for eastern and western parts of the Pre-Caspian Depression

Depth, m	East T °C	West T °C
500	21.2–31.9	23.4–28.4
750	27.0–42.1	37.3–43.0
1000	31.5–52.4	51.4–56.0

can find the relationships between grad T in layers. Larger grad T will be in above-salt layer and sub-salt layer. There is low grad T in salt layer. Hence higher temperatures are achieved on smaller depth in above-salt layer when salt layer exists. It means that in such basins the main phase of oil generation is on smaller depth. And in sub-salt layer the temperature decreases quicker up the section, that preserves the deposits in upper part of sub-salt complex. Hence the salt layer is the important positive factor of oil and gas generation and preservation zones.

The salt diapirs change the surface heat flow in lateral. If the salt layer has thickening up the section then the heat flow increases above the diapir. And heat flow increases in sub-salt layer under the salt diapir too. Hence the salt diapirs are the local positive factors for deposits formation.

If at any stage of basin evolution the heat generation begins in the layer due to exogenic chemical reaction, for example, it changes the temperatures in the sedimentary cover. Let there is the heat generation in the middle layer and there is no heat generation in layers above and below. The analysis shows that existing of the layer with heat generation increases the heat flow above the layer and decreases the heat flow under the layer. Temperature changing in the layer has the parabolic character.

Hence the local increase of the surface heat flow is possible as due to layer of higher heat conductivity as due to heat generation in the layer. But influence of these two factors on underlying layers will be different.

Salt domes and powerful salt complex complicate the regional picture of temperature distribution especially in south-eastern part of the Depression, where salt layer is not deep (100–500 m). Above salt diapir the temperature is 3–5 °C higher than in moulds on the same depth. For deeper horizons there are geothermal “depressions” in the salt diapirs as compared with surrounding terrigenous complexes. Changing of temperature for 500–1000 m depth is 10–21 °C. In western part of Depression the salt domes are deeper (1500–2000 m) and their influence is smaller, Table 2 [3, 16]. All these data are well explained by geothermal modelling.

3 Thermo-Gravimetric Model for the Lithosphere Thickness Definition

Let us consider the heat transfer equation for multilayered medium of the Pre-Caspian Depression and East European Platform lithosphere (Fig. 4):

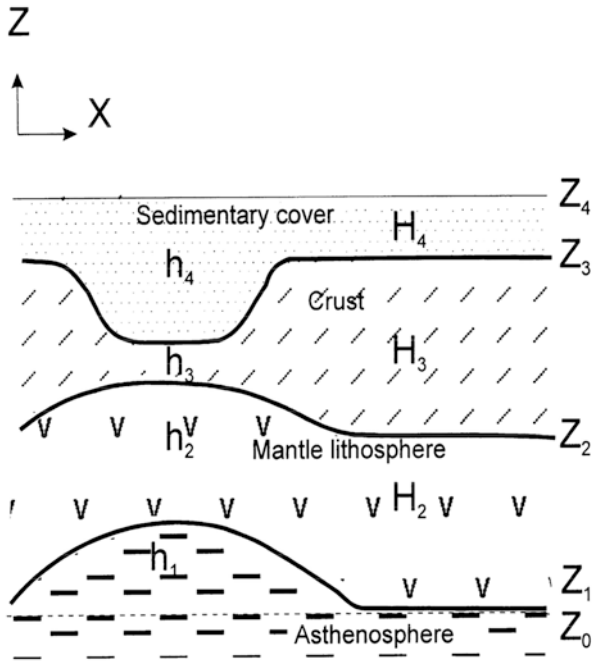


Fig. 4 Principal scheme of the lithosphere structure for the Pre-Caspian Depression and East European Platform
 z – day surface, z – basement surface, z – Moho discontinuity, z – lithosphere-asthenosphere boundary, z – level of isostatic compensation.

$$\begin{aligned} \partial^2 T_i / \partial z^2 &= -Q_i / k_i, \\ T^* &= 0^\circ \text{C}, \quad T_* = 1200^\circ \text{C}, \\ [T_i] &= 0, \quad [k_i \partial T_i / \partial z] = 0, \end{aligned}$$

k_i – heat conductivity, Q_i – heat generation, T^* – temperature of the day surface, T_* – temperature of the lithosphere-asthenosphere boundary, $i = 1 \div 4$.

Then surface heat flow:

$$q^*(x) = - \frac{T_* + \sum_2^n h_i^2 Q_i / 2k_i + \sum_{i=2}^{n-1} h_i / k_i \sum_{j=i+1}^n h_j Q_j}{\sum_2^n h_i / k_i},$$

As radioactive elements are spreaded mostly in the crust, it is possible to put $Q_2 = 0$ in the mantle lithosphere. Then we can get the mantle lithosphere thickness:

$$h_2(x) = - \frac{T_* + q^* \sum_3^n \frac{h_i}{k_i} + \sum_3^n \frac{h_i^2 Q_i}{2k_i} + \sum_{i=3}^{n-1} \frac{h_i}{k_i} \sum_{j=i+1}^n h_j Q_j}{1/k_2 \left(q^* + \sum_3^n h_i Q_i \right)}$$

Let us use the next data for geological-geophysical parameters: $h_4 = 24$ km (thickness of sedimentary cover in the center of Depression), $H_4 = 3$ km (thickness of sedimentary cover of the Platform), $h_3 = 12$ km (thickness of consolidated crust for Depression), $H_3 = 40$ km (thickness of consolidated crust for Platform), $Q_4 = 1$ mcW/m³, $Q_3 = 0.5$ mcW/m³ (basalts), $Q_3 = 2$ mcW/m³ (granites), $k_4 = 3$ W/(mK) (1.7–2.1 for terrigenous rocks and 5.-6.6 for salt), $k_3 = 2.5$ W/(mK), $q^* = 50$ mW/m² for Depression, $q^* = 40$ mW/m² for Platform.

Then we can get $h_2 + h_3 + h_4 = 110$ km and $H_2 + H_3 + H_4 = 180$ km, i.e. asthenosphere upwelling is equal to 70 km under Depression.

Let us consider gravimetric model of the Pre-Caspian Depression. Let for 0-approach the Depression and Platform are isostatically compensated with Z_0 – level of compensation.

Then:

$$\begin{cases} \sum h_i \rho_i = \sum H_i \rho_i, \\ \sum h_i = \sum H_i. \end{cases}$$

ρ_i – densities.

And we can get:

$$h_1 = \frac{(\rho_4 - \rho_2)(h_4 - H_4) + (\rho_3 - \rho_1)(h_3 - H_3)}{\rho_2 - \rho_1},$$

$$H_2 - h_2 = \frac{(\rho_4 - \rho_1)(h_4 - H_4) + (\rho_3 - \rho_1)(h_3 - H_3)}{\rho_2 - \rho_1}.$$

For $\rho_4 = 2.3$ g/cm³ (sedimentary cover), $\rho_3 = 2.7$ (granite) – 2.9 g/cm³ (basalt), $\rho_2 = 3.3$ g/cm³ (lithosphere), $\rho_1 = 3.4$ g/cm³ (asthenosphere) it is possible to get $h_1 = 70$ km, $H_2 - h_2 = 60$ km. I.e. asthenosphere upwelling from gravimetric model is very close to the same value from geothermal model that confirms the model correction. It is possible to say the same about the mantle lithosphere thickening. The same parameters are defined from two different methods which give close results. It increases the result reliability. Both models could be used in more complicated and detailed form.

4 Conclusions

1. Mechanical-mathematical modelling shows that structure of depression is formed on the Earth's surface above rising mantle diapir if diapir is deep and its velocity is low. Stretching in layers can be not large.
2. If the velocity of rising diapir is high or the diapir is not deep the structure of superficial swell can be formed.
3. For every case it is possible to find critical parameters of the problem connecting form of the diapir, its depth and velocity with structure of the Earth's surface.
4. Thermo mechanical modeling shows that surface grad T depends on the basin evolution history and thickness of sedimentary cover.
5. During the basin evolution the oil-gas generation zones arise in the central part, spread to the boundaries, are destroyed in the center and stay in the peritherical parts of the basin only. It gives good agreement with geological data.
6. Low heat flow of the Black sea and South Caspian Depression can be explained by high thickness of the sedimentary cover and by sinking of the lithosphere matter above upwelling mantle diapir.
7. The layer of higher heat generation in the sedimentary cover increases the heat flow above and decreases under the layer.
8. The layer of higher heat conductivity in the sedimentary cover increases the heat flow above and under the layer. The salt layer and the salt diapirs are the positive factors of the formation and preservation of oil and gas generation zones and location of high temperature water.
9. Thermo mechanical modeling gives the possibility to evaluate the mantle diapir upwelling under Depression.

There is no conflict of interests in the chapter.

Acknowledgments This work was supported by a grant from the Russian Science Foundation, (project No. 19-47-02010, "Natural hazards and monitoring for research in Russia and India") and research topics (No. 0142-2014-0027 "Development of the theory and methods of studying the latest tectonics and modern geodynamics of platform and orogenic territories in relation to the assessment of their safety").

References

1. Aksenov AA, Goncharenko BD, Kalinko MK, Kapustin IN, Kirjuhin LG, Razmishljaev AA (1985) Oil-gas potential of subsalt deposits. Nauka, Moscow, p 205
2. Goncharov MA, Koronovskii NV, Svalova VB, Raznitsin YN (2015) The contribution of mantle diapirism to the formation of newly formed basins of the Mediterranean and the Caribbean and the surrounding centrifugal-vergent folded-overlapped orogens. *Geotectonics* 6:80–93
3. Gordienko VV, Zavgorodnjaja OV (1985) Heat flow of the pre-Caspian depression. In: *Geothermal investigations in Middle Asia and Kazakhstan* Nauka, Moscow, pp 251–255
4. Maksimov SP, Dykenshtein GH, Zolotov AN, Kapustin IN, Kirjuhin LG, Razmishljaev AA (1990) *Geology of oil and gas of east-European platform*. Nedra, Moscow. 274pp

5. Sharkov E, Svalova V (2011) Geological-geomechanical simulation of the late cenozoic geodynamics in the alpine-mediterranean mobile belt. *New frontiers in tectonic research – general problems, Sedimentary Basins and Island Arcs*. INTECH, Croatia, pp 18–38
6. Soloviev BA, Svalova VB, Ivanova TD (1991) Thermomechanical model of sedimentary basin formation and evolution on the example of the pre-Caspian depression. In: *Theoretical and experimental investigations of geothermal regime within aquatories*. Nauka, Moscow, pp 93–104
7. Svalova VB (2014) Mechano-mathematical modeling of the formation and evolution of geological structures in connection with deep mantle diapirism. *Monitoring. Sci Technol* 3(20):38–42
8. Svalova VB (1992) Mechanical-mathematical models of the formation and evolution of sedimentary basins. *Sciences de la Terre, Ser Inf* 31:201–208
9. Svalova VB (1993) Mechanical-mathematical simulation of geological structures evolution. *Geoinformatics* 4(3):153–160
10. Svalova VB (1997) Thermomechanical modeling of geological structures formation and evolution on the base of geological-geophysical data. In: *Proceedings of the third annual conference of the International Association for Mathematical Geology IAMG'97, Barcelona, Spain*. Part 2. pp 1049–1055
11. Svalova V (2002) Mechanical-mathematical modeling for the Earth's deep and surface structures interaction. *Proceedings of International Conference IAMG, Berlin*. 5 p
12. Svalova VB, Sharkov EV (1991) Formation and evolution of back-arc basins of the Alpine and Pacific belts (comparative analysis). *Pacific Geol* 5:49–63
13. Svalova VB, Sharkov EV (1992) Geodynamics of the Baikal rift zone (petrological and geomechanical aspects). *Geol Geophys* 5:21–30
14. Svalova VB, Soloviev BA, Ivanova TD (1993) Geodynamics and geothermy of the pre-Caspian depression. In: *Geothermy of seismic and no-seismic zones*. Nauka, Moscow, pp 119–132
15. Zanemonetz (Svalova) VB, Kotelkin VD, Miasnikov VP (1974) Dynamics and lithosphere movements. *Izvestia USSR Acad Sci Ser Phys Earth* 5:43–54
16. The Global Heat Flow Database of the International Heat Flow Commission. <http://www.heat-flow.und.edu/>

Prospects for Identifying and Applied Use of Hydro and Petrothermal Energy Sources in Geodynamically Active Structures of the Eastern Segment of the Central Caucasus



V. B. Zaalishvili, Kh. O. Chotchaev, O. G. Burdzieva, D. A. Melkov,
A. K. Dzhgamadze, V. B. Svalova, and A. V. Nikolaev

1 The Urgency of the Problem

Thanks to its inexhaustible reserves of energy and material resources the supply of energy sources and material resources in modern Russia is ahead of the demand of all economic entities. If such a ratio is preserved even when Russian production reaches global productivity, which will certainly lead to a growth in demand due to a significant expansion of the domestic industries, the current technology of energy resources use will inevitably increase the negative impact on the environment. The environmental consequences of the intensive use of non-renewable energy resources seem to be the main reason not to rely on the country's raw materials and non-renewable energy resources, but to develop a strategy for switching to the use of renewable and environmentally-friendly energy sources, which the leading developed countries of the world community are striving for.

The socio-economic and environmental benefits of using thermal energy from deep-seated hydrothermal deposits and petrothermal foci are quite obvious and, being a promising applied industry, it should be elevated to the rank of state task of innovative development of the energy industry.

V. B. Zaalishvili (✉) · K. O. Chotchaev · O. G. Burdzieva · D. A. Melkov ·
A. K. Dzhgamadze

Geophysical Institute – the Affiliate of Vladikavkaz Scientific Centre of the Russian Academy of Sciences, Vladikavkaz, Russia (GFI VSC RAS), Moscow, Russia

V. B. Svalova · A. V. Nikolaev

Sergeev Institute of Environmental Geoscience of the Russian Academy of Sciences (IEG RAS), Moscow, Russia

© The Author(s), under exclusive license to Springer Nature
Switzerland AG 2021

V. Svalova (ed.), *Heat-Mass Transfer and Geodynamics of the Lithosphere*,
Innovation and Discovery in Russian Science and Engineering,
https://doi.org/10.1007/978-3-030-63571-8_3

For the first time, the idea of thermal energy extraction from underground hot rocks by injection of cold water was expressed at the end of the nineteenth century by K.E. Tsiolkovsky. However, Russia, unfortunately, occupies only 13th place in the list of main countries that use geothermal sources of the Earth as renewable heat and energy, covering, in addition, only 0.03% of the energy consumption.

The use of geothermal sources for heating residential, industrial and social premises and greenhouses is profitable at a heat carrier temperature of 100–150 °C. Such temperatures are reached in almost all continental territories already at depths of 3.5–4.0 km only due to the geothermal gradient of the thermal field of the Earth, without taking into account the local geodynamic features of the active regions. Hydrothermal springs with deep heat additional feeding from local petrothermal objects or magma chambers can reach optimum temperatures for operation at much shallower depths from the Earth's surface, which makes their use highly cost-effective due to low costs for well drilling [1–7].

A significant disadvantage of using low-temperature thermal springs is their mineralization, which contributes to the premature destruction of pipes due to the chemical activity of water. The service life of casing column pipes is less than 10 years since the mineralized heat carrier leads to the overgrowth of the column with iron oxide, calcium carbonate and silicate formations. The problems of erosion, corrosion and salt deposits have a negative impact on the operation of terminal processing equipment and on the unit cost of the final product. The disadvantages include the one-time use of the heat carrier which is discharged into the environment during temperature recovery to the technological minimum, although using the wastewater in agricultural greenhouse facilities, the efficiency can be significantly increased.

As a source of deep heat, one can use the total thermal field of the Earth, which varies with depth in the first approximation according to the geothermal gradient (about 3° per 100 m depth for platforms and 1° for crystalline shields). The local character, confined mainly to individual disjunctive disturbances within the active geosynclinal regions, has a thermal field accumulated in the thermal waters of different genesis. This includes the heat generated by chemical reactions of rising fluids with rocks and groundwater, the reserves of which are estimated in $3 \cdot 10^{31}$ J, exceeding by more than 10 orders of the heat magnitude generated by deformation processes at tectonic stresses. The largest amount of geothermal energy consists in solid hot rocks, where more than 95% of the total resources of underground thermal energy are concentrated. The development of the last ones on the 4–6 km depth accessible for modern drilling technology and with optimum temperature conditions of 180–220 °C is typical for profitable operation for young geosynclinal regions, which is the structure of the Greater Caucasus. In addition, the widely developed network of deep faults of the Central Caucasus (some of which continue to the upper mantle and remain to be active and are channels for a transit of mantle and intracrustal magma) predetermines the prospect of identifying geothermal deformation sites and high-temperature magmatic masses in them.

The world practice of using renewable sources of thermal energy of the Earth shows that hydrothermal sources are profitable in the areas of active Alpine orogenesis, young volcanism, in the areas of large active faults of the Earth's crust with high geothermal parameters (temperature, flow rate), where they are located relatively shallow from the surface, have high temperature conditions and are available for modern drilling technology.

The main factor in the feasibility of petrothermal heat using is the ratio of the temperature at the bottomhole and the depth of the well. Here, global experience of use and calculations show that profitable energy reproduction due to petrothermal heat can be achieved if the temperature at the bottom is 200–250 °C at a depth of 3.5–4.0 km, which is twice the size of the geothermal gradient, i.e. can be only in case of local petrothermal object presence.

The projecting costs of a well of such depth with a drilling diameter at the bottom hole of the order of 8–10 inches will be at least 560–600 million rubles, without taking into account the above-standard unforeseen expenses. Despite the high cost of arranging the heat pipeline, however, during the organization of the normal technological cycle of extracting the heat carrier and transferring its heat to easily transported energy (electrical), the profitability of renewable energy production is confirmed by world practice. The heat pipeline depreciation in this technological cycle reaches more than 90% of all expenses.

Obviously, the profitable use of the Earth's heat based on a geothermal gradient is possible when reaching depths of the order of 6–7 km. Despite the almost twofold increase in expenses, this type of heat has an advantage due to the inexhaustibility of resources.

The technology of selecting the required volume of a high-temperature steam-water mixture can be a chamber process by fracturing or borrowed from the oil industry using horizontal wells in the productive array.

First of all, the development of thermal energy should be realized in the petrothermal massifs located at depths of 2–3 km in the areas of development of young intrusions of granodiorite composition with an absolute age of 2–2.5 million years.

Depending on the size of the intrusive bodies and the degree of erosion, their cooling rate, according to the calculated data, ranges from 180 to 200 °C for one million years, and the beginning of the melt crystallization (the formation of the massif) in the intrusions of this composition occurs at a temperature of 820–900 °C. Considering the age of neo-intrusions, when drilling out the territory of their development, it is quite possible at the depths of 2–2.5 km to open the “dry rocks” with temperatures up to 250–400 °C.

Within the mountainous part of RNO-A, a number of young intrusive massifs outcropping the day surface are known: Midagrabin (headwaters of the Genaldon river), Tepli (headwaters of the rivers of Fiagdon, Arkhondon, Lyadon), Songutidon (headwaters of the Songutidon river) and the hypothetical, blind Tanadon massif (in the upper of the Digorsky gorge). Deep wells can be located in economically developed areas in the immediate vicinity of the exploited highways and transmission lines.

The works carried out in our country and foreign experience confirm the possibility of creating efficient geothermal stations for the generation of heat and electrical energy using the heat of rocks at depths of 3–4 km. Such stations already operate in the USA (Fenton Hill, near Los Alamos) and in France (Alsace). A similar station is built in the south of Chile on the basis of a 2.5 km deep well with a bottomhole temperature of 280 °C.

Experimental industrial work was carried out in Russia in the town of Tyrnyauz on a well drilled to a depth of 4002 m in the granitoids of the El-Dzhurt neo-intrusive complex, whose age is estimated at 2.4 million years. Crystallization of the massif here occurred at a temperature of 750 °C. The temperature at the bottom hole is 232 °C. It should be noted that the massif is exposed and partially eroded. The hydraulic fracture of the mountain massif was realized with the formation of an extensive crack (“dry boiler”). Hot water from the well was practically used for heating residential and industrial premises, but the experimental work was stopped due to the lack of funds. The realized technical and economic analysis of the use of heat energy of dry hot rocks in Tyrnyauz with the help of a geothermal circulating system (GCS) shows the possibility of a relatively quick payback of capital investments. The implementation of such a scheme can be carried out with the help of domestic equipment (for example, geothermal stations produced at the Kaluga plant).

For the geological preparation of construction sites, for the purpose of equipping the mentioned GCS on the territory of the Republic of North Ossetia-Alania, the following sites can be recommended at the present time:

- Genaldon site (in the area of the Upper Karmadon mineral sources);
- Upper Fiagdon site (in the area of the Hilak mineral source);
- Lyadon site (2 km north of the village of Tapankau);
- Arkhonsite (3 km south of the village of Arkhon);
- Songutidon site (7 km south of the village of Dunta);
- Tanadon site (2 km south of the recreation center “Digoria”).

2 Structural-Material Complexes Favorable for the Localization of Petrothermal Sources

According to the concept of the tectonics of lithosphere plates (TLP), the geological structure undergoes regularly alternating periods in the tectonic evolution of the Earth, which are characterized by a certain sequence of geological events and develop against the background of the general directional development of the planet due to its internal energy.

The structural and material complexes of the first-order (according to the regional tectonic zoning scheme) have a sublatitudinal orientation [8], determined by the

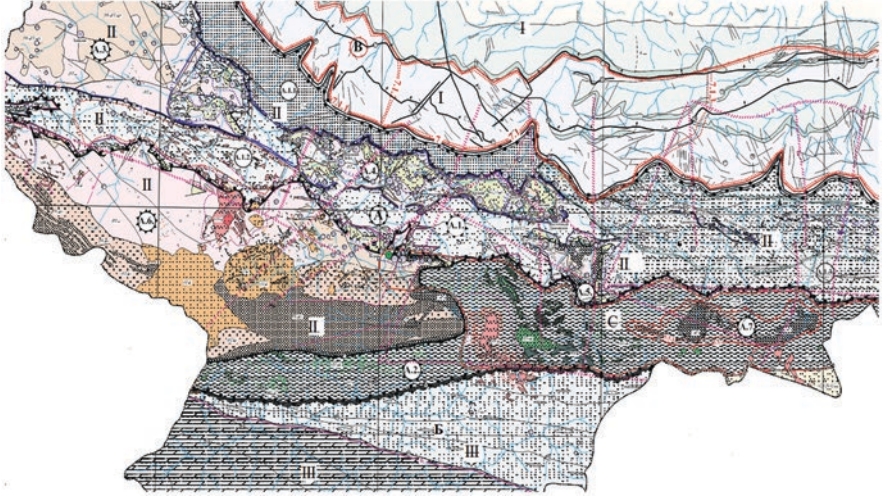


Fig. 1 Structural-tectonic map of the Eastern segment of the Central Caucasus

action of submeridional compressive forces, i.e. anti-Caucasian strike, the main ones of which are shown in Fig. 1. Differentiated structural and material elements of higher orders repeat the spatial orientation of the main structures.

The basis of the structural-and-formational zoning is the data on the geotectonic position of the Caucasus. The territory of the North Caucasus throughout the history available for reconstruction, in general, meets the concept of “rift-related margin of the continent”. The term “rift-related” is understood not as the edges of the platform, but in terms of the characteristics of the unstable, active state of the edge of the platform, periodically leading to the formation of marginal-continental rifts. The concept of a “continent” of the territory of the Greater Caucasus corresponds not only to the continental character of the crust but also to the continental tectonic regime that has been preserved here throughout the entire documented geological history, starting from the Late Proterozoic.

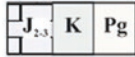
At the same time, some of the structures that arose from time to time belong to the geosynclinal type, without denying in principle their origin as a result of rifting on the continental crust.

The geological development of the territory is determined by the structural-tectonic features of the formation of structural and material complexes, magmatic and volcanic activities, and modern geodynamic activity. These features together are presented in the structure of the Central Caucasus, in the eastern segment of which the mountainous part of the territory of the Republic of North Ossetia-Alania is located.

Legend to the Structural Tectonic Map of the Eastern Segment of the Central Caucasus

Microplates – terrains: I - Pre-Caucasus; II – Bechasynsksk; III – Transcaucasian, C - Mamison-Kazbek zone (relic scar)

B. STRUCTURAL-FORMATIONAL COMPLEX OF THE SCALISTYI RANGE



Carbonate formation of the Scalistyi Range
(northern shelf of the marginal basin compensation stage)

A. DIGOR-OSETINSK STRUCTURAL-FORMATIONAL MEGA ZONE OF THE KIMMERID
(Lower Middle Jurassic rift continental-marginal basin)

A.1 CHEGEM-TEREK STRUCTURAL-FACIAL ZONE (SFZ)

(marginal continental volcanic-plutonic belt (VPB) kimmerid of the Greater Caucasus)

A.1.1 North structural-facial subzone (SFSZ)



Bajocian shallow-lagoon formation, with numerous
plant detritus and woody debris

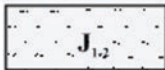


The Toarcian - Aalenian three-membered (argillite-siltstone
with sandstones) flyshoid formation



Pliensbach terrigenous sand formation
(of the marginal continental shallow basin)

A.1.2. Shtulu-Kharess structural-formational subzone



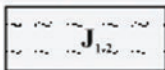
The Pliensbach - Toarcian - Aalenian, terrigenous-flyshoid formation
(clay shale, siltstone, sandstone)



Lower Jurassic effusive and pyroclastic facies of a homodromous
sequentially differentiated basaltic andesit-andesitic formation
(composes vent polygenic subvolcanic-volcanic structures)

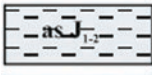
A.1.3. Fiagdon-Terek SFSZ


(with possible submerged elevation of the Chegem –Fiagdon VPB)



The Pliensbach - Toarcian - Aalenian clay-flyshoid carbon formation
(argillite-silt-sandstone) hosting mineralization of the quartz-gold-
polysulphide (ptygmatic) subformation

2. ADAIKHOKH-SHAUKHOKH-DARIAL SFZ
 (the core of the Main Caucasian Geo- anticlinorium)

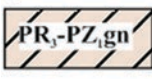
 Lower Middle Jurassic aspid formation of a zone of compensated deflection (schist, quartz sandstone; synsedimentary volcanic rocks of a poorly differentiated andesite-basalt formation)

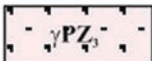
 Early considermental (synsedimentary) poorly differentiated basalt-andesitic formation stratified in the section of the aspid formation

 Kazbek subvolcanic- hypabyssal diabase-picrite formation

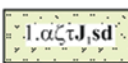

CONSOLIDATED STRUCTURAL-FORMATIONAL BLOCKS (SFB) OF EPIBAIKALIAN-HERCYNIAN FOUNDATION

A.3. Balkar-Digor longitudinal linear SFB
 (the area of steady elevation of the Epipaleozoic basement)

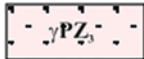
 Upper Proterozoic-Lower Paleozoic formation of the metamorphic Gundarai complex and sialic profile (quartz- mica schist, gneiss, amphibolite)

 Late Paleozoic polyphase granite formation (Belorechensk and Ullukamsk complexes) forms the pre-Jurassic substrate


A.4. Sadon longitudinal linear SFB, the region of the Jurassic terrigenous-mineralogical association broken by the bodies of the volcano-plutonic association – Chegem-Fiagdon VPB (the area of the maximum development of gold-bearing formation)


  Lower Middle Jurassic volcanic-plutonic association of a sequentially differentiated series of andesite-basalt- trachyte (accommodates the mineralization of a gold-silver near-surface formation)

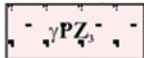
1. Effusive and pyroclastic facies of a homodromous sequentially differentiated basaltic andesite-andesite-dacite-trachyte formation (composes ventr polygenic subvolcanic-volcanic structures)
2. Subvolcanic- hypabyssal facies of microdiorite-granitoporiferous-trachyte formation (dikes, subiacent intrusives, small discordant intrusions)

 The Late Paleozoic polyphase granite formation (Belorechensk and Ullukamsk complexes) forms the pre-Jurassic substrate


A.5. Bakotinsk SFB

 The Lower Jurassic effusive and pyroclastic facies of a homodromous sequentially differentiated basaltic andesite-andesite-dacite-trachyte formation (compiles vent polygenic subvolcano-volcanic structures)

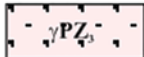
 The Upper Proterozoic-Lower Paleozoic formation of the metamorphic Gundarai complex and sialic profile (quartz- mica schist, gneiss, amphibolite)

 The Late Paleozoic polyphase granite formation (Belorechensk and Ullukamsk complexes) forms the pre-Jurassic substrate

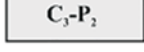
A.6. Laboda-Buron longitudinal linear SFB of the Epibaikalian basement (the area of manifestation of the Alpine tectonic-magmatic activation)

 The Upper-Proterozoic formation of the metamorphic Kassar complex of the mafisalic profile (quartz-mica and amphibolite schist, amphibolites, metatuff horizons, marble)

 The Middle Paleozoic formation of granite-gneiss of the Kassar type


 The Late Paleozoic polyphase granite formation (Belorechensk and Ullukamsk complexes) forms the pre-Jurassic substrate

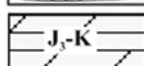
A.7. Shaukhokh-Darial inversion longitudinal linear SFB of the Late Paleozoic basement Formation of grey-colored molasse (transgressive cycle; conglomerates-quartzites, tuff sandstones, carbonaceous phyllite, marbled limestone, horizons of andesite and their tuffs)

 The Middle Paleozoic formation of granite-gneiss of the Darial type


 The Middle Paleozoic formation of granite-gneiss of the Darial type

B. FRAGMENT OF A SHARED SFZ OF THE JURASSIC TERRIGENOUS MIOGEOSYNCLINE

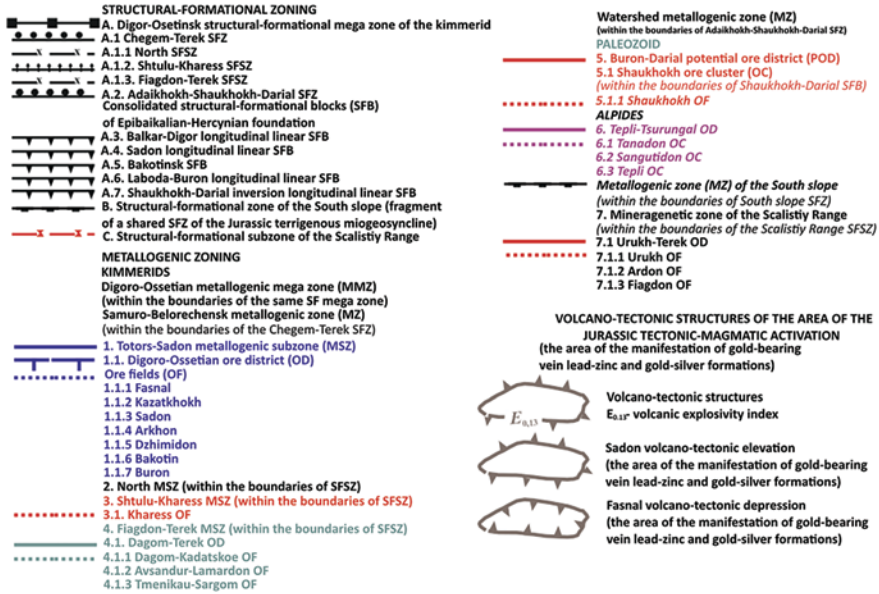
 The Toarcian - Bajocian terrigenous, clay-tuffogenic formation

 Calloway-Oxford carbonate flysch formation (marls, marl limestones, calcareous sandstones, mudstones)

 The Middle Jurassic Tsey diorite - granodiorite formation

 Neogene Tepli diorite -granodiorite formation (complex of small intrusions)

 The Upper Neogene- Quarternary lava complex



The eastern segment of the Central Caucasus, as well as the entire structure of the mega-anticlinorium, is the uplift of the southern edge of the Scythian Plate. Tectonic structures that arose during various collisional events from the Proterozoic to the present and that are recognized with varying degrees of reliability are involved in its structure [9] (Fig. 2). This explains the complexity of the tectonics of the main structures of the territory, represented by fragments of the Pre-Caucasus, Bechasynsk and East Caucasus microplates connected to the East European Plate at the end of Paleozoic (Fig. 1) [10–18].

A series of structural and material complexes of structural-tectonic, volcanic and magmatic nature, destruction and development of folded-block tectonics in the collision era of geodynamic conditions, which to some extent could leave geothermal effects, are noted in the zone of the segment. We give the main ones.

2.1 Cimmerian Folding Zone

The extension to the east of the Sadono-Unal horst and the Fiagdon anticline is the zone of Cimmerian folding. The underthrust of the Scalistiy Range limits the zone of Cimmerian folding from the north, from the south the zone terminates at Tsariit-Tsatadon and Belorechensk faults, separating it from Shaukhokh-Darial uplift.

Within the zone, a number of sub-latitude-oriented tectonic subzones characterized by a certain type of plicative and disjunctive disturbances are distinguished. From the north to the south, the subzones of the northern anticlines, intermediate

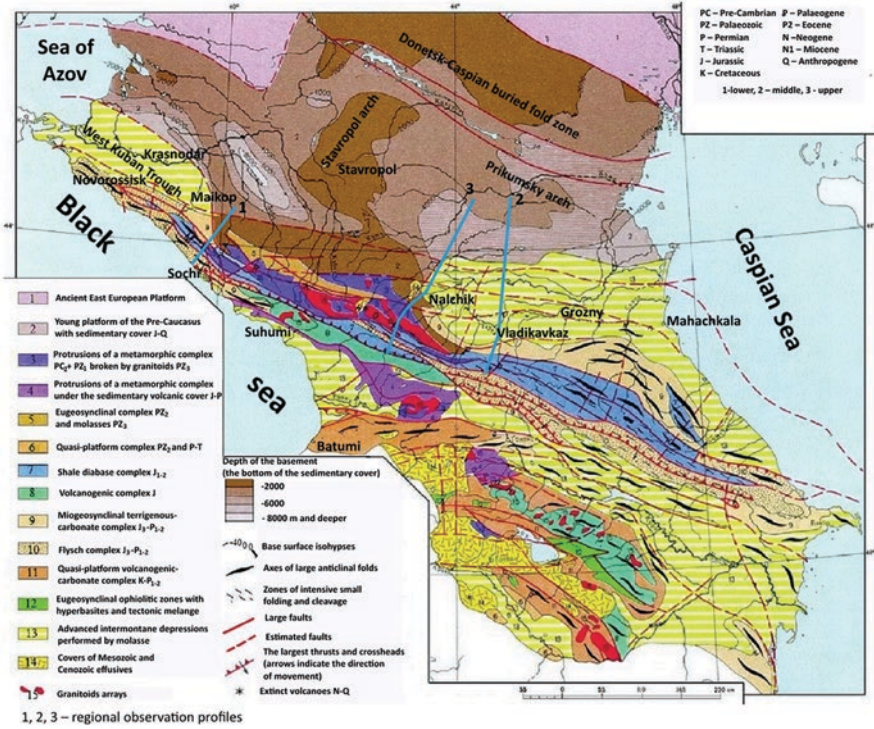


Fig. 2 Geological map of the Caucasus

grabens, central synclines of the Fiagdon-Larsky uplift and the “southern” syncline are singled out.

In general, in terms of its position in the geological structure of the mountainous part of the eastern segment of the Central Caucasus and in its structure, the “southern” syncline of the Cimmerian folding is analogous to the Shtulu-Khares graben-syncline separating the Taymazy-Labagom (Central) and the Balkar-Digor uplifts, and apparently, can be considered to some extent as its eastern segment.

The andesite-dacite tuff-lava volcanogenic formation is replaced by gabbrodiorite-granodiorite and gabbro-diabase dyke formations; magmatic activity is activated. Sedimentary complexes are presented by aspidite and nodular schist, metasandstone and quartzite.

The next stage of the geodynamic situation in the Wilson cycle begins; the interaction of the opening oceanic plate and the continental margin advancing under it begins and, as a result, the activation of basaltoid volcanism associated with the spreading occurs.

2.2 *Central Elevation. (a) Taymazy-Labagom Elevation*

The axial zone of the anticlinorium of the Greater Caucasus in the eastern segment of the Central Caucasus shifts to the south, where it is expressed orographically by the most high-altitude Bokovoy Range. Rocks of various genetic types and a wide age range (from the Proterozoic to the Neogene inclusive, reflecting the different stages of the geodynamic development of the territory) participate in its structure. In the modern look, the main place in the formation of the structural unit belongs to the Epibaikalian-Hercynian structural stage, which has been opened to daylight. The axial zone is represented here by two sublatitudinal horst elevations: Taymazy-Labagom and Shaikhokh-Darial elevations.

According to the material complexes, Taymazy-Labagom elevation is differentiated into two tectonic subzones: Tanadon-Buron and Laboda-Tsmiakom.

The Tanadon-Buron subzone is located in the northern half of the Taymazy-Labagom elevation. It is limited in the north by the depression structure of the Shtulu-Khars graben-syncline, and in the south – by intersection of the Laboda-Karaugom and Tseydon faults. The intersections of these faults are healed by the intrusions of the Karaugom and Tsey massifs of the Digor volcanic-plutonic association of the Middle Jurassic age. The magmatic formations to the zones of large faults of the all-Caucasian orientation and fracturing systems of the north-west strike. Their composition is presented by diorite and gabbro-diorite-granodiorite group of formations.

The Tanadon-Buron subzone consists of five tectonic blocks, of which the western blocks (Tanadon, Rudny and Hupparin) are separated from the eastern ones (Shaikhokh and Buron) by the deep Zgid fault, along which the eastern part of the Tanadon-Buron subzone is raised not less than on 2.5–3 km.

The Laboda-Karaugom fault which borders the western part of the Tanadon-Buron subzone from the south is one of the largest disjunctives of the ancient foundation in this part of the region. The fault can be traced in the west-east direction for 25 km.

The Laboda-Tsmiakom subzone located from the south to the Tanadon-Buron subzone, along the Laboda-Karaugom-Tseydon tectonic zone, is composed of Upper Proterozoic formations of the Mamison-Kazbek suprastructure, represented by crystalline schists of the Kassar suite, belonging to the Buulgen series, and also rocks of the granite-gneiss mid-Paleozoic formation of the Kassar complex. The structural and material complex of the Laboda-Tsmiakom subzone includes also the granodiorite Karaugom and Tsey massifs, as well as stocks and dike complexes of the gabbro-diabase (Kazbek complex) and Middle Jurassic gabbro-diorite-granodiorite (Digor complex) formations.

The Laboda-Tsmiakom subzone consists of two blocks divided by the Karaugom intrusive of granodiorites. The Western (or Watershed) block occupies the ridge part of the Glavnyi Vodorazdelnyi Range between the mountain-glacial massifs of the Laboda (4320 m) and the Burdzhula (4357 m). The Eastern Lagau-Tsmiakom, located between the Lagau and Tsmiakomkhokh mountain massifs, is situated on the slopes of the Bokovoy Range. The block is limited in the north by the Tseydon fault, in the east – by part of the Kolotin thrust, in the south by the zone of the Main thrust. Its western border of the juncture with the Watershed block is destroyed by the intrusion of the granodiorites of the Karaugom massif. Small bodies are tending to its eastern and southern parts and in the northern part the formations of the Middle Paleozoic granite-gneiss formation are predominant. In addition to the above-mentioned granodiorites of the Karaugom and Tsey intrusions, there are also vein derivatives of magmatic formations, as well as countless dikes of the Middle Jurassic gabbro-diabase formation (Digor volcanic-plutonic association).

Within the Taymazy-Labogom elevation the rocks of Buulgen and Maker series contact that is of considerable interest due to the fact that the Maker series lies on the Buulgen and that the Laboda-Karaugom-Tseydon tectonic zone separating these salic and mafic series is nothing more than a large thrust.

2.3 The Shaikhokh-Darial elevation

The Shaikhokh-Darial elevation is the structural and material complex located in the south-eastern part of the eastern segment of the Central Caucasus, where it covers the ridge and slopes of the Bokovoy Range. The elevation integrates the large Shaikhokh and Darial massifs, which are separated by Chachsk cover.

The main feature of the development of the Shaikhokh-Darial structural-facial zone (SFZ) is a local intensive magmatic activity that accompanied sedimentation. At the initial stages, magmatic formations of medium composition were formed, represented by thin horizons of andesitic lavas and their tuffs, stratified in the lower part of the section among quartzitic sandstones and slate schist. The most intense magmatic activity was accompanied by a period of accumulation of clay strata.

Located in the interstream area of the rivers Fiagdon and Gizeldon the Shaikhokh massif is bounded in the north by the southwestern part of the Dzhimara-Godtanadag fault and Tsariit-Tsatadon uplift. Its southern border is bounded by Syrhubarzond overthrust of sublatitudinal orientation. The block is characterized by numerous dikes of the Middle Jurassic gabbro-diabase formation of the Kazbek complex.

The Shaikhokh massif is represented as a folded-block structure with contacts between the suites of the tectonic character, with steeply dipping intra-massive faults of southern inclination. The northern intra-massive blocks are characterized by the wrinkle of Mesozoic rocks in upturned and inclined folds with a wingspan of up to 400–500 m. The rocks of the Shaikhokh massif along the Tsariit-Tsatadon fracture are pulled over sandy-clay deposits of the Cimmerian folding zone.

The Darial massif is the eastern part of the Shaukhokh elevation; it occupies the extreme southeast corner of the eastern segment of the Central Caucasus and is located in the valley of the river Terek. The massif is bounded from the north by the Belorechensk fault and from the south by the Gvilet fault. The basis of the rocks composing the massif is represented by the formations of the Middle Paleozoic granite gneiss formation.

The width of the Darial massif along the valley of the r. Terek is 7 km, and the length within the described area is 20 km.

2.4 Mamison-Kazbek Relic Scar

A relic scar (geosuture) is interpreted as marking the collision zone of continental plates (the Scythian plate and a collage of the southern microplates) and confirms the fact of previously existing (and subsequently closed) sea basin where subduction-type geologic conditions have emerged [19, 20]. The zone has general Caucasian significance and covers part of the Western Caucasus, the entire Central Caucasus, and most of the Eastern Caucasus.

According to the earthquake converted-wave method (ECWM), carried out along the separate regional profiles crossing the Greater Caucasus orogen, there is reason to believe that this zone also has a continuation in the western Caucasus and that between the sources of the river of Mzymta and the valley of the river of Inguri the geosuture is pushed under the Central Caucasus zone.

On the territory of the eastern segment of the Central Caucasus, the geosuture is traced from the Mamison Pass in the west to the Maili-Kazbek massif, stretching along the southern borders of the structural-material complexes of the eastern segment of the Central Caucasus. In the north, the tectonic structures of the Main thrust, the Kolotinsky, Syrhubarzond, Kaidzhin and Gvilet tectonic structures control the geosuture, and in the south – the Adaykom-Kazbek and Cess faults. The relic scar is formed by two formations: Arnag and Cyclaur, in the process of subduction of the oceanic bottom and, especially, collisions of continental plates, turned into a chaotic complex or mixed, which are typical to collision zones of lithospheric plates.

Mamison-Kazbek geosuture appears to be made by remobilized olistostromes of the ophiolite complex, fragments of different sizes of volcanic-sedimentary rocks, tectonized rudaceous terrigenous material. Serpentinous picrites, which are nowhere to be found without andesite-basalt or diabase membrane (the areas of Kliatkom, Arsikom, Midagrabyň), fit well into the scheme of the process of diapirism that took place at the first stage of tectonic mobilization of ophiolites. The subintrusive formations of the Pliocene diorite formation in the structure of the Mamison-Kazbek zone are insignificant and their role is insignificant.

Many researchers who adhere to the concept of a tectonics of lithospheric plates are the supporters of the relic scar rocks moving under the crystalline foundation of the Scythian plate. According to their interpretation, the sedimentary-volcanogenic formations are only partially subducted together with the “absorbed” plate, while

the excess part of the displaced relatively “loose” continental rocks is “pressed” between continental plates that create a kind of cushion in the collision zone, which overthrusts on the edge of the Scythian plates in the form of covers and tectonic plates. Such zones and structures in the Mamison-Kazbek geosuture include Midagraby-Maili, Bubudon-Lyadon and Kurov tectonized intervals and the Kolotinsky and Chachsky covers that separate them.

An example of the formation of tectonized intervals can serve as structures in the rear parts of the Taymazy-Labogom uplift and the Shaukhokh and Darial massifs, which served as peculiar thresholds for sedimentary strata coming from the south. “Resting”, loose sedimentary strata could not move under the dense rocks of the suprastructure and were crinkled, crushed, exfoliated, cataclased and mylonitized. Such tectonized structures include, for example, the Kolotinsky and Kaidzhin covers.

According to the geological observations, three types of olistostrome were found in the Mamison-Kazbek relic scar [21].

The first type includes small blocks of gabbroids located in a thin powdered clay-siltstone matrix without any visible orientation. They are classified as olistolith because of the lack of a visible connection with faults and endo – and exocontact changes. This type was found in the western part of the geosuture, on the slopes of the Bubudon and Kliatkom rivers and on the right bank of the river Dzamarashdon.

The second type of olistostrome is represented by large blocks composed of 70–80% parallel dykes of diabases and gabbro-diabases. Lodged between dykes low-thickness interlayers of enclosing shale are hornfelsed and silicified; andalusite is often developed in them, the blocks are often intensely pyrrhotitized. Occasionally in addition to pyrrhotite chalcopyrite may be presented. The genetic relationship of copper-pyrrhotite ore occurrence is known with this type of olistostrom. Andalusite often is developed in them.

The third type of olistostrome includes shale interbedded with sills and flows of gabbroids and andesite-basalt, as well as blocks completely composed of these magmatic rocks. Olistoblocks of this type are characterized by the fact that the magmatic rocks in them are represented mainly by streamed facies with characteristic spherical separation. Subintrusive formations in these olistoblocks are rare and are represented by single dykes of diabase composition.

As it was noted earlier, among the disjunctive disturbances the most significant tectonic faults limiting the Mamison-Kazbek zone from the north are the Main Caucasian and Syrhubarzon thrusts.

The relic scar is bounded from the south by the Adaykom-Kazbek fault, which consists of a series of parallel fractures, forming a remolded and mylonitized zone with a thickness of 60 m to 1 km. The fall of the fault is steep north (60–80°). The fault zone is characterized by the introduction of a large number of barren quartz veins and lenses. Within the described area, the fault plays the role of a peculiar barrier for Mesozoic magmatic manifestations, which, as follows from the above mentioned, are widely developed north of the fault. South of the Adaykom-Kazbek fault, Mesozoic magmatic manifestations are completely absent. Along this fracture, all geological formations located to the south move under the Mamison-Kazbek geosuture.

Chaotic complexes of sedimentary and tectonic origin are indicators of contrast (in geomorphologic and structural attitude) tectonic zones [22].

Melange marks the position of ophiolite and non-ophiolite joints, convergence and collision of lithospheric plates, microplates, terranes and blocks. Chaotic complexes of sedimentary origin olistostroma indicate the location of underwater ledges and slopes, which distribute geodynamically diverse sedimentation basins.

2.5 *Volcanogenic Formations. Fiagdon Volcano-Plutonic complex (T(?)-Jlf)*

The Fiagdon complex is characterized by basaltoid flows and sheets developed in the composition of the middle subsuite of the Cyclaur suite of basaltoids and the sills and small stocks of subintrusive formations associated with them.

The mafic volcanism of the Fiagdon complex proceeded synchronously with the accumulation of terrigenous material in underwater conditions. Effusive rocks are represented by basaltoid lavas, lava-breccias, among which can be distinguished andesite-basalts, basaltoid of the porphyritic structure – spilites.

The macroscopic and microscopic study of basaltoid magmatism of the Fiagdon complex over a large area of its manifestation did not reveal any signs of regional differentiation. In general, the magmatism of the Fiagdon complex should be considered as a homogeneous tholeiitic series.

In addition to the calculated mineral composition of rocks, the proximity of the considered formations to the tholeiitic series [23] is also confirmed by petrochemical parameters (complex average: $\text{FeO} + 0.9 \text{Fe}_2\text{O}_3 / \text{MgO} = 1.2$; $\text{K}_2\text{O} 1\%$, $\text{Na}_2\text{O} (\text{K}_2\text{O} = 4; \text{Rb} = 10 \text{ g/t}; \text{Sr} = 300 \text{ g/t})$).

The formations of the Fiagdon complex belongs to the magnesian branch of the tholeiitic series, but it should be noted that almost all of the extensive bodies of basaltoids are, to a certain extent, separate, discrete blocks, as if strung together on a single thread. The largest bodies are independent isolated blocks. This pattern is very characteristic for chaotic complexes in which the blocks of basaltoids are olistostromes.

Intrusive formations are joined into plutonic and subvolcanic complexes, reflecting the dynamics and sequence of the geological development of the territory.

2.6 *Middle Paleozoic. Belorechensk Complex Granite Plutonic*

Coarse-grained granitoids, often porphyritic and gneiss metamorphosed, vary in composition from granodiorites, plagiogranites to granites, corresponding to the granitoids of the first phase in the scheme proposed by M.Kh. Srabonyan [24], represent the Belorechensk complex.

Granitoid formations of the Belorechensk complex are fairly widespread in the area within the eastern segment of the Central Caucasus. In the west, their largest massifs are confined to the Balkar-Digorsk uplift, to the boundaries of the protrusions of the infrastructure. Outcrops of granitoids of the Belorechensk complex can be traced in the Sadon-Unal horst, the Fiagdon anticline, the Taymazy-Labagom (Central) uplift and in the squeezed scales of the basement in the Shtulu-Khars graben-syncline.

Coarse-grained non-porphyry granites are among the most widely developed varieties of the Belorechensk complex. They form in plan the stock-shaped and stretched, elongated in the north-west direction bodies. Outcrops of coarse-grained granites are traced by a strip along the northern border of the Uruk protrusion of the infrastructure (headwaters of the Sapvtsek-Uzadon rivers) and exposed in fragments along the southern boundary of the Dashikhokh block (left side of the Uruk river).

In the roof of granite bodies, numerous apophyses of granites into host rocks are usually noted. Contact changes in rocks are minor. As a rule, these changes are noted in the upper slightly eroded parts of the massifs and near flat contacts. Exocontact changes in migmatites of the Upper Balkar complex are not visually identified, which is explained by the proximity of the thermodynamic conditions for the formation of granites and migmatites.

Porphyroblastic granites are traced by a sub-latitudinal strip along the southern border of the Dashikhokh block. They are exposed south of the Skalistyi Range along the Uruk valley. In addition, their small bodies with an area of up to 1–1.5 km² are exposed in the upper reaches of the Sekholadon River, northeast of the town of Vaza-Khokh and in the area between the rivers Haznidon and Lahumedon. Certain massifs of porphyritic granites (from 1.5 to 12.5 km²) are exposed in the southern part of the region in the valleys of the Karaugom (Barzi-Isar mountain), Bartuidon. The host rocks for granites are various migmatites of the Upper Balkar complex. Rare thin (3–5 m) veins and dikes, intersecting migmatized enclosing rocks, occur near exocontact zones and, apparently, are the apophyses of the massifs. Contact changes are practically not observed.

Granites themselves are broken by magmatic formations of a younger age. These are massifs and dikes of two-mica granites of the Ullukamsk complex and the associated veins of muscovite pegmatites and quartz veins. It consists of wide-plagioclase (oligoclase-andesine) crystals with a size of 1.0 × 2.0 to 3.0 × 5.0 mm that are pelitized and sericitized. Plagioclase crystals are corroded with microcline and quartz, and sometimes expanded and deformed, as a result the primary idiomorphic outlines, which are sometimes observed in the microcline, are almost completely lost.

The intrusion of granitoids of the Belorechensk complex was accompanied by a weak thermal-metamorphic effect on host rocks, and, if the anatexite-granite part of the substrate was characterized by palaeogenic-metasomatic replacement, then the other, migmatite part, contact-metamorphic changes are similar to the corresponding changes with epidote-amphibolite metamorphism. Accordingly, the contour of contact-modified rocks in some places acquires an enveloping dome-shaped appear-

ance, a sub-consonant contour of the granite body, which is well traced in the migmatite-gneisses of the substrate along the oriented gneissoidness, restites, melanosome schliers, feverite xenoliths. The traced capacity of dome-shaped over-intrusive formations is from 200 to 600 m, and the more heterogeneous the substrate is, the more distinct and more powerful is the zone of over-intrusive “dome”.

A characteristic feature of migmatite over-intrusive “domes” is the uneven spotty manifestation of high-contrast potassium anomalies of small size, revealed in this area by aerogamma spectrometric explorations [25, 26].

In terms of their physical properties (density, magnetic susceptibility), the Belorechensk granitoids practically do not differ from the migmatites enclosing them and, accordingly, are not reflected in physical fields. When exploring contact zones of Belorechensk granites with the migmatites of the Upper Balkar complex that is enclosing them according to the method of T. Barth (left bank of the Uruk river), migration from migmatites and, accordingly, the input of silicon, sodium and potassium into the granites is observed [27].

The granitoids of the Belorechensk complex on the Digora and Sadon-Unal Horsts of the Fiagdon anticline and the Taymazy-Labagom uplift are the formations of the first phase of the granites of the Main Ridge and Fasnal complexes.

Belorechensk granites are medium and coarse-grained porphyroblast massive, often taxitic rocks. Taxitability is caused, as a rule, by the range of the biotite content, the uneven distribution of the porphyroblast microcline, less often by a change in the grain size. The color is gray, pinkish gray, less often pink.

Characteristic for large microcline crystals is the presence in them of an early internal idiomorphic part, the overgrowing of which by the xenomorphic outer shell according to K. Menerth [28] indicates its metasomatic character. The magnetism of the granites of the Belorechensk complex ranges from $13\text{--}100 \cdot 10^{-6}$, the density is $-2.56\text{--}2.64\text{ g/cm}^3$. The magnetic susceptibility is $6.3 \cdot 10^{-6}$, the density is $2.57\text{--}2.60\text{ g/cm}^3$.

The most part of the veins and dike-shaped bodies, represented by aplites and pegmatites, are located within the taxite differences of granites, in the areas of development of the xenoliths of the Hupparin complex and in the remnants of the roof of crystalline schists.

In geochemical terms, Belorechensk granites are specialized in lead, zinc, copper, and cobalt. All of the ore manifestations of lead and zinc, including the Sadon and Kholst deposits, are spatially conjugated with their outcrops [27].

2.7 Late Paleozoic. Ullukamsk Complex (γ PZ3 U)

Granites of the ullukam complex are widespread intrusive formations of the described area. They are present in the zone of the Main Range, where they take part in the structure of the Balkar-Digor uplift, the Sadon-Unal horst, the Taymazy-Labagom (Central) uplift (blocks: Rudnyi, Saukhokh, Hupparin) and Fiagdon anticline (Bakotin block). Their most significant outcrops are exposed in the upper

reaches of the Karagom, Bartuidon, and in-between Khaznidon-Psygansu rivers [29]. They form small subisometric, irregular, often in the latitudinal direction massifs up to 25 km² in size, exposed by the erosion activity of rivers to a depth of 200 to 2200 meters and variously oriented shallow dikes, usually located near massifs.

The host rocks for the fine-grained two-mica granites are the migmatites of the Upper Balkar complex, the granites of the Belorechensk magmatic complex, as well as the metamorphic formations of the мелкиедайки Vazakhokh complex of the Buron and Kittiberda suites. Contacts with host rocks are igneous, less often tectonic.

Contact changes in granites are weakly manifested and where noted, usually boil down to a decrease in the dimension of the component minerals (quenching zones) and an increase in the amount of muscovite and quartz (apical protrusions and flat-lying contacts). When granites of the Ullukam complex were intruding into granitoids of Belorechensk, the latter were often subjected to microclinization. The veins of pegmatites and aplites associated with granites are confined to the apical parts of the intrusive bodies and the enclosing frame.

The granites of the Ullukam complex are cut by thin dykes of the diabases of the Kazbek complex and dikes of dacites, andesite-dacites of the Teplinsk complex.

2.8 The Prospects for Tectonic Localization of Thermal Medium

If the formation of the main structural-material complexes of the region is of interest from the point of view of magmatism manifestation, then such active deep faults are of interest as transit channels to the host rocks of molten masses, the crystallization of which can form a high-temperature petrothermal object. The position of the main tectonic disturbances on the regional geological section and on the schematic map of the region is shown in Fig. 3.

group of faults on the territory of the Republic of North Ossetia-Alania according to geophysical data.

The Vladikavkaz Fault was situated on the border of the Ossetian Basin with the Lesistyi Range along the southern outskirts of the city of Vladikavkaz. Its presence is confirmed by the gravimetric and seismic works of the correlation refraction method of Grozneftegeofizika, which determine the sharp dip of the Cretaceous base to the north in the foothills of the Terek, Gizeldon and Fiagdon rivers [30–36].

Specialized byseismological explorations based on main modes of the Rayleigh wave the Vladikavkaz fault was investigated along two intersections with an interval of 40 km by researchers of the Schmidt Institute of Physics of the Earth of the RAS and researchers from Geophysical Institute of VSC RAS [37–41]. On a sub-latitudinal profile through the city of Vladikavkaz, a heterogeneous sequence is noted, with a thickness of about 7 km, below which a contrast zone with a thickness

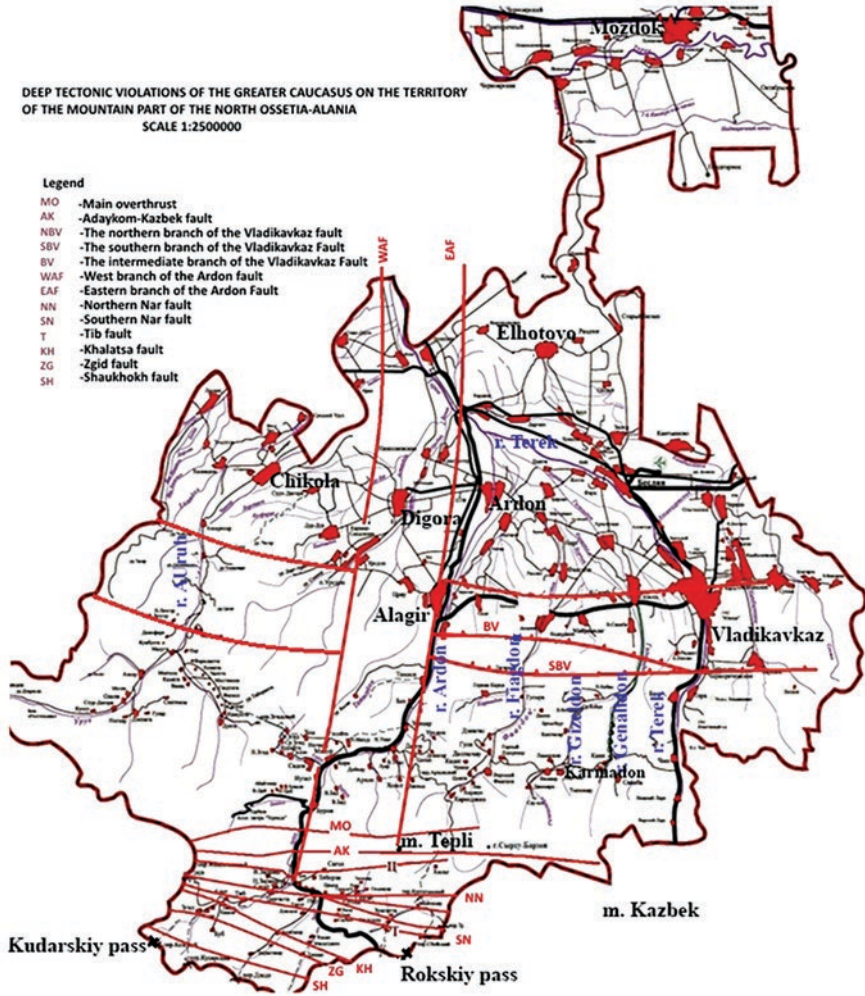


Fig. 3 Location of the Ardon, Vladikavkaz and Adaykom-Kazbek

of up to 5–6 km is observed to a depth of 40 km. Below the non-uniform sequence, to a depth of about 15 km, the zone has a steep northern fall, then fall close to the vertical.

The seismic potential of Possible Seismic Source (PSS) zones of the Vladikavkaz Fault is 6.5–7.1 [42–50]. The manifestation of seismicity can be both deep and medium focus. The shallow focus areas of the PSS, within the Vladikavkaz Fault, are likely to be excluded.

One of the first mentions about the Ardon deep fault appeared in the report [51] on the results of a gravimetric survey of 1: 50,000 scale in the Sadon, Fiagdon-

Assinovsk ore regions of Mountain Ossetia for 1973–1975, when the gravitational step with an amplitude up to 30 mGal was interpreted as the influence of the deep fault.

From this point on, the question of the existence and spatial position of the Ardon fault is not removed from the agenda, when structural-tectonic and seismological problems concerning the territory of the region are solved [52, 53, 54, 55].

To estimate the depth differentiability of the Ossetian Basin section, we used gravimetric data, which were reduced for three different densities of the intermediate layer: 2.0 g/cm³, 2.3 g/cm³ and 2.67 g/cm³. The density value of 2.67 g/cm³ for the intermediate layer makes it possible to estimate the influence of heterogeneities of the consolidated crust and classify the Ardon fault as a deep one, which can be traced to depths of 40 km.

Some authors believe that the Ardon Deep Fault is a component of the Kabardino-Sarpinsk submerging bone seam zone and belongs to the ancient tectonic structures of the Paleozoic – Hercynian orogenic cycle and it has a long-term development and deep-seated formation.

According to the geological and geophysical works, the Ardon deep fault zone, as a single structural zone, is traced from the neointrusivemassif of Tepli mountain, continues in the lower reaches of the Ardon River and then goes through Elkhotovo towards Budennovsk.

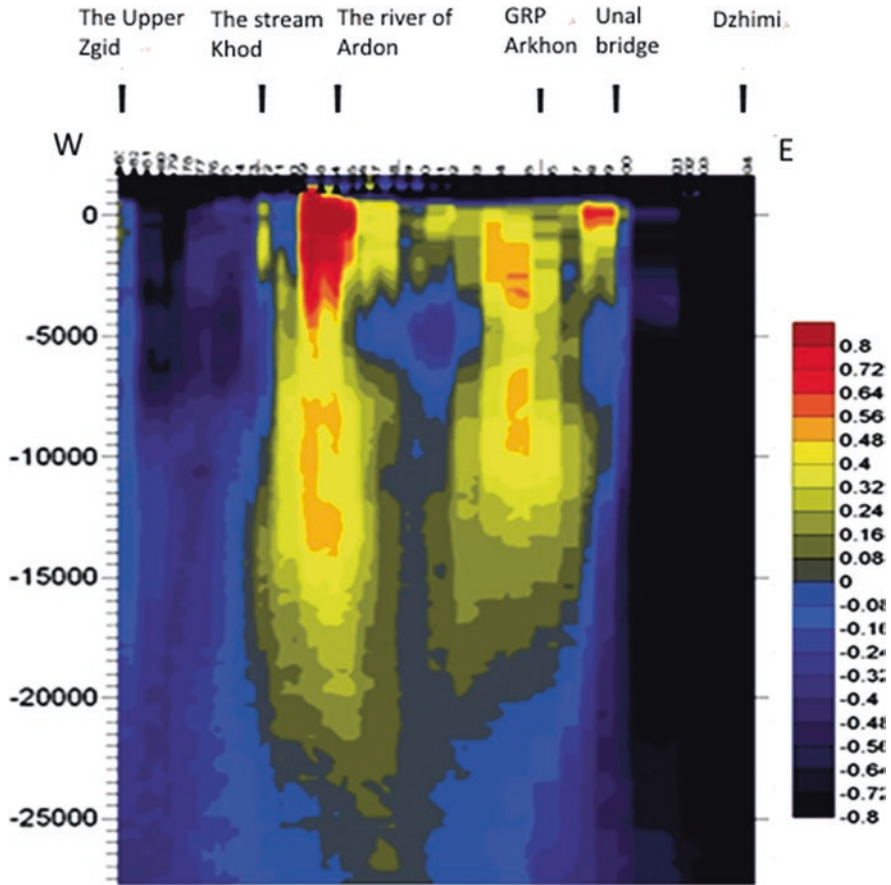
The Ardon Fault in the Tersk-Sunzhensk trough is clearly distinguished in aerial and satellite images by the terraces, it crosses the western margin of the Sunzhensk and Terek anticlinal zones. Using geophysical methods, the fault is revealed, starting from a depth of 2–4 km and confidently traced as the boundary of variously oriented deep structures. In the fault zone in the Pliocene-anthropogenic deposits, there are magmatic blocks with traces of breccia and cataclase (clippens), which indicates its activity.

In the zones of intersection with the faults of the general Caucasian direction, the Ardon fault controls the magmatic activity from the Paleozoic to the Paleogene; a hydrothermal mineralization, activation of hydrothermal processes and seismic hazard are associated with intersection zones. At the intersection of the Sunzha and Terek anticlinal zones with the Ardon fault, uplifts with the highest amplitudes and elevated pressures of Mesozoic-Cenozoic waters confined to Zamankul and Malgobek stress concentration centers are observed.

In the zone of Ardon fault influence Tsey and Songutidon intrusive massifs, the rupture faults of the northeast orientation, in which the ore bodies of the polymetal Zgid and Sadon deposits are located.

Figure 4 shows the velocity model of a geological section along the V. Zgid-Dzhimi observation profile. In the velocity model, two local objects are clearly distinguished, which differ sharply from the host media. The vertical dimensions of the objects substantially exceed the horizontal dimensions, while both objects are almost equal in size. The width of the zone is about 10–12 km and spatially coincides with the estimated azimuth of the strike of the Ardon deep fault in this area. The vertical span of the anomalously expressed object is 20–25 km. The upper part

MSS profile along the Upper Zgid–Dzhimi



Tone scale of deviations from the smoothed regional velocity model V_{SR}

Fig. 4 Velocity model of the geological section in the interpretation of the method of seismic sounding (MSS)

of the zone to a depth of 4.5 km appears more heterogeneous and processed by tectonic movements and deformations than the deep horizons. At depths of 4.5–5.3 km between the branches of the fault, there is a relic of a slightly modified high-velocity environment.

Being a regional submeridional fault that crosses tectonic zones of the all Caucasian orientation, the Ardon fault was seismically active in the past (the Late-Jurassic and Late-Cretaceous eras) and continues to be active to the present (it is associated with numerous mineral springs), which controls PSS zones, which in turn pose a seismic hazard.

In the rocks of the Terek-Caspian trough, the Ardon fault is reflected in abrupt changes in the thickness and facies of individual stratigraphic units of the sedimentary cover [35].

3 Hydrothermal Resources of the Region

Hydrothermal resources of the region can be estimated from the data of numerous wells, drilled purposefully for direct searches of mineral and thermal waters or sink for solving oil prospecting tasks.

44 wells out of the 102 structural and oil prospect wells drilled in 22 parts of the region have depths from 1000 to 3168 m, the remaining wells range from 500 to 998 m. Analysis of temperature regimes in the bottomhole part of the drilled wells allows us to distinguish two areas with anomalous temperature deviations of hydrothermal waters.

Lower-Karmadon (Fig. 3) – confined to the junction of open tearing cracks with the most elevated parts of the basement in anticlinal folds. Taking into account that in the Quaternary period right up to Wurm an outflow of andesitic lavas from the Kazbek volcanic center took place, the Lower-Karmadon mineralized thermal waters deposit is a manifestation of the influence of the heat field of the cooling substrate of extinct volcanic foci. Despite the fact that according to geophysical data, the likelihood of volcanic activity of Kazbek and Tepli volcanoes is excluded according to the gravity field data above them, which is characterized by relatively positive values caused, as it was noted above, by the surface layer with an excess density of 0.15 g/cm^3 , upper and lower boundaries of which are at depths of the order of 0.5 and 4.5 km. This layer appears to be a strata of deep-water Lower-Jurassic sediments with products of basic magmatism (dikes, intrusions, sills of the Kazbek diabase belt), which lies on the crystalline basement.

The volcanic structures of Tepli and Kazbek are not accompanied by local gravitational minimum anomalies similar to the Elbrus volcano, which excludes the presence of a chamber with a liquid substrate and negates the assumption of Kazbek or Tepli volcano [36, 37]. However, this does not mean that the fluids in the chambers have cooled to a temperature allowed by the geothermal gradient, as evidenced by the hot mineralized springs coming to the surface in the district and the thermal waters self-draining from the wells with elevated geothermal gradients. The heat flow around Kazbek and Teplivolcanic foci (petrothermal heat) of neovolcanism continues to heat the circulating waters, possibly simultaneously enriching them with mineral components.

Considering the last eruption of the Kazbek volcano (6000 years ago), the temperature of the volcanic substrate (about $900 \text{ }^\circ\text{C}$) and the temperature gradient of cooling of the “extinct” volcano $180\text{--}2000 \text{ }^\circ\text{C}$ over 1 million years, we can be sure that there is a high temperature environment in the chamber located on depth of about 5–7 km. Post-volcanic gas-hydro-thermodynamic effects on the Kolka Glacier, through opening cracks and rupture faults during an earthquake, is the

cause of historically recorded periodic catastrophic emissions (1752, 1834–1835, 1902, 1969–1970, 2002). The history of the dynamics of the Kolka glacier until 1752 is unknown [56–60].

The average temperature of the hydrotherms at the bottomhole of a series of exploration and production wells in the Lower-Karmadon area, mostly drilled to a depth of 420–520 m (one well -724 m), varies within 30–40 °C [61], which exceeds the geothermal gradient of the region, which according to observations of the temperature regime in the workings of the Sadon mine is 3°C per 100 m of deepening (at a depth of 1500 m from the day surface, the temperature in the workings reaches 45 °C).

In the bottomhole part of well No. 10 (depth 724 m), the temperature of the hydrothermal field reaches 54 °C, i.e. the geothermal gradient for the Lower-Karmadon open-pit mine is of the order of 6–7 °C, which characterizes the high potential of the petrothermal object. With such a temperature profile of the section, a renewable hydrothermal fluid with a temperature of 250 °C, sufficient to generate electricity, can be obtained at a well depth of 3500–3600 m.

In 1990–1993 as part of the program to expand the medical profile of the Tamisk sanatorium, at the stage of detailed searches for therapeutic-drinking and thermal waters, well No. 1BT was drilled to a depth of 2370 m. The well is located on the right bank of the Ardon river 2.5 km to the southeast of the town of Alagir RNO-A on the southern outskirts of Biragzang village (Fig. 3). Thermal ($T = 53$ °C) therapeutic-drinking mineral water was obtained in the well from sediments of the aquiferous complex of the Goteriv-Barrem suits of the Lower-Cretaceous (int. 2064–2160 m), operating reserves of 500 m³/day in category C₂ in the amount of 500 m³/day [2, 62].

The geothermal gradient is 2.24 °C, but the structure in which the well was drilled is of particular interest. As can be seen from Fig. 3, the well was driven at the intersection of the eastern border of the Ardon deep fault and the southern branch of the Vladikavkaz fault, characterized by active seismotectonic structures that have a continuation in the subcrustal environment (in the upper mantle) [42]. According to calculations, the seismic potential of the Vladikavkaz fault is estimated at 6.8–7.1 units of magnitude. Its activity is confirmed by the frequent earthquakes of magnitude 3–4 units in the area of Alagir, located at the intersection of the Ardon and Vladikavkaz faults.

The presence of thermal waters in the Hauterivian – Barreme sediments may indicate the influence of a local petrothermal object in the zone of tectonic faults or the existence of an active zone of PES at the intersection of these faults in the form of deformation friction, stress discharge, an influx of molten masses, etc.

With this interpretation of the results of the well No.1BT, a low geothermal gradient can be caused by the occurrence of a petrothermal object at considerable depth (4–5 km). When the thickness of the terrigenous-sedimentary strata of the Ossetian plain in the zone of maximum deflection of about 9 km (excluding the subsalt complex), sediments below 4.5–5.0 km are represented by Cretaceous and Jurassic sediments that crop out at the location of the well No.1BT, i.e. a sharp pinching-out of the Ossetian basin to the south in the zone of junction with the structure of the

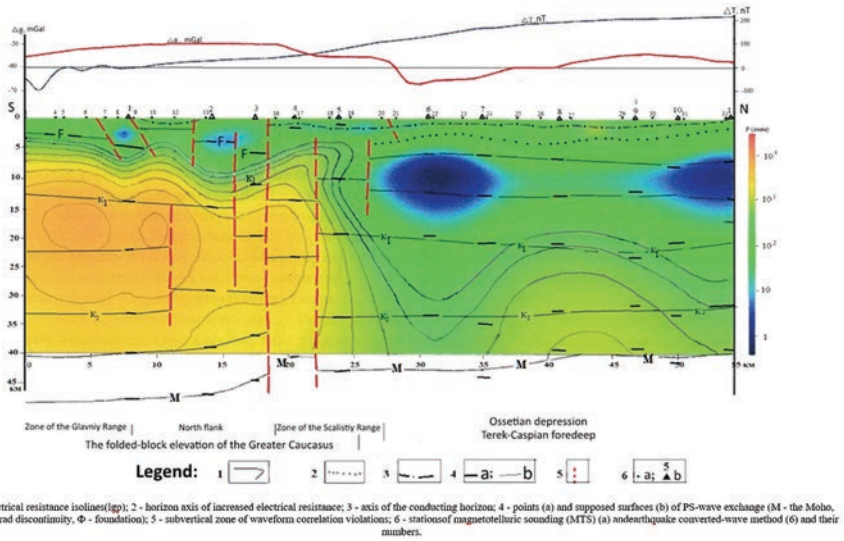


Fig. 5 Deep geological and geophysical model of the southern flank of the Genaldon profile

LesistiyRange of the fold-blocky uplift of the Greater Caucasus occurs. These two structures are separated by a fault zone, which is noted in the interval between the 17th and 28th kilometers of the studied Genaldon profile (Fig. 5). It is characterized by sharp displacements of the axes of electrical conductivity and the boundaries of the exchange of PS waves and increased gradients of the gravitational field. The deep fault zone, the thickness of which reaches 10 km, is a regional Pre-Caucasian fault and characterizes the junction zone of the Alpine Fold Region and the Scythian Platform. The zone is largely overlapped by the SkalistiyRange monocline complex, which represents the boundary structure between the Greater Caucasus orogen and the Terek-Caspian depression. Quantitative calculations for the gravitational step, observed at 28–29 km of the profile, have a northern incidence of the separation plane at angles of 65–70° with an effective density of about -0.1 g/cm^3 .

1 – electrical resistance isolines(lgp); 2 – horizon axis of increased electrical resistance; 3 – axis of the conducting horizon; 4 – points (a) and supposed surfaces (b) of PS-wave exchange (M – the Moho, K – Conrad discontinuity, Φ – foundation); 5 – subvertical zone of waveform correlation violations; 6 – stations of magnetotelluric sounding (MTS) (a) and earthquake converted-wave method (6) and their numbers.

The implementation and effective operation of heat objects at such depths is unlikely, and the optimality of selecting the location of the well No. *IBT* in the complex of geological, hydrogeological signs and paradigms for the existence of the active deep zones of the Ardon and Vladikavkaz faults involves deepening the No. *IBT* well in the subsalt complex to depths of about 4.5–5.0 km or the establish-

ment of a new well at a design depth of 4.0–4.5 km, having previously evaluated the section for the transition of a low-resistivity section to a high-resistivity one at the depths of the projected drilling.

With the continuation of deep faults into the mantle sphere, they can serve as collectors of the mantle substrate and hot fluids, the crystallization of which can form petrothermal objects that differ from host rocks in their physical characteristics. Such objects with a rich set of chemical elements can enrich the water circulating around their easily soluble elements, forming thermal mineralized waters.

4 Conclusions

A brief review of the results of structural and oil prospecting wells with limited information on the temperature regime of the sections does not allow for a detailed differentiation of the studied territory for classification by temperature. Since the direction of using the petrothermal heat is new and the study of the thermal field was not conducted, an analysis of the prospects for the development and use of geothermal sources was carried out based on observations of hydrothermal mineral springs, with reasonbelieving that hydrothermal sources are, in general, the result of petrothermal heat.

The available database allows to distinguish two areas at the first stage: Lower Karmadon (the average operational depth is about 450–500 m, connected to one degree or another with the late volcanic activity of Kazbek volcano) and Biragzang (the operating depth is 2370 m, coinciding with the articulation of the eastern side of the meridional Ardon deep fault and latitudinal Vladikavkaz fault). It seems efficient and cost-effective to use the renewable hydrothermal heat carrier by the circulating heating method based on the lavas of andesidacite from the Kazbek and Tepli volcanic centers, the Kion magmatic massif, the Lower Karmadon hydrothermal source and the seismological sources of active deep fractures [42].

The temperature indicator of 223 °C at a depth of 4002 m of the Tyrnauz deep well is a confirmation of the high thermal potential of the geodynamically active zones of the Central Caucasus for the localization of hydro- and petrothermal heat carriers satisfying efficient and cost-effective operation at well depths of 3500–4000 m.

At the initial stage, it is advisable to perform aerial thermal imaging of the mountainous part of the region in order to highlight promising areas with high potential for petrothermal heat.

Acknowledgments The research was supported by Russian Science Foundation (Project No. 19-47-02010 RSF-DST(2018):” Natural hazards and monitoring for mountain territories in Russia and India”.

References

1. Gnatus NA (2006) Thermal energy of the Earth as the basis of future heat power industry. *Novosti teplosnabzheniya* 12
2. Zaalishvili VB, Dzhgamadze AK (2015) Geothermal waters of North Ossetia. In: Proceedings of the international scientific-practical conference “Geoenergy”, June 19–21, 2015. Grozny: GGNTU, Makhachkala: ALEF, pp 52–60
3. Zaalishvili VB, Melkov DA, Burdzieva OG (2015) Possibilities of geothermal energy use on the North Caucasus (a view on a problem from Azores example). *Ecol Environ Conserv* 21(S Dec):145–149
4. Burdzieva OG, Zaalishvili VB, Beriev OG, Kanukov AS, Maysuradze MV (2016) Mining impact on environment on the North Ossetian territory. *Int J Geomate* 10(19):1693–1697
5. Burdzieva OG, Zaalishvili VB, Aiskhanov SK, Kanukov AS, Margoshvili MT, Yakhikhazhiev SK (2019) Environmental State of North Caucasus Region, Caused by Mining Activities. In: VIII science and technology conference “Contemporary Issues of Geology, Geophysics and Geo-ecology of the North Caucasus” (CIGGG 2018) Atlantis Press, 2019
6. Golik VI, Burdzieva OG, Zaalishvili VB, Kanukov AS, Melkov DA, Arkhireeva IG, Dzobelova LV (2019) Problems of seismic safety of ore mining. In: VIII science and technology conference “Contemporary Issues of Geology, Geophysics and Geo-ecology of the North Caucasus” (CIGGG 2018) Atlantis Press, 2019
7. Zaalishvili V, Dzhgamadze A, Gogichev R, Dzeranov B, Burdzieva O (2018) Changes in the qualitative characteristics of groundwater of the Ossetian artesian aquifer. *Int J Geomate* 15(51):22–30
8. Milanovsky EE, Khain VE (1963) Geological structure of the Caucasus. Moscow University, Moscow. pp 222–296
9. Zonenshain LP, Kuzmin MI, Natapov LM (1990) Tectonics of lithosphere plates on the territory of the USSR, vol 2. Nedra, Moscow, pp 168–175
10. Baranov GI, Grekov II (1982) Geodynamic model of the greater Caucasus. In: Collection of the reports at the 2nd Caucasus geodynamics seminar in Tbilisi, Apr.1980. Nauka, Moscow, p 51
11. Baranov GI (1991) Tectonic studies in the North Caucasus. In: Abstracts of the VII territorial conference on geology and minerals of the North Caucasus. Essentuki, pp 91–93
12. Baranov GI, Omelchenko VA, Prutsky NI (1995) The sequence of tectonic events and their expression in the modern structure of the North Caucasus. In: Main problems of geological study and use of the mineral resources of the North Caucasus: materials of the VIII anniversary conference on geology and mineral resources. Essentuki, pp 63–77
13. Compilation of a specialized geological base of 1: 50000 scale for a predictive metallogenic map of Mountain Ossetia: a research report. Book 2 / Sevogeologoozvedka; chief Oikhovskiy G.P., Tibilov S.M. – Vladikavkaz, 1998. pp 55–68
14. Chotchaev KhO, Zaalishvili VB, Shempelev AG, Berger MG, Burdzieva OG, Zaks TV, Makiev VD, Trofimenko SN (2019) Structural-material complexes as indicators of geodynamic situations by example of eastern part of Central Caucasus. In: VIII science and technology conference “contemporary issues of geology, geophysics and geo-ecology of the North Caucasus” (CIGGG 2018). Atlantis Press
15. Rogozhin EA, Milyukov VK, Zaalishvili VB, Ovsyuchenko AN, Mironov AP, Gorbatikov AV, Melkov DA, Dzeranov BV (2019) Characteristics of modern horizontal movements in central sector of greater Caucasus according to GPS observations. In: VIII science and technology conference “contemporary issues of geology, geophysics and geo-ecology of the North Caucasus” (CIGGG 2018). Atlantis Press
16. Zaalishvili VB, Chotchaev KhO., Magkoev TT, Melkov DA, Nikolaev AV, Svalova VB, Arkhireeva IG, Dzeranov BV (2019) Physical fields as derivative of deformation of rock massifs and Technology of Their Monitoring. In: VIII science and technology conference “contemporary issues of geology, geophysics and geo-ecology of the North Caucasus” (CIGGG 2018). Atlantis Press

17. Zaalishvili VB, Chotchaev KO, Shempelev AG, Melkov DA, Burdzieva OG, Parada SG, Dzeranov BV, Dzhgamadze AK (2019) Geodynamic situation in Central Caucasus and structural complexes on depth section of Genaldon profile. In: VIII science and technology conference "contemporary issues of geology, geophysics and geo-ecology of the North Caucasus" (CIGGG 2018). Atlantis Press
18. Zaalishvili VB, Yurkov AK, Melkov DA, Kozlova IA, Kanukov AS, Demezko DY, Morozov PS (2019) Assessment of sensitivity zone of radon and temperature measurements in study of process of tectonic earthquakes preparation. In: VIII science and technology conference "contemporary issues of geology, geophysics and geo-ecology of the North Caucasus" (CIGGG 2018). Atlantis Press
19. Baranov GI (1991) The pre-Hercynian structure of the greater Caucasus. In: Abstracts of the VII Regional Conference on Geology and Minerals of the North Caucasus. Essentuki, pp 104–106
20. Baranov GI (1995) Geodynamic development of the Greater Caucasus in the Paleozoic. In: The main problems of geological study and use of the mineral resources of the North Caucasus: materials of the VIII anniversary conference on geology and mineral resources. Essentuki, pp 54–56
21. Parnachev VP (2014) The bases of geodynamic analysis. Publishing house NTL, Tomsk, pp 243–277
22. Schulz SS, Ergashev SE, Gvozdev VA (1991) Geodynamic reconstruction: a methodological guide. Nedra, Leningrad, p 144
23. Zonenshain LP, Kuzmin MI, Moralev VM (1976) Global tectonics, magmatism and metallogeny. Nedra, Moscow, p 231
24. Srabonyan MKh, Snezhko VA, Dolya AN, Potapenko YuYa (1995) Magmatic complexes of the North Caucasus and the problem of their systematization. In: Proceedings of the VIII Anniversary conference on geology and minerals. Essentuki, pp 43–63
25. Snytko AS, Zhukov BV (1991) Comprehensive aerogeophysical works of 1:25 000 scale on Urukhsakaya area. Nevskgeologiya, Leningrad, p 39
26. Lebedko GI, Usik VI (1985) Geochronology of the North Caucasus. RSU, Rostov-on-Don, p 148
27. Enna NL, Kirichko YA, Pismennyi AN (1997) Reporting materials on additional site exploration (ASE)-50. Pages: K-38-28-B; K-38-39-B; K-38-40-a. Urukhsakaya geological-mapping party (GMP). Essentuki
28. Menert K (1971) Migmatites and the origin of granites. Mir, Moscow
29. Korsakov SG, Semenukha IN, Gorbova SM (2002) State geological map of the Russian Federation / – 1: 200 000. Second edition. Caucasian series, sheet L-37-XXXIV. VSEGEI, St/Petersburg, p 182
30. Sterlenko YA, Krisyuk IM, Dagayev LA (1978) To the tectonic zoning of mountain Ossetia and mountain Chechen-Ingushetia. In: Collection of works. Questions of petroleum geology, hydrogeology and geophysics of the Caucasus. Grozny, pp 53–59
31. Shempelev AG (2008) The deep structure of the Kazbek megablock of the Greater Caucasus. In: Proceedings of the XLI Tectonic Meeting "General and Regional Problems of Tectonics and Geodynamics". Moscow, pp 463–467
32. Fedotov SA, Utkin IS, Zaalishvili VB, Utkina LI (2011) Evaluation of the possibility of using the heat accumulated by the magmatic source of the Elbrus volcano in the enclosing rocks for the production of electricity. Geol Geophys South Russ 11(1):32–37
33. Zaalishvili VB, Nevskaya NI, Nevsky LN, Shempelev AG (2014) On the peculiarities of geophysical fields above the Elbrus and Kazbek. Geol Geophys South Russ 14(4–2):27–33
34. Shempelev AG, Zaalishvili VB, Kukhmazov SU (2017) Deep structure of the western part of the Central Caucasus from geophysical data. Geotectonics 51(5):479–488
35. Zaalishvili VB, Nevskaya NI, Nevskii LN, Shempelev AG (2015) Geophysical fields above volcanic edifices in the North Caucasus. J Volcanol Seismol 9(5):333–338

36. Zaalishvili VB, Burdzieva OG, Dzhgamadze AK (2015) Geothermal waters of North Ossetia. *Ecol Environ Conserv* 21(S Dec):151–155
37. Gorbatikov AV, Ovsyuchenko AN, Rogozhin EA (2011) The structure of the zone of the Vladikavkaz fault according to the results of a study by a complex of geological and geophysical methods. *Geol Geophys South Russ* 11(2)
38. Rogozhin EA, Gorbatikov AV, Zaalishvili VB, Stepanova MY, Kharazova YuV ANV, Melkov DA, Dzeranov BV, Dzeboev BA, Gabaraev AF (2013) New ideas about the deep structure of the Ossetian sector of the greater Caucasus. *Geol Geophys South Russ* 13(4):3–7
39. Gorbatikov AV, Rogozhin EA, Stepanova MY, Kharazova YV, Andreeva NV, Perederin FV, Zaalishvili VB, Melkov DA, Dzeranov BV, Dzeboev BA, Gabaraev AF (2015) The pattern of deep structure and recent tectonics of the greater Caucasus in the Ossetian sector from the complex geophysical data. *Izvestiya Phys Solid Earth* 51(1):26–37
40. Rogozhin EA, Gorbatikov AV, Zaalishvili VB, Stepanova MY, Andreeva NV, Kharazova YV (2015) New data on the deep structure, tectonics, and geodynamics of the greater Caucasus. *Dokl Earth Sci* 462(1):543–545
41. Zaalishvili VB, Chotchaev KhO, Melkov DA, Kanukov AS, Magkoev TT, Gabeeva IL, Dzobelova LV, Shepelev VD (2019) complex analysis of geological data and use of velocity model of MMS on Central Caucasus sections. In: VIII science and technology conference “contemporary issues of geology, geophysics and geo-ecology of the North Caucasus” (CIGGG 2018). Atlantis Press
42. Zaalishvili VB, Rogozhin EA (2011) Assessment of seismic hazard of territory on basis of modern methods of detailed zoning and seismic microzonation. *Open Construct Build Technol J* 5:30–40
43. Zaalishvili V (2016) Spectral characteristics of seismic waves at strong ground motions. *Int J Geomate* 10(20):1706–1717
44. Zaalishvili V, Melkov D, Gabeeva I (2016) Expected seismic intensity assessment taking into account local topography site effect. *Int J Geomate* 10(19):1680–1686
45. Zaalishvili V, Melkov D, Kanukov A, Dzeranov B (2016) Spectral-temporal features of seismic loadings on the basis of strong motion wavelet database. *Int J Geomate* 10(19):1656–1661
46. Zaalishvili VB, Kanukov AS, Melkov DA, Makiev VD, Dzobelova LV (2018) Development of a unified model of geoinformation system for city planning and integration. *Int J Geomate* 15(51):160–166
47. Zaalishvili VB, Melkov DA, Kanukov AS, Dzeranov BV, Shepelev VD (2016) Application of microseismic and calculational techniques in engineering-geological zonation. *Int J Geomate* 10(19):1670–1674
48. Ganapathy GP, Zaalishvili VB, Melkov DA, Dzeranov BV, Chernov YuK, Kanukov AS (2019) Soil Liquefaction Susceptibility Assessment of Mozdok City (North Ossetia, Russia). In: VIII Science and Technology Conference “Contemporary Issues of Geology, Geophysics and Geo-ecology of the North Caucasus” (CIGGG 2018) Atlantis Press
49. Kharebov CS, Zaalishvili VB, Zaks TV, Baskaev AN, Archireeva IG, Gogichev RR, Maysuradze MV, Chitishvili MI (2019) Influence of soils on impact parameters of seismic effect. In: VIII science and technology conference “contemporary issues of geology, geophysics and geo-ecology of the North Caucasus” (CIGGG 2018). Atlantis Press
50. Zaalishvili VB, Melkov DA, Gabeeva IL, Makiev VD, Kanukov AS, Gabaraev AF, Morozov FS, Tuavev GE (2019) Macroseismic manifestation of seismic events of different intensity on territory of Vladikavkaz. In: VIII science and technology conference “contemporary issues of geology, geophysics and geo-ecology of the North Caucasus” (CIGGG 2018). Atlantis Press
51. Kvyat ZG, Tibilov SM Report on a gravimetric survey of 1: 50000 scale in the Sadon and Fiagdon-Assinovsky ore regions of the mountain Ossetia for 1973–1975 period. Geopartiya, Nalchik
52. Svalova VB, Zaalishvili VB, Ganapathy GP, Nikolaev AV (2018) Natural hazards and disasters in mountain areas. *Geol Geophys South Russ* 18(2):99–115

53. Zaalishvili VB, Nevskaya NI, Nevsky LN, Melkov DA, Shempelev AG (2012) Monitoring of hazardous geological processes in the area of the supposed Ardon fault and in the section of the pipeline route from the villages of Dzuarikau to the border of the RNO-Alania. *Geol Geophys South Russ* 12(4):25–32
54. Krisyuk IM, Smirnova MN (1966) About the Ardon deep fault. *Proceedings of GSTOU*, issue 29, pp 28–30
55. Nechaev YuV SAP (2007) New technologies for monitoring the internal structure of volcanoes. *Bull Vladikavkaz Scientific Center* 7(4)
56. Zaalishvili VB, Nevskaya NI, Mel'kov DA (2014) Instrumental geophysical monitoring in the territory of northern Caucasus. *Izvestiya Phys Solid Earth* 50(2):263–272
57. Zaalishvili VB, Melkov DA (2014) Reconstructing the Kolka surge on September 20, 2002 from the instrumental seismic data. *Izvestiya Phys Solid Earth* 50(5):707–718
58. Zaalishvili VB, Berger MG, Maliev IN, Melkov DA, Kanukov AS, Makiev VD (2016) Development of the instrumental monitoring system of the Kazbek volcanic center. *Geol Geophys South Russ* 16(4):44–51
59. Zaalishvili VB, Melkov DA, Dzeranov BV, Morozov FS, Tuaevev GE (2018) Integrated instrumental monitoring of hazardous geological processes under the Kazbek volcanic center. *Int J Geomate* 15(47):158–163
60. Zaalishvili VB, Chotchaev KO, Shempelev AG (2018) Signs of the geodynamic situation and elements of the structural-material complexes of the Central Caucasus in the deep section of the Genaldon profile. *Geol Geophys South Russ* 18(4):58–74
61. Bulatsev GP, Grigorovich VS (1988) Report on the results of exploration at the Korinsky field with the calculation of operating reserves as of December 01, 1988, Vladikavkaz
62. Dzhgamadze AK, Paschenko VI (2008) Report on the results of hydrogeological studies on well No. 1BT with the calculation of operating reserves of thermal mineral waters as of July 01, 2008

Models of Geothermal Areas: New Insights from Electromagnetic Geothermometry



Viacheslav V. Spichak and Olga K. Zakharova

1 Introduction

Temperature estimation in the Earth's crust is usually based on temperature logs or heat flow gradient data. Actual measured temperature data are limited to the bore-hole depths amounting in most cases to 1–3 km. Studies of hydrothermal processes showed that specific properties of the underground fluid composition are closely related to the geothermal conditions of their formation.

Therefore, studying these properties provides information about the thermal state of the interior that complements the results of direct thermometry and serves as a basis for forecasting the deep geothermal conditions in scantily explored regions.

The temperature dependency of the composition of some characteristic hydrothermal components is established experimentally with so-called indirect geothermometers. Using empirical or semi-empirical formulas, one can roughly estimate the “base depth” temperature from the known amount or proportion of these components in areas of surface manifestations of thermal activity. Researchers often use indirect estimates based on geological (Harvey and Browne [19]), geochemical [21] or gas composition [2] data to guess the temperature at characteristic depths.

Despite the fact that the aforementioned indirect geothermometers could serve as useful tools for estimating temperatures at some depths and, thus, for constraining the sub-surface temperature, they cannot be used neither for constructing the temperature distribution in the studied area nor for its interpolation / extrapolation from the temperature well logs.

Using the electrical resistivity data of rocks seems to be the most natural approach to indirectly estimate temperature, because this property is commonly a function of

V. V. Spichak (✉) · O. K. Zakharova
Goelectromagnetic Research Centre IPE RAS, Moscow, Troitsk, Russia

© The Author(s), under exclusive license to Springer Nature
Switzerland AG 2021

V. Svalova (ed.), *Heat-Mass Transfer and Geodynamics of the Lithosphere*,
Innovation and Discovery in Russian Science and Engineering,
https://doi.org/10.1007/978-3-030-63571-8_4

temperature. Temperature dependence of the electrical resistivity of rocks permits its use for the temperature estimation using some empirical formula. Similar methods can be used accordingly on a regional or even global scale based on empirically matched data [28] or data determined from the global magnetovariational sounding [14]. At the same time, the complex, non-homogeneous structure of the Earth and the lack of information about its properties allow construction of only very crude temperature models based on assumptions regarding the electrical conductance mechanisms.

On the other hand, the electromagnetic (EM) sounding of geothermal areas (see, for instance, the review paper by [34], and references therein) may provide indirect temperature estimation in the Earth's interior based on electromagnetic measurements at the surface. Spichak and Zakharova [35] have developed an indirect EM geothermometer, which does not require prior knowledge or guessing regarding the electrical conductance mechanisms in the Earth's crust. In this paper, we review the application of EM geothermometry to the location of the deep heat sources, estimating dominating heat transfer mechanism at large depth and constraining location of supercritical reservoir.

2 Electromagnetic Geothermometry

Parameter estimation in the space between the drilled boreholes is usually carried out by linear interpolation or geostatistical tools based on the spatial statistical analysis of the approximated function, "kriging" being the most often used procedure. Using the electrical resistivity profiles revealed from the electromagnetic sounding data one could reduce the interpolation errors since in this case the database is increased due to adding new (resistivity) data related somehow to the temperature. Unlike other indirect geothermometers it enables the temperature estimation in the given locations in the earth, which makes it an indispensable tool in geothermal exploration and exploitation of the geothermal systems.

Spichak et al. [40] have shown that the temperature interpolation accuracy in the interwell space is controlled mainly by 4 factors related to the characteristics of the space between the place where the temperature profile is estimated and related EM site: faulting, meteoric and groundwater flows, spacing, and lateral geological heterogeneity (though, the latter factor being less restrictive, if appropriate EM inversion tools are used). Therefore, prior knowledge of the geology and hydrological conditions in the region under study can help to correctly locate the EM sensors with respect to the areas where the temperature is to be predicted and thereby reduce the estimation errors.

Optimal methodologies for calibration of the indirect electromagnetic geothermometer in different geological environments were developed [37, 40]. It was shown that the temperature estimation by means of the EM geothermometer calibrated by 6–8 temperature logs results in 12% average relative error. Prior knowledge of the geology and hydrological conditions in the region under study can help

to correctly locate the EM sensors with respect to the sites where the temperature is to be predicted and thereby reduce the estimation errors up to 5–6%.

Special attention was paid to the application of indirect EM geothermometer to the temperature extrapolation in depth [36]. The results obtained in the Tien Shan area indicate that the temperature extrapolation accuracy essentially depends on the ratio between the well length and the extrapolation depth. For example, when extrapolating to a depth twice as large as the well depth the relative error could be less than 2%. This result makes it possible to increase significantly the deepness of indirect temperature estimation in the earth's interior based on the available temperature logs, which, in turn opens up the opportunity to use available temperature logs for estimating the temperatures at depths, say, 3–10 km without extra drilling [29, 30].

EM geothermometry was successfully used for deep temperature assessment in the geothermal areas Soultz-sous-Forêts, France [32], Hengill, Iceland [39] and Travale, Italy [31]. Below we briefly discuss the main findings of these studies summarized in the monograph [38].

3 Constraining Supercritical Reservoir

It is often necessary to recognize the type of the heat carrier circulating in the geothermal system. In particular, it is difficult to distinguish between hot aqueous and gaseous fluids solely basing on the electrical resistivity and/or seismic velocities' cross-sections without prior information, which may come from geology, geochemistry, well logs, etc. However, even joint analysis of the resistivity and seismic velocities data does not always provide enough information, which might enable to draw conclusions on the type of geothermal fluids (see, for instance, [20]). On the other hand, using temperature model of the study area may provide necessary information for constraining location of geothermal reservoirs, particularly, at large depth.

This could be illustrated by the case study of the Travale geothermal area, Southern Tuscany, Italy (Fig. 1). For better understanding of the thermal structure of this area Gola et al. [17] systematized available structural, geological, geochemical, geochronological, petrological and geophysical data published by many researchers during last 30 years. According to this paper there are two main geothermal reservoirs in this area: the "shallow reservoir" hosted in the evaporite-carbonate units (about 0.7–1.0 km b.g.l. on average and with temperature from 150 °C to 260 °C) and the "deep reservoir" hosted in the metamorphic succession and Neogene granitoids (about 2.5–4.0 km b.g.l. and with temperature from 300 °C to 350 °C) [5, 27]. Fluids dominantly of meteoric origin at vapor phase circulate in both reservoirs [9]. The meteoric recharge occurs through the carbonate outcropping formations; besides a lateral input from the regional aquifers surrounding the hydrothermal reservoirs is also assumed, presumably induced by the actual exploitation process [9, 27].

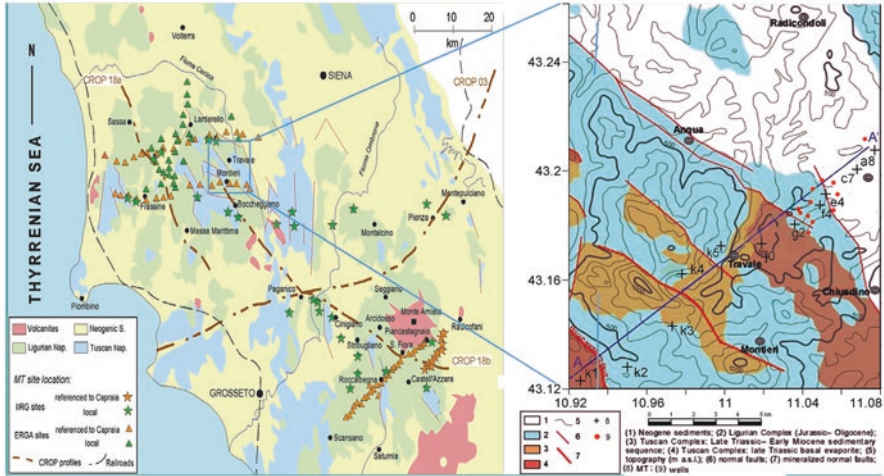


Fig. 1 (a) The simplified tectonic scheme of the region and its location; (b) location of MT profile AA' (MT sites are marked by crosses) [7, 24]

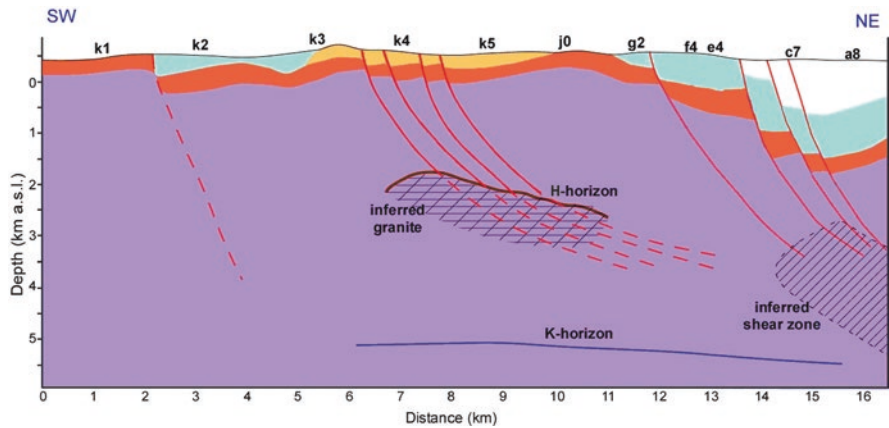


Fig. 2 The schematic section cutting the geological structures along the eastern boundary of the Pomarance basin along AA' profile (see its location in the Fig. 1b), which accommodates the Travale geothermal anomaly (Modified after Bellani et al. [4]). The temperature isolines are marked in °C

2D and 3D seismic exploration activities carried out in the last decades provided evidences of two distinct seismic markers, referred to as “H-horizon” and “K-horizon” (shown in Fig. 2), discontinuously characterizing the entire area. Drilling data show that in some cases the H-horizon is located in correspondence of the thermo-metamorphic aureole of Neogene granitoids [6] and many wells produced super-heated steam from this level. The deeper K-horizon has similar amplitude pattern, but locally showing bright spot features and a more continuous spatial

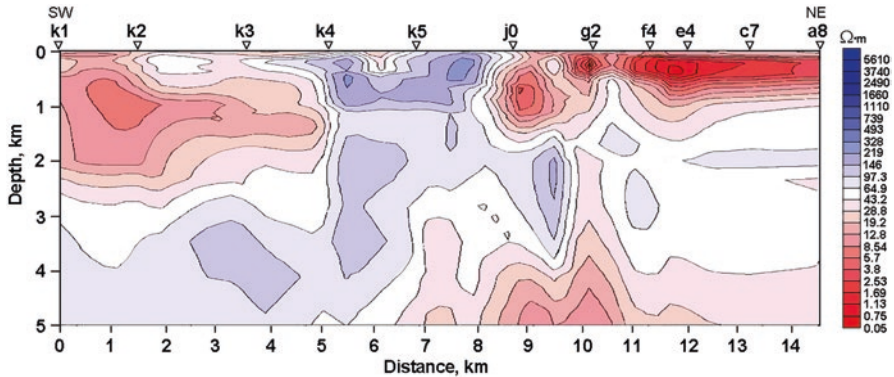


Fig. 3 Electrical resistivity model of the Travale area along profile AA' revealed from magnetotelluric data [26]

extension with respect to H-horizon. The nature and the origin of these horizons are still under debate since 1983 (e.g., [3, 8, 23]), as it has not yet been drilled with the presumable exception of the San Pompeo 2 well. The thermobaric conditions extrapolated at this level ($P \approx 30$ MPa and $T > 400$ °C) do not seem to be compatible with the deep geothermal reservoir so far exploited characterized by a sub-hydrostatic pressure controlled by its current super-heated steam condition [27].

Uncertainties mentioned above could be reduced by considering the resistivity and temperature models of this area. Pushkarev [26] has built a 2D electrical resistivity model along profile AA' shown in Fig. 1b (Fig. 3). It is seen that resistivity manifests heterogeneous behavior, which correlates with large seismic anisotropy (16%) [25] and generally ranges from 10 to 100 Ω.m, which indicates presence of fluid saturated rocks.

Spichak [31] has used EM geothermometer for constructing the temperature model along the same profile (Fig. 4) basing on the resistivity model mentioned above and temperature well logs available in this area. Its analysis explains the observations not addressed by previous conceptual models of this area. In particular, the isotherm $T_{SCF} = 375$ °C characterizing possible appearance of supercritical fluids practically coincides with the upper reflection horizon H (see Fig. 2 for its location) while the isotherm $T_{BDT} \approx 550-600$ °C characterizing granite solidus corresponds to location of the lower reflection horizon K.

These inferences could be interpreted as follows. The lower reflection horizon K marks transition from cooling partially melted magmatic intrusion (below the depth of 5 km) being in a plastic state to brittle granitic massif (above the isotherm $T_{BDT} \approx 600$ °C) filled by mixture of deep magma waters migrated towards shallow levels, products of water – rock interaction and meteoric waters [7] being in a supercritical state under the pressure above 220 Kbar and temperature ranging between T_{SCF} and T_{BDT} . The wave velocity contrast at the lower reflection horizon K could be caused by sharp decrease of the dissimilar shear rigidity during transition from brittle to ductile medium [11].

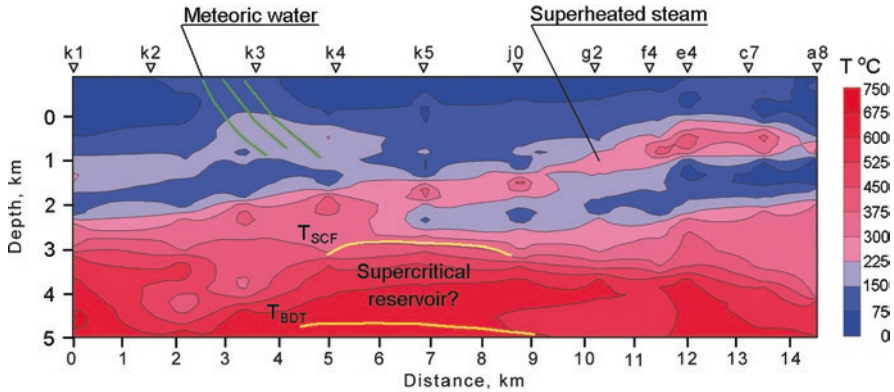


Fig. 4 Temperature model of the Travale area along profile AA' built using EM geothermometer [31]. T_{SCF} and T_{BDT} indicate locations of isotherms corresponding to supercritical fluid threshold and brittle/ductile transition, accordingly

At shallow depths (< 2 km) decreasing pressure and temperatures support transition from supercritical fluids below location of the isotherm T_{SCF} and superheated mixture of steam and gas. However, this transition is not so sharp as that between brittle and ductile rocks at the depth of the isotherm T_{BDT} . Accordingly, the upper reflection horizon H separating supercritical fluids at temperatures above T_{SCF} and heavily fractured gas-steam bearing rocks manifests non-continuous behavior. It is worth mentioning in this relation that shallow (0–2 km) inclined slab beneath the sites k5-f4 (Fig. 4) often interpreted as a “shallow reservoir” (see, for instance, [17], and references therein) could be considered as a channel of transportation of the hot steam from supercritical reservoir to the surface.

4 Heat Sources and Seismicity

The application of the indirect EM geothermometer enables building 3-D temperature model of the study area, which could offer a comprehensive database for further analysis in geothermal terms. It was used by Spichak et al. [39] for detecting heat sources and explaining the seismicity structure in the Hengill geothermal area (Iceland).

The high-temperature Hengill area is a triple junction zone of intersection of the Western Volcanic Zone (WVZ), the Reykjanes Peninsula Rift (RPR), and the South Icelandic Seismic Zone (SISZ), which is located in the southwest of the island (Fig. 5, upper panel). The Hengill volcanic complex comprises several interconnected geothermal fields located in different directions with respect to the Mt. Hengill (marked by H in Fig. 5, lower panel): the Hveragerdi (Hv) area in the southeast; the Nesjavellir (Ne) area in the northeast, and Hellisheidi (He) area in the southwest.

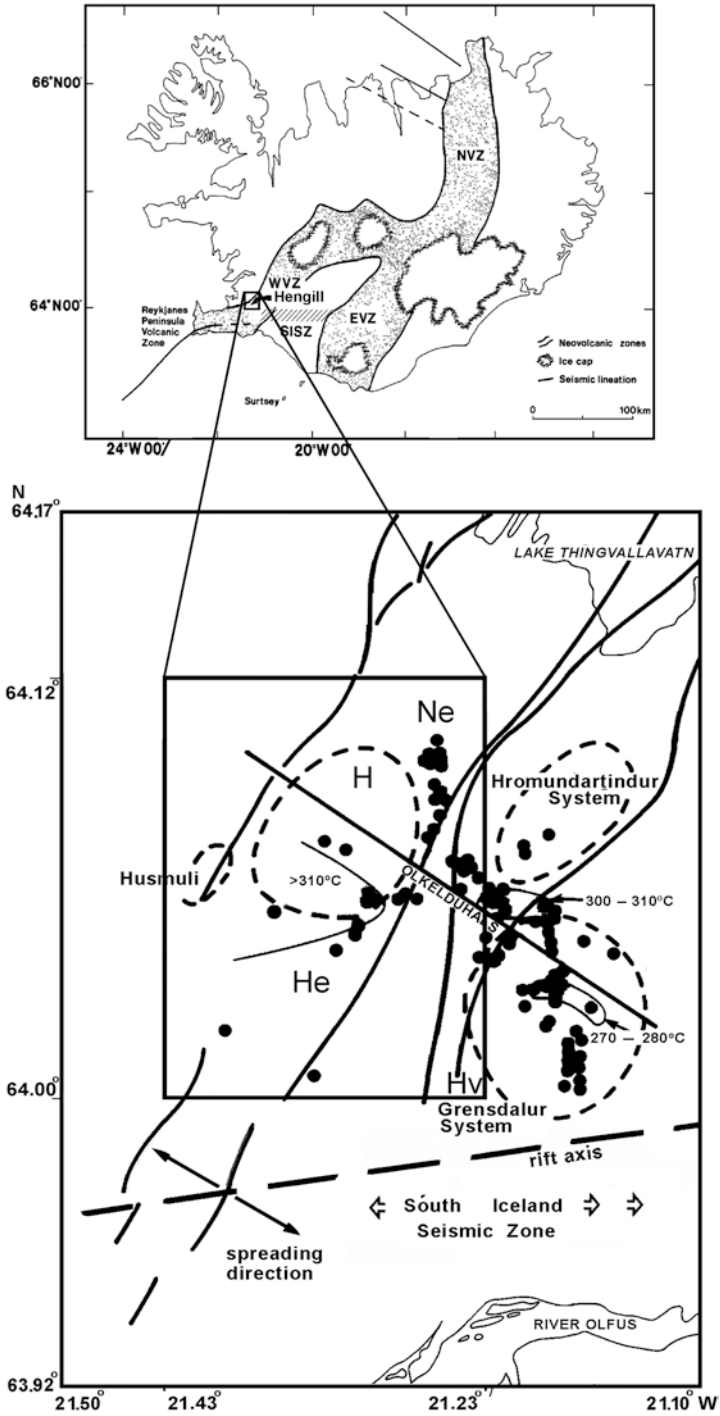


Fig. 5 Upper panel: map of the study area. Lower panel: schematic tectonic map of the Hengill triple junction. Bold lines indicate the NNE trending eruption/fissure zones. The eruptive centers are outlined by dashed lines. Hot springs and fumaroles are indicated by dots. The line connecting the Hengill and Grendalur volcanoes indicates the axis of the transverse tectonic structure. Rectangle bounds the studied area. (Modified from Foulger and Toomey [16])

Overall, the region and its immediate vicinity hosts four centers of volcanic activity (Fig. 5, lower panel): the Hengill area mentioned above, as well as the Grensdalur, Hromundartindur, and Husmuli areas. The Hengill volcanic complex comprises an active central volcano and a swarm of fractures trending north-northeastwards (Fig. 6). The secondary tectonic structural trend, transverse to the dominant NNE-SSW trend of the signs of crustal accretion, has developed in the zone connecting the centers of the Hengill and Grensdalur volcanic complexes and extending along the Olkelduhals line (Fig. 5, lower panel).

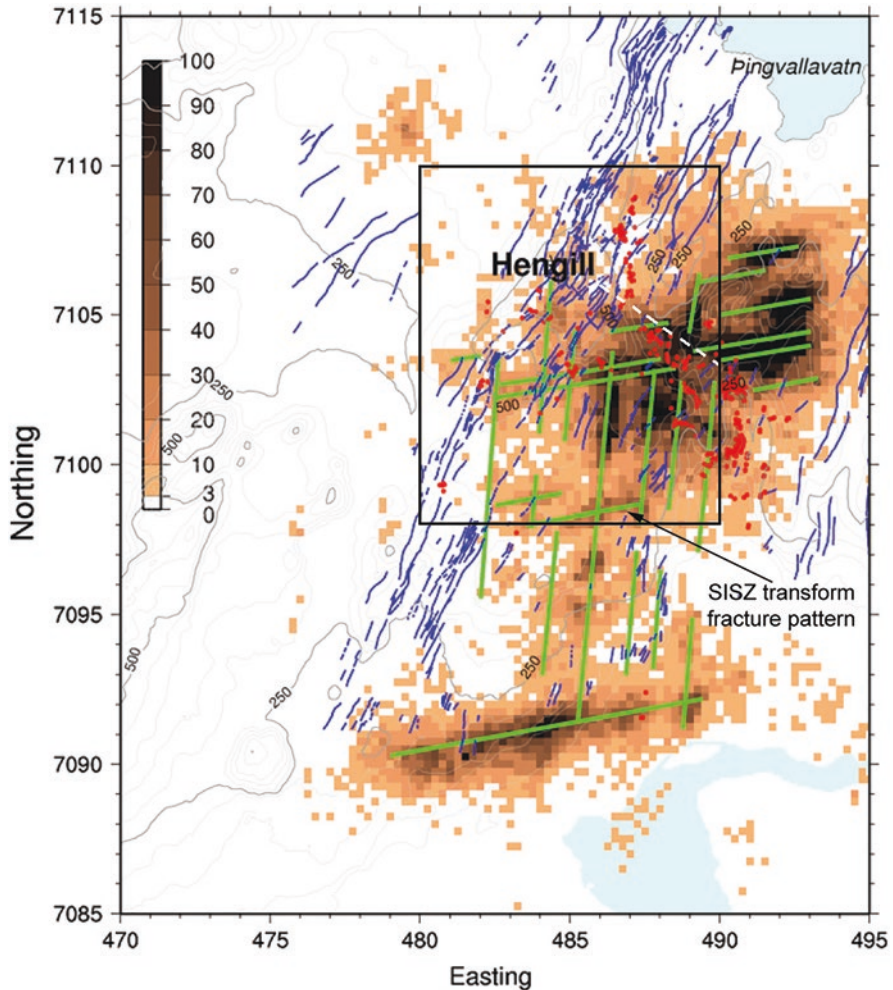


Fig. 6 Density of seismic epicentres from 1991 to 2001 and inferred transform tectonic lineaments (thick lines) based on the overall distribution of the seismicity (thin lines - faults and fissures mapped on the surface). Rectangle bounds the studied area indicated in the Fig. 5. (Redrawn from Árnason et al. [1])

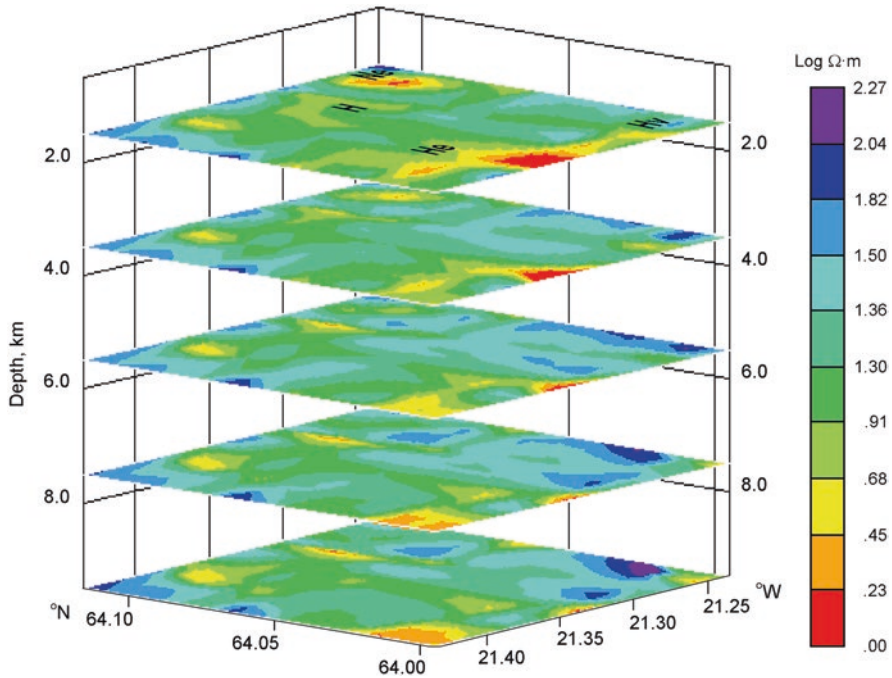


Fig. 7 Slices of the electrical resistivity distribution in the Hengill area at different depths [33]

Spichak et al. [33] have built 3-D electrical resistivity model of the Hengill geothermal area up to the depth of 20 km (Fig. 7). Basing on this model the authors indicated that the heat source in the upper crust of the region could be the upflow of highly conductive material from below 20 km, its accumulation in the subsurface reservoirs and further spreading in the rheologically weak layer at depths 5–15 km. The obtained results confirm the mantle origin of the heat sources in this region, which was hypothesized earlier. Meanwhile, no continuous well conductive layer with resistivities less than 10 Ohm.m is detected in the depth range 10–25 km. Instead local well conducting areas were found linked with each other both in horizontal and vertical directions.

Spichak et al. [39] have constructed the first 3-D temperature model of the Hengill geothermal area (Figs. 8 and 9). The analysis of the temperature model enabled to draw important conclusions about the structure of this geothermal area, location of heat sources, seismicity pattern, etc., and formulate a new conceptual model of the Icelandic crust. According to this model the background temperature of the Icelandic crust above 20 km does not exceed 400°C. It is overlapped by a network of interconnected high-temperature low resistive channels, which braid through the crust mainly at a level of 10–15 km and root to a depth greater than 20 km.

Accordingly, the probable heat sources feeding the geothermal system are supposed to be the intrusions of the hot partially molten magma upwelling from the mantle through the faults and fractures. In particular, it was inferred that the

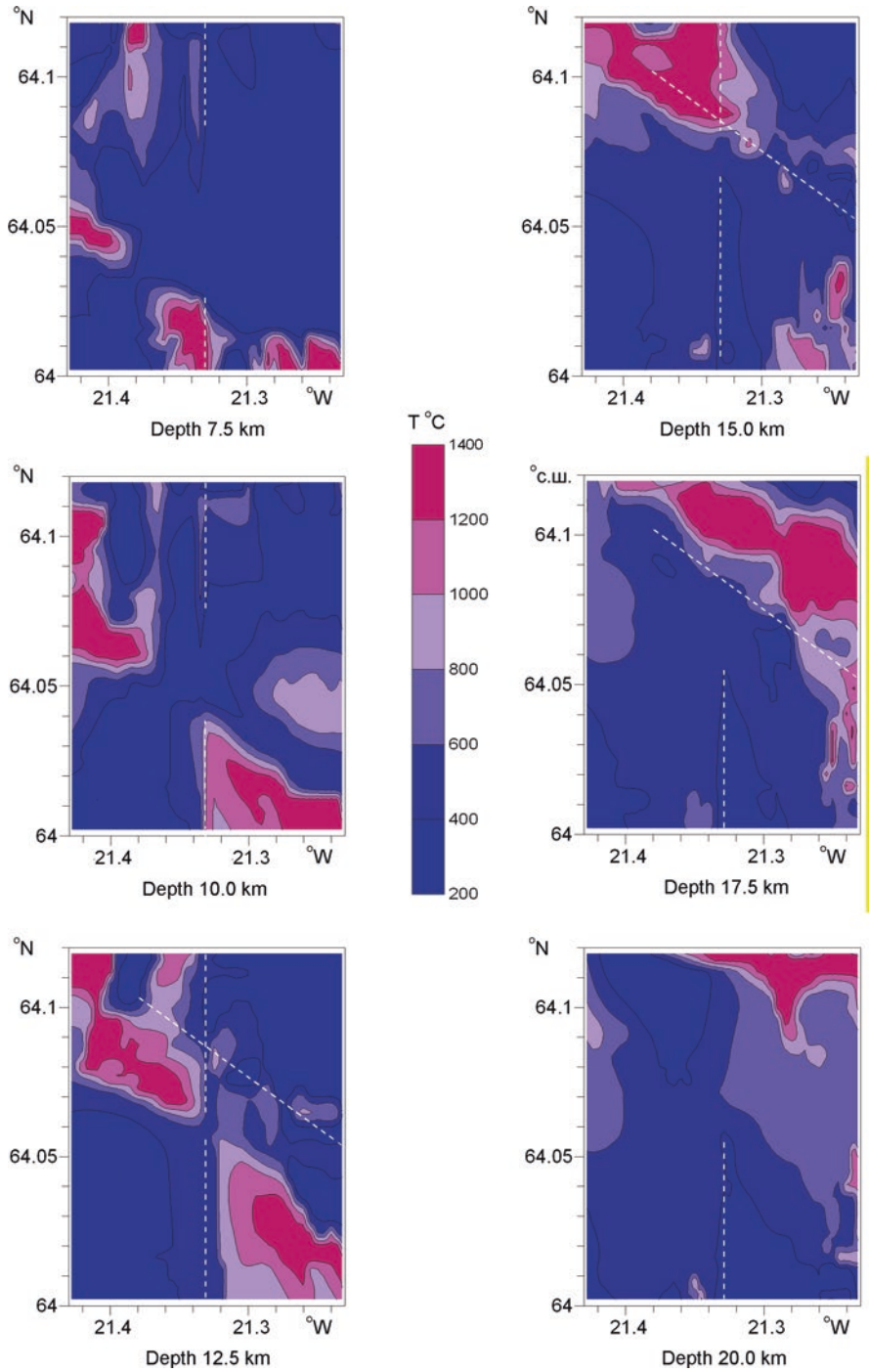


Fig. 8 Slices of the temperature distribution in the Hengill area at different depths [39]. Vertical dashed line indicates the hypothesized location of the deep transform fault; diagonal dashed line marks the projection of the Olkelduhals transverse tectonic structure indicated in the Figs. 5–6

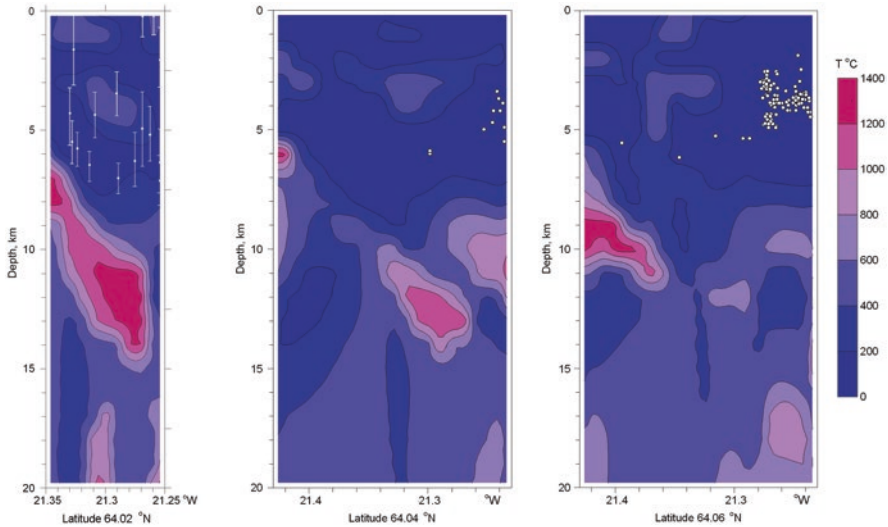


Fig. 9 Temperature cross-sections in the Hengill area at different latitudes. Bars are redrawn from Stefansson et al. [41]. White dots indicate the earthquake hypocenters according to Jousset et al. [20]

unusually high temperatures (1100 °C) detected at the depth 2 km of the study area [15] could originate from the molten liquid magma (with temperature higher than liquidus) upwelling from the mantle and finally accumulating in the shallow magma pockets at depths 2–5 km (Fig. 9). The comparison between the vertical temperature cross-sections and the projections of the earthquake hypocenters showed that they all are located in the areas where temperature does not exceed 400°C (see locations of hypocenters in the Fig. 9), which is a gabbro solidus in a silica-rich Icelandic crust.

Joint analysis of the temperature and resistivity models together with the gravity data enabled to discriminate the locations of relict and active parts of the volcanic geothermal complex. Figure 10 indicates Bouguer gravity anomaly map, where four adjacent domains (see their locations in Fig. 5, lower panel) correspond to the regions in the crust with different thermal regimes: in the Husmuli (I) and Grensdalur (III) large massifs of the solidified magma are cooling while in more active Nesjavellir (II) and Hellisheidi (IV) areas the upwelling of the partially molten magma or hot fluids takes place. They are separated by a deep SN fault and the Olkelduhals transverse tectonic structure (marked in the Fig. 10 by dashed lines). The deep fault is traced in the horizontal slices of both electrical resistivity (Fig. 7) and temperature (Fig. 8) and coincides with the supposed location of the hypothesized transform fault submeridionally striking in the southern part of the region (Fig. 6).

This, in turn, explains the observed seismicity pattern by different geothermal regimes in four adjacent parts of the area separated by the deep S–N fault constrained between the meridians 21.31° and 21.33°W and a WNW–ESE diagonal band running beneath the second-order tectonic structure of Olkelduhals.

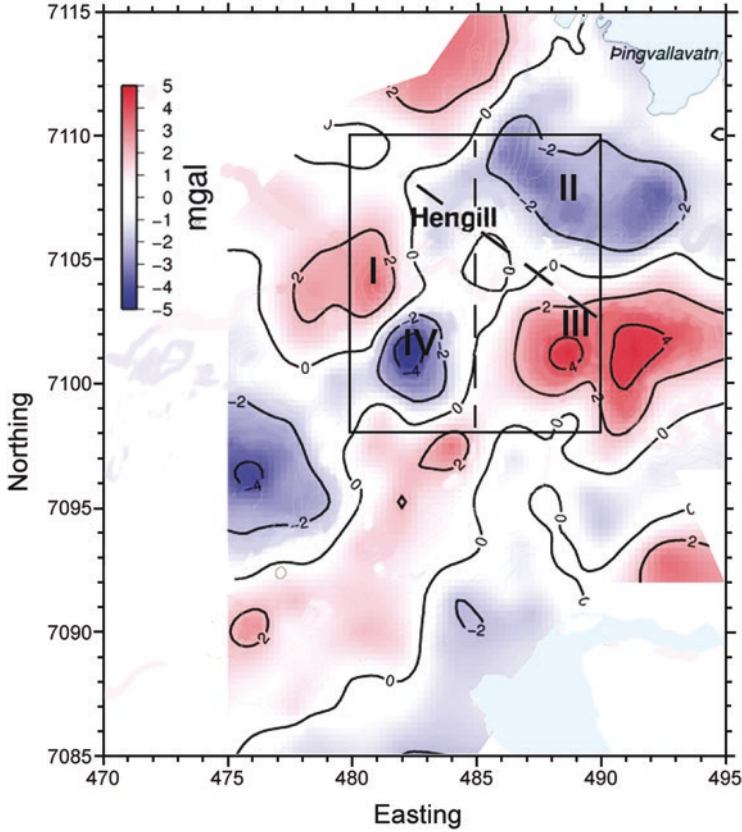


Fig. 10 Residual Bouguer anomaly map (Modified after Árnason et al. [1]); I-IV indicate gravity anomalies; vertical dashed line indicates projection of the deep resistivity and temperature fault; diagonal dashed line marks the axis of the Olkelduhals transverse tectonic structure. Rectangle bounds the studied area

5 Estimating the Dominating Heat Transfer Mechanism and Fluid Circulation Paths

An indirect electromagnetic geothermometer was used by Spichak et al. [32] for deep temperature estimations in the Soultz-sous-Forêts geothermal area (France) (Fig. 11) using magnetotelluric (MT) sounding data collected along the profile AB. Validation of temperature assessment carried out by comparison of the forecasted temperature profile with temperature log from the deepest borehole has resulted in the relative extrapolation accuracy less than 2%. It was found that the resistivity's uncertainty caused by MT inversion errors and by possible effects of external factors very weakly affects the resulting temperature, the latter being influenced mainly by the ratio between the borehole and extrapolation depths.

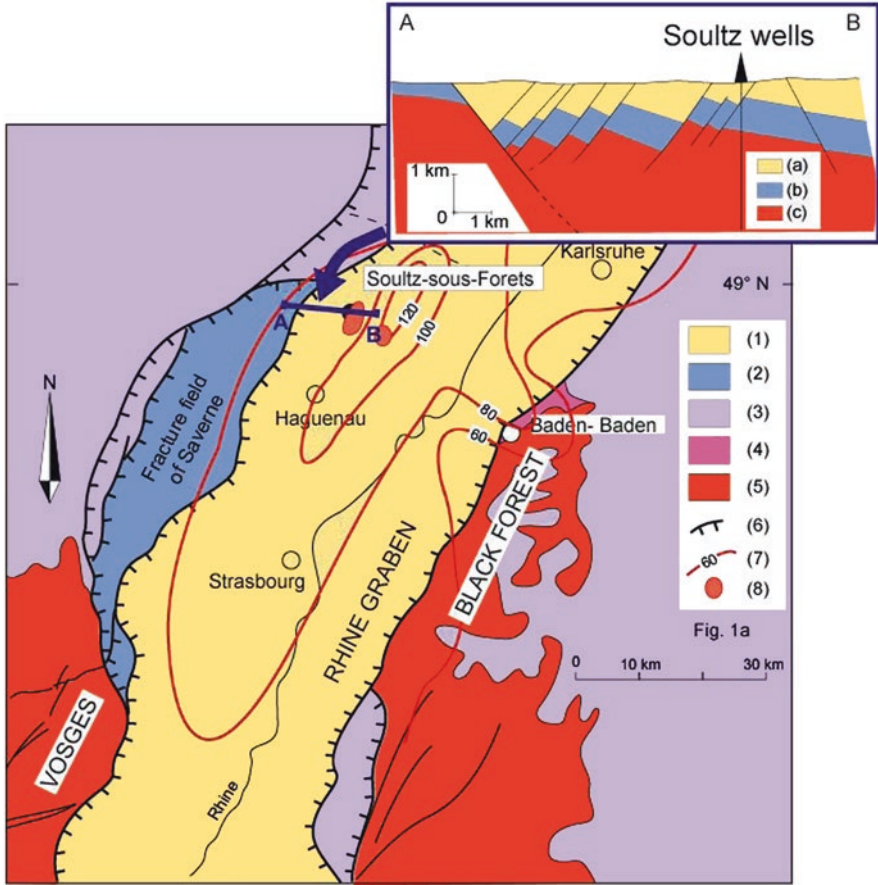


Fig. 11 Location of the EGS Sultz site and geology of the Upper Rhine Graben: (1) Cenozoic sediments, (2) Jurassic, (3) Trias, (4) Permian, (5) Hercynian basement, (6) Border faults, (7) Temperature distribution in °C at 1500 m depth [18], (8) Local thermal anomalies [18]. Simplified cross-section through profile AA': (a) Cenozoic filling sediments (b) Mesozoic sediments, (c) Paleozoic granite basement [12]

2D inversion of MT data has resulted in the electrical resistivity section along profile AB (Fig. 12). Application of EM geothermometer enabled to build the temperature cross-section up to the depth 5000 m (Fig. 13). It manifests local temperature maxima at large depths beneath the wells GPK2 and RT1/RT3 indicating appropriate heat sources located at large depths.

Another remarkable feature of the temperature cross-section concerns to the isotherms' sinusoidal shape in the horizontal direction that supports the hypothesis on the deep rooted fluid circulation in the Sultz fractured granitic basement [10, 22]. The analysis of the temperature profile in GPK2 location beneath 5000 m has shown

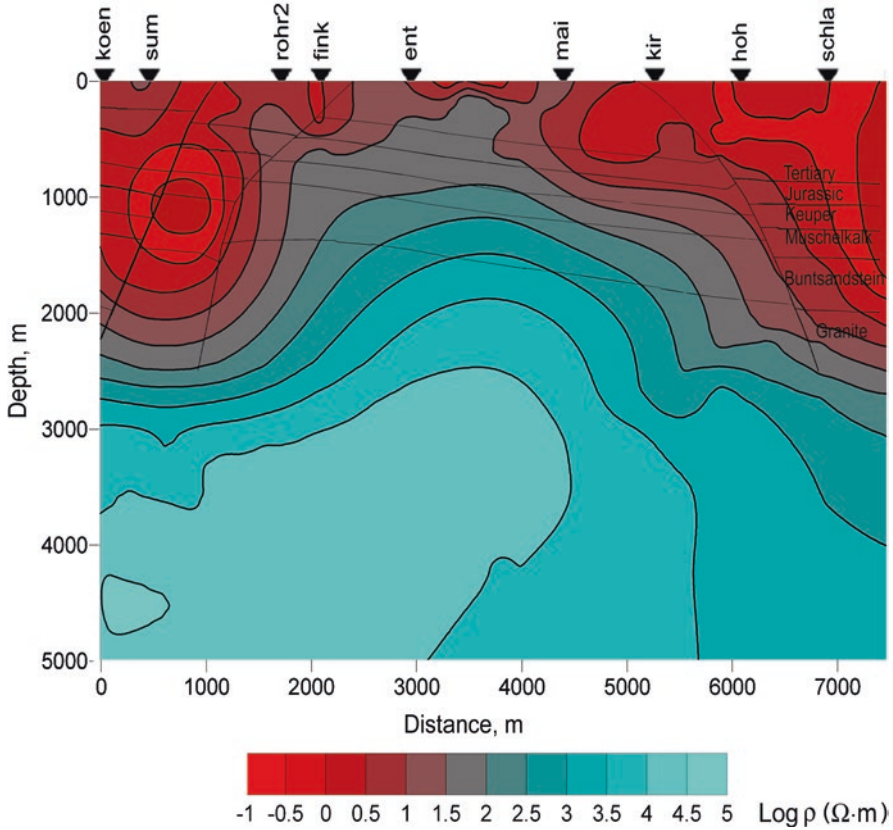


Fig. 12 Electrical resistivity cross-sections along the profile AA' (Sultz-sous-Forêts, France) [32]. Triangles indicate locations of MT sites

that its behavior continues to be of the conductive type (as in the depth range 3700–5000 m) up to the depth 6000 m, while manifesting convective type below this depth (Fig. 14b).

It is worth mentioning in this connection that a common way of searching for the fluid circulation paths at large depths basing only on the electrical resistivity cross-sections (see, for instance, [24]) may lead to incorrect inferences, since the low resistivity anomalies could be caused by a number of reasons. Using of the temperature cross-sections may reduce the uncertainty and help to trace the fluid flows (see previous sections).

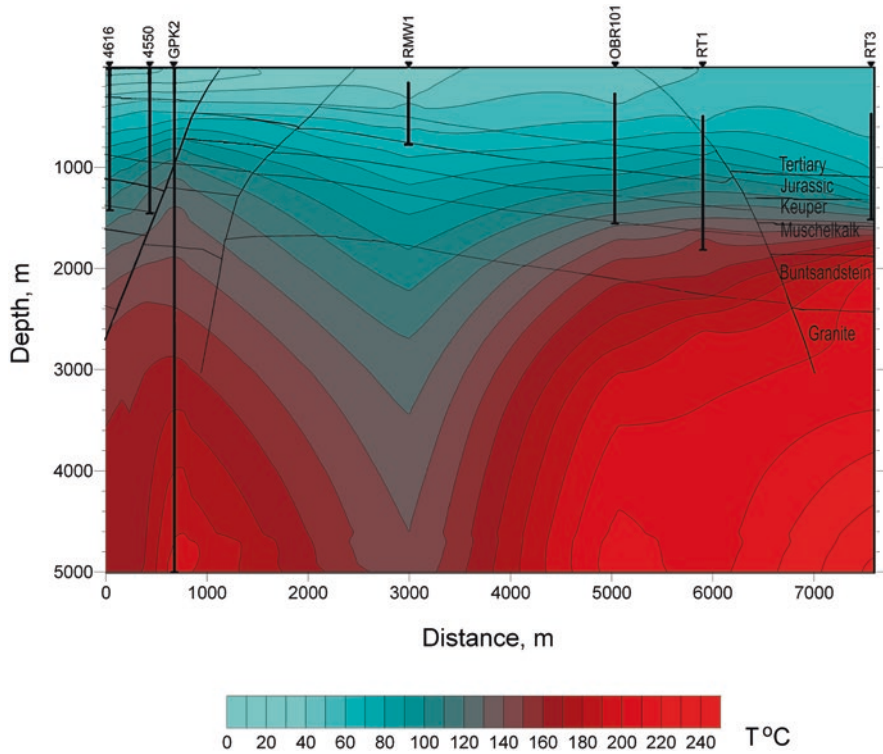


Fig. 13 Temperature cross-section along the profile AA' (Soultz-sous-Forêts, France) [32]. Vertical solid lines indicate boreholes' locations in the vicinity of the profile AA'

6 Conclusions

The studies carried out using indirect EM geothermometer lead to the following conclusions.

The temperature estimates obtained with indirect EM geothermometers could be based on its advance calibration of electrical resistivity - temperature relationships in a few wells. Due to this the temperature estimates do not depend explicitly on alteration mineralogy or other factors influencing the temperature reconstruction in different geological environments.

The temperature interpolation accuracy in the interwell space is controlled mainly by 4 factors related to the characteristics of the space between the place where the temperature profile is estimated and related EM site: faulting, meteoric and groundwater flows, spacing, and lateral geological heterogeneity (though, the latter factor being less restrictive, if appropriate EM inversion tools are used). Therefore, prior knowledge of the geology and hydrological conditions in the region under study can help to correctly locate the EM sensors with respect to the areas where the temperature is to be predicted and thereby reduce the estimation errors.

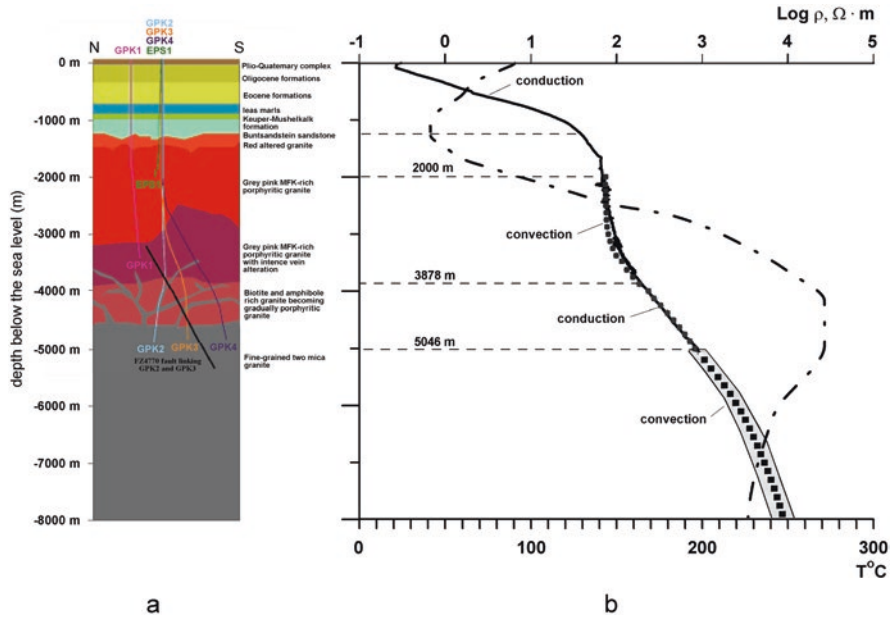


Fig. 14 (a) 2D conceptual model of the geology at Soultz-sous-Forets (modified after [13]); (b) temperature extrapolation in the well GPK2 for the depth range 5046 m – 8175 m. The temperature well log is indicated by solid line, forecasted temperature – by crosses, log resistivity profile is marked by dashed – dotted line. Hatched area indicates the bars corresponding to 10% uncertainty in the resistivity model used for the temperature forecast. (Modified after Spichak et al. [32])

Application of the indirect electromagnetic geothermometer allows high accuracy temperature estimation at depths exceeding the depths of drilled wells for which temperature data are available. Electromagnetic geothermometer could provide the spatial temperature models in the absence of manifestations of geothermal activity on the surface. They, in turn, offer a comprehensive database for drawing conclusions regarding location of the heat sources, fluid type and its circulation paths, and supercritical fluids at large depths not accessible by available boreholes.

Acknowledgements This study was carried out partly due to support of RSCF (grant N20-17-00155).

References

1. Árnason KH, Eysteinnsson E, Hersir GP (2010) Joint 1D inversion of TEM and MT data and 3D inversion of MT data in the Hengill area, SW Iceland. *Geothermics* 39:13–34
2. Arnorsson S, Gunnlaugsson E (1985) New gas geothermometers for geothermal exploration-calibration and application. *Geochim Cosmochim Acta* 49(6):1307–1325

3. Batini F, Bertini G, Bottai A et al (1983) San Pompeo 2 deep well: a high temperature and high pressure geothermal system. In: Extended abstract of third international seminar on results of EC research and demonstration projects in the field of geothermal energy: 341–353
4. Bellani S, Brogi A, Lazzarotto A et al (2004) Heat flow, deep temperatures and extensional structures in the Larderello geothermal field (Italy): constraints on geothermal fluid flow. *J Volcanol Geotherm Res* 132:15–29
5. Bertani R, Bertini G, Cappetti G et al (2005) An update of Larderello-Travale/Radicondoli deep geothermal system. In: Extended abstract for the world geothermal congress, Antalya, Turkey
6. Bertini G, Casini GG et al (2006) Geological structure of a long-living geothermal system, Larderello, Italy. *Terra Nova* 18(3):163–169
7. Brogi A, Lazzarotto A, Liotta D et al (2005) Crustal structures in the geothermal areas of southern Tuscany (Italy): insights from the CROP 18 deep seismic reflection lines. *J Volcanol Geotherm Res* 148:60–80
8. Cameli GM, Dini I, Liotta D (1993) Upper crustal structure of the Larderello geothermal field as a feature of post-collisional extensional tectonics, Southern Tuscany, Italy. *Tectonophysics* 224(4):13–423
9. Celati R, Cappetti G, Calore C et al (1991) Water recharge in Larderello geothermal field. *Geothermics* 20:119–133
10. Clauser C, Villinger H (1990) Analysis of conductive and convective heat transfer in a sedimentary basin, demonstrated for the Rhein graben. *Geophys J Intern* 100:393–414
11. Carzione JM, Poletto F (2013) Seismic rheological model and reflection coefficients of the brittle-ductile transition. *Pure Appl Geophys* 170:2021–2035
12. Dezayes C, Chevremont P, Tourliere B et al (2005) Geological study of the GPK4 HFR borehole and correlation with the GPK3, borehole (Soulz-sous-Forêts, France). BRGM/RP-53697-FR. Technical Report, BRGM
13. Dezayes C, Genter A, Hooijkaas G (2005) Deep-seated geology and fracture system of the EGS Soutz reservoir (France) based on recent 5km depth boreholes. In: Proceedings of the world geothermal congress, Antalya, Turkey
14. Dmitriev VI, Rotanova NM, Zakharova OK (1988) Estimations of temperature distribution in transient layer and lower mantle of the Earth from data of global magnetovariational sounding. *Izvestiya RAN ser Fizika Zemli* 2:3–8. (in Russian)
15. Elders WA, Fridleifsson GO (2010) The science program of the Iceland Deep Drilling Project (IDDP): a study of supercritical geothermal resources. In: Expanded abstracts of the world geothermal congress, Bali, Indonesia
16. Foulger GR, Toomey DR (1989) Structure and evolution of the Hengill-Grensdalur volcanic complex, Iceland: geology, geophysics, and seismic tomography. *J Geophys Res* 94(B12):17511–17522
17. Gola G, Bertini G, Bonini M et al (2017) Data integration and conceptual modeling of the Larderello geothermal area, Italy. *Energy Procedia*. <https://doi.org/10.1016/j.egypro.2017.08.201>
18. Haenel R, Legrand R, Balling N et al (1979) Atlas of subsurface temperatures in the European Community. Th. Schafer Druckerei GmbH, Hannover
19. Harvey CC, Browne PRL (1991) Mixed-layer clay geothermometry in the Wairakei geothermal field, New Zealand. *Clays Clay Miner* 39:614–621
20. Jousset P, Haberland C, Bauer K et al (2011) Hengill geothermal volcanic complex (Iceland) characterized by integrated geophysical observations. *Geothermics* 40:1–24
21. Kharaka YK, Mariner RH (1989) Chemical geothermometers and their application to formation waters from sedimentary basins. In: Naeser ND, McCulloch T (eds) *Thermal history of sedimentary basins*. S.C.P.M. Special issue, Springer, pp 99–117
22. Le Carlier C, Royer JJ, Flores EL (1994) Convective heat transfer at Soultz-sous-Forêts geothermal site: implications for oil potential. *First Break* 12(11):553–560
23. Liotta D, Ranalli G (1999) Correlation between seismic reflectivity and rheology in extended lithosphere: southern Tuscany, inner Northern Apennines, Italy. *Tectonophysics* 315:109–122

24. Manzella A, Spichak V, Pushkarev P et al (2006) Deep fluid circulation in the Travale geothermal area and its relation with tectonic structure investigated by a magnetotelluric survey. In: Expanded abstracts of the 31th workshop on geothermal reservoir engineering, Stanford University, USA
25. Piccinini D, Saccorotti G (2018) Observation and analysis of shear wave splitting at the Larderello-Travale geothermal field, Italy. *J Volcanol Geotherm Res* 363:1–9
26. Pushkarev PY (2007) 2D resistivity model of the Travale geothermal field revealed from MT data. In: Proceeding of the workshop INTAS project, Pisa, Italy
27. Romagnoli P, Arias A, Barelli A et al (2010) An updated numerical model of the Larderello-Travale geothermal system, Italy. *Geothermics* 39:292–313
28. Shankland T, Ander M (1983) Electrical conductivity, temperatures, and fluids in the lower crust. *J Geophys Res* 88(B11):9475–9484
29. Spichak VV (2013) A new strategy for geothermal exploration drilling based on using of an electromagnetic sounding data. In: Expanded abstract of the international workshop on high enthalpy geothermal systems. San-Bernardino, California
30. Spichak VV (2014) Reduce geothermal exploration drilling costs: pourquoi pas?! In: Expanded abstract of the D-GEO-D conference, Paris, France
31. Spichak VV (2019) Temperature models of geothermal areas: lessons learned from electromagnetic geothermometry. In: Proc. Int. Workshop on Water Dynamics. Sendai, Japan
32. Spichak V, Geiermann J, Zakharova O et al (2015) Estimating deep temperatures in the Soultz-sous-Forêts geothermal area (France) from magnetotelluric data. *Near Surface Geophys* 13(4):397–408
33. Spichak V, Goidina A, Zakharova O (2011) 3D geoelectrical model of the Hengill volcanic complex (Iceland). *Trans KRAUNZ* 1(19):168–180. (in Russian with English abstract)
34. Spichak VV, Manzella A (2009) Electromagnetic sounding of geothermal zones. *J Appl Geophys* 68:459–478
35. Spichak VV, Zakharova OK (2007) Temperature estimation in the earth's interior from the ground electromagnetic sounding data. *Izvestiya Phys Solid Earth* 6:68–73
36. Spichak VV, Zakharova OK (2009) The application of an indirect electromagnetic geothermometer to temperature extrapolation in depth. *Geophys Prospect* 57:653–664
37. Spichak VV, Zakharova OK (2012) The subsurface temperature assessment by means of an indirect electromagnetic geothermometer. *Geophysics* 77(4):WB179–WB190
38. Spichak VV, Zakharova OK (2015) *Electromagnetic geothermometry*. Elsevier, Amsterdam
39. Spichak VV, Zakharova OK, Goidina AG (2013) A new conceptual model of the Icelandic crust in the Hengill geothermal area based on the indirect electromagnetic geothermometry. *J. Volcanol/Geotherm Res* 257:99–112
40. Spichak VV, Zakharova OK, Rybin AK (2011) Methodology of the indirect temperature estimation basing on magnetotelluric data: northern Tien Shan case study. *J Appl Geophys* 73:164–173
41. Stefansson R, Gudmundsson JB, Roberts MJ (2006) Long-term and short-term earthquake warnings based on seismic information in the SISZ. In: *Veðurstofa Íslands – Greinargerð, Icelandic Meteorological Office, Rep. 06006*, 53 pp. Reykjavik

Explosive Processes in Permafrost Areas – New Type of Geocryological Hazard



A. N. Khimenkov, D. O. Sergeev, A. N. Vlasov, D. B. Volkov-Bogorodsky,
G. S. Tipenko, V. P. Merzlyakov, and Y. V. Stanilovskaya

1 Introduction

This paper discusses explosive processes in perennial frozen soils, which are triggered by the natural and man-made causes. Some of them have been described for a long time and are associated with water freezing in confined conditions (explosions of hydrolaccoliths and icing mounds). Others are associated with gas emissions during drilling. And the latest explosive processes have been observed in the last 5 years and associated with natural emissions of underground gases without any anthropogenic impacts.

These processes relate to physical explosions associated with the occurrence of internal pressure build up in a cavity saturated by fluid or gas until the pressure reaches the maximum allowable stress limit for the host sediments. Explosions are often triggered by uncontrolled release of potential energy from compressed gas trapped in confined spaces in the deposits [14]. The key reason for occurrence of explosive events is not a chemical reaction, but rather a physical process related to release of inner energy of liquid or gas over a short time period.

A. N. Khimenkov (✉) · D. O. Sergeev · G. S. Tipenko · V. P. Merzlyakov
Sergeev Institute of Environmental Geoscience RAS (IEG RAS), Russia, Moscow

A. N. Vlasov · D. B. Volkov-Bogorodsky
Institute of Applied Mechanics of the Russian Academy of Sciences, Russia, Moscow
e-mail: iam@iam.ras.ru

Y. V. Stanilovskaya
Total S.A., France, Paris
e-mail: yulia.stanilovskaya@total.com

© The Author(s), under exclusive license to Springer Nature
Switzerland AG 2021

V. Svalova (ed.), *Heat-Mass Transfer and Geodynamics of the Lithosphere*,
Innovation and Discovery in Russian Science and Engineering,
https://doi.org/10.1007/978-3-030-63571-8_5

1.1 Natural Explosions of Hydrolaccoliths

During the studies conducted in 1930s on the Yamal peninsula, V.I. Andreev recorded the narrative of the Nenets, indicating that in the Baidaratskaya tundra in the winter there was a loud (deafening) noise (explosion) from the side of mound and after a surface icing was found. In view of the above, the author suggested that there was a cavity below the surface ice and it was filled by water and may be partially saturated with gas, which were erupted at the surface during deep cracking of mounds [1]. In the course of the study focused on evolution of fluvial-lacustrine systems across the South Trans-Baikal region, O.I. Bazhenova [3] amassed evidence and acquired supporting data related to explosion of hydrolaccoliths formed in the lacustrine depressions. Explosions of mounds are often accompanied by a strong noise similar to that of a gunshot, which can be audible in the radius of 7–10 km. Explosion events often result in formation of new forms of landscape represented by craters. Diameter of craters may vary in the range from 1 m to 15–25 m, and depth may vary from 2 to 5 m. A large volume of soil material is usually erupted from craters and lifted to the surface during explosions (508 m³). The largest ice fragment with layers of sand, gravel and pebble had the thickness of 2 m, width of 6–9 m and length of 18 m [31]. During explosion of the mound occurred on June 27, 1938 in close vicinity to Byrtsa village, the ice, sand and pebble were blown out, lifted to the height of 8–12 m and scattered away at the radius of 15 m [34]. A.N. Sklyarevskaya [4] witnessed an explosion of a large size hydrolaccolith at the bottom of Arangot pad on May 24, 1964 at 2 p.m. The noise from explosion was clearly audible at the radius of 6 km. During explosion large amount of sand and gross material with ice blocks with the size of 2×1,5×0,7 m were erupted from the central part of the mound. The explosion resulted in formation of an elongated crater with the following size: length of 15 m, width of 2–4 m and depth of 2 m [4]. The reason for natural explosions discussed herein is freezing of water saturated horizons (aquifers). Nevertheless, only presence of gas component could ensure development of favorable conditions for explosions and support high power and force of the said explosions. Building up of compressed gas results in accumulation of potential energy and consequent explosion when mounds' inner pressure exceeds resistivity and strength of the top soil.

1.2 Anthropogenic Explosions in Permafrost

From the beginning of the extensive exploration for oil and gas in the Arctic region there has been instances of gas emissions with blow outs of drilling tools and mud, degassing of washing fluids, etc. For example, in the Anabaro-Khatanga inter-fluvial region there has been gas emissions reported at the depth of 70–120 m [36]. Exploration and subsurface mining operations performed in the areas of placer deposits in permafrost on the North East of Russia were often accompanied by gas emissions from depths of up to 100 m [12]. Geotechnical surveys for construction

of the Yuribey River's bridge in the Yamal peninsula were conducted in 1986–1990. During the survey more than 200 geotechnical wells were drilled to the depth from 10 to 53 m. In most wells, gas emissions were reported [36]. Sand and small size ice eruptions were multiply recorded during drilling. In one instance there was an intense release of a drilling tool with the total weight of 150 kg that was thrown up at the height of 12 m from the wellhead. In one of the wells there was a constant gas flare burning for more than one month. In some other wells there were short duration bursts during gas ignition [2]. Gas emissions were documented during drilling of geotechnical wells in the upper section of the permafrost (up to 20–30 m) in the Zapolyarnoye oil and gas condensate field (OGCF) situated on the north of Western Siberia. The thickness of permafrost in the field is estimated at 500 m. According to OJSC Fundamentproekt, during drilling of geotechnical wells of 20 m depth at the construction site of the gas treatment facility (UKPG-2C) for the Zapolyarnoye OGCF, gas emissions were reported in a number of wells. These gas releases occurred at the intervals of unconsolidated frozen sands at the depth of 13.0–13.8 m and 14.0–14.5 m. Gas burning at wellheads continued for 24 h. Pursuant to information of KRIOS company, which in the summer of 2003 conducted drilling of permafrost observation wells with depth of 250 m, gas emissions in the permafrost in the Zapolyarnoye OGCF came from the 90–250 m interval [36]. During well drilling in the Tota-Yakhinsky field (the Gydan Peninsula) in 1986, there was a gas emission with a consequent blow out of 12 m³ drilling mud from the depth of 115 m. The gas coming from the wells was burning for 3 months [36]. Gas emissions in the Yamburg gas condensate field have been registered at 45–55 m depth in 450 m permafrost thickness [28]. The permafrost thickness in the southern sector of the Bovanenkovo GCF (northwest part of the Yamal Peninsula) varies up to 320 m. Majority (85%) of gas emissions in the Yamal deposits are recorded from the depth of 60–80 m; this horizon is traceable for 120 km² area [13].

Relatively high gas content within the permafrost has been reported both in the onshore and offshore zones as well as under the sea bottom in Arctic seas. Large size gas emission from the well situated on the shelf of the Pechora Sea was documented by V.P. Melnikov et al. [29]. Drilling operations were conducted from the floating drilling rig at the location with water depth of 64 m. The large size gas emission was occurred at 50 m depth below the sea bed when drilling through the frozen clays. The gas and water fountain reached the height of 10 m above the deck of the vessel. Ten days later, the echometer survey indicated presence of underwater gas fountain (height of 10 m, diameter of 10 m) at the drilling site. During core recovery from the permafrost, the mud jacket of the samples swelled and ice cracked. These processes are instigated by dissociation of gas hydrates, which are present in the samples [29].

Permafrost, where drilling operations took place, is an important element of any explosive process captured herein. No explosion would occur if it had not been in the permafrost. These explosions were instigated by a sharp pressure drop and temperature increase at the 14–120 m interval. Experts recognize that the most probable explanation for occurrence of such blowouts is dissociation of gas hydrates in permafrost.

1.3 Explosions Contributing to Formation of Gas Emission Craters

A round shape gas emission crater (GEC) with the depth of 70 m was discovered in 2014 in the Yamal peninsula, 30 km south of the Bovanenkovo OGCF [5]. A concentric build up composed of erupted soils was next to the crater. Several craters with similar shape and size were discovered later on the north of the Western Siberia. Currently, the total of 8 craters have been documented: location of 7 craters used from the publication [24] adding ErkGEC, the coordinates of Osokin’s craters are still unknown (Fig. 1).

GEC-1 (Central Yamal) located 30 km to the south of the Bovanenkovo OGCF (Fig. 2). GEC-2 (Central Yamal) located 20 km to the north of GEC-1 and 10 km to the south of the Bovanenkovo OGCF [9, 32] (Fig. 3). GEC-3 (Central Yamal) located 10 km to the west of the GEC-2 (Fig. 4).

AntGEC (on the southwest of the Gydan peninsula) is located 90 km away from Antipayuta [22] (Fig. 5). YeniGEC (on the east of the Gydan peninsula) is situated in the southwest of the Yenisei Bay and on the left bank of the Mongoche River, next to the Deryabinsky gas field (Fig. 6). The frozen soils and ice blocks discovered in close vicinity to the crater were as large as 3×5 m. SeYKhGEC (North-eastern Yamal) was found at the distance of 34 km to the northwest of the Seyakha village and in the flood-plain of the Mordy-Yakha River. During gas blowout there was a gas ignition. This assumption is supported by the presence of charred sand and plants on the parapet [7] (Fig. 7). ErkGEC (South Yamal) was discovered in summer of 2017 in the flood plain of the Erkuta-Yakha River (Fig. 8), 220 km to the north of Salekhard town. Osokin’s gas emission crater is located on the Yamal Peninsula, but coordinates are still unknown (Fig. 9).

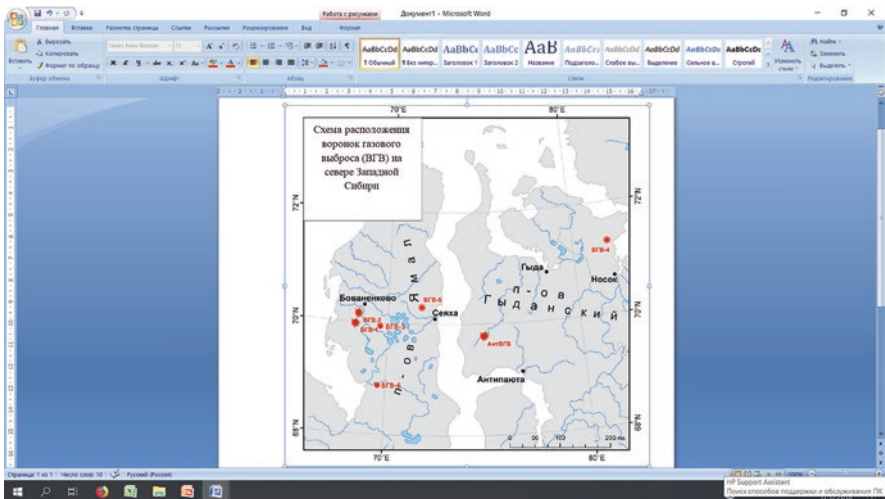


Fig. 1 Overview map of 7 gas emission craters location on the north of Western Siberia from the publication [24] adding ErkGEC. The coordinates of Osokin’s craters are unknown.



Fig. 2 Photo of GEC-1 from publication [16].

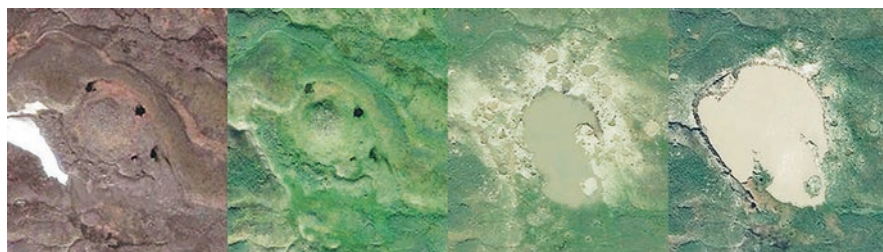


Fig. 3 Satellite images of GEC-2 from publication [8]: 1 – July 4, 2009; 2 – July 30, 2010; 3 – July 21, 2013

The analysis of survey data on gas emission craters situated on the north of Western Siberia allowed making some generalizations:

1. All craters are located on the so-called “warm” landscape. GEC-1 is developed at the interface between khasyrey and lower section of the slope populated by bushes, GEC-2 is formed within the borders of the creek valley, GEC-3 and YeniGEC are appeared on the shore of the water body, Seyakha crater (SeYkhGEC) is created in close vicinity to the riverbed, Erkuta crater (ErkGEC) is occurred within the flood plain of the river, in close vicinity to the oxbow lake at the spot covered by bushes, Antipayuta crater (AntGEC) is developed on the



Fig. 4 GEC-3 from publication [8]: a – photos taken from helicopter on April 27, 2013 (S.A. Nikitenko), b – satellite image, August 2015.



Fig. 5 Antipayata gas emission crater (AntGEC). (Photo: M. Lapsuya)

site of a well-warmed sandblow, on the edge of the terrace surface destroyed by thermal erosion processes, Osokin's crater is located at the bottom of the low land populated by bushes.

2. All discovered craters have round shape, diameter of 10–20 m and depth of 20–70 m.
3. Walls or erupted blocks for all craters have ice containing soils or ground ice.
4. The erupted soils is placed concentrically around crater edges. The radius of erupted soils is up to 100 m. This indicates a significant pressure during the explosion.



Fig. 6 Fragments of ice-rich permafrost erupted from YeniGEC on April 2013. (Photo: S. Yaptune)

5. In some sites (GEC-1, GEC-2, AntGEC, YeniGEC, SeYkhGEC, ErkGEC) frost mounds of 2–6 m height were observed prior to explosions. Indicative duration of frost mound life before explosion is from 2 years (ErkGEC) to 70 years (GEC-1). Indirect data (dendrological studies, verbal communications provided by indigenous population) indicates that growth rate of frost mounds prior to explosion may vary from 0.7 cm/year (GEC-1) to 200 cm/years (ErkGEC).
6. In the craters (GEC-1, SeYkhGEC), in which it was possible to make an analysis of gas composition, methane was detected. This coincides with the gas composition in permafrost samples recovered from observation wells of the Bovanenkovo field, where methane is estimated at 98.4–99.9 % [13].
7. In some instances, crater's explosions were accompanied by gas ignition (YeniGEC, SeYkhGEC).

According to opinion of specialists involved in gas emission crater's inception and evolution studies (incl. V.I. Bogoyavlensky [6, 9], M.O. Leibman, A.I. Kizyakov [26], M.I. Eпов, I.N. Eltsov, V.V. Olenchenko et al. [16], S.N. Buldovich, V. Khilimonyuk et al. [10], A.N. Khiminkov et al. [18–20] and others), the features have been formed due to subsurface gas release. Nevertheless, opinion split on the subject of origin of gas contributing to blowout. In terms of origin, the gas may be



Fig. 7 Fragments of frozen soils erupted from SeYkhGEC in the valley of the Se-Yakha River, July 2017. (Photo: YANAO Administration)



Fig. 8 Erkuta gas emission crater (ErkGEC) in the flood plain of the Erkuta-Yakha River. (Photo: YANAO Administration)



Fig. 9 Osokin's crater situated on the Yamal peninsula (Photo: A. Osokin, 26.07.2013).

catagenetic coming from deep horizons underlying the permafrost, and biochemical gas formed as a result of bacteria's activity as well as mixed type origin gas.

2 Overview of Hypotheses of Gas Emission Crater Genesis

2.1 Hypothesis of V.I. Bovoyavlensky

Permafrost serves as a good regional seal which prevents vertical gas migration. Due to the irregular distribution of formation pressure, gas migrates sub-horizontally with consequent release at the surface or in the water body through weak zones (faults, thermokarst lakes with taliks, frost mounds) [7]. The GEC-1 and GEC-2 are encountered at the zone corresponding to the excessive heat flow [7]. This assumption requires additional supporting evidence. The results of studies conducted in the Yamal crater (GEC-1) show that there is a permafrost below the crater [16, 30]. Therefore, gas migration should run through the permafrost, but compelling arguments shall be provided to support this theory.

2.2 Hypothesis of M.O. Leibman

The positive temperature extremum in summer of 2012 resulted in temperature raise in the gas hydrates containing permafrost and consequent gas release due to its dissociation (predominately methane) and formation of craters [26]. To support this hypothesis, it will be necessary to find out if exposure to abnormal heating during 1 or 2 summer seasons may have an impact on dissociation of gas hydrates located at the depth of 60 m and somehow impact gas accumulation and migration within the permafrost. Soil temperature surveys in the region of Marre-Sale show absence of evidence to assume any sharp temperature variations [15].

2.3 Hypothesis of I.D. Streletskaya

The findings from the studies conducted in the Yamal crater (GEC-1) have been used to make an assumption that methane might accumulate and fill in the cavity, which corresponding to the “grotto” of 5 m high from the bottom of the crater and in the upwards direction. After formation of the crater, all methane was released to the surface and consequently mixed with the air [33]. The presence of the cavity with a height of about 5 m and a radius of 2 m must be justified in terms of formation mechanisms and the possibility of long-term existence.

2.4 Hypothesis of S. Buldovich, V. Khilimonyuk. Buchkov et al.

Explosion of the sub-lake talik was the key reason for formation of the Yamal crater. Thickness of permafrost overlying the talik at the time of explosion varied in the range from 7 to 9 m. The talik was composed of water-soil mixture saturated with gas and containing dissolved gas (primarily, CO₂) of biogenic origin. The upper section of the talik was represented by a gas layer [10].

The cryogenic eruption event was instigated by thermal cracking (ice wedges) in the frozen cap and comprised of a number of stages.

At the first stage (which lasted few minutes), gas release primarily occurred in the upper zone of the talik with consequent gas migration through cracks and expands adiabatically. At the second stage (hydraulic), which lasted few hours, the water was outpouring and gas was released from solution. These processes resulted in upwards migration of gas and water fluid. The last stage (duration from 5 to 25 h) consisted of eruption of unfrozen soils and release of gas from pore water present in the unfrozen soils or release of CO₂ as a result of dissociation of gas hydrates. The hypothesis of the authors is based on the analysis of the samples recovered at the depth of 10–17 m and corresponds to the upper part of the crater only. The original depth of the Yamal crater (GEC-1) was 60 m. Application of the conclusions derived

for the upper zone of the crater to the deeper sections requires additional supporting evidence. The deeper part of the crater is characterized by a high methane content [25, 33]. The methane content in the lake water, which was formed in the crater during the first 3 years of monitoring is still very high. This is a sign of an active gas source situated under the bottom of the lake [25]. During formation of the craters SeYkhGEC and ErkGEC, there were gas ignition and combustion events and this is indicative of methane presence. These facts are not in line with the assumption that dissociation of carbon dioxide hydrate is the key reason for formation of gas emission craters. Nevertheless, for some cases this possibility exists.

2.5 Hypothesis of M.I. Epov, I.N. Eltsova, V.V. Olenchenko

The key reason for formation of the Yamal crater (GEC-1) was gas hydrates dissociation at the depth of 60–80 m [16]. The source of the high heat flux may correspond to a large size oil and gas structure. This heat flow resulted in gas hydrates exposure in the upper part of the cross section. In addition, some geomorphologic and geophysical features have been identified in the study area to indicate the presence of faults with crater located at the crossing point of such faults.

It is very likely that exposure to the heat flow resulted in triggering dissociation processes in gas hydrates contained within the permafrost. It is still not clear how fragments of frozen soils were lifted up to the surface from the depth of 60 m. According to the calculations of V.P. Merzlyakov [19], the formation pressure required to ensure lifting of the soils from the indicated depth shall be 10 MPa. In the course of gas hydrate dissociation at temperatures below zero, the generated pressure is not exceeding 2.6 MPa [17]. The increased heat flow has not been proven for other craters. Therefore, this hypothesis requires further verification.

2.6 Hypothesis of the Authors (A.N. Khimenkov et al.)

Recognizing potential variations in the origin of gas, availability of different heat sources and different mechanisms for formation of craters, the authors presume that the proposed mechanism will address all inconsistencies and uncertainties captured above. We believe that the main source of gas causing the explosive processes in permafrost is hydrate-containing frozen soils, and the reason for heating upsetting gas hydrate equilibrium state is lakes widespread in the Western Siberia [19]. Preparation of explosion is a staged process [18, 20].

1. The main driving factor that triggers all consequent events is a localized heating of permafrost. Heating of the permafrost below the lake resulted in development of the talik and thawing zone characterized by a higher temperature compared to that of the adjacent soils. At the presence of the local heating under the lake,

frozen soils temperature increase within negative values. Permafrost temperature in the localized heated areas under lakes usually vary in a range from $-1 \dots -3$ °C.

2. After the temperatures in the layer of gas hydrates occurring in the 60–80 m interval [30] exceed the values ensuring their steady state, the process of dissociation begins with methane release at initial pressure 2.2–2.6 MPa [17].
3. The gas under pressure begins to filter into the weaker high-temperature frozen soils. The overpressured gas saturates permafrost, thus, reducing soil strength and triggering plastic deformation of ice. Development of new fractures and dislocations stimulate an increase in gas migration velocity. Gas expulsion processes (due to migration) trigger gas hydrate dissociation and gas pressure build up and stabilization at the original level. These processes contribute to preservation of high pressure in migrating gas bubbles. Gradually, in the area of a “common filtration unit”, an ice-soil gas-saturated stock is formed that penetrates the permafrost. The pressure in gas bubbles located at any depth along the stock will correspond to the pressure in hydrate dissociation zone. The ice-soil stock is forced to move upwards due to a combination of high pressure in permafrost and vertical upwards pressure.
4. The upwards migration of gas saturated ice-soil mass results in plastic deformation of the upper zone of thawing sediments (of talik) with consequent heaving and freezing. This leads to formation of a low temperature 6–8 m thick frozen layer, which is impervious to gas. This layer serves as a sealing barrier that prevents vertical movement of the gas flow in the upwards direction. Deformation of the sealing horizon under the influence of the underlying pressure may result in development of frost mounds.
5. When plastic deformation at the top of the permafrost reaches its limit, the seal breaks and soil-ice mixture saturated with gas erupts under over pressure [18, 19, 21].

Different initial conditions and diverse combinations of processes occurred during preparation for explosion result in different scenarios of gas emission crater evolution: from gas migration to sub-lake talik (in the case of a large and deep lake) to explosion without mound formation (in the case of gas hydrates location at a shallow depth, and their rapid decomposition).

3 Permafrost Temperature Increase Due to Impact of Surface Water

Low-temperature frozen soils in natural conditions are not permeable to gas. Nevertheless, some external impacts and special conditions may stimulate development of gas permeable zones in permafrost. One of the driving factors stimulating

development of these zones is a temperature increase to the level of phase transition. Surface water bodies are the most efficient sources of heat in natural environment. Lakes provide both fast heating of permafrost located under them and a rapid return to the original temperature state when lakes drainage. In case of the closed talik formation below water body, a binary structure of soils is created. Directly underlying the water body the soils are characterized by the positive temperatures (talik) and high-temperature frozen soils occur below. This concept can be illustrated using study results of Lake Illisarvik located in the Mackenzie Delta. The size of the lake is 300 m by 600 m, the maximum depth is 4.5 m. The average annual temperature of permafrost in the vicinity of the lake varies in the range from -8 to -10 °C. The permafrost thickness ranges from 400 to 600 m. The total of 10 wells have been drilled of 15–87 m depth. In the deep-water of the lake, the boundary of the thawed soils is defined at 24 m with underlying frozen soils with temperatures declining with depth and reaching -3 °C at 90 m [11].

For the north of Western Siberia, where gas emission craters were discovered, there are no temperature data for the sediments. Assessment of the impact of lakes on temperature variations in permafrost can be based on analysis of temperature measurements in wells drilled on the khasyreys (on the bottom of drained lakes). Temperature measurements acquired from the khasyreys surfaces may vary in the range from -3 °C to -2.5 °C for the third marine terrace and from -1.8 °C to -1.6 °C for the floodplain [13]. Outside the lake influence zone, the permafrost temperatures at the depth of 60–80 m for the third marine terrace and floodplain vary in the range from -5.5 °C to -5 °C [13].

In areas of local heating of permafrost due to exposure to the surface water body, the frozen soils experience volumetric heat deformations with development of cracks. The strength of frozen soils and ice reduces and the porosity increases, forming the well-developed system of filtration channels connecting the pores to each other. These processes lead to pressure release in the areas exposed to heat, thus, resulting in increased permeability to gas. Localized heating of permafrost produces plowing effect and boosts permeability to gas. Therefore, local conditions for development of a gas-saturated zone develop even before the appearance of a gas source in the permafrost. Heated zones under the water bodies not only stimulate development of favorable conditions for fluids accommodation into it, but also controls the shape of the space where these processes may occur. It means that the heated soils zone also forms a cylindrical channel filled with high temperature permafrost. Analysis of the geophysical data indicates that cone shape areas form under the lakes. These cones characterize by development of distorted and deformed zones along the borders of crystals, where unfrozen water content increases, and gas inclusions expand and form channels between themselves [27].

4 Fluid Dynamics Processes During Formation of Gas Emission Craters

Currently, the focus of the study performed for better understanding of natural explosive processes in the cryolithozone is given to the stage of deformation of the frozen cap. This path is not constructive, since it is based on the consideration of only one final stage in the gas emission crater evolution. Such approach does not reveal the reasons of inception and evolution of natural explosive processes in permafrost even if the gas origin itself is detected.

Self-developing gas dynamic geosystems (compose of several connected zones: primary gas generation, transit and accumulation) forms regardless of gas genesis, conditions instigating gas redistribution, and distance of gas migration. This geosystem has clearly defined boundaries, specific morphology, properties and structural bonds controlled by typical structural features of the frozen soils and temperature field anisotropy. Each zone corresponds to the specific phase of gas redistribution in permafrost. Realization of all stages of gas accumulation results in explosion.

Gradually filtered gas accumulates and forms a single flow through the permafrost. While migrating through cracks and micropores, the overpressured gas is not only filtered through the frozen soils, but also deforms its. Irregularity of gas redistribution leads to development of plastic and rupturing deformations. When pressures exceeding the limit of long-term strength are reached, the ice-rich soils may start flowing and push out the overlying sediments. Gas and ice predominantly move in the upwards direction. This determines the development of frost mounds.

Within the fluid-dynamic geosystem, a continuous filtration flow or “common filtration unit” is formed where gas fluid migrates from high pressure areas to low pressure areas (usually in the vertical direction). The gas fluids of that flow are characterized by macro parameters (migration velocity, pressure, temperature, etc.). The “common filtration unit” with unsteady state is heterogeneous and has pressure gradients in different sectors providing filtration mass transfer in permafrost. This is the reason why gas fluids exert a force on the walls of pores and cracks, thus, stimulating their expansion [35, 23].

The life cycle of the gas dynamic geosystem analyzed herein is controlled by multiple parameters, therefore, it can be assumed that each geosystem will have different evolution scenario. With an appropriate ratio of internal and external factors, it can lead to the GEC formation, which is only the final stage of the full life cycle of the given geosystem. The conditions under which this occurs are considered by us earlier [18, 19].

Allocation of self-developing gas-dynamic geosystems as the main object of the study of explosive processes in cryolithozone will allow not only to define trends and direction of their development, but also to develop a scientifically based method for forecasting future behavior in case of fluctuations of global climate or human impacts on permafrost.

At present, there is still not enough knowledge to build a unified theory of the formation of such complex and diverse class of phenomena, as gas emission craters. This will require nontrivial and innovative approaches that do not fit into the mainstream of the traditional statements existing in geocryology. In particular, a solution can be found within the concept of the fluid dynamic geosystems in cryolithozone [18, 19].

5 Conclusion

It is well known that thawing of permafrost may have a significant release of the greenhouse gases into the atmosphere. The data presented in this paper show that this effect may also take place in frozen state. Even relatively insignificant temperature increase in gas hydrates bearing permafrost may trigger dissociation of them, result in natural explosive processes and emission of greenhouse gas.

In the course of the Arctic exploration, the thermal impact on permafrost and the danger of explosive processes will increase for engineering structures. Nevertheless, this group of processes has never been accounted for project solutions and forecasts of infrastructure permafrost interaction. Moreover, these processes are not included to the group of hazardous geological processes.

Important role in formation of gas emission craters is played by gas migration process through permafrost. Meanwhile, this process is practically not studied. For better understanding of the phenomena, first of all, it is necessarily to build a filtration and deformation model based on common representation of gas filtration and plastic deformation processes in frozen soils. Further study of these processes is seem to be problematic due to the lack of appropriate conceptual and terminological base, developed classifications and systematizing indicators.

The project is executed in compliance with the government assignment # 0142-2019-0029 and financed by the Russian Foundation for Basic Research (grant 17-05-00294) for investigation of gas migration in permafrost.

References

1. Andreev VI (1936) Hydrolaccoliths (bulgunnyahs) in the West Siberian tundra. *News State Geogr Soc* 68(2):186–210
2. Are FE (1998) The problem of the emission of deep gases into the atmosphere. *Earth's Cryosphere II*(4):42–50
3. Bazhenova OI (2013) Modern dynamics of lake-fluvial systems of the Onon-Torei High Plain (South Transbaikalia). *Bull Tomsk State Univ* 371:171–177
4. Bogomolov NS, Sklyarevskaya AN (1969) On the explosions of hydrolaccoliths in the southern part of the Chita region. *Icings of Siberia*. Nauka, Moscow, pp 127–130
5. Bogoyavlensky VI (2015) Gas and oil emissions onshore and offshore in the Arctic and the World Ocean. *Drill Oil* 6:4–10

6. Bogoyavlensky VI (2016) Natural and man-made threats in the development of oil and gas fields in the Arctic and in the World Ocean. *Noosphere* 1:48–67
7. Bogoyavlensky VI (2018) Gas-hydrodynamics in gas emission craters. *Arctic Ecol Econ* 1(29):48–54
8. Bogoyavlensky VI, Bogoyavlensky IV, Nikonov RA (2017) Results of satellite and expeditionary studies of large gas emissions in Yamal in the area of the Bovanenkovo field. *Arctic Ecol Econ* 3(27):4–17
9. Bogoyavlensky VI, Mazharov AV, Pushkarev VA, Bogoyavlensky IV (2015) Gas emissions from the Yamal peninsula cryolithozone. *Drill Oil* 7:8–13
10. Buldovich SN, Khilimonyuk VZ, Bychkov AY, Ospennikov EN, Vorobyev SA, Gunar AY, Gorshkov EI, Chuvilin EM, Cherbunina MY, Kotov PI, Lubnina NV, Motenko RG, Amanzhurov RM (2018) Cryovolcanism on the Earth: origin of a spectacular crater in the Yamal Peninsula (Russia). *Sci Rep* 8
11. Burges M, Judge AS, Taylor A, Allen DV (1982) Ground temperature studies of permafrost growth at a drained lake site, Mackenzie Delta. *Proceedings of the 4th Canadian Permafrost conferences*: 3–11.
12. Chaban PD (1991) About gas hydrates in permafrost placers. *Kolyma* 6:18–19
13. Cryosphere of oil and gas condensate fields of the Yamal Peninsula (2013) T. 2. The cryosphere of the Bovanenkovo oil and gas condensate field / Ed. YuB Badu, NA Gafarova, EE Podborny. Moscow: Gazprom Expo, 424 p.
14. Devisilov VA, Drozdova TI, Timofeeva SS (2012) Theory of combustion and explosion. Practice: study guide. Moscow: Forum, 352 p
15. Dubrovin VA, Kritsuk LN, Polyakova EI (2015) Temperature, composition and age of the Kara Sea shelf deposits in the area of the Marre-Sale geocryological station. *Earth's Cryosphere* XIX(4):3–16
16. Eпов MI, Eltsov IN, Olenchenko VV, Potapov VV, Kushnarenko ON, Plotnikov AE, Sinitsky AI (2014) The Bermuda triangle of Yamal. *Science First-Hands* 5(59):14–23
17. Istomin VA, Chuvilin EM, Sergeeva DV, Bukhanov BA, Stanilovskaya YV, Badets C (2018) Influence of the component composition and gas pressure on ice and hydrate formation in gas-saturated pore solutions. *Oil Gas Chem* 2:33–42
18. Khimenkov AN, Stanilovskaya YV (2018) Phenomenological model of the formation of gas emission craters on the example of the Yamal crater. *Arct Antarct* 3:1–25
19. Khimenkov AN, Stanilovskaya YV, Sergeev DO, Vlasov AN, Volkov-Bogorodsky DB, Merzlyakov VP, Tipenko GS (2017) The development of explosive processes in the cryolithozone in connection with the formation of the Yamal crater. *Arct Antarct* 4:3–37
20. Khimenkov AN, Sergeev DO, Stanilovskaya YV, Vlasov AN, Volkov-Bogorodsky DB, Merzlyakov VP, Tipenko GS (2019) Structural transformations of permafrost before the formation of the Yamal Craters. Natural hazards and risk research in Russia. Innovation and discovery in Russian science and engineering. Springer, pp 305–316.
21. Khomutov AV, Kizyakov AI, Leibman MO, Dvornikov YA (2017) Gas emission craters: in the process of studying their formation conditions. *Khold'Ok!* 15:5–13
22. Kizyakov AI, Sonyushkin AV, Khomutov AV, Dvornikov YA, Leibman MA (2017) Assessment of the relief-forming effect of the formation of the Antipayutinskaya gas emission crater according to satellite stereo data. *Modern Problems of Remote Sensing of the Earth from Space*, 14 (4): 67–75.
23. Leibman MO, Dvornikov YA, Khomutov AV (2017) Chemical features of the lakes water and gas emission craters in the marine sediments of the north of Western Siberia. *Proceedings of the XXII international scientific conference on marine geology* 4: 117–121.
24. Leibman MO, Dvornikov YuA, Khomutov AV, Kizyakov AI, Vanshtein BG (2018) Main results of 4-year gas-emission crater study. *Proceedings of 5th European conference on Permafrost, France*, pp. 293–294.

25. Leibman MO, Dvornikov YA, Streletskaya ID, Khomutov AV, Kizyakov AI, Vanshtein BG, Semenov PB (2018) Connection of gas emission craters with methane release on the north of Western Siberia. *Degassing of the Earth: geology and ecology*. Moscow:1–3
26. Leibman MO, Kizyakov AI (2016) New natural phenomenon in the permafrost zone. *Nature* 2:15–24
27. Majorowicz J, Osadetz K, Safanda J (2015) Models of talik, permafrost and gas hydrate histories – Beaufort Mackenzie Basin, Canada. *Energies* 8:6738–6764
28. Melnikov PI, Melnikov VP, Tsarev VP, Degtyarev BV, Mizulina NB, Popov AP, Bereznyakov AI, Svechnikov AM (1989) On the generation of hydrocarbons in the permafrost. *Proc Acad Sci USSR Geol Ser* 2:118–128
29. Melnikov VP, Spesivtsev VI, Kulikov VN (1997) On jet degassing of hydrocarbons as a source of ice growth on the shelf of the Pechora Sea. *Results of the fundamental studies of the Earth's cryosphere in the Arctic and Subarctic*. Novosibirsk: Nauka, pp 159–269.
30. Olenchenko VV, Sinitsky AI, Antonov EU, Eltsov IN, Kushnarenko ON, Plotnikov AE, Potapov VV, Epov MI (2015) The results of geophysical studies of the territory of the geological phenomena “Yamal crater”. *Earth's Cryosphere* XIX(4):94–106
31. Petrov VG (1930) Icings on the Amur-Yakut highway. *Academy of Sciences of the USSR, Leningrad*. 177 p
32. Sizov OS (2015) Remote analysis of the effects of surface gas emissions in the north of Western Siberia. *Geomatics* 1:53–68
33. Streletskaya ID, Leibman MO, Kizyakov AI, Oblogov GE, Vasilyev AA, Khomutov AV, Dvornikov YA (2017) Ground ice and their role in the formation of a gas emission crater on the Yamal Peninsula. *Bulletin of Moscow University. Series 5: Geography* 1(2):91–99
34. Strugov AS (1955) Hydrolaccolith explosion (Chita region). *Nature* 6:117
35. Trofimov VA (2012) Determination of gas pressure in a coal layer. *Proc Int Sci Symp “Miner's Week”* 1:324–345
36. Yakushev VS (2009) Natural gas and gas hydrates in the cryolithozone. *VNIIGAZ, Moscow*. 192 p

Borehole Temperature Measurements Under Free Thermal Convection



Dmitry Yu Demezhko, Bogdan D. Khatskevich, and Mansur G. Mindubaev

1 Introduction

One of the main methods of geothermics is temperature measurements in boreholes. Development of modern equipment provides high accuracy, stability, spatial and temporal resolution of temperature measurements that significantly expands geological applications of borehole temperature data. In addition to traditional applications, methods for studying fine hydrogeological effects [1, 8, 24, 25, 28] as well as geodynamic processes in seismically active zones using a downhole temperature monitoring [4, 12, 13, 31] are being developed. However, temperature noise caused by free thermal convection (FTC) of a fluid or air in boreholes limits the accuracy of temperature measurements. Acoustic noise generated by FTC is a serious obstacle to seismic monitoring in wells [26].

In water-filled boreholes FTC occurs when due to a positive temperature gradient a warmer and hence a lighter fluid is located below colder and heavy one. Ascending and descending water flows tend to even out density and temperature heterogeneities, but rock temperature field maintains a positive gradient.

The dimensionless Rayleigh number Ra determines the occurrence and development of convection. For borehole conditions (vertical cylinder):

$$Ra = \frac{g\beta r^4}{\nu a} G \quad (1)$$

where r is inner borehole radius, G – temperature gradient, g – acceleration due to gravity, ν – kinematic viscosity, a – thermal diffusivity, β – thermal expansion coef-

D. Y. Demezhko (✉) · B. D. Khatskevich · M. G. Mindubaev
Institute of Geophysics, UB RAS, Yekaterinburg, Russia

ficient. The parameters β , ν , a depend on temperature. The critical value of the Rayleigh number Ra_{crit} which determines the onset of convection lies within the range of 68–216 depending on the ratio of the fluid thermal conductivity and the thermal conductivity of surrounding rock λ_f/λ_m [19]:

$$Ra_{crit} = \frac{96}{5(1+7\lambda_f/\lambda_m)} \left[3(33+103\lambda_f/\lambda_m) - \sqrt{3(2567+14794\lambda_f/\lambda_m+26927(\lambda_f/\lambda_m)^2)} \right] \quad (2)$$

Thermal effects of FTC have been observed in many boreholes with a positive temperature gradient [3, 6–8, 12, 16, 18, 20, 29, 30, 32]. Figure 1a shows examples of temperature records in the kun-1 borehole (Kunashir Island, Russia). The measurements were carried out using thermistors with a resolution of ~ 0.001 K. At a depth of 20 m, where temperature gradient is close to zero, convective temperature noise is absent, but already at a depth of 80 m with a gradient of 100 K/km, the range of temperature fluctuations reaches 0.08 K. Convective temperature noise can also occur under a negative gradient. We recorded this phenomenon in a shallow water-filled hole (Fig. 1b). When water temperature value falls within the range of 0 to +4 °C, thermal expansion coefficient of water β becomes negative, and the Rayleigh number is again positive.

Despite the importance of the problem of free thermal convection for the development of high-precision borehole temperature measurements, it was not given due attention until recently. Existing approaches are based on the ideas about the structure of convective currents formed in the first half of the last century. According to these ideas ([33]; Diment and Urban, 1983; [3, 7]) FTC currents are organized as a vertical sequence of convective cells (like a Rayleigh-Benard cells in a flat layer) having a certain vertical dimension, determining the amplitude of temperature noise.

Based on the results of numerical modeling and the experiments conducted in a laboratory and in real boreholes, we are showing that the system of convective currents is organized otherwise and evaluating main FTC characteristics.

2 Numerical Modeling

First numerical simulations were carried on for a water-filled vertical channel of square section with side $2r$ [27]. A constant temperature gradient G was maintained at the channel boundaries. Numerical simulation of a square channel is easier to realize than a cylindrical one. At the same time, such a model describes quite well a real borehole with a diameter of $2r$. Due to the stabilizing effect of viscosity in the corners, the “effective” section of the square channel is somewhat less than real one [19]. The FTC equation system was solved in the Boussinesq approximation. The following units were chosen: half-width of the horizontal section r for the length; r^2/a_w where a_w is thermal diffusivity of water for the time; a_w/r for the speeds; Gr for the temperature.

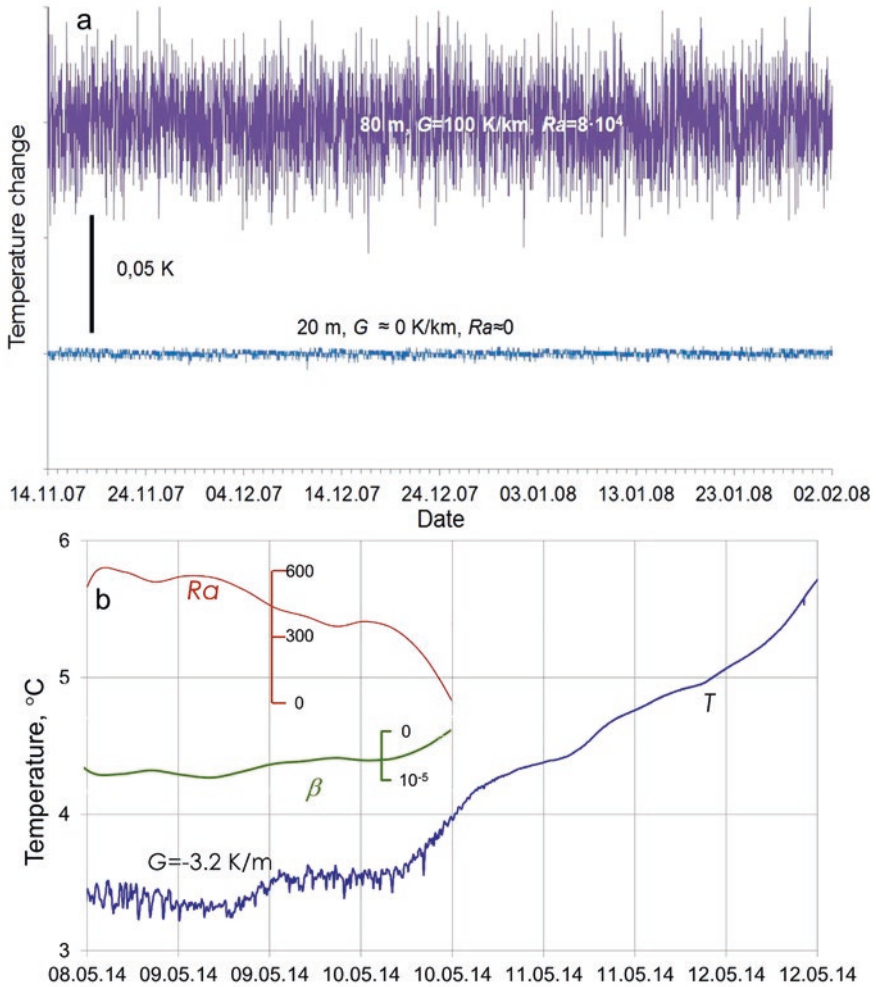


Fig. 1 Temperature noise caused by free thermal convection in water-filled boreholes: (a) under positive temperature gradient (in the 300-m borehole kun-1, Kunashir Island), (b) under negative temperature gradient (in shallow hole in Yekaterinburg)

Simulation was made under the following parameters: $Ra = 1500$, the Prandtl number $Pr = 8$, and the aspect ratio (the ratio of channel length to its half width) equal to 40. Figure 2a,b shows typical patterns of spatial distributions of temperature deviations δT from its undisturbed value (determined by temperature gradient), and the vertical velocity component u_z . In the central part of the channel FTC currents are organized as helical ascending and descending jets. At the upper and lower boundaries the helical system is broken. Near the upper boundary the descending cold jet is located inside the ascending one and vice versa near the lower boundary. A similar helical pattern of FTC currents was also obtained by Khoroshev [23].

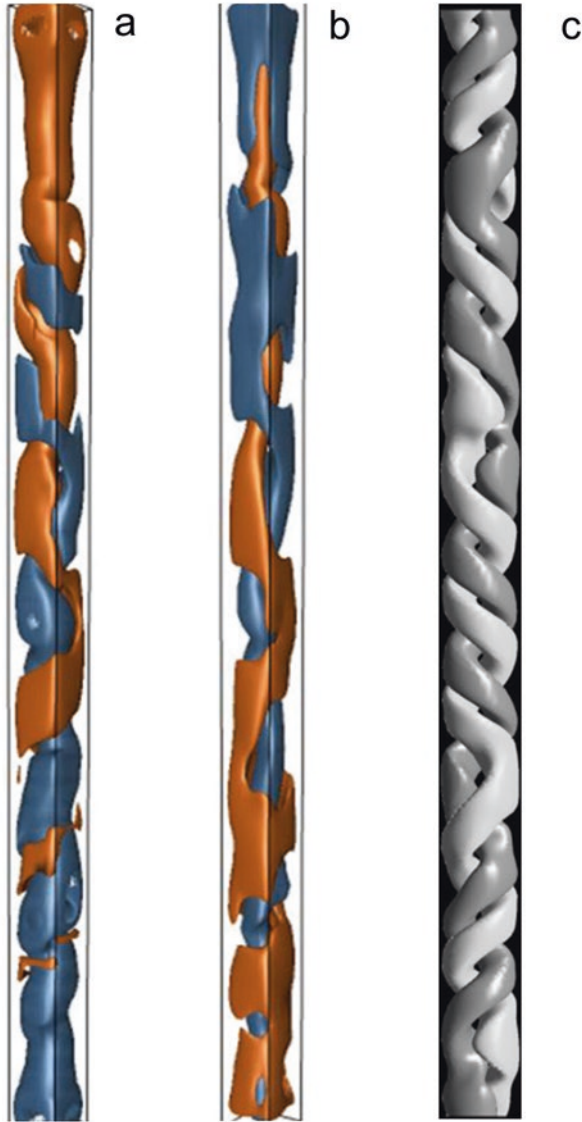


Fig. 2 Numerical modeling of the FTC currents' structure: (a, b) isosurfaces of temperature anomalies δT and the vertical velocity component u_z [27]; (c) isosurfaces of the vertical velocity component u_z [23]

In the second version of the numerical simulation, we have attempted to quantify the FTC characteristics for different values of the Rayleigh number [14]. A vertical square channel surrounded by a rock massif which thermal diffusivity a_m is different from the fluid's one a_w ($a_m/a_w = 6$), was considered. A constant temperature gradient

G was maintained on the outer edges of the massif far enough from the channel. We identified two types of temperature effects: short-term temperature fluctuations relative to its mean value and a long-term effect manifested as a decrease in geothermal gradient. It is important to take into account the long-term effect in assessment of the global heat balance of the Earth using heat flow measurements in boreholes. Temperature studies under FTC could lead to underestimating of a heat flow value.

As the Rayleigh number increases, the components of currents' velocity (averaged over the channel section) increase:

$$v_i = k_i \frac{a_w}{r} \sqrt{Ra - Ra_{cr}}, \tag{3}$$

where indices $i = "f", "z", "h"$ denote the modulus of full vector, vertical and horizontal components, respectively; $k_f = 2.3, k_z = 1.9, k_h = 1.1$ (Fig. 3). The ratio v_h/v_z is also increasing. It will be shown below that faster growth of horizontal component of the velocity is due to the increasing speed of the helical rotation system.

The amplitude of temperature fluctuations (expressed by the standard deviation from the mean value) is practically independent of the Rayleigh number, but is determined by geothermal gradient and channel radius: $\sigma \approx 3Gr$. The Rayleigh number determines spectral composition of the fluctuations. The higher the Rayleigh number, the more high-frequency fluctuations.

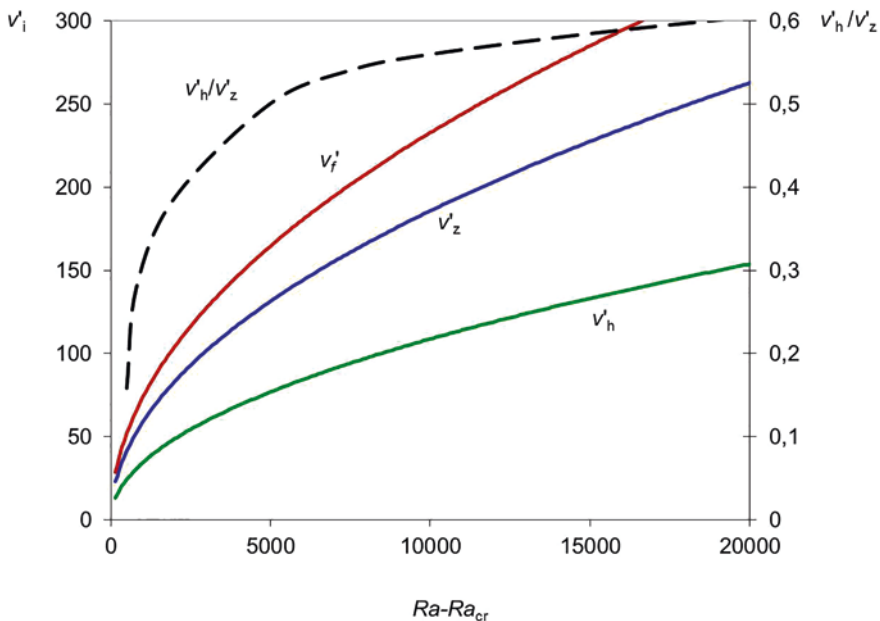


Fig. 3 Dependence of the dimensionless components of currents' velocity v' on the Rayleigh number. The average dimensional velocity is calculated as $v = v' a_w / r$

3 Infrared Thermography Method

The method of infrared thermography was developed for laboratory studies of FTC structure. The method is based on registration of temperature anomalies arising on outer walls of a vertical water-filled pipe in which the conditions of convection are maintained (Fig. 4). Temperature gradient on the pipe outer walls provides an upward flow of warm air from a toroidal heater. Temperature measurements are carried out using an infrared camera. Camera installation equipment provides the ability to move it vertically, horizontally and around the cylinder within $\pm \pi / 2$.

The measurements were carried out using an infrared camera Testo 875 in the central part of the pipe after two hours of heating and the onset of a stable convective regime. Measurements included 45-minute temperature monitoring with minute sampling of images for a given camera position. Spatiotemporal sweeps of temperature anomalies were constructed using these data (Fig. 5a). To evaluate the

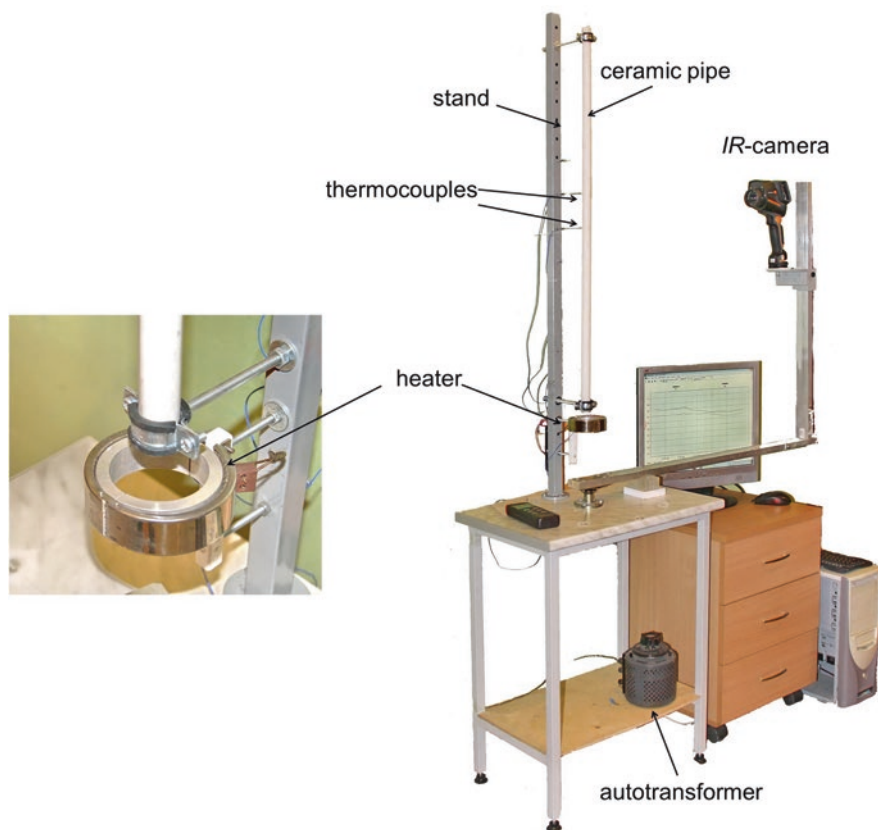


Fig. 4 Laboratory stand for FTC study

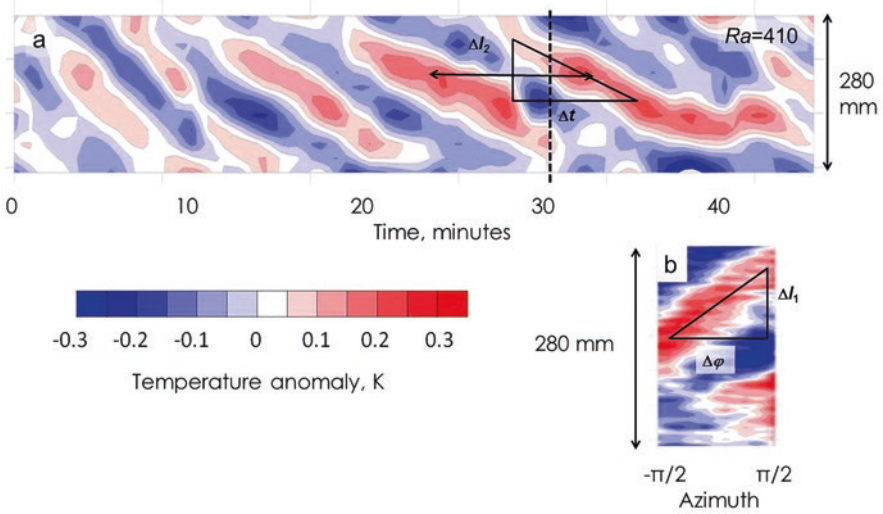


Fig. 5 Infrared thermography of water-filled pipe. (a) – spatiotemporal sweep (at fixed IR-camera position); (b) – azimuthal sweep (at fixed time – 32-th min)

anomalies on the walls, temperature trend corresponding to the mean value of temperature gradient was subtracted from the central temperature profile of each image. Measurements for azimuth sweeps (from $-\pi / 2$ to $+\pi / 2$ through $\pi / 4$) were taken before the start of the monitoring, as well as at the 16th and 31st minutes and after the end of the monitoring (Fig. 5b).

Distinct temperature anomalies appear at $Ra = 279$. Inclined anomalies on the azimuth sweep (Fig. 5b) indicate that the ascending and descending currents are organized as a system of helical jets. The anomaly inclination on the spatiotemporal sweep (Fig. 5a) is clearly manifested when $Ra \geq 322$ and indicates the rotation of the entire helical system around the cylinder axis. The slope of the anomaly on azimuth sweep $\eta_1 = \Delta l_1 / \Delta \varphi$ determines the direction of helical twist ($\eta_1 > 0$ for right helix, $\eta_1 < 0$ for left helix) and helical pitch $h = 2\pi \eta_1$. The slope of the anomaly on an angular velocity of rotation $\omega = 2\pi / \tau = \eta_2 / \eta_1$.

An experiment using a pipe with 20 mm internal diameter has confirmed the conclusions obtained by numerical modeling. FTC currents represent a helical system with the Rayleigh number slightly exceeded its critical value. The system rotates around a vertical axis. Helix pitch decreases from 270 to 130 mm (Fig. 6) as the Rayleigh number increases from 280 to 2800. On the contrary, angular velocity of rotation increases from 0.7×10^{-2} to 3.4×10^{-2} rad/s (Fig. 7). The experiment also confirmed the previously obtained dependence of the standard deviation of temperature fluctuations on geothermal gradient and inner radius of a borehole (this dependence will be discussed in more detail in the next section). Although a small-diameter pipe was used in the experiment, it is easy to generalize the results to the conditions of real boreholes using similarity laws.

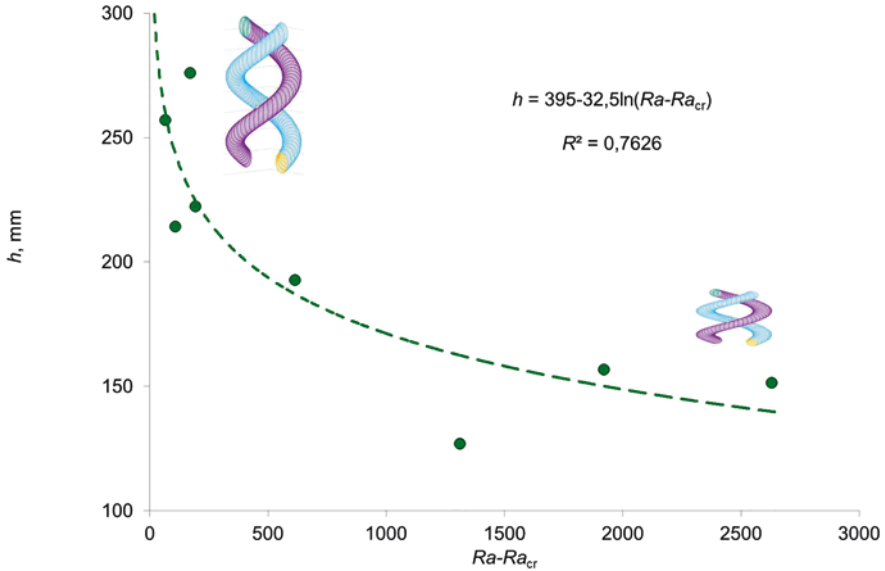


Fig. 6 Dependence of helical pitch (h) on the Rayleigh number ($Ra - Ra_{cr}$)

4 Research in Real Boreholes

4.1 Temperature Noise Estimation

Estimation of the amplitude of temperature noise caused by FTC prior to temperature measurements or a long-term temperature monitoring is one of the important problem in geothermal research. Until now, the use of the relations proposed for this assessment has been requiring knowledge of the vertical size of a convective cell — a characteristic arising from a misconception about the structure of FTC currents. Diment and Urban [17] estimated a maximum range of temperature fluctuations using the relation $\Delta T_{\max} = AGr$, where the dimensionless constant A is defined as the ratio of the vertical size of a convective cell to borehole radius. At the same time, convincing experimental estimates of the vertical size of a cell have not been obtained since then.

We proposed the dependency in which borehole radius is the only characteristic size. To check the validity of the relation $\sigma/r = kG$, we analyzed the data of temperature monitoring obtained both in a laboratory setup and in real boreholes. Collected data cover three orders of temperature gradient change – from 0.01 to 10 K/m (Fig. 8, Table 1). Most of points on the graph lie within the range $\sigma/r = (3 \div 1.5)G$. The coefficient decrease below 1.5 can be explained by the influence of borehole equipment occupying a certain part of the hole space or by the influence of drilling fluid of increased viscosity – factors contributing to the suppression of FTC. It is more difficult to explain the coefficient increase $k > 3$. Most

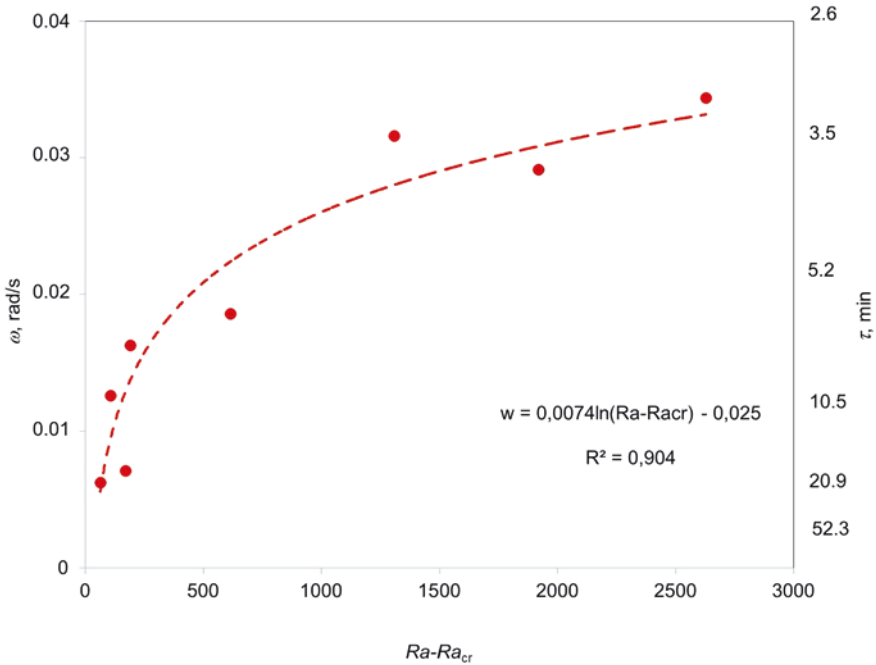


Fig. 7 Dependence of angular velocity (ω) and period of rotation (τ) on the Rayleigh number ($Ra - Ra_{cr}$)

of the points lying above the line $k = 3$ were obtained during a laboratory experiment. They most likely reflect an underestimation of temperature gradient determined under its instability over a small interval.

4.2 Convection Suppression Devices

Misconceptions about FTC structure implemented in all known technical means for suppressing convection in borehole. They divide a borehole into separate vertical intervals, for example, using packers [5, 10], or horizontal discs (shields) [2, 21, 34]. It is assumed that these intervals should be less than the vertical size of a convective cell.

Since FTC currents form a rotating helical system and are not limited vertically, the most effective method of suppressing FTC is to divide a borehole with vertical shields into separate sectors or segments (Fig. 9a,b). These shields reduce the effective cross section of a borehole and the Rayleigh number on the one hand and prevent the system rotation on the other hand ([22] – No. ...). The amplitude of temperature fluctuations decreased by 6 times (Fig. 9c) after the device (Fig. 9a) was installed in the borehole.

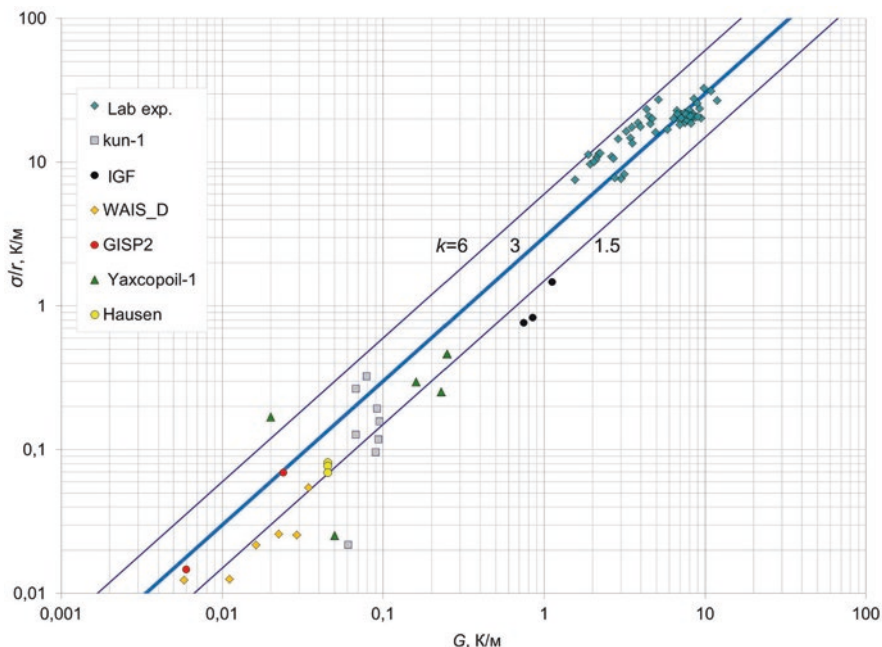


Fig. 8 Experimental dependence of the amplitude of temperature fluctuations (standard deviation) normalized to the borehole radius r from temperature gradient G . Straight lines correspond to the relations $\sigma/r = kG$

Table 1 Data to construct Fig. 8

Borehole	Observations	Borehole radius, mm	Temperature gradient, mK/m	σ , mK	Ra	Fluid	References
Lab experiment	54	10	1550–11,900	152–665	340–3500	Water	[15]
Kun-1 (Kunashir, Russia)	8	52–84	61–95	8–17	8800–67,800	Water	[12]
Yaxcopoil-1 (Mexico)	5	118	20–250	3–55	1,3105–1,6106	Water	[8]
WAIS_D (Antarctica)	6	81,5	6–25	1–5		Isopar-k	[11]
GISP2 (Greenland)	2	90,5	6–24	1–6		n-butyl acetate	[9]
IGF (Yekaterinburg, Russia)	3	50	740–1120	19–37	450–860	Water	
Hausen (Switzerland)	3	87,5	45	6–7	1550	Water	[29]

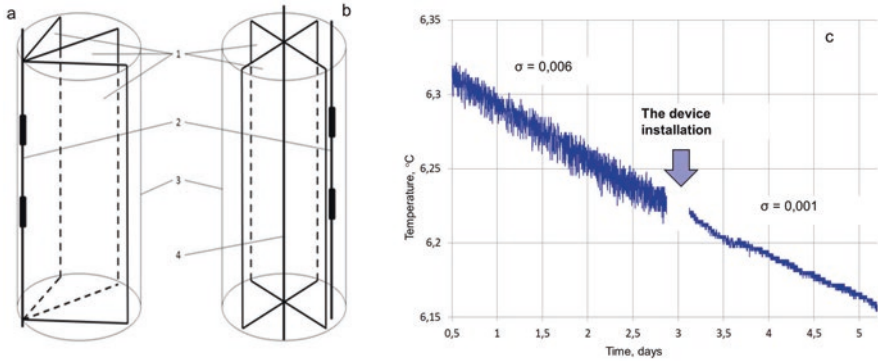


Fig. 9 The scheme of the device for suppressing the FTC temperature noise [22] and its location in the well: (a) – on a string of temperature sensors, (b) – on a separate rope. 1 – polymer film strip, 2 – string of temperature sensors, 3 – borehole, 4 – rope; (c) – an example of suppression of the FTC temperature noise in borehole

5 Conclusion

A new laboratory method for studying free thermal convection in water-filled boreholes has been developed. The method is based on infrared thermography of temperature anomalies appearing on outer walls of the vertical water-filled ceramic pipe where convection conditions are maintained.

Numerical modeling and results of laboratory and field studies show that:

1. Convective currents form a system of 2–4 helical jets rotating around a vertical axis. The velocity of currents, system rotation frequency, and helical pitch depend on the Rayleigh number value.
2. The unsteady nature of the currents generates temperature noise with the amplitude (standard deviation σ) depending on geothermal gradient G and the inner borehole radius r as $\sigma = (3 \div 1.5)Gr$. The Rayleigh number determines the spectral composition of the noise: the high-frequency component of noise rises as Ra increases.
3. Most effective way of temperature noise suppressing is to install a device on the measurement interval made of vertical shields of a polymer film interconnected in such a way that they divide a borehole into separate sectors or segments.

The studies were carried out with the support of the Russian Foundation for Basic Research, project No. 19–05–00050-a (field research in boreholes, development and full-scale testing of devices for suppressing the FTC) and state funded topic of R&D no. 0394-2020-0002 (mathematical modeling, investigations on the laboratory unit for modeling free thermal convection)

References

1. Anderson MP (2005) Heat as a ground water tracer. *Ground Water* 43(6):951–968
2. Beck A, Jaeger JC, Newstead G (1956) The measurement of the thermal conductivities of rocks by observations in boreholes. *Aust J Phys* 9(2):286–295
3. Berthold S, Börner F (2008) Detection of free vertical convection and double-diffusion in groundwater monitoring wells with geophysical borehole measurements. *Environ Geol* 54(7):1547–1566
4. Buntebarth G, Chelidze T (eds) (2005) Time-Dependent Microtemperature and Hydraulic Signals Associated with Tectonic/Seismic Activity. Tbilisi 4–108
5. Burkhardt H, Honarmand H, Pribnow D (1995) Test measurements with a new thermal conductivity borehole tool. *Tectonophysics* 244:161–165
6. Cermak V, Safanda J, Bodri L (2008a) Precise temperature monitoring in boreholes: evidence for oscillatory convection? Part I. experiments and field data. *Int J Earth Sci* 97(2):365–373
7. Cermak V, Bodri L, Safanda J (2008b) Precise temperature monitoring in boreholes: evidence for oscillatory convection? Part II: theory and interpretation. *Int J Earth Sci* 97(2):375–384
8. Cermak V, Safanda J, Bodri L (2010) Thermal instability of the fluid column in a borehole: application to the Yaxcopoil hole (Mexico). *Int J Earth Sci* 99(6):1437–1451
9. Clow GD (1999) GISP2-D temperature (Dataset). PANGAEA <https://doi.org/10.1594/PANGAEA.55517>
10. Colombani N, Giambastiani BMS, Mastrocicco M (2016) Use of shallow groundwater temperature profiles to infer climate and land use change: interpretation and measurement challenges. *Hydrol Process* 30(14):2512–2524
11. Cuffey KM, Clow G (2014) Temperature profile of the West Antarctic ice sheet divide deep borehole (Dataset) <http://www.usap-c.org/view/dataset/609550>
12. Demezhko DY, Yurkov AK, Utkin VI, Klimshin AV (2012a) On the nature of temperature variations in borehole kun-1 (Kunashir Island). *Russ Geol Geophys* 53(3):313–319. <https://doi.org/10.1016/j.rgg.2012.02.008>
13. Demezhko DY, Yurkov AK, Utkin VI, Shchapov VA (2012b) Temperature changes in the KUN-1 borehole, Kunashir Island, induced by the Tohoku Earthquake (March 11, 2011, M = 9.0). *Dokl Earth Sci* 445(1):883–887
14. Demezhko DY, Mindubaev MG, Khatskevich BD (2017) Thermal effects of natural convection in boreholes. *Russ Geol Geophys* 58(10):1270–1276
15. Demezhko DY, Khatskevich BD, Mindubaev MG (2019 –in print) Investigation of free thermal convection in water filled vertical cylinder using infrared thermography. *Russ Geol Geophys*
16. Diment WH (1967) Thermal regime of a large diameter borehole: instability of the water column and comparison of air- and water-filled conditions. *Geophysics* 32:720–726
17. Diment WH, Urban TC (1983) A simple method for detecting anomalous fluid motions in boreholes from continuous temperature logs. *GRC Trans* 7:485–490
18. Eppelbaum LV, Kutasov IM (2011) Estimation of the effect of thermal convection and casing on the temperature regime of boreholes: a review. *J Geophys Eng* 8(1):1–10
19. Gershuni G, Zhukhovitskii E (1976) Convective stability of incompressible fluids. Keter Publishing House, Jerusalem
20. Gretener PE (1967) On the thermal instability of large diameter wells—an observational report. *Geophysics* 32:727–738
21. Harries JR, Ritchie AIM (1981) The use of temperature profiles to estimate the pyritic oxidation rate in a waste rock dump from an openpit mine. *Water Air Soil Pollut* 15(4):405–423
22. Khatskevich B D, Demezhko D Yu, Mindubaev M G (2019) Sposob temperaturnogo monitoring v vodonapolnennykh skvazhinakh [the way to temperature monitoring in water filled boreholes]. Patent RF,no. 2678174, 2019
23. Khoroshev AS (2012) Numerical study of free convective flows in extended vertical cylindrical areas under a constant vertical temperature gradient on the side surface. *VESTNIK of Samara University. Aerosp Mech Eng* 5–1(36):46–48. (in Russian)

24. Klepikova MV, Roques C, Loew S, Selker J (2018) Improved characterization of groundwater flow in heterogeneous aquifers using granular polyacrylamide (PAM) gel as temporary grout. *Water Resour Res* 54(2):1410–1419
25. Lapham WW (1989) Use of temperature profiles beneath streams to determine rates of vertical ground-water flow and vertical hydraulic conductivity. Dept. of the interior, US geological survey; USGPO; Books and Open-File Reports Section, US Geological Survey 2337
26. Lee WH, Jennings P, Kisslinger C, Kanamori H (eds) (2002) International handbook of earthquake & engineering seismology. Part A. Elsevier, p 312
27. Mindubaev MG, Demezko DY (2012) Free thermal convection in boreholes: numerical modeling and experimental data. *Monitoring. Sci Technol* (“MST”) 4(13):12–18. (in Russian)
28. Pehme P, Parker BL, Cherry JA, Blohm D (2014) Detailed measurement of the magnitude and orientation of thermal gradients in lined boreholes for characterizing groundwater flow in fractured rock. *J Hydrol* 513:101–114
29. Pfister M, Rybach L (1995) High-resolution digital temperature logging in areas with significant convective heat transfer. *Geothermics* 24:99–100
30. Sammel EA (1968) Convective flow and its effect on temperature logging in small-diameter wells. *Geophysics* 33(6):1004–1012
31. Shimamura H, Ino M, Hikawa H, Iwasaki T (1985) Groundwater microtemperature in earthquake regions. *Pure Appl Geophys* 122(6):933–946
32. Urban TC, Diment WH, Nathenson M (1978) East Mesa geothermal anomaly, Imperial County, California: significance of temperatures in a deep drill hole near thermal equilibrium. *Geotherm Resour Counc Trans* 2(2):667–670
33. Van Der Merwe JH (1951) The influence of convection on measured borehole temperatures. *S Afr J Sci* 47(8):235–238
34. Vroblesky DA, Casey CC, Lowery MA (2006) Influence of in-well convection on well sampling. U.S. Geological Survey Scientific Investigations Report 5247 13 pp

Geothermal Regime of Groundwater in Moscow Under Anthropogenic Impact



Gleb I. Batrak

1 Introduction

Moscow is one of the largest cities in the world, occupying an area of 1081 square kilometer. Density of the population also is very high and is about 10,000 people per square kilometer. The infrastructure of the city is powerfully developed, however significant part of it is in unsatisfactory condition. The majority of infrastructure objects promote heat contamination of the city environment. The significant share of the contamination is in geological environment. Water-caring communications, plants, buildings with heat losses, ponds and rivers are the main sources of the contamination.

1.1 Climate Factor

The temperature of the upper part of soils and of the shallow ground waters strongly depends on temperature of air and atmospheric precipitation. For the last 100 years the mid-annual air temperature in Moscow has risen on 2,5 °C (Fig. 1, 2). On the average in the Northern hemisphere — on 0,8 °C, and 0,6 °C took last 30 years (Fig. 3). The difference between temperature on suburbs and in city centre reaches 3–4 degrees. Therefore vegetation in the city centre comes in 10 days earlier. During recent years it is possible to observe a so-called phenomenon as “islands of heat” – average air temperature on Fridays is 0.7 degrees more than in other days. In days off the city cools down a little, but starting on Monday cars and factories begin to heat the environment, achieving a local maximum of warming on Friday.

G. I. Batrak (✉)
IEG RAS, Moscow, Russia

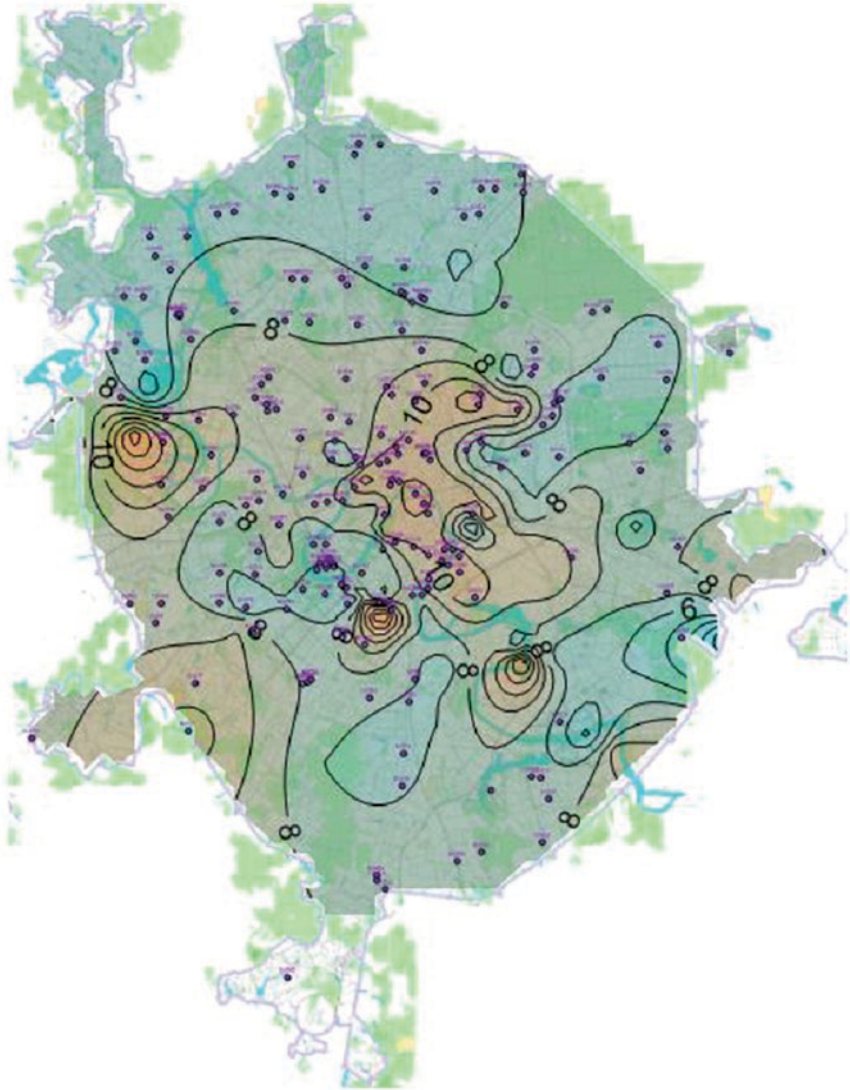


Fig. 1 The minimum groundwater temperature over many years, °C

It is visible on the diagrams that the air temperature in Moscow steadily increases. One part of a trend is caused by global processes and another part is caused by local urban activity in the city. All these result in an additional heating of the lithosphere from the surface.

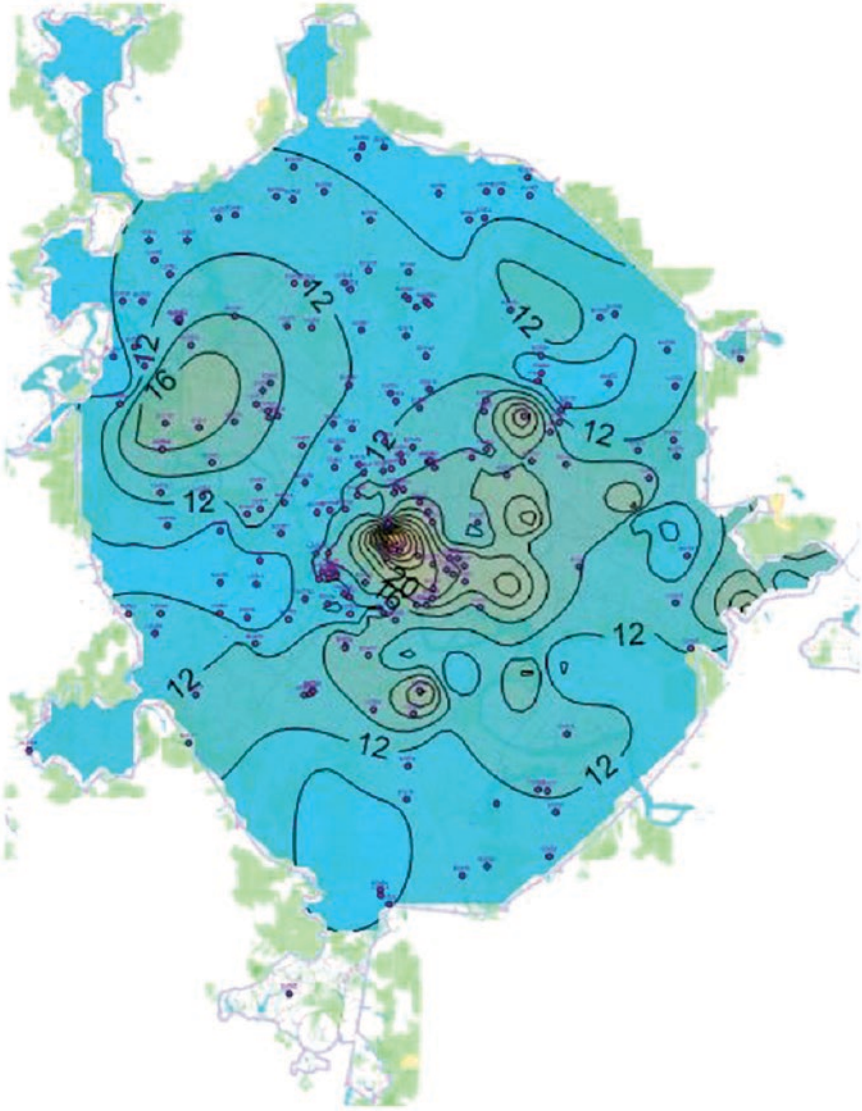


Fig. 2 Maximum groundwater temperatures over many years, °C

1.2 Soil Temperature

The influence caused by urban change of temperature regime of the top layers of the lithosphere now represents a serious environmental problem. The sources of heating are: the dumps of hot technological waters in the rivers and open reservoirs, leaks of technical water supply and industrial conditioners, warmed underground



Fig. 3 Long-term temperature amplitudes according to one-time measurements, °C

constructions, water-caring communications, tunnels, collectors etc. As a result in the territory of Moscow at average depths of 10–30 m, a steady geothermal anomaly with excess of temperature 2–6 degrees above background is observed. The anomaly is much bigger than the administrative border of the city and reaches a part of forest-covered zone to the west, south and east directions from the capital. Warming up of sandy-argillaceous soils in Moscow does not cause its structural changes, but promotes change of clay and organic soils properties that result in some surface

subsidence. Heating of rocks causes increase of aggression in relation to concrete and metal of designs. The depth and periods of soil freezing are also powerfully violated in contrast with the background region. Below a frost penetration depth of 1.6 m the soil temperature is characterized by the following values (Fig. 4):

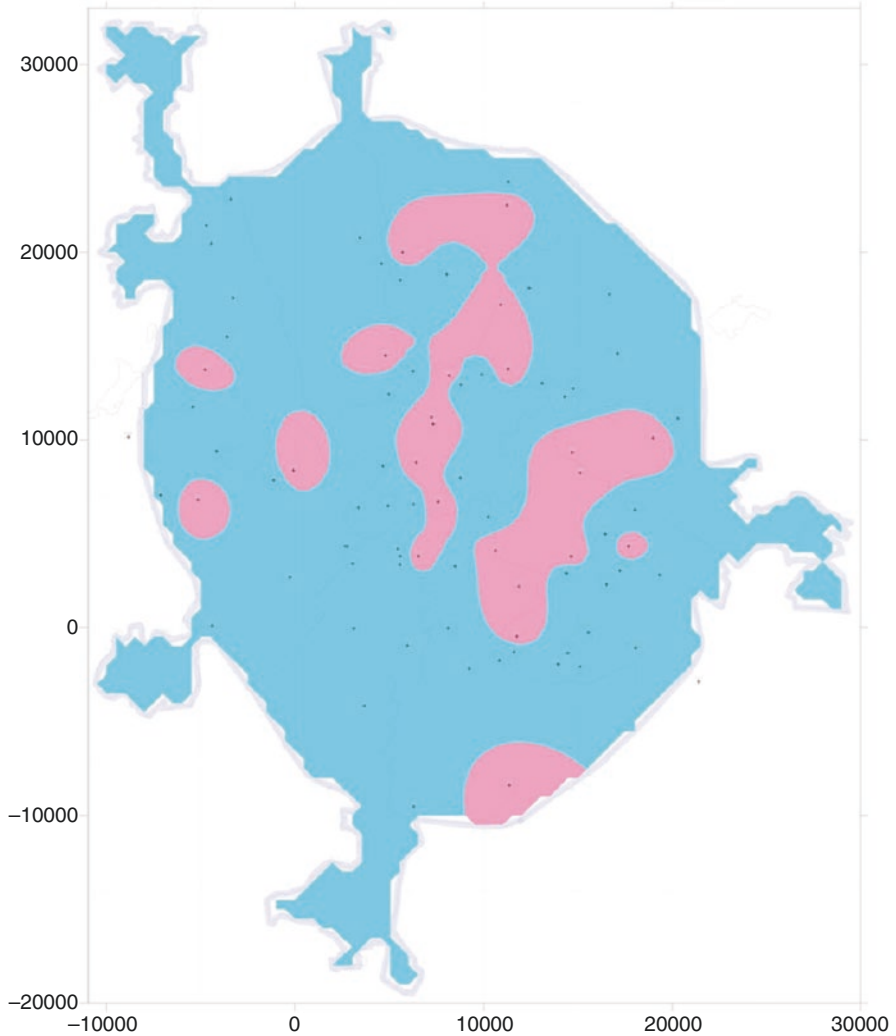


Fig. 4 Trends in groundwater temperature for 2014–2015, °C (red temperature rise is shown, blue – decrease)

1.3 Regularities of the Formation of Long-Term Temperature Regime of Groundwater

The formation of a long-term amplitude in groundwater temperatures in the city is largely due to technogenic factors. In the long-term view, the average annual air temperatures in the city are very stable. In addition, for shallow groundwater, the average annual temperature values have oscillation amplitudes much less than the intra-annual ones. For deeper groundwaters, this ratio may decrease. However, due to the distance from the earth's surface, long-term trends have small slope angles. Therefore, the pattern remains. Under conditions of technogenic disturbance, long-term amplitudes exceed seasonal amplitudes. This phenomenon can be observed in about 40% of cases. Most of the city's territory has been in a stable temperature regime for the last 10 years. Approximately half of the territory is experiencing a slight downward trend in temperatures. In the rest of the territory, the temperature rises with varying degrees of intensity. An important characteristic of the long-term regime is the cyclical nature of the average annual temperatures of groundwater. However, a nine-year series of observations does not reveal cycles for more than four years. And those are not entirely reliable.

1.4 Violation of the Temperature Regime

According to archival data, by the end of the twentieth century, as a result of the introduction of high-precision thermometric studies in a large number of observation wells into regime observations, a significant violation of the temperature regime in the territory of Moscow was revealed both in the development interval of the groundwater horizon and in the development interval of the exploited horizons of the Carboniferous (Fig. 1–4). The area with a disturbed temperature regime of groundwater was most clearly recorded by the nature of the temperature distribution at the depth of the “neutral layer”. A characteristic feature here is also the presence of maximum average annual temperatures at a depth of 20–40 m. The average annual temperature at this depth from the periphery of the city to the center increased from background values of 6.5–7 °C to 12.0 °C, and in some areas of the central part to 15–20 °C and more. The amplitude of the change in the annual temperature at the indicated depths is 0.5–2.0 °C.

Part II

Heat Transfer

Geothermy of the Continental Margins of Eastern Russia



Pavel Gornov

1 Introduction

The region under study is located in the active “transition zone” from the Eurasian continent to the Pacific Ocean. In this paper, by the transition zone is meant not only the continent–ocean border area (continental coastline, marginal seas, island arcs, and deep-sea trenches) but also the margins of intercontinental regions of the Eurasian continent with different structures and regimes of development. The transition zone is a natural buffering and damping regulator of the interaction between the Eurasian and Pacific plates and a number of lower-order plates (Okhotsk, North China, Amur block). At the boundary between the Mesozoic and Cenozoic Eras, active tectonic, magmatic, and geodynamic processes occurred in the transition zone, which were most likely responsible for the diverse geothermal regime and high no uniformity of measured heat-flow values.

In the study region, there are Precambrian platforms, massifs with a metamorphosed ancient basement, Paleozoic–Cenozoic accretion and collision-folded systems, numerous Mesozoic–Cenozoic superimposed and volcano plutonic belts, the marginal Seas of Okhotsk and Japan, and the Kuril–Kamchatka and Japanese island arc system (Fig. 1).

The state of geothermal exploration in the region is uneven; a relatively dense network of heat flow measurements is available in water areas adjacent to the north-eastern margin of Eurasia and in sedimentary basins of the region. Available geothermal information allows a reliable characterization of the thermal fields of almost all structural-formation zones in the region.

P. Gornov (✉)
ITIG FEB RAS, Khabarovsk, Russia
e-mail: gornov@itig.as.khb.ru; itig@itig.as.khb.ru

© The Author(s), under exclusive license to Springer Nature
Switzerland AG 2021

V. Svalova (ed.), *Heat-Mass Transfer and Geodynamics of the Lithosphere*,
Innovation and Discovery in Russian Science and Engineering,
https://doi.org/10.1007/978-3-030-63571-8_8

123

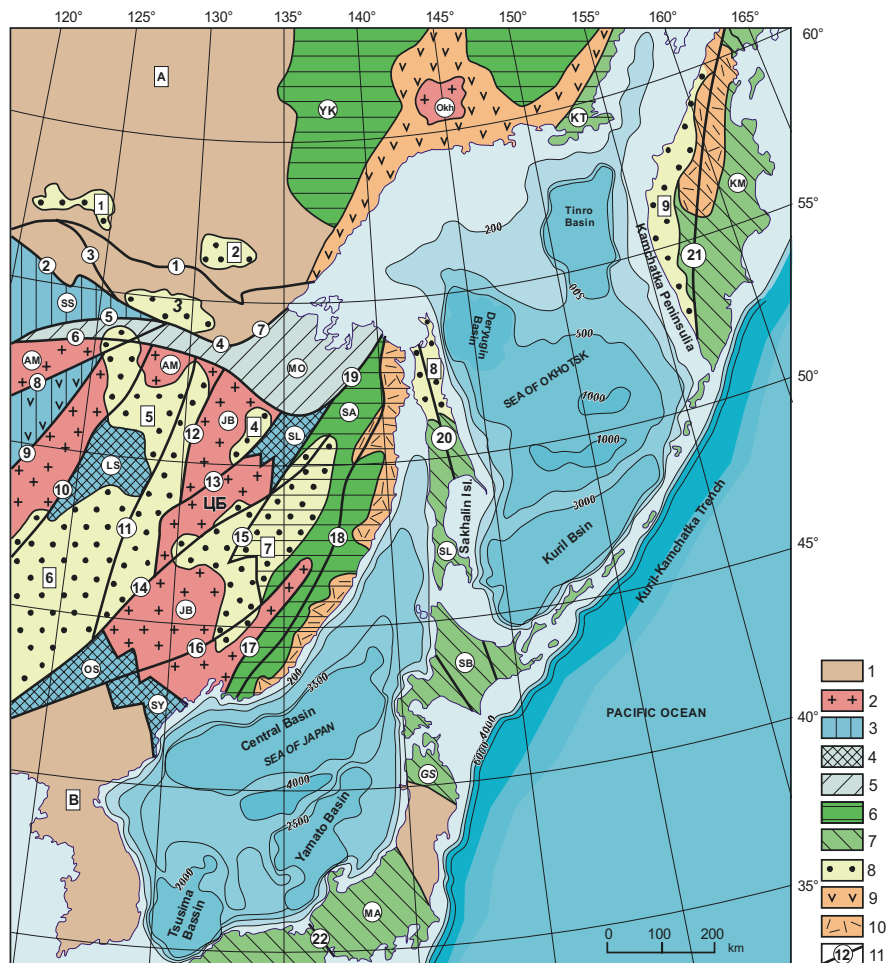


Fig. 1 Diagram of the tectonic zoning of the continent–ocean transition region in northeastern Eurasia

Compiled using the materials [18, 23, 26, 28, 31, 38]

1—ancient platforms, letters in a rectangle: Siberian (A), North China (B); 2— microcontinents with a Precambrian basement, letters in circles: Argun–Mamyn (AM), Dyagdachi (D), Jiamusi–Bureya (JB), Khanka (KH); 3–7— orogenic belts, numbers in circles: 3—Caledonian: Selenga–Stanovoy (SS), North Khingan (NK); 4— Hercynian: Lunjiang–Selemdzha (LS), Ondor Sum (OS), Silamulun–Yienben (SY), Suluk (SL); 5—Late Hercynian–Indosinian: Mongol–Okhotsk (MO); 6—Cimmerian: Sikhote-Alin (SA), Verkhoyansk–Kolyma (VK), Kolyma–Tanor (KT); 7— Late Cimmerian–Alpine: Kamchatka (KM), Sakhalin (SL), Sanbagawa (SB), Gyeongsang (GS), Mino–Tambo–Ashio (MA); 8—Mesozoic–Cenozoic sedimentary basins and depressions, numbers in squares: 1—Chulman, 2—Toko, 3—Upper Zeya, 4—Bureya, 5—Amur–Zeya, 6—North China, 7—Middle Amur, 8, North Sakhalin, 9—West Kamchatka; 9–1— volcanic belts: 9—Mesozoic, 10—Late Mesozoic–Cenozoic; 11—main faults, numbers in circles: 1—Stanovoy; 2—Dzheltulak; 3—Unakha; 4—Lanskoe; 5—North Tukuringra; 6—South Tukuringra; 7—Uligidan; 8—Derbugan; 9—Qinling; 10—Nenjiang; 11—Harbin; 12—West Turan; 13—Khingian; 14—Ilan–Itun; 15, Kukan; 16—Dunmi–Alchan; 17—Arseniev; 18—Central Sikhote–Alin; 19—Paukan, 20—Central Sakhalin, 21—Main Kamchatka; 22—Fossa Magna fault zone.

Since the last map constructions [1–3, 9, 11, 12, 19, 29, 30, 33, 36] new heat-flow measurement data have been reported [10, 15, 37], new geoinformation technologies have been developed, and new opportunities for developing more detailed and accurate geothermal models have appeared. Based on this, the objectives of this study were to generalize and analyze available geothermal information, to construct a heat-flow distribution map, and, on its basis, to determine the Moho (M) temperature and the thickness of the “geothermal” lithosphere and to construct distribution maps of these quantities.

2 Method of Developing Thermo Physical Models

The initial data for the calculations were data on heat-flow, the thermo physical characteristics of rocks, and the deep structure, which were used to evaluate temperatures in the lithosphere of the region. The deep structure of the main types of the Earth’s crust and the upper mantle was constructed using the data of [4, 5] and numerous seismic profiles (>50) of our own construction. Based on this, the model of a predominantly layered distribution of thermo physical parameters of the Earth’s crust and lithosphere was chosen.

Over the years, there have been extensive experimental and theoretical studies of the thermo physical characteristics of various types of rocks (thermal conductivity, thermal diffusivity, heat generation [24, 6, 8, 9, 14] and their distribution in the layers of the Earth’s crust and upper mantle [3, 8, 13, 27]. In the calculations, the dependence of the thermal conductivity on temperature and radiant heat transfer was taken into account. Based on these data and taking into account deep-structure models, densities of crustal layers, and longitudinal velocities of seismic waves, the following values of the thermal conductivity and heat generation in the layers of the Earth’s crust and upper mantle were chosen (Table 1).

Table 1 Thermophysical characteristics of the regions tectonosphere

Layer type	Island arc crast		Shelf		Continental margins		Oceanic crust	
	λ	A	λ	A	λ	A	λ	A
Unconsolidated sediments	–	–	–	–	–	–	1.0	1.0
Consoldated sediments	1.8	0.8	–	–	1.6	0.8	–	–
Upper crust	2.4	1.0	2.4	1.0	2.4	1.0	–	–
Middle crust	2.5	0.3	2.5	0.3	2.5	0.3	2.5	0.3
Lower crust	2.6	0.2	2.6	0.2	2.6	0.2	2.6	0.14
Upper matle	5	0.04	5	0.04	5	0.04	6	0.04

Note. λ , Coefficient of thermal conductivity (W/mK); A, heat generation (W/m³)

Estimates of the unsteady thermal regime of the lithosphere of the region [35, 36] show that 30–40 million years after the last tectonic magmatic activity in the region, the unsteadiness of the thermal field has significantly decreased, except in the areas of contemporary volcanism, zones of unloading of underground fluids, and sedimentary basins of great thickness. The thermal unsteadiness effect is extremely difficult to quantify because of the uncertainty or lack of initial data necessary for this. It is quite correct to assume that, at present, the thermal regime of the region is generally steady-state and can be modeled using a two-dimensional steady-state heat-conduction equation with variable coefficients, whose numerical solution is found using the finite-difference method (grid method) [21, 22, 34].

Without going into a discussion of the physical and geological nature of the interface between the lithosphere and asthenosphere and the Moho, we note that the lithosphere is a solid, fairly rigid shell of the Earth, whose lower boundary may be located in zones of partial melting of the upper mantle and is determined by various geophysical methods. The inhomogeneity of the relief of its base varies widely according to different data. It is also assumed that in the upper mantle, there is a rheological boundary, or, more precisely, a region that separates the overlying lithosphere from the underlying asthenosphere, whose thickness reaches a few tens of kilometers. The same can be said of the Moho because of the “fuzziness” in the determination of reflector depths, whereby the transition from the crust to the upper mantle extends vertically for 20 km in the Baltic Shield and for 5 km in Western Europe [20].

In this paper, both Moho temperatures and the depths of the base of the lithosphere are tied to the conventional rigid boundaries—the Moho depth and the depth of the solidus temperature of the mantle material (dry peridotite). The temperature of the beginning of rock melting varies from 1050 °C to 1300 °C, according to different authors [3, 8, 27]. We determined its value equal to 1200 °C. This temperature corresponds to zones of partial melting of the mantle (dry peridotite), and the depths of geoisotherms of this temperature determine the lithosphere thickness (the “geothermal” method of determining the lithosphere thickness).

At each point of heat-flow determination, the temperature distribution was calculated to depths of 200 km at intervals of 1–10 km, and the obtained values were used to determine Moho temperatures and the depths of 1200 °C geoisotherm. In the calculations, heat-flow values less than 40 and more than 120 mW/m² were excluded. In the map of the lithospheric thickness, the regions of rise of the asthenosphere to the surface are bounded by the 60 km isoline and subsidence regions by the 180 km isoline. The distribution maps of heat flow, lithosphere thickness, and Moho temperatures were constructed using ArcGIS geostatistical Analyst.

3 Results of Geothermal Studies of the Region

3.1 *Geothermal Parameters of the Continental Part of the Region*

The continental part of the continent–ocean transition in the north of Eurasia has low geothermal parameters. The strike of heat-flow anomalies generally corresponds to the direction of geomorphological and tectonic structures. In the east of Russia, heat-flow anomalies are oriented north-south and northwest, similar to the structures, and in the northeast of China, northeast and roughly north-south. The average heat-flow values of the tectonic structures of the region vary from 50 to 90 mW/m². Maximum values are obtained for volcanic belts (70–90 mW/m²) and sedimentary, mainly petroleum, basins of the region (80–90 mW/m²), and minimum values for Precambrian blocks, massifs, and orogenic belts (45–60 mW/m²).

The heat flow of Precambrian blocks and massifs is primarily determined by the radiogenic heat generation of rocks, the great thickness of rocks with high thermal conductivity, and prolonged surface cooling of these structures. Within the Siberian platform, the heat flow varies from 30 to 65 mW/m² with an average of 42 mW/m², and the geothermal gradient from 10 to 30 K/km. Blocks with an elevated heat flow of 45–50 mW/m² are characterized by high radiogenic heat generation of rocks. The heat flow of the central part of the Aldan–Stanovoy shield is 30–50 mW/m². In the eastern part of the shield, the heat flow varies from 35 to 65 mW/m². In the north, the platform cover region has heat-flow values of 20–50 mW/m²; low values of 20–30 mW/m² can be explained by a set of factors, such as the long-term tectonic passivity of lithosphere blocks, the great thickness of rocks with high thermal conductivity and low heat generation, and long-term surface cooling. Higher heat flows (45–60 mW/m²) are noted in the South Yakutian superimposed Mesozoic basins (Chul'man and Ytymdzha). In the Toko Basin, elevated heat flows of 65–80 mW/m² are obtained, which may be related to mantle and asthenospheric diapirism and the high mantle component of the heat flow. Slightly higher heat flows are observed in the North China Platform. Measured heat-flow values vary from 30 to 82 mW/m², with an average value of 56 mW/m². Most of the points of heat-flow determining are confined to rift-related depressions. All of them have elevated heat flows (60–80 mW/m²) and geothermal gradients (30–40 K/km).

In the orogenic belts of the region, the average heat flows (50–60 mW/m²) and geothermal gradients (20–30 K/km) are higher than those in the Precambrian blocks and massifs. Regularity is observed in the changes in the geothermal characteristics as a function of age. The heat flow and geothermal gradient are higher in younger folding regions. Thus, in the Early Paleozoic Selenga–Stanovoy orogenic belt, the heat flow is 45–50 mW/m² and the geothermal gradient is 20–25 K/km. The heat flow and geothermal gradient of the Mesozoic orogenic belts increase to 55–60 mW/m² and 30 K/km, respectively. The average heat flow and geothermal gradient of the

Late Mesozoic Sikhote-Alin orogenic belt are 55 mW/m^2 and 25 K/km . The southern part of the belt has elevated heat-flow values $>60 \text{ mW/m}^2$ confined to the crosscutting extensional structures and shear dislocation zones responsible for Late Cenozoic mafic magmatism. Examples of such areas are the Shkotovo and Shufan basalt plateaus in southern Primorye and the Samarga and Sovgavan plateaus on the coast of the Tatar Strait.

Among the volcanic belts, maximum geothermal parameters (85 mW/m^2 and 42 K/km) are observed for the marginal continental South Korea belt [17]. Minimum values of heat flow ($60\text{--}70 \text{ mW/m}^2$) and geothermal gradient ($25\text{--}30 \text{ K/km}$) are established for intracontinental belts (Yinshan and Great Hingan). Among the latter, there are belts (Umlekan–Ogodzha and Dahingan) with elevated values of geothermal parameters. The values of heat flow and geothermal gradient for them are 80 and 72 mW/m^2 ; 35 and 30 K/km , respectively. Noticeable change in the geothermal characteristics as a function of the thickness of the crust of volcanic belts is not observed. Slight increase in heat flow for belts with reduced crust thickness is not accompanied by an increase in the geothermal gradient. It should be noted that volcanic belts, as a rule, correspond to an abrupt change in the thickness of the Earth's crust. The differentiation of the geothermal characteristics of volcanic belts of different age is less pronounced than for folded systems. There is an increase in the average values of heat flow and geothermal gradient of Cenozoic volcanic belts compared to their values for Mesozoic–Cenozoic belts and Paleozoic volcanic fields. The latter are similar in the average heat flow and are characterized by a smooth increase in the geothermal gradient as they rejuvenate. Some volcanic belts may not follow these trends. Thus, the South Korea belt, composed mainly of Mesozoic volcanics with a subordinate development of Cenozoic volcanics, has comparable or higher values of heat flow and geothermal gradient than volcanic Cenozoic belts [25].

The best explored parts of the study region are sedimentary basins, most of which belong to the Mesozoic–Cenozoic rift-related structures of the continental margins. They all have high geothermal characteristics, especially in depressions of the North China sedimentary basin (Bohai, Liaohe, and Sunlyao), in which the heat flow (on average $70\text{--}80 \text{ mW/m}^2$) and the geothermal gradient ($30\text{--}40 \text{ K/km}$) are considerably higher than those in the surrounding areas ($50\text{--}55 \text{ mW/m}^2$ and $20\text{--}25 \text{ K/km}$). This is most likely due to the intense removal of deep heat from the heated mantle and asthenospheric diapirs along the destructive zones formed as a result of cracking and extension of the Earth's crust and upper mantle. High heat flows were determined in basins with a thick sedimentary cover: Upper Bureya, Upper Zeya, and Toko ($80\text{--}90 \text{ mW/m}^2$), which may be related to heat shielding by a thick layer of weakly lithified clastic deposits and the increased radioactivity of cover rocks. The Middle Amur basin is characterized by low differentiated heat-flow values of about $40\text{--}60 \text{ mW/m}^2$ with an average of 55 mW/m^2 and a geothermal gradient of $20\text{--}30 \text{ K/km}$.

The geothermal parameters of the main tectonic structures of the region are summarized in Table 2.

Table 2 Geothermal parameters of the main tectonic structures of the northeastern Eurasia

Tectonic structure	Geothermal gradient, K/km	Thermal conductivity, W/mK	Thermal flow, mW/m ²	Number of measurements	Temperature at Moho boundary, °C	Lithosphere thickness, km	Earth's crust, km
Siberian platform	10–30	2.28	42	> 100	400–600	140–180	40–44
Jiamusi–Bureya massif	20–25	2.36	50	27	400–600	120–130	35
Khankai massif	25–30	1.71	55	16	500–600	140–160	34
North China platform	25–30	1.95	56	> 100	400–600	120–140	35
Selenga–Stanovoy orogenic belt	20–25	1.90	50	15	500–600	140–160	40
North Khingan orogenic belt	25–30	2.09	60	25	600–700	140–150	39
Sikhote-Alin orogenic belt	25–30	1.83	55	30	500–700	120–140	36
Sikhote-Alin volcanogenic belt	30–35	2.18	70	15	650–750	100–120	35
Dahingan volcanogenic belt	30–35	2.20	72	15	700–800	100–120	38
Yinshan volcanogenic belt	25–30	2.25	70	19	600–700	100–120	34
Umlekan–Ogodga volcanogenic belt	35–40	1.95	80	3	700–800	80–100	38–40
South Yakutian group of depressions	20–25	2.80	60	20	600–700	140–160	42–44
Bureya depression	35–40	2.85	90	4	800–900	70–80	34–36
North Baikal group of depressions	20–25	2.70	50	17	400–500	120–140	40–44

(continued)

Table 2 (continued)

Tectonic structure	Geothermal gradient, K/km	Thermal conductivity, W/mK	Thermal flow, mW/m ²	Number of measurements	Temperature at Moho boundary, °C	Lithosphere thickness, km	Earth's crust, km
Upper Zeya depression	40–45	2.20	90	2	800–900	70–80	38–40
Middle Amur depression	20–30	2.12	55	10	500–600	100–120	32–34
Amur-Zeya depression	20–25	2.21	45	9	400–500	140–160	38–40
North China sedimentary basin	35–40	1.73	70	> 100	700–800	90–100	30–32

3.2 Geothermal Parameters of the Marginal Seas of the Region

The heat flow of the marginal seas is high (80–150 mW/m²) and shows a general trend of being considerably higher in depressions and troughs than on hills. The average heat flow of the Sea of Japan is 95 mW/m². Most of the water area is covered by anomalies; in large positive anomalies, the heat flow reaches 100–150 mW/m², and in the southern part of the Tatar Strait, it exceeds 100 mW/m². The average heat flow of the Okhotsk Sea in the central and southern parts is 85 mW/m². Elevated heat flows of 85–120 mW/m² are observed in the Deryugin and Tinro troughs and the Kuril basin. The Central Okhotsk uplift is characterized as a zone of relatively low heat flow—60 mW/m². Maximum seismic activity in the junction zone of the Kuril–Kamchatka and Japanese island arcs is observed on the contact line of anomalously high and low heat flows. Here the horizontal temperature gradient reaches 50 °K/km, which can give rise to thermoplastic stresses [7]. The epicenters of catastrophic earthquakes fall quite accurately on this line. In the vicinity of deepwater troughs, the heat flow is lower than the average oceanic value and is 40–50 mW/m². In the Kuril–Kamchatka and Japan island arcs regions, the heat flow rises to 80–120 mW/m², and in the zones of back-arc spreading (Honshu and Kuril basins), the heat flow at some measurement points reaches anomalously high values of 140–180 mW/m², which may be due to the hydrothermal and volcanic activity of the Earth's interior (Fig. 2).

3.3 Moho Temperatures and the Thickness of the “Geothermal” Lithosphere

In the Asian-Pacific transition zone of North Eurasia, all types of the Earth's crust are represented [16]. The continental crust is 38–44 km thick, the oceanic crust 8–12 km thick, and the transitional crust 12–34 km thick. Maximum crust thickness (38–44 km), low heat flows (40–55 mW/m²), and minimum Moho temperatures (500–700 °C) are observed on ancient platforms and Precambrian blocks and massifs. Moho temperatures at these structures are mainly determined by radiogenic heat generation (²³⁸U and ²³²Th) in the Earth's crust, and temperatures of 600–700 °C are, as a rule confined, to areas with a granite-metamorphic layer of increased thickness.

The heat flow and Moho temperature increase with decreasing thickness and age of the crust. The Moho temperatures of orogenic belts vary from 500 °C (Caledonian Selenga–Stanovoy) to 700–800 °C (Late Cimmerian–Alpine Sakhalin and Kamchatka belts). In the Mesozoic–Cenozoic sedimentary basins of the region, the thickness of the Earth's crust is reduced to 30–35 km, and most of them have a rift-related nature and high geothermal activity. The Moho temperatures increase from 600–700 °C (North Baikal group of troughs) to 800–900 °C in the depressions of

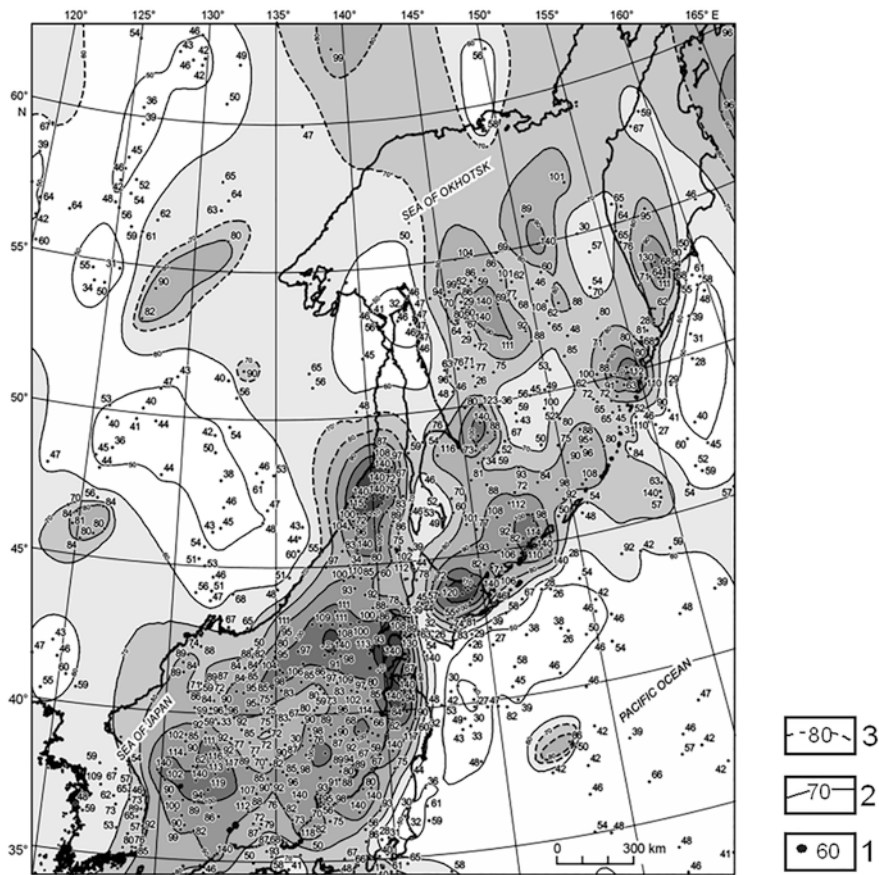


Fig. 2 Map of the heat flow of the continent–ocean transition region of northeastern Eurasia. 1, heat-flow measurement points (mW/m^2); 2 heat-flow isolines; 3, presumed heat-flow isolines. Heat-flow values from [10, 15]

the North China sedimentary basin. Relatively high Moho temperatures are typical of the marginal continental volcanic belts: the Mesozoic Okhotsk–Chukotka and Sikhote-Alin belts ($650\text{--}750\text{ }^\circ\text{C}$) and the Late Mesozoic–Cenozoic South Korea belt ($700\text{--}800\text{ }^\circ\text{C}$) (Fig. 3).

Maximum Moho temperatures and minimum lithosphere thickness are, as a rule, characteristic of deep-sea basins of marginal seas. In the axial parts of these structures, the lithosphere thickness is $40\text{--}50\text{ km}$ and the Moho temperatures are $900\text{--}1000\text{ }^\circ\text{C}$; on the margins of the structures, the lithosphere thickness is increased to $60\text{--}70\text{ km}$ and the Moho temperatures are $600\text{--}800\text{ }^\circ\text{C}$. Minimum Moho temperatures of $500\text{--}700\text{ }^\circ\text{C}$ and maximum lithosphere thickness of $90\text{--}120\text{ km}$ are established within deep-sea trenches. On the island arcs of the region, the thermal field is sharply unsteady. Partial melting zones and magmatic sources may lie at depths of

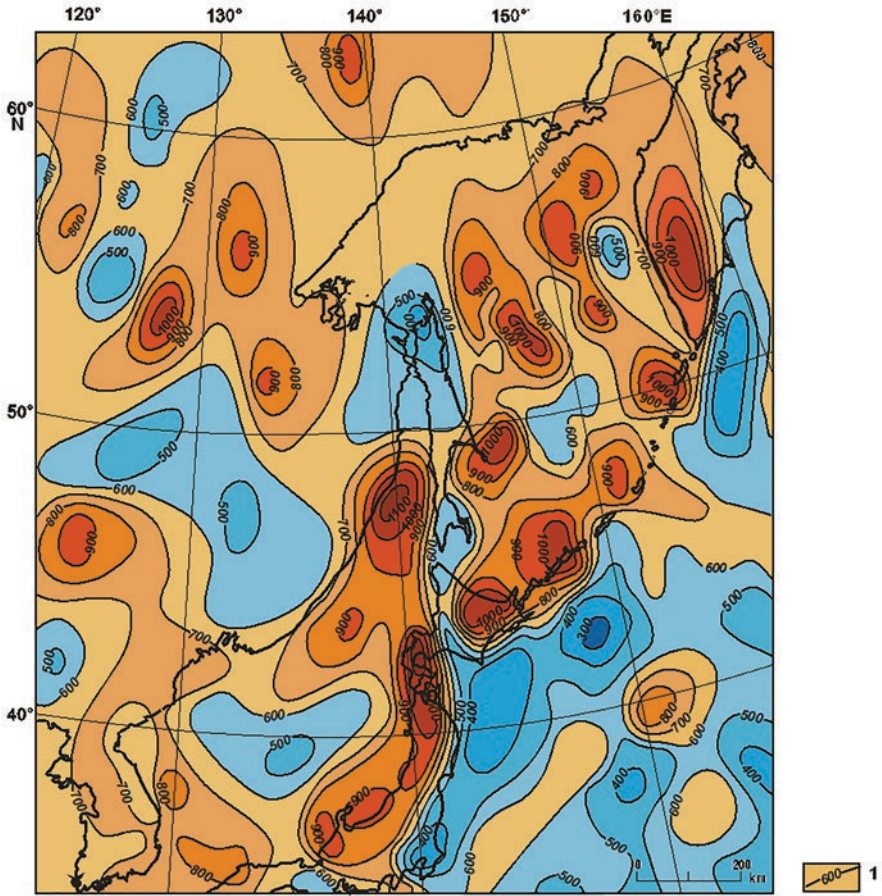


Fig. 3 Moho temperatures of the continent–ocean transition in northeastern Eurasia. 1, isotherms on the surface of M, °C

20, 40, and 60 km with a temperature of about 1200 °C. It is most likely that the partial melting zone does not have a clear level here, and the lithosphere is saturated with numerous magmatic sources located at different depths. The heat flow and the lithosphere thickness naturally depend on the age of the last tectonic-magmatic activity.

The depths to the top of the asthenosphere of the region vary, according to geothermal data, from 60–70 km (Tsushima, Central Japanese, and South Kuril) to more than 180 km (north of the Siberian Platform). A rise of the top of the asthenosphere (90–110 km) is observed on the southern margin of the Aldan–Stanovoy shield and the Mongol–Okhotsk orogenic belt at their junction with the Sikhote-Alin orogen. The Sikhote-Alin orogen is recorded as a gradual west-east decrease in lithosphere thickness from 100 to 80 km, except in the Lower Amur region, in which the lithosphere thickens to 130–140 km. In the south of the region, the area of

reduced lithosphere thickness of 80–100 km corresponds to the eastern block of the North China Platform. The southeastern part of the Siberian Platform has a thickened lithosphere of 130–160 km on the Aldan–Stanovoy shield and more than 170–190 km on the north of the platform. In the Japanese and Kuril–Kamchatka trenches, the lithosphere thickness is 120–140 km. Reduction in lithosphere thickness occurs in all deep-sea trenches to 50–70 km and its thickening to 90 km is observed on the hills of the Japan and Okhotsk seas (Fig. 4).

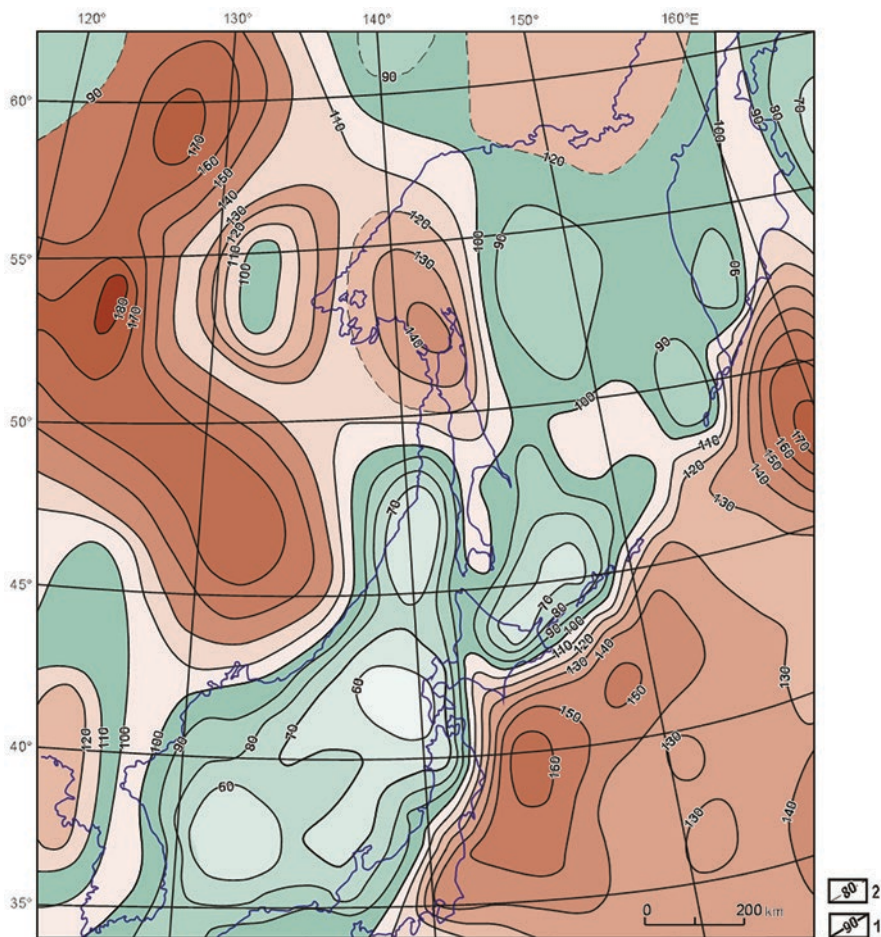


Fig. 4 Lithosphere thickness in the continent–ocean transition region in northeastern Eurasia. 1, lithosphere thickness isolines (km); 2, presumed lithospheric thickness

4 Conclusions

We believe that the thermal field is the least studied and the most controversial of all the physical fields of the Earth. This is primarily due to the fact that all our knowledge about the distribution of heat sources and heat-transfer mechanisms in the Earth are based on measurements performed at small depths (a few kilometers). Moreover, these data do not have unambiguous interpretation. To date, both the method and analytical equipment for heat-flow measurements are imperfect. Direct (*in situ*) qualitative methods for measuring the heat flow on the mainland are not available. All heat-flow measurements are tied to wells in which the temperature gradient and the thermal conductivity of rocks penetrated by a well are separately measured and their product yields the heat-flow value at the observation point. For regions of the Earth deeper than 10 km and further, available data on the temperature distribution are very scarce and unreliable, and the location of heat sources and the heat-transfer mechanism are not exactly known. Nevertheless, the construction of temperature models at the boundaries separating the Earth's crust from the upper mantle and the lithosphere from the asthenosphere is very important, in our opinion, since temperatures directly or indirectly cause most of the tectonic and magmatic processes at the interfaces between the two most important spheres of the Earth.

The thermal field of the region was analyzed. The values of geothermal parameters in the study region are not high. The average heat flows for the tectonic structures in the region have a small variation of 50–70 mW/m²; maximum values are characteristic of volcanic belts (90–200 mW/m²) and sedimentary, mainly petroleum, regional basins (80–90 mW/m²), and minimum values are observed for Precambrian blocks, massifs, and orogenic belts (50–53 mW/m²).

The heat flow of marginal seas is high, 80–150 mW/m² and shows a general trend of being considerably higher in basins and depressions than on hills. In the vicinity of deep-sea trenches, the heat flow is lowered relative to the mid-oceanic value and is 40–50 mW/m². This may be due to the subduction of the Pacific plate under the Eurasian plate, resulting in shielding of the mantle component of the heat flow, as well as to thermal water circulation within the seabed crust. There are also other models of the low heat flow in the zone of seabed trenches. The factors responsible for the low heat flow in the Central Hokkaido–Sakhalin narrow zone may be the formation of a high-temperature source in the mantle, the occurrence of convective heat and mass transfer with a small adiabatic gradient, in part, heat absorption due to metamorphism and granitization, and, to a lesser extent, a decrease in the heat flow under the influence of refraction, sedimentation, and thrusts.

In the continent–ocean transition region, there are numerous positive anomalies with heat flows exceeding 100 mW/m², which are mainly confined to deep-sea trenches of marginal seas, the Kuril–Kamchatka and Japanese island arcs, and the southern Tatar Strait region. The thermal field of these structures is most likely unsteady, but the thermal unsteadiness effect is extremely difficult to quantify due to the uncertainty or lack of initial data necessary for this; in general, they do not determine the overall heat-flow distribution pattern in the region.

Both Moho temperatures and the depths to the top of the asthenosphere primarily depend on heat-flow values. The heat flow and lithospheric thickness are inversely related to each other. Elevated and high heat flows are recorded in areas with reduced lithospheric thickness and high Moho temperatures. This may be indicative of the thermal activity of the upper mantle, thermal destruction of the Earth's crust, and, partly, its heat-shielding effect. The mantle component of the heat flow of marginal seas is 80–90% of the total, whereas for continental margin areas, the mantle heat flow does not exceed 30–40%. Local anomalies of heat flow, temperature, and lithospheric thickness of a few tens of kilometers are due to the irregularity of relief forms, contrasting heat conductivity of the lower layers of the sedimentary cover relative to the enclosing strata of the crystalline foundation, and the presence of additional heat sources. In this case, the heat-flow amplitude can be 2–3 times higher than the average value for the region, and the source of these anomalies is at depths of a few tens of kilometers.

For heat-flow values <40 mW/m², the “geothermal” method for determining the lithosphere thickness yields poor-quality results. For these values, existing models of the heat generation of the crust determine the entire surface heat flow, and the heat removal from the depths of the Earth is as if absent, which is unlikely, and at depths of 200 to 300 km, the temperature does not reach the melting point of rocks. For low heat flows, the lithosphere thickness exceeds 200 km and such regions can act as “viscous anchors” [27]. The region of the most probable location of the pole of rotation of the Amur plate is given in [32] 57° to 60° N and 117° to 123° E; it is characterized by reduced heat flow (40–50 mW/m²) and increased lithosphere thickness (180–200 km).

References

1. Artemieva IM (2006) *Tectonophysics* 416
2. Artemieva IM, Mooney WD (2001) *J Geophys Res* 106
3. Chermak V (1982) *Izv. AN SSSR, Fizika Zemli* 1
4. Chuikova NA, Stroev PA, Koryakin ED, Grushinskii AN, Maksimova TG (1998) *Fizika Zemli*, 9
5. Didenko AN (ed) (2010) *Deep structure and metallogeny of East Asia* [in Russian]. Dal'nauka, Vladivostok
6. Dorofeeva RP (1986) *Geologiya i Geofizika* 27
7. Duchkov AD, Sokolova LS (2014) *Interexpo Geo-Siberia* 2
8. Duchkov AD, Lysak SV, Balobaev VT (eds) (1987) *Thermal field of the interior of Siberia* [in Russian]. Nauka, Novosibirsk, p 197
9. Duchkov AD, Sokolova LS, Rodyakin SV, Chernysh PS (2014) *Geologiya i Geofizika* 55 (5–6)
10. *Geothermal Atlas of Siberia and the Far East* <http://www.maps.nrcgit.ru/geoterm/> (2014)
11. Gordienko VV, Andreev AA, Bikkenina SK, Van'yan LL, Veselov OV, Erokhov VV, Zhil'tsov EG, Zavgorodnyaya OV, Kulik SK, Logvinov IM, Lyapishev AM, Martanus ER, Moroz YF, Soinov VV, Solov'ev VN, Tarakanov RZ (1992) *Tectonosphere of the Pacific margin of Asia* [in Russian]. FEB RAS, Vladivostok. p 236
12. Gornov PY (1998) *Thermal regime of the Earth's crust of the Far East of Russia*. In: *Structure and evolution of the geospheres* [in Russian]. Khabarovsk, pp 169–171

13. Gornov PY, Goroshko MV, Malyshev YF, Podgornyi VY (2009) *Geologiya i Geofizika* 50 (5)
14. Gornov PY (2015) *Geologiya i Geofizika* 56 (3)
15. Global heat flow database (IHFC) <http://www.heatflow.und.edu> (2011)
16. Khain EV, Lomize MG (1995) *Geotectonics with the basics of geodynamics* [in Russian]. Izd. Mosk. Univ., Moscow, p 480
17. Kim, H.C, Lee, Y. (2007) *J Geophys Res* 12
18. Li JH, Kroener A, Qian XL, O'Brien P (2000) *Acta Geol Sin* 74(2)
19. Levin LE (2006) Structure of the thermal lithosphere and asthenosphere beneath the oceans and continents. *Geotektonika* 5
20. Lobkovskii LI, Nikishin AM, Khain VE (2004) Modern problems of geotectonics and geodynamics [in Russian]. Nauchnyi Mir, Moscow, p 612
21. Lyubimova EA, Lyuboshits VM, Parfenyuk OI (1983) Numerical models of the thermal fields of the earth [in Russian]. Nauka, Moscow, p 125
22. Lyuboshits VÌ (1976) *Izv. AN SSSR, Fizika Zemli* 9
23. Mossakovskii AA, Ruzhentsov SV, Samygin SG, Kheroskova TN (1993) *Geotektonika*, 6
24. Malyshev YF (1977) Geophysical studies of the Precambrian of the Aldan Shield [in Russian]. Nauka, Moscow, p 128
25. Malyshev, Yu.F., Lipina, E.N. *Tikhookeanskaya Geologiya*, 1 (1994)
26. Parfenov LM, Berzin NA, Khanchuk AI, Badarch G, Belichenko VG, Bulgatov AN, Dril' SI, Kirillova GL, Kuz'min MI, Nokleberg U, Prokop'ev AV, Timofeev VF, Tomurtogoo O, Yan' X (2003) *Tikhookeanskaya Geologiya* 22(6)
27. Pollack H, Chapman DS (1977) *Tectonophysics* 38
28. Ren J, Wang Z, Chen B (1999) Geological Publishing House, Beijing. p 32
29. Shevaldin YV, Balabashin VI, Kiselev YV (1984) Nauka, Moscow. pp 66–74
30. Sychev PM, Veselov OV, Volkova NA, Soinov VV (1982) *Tikhookeanskaya Geologiya*, 6
31. Tectonics, deep structure, and metallogeny in the junction zone between the Central Asian and Pacific belts. Explanatory note to a 1:1,500,000 tectonic map (in Russian). FEB RAS, Vladivostok–Khabarovsk, 2005. p 264
32. Timofeev VY, Kazanskii AY, Ardyukov DG, Metelkin DV, Gornov PY, Shestakov NV, Boiko EV, Timofeev FV, Gil'manova GZ (2011) *Tikhookeanskaya Geologiya* 30(4)
33. Tuezov IK (1988) Map of the heat flow of the Pacific Ocean and adjacent continents [in Russian]. (Far Eastern Scientific Center of the USSR Academy of Sciences Khabarovsk 1988
34. Tuezov IK, Epaneshnikov VD *Izv. AN SSSR, Fizika Zemli*, 7 (1987)
35. Tuezov IK, Epaneshnikov VD, Hayakawa M (1995) Geothermics: regional problems, modeling, and applications [in Russian]. Nedra, Moscow, p 303
36. Veselov OV, Volkova NA, Eremin GD, Soinov VV, Kozlov NA (1974) *Dokl. AN SSSR* 217(4)
37. Wang JV (ed) (1996) *Geothermics in China*. Seismological Press, Beijing, p 299
38. Zonenshain LP, Kuz'min MI, Natapov LM (1990) Tectonics of lithospheric plates of the USSR territory (in Russian). Nedra, Moscow, p 662

On Geothermal Problems of the Marginal Seas



Alexander Muravyev

1 Introduction

The first measurements of the heat flow in the marginal seas were carried out in 1962 in the Caribbean Sea and the Aleutian Basin of the Bering Sea [18, 22]. To date, geothermal studies have covered most of the marginal basins, and the total number of measurements in them exceeds 5000. The results are summarized in a number of works [4, 51, 77, 87, 115, 122, and many other works].

Significant contribution to the theoretical and experimental geothermics of the marginal seas is associated with research by leading scientific centers and institutes, such as the Lamont Geological Observatory, the Scripps Oceanographic Institute, the University of Tokyo, the Geological Institute of the Russian Academy of Sciences, the Institute of Earth Physics of the Russian Academy of Sciences, the Institute of Oceanology of the Russian Academy of Sciences, the Institute of Marine Geology and Geophysics of the Far East Branch RAS and a number of other organizations.

2 Specifics of Heat Flow Distribution and Thermal Regime of Island-Arc Systems

In the nature of the distribution of heat flow in the “island arc – marginal sea” system, the first systematic studies [106] already revealed a number of general patterns characteristic of almost all island arc systems:

A. Muravyev (✉)
GIN RAS, Moscow, Russia

1. A decrease in the heat flow to 30–50 mW/m² is usually observed between the deep-sea trench and the volcanic front of the island arc.
2. In the volcanic zones of island arcs and continental margins, the heat flow is generally higher (40–100 mW/m²), but it is characterized by a very large scatter.
3. In back-arc basins, the heat flow is usually high (80–160 mW/m²) and relatively stable.

The distribution of heat flow in marginal seas, as well as on continents and oceans, depends on the age of the last event of tectonic-magmatic activity [77, 86, 87, 115], and the experimental dependences are very similar to that observed at mid-ocean ridges and back-arc basins [4, 122]. Such a coincidence gave grounds for setting the problem of the applicability of fundamental theoretical developments of the spreading concept to back-arc basins, in particular, to the estimation of the time of their formation. For many back-arc basins, their age was estimated from geothermal data, which was later confirmed by deep-sea drilling, analysis of magnetic anomalies, geological data and tectonic reconstruction [78, 89, 90, etc.].

According to the concept of plate tectonics and seafloor spreading, the heat flow through the ocean floor is expressed by a function [52]:

$$q_s = (T_m - T_s) / (\pi \alpha t)^{1/2} = \lambda (T_m - T_s) (u / \pi \lambda \alpha)^{1/2} \quad (1)$$

where T_s is the temperature on the bottom surface (°C), T_m is the temperature of the asthenosphere (°C), α is the thermal diffusivity (m²/s), λ is the thermal conductivity of the lithosphere (W/m·K), t is the age of the basement (Ma) or:

$$q_s = C \cdot t^{-1/2} \quad (2)$$

where $C = 473$, ($t < 120$ Ma), as derived by B. Parsons and J. Sclater [64], or $C = 502$ ($t < 80$ Ma), as estimated by C. Lister [47]; [q] = mW/m².

Relations (1) and (2) are also valid for marginal seas, but due to the diversity of geodynamic conditions, regional average values of heat flux may shift relative to the theoretical dependence. This must be considered when assessing the age of their basement.

Table 1 and Fig. 1 summarize the heat flow data for different marginal seas. It shows the average values of the measured conductive heat flow with a standard deviation and the age intervals of the formation of the basin, established independently by geological and geophysical methods and drilling.

For a number of basins of the marginal seas (the eastern part of Parece Vela, Solomon Sea, Tasman Sea, Coral Sea, South China basin, Venezuelan basins, etc.) the ratio $q(t)$, calculated by the equation (2), is fair. Geological data on these seas suggest their spreading origin, similar to that of the oceans. The sufficiently high thickness of sediments (several hundred meters) in these seas provides the conductive character of cooling of the lithosphere. Noticeable deviations of the average heat flow values from the theoretical curve are associated with such phenomena as sedimentation, hydrothermal circulation, and repeated thermal activation.

Table 1 Heat flow and age of marginal seas

Sea/Basin	Abbreviation	Index	q_0 , mW/ m ²	References	Age, Ma	References
Balearic basin	BA	3, 5	92 ± 10	[35]	20–25	[35]
Tyrrhenian Sea (1)	TR1	3, 5	134 ± 8	[35]	7–12	[35]
Tyrrhenian Sea (2)	TR2	3, 5	151 ± 10	[35]	5–8	[35]
W. Alboran basin	WA	2, 5	69 ± 6	[68]	T; N1	[13]
E. & S. Alboran basins	EA	2, 4	124 ± 8	[68]	24–7	[13]
Andaman Sea	AN	1, 2	131 ± 41	[17]	0–9	[17, 85]
Venezuelan basin	VE	5	56 ± 12	[115]	59–83	[16]
North Fiji basin	NF	1, 2	116 ± 60	[115]	0–3	[117]
South Fiji basin	SF	4	96 ± 19	[115]	28–36	[117]
Tasman Sea	TA	5	53 ± 10	[69]	52–85	[116]
Coral Sea/Queensland basin	CO	5	60 ± 12	[12]	56–62	[117]
Bismarck Sea/Manus basin	BS	1, 3	195 ± 41	[93]	0–3,5	[99]
Solomon Sea	SO	5 (4)	86 ± 10	[6, 32]	28–39	[32]
Sulu Sea	SU	4	89 ± 7	[6]	41–47	[44]
Sulawesi Sea	SL	5	56 ± 22	[6]	65–72	[44]
Caroline basin	CA	5	85 ± 31	[6]	28–36	[44]
Shikoku basin	SH	5, 2	82 ± 29	[6]	14–24	[83]
Philippine basin	PL	4, 2	68 ± 22	[6, 62, 88]	39–50	[49, 59, 60]
Parece Vela basin (W)	PV1	5, 2	40 ± 40	[62, 88]	18–31	[43, 57]
Parece Vela basin (E)	PV2	5, 3	87 ± 8	[62, 88]	18–31	[43, 57]
Mariana trough	MT	1, 2	137 ± 89	[3, 30, 88]	0–6	[34, 58, 79]
South China Sea (□3)	SC1	5	88 ± 6	[100]	27–33	[100]
South China Sea (N1)	SC2	5	107 ± 4	[100]	19–23	[100]
Okinawa Trough	OK	1	140 ± 115	[50, 121]	0–2; (20)	[50, 96]
Japan Sea/Japan basin	JP	5, 3	96 ± 14	[123]	30	[96, 97]
/ Yamato basin	YM	5, 3	97 ± 12	[123]	15	[96, 97]
/ Tsushima basin	TS	5, 3	96 ± 6	[123]	20	[123]
/ Tartary trough	TT	5, 3	99 ± 15	[123]	20	[123]
Sea of Okhotsk/Kurile basin	KU	(4), 3	81 ± 13	[112]	25	[55, 111]
/ Deryugin basin	DE	(4), 3	87 ± 45	[91, 113]	20	[111]
Bering Sea/NE Komandorskaya basin	KM1	5, 3	81 ± 8	[42, 61]	25–40	[8]
Bering Sea/SW Komandorskaya basin	KM2	1, 3	137 ± 32	[61, 115]	0–10	[73, 80]
Bering Sea/Aleutian basin	AL	4, 3	58 ± 16	[42, 88]	117– 132	[14]
Bering Sea/Bowers basin	BR	5, 3	80	[18, 115]	30 ± 5	[73]

Notes: In column (2) abbreviated names are given corresponding to Fig. 1. The index in column (3) characterizes the most important regional geological factors determining the heat flow: 1 – modern back-arc spreading; 2 – hydrothermal circulation; 3 – intensive sedimentation; 4 – two-stage cooling; 5 – post- spreading (single stage) cooling of lithosphere

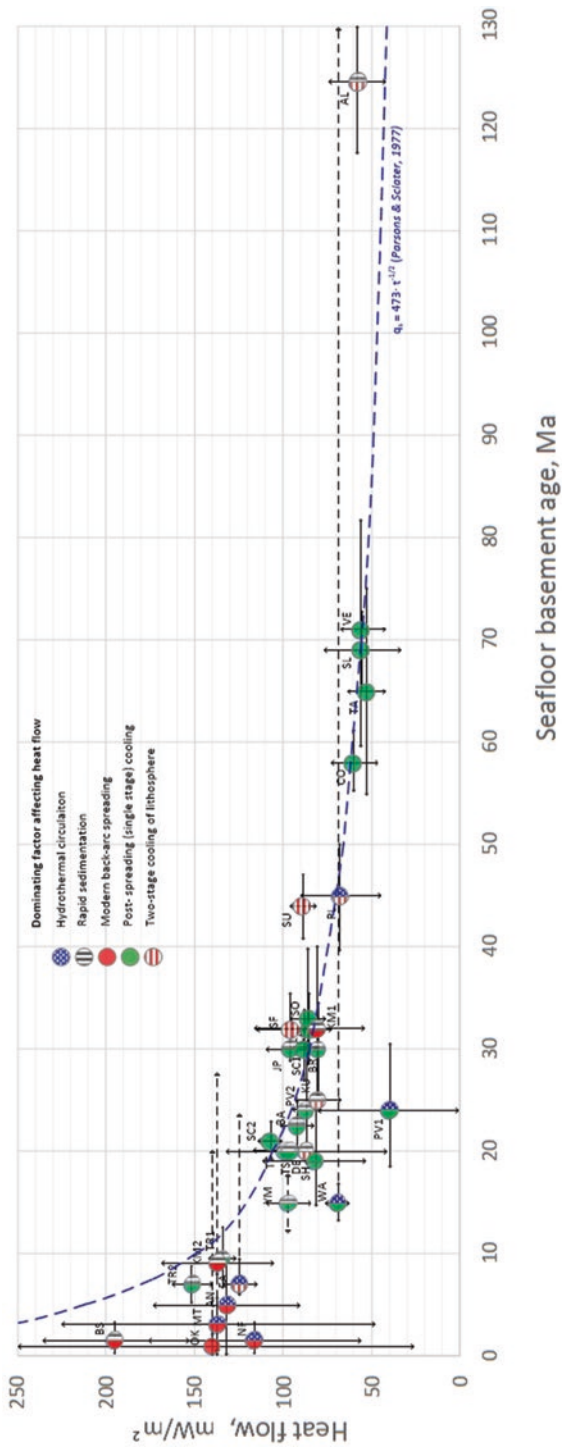
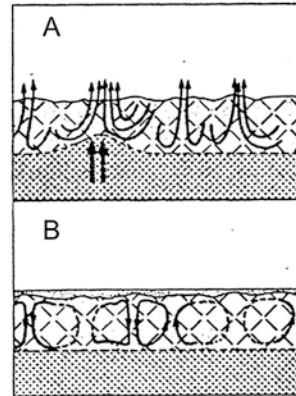


Fig.1 Heat flow and age of the marginal seas and basins

Fig. 2 The nature of the hydrothermal circulation in the fractured basaltic layer (a) – in the absence of bottom sediments (convective + conductive heat transfer); (b) – in the presence of a sedimentary layer (conductive heat transfer through sediments). (After C. Lister [46])



In the young back-arc basins (such as Lau basin, North Fiji basin, Mariana trough), the heat flow distribution is also similar to that observed in the centers of the spreading of the oceans, i.e. characterized by a high average value with a very large dispersion of measured values. The scatter of data is mainly determined by the hydrothermal convective heat transfer, leading to an underestimation of the conductive heat flow in the axial zone. Water circulation is facilitated by the absence or non-ubiquitous development of sediment cover (Fig. 2), and the measured conductive component (q_m) here is only part of the total heat loss (q_t):

$$q_m \approx q_t - q_{\text{conv}} \quad (3)$$

The effect of water circulation can affect the heat flow in more ancient basins, where the basement is heavily fractured, and the thickness of the sediments is small (like in the western part of the Parece Vela basin, Philippine Sea) [57, 71, 72].

Among the young back-arc basins, the highest heat flow is characterized by the Manus basin in the Bismarck Sea. The Manus basin is a unique area where specific conditions – a thick layer of precipitation and a very young (0–3, 5 Ma) age of the crust – allow direct geothermal measurements to determine the total heat flow in a modern back-arc spreading center. The average of 8 measurements made on the 10th cruise of the RV “Vulkanolog” is 195 ± 41 mW/m² [93]. The total heat flow corrected for sedimentation [21], may exceed here 300 mW/m².

Very high values (over 1000 mW/m²) were also obtained in the Okinawa trough [121], although the average heat flow here is 140 ± 115 mW/m². In the area of 27° 34.4 N, 127° 08.6 E with the help of underwater vehicles, foci of open hydrothermal discharge were found on seamounts with a height of up to 5–6 m and a width of up to 15–25 m, with a temperature inside the hill at a depth of 40 cm to 20–50 °C; water in the sources is enriched with methane [40]. The development of the trough is considered as a result of seafloor spreading in the range of 9–20 million years ago [50] and the latest (0–2 million years) magmatic activation in the rear of the Ryukyu arc.

Another factor that underestimates the average heat flow on a regional scale is sedimentation. Its role is important for the basins with long-term intensive

sedimentation (such as Bering Sea, Sea of Okhotsk, Japan Sea, etc.). The magnitude of the correction can be accurately calculated in the presence of the deep sea drilling wells and seismic sections. Convenient nomograms for rapid estimates of the correction for sedimentation are presented in [21].

Very detailed heat flow study in the Sea of Japan has been carried out [124]; its values are homogeneous and are 95 and 97 mW/m² for the valleys of Japan and Yamato, respectively. Basement age is less well known; estimates based on drilling data, seismic stratigraphy, basement depth and geothermal data indicate an age of about 30 Ma for the Japan Basin and 10–15 Ma for the Yamato Basin [96]. The reduced heat flow within the Yamato basin can be explained by the structural factor [39].

Heat flow is slightly higher than the theoretical one observed in the South Fiji, Sulu and Aleutian basins. To explain such deviations, the model of two-stage cooling of the lithosphere is used [42, 115], proposed for basins, which are considered to be the fragments of ancient oceanic crust, separated by subduction zones (like Aleutian and Philippine basins). According to this model, the thermal evolution of the lithosphere of such depressions undergoes two stages: (1) post-spreading cooling within the ocean to 40–45 mW/m²; (2) additional thermal impulse of about 40 mW/m² due to a sharp change in the geodynamic framework and re-cooling to the current values of the heat flow. The Aleutian and Philippine basins must be presently at the end of the second stage.

In some cases, the nature of the geothermal field in island-arc systems is difficult to explain using simple subduction models. One such example is the Nankai Trough, framing southwestern Japan. Both direct measurements of the heat flow and its estimates from the depth of the base of the gas hydrates layer [119] show that from the island arc, the heat flow increases down the slope from 40 to 90 mW/m² and reaches a maximum – more 130 mW/m² – on the trench axis. The most likely explanation for this phenomenon is that this is the result of the subduction of the young (14–25 Ma) hot lithosphere of the adjacent Shikoku basin. The thickness of the lithospheric plate according to estimates of the dispersion of surface waves [84], is 30 km. An alternative explanation is to increase the heat flow by 20–40 mW/m² compared to the hypogene heat flow due to the squeezing of hot fluids from sediments during the subduction process [120].

A complex picture of the geothermal field distribution is also observed in the Sea of Okhotsk. High heat flow (80–100 mW/m²) is noted here not only in the back-arc basins (in particular, in the Kuril basin), but also in the inner parts of the sea – near the eastern coast of Sakhalin, in the depressions of Deryugin and Tinro [91, 112]. In the central and western parts of the sea, the heat flow is lower: 50–70 mW/m² in the area of the uplift of the Institute of Oceanology and 35–45 mW/m² along the west coast of Kamchatka. Probably, the Sea of Okhotsk can be considered as a destructive continental margin that has undergone several episodes of diffuse back-arc spreading during the Cenozoic period [55].

Thus, the magnitude of the heat flow and the nature of its distribution in the marginal seas are diverse and depend on the age of the basement (or the time of the last tectonic-thermal activation), the mechanism of formation of the marginal basin and

specific geological features. But in general, the law of cooling of the lithosphere of the oceans and marginal seas is the same, and taking into account regional geological features, it can be used to estimate the age of the magmatic basement of marginal seas.

3 Some Aspects of Geodynamics of Island Arc Systems

Geodynamic and thermomechanical processes in island-arc systems are extremely complex and have not yet been studied sufficiently. Considered quite a few models with which attempts were made to explain the main features of geodynamics, including the distribution of heat flow and deep temperatures in the lithosphere of island arc systems [4, 6, 19, 20, 25, 31, 33, 38, 48, 101–103, 107]. The geological history of each marginal sea has its own specifics.

At the same time, three main mechanisms of formation of back arc basins are distinguished: (1) the isolation of fragments of the ancient oceanic plate by an island arc [29, 70, 76], for example, the Aleutian and Philippine basins; (2) back-arc stretching along the plate shear boundaries, as in the Andaman Sea [104]; (3) back-arc spreading associated with the subduction process [37] and currently taking place in Okinawa, Mariana, Lau, and others. As on the mid-ocean ridges, active arc-spreading is associated with stretching of the lithosphere and ascent of the asthenosphere, partial melting, expressed in intense modern igneous, volcanic and hydrothermal processes. It is assumed that the source of energy for these processes may be additional heat arising in the upper zone of the plunging cold lithospheric plate due to friction [25], as well as additional heat transfer from the mantle by convective currents, as follows from seismic tomography data [2]. It is believed that the ascending mantle convection responsible for the discovery of a number of marginal seas (such as Tasman Sea, South China Sea) may not be associated with subduction [10, 27].

In a separate group should be allocated seas, which are relict fragments of the “closing” ocean between the convergent margins of large lithospheric plates (e.g., Mediterranean Sea is a remnant of Paleo-Tethys Ocean). The heat flow in this case, in general, corresponds to the age of the basement, but may be significantly underestimated due to high sedimentation rates (Black and Caspian Seas). The Eastern basin of the Black Sea experiences subduction under the Crimea and the Caucasus, while the Western basin subducts under the northern coast of the Anatolian Peninsula. The Central Black Sea uplift obviously represents a left-lateral transform fault zone. The average heat flow for 770 measurements in the region from the global database [24] is 51 ± 39 mW/m². This value corresponds to the Upper Cretaceous (Santonian) age of the basement, ~86 Ma.

To explain the observed distribution of heat flow in the back-arc areas, besides an additional heat source, it is assumed that the high effective thermal conductivity which is several times higher than the normal conductive thermal conductivity [25] due to penetrating convection of rising magma streams. The role of the ascending

mass-flow of silicate substance in the geothermal regime of island-arc systems is confirmed by the analysis of the correlation of isotopic ratios of $^3\text{He}/^4\text{He}$, $^{87}\text{Sr}/^{86}\text{Sr}$ [67, 74].

Thermal subduction models are based on the numerical solution of the heat equation, which takes into account material movement and internal heat sources [11]:

$$\frac{dT}{dt} + v \cdot \nabla T = \frac{1}{\rho \cdot C_p} [\nabla(\lambda \cdot \nabla T) + A] \quad (4)$$

where $T = T(x, z, t)$ is the temperature distribution, t is time, v is the speed of the subduction, A is heat generation, λ is thermal conductivity, ρ is density, C_p is specific isobaric heat capacity of rocks. The thermodynamic conditions and the depth of melting of the rocks of the upper layers of the oceanic crust – marine sediments and serpentinized basalts enriched with volatile ones – vary depending on the subducting slab angle and the speed [75]. Accordingly, these parameters affect the distance of the volcanic front from the trench axis and the petrological characteristics of island arc volcanism.

The problem of the specific conditions under which the opening of the back-arc basin in the rear of the arc begins is not yet fully resolved. In a number of models, secondary convection in the post-arc mantle wedge is considered as an independent cause of back-arc spreading [7, 54, and others], while physical modeling shows that although compression is applied in the overriding plate convergence zone, stretching may occur [82].

The heat of friction (Q_f) depends on the magnitude of the shear stress (τ) at the contact of the plates and the speed of their relative displacement (v):

$$Q_f = v \cdot \tau \quad (5)$$

In various models, the value of τ varies from $\tau = 0$ MPa [120] to $\tau \geq 100$ MPa. In models that take into account the pressure of the pore fluid and the rheological properties of rocks depending on P-T conditions, for example [107], it is calculated that the temperatures at the interface of the plates and in the extended plate are determined by subduction of the cold plate and friction warming up. In these models, the average value of shear stresses at the contact of the plates between the axis of the trench and the volcanic arc varies from 10 to 40 MPa.

Heat can be released not only along the seismic focal zone, but also during deformation in the upper parts of the lithosphere [53]. The release of friction heat increases with an increase in the subduction rate, but the role of friction heat decreases with increasing temperature. In the works [36, 101] it is shown that if we consider the medium as a Newtonian fluid with viscosity depending on temperature, then these parameters are related as: $Q_f \sim v^n$, $0 < n < 1$. This means a relatively small increase in T and Q with increasing v . The lack of heat flow correlation with the subduction rate confirms this result, although the thermal regime of island-arc systems can reflect not only modern subduction processes, but also processes of the past. In the absence of frictional heating, immersion of the cold oceanic plate would

lead to effective cooling of the mantle, the greater, the higher is the subduction velocity.

Thermal models of subduction with different angles (26.6° and 45°) and different speeds of subduction (from 7 to 50 mm/year) are considered in [94]. The temperature distribution in this model is strongly dependent on the rate of immersion of the plate.

An important parameter determining the nature of tectonic processes and the thermal regime of island-arc systems is the age of the sinking plate. The classification of subduction zones depending on the age of the moving plate and the nature of tectonic-magmatic processes is given in [105] (Table 2). In this paper, two modes of subduction are distinguished – Chilean type and Mariana type.

The Chilean type characterizes the subduction of young (up to 50 million years) oceanic plates, which have not yet had time to cool enough, to the continental margin. It is characterized by a gentle angle of upward movement, the predominance of compression stresses, strong thrust-type earthquakes, calc-alkaline magmatism, and the absence of a back-arc basin. Typical examples are the Pacific margins of South and Central America.

The Mariana type characterizes the subduction of an ancient oceanic plate under another oceanic plate. Features of this type are the steep fall of the Benioff zone, the lack of an accretionary prism, strong earthquakes, the prevailing stretching conditions, high heat flow in the back arc area and back arc spreading, like it occurs in Mariana trough and Okinawa trough [26, 45, 105]. It is noted [95] that with a steep fall of the Benioff zone, arcuate central type spreading occurs (the Mariana trough), and in the case of a gentler fall, diffuse spreading (for example, in the basins of the Sea of Japan, the Lau Basin).

The embedding of a new island arc occurs at a time when the forces of tangential compression from the mid-ocean ridge and the gravitational “sliding” of the plate in the subduction zone overcome the forces of friction between the oceanic plate and the asthenosphere and the forces of viscous resistance in the subduction zone. The farther from the center of spreading, the greater the friction surface between the lithosphere and the asthenosphere. At a certain point, the driving forces are not enough to continue the subduction process under the old island arc or continental base, and the “conveyor” is being rebuilt. A new subduction zone in the ocean is formed in the place where tectonic stresses exceed the tensile strength of the oceanic lithosphere. Such scenario is considered for the Aleutian basin about 65 M.y. ago, when part of ancient Kula plate was trapped as a result of subduction zone jump from Alaska margin to about 1000 km to the south. Similarly, the eastward migration of subduction zone during the Cenozoic formed the modern shape of Philippine Sea.

Volcanism on the island arc does not begin immediately, but after the subducted plate reaches the depth of partial melting of marine sediments and serpentinized basalts, that is, at temperatures above 600°C at a pressure of about 20 kbar (≈ 60 km). Therefore the time delay of the onset of volcanism after subduction axis jump-over depends on the angle and speed of the moving plate and may take few million years.

Table 2 Comparative geodynamic characteristics of some subduction zones according to data [23, 28, 63, 105, and others]

Subduction zone	Stress class	Subducting slab age, Ma	Angle of Subduction	$V_{on}+V_{sn}$ mm/year	V_{on} mm/year	Max. depth of Benioff zone, km	Crustal thickness, km
Aegean	1		35	7	-3	180	25-30
Andaman	1	72 ± 5	40-50	15-29	-(31-45)	210	6-10
Sumatra	5	55 ± 5	30	75	-3	650	30
Java	5	138 ± 10	55	82		600	25-30
Philippine	5	50-60	63	74	1	620	20
Ryukyu	2	50	45	47	1	240	25
SW Japan (Nankai)	5	21	30	35	1	70	27-36
NW Japan	6	112-130	30-40	105	2	600	27-36
New Zealand	3	98	67	33		300	36
Kermadec	1	75-113	50-65	68	-24	700	18
Tonga	1	75-120	53	68	-33	650	12
New Hebrides	1	43-52	60-70	91	63	670	28
South Solomon	4	28-36	40-60	35	-27	150	15-20
New Britain	1	50 ± 10	65-80	-40	-98	600	20-40
Mariana	1	150-180	90	34	-71	600-700	15-18
Izu Bonin	2	146	65	58	-34	500-550	15-18
Kurile	(5)	119	50-55	88	-2	650	15-30
Kamchatka	(5)	90 ± 15	50	88		550	25-45
Central Aleutian	4	54	65	63	10	260	18-25
Alaska	6	46	40-55	70	8	150	30
NW Mexico	6	9-30	20-25	62	20	150-260	30
Central America	3	23 ± 5	65	65		200	42
Less Antilles	4	68-80	40-65	37	10	230	30-35
Colombia	6	15 ± 10					65
Peru (10°N)	6	45	15-60	79	27	520-600	40-70
Chile (30°S)	7	48	15-45	88	28	500-600	40-70
South Sandwich	1	49	70-80	9	-8	260	20

Notes: Stress classes: 1 – tension (active back-arc spreading); 2 – weak back-arc spreading; 3 – weak stretching, faults, but without crustal thinning; 4 – ±; 5 – weak folding, reverse faults; 6 – folding, reverse faults; 7 – folding, thrusts. V_{sn} is the normal continentward component of the speed of the subducted plate; V_{on} is the normal oceanward component of the speed of the overriding plate

The patterns of change of island-arc magmatic series in time and space also reflect the features of the thermal mode of subduction. The study of the petrological zonation of island arcs [56] shows that, in general, a magmatic series is observed across the strike of the arc: tholeiitic basalts – high-alumina – K-Na – sub-alkaline – alkaline olivine basalts. According to Kushiro [41], tholeiitic calc-alkaline rocks are derivatives of the peridotite mantle: if the water content is low and the temperatures are high, then the tholeiitic series prevails, whereas with an increased water content and relatively low temperatures, the calc-alkaline type of volcanism prevails. For this reason, with a standard course, tholeiitic magmatism usually manifests itself in the early stage of the subduction zone (since the mantle had not yet cooled, and the sinking plate did not reach the depths of the dehydration zones. This sequence can, however, be disturbed during a non-standard magmatic evolution, for example, manifestation of K-Na – subalkaline basites at different stages of development of island arcs [9].

The volatile content plays an important role in the processes of melting and temperature distribution in the lithosphere of island-arc systems. According to the available definitions, island-arc lavas contain about 0.5% by weight of water [75, 125]. With this amount of water, the solidus temperature of pyrolite decreases to 1050 °C against 1200 °C for dry rocks [118]. Of particular importance is the dehydration of rocks, in particular, dragging down sediments into subduction zone, considered in a number of works [5, 15, 65]. A significant amount of free and chemically bound water is contained not only in the sediments, but also in the upper 1–3 km of the “second layer” of the oceanic crust. The deep-sea drilling well No. 504B, which reached a depth of 1075 m in basalts, showed that the volatile content in the base rocks is heterogeneous and amounts to 0.5–1.0 wt.% H₂O and 0.1 wt.% CO₂ in pillow basalts. The dyke complex contains respectively, 1–3 wt.% H₂O and 0.05–0.1 wt.% CO₂ [1].

The increase in water content in basalts with distance from the axis of the mid-oceanic ridge, apparently, is the result of the interaction of igneous rocks with oceanic water along the deep faults leading to the serpentinization of peridotites (Fig. 3). The thermodynamic conditions of the “window of serpentinization” of the

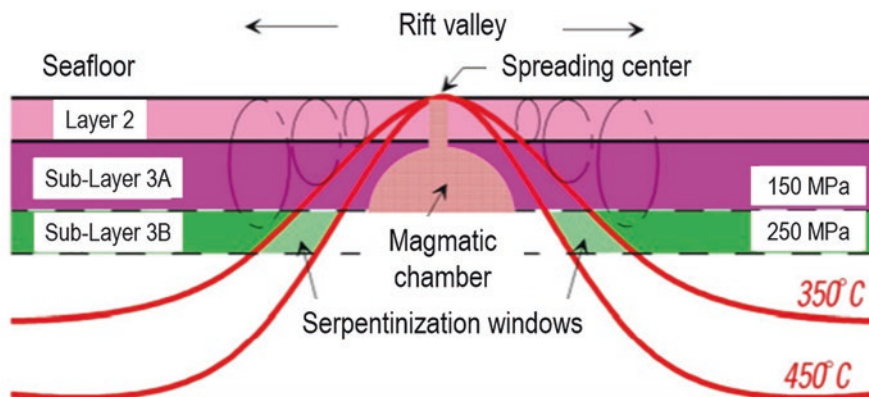
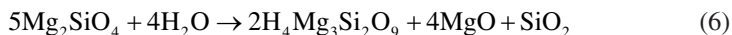


Fig. 3 Formation of Serpentinite Sub-Layer 3B of the Oceanic Crust

oceanic lithosphere correspond to temperatures of 90–500 °C, and with a high iron content in olivine, intensive serpentinization begins at lower temperatures from 25 °C [110]. Laboratory experiments have shown that a reaction is likely in which olivine is replaced by the same amount of serpentine, and an excess of MgO and SiO₂ is carried into solution. This can be approximated by the following equation:



Recycling of volatile substances contained in the subducted oceanic crust is confirmed by the analysis of the isotopic composition of volcanic gases above subduction zones [92], while the degree of recycling of silicate matter remains problematic [81].

Dehydration of rocks in the subduction zones occurs at depths of 80–125 km, while about 200 kJ are absorbed per 1 kg of rock [5], which reduces the thermal effect of frictional heating. For example, in the subduction zone at the Japan trench, the equivalent reduction in heat flow due to dehydration is estimated at 8–10 mW/m² [25]. In addition, in the dehydration zone, the frictional heat should sharply decrease, since the pore pressure of water greatly reduces the strength of rocks. Dehydration thus leads, at least, to partial self-compensation of the thermal effect and the melting effect caused by the presence of volatiles. Fluid flows ascending along cracks, in turn, cause reactions of retrograde metamorphism with a high exothermic effect (about 30 kJ/mol H₂O) in the extended plate and significantly inhibit the cooling of the latter [66] (Fig. 4).

Along with the heat of friction and the dehydration effect, phase transitions and adiabatic compression can play a significant role in the thermal regime of island-arc systems, the geothermal effect of which was estimated in the work [25]. During the phase transitions, basalt – eclogite and olivine – spinel are released, respectively, 63 and 334 kJ/kg (15 and 60 cal/g), respectively. According to J. Verhoogen [114], when olivine is converted into spinel, the temperature increases by 160 °C, which corresponds to an increase in heat flow by about 65 mW/m².

The temperature rise due to adiabatic compression is:

$$\frac{dT}{dz} = \frac{\beta \cdot g}{C_p} \cdot T \quad (7)$$

Where $\beta = \frac{1}{V} \left(\frac{dV}{dT} \right)_p$ is coefficient of volume expansion, g – acceleration of gravity, C_p – isobaric heat capacity.

For subduction of the lithospheric plate 60 km thick at an angle of 50° to a depth of 300 km during 30 million years (Japan trench), additional heat generation due to adiabatic compression is about 20 mW/m² [25]. Calculations show that for simultaneous heating of the “cold” plate and melting, additional heat generation is required, of the order of 250 mW/m². The problem of localization of such a quantity of thermal energy requires further study.

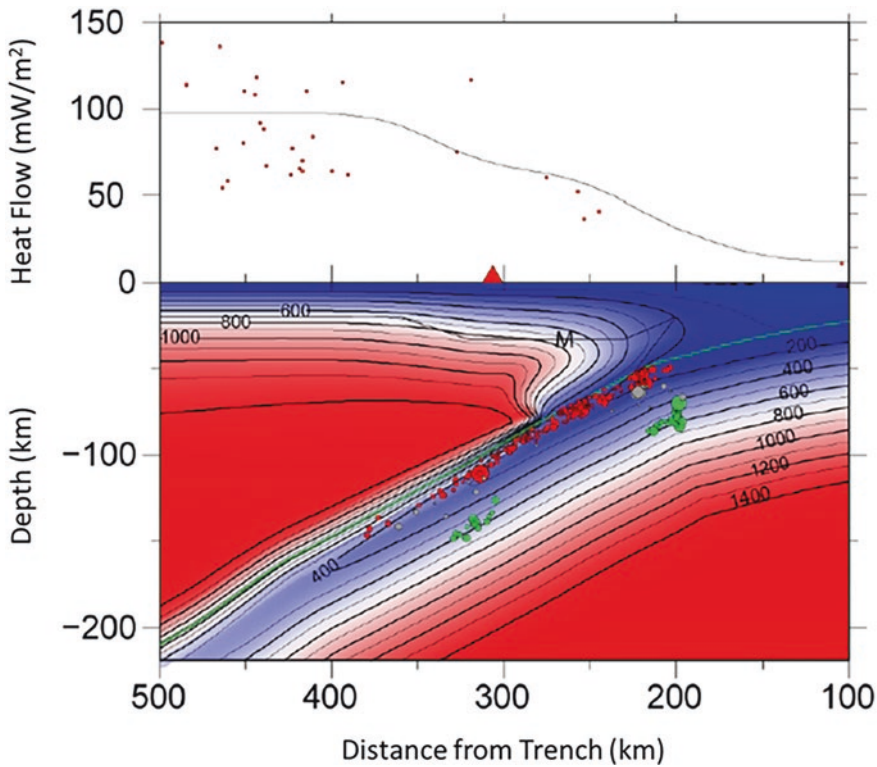


Fig. 4 Thermal model [109] and seismicity of the Pacific Plate in the Tohoku subduction zone, NE Honshu [108]. (Top:) The predicted heat flow (solid line) compared with observations (from [98]). The position of the volcanic arc is shown by a red triangle. Seismicity within 10 km on each side of this profile is shown in circles by the distance from the plate surface, approximately indicate the upper plane (depth from 0 to 10 km in red) and the lower plane – a doubled Wadati -Benioff zone (> 25 km in the green zone). Seismicity at a depth of 10–25 km is shown in gray

Comparison of thermal regime of marginal seas leads to a number of general conclusions:

1. The distribution of heat flow in the marginal seas, as well as on the continents and oceans, depends on the age of the last stage of tectonic-magmatic activity, and the experimental dependences practically coincide for the mid-ocean ridges and back-arc basins. The most important geological factors affecting the deviation of the observed heat flow in the marginal seas from the “theoretical” curve of heat flow – age dependence for cooling of the oceanic lithosphere are: hydro-thermal circulation, rapid sedimentation, and one- or two-stage cooling scenario of the lithosphere. General applicability of fundamental theoretical developments of the spreading concept to back-arc basins enables estimating the time of their formation.

2. There is a genetic relationship between the tectono-thermal regime of island-arc systems with the geological and geophysical parameters of the subduction zones – age and topography of the basement, speed of movement, slope of the Benioff zone. The thermal regime is reflected in the petrological and geochemical features of island arc and back-arc magmatism.
3. The back-arc spreading and island-arc magmatism are due to a powerful additional heat source, leading to melting near the contact of the moving plate with the mantle wedge located above. Adiabatic compression of the substance of the moving plate gives an increase in temperature by 15–20%, and phase transitions by 10–15%.
4. The release of water during the dehydration of serpentinites and other water-containing minerals leads to mutually compensating effects: a decrease in the solidus temperature on the one hand, the absorption of heat and a decrease in friction heat generation on the other. In the block pulled over, exothermic reactions of retrograde metamorphism restrain the cooling caused by the advance of the cold block.
5. Conductive heat transfer explains the minimum heat flow above the trenches but does not explain the maximum behind the island arcs; the heat flow maximum and the volcanic axis do not necessarily coincide.

Acknowledgements The author is grateful to the colleagues – Prof. M.D. Khutorskoy and Dr. B.G. Polyak for useful discussions and valuable comments. The work does not contain any conflicts of interest.

References

1. Alt JC, Muehlenbachs K, Honnorez JJ (1986) Oxygen isotopic composition and calculated equilibrium temperatures of formation for vein carbonates from DSDP Hole 504B. PANGAEA. <https://doi.org/10.1594/PANGAEA.713297>
2. Anderson DL, Dziewonsky AM (1984) Seismic tomography. In the world of science. No. 12, pp 16–26 (in Russian)
3. Anderson RN (1975) Heat flow in the Mariana marginal basin. *J Geophys Res* 80:4043–4048
4. Anderson RN (1980) Update of heat flow in the east and southeast Asian seas. In: Hayes DE (ed) *The tectonic and geologic evolution of southeast Asian seas and islands*, Geophysics Monograph, vol 23. American Geophysical Union, Washington, DC, pp 319–326
5. Anderson RN, Uyeda S, Miyashiro A (1976) Geophysical and geochemical constraints at converging plate boundaries—Part I: Dehydration in the downgoing slab. *Geophys J Int* 44:333–357
6. Anderson RN, Langseth MG, Hayes DE, Watanabe T, Yasui M (1978) Heat flow, thermal conductivity, thermal gradient. *Geophysical atlas of the East and Southeast Asian seas*. I.D.O.E.
7. Andrews DJ, Sleep NH (1974) Numerical modelling of tectonic flow behind island arcs. *Geophys J Roy Astron Soc* 38:237–251
8. Baranov BV, Seliverstov NI, Murav'ev AV, Muzurov EL (1991) The Komandorsky Basin as a product of spreading behind a transform plate boundary. *Tectonophysics* 199(2–4):237–269

9. Bogatikov OA, Tsvetkov AA, Kovalenko VI (1987) Magmatic evolution of island arcs. In: Petrology and geochemistry of arcs and marginal seas. Moscow, Chap.6, pp 313–331 (in Russian)
10. Bogdanov NA (1988) Tectonics of the deep-sea basins of the marginal seas. Nedra, Moscow, 221 pp (in Russian)
11. Carslaw G, Jaeger D (1964) Thermal conductivity of solids. Nauka, Moscow, p 487. (in Russian)
12. Choi DK, Stagg HMJ, et al (1987) “Rig Seismic” research cruise 6: Northern Australia heat flow post cruise report. Australian Government Publication Service, 40 pp
13. Comas MC, Garcia-Dueñas V, Jurado MJ (1992) Neogene tectonic evolution of the Alboran basin from MCS data. *Geo-Mar Lett* 12:157–164
14. Cooper AK, Marlow MS, Scholl DW (1976) Mesozoic magnetic lineations in the Bering Sea marginal basin. *J Geophys Res* 81:1916–1934
15. Delany JM, Helgeson HC (1978) Calculation of the thermodynamic consequences of dehydration in subducting oceanic crust to 100 kb and > 800 °C. *Am J Sci* 278:638–686
16. Donnelly TW et al (1973) Basalts and dolerites of Late Cretaceous age from the Central Caribbean. In: Edgar NT et al (eds) Initial reports of DSDP, Leg 15. US Government Print Office, Washington, DC, pp 989–1011
17. Eguchi T, Uyeda S, Maki T (1979) Seismotectonics and tectonic history of the Andaman Sea. *Tectonophysics* 57:7–51
18. Foster TD (1962) Heat flow measurements in the Northwest Pacific and in the Bering Sea. *J Geophys Res.* 67:2991–2993
19. Furlong KP, Chapman DS, Alfeld PW (1982) Thermal modeling of the geometry of subduction with implications for the tectonics of the overriding plate. *J Geophys Res.* 87(B3):1786–1802
20. Furukawa Y, Uyeda S (1989) Thermal state under Tohoku arc with consideration of crustal heat generation. *Tectonophysics* 164:175–187
21. Galushkin YI, Smirnov YB (1987) Thermal history of sedimentary basins. Express heat flow estimation methods. *Geol Geophys* 11:105–112. (in Russian)
22. Gerard R, Langseth MG, Ewing M (1962) Thermal gradient measurements in the water and bottom sediments of the Western Atlantic. *J Geophys Res* 67:785–803
23. Gill JB (1981) Orogenic andesites and plate tectonics (ed Wyllie PJ). Springer, 390pp
24. Hasterok D (2016) Global heat flow database. www.heatflow.org/
25. Hasebe K, Fujii N, Uyeda S (1970) Thermal processes under island arcs. *Tectonophysics* 10:335–355
26. Hawkins JW, Lonsdale PF, Macdougall JD, Volpe AM (1990) Petrology of the axial ridge of the Mariana Trough backarc spreading center. *Earth Planet Sci Lett* 100:226–250
27. Hayes DE (1984) The marginal seas of southeast Asia. In: History and origin of marginal and inland seas. 27th IGC Reports vol.6. Part II. Nauka, Moscow, pp 30–44. (in Russian)
28. Hilde TWC (1983) Sediment subduction versus accretion around the Pacific. *Tectonophysics* 99:381–397
29. Hilde TWC, Uyeda S, Kroenke L (1977) Evolution of the western Pacific and its margin. *Tectonophysics* 38(1–2):145–165
30. Hobart MA, Anderson RN, Fujii N, Uyeda S (1983) Heat flow from hydrothermal mounds in two million-year-old crust of the Mariana Trough which exceeds two watts per meter 2. *EOS Trans Am Geophys Union* 64:315
31. Honda S (1985) Thermal structure beneath Tohoku, northeast Japan – a case study for understanding the detailed thermal structure of the subduction zone. *Tectonophysics* 112:69–102
32. Honza E, Davies HL, Keene JB, Tiffin DL (1987) Plate boundaries and evolution of the Solomon Sea region. *Geo-Marine Lett* 7:161–168
33. Hsui AT, Toksoz MN (1981) Back-arc spreading: trench migration, continental pull or induced convection? *Tectonophysics* 74:89–98
34. Hussong DM, Uyeda S (1982) Initial reports of deep sea drilling project, Leg 60. US Government Print Office, Washington, DC, 929 pp

35. Hutchison J, Von Herzen RP, Loudon KE, Sclater JG, Jemsek J (1985) Heat flow in the Balearic and Tyrrhenian basins Western Mediterranean. *J Geophys Res* 90(B1):685–701
36. Ida Y (1983) Thermal and mechanical processes producing arc volcanism and back-arc spreading. In: *Arc volcanism: Physics and tectonics*. Tokyo, pp 165–175
37. Karig DE (1971) Structural history of the Mariana island arc system. *Geol Soc Amer Bull* 83:323–344
38. Karig DE (1983) Temporal relationships between back arc basin formation and arc volcanism with special reference to the Philippine Sea. In: Hayes DE (ed) *The tectonic and geologic evolution of Southeast Asian Seas and Islands*, P.2, Geophysics Monograph 27. American Geophysical Union, Washington, DC, pp 318–325
39. Khutorskoy MD (1982) Heat flow in areas of structural geological heterogeneity. In: *Proceedings of GIN USSR*, vol 353. Nauka, Moscow, p 77 (in Russian)
40. Kimura M, Uyeda S, Kato Y, Tanaka T, Yamano M, Gamo T, Sakai H, Kato S, Izawa E, Oomori T (1989) Active hydrothermal mounds in the Okinawa trough back-arc basin, Japan. *Tectonophysics* 145:319–324
41. Kushiro I (1978) Density and viscosity of hydrous calc-alkalic andesite magma at high pressures. *Carnegie Inst Washington Yearbook* 77:675–677
42. Langseth MG, Hobart MA, Horai K (1980) Heat flow in the Bering sea. *J Geophys Res* 85:3740–3750
43. Langseth MG, Mrozowski CL (1980) Geophysical surveys for Leg 59. In: *Initial reports of DSDP*, 59. Washington, DC, pp 487–502
44. Lee CS, McCabe R (1986) The Banda-Celebes-Sulu basins: a trapped piece of Cretaceous-Eocene oceanic crust? *Nature* 322:51–54
45. Lee CH, Shor GG, Bibee LD, Lu RS, Hilde TWC (1980) Okinawa Trough: origin of a back-arc basin. *Mar Geol* 35:219–241
46. Lister CRB (1972) On the thermal balance of the mid-ocean ridge. *Geophys J Roy Astr Soc* 26:515–535
47. Lister CRB (1977) Estimates for heat flow and deep rock properties based on boundary layer theory. *Tectonophysics* 41:157–171
48. Lobkovsky LI (1988) Geodynamics of the zones of spreading, subduction and two-tier plate tectonics. Nauka, Moscow, p 252. (in Russian)
49. Loudon KE (1977) Paleomagnetism of DSDP sediments, phase shifting of magnetic anomalies, and rotations of the West Philippine Basin. *J Geophys Res* 82:2989–3002
50. Lu RS, Pan JJ, Lee TC (1981) Heat flow in the southwestern Okinawa Trough. *Earth Planet Sci Lett* 55(2):299–331
51. Matsubayashi O, Nagao T (1988) Compilation of heat flow onshore and offshore the Southeast Asia. *Tectonics of Eastern Asia and Western Pacific continental margin*, vol 22. DELP Publication, Tokyo, pp 125–126
52. McKenzie DP (1968) The influence of boundary conditions and rotation on convection in the Earth's mantle. *Geophys J R Astron Soc* 15:457–500
53. McKenzie DP (1969) Speculations on the consequences and causes of plate motions. *Geophys J* 18:1–32
54. McKenzie DP, Sclater JG (1968) Heat flow inside the island arcs of the northwestern Pacific. *J Geophys Res* 73:3173–3179
55. Melankholina EN (1988) Tectonics of the North-West Pacific. Relationship of the structures of the ocean and the continental margin. In: *Proceedings of the Geological Institute, Academy of Sciences*, vol. 434, p 218 (in Russian)
56. Miyashiro A (1974) Volcanic rock series in island arcs and active continental margins. *Am J Sci* 274:321–355
57. Mrozowski CL, Hayes DE (1979) The evolution of the Parece Vela Basin, eastern Philippine Sea. *Earth Planet Sci Lett* 46:49–67
58. Mrozowski CL, Hayes DE, Taylor B (1982a) Multichannel seismic reflection surveys of Leg 60 sites, DSDP. *Initial Rep DSDP* 59:57–69

59. Mrozowski CL, Hayes DE, Taylor B (1982b) Complexities in the tectonic evolution of the West Philippine basin. *Tectonophysics* 82:1–24
60. Murauchi S, Den N, Asano S, Hotta H, Yoshii T, Asanuma T, Hagiwara K, Ichikawa K, Sato T, Ludwig WT, Ewing JI, Edgar HT, Houtz RE (1968) Crustal structure of the Philippine sea. *J Geophys Res* 73:3143–3171
61. Muraviev AV (1988) Heat flow in the southern part of Komandorskaya basin. In: *Geothermal studies at seafloor*. Nauka, Moscow, pp 59–68 (in Russian)
62. Muraviev AV, Smirnov YB, Sugrobov VM (1988) Heat flow along the Philippine Sea Geotraverse. *Dokl Akad Nauk USSR* 299:189–194. (in Russian)
63. Otsuki K (1989) Empirical relationships among the convergent rate of plates, rollback rate of trench axis and island arc tectonics: “Laws of convergent rate of plates”. *Tectonophysics* 159(1–2):73–94
64. Parsons B, Sclater JG (1977) An analysis of the variation of ocean floor Bathymetry and heat flow with age. *J Geophys Res* 82:803–827
65. Peacock SM (1987) Thermal effects of metamorphic fluids in subduction zones. *Geology* 15:1057–1060
66. Peacock SM (2013) Thermal and petrologic structure of subduction zones. *Geophysics monograph series*. Book Editor(s): Bebout GE, Scholl DW, Kirby SH, Platt JP
67. Polyak BG (1988) Heat and mass flow from the mantle in the main structures of the earth's crust. Nauka, Moscow, p 192. (in Russian)
68. Polyak BG, Fernández M, Khutorskoy MD et al (1996) Heat flow in the Alboran Sea, western Mediterranean. *Tectonophysics* 263:191–218
69. Popova AK, Smirnov YB (1981) Tasman Sea and trenches of the South-Western Pacific. In: *Methodical and experimental basics of geothermics*, pp 178–181 (in Russian)
70. Pushcharovsky YM (1972) Introduction to the tectonics of the Pacific segment of the Earth. Nauka, Moscow, p 222. (in Russian)
71. Rodnikov AG, Isezaki N, Shiki T, Uyeda S, Liu G (eds) (1991) The North China Plain – Philippine Sea – Mariana Trench Geotraverse. Nauka, Moscow, p 152. (in Russian)
72. Rodnikov AG, Rodkin MV, Stroev PA, Uyeda S, Isezaki N, Shiki T (1996) Deep structure and geophysical fields along the Philippine Sea Geotraverse. *Phys Solid Earth* 32(12):1010–1017
73. Rubenstone JL (1984) Geology and geochemistry of early Tertiary submarine volcanic rocks of the Aleutian islands, and their bearing on the development of the Aleutian island arc. PhD Thesis, Cornell University, Ithaca, 350 pp
74. Sano Y, Wakita H (1985) Geographical distribution of $3\text{He}/4\text{He}$ ratios in Japan: implications for arc tectonics and incipient magmatism. *J Geophys Res* 90(B10):8729–8741
75. Schmidt MW, Poli S (1998) Experimentally based water budgets for dehydrating slabs and consequences for arc magma generation. *Earth Planet Sci Lett* 163:361–379
76. Scholl DW, Buffington EC, Marlow MS (1975) Plate tectonics and structural evolution of the Aleutian-Bering Sea region. In: Forbes RB (ed) *Contributions to the geology of the Bering sea basin and adjacent regions*. Geological Society of the American Memoirs, vol 151, pp 1–32
77. Sclater JG, Ritter UG, Dixon FS (1972) Heat flow in the Southwestern Pacific. *J Geophys Res* 77(29):5697–5704
78. Sclater JG, Karig DE, Lawver LA, Loudon K (1976) Heat flow, depth, and crustal thickness of the marginal basins of the south Philippine Sea. *J Geophys Res* 81:309–318
79. Scott R, Kroenke L (1980) Evolution of back arc spreading and arc volcanism in the Philippine Sea: interpretation of Leg 59 DSDP results. In: Hayes DE (ed) *The tectonic and geologic evolution of southeast Asian seas and islands*. *Geophysics Monograph* 23. AGU, Washington, DC, pp 283–291
80. Seliverstov NI, Avdeiko GP, Ivanenko AN, Shkira VA, Khubunaya SA (1986) New submarine volcano in the western part of Aleutian island arc. *Volcanol Seismol* 4:3–17
81. Sharaskin AY, Karpenko SF (1987) Subduction in the light of geochemical data. In: *The structure of seismic focal zones*. Nauka, Moscow, pp 110–122 (in Russian)

82. Shemenda AI (1985) Modeling the spreading mechanism of some types of marginal seas. *Oceanology* 25(2):265–273. (in Russian)
83. Shih T (1980) Marine magnetic anomalies from the Western Philippine Sea: implications for the evolution of marginal basins. In: The tectonic and geologic evolution of Southeast Asian seas and islands, *Geophysics monograph*, 23. AGU, Washington, DC, pp 49–85
84. Shiono K, Sacks IS, Linde AT (1980) Preliminary velocity structure of Japanese Islands and Philippine Sea from surface wave dispersion. *Yearbook Carnegie Inst Washington* 79:498–505
85. Singh SC, Moeremans R (2017) Anatomy of the Andaman–Nicobar subduction system from seismic reflection data. Chapter 13. *Geological Society, London, Memoirs* 47:193–204. <https://doi.org/10.1144/M47.13>
86. Smirnov YB, Sugrobov VM (1979) Earth heat flow in the Kuril-Kamchatka and Aleutian provinces. I. Heat flow and tectonics. *Vulkanol Seismol* 1:59–73 (in Russian)
87. Smirnov YB, Sugrobov VM, Galushkin YI (1982) Heat flow in the junction zone of the Aleutian-Kamchatka island arc system. *Vulkanol Seismol* 6:96–115
88. Smirnov YB, Yamano M, Uyeda S, Galushkin YI, Muraviev AV, Sugrobov VM, Ruhui Z, Qianfan W, Li R, Wanxia Z (1991) Heat flow. In: Rodnikov AG, Isezaki N et al (eds) *The North China Plain – Philippine Sea-Mariana Trench Geotraverse*. Moscow, Nauka, pp 97–119
89. Stein CS, Stein S (1992) A model for the global variation in oceanic depth and heat flow with lithospheric age. *Nature* 359:123–129
90. Stein CS, Stein S (1994) Constraints on hydrothermal heat flux through the oceanic lithosphere from global heat flow. *J Geophys Res* 99(B2):3081–3096
91. Soinov VV, Solovyev VN, Vlasenko VN, Salman AG (1984) Heat flows through the bottom of the Deryugin Sea of Okhotsk Sea. In: *Theoretical and experimental studies on the geothermics of seas and oceans*. Nauka, Moscow, pp 63–66. (in Russian)
92. Staudacher T, Allegre CJ (1988) Recycling of oceanic crust and sediments: the noble gas subduction barrier. *Earth Planet Sci Lett* 89:173–183
93. Sugrobov VM, Gorshkov AP, Smirnov YB (1983) The New Guinea Sea. In: *Methodical and experimental fundamentals of geothermy*. Nauka, Moscow, pp 173–178. (in Russian)
94. Sydora LJ, Jones FW, Lambert RSJ (1980) Model calculations of the thermal fields of subducting lithospheric slabs and partial melting. *Tectonophysics* 62:233–249
95. Tamaki K (1985) Two models of back-arc spreading. *Geology* (7):475–478
96. Tamaki K (1986) Age estimation of the Japan Sea on the basis of stratigraphy, basement depth and heat flow data. *J Geomag Geoelect* 38:427–444
97. Tamaki K, Pisciotto K, Allan J et al (1990) Background, objectives, and principal results, ODP LEG 127, Japan Sea. *Proceedings of the Ocean Drilling Program. Initial Rep* 127:5–33
98. Tanaka A, Yamano M, Yano Y, Sasada M (2004) Geothermal gradient and heat flow data in and around Japan (I): appraisal of heat flow from geothermal gradient data. *Earth Planets Space* 56:1191–1194
99. Taylor B (1979) Bismarck Sea: evolution of a back-arc basin. *Geology* 7:171–174
100. Taylor B, Hayes DE (1983) Origin and history of the South China Sea Basin. In: Hayes DE (ed) *The tectonic and geologic evolution of Southeast Asian Seas and Islands*, *Geophysics monograph* 23. American Geophysical Union, Washington, DC, pp 89–104
101. Turcotte DL, Schubert G (1973) Frictional heating of the descending lithosphere. *J Geophys Res* 70:5876–5886
102. Turcotte DL, Schubert G (1982) *Geodynamics – application of continuum physics to geological problems*. Wiley, New York, 450 pp
103. Uyeda S (1977) Some basic problems in the trench-arc-back arc systems. *American Geophysical Union. Maurice Ewing Ser* 1:1–14
104. Uyeda S (1982) Subduction zones: an introduction to comparative subductology. *Tectonophysics* 81(3–4):133–159
105. Uyeda S, Kanamori H (1979) Back-arc opening and the mode of subduction. *J Geophys Res* 84:1049–1061

106. Uyeda S, Vacquer V (1968) Geothermal and geomagnetic data in and around the island arc of Japan. *Geophys Monogr AGU* 12:349–366
107. Van den Beukel J, Wortel R (1988) Thermo-mechanical modelling of arc-trench regions. *Tectonophysics* 154:177–193
108. Van Keken PE, Kita S, Nakajima J (2012) Thermal structure and intermediate-depth seismicity in the Tohoku-Hokkaido subduction zones. *Solid Earth* 3(2):355–364
109. Van Keken P, Wilson C (2017) Thermal structure of subduction zones/Carnegie Inst. For Science, Washington, DC
110. Velinsky VV, Tretyakov GA, Simonov VA (2004) Physicochemical modeling of the serpentinization process and the role of oceanic serpentinites in hydrothermal ore formation. *Izv Tomsk Polytech Univer.* 307(1):57–63. (in Russian)
111. Veselov OV (2005) Geothermics of tectonosphere of the Japan Sea – Sea of Okhotsk region. PhD Thesis, Khabarovsk, 2005, p 28
112. Veselov OV, Volkova NA, Soinov VV (1983) Transition zones of the Okhotsk, Japanese and Philippine provinces. In: *Methodical and experimental fundamentals of geothermy*. Nauka, Moscow, pp 168–171. (in Russian)
113. Veselov OV, Semakin VP, Kochergin AV (2018) Heat flow and neotectonics of the area of the Deryugin basin (Sea of Okhotsk). *Transit Zone Geosyst* 2(4):312–322. (in Russian)
114. Verhoogen J (1965) Phase changes and convection in the Earth's Mantle. *Phil Trans Roy Soc A* 258:276–283
115. Watanabe N, Langseth MG, Anderson RN (1977) Heat flow in back-arc basins of the western Pacific. In: Talwani M, Pitman WC (eds) *Island arcs, deep sea trenches and back-arc basins*. American Geophysical Union, pp 137–161
116. Weissel JK, Hayes DE (1977) Evolution of the Tasman Sea reappraised. *Earth Planet Sci. Lett.* 36:77–84
117. Weissel JK, Watts AB (1979) Tectonic evolution of the Coral Sea basin. *J Geophys Res* 84:4572–4582
118. Wyllie PJ (1977) Magmas and volatile components. *Am. Mineral.* 64:469–500
119. Yamano M, Uyeda, Aoki Y, Shipley TH (1982) Estimates of heat flow derived from gas hydrates. *Geology* 10:339–343
120. Yamano M, Honda S, Uyeda S (1984) Nankai Trough: a hot trench? *Mar Geophys Res* 6:187–203
121. Yamano M, Uyeda S, Kinoshita H, Hilde TWC (1986) Heat flow measurements. Report on DELP-1984 cruise in the middle Okinawa trough. *Bull ERI, Tokyo* 61:251–267
122. Yamano M, Uyeda S (1988) Heat flow. In: Nairn AEM, Stehli FG, Uyeda S (eds) *The ocean basins and margins*, vol. 7B. Plenum Publishing Corporation, pp 523–557
123. Yamano M, Shevaldin YuV, Zimin PS, Balabashin VI (1996) Heat flow of the Japan Sea. In: *Geology and geophysics of the Japan Sea*. Ser. Japan-Russian monograph (JRM) Tokyo. Terra Scientific PC, pp 61–74
124. Yoshii T, Yamano M (1983) Digital heat flow data file around Japanese Islands. Tokyo
125. Zellmer GF, Edmonds M, Straub SM (2014) Volatiles in subduction zone magmatism. *Geol Soc Lond Spec Publ* 410:1–17

Heat Flow Asymmetry on the Mid-Oceanic Ridges of Northern and Southern Earth Hemispheres



M. D. Khutorskoy and E. A. Teveleva

Detailed heat flow studies within the slopes of the mid-oceanic ridges and adjacent abyssal basins have shown that its distribution is not symmetric everywhere relative to the ridge axis in the same-type zones, but is subject to a complex redistribution mechanism that depends on many geological causes associated with tectonics and features of the structure of the lithosphere of these zones.

The presence of the geothermal asymmetry of the mid-ocean ridges (MOR) slopes, adjacent abyssal basins and passive parts of the transform faults in the Atlantic, Indian and Pacific Oceans was justified and confirmed on the basis of statistical processing of data from the global heat flow database along the geotraverses, Crossing MOR and covering the above structural elements of the oceanic crust [13, 14, 16, 27, 28]. It is important to note that the MOR asymmetry is observed not only in the thermal field, but also in other geophysical fields: magnetic [7] and gravity [3], and also in the crust structure [22, 31].

The nature of this phenomenon was repeatedly discussed, and various geological and geophysical models were proposed to explain the existing asymmetry. Some researchers note the existence of different oceanic plates spreading rates on different sides of the ridges axis [22, 32], others believe that the geodynamic processes in the adjacent plates differ, and on one of them the compression regime, which replaced the initial tension situation, creates overthrust structures characteristic for compression [3, 31].

We previously proposed to consider the influence of the Coriolis force [15], which acts on any mass, moves along the radius of the rotating Earth and diverts this mass from the orthogonal trajectory, respectively, to the west in the southern hemisphere and to the east – in the northern hemisphere. An upward flow of magma in the divergent zones of the middle ridges can be considered as such a “mass”. The

M. D. Khutorskoy (✉) · E. A. Teveleva
Geological Institute of the Russian Academy of Sciences, Moscow, Russia

deviation of this flow from a trajectory orthogonal to the planet's surface determines the observed geothermal asymmetry.

The purpose of this paper is a comparative analysis of the heat flow distribution along geotraverse crossing MOR in the southern and northern hemispheres of the planet. Naturally, we consider those MOR intersections, which are most representative of heat flow measurements. The compilation of measured heat flow values is reflected in global databases [9, 12, 26, 29].

To establish the fact of geothermal asymmetry on the MOR slopes, we compared heat flow data for the same type of elements along the long profiles (geotraverses) crossing the ridges in the World Ocean: the Mid-Atlantic ridge, the East Pacific Rise and the West Indian Ridge (Fig. 1). Statistical sampling for each of these geotraverses is quite representative (Table 1) for comparative analysis.

The proof of the possible geothermal asymmetry of structural morphological elements along geotraverses is based on a statistical comparison of empirical data related to different its parts, in our case, to its western and eastern strike.

To verify of the statistically significant difference in the mean heat flow values, the parametric Cramer-Welch criterion (T) was used in the samples, the value of which is found from the formula [8]:

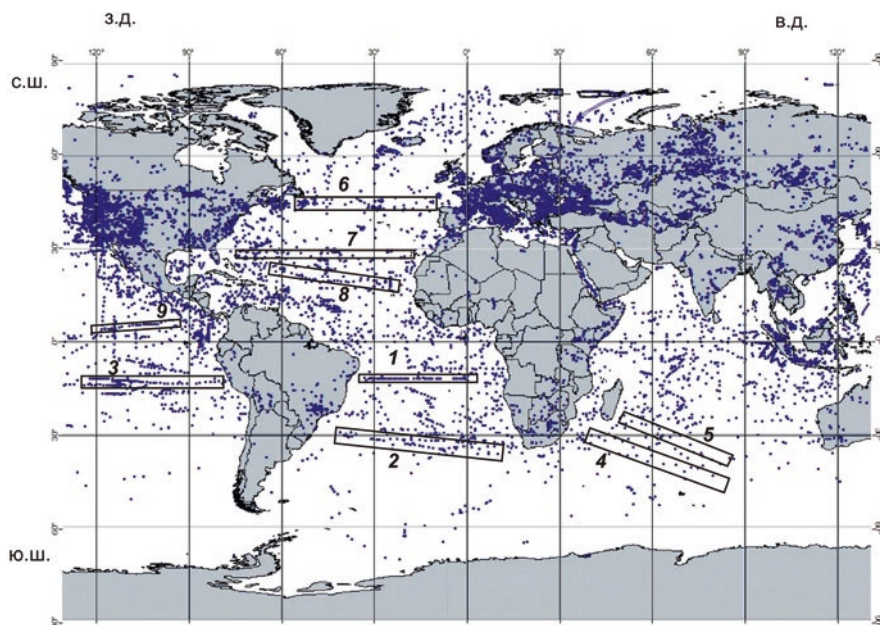


Fig. 1 The scheme of the location of the measurement points of the heat flow and the investigated geotraverses in the World Ocean (see the text for the numbers)

Table 1 Statistical characteristics of geotraverse in the southern hemisphere of the Atlantic Ocean

No. geotraverse	No.1 Angola-Brazil		No. 2 -31°S	
	West	East	West	East
Average heat flow value	62	39	91	61
Standart deviation	25	21	94	62
Number of measurement	16	18	6	27
Cramer-Welch criterium	3,0		0,99	
Confidence probability	99%		80%	

$$T = \frac{\sqrt{mn} * (\bar{x} - \bar{y})}{\sqrt{ns_x^2 + ms_y^2}},$$

where \bar{x} , s_x^2 , n и \bar{y} , s_y^2 , m , respectively, sample means, variances, and the amount of data from two comparative samples. If $T < \varphi\left(1 - \frac{\alpha}{2}\right)$, where $\varphi\left(1 - \frac{\alpha}{2}\right)$ – is the inverse of the normal distribution function from the significance level α , where $\alpha = 1 - P$, P is the confidence probability, then the hypothesis of homogeneity of the mean heat flow values, i.e. the existence of asymmetry is not confirmed. If $T \geq \varphi\left(1 - \frac{\alpha}{2}\right)$, then the hypothesis is accepted that the average values for the considered feature are non-uniform, and the asymmetry is confirmed. With a significance level $\alpha = 0.05$ (at $P = 95\%$), the critical value of the Cramer-Welch criterion is $T = 1.96$. Therefore, if the value of the criterion does not exceed this value, then it is necessary to accept the hypothesis of homogeneity of the sample data by the mean value. If the value of the criterion is greater than or equal to the critical value then the samples by the mean value are recognized as different.

1 Southern Hemisphere of the Earth

In the southern hemisphere, we analyzed the heat flow distribution along five geotraverses: (1) Angola-Brazil geotraverse (12°S), (2) geotraverse along 31°S – in the Atlantic Ocean; (3) geotraverse 15°S – in the Pacific Ocean, as well as geotraverse in the Indian Ocean: (4) the southern part of the Crozet-Mozambique Basin and (5) the northern part of the Crozet-Madagascar (Fig. 1).

1.1 Atlantic Ocean

Most of the geothermal data for the Angolo-Brazilian geotraverse (No.1) was obtained during many years of expeditionary geological and geophysical research by VNIIOceangeology [18, 25, 27, 30].

Within the Angola-Brazil geotraverse, detailed heat flow measurements, gravitational and magnetic fields, the bottom relief, and a large volume of seismic surveys were carried out.

The bottom morphostructure along the geotraverse conform to the traditional transoceanic structures scheme [22]. In the central part of the geotraverse there is a mid-Atlantic uplift, on both sides of which abyssal plates lie (the Angolan and Brazilian basins) and the marginal-continental flexures (African and South American continental slopes with foothills) interfaced with plates (Fig. 2). The listed first-order structures are complicated by a system of subordinate and superimposed morphostructures: mosaic-cellular and linear-ridge uplifts, plateaus, troughs, volcanic buildings of central type are distinguished. Despite the smooth interface of structures in general, longitudinal zones relative to the middle ridge of the zone are contacted by faults. Based on the landscape characteristics (size, amplitude, orientation), the asymmetry of the wings of the median uplift is noted: in the formation of

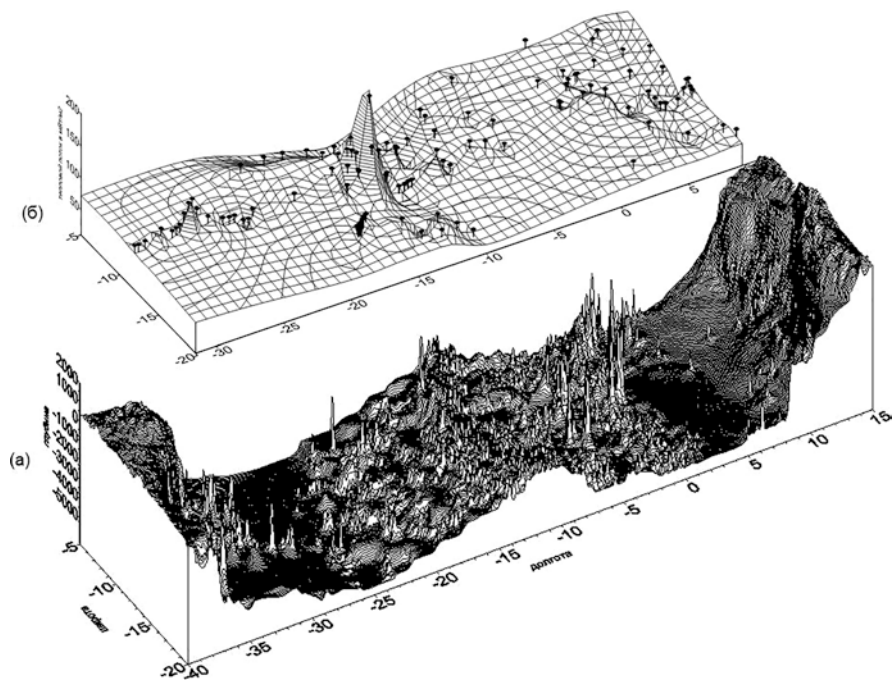


Fig. 2 The relief of the bottom (a) and the heat flow (b) along the Angola-Brazil geotraverse

the basalt bed, the tectonic -magmatic activity was most intensively manifested in the western “Brazilian” wing [25].

The structure of the magnetic field of the western and eastern flanks of the uplift is also asymmetric. The anomalies of the western flank are characterized by a relatively high intensity (up to 150 nT) and a more consistent linearity. They are well identified up to the 33rd anomaly inclusive. Anomalies of the eastern flank are characterized by smoothed (up to 100 nT) fragmentarily linear field with alternating signs, and the correlation is quite arbitrary here [18]. Asymmetry in the structure of the anomalous magnetic field of the western and eastern flanks of the middle elevation is also established on the geomagnetic cross-section: the surface of the lower edges of magnetized bodies on the western flank does not deeper than 12 km, and in the east reaches 20 km from the ocean surface.

According to the data of CDP, there are structural seams buried beneath the sedimentary cover. On the seismic section, they are expressed in the form of a powerful reflector that passes through the entire crust and displaces the Moho surface. Although these seams are not expressed either in the bottom relief or in the gravitational field, in the structural plan they also give grounds for assuming the asymmetry of the underlying tectonic processes. On the Angolan seam, the oceanic lithosphere is advancing on the surface of the paleocontinental slope toward the continent, and on the Brazilian slope listric slipping off is observed.

The observed asymmetry in the deep structure of the slopes and abyssal basins along the geotraverse, as well as in the magnetic field, is naturally related to the difference in the energy of the geodynamic processes, which can be judged from the analysis of geothermal data. They showed, at statistical processing and calculation of the Cramer-Whelch criterion, a significant difference in heat flow on different sides of Mid-Atlantic Ridge. Thus, the average heat flow to the west of the Mid-Atlantic Ridge is 62 mW/m², and to the east 39 mW/m² (Table 1).

Discussing the reasons for the geothermal asymmetry of the ridge, we can agree in the first approximation with the authors of the report [25, p. 21], who explain it “... by the absence of a single mechanism for the formation of the oceanic lithosphere”, but the result obtained by us suggest the presence of additional deep thermal sources, which caused an increase in heat flow on the western flank of the ridge in the geotraverse zone.

We can assume either the presence of different lithosphere thicknesses from the western and eastern sides of the ridge (in this case, differences in the background heat flow values will remain in the stationary geothermal field), or the action of non-stationary and later geodynamic processes that altered the thermal structure of the already formed oceanic lithosphere.

The first of our assumptions does not agree with the independent geophysical results obtained in the study of geotraverse, and also with estimates of the lithosphere thicknesses from the bottom bathymetry data [19]. The second assumption is more real, because structural heterogeneity and the presence of superimposed tectonic processes in the formed lithosphere is confirmed by magnetometry and seismic profiling data.

Geotraverse along 31°S stretches from the Cape basin in the east to the Plateau Rio-Grande in the west of the Atlantic Ocean. In the geotraverse strip, there are 6 measurements to the west of the Mid-Atlantic Ridge and 27 measurements to the east. Applying the same method of data comparison, we calculated that the average heat flow west of Mid-Atlantic Ridge is 91 mW/m², and to the east 61 mW/m², i.e. came to a similar result: the western flank of the Mid-Atlantic Ridge on the geotraverses of the southern hemisphere in the Atlantic has a higher heat flow (See Table 1).

As was announced above, we will discuss more general and universal models for explaining the observed asymmetry of heat flow after characterizing all geotraverses.

1.2 *Pacific Ocean*

In the southern hemisphere of the Pacific Ocean, we examined one geotraverse crossing the East Pacific Rise at 15°S. The East Pacific Rise represents one of the main links of the global chain of mid-oceanic ridges. In the southeastern Pacific it serves as a boundary between the Pacific plate in the west and the plates of the Antarctic, Chilean, Nazca and Cocos in the east. Morphologically, the uplift is expressed in the form of a wide (1000–1200 km) swell with gentle slopes dissected into large and small blocks, among which submarine volcanic mountains or volcanic arrays are elevated. Parallel to the main axis of the East Pacific Rise, sometimes there are clay-volcanic uplifts of relatively small extent. The crest of the East Pacific Rise is located at a depth of 2–3 km, and only a few individual volcanoes rise to less than 2 km. The highest point of the ridge in this part of the ocean is Easter Island, located in the zone of its connection with the latitude-volcanic Sala y Gomez ridge.

The peculiarity of the East Pacific Rise, which distinguishes it from other middle ridges, is the absence of a longitudinal rift valley and its ridge framing, which is explained by the high rate of spreading (up to 16 cm/year), at which abundant masses of magmatic material arriving at the surface completely fill rift valley [21, 22].

Sedimentary layer on the rise is quite thin, and in a number of places and generally absent. The second layer, represented mainly by basalts, has a thickness of 1 km, and the “basalt layer”, which, judging by the results of dredging on the Heizen fault in the 24th cruise of the “Academik Kurchatov” R/V, consists of amphibolite shales, 6–3.7 km, which is almost 2 km less than the thickness of this layer outside the East Pacific Rise. G. Menard in his works called the East Pacific Rise as a meganticlinal uplift of the oceanic crust, in which the layers gradually become thinner as they approach the crust [6].

Throughout the course of the East Pacific Rise, it is dissected by numerous transform faults, over which its blocks are sometimes displaced over considerable distances. For example, the displacement of the East Pacific Rise axis in the Heisen and Tharp faults of the Eltanin transform system between 53 and 57°S reaches 15° in

longitude, i.e. more than 1500 km. The nature of the displacements varies along the strike of the East Pacific Rise: to the south of the parallel 40°S the right-hand displacements predominate, between 40° and 20°S – left-sided, and northern of 20°S, right up to the junction with the latitudinal Galapagos uplift, again right-sided ones predominate.

Many researchers also note similar features in the geophysical fields of the southern part of the mid-Atlantic [17]. This similarity is expressed in identical anomalies of the total geomagnetic field vector and gravitational anomalies in the free air reduction.

American and Canadian scientists obtained the main volume of geothermal measurements in this part of the Pacific Ocean. Nevertheless, about 50 heat flow measurements were carried out by Russian scientists, including the authors of this work, during the 14th cruise of the “Dmitry Mendeleev” R/V and the 24th cruise of the “Akademik Kurchatov” R/V [30].

Geotraverse area 15°S is characterized by the highest geothermal knowledge from all considered objects. A total of 7260 heat flow measurements were analyzed here, of which 3740 are located western of the East Pacific Rise axis, and 3520 are to the east. The calculation of the statistical difference in the sample showed that at this intersection of the East Pacific Rise there is a significant asymmetry of the heat flow: its mean value to west of the ridge is 88 mW/m², and to the east 72 mW/m² (Table 2).

1.3 Indian Ocean

In this paper, we analyzed heat flow distribution on the flanks of the South-West Indian Ridge (Fig. 3). It is morphologically divided into the West-Indian ridge and the African-Antarctic ridge, the connection of which occurs in the zone of the Prince Edward transform fault at 37°E (Fig. 3). The ridges are characterized by an intensely subdivided relief with a height difference of up to 4 km. They are intersected by numerous transform faults, displacing the modern spreading axis sometimes for tens of miles [32].

Table 2 Statistical characteristics of geotraverse in the southern hemisphere of the Pacific Ocean

No. geotraverse	No.3 -15°S	
West/east	West	East
Average heat flow value	88	72
Standart deviation	61	59
Number of measurement	3745	3520
Cramer-Welch criterium	2,84	
Confidence probability	99%	

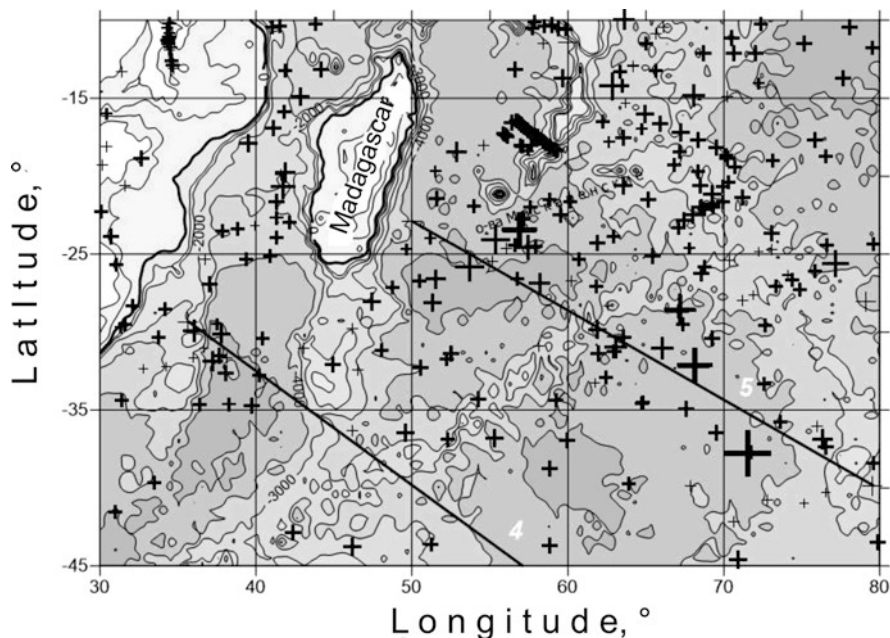


Fig. 3 Bathymetric map of the southwestern part of the Indian Ocean (cross-section of isobaths – 1000 m) and location of points of heat flow measurement (crosses). The size of crosses is proportional to the amount of heat flow. 4–5 – geotraverse, along which statistical processing of geothermal data was carried out

South-West Indian Ridge refers to slowly spreading ridges [10]. The spreading rate here, on the average, does not exceed 14 km/million years (1.4 cm/year), and the accretion of the crust on both sides of the ridge axis is sharply asymmetric. So, on the “Antarctic” side it is 8.5 km/million years, and on the “African” side it is 5.5 km/million years [4]. Along the strike of South-West Indian Ridge, structural asymmetry is also observed. The parts of the ridge lying west of the Andrew Bayne transform fault (30°E) and east of the Malville transform fault (61°E) are characterized by an abnormally deep axial valley, oblique spreading, a small central magnetic anomaly and unstable morphological manifestation at the bottom of transform faults passive parts [4, 24].

Such properties of the peripheral parts of South-West Indian Ridge allow us to assume that they have a relatively “cold” mantle, a strong and thick lithosphere and limited magma reserves. On the contrary, the central part of South-West Indian Ridge, between 30 and 61°E, is characterized by superficially manifested transformations in the relief, orthogonal spreading and a pronounced central magnetic anomaly [24]. Within this part of South-West Indian Ridge, between the transform faults of Atlantis II (56°45'E) and Navar (58°40'E), lies a segment which, judging by the spreading rate, can be compared with most segments Mid-Atlantic ridge.

Thus, South-West Indian Ridge is characterized by structural and morphological asymmetry along and across its strike.

In the southwestern part of the ocean, since the late 60s of the twentieth century, expeditions to American, French and Japanese research vessels have been carried out repeatedly, including heat flow measurements [1, 2, 5, 11]. The compilation of the measured heat flow values is reflected in global databases [9, 12, 26, 29]. Figure 3 shows all known points of measurement in this part of the Indian Ocean.

To establish the fact of geothermal asymmetry on the flanks of West Indian Ridge, we compared the samples of heat flow data along two long geotraverses crossing the ridge (Fig. 3). Statistical sampling for each of these geotraverses is quite representative (Table 3) for comparative analysis.

Thus, in the southwestern part of the Indian Ocean, we note the presence not only of a structural but also a geothermal asymmetry of the West Indian Ridge relative to its axis. The western slope and the adjacent abyssal basin are characterized by a higher heat flow than the eastern part of the West Indian Ridge in the strip of both geotraverses.

Summing up the statistical analysis of the asymmetry of the MOR of the southern hemisphere, we note that for all crossings of ridges in the three oceans of the Earth, the western flank has a higher heat flow than the eastern one.

2 Northern Hemisphere of the Earth

In the northern hemisphere four geotraverses were considered: (6) geotraverse 45°N, (7) Canary-Bahamian geotraverse (28°N), (8) geotraverse 19°N, – in the Atlantic and (9) geotravers 10°N in the Pacific Ocean.

2.1 Atlantic Ocean

Geotraverse 45°N extends from the Bay of Biscay in the east to the Newfoundland depression in the west, crossing the Mid-Atlantic Ridge by 28°W. The area has been studied by all geological and geophysical methods. Heat flow measurements here

Table 3 Statistical characteristics of geotraverse in the Indian Ocean

No. geotraverse	No.5		No. 4	
	West	East	West	East
Average heat flow value	76	48	124	77
Standart deviation	59	30	79	40
Number of measurement	65	28	12	48
Cramer-Welch criterium	2,38		2,9	
Confidence probability	99%		99%	

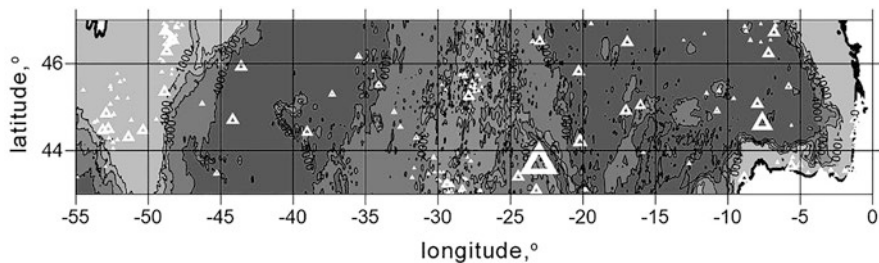


Fig. 4. The relief of the bottom and the points of measurement of the heat flow (triangles) in the region of geotraverse 45°N. The size of the triangles is proportional to the value of the heat flow

Table 4 Statistical characteristics of geotraverse in the northern hemisphere of the Atlantic Ocean (No.6)

No. geotraverse	No.6	
West/east	West	East
Average heat flow value	69	84
Standart deviation	57	43
Number of measurement	95	200
Cramer-Welch criterium	2,6	
Confidence probability	99%	

are more than 250 (Fig. 4). The range of the heat flow is very wide. The minimum value is 25 mW/m², and the maximum value is 180 mW/m². Note that the Mid-Atlantic Ridge in this region is not characterized by the most extreme values, which is usually associated with a decrease in the conduction heat flow due to heat and mass transfer in the rift valley of the ridge.

The maximum heat flow values refer to the eastern slope of the Mid-Atlantic Ridge in the region of the 8-10th magnetic anomalies. Further to the east, in the Bay of Biscay, heat flow decreases somewhat, but, nevertheless, remains elevated compared to the Newfoundland depression. A comparison of heat flow samples to the west and east of the Mid-Atlantic Ridge axis showed that the sample in the east has a statistically significant excess of the average values above the sample in the west (Table 4).

The position of the Canary-Bahamian geotraverse (23–29°N) is chosen so that it intersects only one divergent plate boundary (Mid-Atlantic Ridge) (Fig. 5), which functioned throughout the history of the Atlantic expansion. The geotraverse strip covers the region most representative for the processes of accretion and evolution of the oceanic crust in a slow spreading environment, as located between the most distant from each other Atlantic transform faults – Kane and Atlantis [18].

According to the seismic results, two earth crust types are distinguished in the geotraverse area, with a certain wave field structure and velocity characteristics, the normal and anomalous crust. Normal crust is characterized by the presence of three seismic complexes: the first seismic complex, which, in accordance with the features of the wave field, is compared with the pillow-lavas and basalt flows in the ophiolite sections; the second – (acoustically transparent horizon) is interpreted as a complex of parallel dikes; the third seismic complex, due to the presence of

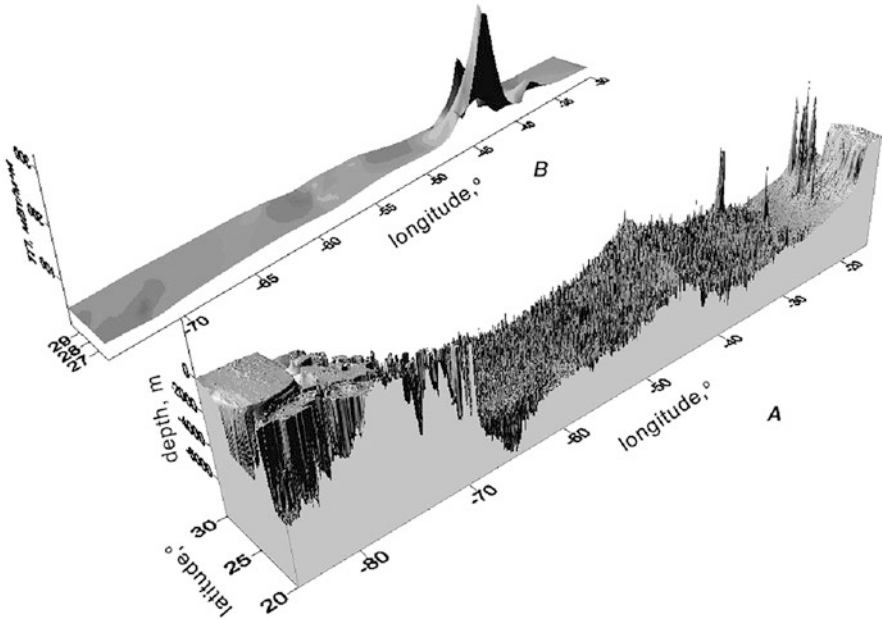


Fig. 5 Block diagrams of the bottom relief (a) and heat flow (b) along geotraverse No. 7 (Canaro-Bahamian)

dynamically expressed reflecting areas and inclined reflectors, corresponds to the lower parts gabbroids of the typical ophiolites section. On most temporary sections of the seismic reflection survey, the Moho section is highlighted, marking the transition from “layered” to “nonlayered” recording. On the seismic reflection profiles in the Canary-Bahamian geotraverse band, there are also areas where the wave fields have anomalous features: saturation with diffraction axes or reflecting the boundaries of a complex structure (inclined and “spike-shaped” reflectors).

Manifestations of asymmetry on the geotraverse were noted in the analysis of the “root dependence” of the relief on the slopes of the Mid-Atlantic Ridge [19], the gravitational free air anomalies [6, 17] and heat flow [28]. However, a statistical comparison of the geothermal characteristics of the same morphological elements along the Canary-Bahamian geotraverse revealed their heterogeneity. For example, a comparison of heat flow statistics in abyssal basins showed that in the Canary Basin in the geotraverse strip, heat flow is statistically significantly higher than in the southern part of the North American (Bahamian) basin. At the same time, a comparison of heat-flow distribution on the slopes of Mid-Atlantic Ridge did not reveal a significant difference from the east and west sides of the ridge axis.

The emergence of a new, much more representative database on heat flow [9] made it possible to significantly increase the analyzed sample in the Canary-Bahamian geotraverse. If earlier in the geotraverse strip we analyzed 42 measurements, in the last base we included about 600 measurements for the same coordinates.

Table 5 Statistical characteristics of geotraverse in the northern hemisphere of the Atlantic Ocean (No.7)

Canary-Bahamian geotraverse No.7		
West/east	West	East
Average heat flow value	78	105
Standart deviation	56	79
Number of measurement	565	36
Cramer-Welch criterium	1,99	
Confidence probability	95%	

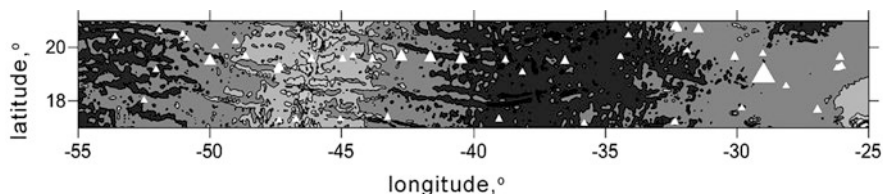


Fig. 6 Relief and position of measurement points of heat flow (triangles) along the geotraverse 19°N (the size of the triangles is proportional to the value of the heat flow)

Table 5 shows the results of statistical processing of heat flow samples in the western and eastern the geotraverse periphery. Calculations showed that in the total sample the excess of the average heat flow to the east of MAR is statistically significant compared to the sample of geothermal data to the west of the ridge.

Figure 6 shows the relief of the bottom in the geotraverse area of 19°N (No. 8). This earth's crust block is almost unaffected by transform displacements and can be considered as a tectonotype of the symmetrical arrangement of the ocean floor morphological elements: slopes of Mid-Atlantic Ridge and adjacent abyssal basins.

However, a comparison of heat flow samples generated from measurements on different sides of the Mid-Atlantic Ridge axis showed a statistically significant difference – the eastern flank of the geotraverse has a higher average heat flow (Table 6).

2.2 Pacific Ocean

In the Pacific, only one geotraverse in the northern hemisphere satisfies the condition of sufficient geothermal study. This geotraverse is No. 9, crossing the EPR at 10°N. More than 5000 heat flow measurements were obtained along this geotraverse by efforts of mainly American researchers [20, 23, 34]. The overwhelming number of measurements lies in the range of 65–100 mW/m². Only about 20 points are characterized by hurricane values of 250–260 mW/m², gravitating towards the axis of the East Pacific Rise. Statistical analysis showed a slight but significant dif-

Table 6 Statistical characteristics of geotraverse in the northern hemisphere of the Atlantic Ocean (No.8)

19°N, No.8		
West/east	West	East
Average heat flow value	74	93
Standart deviation	51	100
Number of measurement	22	30
Cramer-Welch criterium	1,34	
Confidence probability	82%	

Table 7 Statistical characteristics of geotraverse in the northern hemisphere of the Pacific Ocean (No.9)

10°N, No.9		
West/east	West	East
Average heat flow value	69	74
Standart deviation	53	56
Number of measurement	2829	3160
Cramer-Welch criterium	1,49	
Confidence probability	87%	

ference in heat flow of the East Pacific Rise flanks: the eastern flank has a higher average value than the western flank (Table 7).

2.3 *The Discussion of the Results*

A comparison of geothermal data for geotraverse flanks crossing all the MORs in the Worls oceans revealed a statistically significant asymmetry of heat flow that varies in direction in the southern and northern the Earth hemispheres: in the southern hemisphere, higher heat flow characterises the western flanks of geotraverses, and in the north – the eastern flanks (Fig. 7).

The explanation of this phenomenon requires not only the correction of the basic principles of the ocean bottom spreading paradigm, but also the more global, planetary causes of asymmetry in the fast and slowly spreading ridges. There are at least two possible causes that complicate the symmetrical divergence mechanism. They include differing age of tectonic plates blocks on opposite sides of the axis of the ridge and/or the imposition of secondary processes on primary spreading, which proceed with the release or energy absorption. Among such processes, we can point to the expansion of the crust in the accretion zone and in adjacent abyssal basins, which is accompanied by the formation of listric faults, as well as the formation of shaded blocks shielding the deep heat flow. With these tectonic processes, the complex redistribution of convective flows in the oceanic lithosphere upper part, which is fixed in the geothermal field by the presence of anomalously high and anomalously low (and even zero) heat flow values, is inextricably linked.

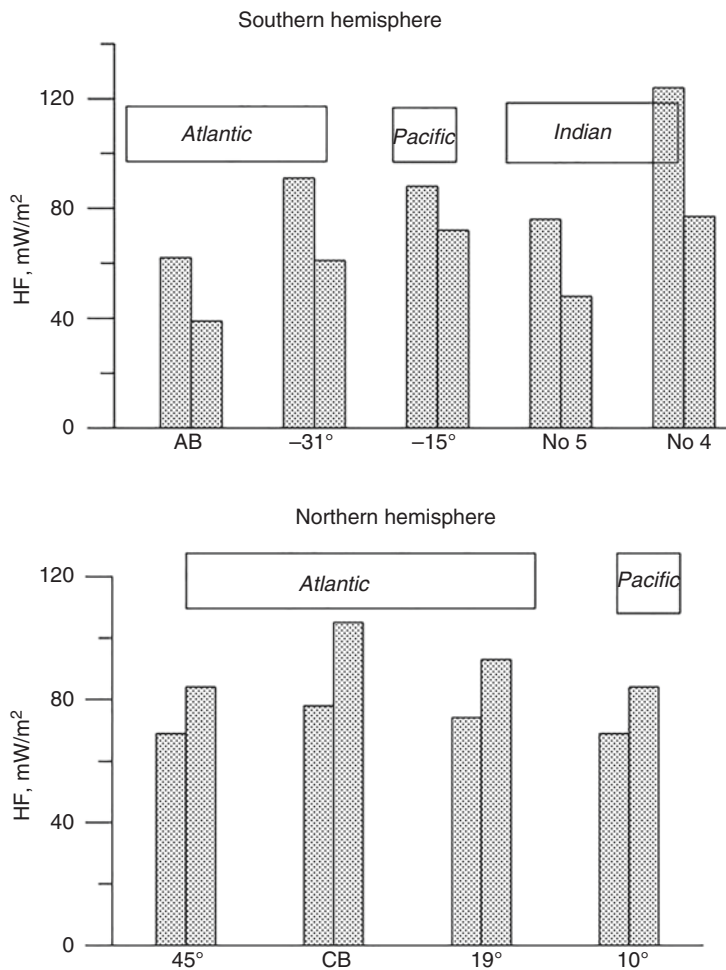


Fig. 7 Histograms of the arithmetic mean heat flow distribution along geotraverses in the southern and northern Earth's hemispheres

The existing methodology for the age of the second layer of the oceanic crust calculating according to geothermal data (eg, [33]) is based on the assumption of equal spreading speed on both sides of the oceanic ridges axis. Based on this, formula is derived that allows us to calculate the age of the bottom (t) from the measurements of the heat flow (q):

$$q = \lambda \cdot T_a / \sqrt{\pi a t},$$

where λ is the lithosphere thermal conductivity; T_a is the temperature of the asthenosphere; a is the thermal diffusivity, as well as the derivative of the other formula for estimating lithosphere thickness (H_L):

$$H_L = (T_s / T_a) \sqrt{\pi at},$$

where T_s is the solidus temperature of the mantle substance. The presence of geothermal asymmetry greatly complicates the application of these formulas and suggests another, more complex model for quantitative estimates of the oceanic lithosphere parameters. Previous studies of the oceanic crust age correlation with respect to magnetic anomalies and heat flow magnitude have not established a significant correlation [3].

The idea of the geothermal asymmetry existence makes it possible to explain the reason for the correlation absence. These factors undoubtedly need to be taken into account when analyzing the geothermal field of the oceanic crust, but they do not explain the different “direction of asymmetry” in the northern and southern hemispheres. Above we mentioned the influence of the Coriolis force, which invariably manifests itself on a rotating Earth.

On any material point of the Earth (m), due to its counterclockwise rotation with angular velocity (ω), the Coriolis force $F_k = 2m \cdot v \cdot \omega \cdot \sin\varphi$, will act, which in the southern hemisphere will shift the mass to the left relative to the radius (Fig. 8), and in the north, respectively, to the right.

In divergent zones this mass is magma, accumulated in the asthenospheric mantle reservoir and moving inside it under the Coriolis force action (Fig. 9). The excess enthalpy of this mass determines the specific convective and conductive heat flow distribution, which we observe in the divergent zones. Convective discharge of the deep heat and mass flux is directed strictly along the fault rift zone and is ultimately

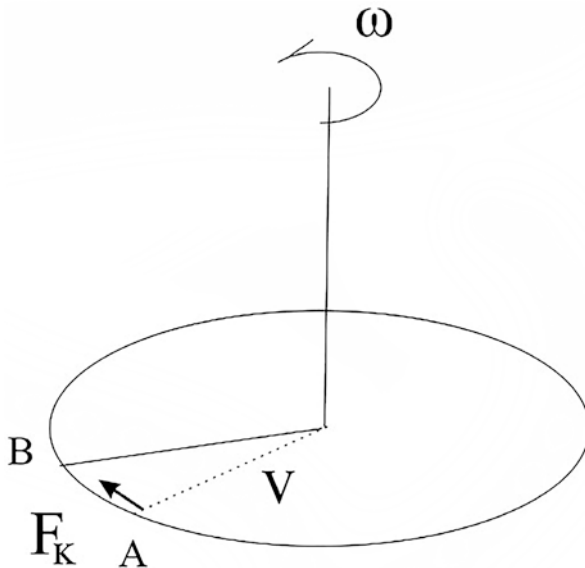


Fig. 8 The action of the Coriolis force (explanations in the text)

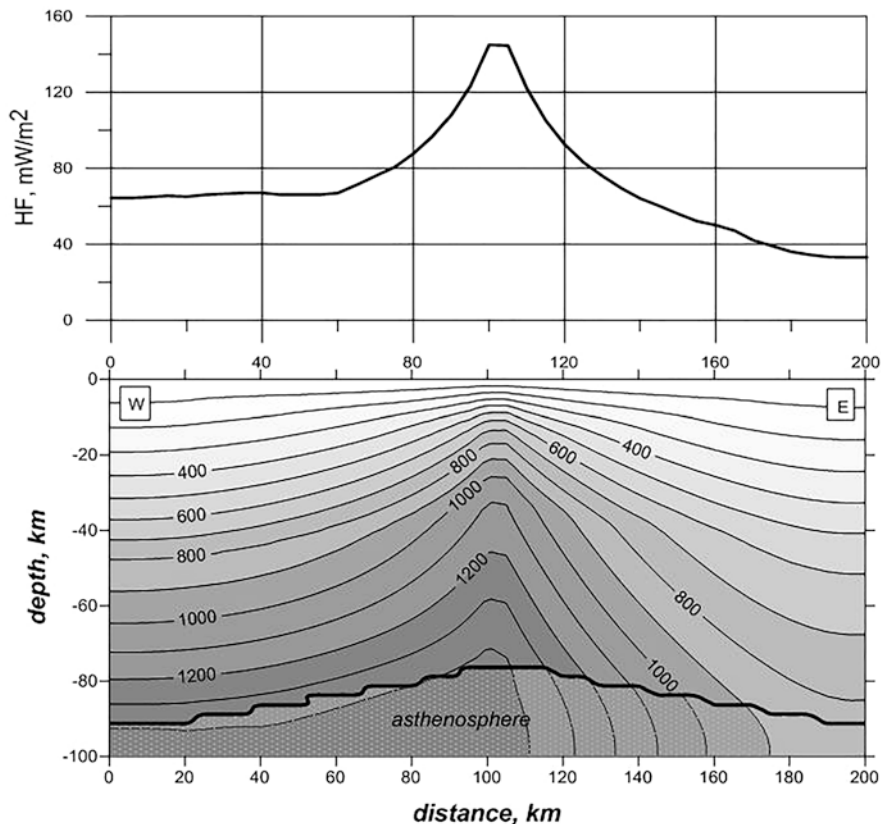


Fig. 9 Geotemperature field, $T, ^\circ\text{C}$ (below) and heat flow (mW/m^2) (above) asymmetry across mid-oceanic ridge (this example for the Southern Earth's hemisphere)

expressed in the form of volcanic manifestations on the sea bottom. At the same time, the main source of conductive heat flow on the MOR flanks and in adjacent abyssal depressions is the presence of fractional molten mantle material in the asthenospheric reservoir. The concentration of magma in this reservoir is asymmetric, due to the Coriolis force influence (see Fig. 9). The appearance of more high-enthalpy mass on one of the flanks explains the observed conductive heat flow asymmetry.

We propose to introduce a “quantitative indicator of geothermal asymmetry”, which is characterized by the absolute value of the difference in heat flow average values on the opposite geotransverse flanks: $\delta q = |q_1 - q_2|$. Due to the increase in Coriolis force along the Earth poles directions, this indicator should be greater for geotransverse at high latitudes than at near equatorial ones. In Fig. 10, the δq value is plotted along the ordinate axis for all the studied geotransverse as a function of its location latitude. Fitting approximation (dotted curve) has the shape of a parabola with a minimum at the equator latitude.

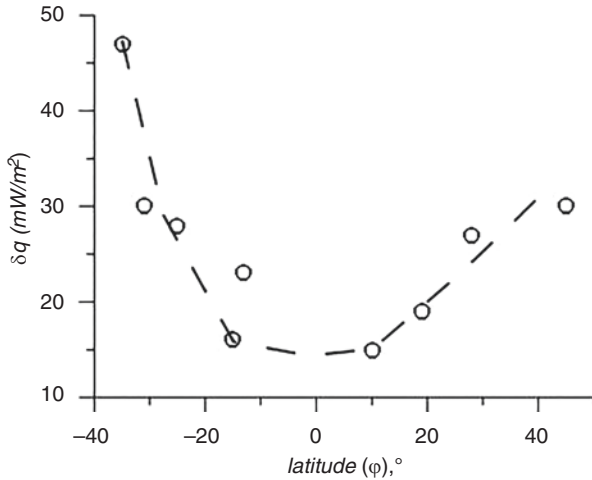


Fig. 10 Relationship of the geothermal asymmetry sign δq from geotraverse latitude

The amplitude of the displacement of the magmatic stream will be greater at high latitudes (ϕ) than when approaching the equator. Under the action of the same force, the material point in the northern hemisphere will deviate to the east relative to the trajectory orthogonal to the surface of the planet.

Geotraverses No. 1–5 are located in the southern hemisphere, therefore the flow of rising magma invariably deviates to the west, which explains the observed asymmetry in the World Ocean.

For geotraverses No. 6–9 located in the northern hemisphere, the eastern flank of the geotraverse turns out to be more “warm”, which can also be unambiguously associated with the influence of the Coriolis force.

Thus, we confirmed with the help of statistical analysis that in geotraverses of the southern hemisphere of the Earth, crossing the mid-oceanic ridges, their western flank has a higher mean arithmetic heat flow, and in the geotraverses of the northern hemisphere it is the eastern flank. The influence of the Coriolis force can be considered as the universal cause of this pattern, which, when the planet rotates, tilts the ascending stream of magma and other products of eruptions in divergent zones, respectively, to the west – in the southern hemisphere, and to the east – in the northern hemisphere.

Acknowledgements The work was carried out with financial support of the state budget theme No. 0135-2019-0040, with financial support the RFBR Grant (No. 19-05-00014) and with financial support of the Program of Russian Academy Sciences Presidium No. 49.

References

1. Anderson RN, Langseth MG, Hobart MA (1979) Geothermal convection through oceanic crust and sediments in the Indian Ocean. *Science* 204:828–832
2. Anderson RN, Langseth MG, Sclater JG (1977) The mechanisms of heat transfer through the floor on the Indian Ocean. *J Geophys Res* 82:3391–3409
3. Budanov VG, Ermakov BV, Podgornykh LV (1997) Geophysical asymmetry of the wings of mid-Atlantic ridge (MAR): gravity, magnetic fields, heat flow. European Geophysical Society, *Annales Geophysical*, part I, Society Symposia, Solid Earth Geophysics & Natural Hazards, Supplement I to Volume 15, SE27 Tectonic evolution and thermal structure at mid-ocean ridges, p 161
4. Cannat M, Rommevaux-Jestin C, Sauter D, Deplus C, Mendel V (1999) Formation of the axial relief at the very slow spreading Southwest Indian Ridge (49° to 69°E). *J Geophys Res* 104:22825–22843
5. Courtney RC, Recq M (1986) Anomalous heat flow near the Crozet Plateau and mantle convection. *Earth Planet Sci Lett* 79:373–384
6. Gainanov AG (1980) Gravimetricheskie issledovaniya zemnoi kory okeanov [Gravimetric studies of the Earth's crust of the oceans]. Moscow State University, Moscow, 240 p. (In Russ.)
7. Glebovskii VY, Kaminskii VD, Osipov VA (1986) Struktura anomal'nogo magnitnogo polya ot sredinnogo khrebtta do Angol'skogo shel'fa [Structure of an anomalous magnetic field from the middle ridge to the Angolan shelf]. *Litosfera Angol'skoi kotloviny i vostochnogo sklona Yuzhno-Atlanticheskogo khrebtta* [The lithosphere of the Angolan basin and the eastern slope of the South Atlantic Ridge]. Leningrad, pp 70–80. (In Russ.)
8. Gmurman VE (2005) *Teoriya veroyatnostei i matematicheskaya statistika* [Theory of probability and mathematical statistics]. Vysshaya shkola Publication, Moscow, pp 327–349. (In Russ.)
9. Hasterok et al. <http://heatflow.org/data>
10. Hosford A (2001) Crustal accretion and evolution at slow and ultra-slow spreading mid-ocean ridges. Doctoral dissertation, Massachusetts Institute of Technology, 254 p. <http://hdl.handle.net/1721.1/58441>
11. Hyndman RD, Langseth MG, Von Herzen RP (1987) Deep Sea Drilling project geothermal measurements: a review. *Rev Geophys* 25(8):1563–1582
12. Jessop AM, Hobart MA, Sclater JG (1976) The world heat flow collection – 1975. Geothermal Series 5, Energy, Mines and Resources, Earth Physics Branch, Ottawa
13. Khutorskoy MD, Polyak BG (2017) Teplovoi potok v transformnykh razlomakh Severnoi Atlantiki i Yugo-Vostochnoi Patsifiky [Heat flow in the transform faults of the North Atlantic and South-Eastern Pacific]. *Geotektonika = Geotectonics* 2:55–66. (In Russ.)
14. Khutorskoy MD, Teveleva EA (2016) Teplovoi potok v abissal'nykh kotlovinakh Patsifiky i Atlantiki [Heat flow in the abyssal basins of Pacific and Atlantic]. *Monitoring. Nauka i tekhnologii = Monit Sci Technol* 4(29):20–27. (In Russ.)
15. Khutorskoy MD, Teveleva EA (2018) O geotermicheskoi asimmetrii yugo-zapadnogo Indiijskogo khrebtta [On the geothermal asymmetry of the southwestern Indian ridge]. *Monitoring. Nauka i tekhnologii = Monit Sci Technol* 1:6–16. (In Russ.)
16. Khutorskoy MD, Teveleva EA, Podgornykh LV (2017) Geotermicheskaya asimmetriya transformnykh razlomov ekvatorial'noi chasti Atlanticheskogo okeana [Geothermal asymmetry of transform faults in the equatorial part of the Atlantic Ocean]. *Doklady akademii nauk = Proc Acad Sci* 475(3):325–328. (In Russ.)
17. Kuo B-Y, Forsyth DW (1988) Gravity anomalies of the ridge transform system in the South Atlantic between 31 and 34,5°S. Upwelling centers and variation in crustal thickness. *Mar Geophys Res* 10:205–232
18. Mashchenkov SP, Pogrebetskii YE (1995) Simmetriya i asimmetriya SAKh po materialam kompleksnykh geofizicheskikh issledovaniy na atlanticheskikh geotraversakh [Symmetry and asymmetry of the MAR on the basis of data from complex geophysical studies on Atlantic geo-

- traverses]. *Geologiya i mineral'nye resursy Mirovogo okeana* [Geology and mineral resources of the World Ocean]. VNIIOkeanologiya Publication, St. Petersburg, pp 64–79. (In Russ.)
19. Mashchenkov SP, Pogrebitsky YE, Astafurova EG et al (1998) Glubinnoe stroenie i evolyutsiya litosfery Tsentral'noi Atlantiki (rezul'taty issledovaniya na Kanaro-Bagamskom geotraverse) [Deep structure and evolution of the lithosphere of the Central Atlantic (research results on the Canary-Bahamian geotraverse)]. VNIIOkeanologiya Publications, St. Petersburg, 290 p. (In Russ.)
 20. McKenzie DP, Sclater JG (1969) Heat flow in the eastern Pacific and sea-floor spreading. *Bull Volcanol* 33:101–118
 21. Menard HW (1966) Fracture zones and offsets of the East-Pacific rise. *J Geophys Res* 71(2):682–685
 22. Naryshkin GD, Pogrebitsky YE (1986) Morfostruktura dna Yugo-Vostochnoi Atlantiki [Morphostructure of the bottom of the South-East Atlantic]. *Litosfera Angol'skoi kotloviny i vostochnogo sklona Yuzhno-Atlanticheskogo khrebtva* [The lithosphere of the Angolan basin and the eastern slope of the South Atlantic Ridge], Leningrad, pp 10–23. (In Russ.)
 23. Parsons B, Sclater IC (1977) An analysis of the variation of ocean floor bathymetry and heat flow with age. *J Geophys Res* 82(5):883–890
 24. Patriat P, Sauter D, Munsch M, Parson L (1997) A survey of the Southwest Indian Ridge axis between Atlantis II Fracture zone and the Indian Ocean Triple Junction: regional setting and large-scale segmentation. *Mar Geophys Res* 19:457–480
 25. Pogrebitsky YE, Goryachev YV, Osipov VA, Trukhalev AI (1990) Stroenie okeanicheskoi litosfery po rezul'tatam issledovaniya na Angolo-Brazil'skom geotraverse [The structure of the oceanic lithosphere from the results of studies on the Angola-Brazil geotraverse]. *Sov. geologiya = Soviet Geol* 3:8–22. (In Russ.)
 26. Podgornykh LV, Khutorskoy MD (1997) Planetarnyi teplovoi potok [Planetary heat flow]. A map of scale 1: 30 000 000 and an explanatory note to it. Orgservis LTD, Moscow/St. Petersburg, 65 p. (In Russ.)
 27. Podgornykh LV, Khutorskoy MD (1998) Asimetriya raspredeleniya teplovogo potoka vdol' Angolo-Brazil'skogo geotraversa (Yuzhnaya Atlantika) [Asymmetry of heat flow distribution along the Angola-Brazil geotraverse (South Atlantic)]. *Doklady RAN = Proc Russ Acad Sc* 355(4):212–215. (In Russ.)
 28. Podgornykh LV, Khutorskoy MD (1999) Geotermicheskaya asimetriya sredinnykh khrebtov Mirovogo okeana [Geothermal asymmetry of the medial ridges of the World Ocean]. *Geotektonika = Geotectonics* 3:21–42. (In Russ.)
 29. Pollack HN, Hurter SJ, Johnston JR (1992) Global heat flow data set. World Data Center A for Solid Earth Geophysics. NOAA E/GCI, Boulder
 30. Popova AK, Smirnov YB, Khutorskoy MD (1984) Geotermicheskoe pole transformnykh razlomov. Glubinnye razlomy okeanskogo dna [Geothermal field of transform faults. Deep faults in the ocean floor]. Nauka Publications, Moscow, pp 78–87. (In Russ.)
 31. Pushcharovsky YM, Peive AA, Raznitsin YN, Bazilevskaya ES (1995) Razlomnye zony Tsentral'noi Atlantiki [Fault zones of the Central Atlantic]. *Tr. GIN RAN* [Proceedings of the Geological Institute of the Russian Academy of Sciences], 495. GEOS Publications, Moscow, 163 p. (In Russ.)
 32. Shreider AA (2001) Geomagnetnye issledovaniya Indiiskogo okeana [Geomagnetic studies of the Indian Ocean]. Nauka Publications, Moscow, 320 p. (In Russ.)
 33. Sorokhtin OG (1974) Global'naya evolyutsiya Zemli [Global evolution of the Earth]. Nauka Publications, Moscow, 184 p. (In Russ.)
 34. Von Herzen RP, Uyeda S (1963) Heat flow through the eastern Pacific ocean floor. *J Geophys Res.* 68(14):4219–4250

The Correlation Between Earth Heat Flow and Oil and Gas Potential – Fundamental Pattern of Western Siberia



Margarita F. Galieva, Daniil S. Krutenko, and Galina A. Lobova

1 Introduction

Present work is related to the enhancement of possibilities of Geothermy as a geophysical method for solving forecast and prospecting problems of Petroleum Geology [9].

Key role belongs to fundamental geodynamic parameter – the deep heat flow density [10]. This is the main parameter, determining the thermal history of potentially oil source sediments, the realization degree of generation potential of organic matter, the syngensis of foci of hydrocarbon generation and accumulating reservoirs [4]. To the point, the following is a quotation from monograph [13]: “Thus, according to the new obtained data about deep heat flow, a widespread viewpoint concerning the omnipresent confinedness of oil and gas deposits to *geotemperature anomalies* zones is not confirmed. Nevertheless, it is found out that the majority of hydrocarbon accumulations are located in zones of substantial lateral inhomogeneity of *the deep heat flow*” (*italics* by article authors).

Objects for present research are territories of localization of hydrocarbon fields in the northern part of Yamalo-Nenets Autonomous Okrug, where oil and gas potential is associated, predominantly, with the Lower Cretaceous deposits of the Akhskaya suite, and in Tomsk Region, which geological section contents deposits in the Upper Jurassic as well as in the contact zone of the Paleozoic and the Mesozoic and in the Inner Paleozoic.

Research purpose is to investigate consistent patterns of the deep heat flow changes, to evaluate the correlation between the heat flow peculiarities and localization of hydrocarbon fields and to define possible prospecting geothermal criteria of

M. F. Galieva (✉) · D. S. Krutenko · G. A. Lobova
National Research Tomsk Polytechnic University (TPU), Tomsk, Russia

© The Author(s), under exclusive license to Springer Nature
Switzerland AG 2021

V. Svalova (ed.), *Heat-Mass Transfer and Geodynamics of the Lithosphere*,
Innovation and Discovery in Russian Science and Engineering,
https://doi.org/10.1007/978-3-030-63571-8_11

oil and gas potential through the example of the territories, which were mentioned earlier.

Investigation and evaluation have been carried out, foremost, based on *calculated* values of the deep heat flow density from the base of a sedimentary section, besides the *experimental* determinations of the deep heat flow have been also analysed.

2 The Methodology of Deep Heat Flow Calculation

The deep heat flow is determined by solving inverse problem of Geothermy with the aid of software package tools for 1D basin modelling [6].

Solution is performed within the parametric description of the sedimentation history and the history of thermophysical properties of the sedimentary layer only, beginning from the Jurassic, without invoking information about the nature of heat flow and geodynamics below the base of the sedimentary section. For the conditions of Western Siberia, characterized, starting from the Jurassic time, by the quasistationarity of the deep heat flow [1, 14], the solution of the inverse Geothermy problem – determining the density of heat flow – is carried out uniquely.

To solve the inverse problem of Geothermy, we use as “observed” both measurements of reservoir temperatures obtained during well tests and temperature logs of steady-state boreholes (Method of definite geotemperature gradient, DGG) and also geotemperatures recalculated from the values of vitrinite reflectance (VR). The geotemperatures from VR are included immediately in a rigorous mathematical form. No separate “calibrations” for VR temperatures are required.

The first boundary condition of the model is determined by the temperature of the surface of sedimentation in the Mesozoic-Cenozoic, i.e. paleoclimate factor, and is given as a piecewise linear function of the “local” secular temperature pattern on the Earth’s surface. The “local” secular temperature patterns of the Arctic zone and the south-eastern part of Western Siberia were built on the basis of synthesis of experimental definitions and paleoclimatic reconstructions [7, 8].

Parametrization of sedimentary section, exposed by a well, which defines parameters of sedimentation and thermophysical model, accepts in compliance with the lithologic and stratigraphic dedicated breakdown.

Petrophysical dependences of thermal conductivity of sediments on their lithology and density are used for setting the thermal conductivity of rocks [5]. The coefficients of thermal diffusivity and thermal extraction density of radioactive sources were determined according to the lithology of stratigraphic sequence as well. The formation, existence and degradation of the permafrost and ice mass in the Neopleistocene and Holocene are taken into account as a kind of dynamic lithologic and stratigraphic complexes with anomalous values of thermal conductivity, thermal diffusivity and density.

The upper boarder of sedimentation mass – depositional surface, daylight surface. Therefore, paleotemperature reconstructions immediately are conjugated with

paleostructural reconstructions. The sedimentation rate in the model may be set to zero and negative values, that allows to take into account non-depositional hiatus and denudation.

The main criterion for the accuracy of the results of modeling is the *optimal* consistency (“discrepancy”) of the maximum calculated geotemperatures with the “observed” temperatures of the “maximum paleothermometer” – temperatures determined by VR. *The optimality* of the “discrepancy” of calculated geotemperatures with “observed” reservoir temperatures is equally important. The optimal “discrepancy” is the mean square difference between the calculated and “observed” values, which is equal to the error of observations [16]. In our case, the error of observations is of the order of ± 2 °C [6].

The important criterion for the accuracy of the results of modelling is the consistency between the calculated values of the heat flow density and the data of its experimental determination in the study area.

3 The Heat Flow of Yamal

The Mesozoic-Cenozoic sedimentary cover in the study area began to form in the Lower Jurassic. In this time *Kiterbyutskaya argillaceous suite* J_{1t} , which had an oil-source potential, was accumulating. Till the end of the Volgian Age the marine transgression has expanded, *Bazhenov formation* ($J_{3tt}+K_1b$), which is the most enriched in organic matter, was accumulating. According to the average VR value – $R_{vi}^0=0,96\%$ – the Bazhenov formation is in the end of the main oil generation zone within the limits of the Arctic area.

Marine regime has prevailed since the Aptian-Cenomanian until the beginning of the Eocene. Thickness analysis of Paleogene-Neogene testified that sedimentation had gone to the middle of the Miocene for 32 million years (Nyurolskaya, Tavdinskaya, Atlymskaya, Novomikhaylovskaya, Turtasskaya, Abrosimovskaya formations) and amounted to 335–535 m, then these sediments have been degraded in the Early Bicheul time.

In the Middle Miocene-Early Pliocene, since the end of the Bicheul time and till the end of the Novoportov accumulation had gone of the order of 100 m thick sediments, which in the subsequent stage of positive tectonic movements over 1.3 million years were denudated. With the onset of the Late Miocene, Pliocene-Quaternary lacustrine-alluvial sediments accumulated.

The Middle Jurassic oil and gas complex (OGC) includes reservoirs in Vimskaya suite ($J_2b_1^1$) with YuYa₇₋₉ formations and Malyshevskaya suite ($J_2b_2^2-bt_{1-2}$) with YuYa₂₋₄ formations in lower subsuite. *The Upper Jurassic OGC* combines Nurminskaya suite ($J_2bt^3-k+J_3ok-tt_1$), while *the Cretaceous* – Akhskaya, Tanopchinskaya and Yarongskaya the Lower Cretaceous suites. Achimovskaya sequence is identified in the bottom of the Cretaceous with a group of Ach formations.

Stratigraphic breakdowns, well testing results and VR data of deep wells (Database of the Trofimuk Institute of Petroleum Geology and Geophysics of Siberian Branch of Russian Academy of Sciences, 2018) are invoked for purpose of building sedimentation and thermophysical 1D-models. The breakdowns are accepted considering the dynamic of tectonic events during the formation of sedimentary section in the territory of Yamal. Account the permafrost performed beginning from 0.52 million years ago, while ice mass – beginning from 0.182 million years ago. [7]. The glacier has completely degraded by the time of 15 thousand years ago (the end of the Sartan time).

The scheme of heat flow density of Yamal (Fig. 1a) was built using *calculated* values of heat flow density from the base of the sedimentary section in 8 wells and data of *experimental* determinations of deep heat flow density in 12 wells [11].

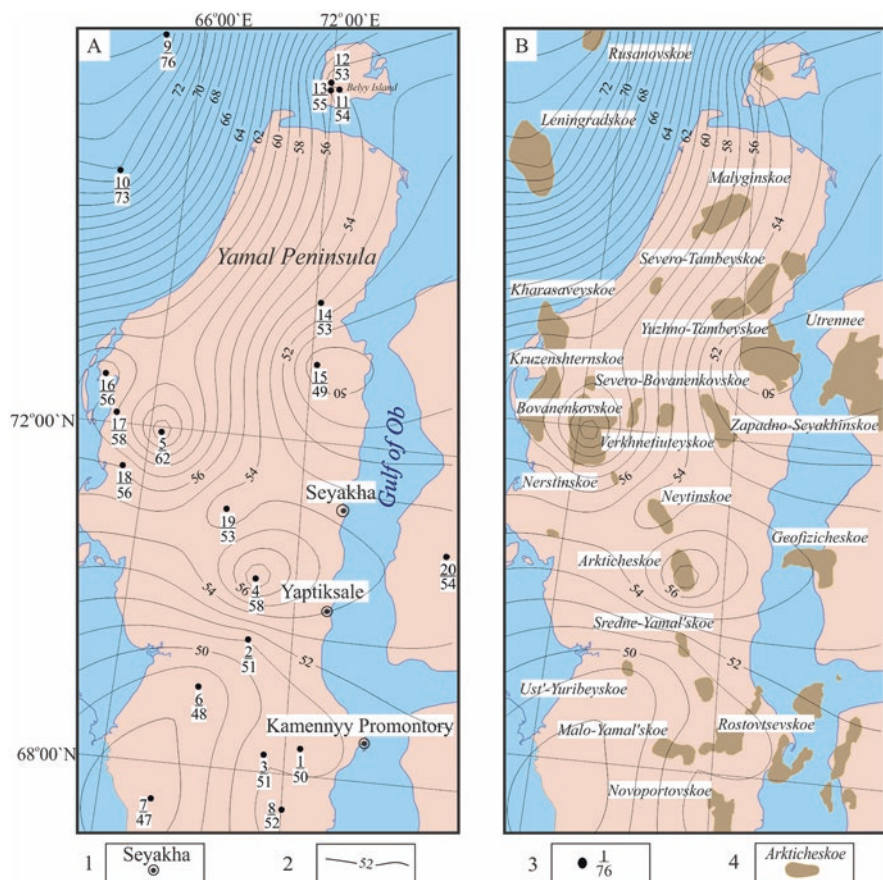


Fig. 1 The Yamal Peninsula. The heat flow (a) and its correlation with hydrocarbon deposits (b): 1 – residential place and its name; 2 – isolines of deep heat flow values; 3 – well, the numerator is an identification number, the denominator – heat flow density value, mW/m²; 4 – field outline and the name

It is interesting to match calculated values of the heat flow, obtained with the authors' methodology [6], with calculated values of heat flow, obtained earlier via use of the physical-mathematical model of A.R. Kurchikov [13]. Thus, cataloged values of the heat flow density [13] in wells of Kharasaveyskoe, Kruzenshternskoe and Bovanenkovskoe fields are in the range of 56–62 mW/m², whereas the scheme (Fig. 1) gives the range of 57–62 mW/m². And then cataloged values of the heat flow density [13] in wells of Arkticheskoe and Sredne-Yamal'skoe fields are in the range of 54–56 mW/m², whereas the scheme (Fig. 1) gives the range of 51–57 mW/m².

It is possible to see the following peculiarities in the scheme (Fig. 1b): “positive anomaly” (for example, Bovanenkovskoe area); “negative anomaly” (Yuzhno-Tambeyskoe area); “bay-shaped configuration of isolines” (Rostovtsevskoe area); “non anomalous field” (Sredne-Yamal'skoe area).

Analysis of correlation between the heat flow and localization of 13 well-known fields shows the following. 6 fields are in the zones of *positive anomalies* of heat flow (46% of the total number), the biggest among them – Bovanenkovskoe and Arkticheskoe. 1 field is in the zone of *negative anomaly* of the heat flow (8%) – Yuzhno-Tambeyskoe. 4 fields are in the zones of *bay-shaped configuration of isolines* (31%): Kruzenshternskoe, Neytinskoe, Rostovtsevskoe and Novoportovskoe.

Consequently, *in the order of 80–85% of known hydrocarbon fields of Yamal are associated with anomalous features of the deep heat flow.*

4 The Heat Flow of Ostaninskoe Group of Fields (Tomsk Region)

The study area is located in Parabel District of Tomsk Region between rivers the Chuzik and the Chizhapka (Fig. 2). As to sediments of the platform cover the research territory is in the articulation zone of two tectonic structures of the first order: Nyurol'skaya megadepression and the south part of Srednevasyuganskiy megaswell. The Jurassic sedimentary rocks rest with non-depositional hiatus and angular unconformity on erosional suppression of the Paleozoic carbonate rocks of the Devonian-Lower Carboniferous.

Oil and gas fields, mainly, are associated with the Upper Jurassic sandy reservoirs of horizon Yu1. Hydrocarbon deposits are concentrated in anticline, fault-bounded traps of the Upper and Middle Jurassic and *in the oil-and-gas horizon of weathering crust (M formation) and in the Inner Paleozoic (M₁ formation)* (Table 1). The deposits of the uppermost part of basement rocks are relating to metasomatically altered bioaccumulated limestones, which represent as reservoir rocks of porous-fissured type.

Commonly spread in the study territory the Upper Jurassic *Bazhenov Formation* is an oil source rock *for the Middle and Upper Jurassic OGC* [2]. Potentially oil-source the Lower Jurassic *Togurskaya suite* is accepted as a traditional hydrocarbon source *for the pre-Jurassic OGC* [12]. However, this formation has quite limited

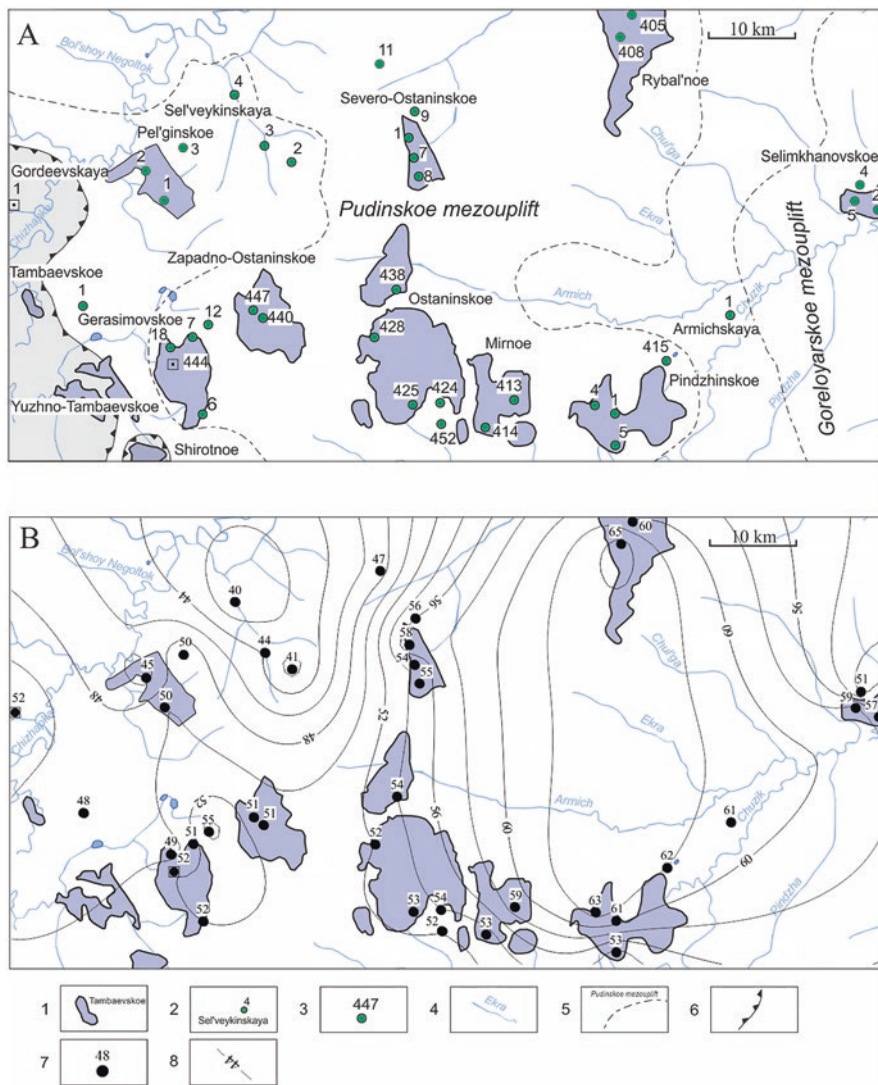


Table 1 Oil and gas potential of Ostaninskoe group of fields (according to the database of Tomsk branch of the “Territorial fund of geological information, Siberian federal district”, 2018)

Field	Oil and gas complex	Inflows (formation)		Fluid type
		Commercial	Noncommercial	
Mirnoe	The Upper Jurassic	Yu ₁ ¹⁻²	–	OGC
Rybal'noe	The Upper Jurassic	–	Yu ₀	O
		Yu ₁ ¹ , Yu ₁ ³ , Yu ₁ ⁴	–	O
	The Paleozoic	–	M	O
Pindzhinskoe	The Upper Jurassic	Yu ₁ ¹ , Yu ₁ ²	–	O
	The Middle Jurassic	–	Yu ₈	G
	The pre-Jurassic	–	M	OGC
Ostaninskoe	The Upper Jurassic	Yu ₁ ¹ , Yu ₁ ² , Yu ₁ ³ , Yu ₁ ⁴	–	GC
	The Middle Jurassic	Yu ₃ , Yu ₄	–	GC
	The pre-Jurassic	M, M ₁	–	OGC
Severo-Ostaninskoe	The pre-Jurassic	M	–	OGC
Gerasimovskoe	The Upper Jurassic	Yu ₁ ¹⁻² , Yu ₁ ³ , Yu ₁ ⁴	–	GC
	The Middle Jurassic	Yu ₂	–	GC
		–	Yu ₇	O
		–	Yu ₈	O
		–	Yu ₉	O
		Yu ₁₀	–	OGC
		Yu ₁₁	–	GO
	Yu ₁₂	–	GO	
	The Lower Jurassic	Yu ₁₄	–	GO
		Yu ₁₅	–	GO
The pre-Jurassic	M, M ₁	–	GO	
Selimkhanovskoe	The Upper Jurassic	Yu ₁ ¹⁻²	–	OGC
		Yu ₁ ³⁻⁴	–	GO
	The Middle Jurassic	–	Yu ₂	O
	The pre-Jurassic	M	–	OGC
Pel'ginskoe	The Upper Jurassic	Yu ₁ ¹	–	GO
Tambaevskoe	The Middle Jurassic	–	Yu ₆ , Yu ₇	GO
	The pre-Jurassic	M	–	GO
Yuzhno-Tambaevskoe	The Lower Jurassic	–	Yu ₁₄	O
	The pre-Jurassic	M, M ₁	–	GO
Shirotnoe	The Middle Jurassic	Yu ₁₃	–	OGC
		–	Yu ₁₀	O
	The Lower Jurassic	–	Yu ₁₅	GO
		–	Yu ₁₆	O
The pre-Jurassic	–	M	OGC	

Fluid type: G – gas, O – oil, GC – gas condensate, OGC – oil and gas condensate, GO – gas and oil.

spread – the south-western edge of the study area (Fig. 2a). In this connection it is impossible to except the version, which suggests accounting *the Devonian strata* as a hydrocarbon generating source for the pre-Jurassic reservoirs [15]. The hypothesis of “*Bazhenov source of origin*” of the pre-Jurassic hydrocarbon deposits is more disputable and it has only indirect arguments [3].

The calculations of the heat flow density performed for geological sections of 35 exploratory and 2 parametric wells on the study area (Fig. 2). Data of deep well testing (reservoir temperatures) and temperature logs DGG were investigated and summed up from primary “well historical data”, reserve calculation reports, operational analysis reports and generalization of geological and geophysical database of Tomsk Region (the database of Tomsk branch of the “Territorial fund of geological information, Siberian federal district”, 2018). VR values determined in the Laboratory of Oil and Gas Geochemistry of the Institute of Petroleum Geology and Geophysics of Siberian Branch of Russian Academy of Sciences (Novosibirsk).

The comparison of modelling temperatures with reservoir temperatures and with temperatures determined by DGG and by VR is performed. The calculated model of heat distribution in the sedimentary section coincides with “observed” values in the optimal way at a level of ± 2 °C.

The reliability of the results of paleotemperature modelling is confirmed consistency of the obtained *calculated* values of the heat flow density with *experimental* determinations of A.D. Duchkov [17]. Experimental data is limited with isoline of 60 mW/m², calculated values are in the range of 41–65 mW/m².

The following anomalous peculiarities are observed in the map of the deep heat flow distribution (Fig. 2b): “positive anomaly”, “gradient zone”, “negative anomaly”, “bay-shaped configuration of isolines”.

Hydrocarbon fields in the eastern part of the territory are associated with the remarkable *gradient zone*, which surrounds a large *positive anomaly*. There 6 fields are located: Rybal'noe, Selimkhanovskoe, Pindzhinskoe, Mirnoe, Ostaninskoe, Severo-Ostaninskoe, that accounts 50% of the total number of the fields in the study area. 3 fields (25%) are *in the zone of bay-shaped configuration of isolines* – Pel'ginskoe, Gerasimovskoe, Zapadno-Ostaninskoe. Remarkably, hydrocarbon fields are absent in the zone of *negative anomaly* of the heat flow in the north-western part of the territory.

Therefore, 9 fields (75%), which are located in the study area, are associated with the anomalous features of the deep heat flow distribution. 3 fields – Shirotnoe, Yuzhno-Tambaevskoe, Tambaevskoe, do not correlate with the anomalous peculiarities of the heat flow.

Independently important to note, that Selimkhanovskoe, Ostaninskoe, Severo-Ostaninskoe and also Gerasimovskoe fields, within which deposits are exposed with commercial hydrocarbon inflows, are associated with the substantial lateral inhomogeneity of the heat flow density (*gradient zones*) (Table 1). Pindzhinskoe, Mirnoe and Rybal'noe fields are also included in the remarkable *gradient zone*, within them it is possible to *forecast* deposits with commercial hydrocarbon inflows.

Yuzhno-Tambaevskoe and Tambaevskoe fields, within which deposits are exposed with commercial hydrocarbon inflows, are separated from anomalous

peculiarities of the heat flow. Interesting to point, that particularly these fields are located within the borders of spread of potentially oil-source the Lower Jurassic Togurskaya suite.

5 Conclusion

The scheme and the map of the deep heat flow were built for the territory of localization of the Arctic hydrocarbon fields of Yamal and the fields of Tomsk Region, where the Paleozoic oil deposits were exposed in geological section. It was stated that 75–80% of hydrocarbon fields, which were located in the study areas, correlated with the anomalous peculiarities of the deep heat flow distribution.

The reliability of calculated values of Yamal heat flow was reasoned with performing of the classical geophysical criterion – criterion of “discrepancy”, consistency with earlier revealed tendency of the heat flow density increase towards the north-western direction, comparability with the catalogue of calculated values of the heat flow, which was presented in earlier published monographic work [13]. The reliability of calculated values of the heat flow of Ostaninskoe group of fields of Tomsk Region was substantiated with performing the criterion of “discrepancy”, consistency with the map of the heat flow determinations of Western Siberian Plate.

The confinedness of fields with commercial hydrocarbon inflows from the deposits of pre-Jurassic OGC to the strongly marked *gradient zone* of the heat flow density values was placed emphasis through the example of Ostaninskoe group of fields. This allows to forecast getting commercial inflows from the pre-Jurassic OGC in Pindzhinskoe, Mirnoe and Rybal'noe fields.

Afore-named characterize lateral inhomogeneity of the heat flow (*gradient zones*), probably, not as forecast criterion of oil and gas potential, but rather as an existence of the fundamental correlation between the intensity of naftidogenesis and lateral inhomogeneity of the deep heat flow of Western Siberia.

Acknowledgments *The authors thank Professor V.I. Starostenko and Professor M.D. Khutorskoy for the constant attention to our research.*

References

1. Duchkov AD, Galushkin YI, Smirnov LV, Sokolova LS (1990) The evolution of the sedimentary cover temperature field of the West Siberian Plate. *Russ Geol Geophys* 10:51–60
2. Fomin AN (2011) Catagenesis of organic matter and petroleum potential of the Mesozoic and Paleozoic sediments of the West Siberian megabasin. IPGG SB RAS, Novosibirsk
3. Galieva MF, Krutenko DS (2019) Geological and geophysical evidences favouring the hypothesis “Bazhenov source of origin” of pre-Jurassic oil deposits of Ostanino group of fields (Tomsk region). Proceedings of the 2-nd All-Russ. Sci. Conf. of young researchers and students, dedicated to the 85th anniversary of ac. A.E. Kontorovich: Contemporary Problems

- of oil and gas Geology of Siberia. Trofimuk Institute of Petroleum Geology and Geophysics of Siberian Branch of Russian Academy of Sciences (IPGG SB RAS); Novosibirsk State University. Novosibirsk, Russia. pp 22–25
4. Isaev VI (2004) Paleotemperature modeling of the sedimentary section, and oil-and-gas generation. *Russ J Pac Geol* 23(5):101–115
 5. Isaev VI, Gulenok RY, Veselov OV, Bychkov AV, Soloveychik YG (2002) Computer technology of integrated assessment of oil and gas potential of sedimentary basins. *Oil Gas Geol* 6:48–54
 6. Isaev VI, Iskorkina AA, Lobova GA, Starostenko VI, Tikhotskii SA, Fomin AN (2018) Mesozoic–Cenozoic Climate and Neotectonic Events as Factors in Reconstructing the Thermal History of the Source-Rock Bazhenov Formation, Arctic Region, West Siberia, by the Example of the Yamal Peninsula. *Izvestiya Phys Solid Earth* 54(2):310–329
 7. Isaev VI, Iskorkina AA, Kosygin VY, Lobova GA, Osipova EN, Fomin AN (2017) Integrated assessment of paleoclimate factors of reconstructing thermal history of petromaternal Bazhenov suite in arctic regions of Western Siberia. *Bull Tomsk Polytech Univ Geo Assets Eng* 328(1):13–28
 8. Isaev VI, Iskorkina AA, Lobova GA, Fomin AN (2016) Paleoclimate’s factors of reconstruction of thermal history of petroleum bazhenov and togur suites southeastern Western Siberia. *Geofizicheskii zhurnal* 38(4):3–25
 9. Isaev VI, Iskorkina AA, Lobova GA, Luneva TE, Osipova EN, Ayupov RSh, Igenbaeva NO, Fomin AN (2018) Mesozoic-Cenozoic climate and the geothermal regime of the oil source Kiterbyutskaya suite of the Arctic region of Western Siberia. *Georesources* 20(4) Part 2: 386–395
 10. Khutorskoy MD (1996) Introduction to Geothermy: lecture course. RUDN Publishing House, Moscow
 11. Khutorskoy MD, Akhmedzyanov VR, Ermakov AV et al (2013) Geothermy of Arctic seas. GEOS, Moscow
 12. Kostyreva EA (2005) Geochemistry and genesis of Paleozoic oil of south-eastern Western Siberia. Novosibirsk, SB RAS Publishing House, “Geo” Branch
 13. Kurchikov AR (1992) Hydrogeothermal criteria of oil-and-gas potential. Nedra, Moscow
 14. Kurchikov AR (2001) Geothermal regime of hydrocarbon accumulations in Western Siberia. *Russ Geol Geophys* 42(11–12):1846–1853
 15. Lobova GA, Isaev VI, Kuz'menkov SG, Luneva TE, Osipova EN (2018) Oil and gas reservoirs of weathering crusts and Paleozoic basement in the southeast of Western Siberia (forecasting of hard-to-recover reserves). *Geofizicheskii zhurnal* 40(4):73–106. (In Russ.)
 16. Strakhov VN, Golizdra GYa, Starostenko VI (2000) Theory and practice of interpreting potential fields: Evolution in the 20th century. *Izvestiya Phys Solid Earth* 36(9):742–762
 17. Western Siberia (2000) Geology and mineral resources of Russia. In 6 volumes, vol 2, St. Petersburg, VSEGEI Publishing House

Part III
Fluid Transfer

Influence of Hydrodynamic Conditions on the Mass Transfer of Pollutants in the Areas of Liquidated Mines



Gleb Batrak

1 Introduction

Currently, mining is increasingly based on deposits with complex and very complex hydrogeological conditions [1]. The regimes of the levels and flow rate of mine water are the most important characteristics, since it directly depends on maintaining a safe depth of the water level to prevent developing of exogenous processes in the developed area, as well as the cost of maintaining this depth [2, 3].

The hydrodynamic regime is a key indicator in the flooding of single mines and systems of hydraulically coupled mines. The rate of water level rise in the mine, the period of the mine flooding, the position of the water level after the flooding and the possibility of reaching it on the surface, the flow rate of water that will be poured onto the surface or selected by the water reduction system in order to maintain a safe level of mine water, as well as the chemical composition of groundwater and its variability over time are the parameters under forecast. The hydrodynamic regime is a reflection of the existing balance of mine water, therefore it is necessary in the preparation and verification of any forecast models.

The forecasts of mine flooding are very different from most hydrogeological forecasts, including those compiled for open pit mining. This specificity is that in addition to rocks, these natural-technical systems contain large capacities of empty space at the time of development. Water in this space flows much faster than in rocks. Its flow no longer obeys the laws of continuum mechanics, but obeys the laws of hydraulics. In fact, the mines are an underground tank of complex shape with permeable walls. In cases where there are several hydraulically connected shafts, water can flow between them, both relatively slowly and catastrophically quickly.

G. Batrak (✉)
IEG RAS, Moscow, Russia

© The Author(s), under exclusive license to Springer Nature
Switzerland AG 2021

V. Svalova (ed.), *Heat-Mass Transfer and Geodynamics of the Lithosphere*,
Innovation and Discovery in Russian Science and Engineering,
https://doi.org/10.1007/978-3-030-63571-8_12

191

Currently, there are several forecasting techniques. Some of them are based on linearized, i.e. simplified dependences of the rate of rise of the water level and the decrease in water inflow from depth. Part of it is based on balance equations, in which the calculation of the volumes of worked out space plays the most important role. In simple cases, regression curves give good convergence. The most promising, nevertheless, is the method of three-dimensional numerical simulation of water filtration. However, all these methods encounter objective difficulties in combining the requirements for the accuracy and reliability of forecasts with the quality of the source data that can form the basis of these forecasts. In addition, the latter method in the case of flooded mines has the complexity that takes a lot of effort and time to collect and prepare the initial information, which is often not enough. This is because the hydrogeological forecast in many cases is made after the closure of the mines.

2 Factors and Conditions for the Formation of the Regime

The initial materials for studying the patterns of groundwater regime formation in liquidated mines were the mines of Primorye, Pechora, the Moscow Region basin, the East Donbass and the Slantsevsky District of the Leningrad Region.

Based on the study of these regions, the main factors and conditions for the formation of the groundwater regime of the liquidated mines were summarized (Table 1). Moreover, under the conditions here we mean the natural and technogenic environment that remains virtually unchanged during the flooding of the mines, and factors are processes that, changing themselves, also change the regime of groundwater.

3 Patterns of the Hydrodynamic Regime Formation at Flooded Mines

Stopping forced drainage from the mine leads to a sharp decrease in the depth of the depression funnel, which, in the absence of a safe maintained level of mine water, reaches fully compensated levels, which in some cases is accompanied by the release of water to the earth's surface. The so-called compensatory hydrodynamic regime is impaired; both natural and artificial components of vibrations are present in it. The classic laws of this regime are:

1. Reducing the influence of intra-annual dynamics due to the infiltration nutrition of groundwater with depth. So, at a depth of several hundred meters, oscillations due to the vertical component of the power are practically not traced. At depths of 100 or less meters, such fluctuations can be recorded very clearly.

Table 1 The main conditions and factors of the formation of the groundwater regime of the liquidated mines

Conditions		Factors	
Natural	Technogenic	Natural	Technogenic
Open fracturing (karst)	Volume of worked out space	Precipitation regime	Water withdrawal regime (how much pumping equipment is turned on and with what frequency)
Complications by tectonic disturbances	Three-dimensional configuration of the worked-out space	Inflow from borders	Transition from underground to submersible drainage
The presence of compression and extension zones	The condition of pillars	Crushing of pillars by rock pressure	Functioning of hydraulically connected mines where mining continues
The permeability of the material filling tectonic disturbances	The presence of failures between the mines, their throughput section, depth of location and condition	Collapse of the roof of the worked out space	Changes in technology
Introduction of "lateral rocks"	Supported drainage rate	Variability of the coefficient of residual voidness as the flooding	Transfer of underground drainage from one horizon to another
	The number and power of the worked-out seams	reverse colmatation of crushed mine workings with increasing pressure gradients	

2. With regard to long-term dynamics, its manifestation depends to a large extent not only on depth to level, but also on the geological structure of the territory. So, with a shallow bedding of layers, the penetration of atmospheric rain and melt water is hampered by the need to overcome water of poorly permeable sediments during the alternation of geological layers. In this case, nutrition can stretch for years, and peaks due to high water content have much smoother amplitudes and a time delay in manifestation. With a steep bed of infiltrating waters, it becomes possible to quickly penetrate into groundwater, often within one season. This leads to peak rises in groundwater levels or to peak dewatering loads, which must be taken into account when creating water reduction projects. So, the neighboring mine areas, which had the same rainfall for one year, but different geological structure, demonstrate different dynamics of level recovery.
3. The greater depth of the mine water level, the faster rise the rate. This regularity is explained by large flow gradients at the initial stages of flooding and accordingly a more rapid influx of water from the borders.
4. When the rising level of groundwater reaches the next developed horizon, the rate of rise sharply slows down during the period of filling the mine workings.

After filling, the ascent rate returns to the previously noted pattern. The duration of the deceleration period is determined by the capacitive properties of the developed horizon.

5. If there is a hydraulically coupled system of interacting shafts, new ones are added to the above patterns. When the water level in the mine reaches the current hydraulic link with another mine having a lower water level, the lift stops until the water level of the second mine reaches the hydraulic link and then rises in both mines with a high degree of synchronism.

4 The Effect of Undermining the Territory on the Groundwater Regime of the Upper Horizons

With the technology of mining coal seams with lavas, the collapsed areas of the coal-bearing layer collapse, the thickness of which can vary from less than one meter to several meters. In the presence of several worked out horizons, the volume of developed space increases several times. As a result, especially with shallow bedding, overlying rocks are deformed, which leads to subsidence of the earth's surface and the formation of anthropogenic relief. In the coal basin of the Moscow Region, precipitation reaches a few meters, and, for example, in Primorye it reaches 15–20 m. Moreover, the areas on which the pillars were left retain surface marks that existed before the start of work. As a result, the relief may be a hill of technogenic genesis. Often secondary settling troughs of small sizes are formed on the settled territory, complicating the surface of the larger trough.

If the liquidation of the mines was carried out with the support being left, the subsequent subsidence occurs more smoothly. All this leads to varying degrees of deformation of aquifers and water-resistant layers over the developed space. The geological section changes significantly. Even with plastic deformations, an overflow of aquifers often occurs, a violation of the integrity of the aquifers, leading to an intensification of water exchange between the horizons.

From the point of view of the groundwater regime, this leads to an equalization of groundwater levels in different horizons and to an increase in the synchronism of their changes under the influence of natural and technogenic factors. A decrease in the hypsometric marks of the earth's surface leads to a decrease in depths to the level of groundwater in the upper horizons. When changing the geometry of the underground space, the direction of the flow of groundwater sometimes changes, although, as a rule, locally.

An additional anthropogenic load in the reclaimed territories may further change the conditions for the formation of groundwater. Ponds and dams, a covered erosion network, roads blocking the water, sedimentation tanks and tailing dumps – all this makes changes to the balance of groundwater and affects their regime.

This can lead to undesirable consequences for settlements located in the impact zone. So, in the Tula region in the village of Dedilovo there are two mines closed in

the mid-90s: Dedilovskaya and Komsomolskaya. Both mines are located on high watershed areas. After the mines were decommissioned, levels restored, however, including due to subsidence of the surface, the groundwater balance changed, which caused flooding of houses located in the lowland at the confluence of the Olen and Shivorona rivers. If during operation the pumped-out water with a volume of 1134 cubic meters per day merged into the tributaries of the Olen River, and the rivers were full-flowing, and the groundwater levels were lower due to overflow to lower lying horizons during drainage of mines even in the riverine areas, then after the liquidation of the mines the rivers became shallow and groundwater levels have risen. At the same time, the subsidence of the earth’s surface by an average of two meters exacerbated the situation with flooding.

Based on the available data, the main polluting components in mine waters over the Russia’s territory are iron and manganese everywhere, and in many regions mine water contains a high concentration of other heavy metals – lithium, nickel, beryllium and aluminum. In several regions an increased content of phenols (Kuzbass, Primorsky Krai, Sakhalin Oblast), as well as sulfates, chlorides, nitrates and nitrites was observed. The mine waters of the Kizelovsky coal basin are the most polluted in the world (Fig. 1).

5 Errors in Forecasts of the Hydrodynamic Regime of Mine Water

As for the natural regime, the main methods for predicting the regime of groundwater of flooded mines are balance, hydrodynamic, and genetic-statistical. Today the main place is occupied by the balance method. The large volume of worked out space, known with high accuracy and spatial reference, makes it possible to sufficiently qualitatively predict the rate of level rise and the volume of water in the massif. The main difficulty here is the uncertainty of knowledge about the state of hydraulic connections between the mines. In some cases, we may not know if connecting mine workings exist. If they are present on worked out horizons, they can be fully or partially closed under the influence of rock pressure. A difficult problem is

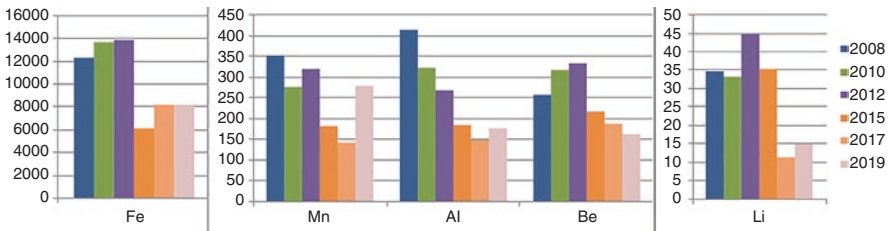


Fig. 1 Regime of main pollutants in mine water, Kizelovsky coal basin. Vertical axis – times exceeding the maximum permissible concentration

the presence of abnormal pillars of rocks that filter water through themselves. However, with high pressure gradients in neighboring mines, the whole can simply be squeezed out and a new hydraulic connection is formed.

In the hydrodynamic method, both analytical solutions and numerical ones can be used by constructing hydrodynamic models. The first approach gives rough approximations due to the inability to take into account the entire complex underground infrastructure. Numerical models allow you to specify the whole variety of natural and technogenic conditions, but rarely provide an opportunity to qualitatively reproduce the situation that developed before the development of the field, since development began a long time ago, sometimes in the 19th century, and reliable geological data of that time were not preserved.

Separately, it is necessary to distinguish various kinds of linearizations and asymptotics obtained by significantly simplifying the equations of hydrodynamics, for example, the quadratic dependence of the influx on the water decrease. In some cases – with a lack of time for forecasting or the scarcity of initial data – they are the main tool for an operational assessment of the situation.

The genetic-statistical method in this case mainly uses an apparatus of various kinds of regression dependencies, which also give a rather qualitative result, although it is more preferable in the absence of several hydraulically connected mines.

Accordingly, the number of mines in a hydraulically coupled group also refers to uncertainties. In the presence of two hydraulically connected mines, each of which is supposed to be equipped with a drainage system, the distribution of the flow between them is not precisely determined. The conductivity of tectonic disturbances is difficult to determine, especially with lithological variability of the section.

As you know, in the underworked mass during its mining, a zone of random collapse is formed, above the zone of increased fracturing, then the zone of deflection. This pattern is characteristic of a gentle fall of the layers. During a steep fall, especially at a low power of the worked-out formation, the worked-out space becomes closer to the vertical. Such a mine can collapse under the influence of rock pressure with virtually no formation of a fractured zone.

The rate of level rise is an indicator of the flow between the mines only over a relatively long period of time, usually the first months, since the capacitive properties in the vertical section change (due to residual voidness and natural anisotropy), and in the shaft where the water flow began, the speed level rise may even slow down, which has been repeatedly recorded.

Forecast uncertainties are also associated with the difficulty in estimating the hydraulic connection between aquifers in the vertical section, which was a consequence of the disturbance of the water-resistant strata under the influence of underground mining. If there are abnormal pillars between the mines, they may be crushed and water breakthrough into the adjacent mine. This requires a large hydrodynamic pressure, i.e. the water level in one of the mines should be significantly, as a rule, several hundred meters higher than in the other mine. Then, in the groundwater regime of a flooded mine, a temporary decrease in water level may form. Given the

possibility of having non-normative pillars at different levels, such events in the groundwater regime can occur repeatedly.

It is difficult to evaluate the variability of the filtration properties, which cannot be estimated by experimental filtration work, especially with deep bedding. As is known, fracturing of rocks damps with depth, however, the nature of damping and characteristic depths are rarely known. Under certain conditions, volumes of water hanging above underground workings in parts of the rock mass isolated in the filtration relation may be unknown. Often the data on water inflow into the mines during their operation, as well as the reliability of mining plans, especially for very old used formations, are often questionable. For these reasons, it is not always possible to even determine the direction of movement of groundwater during flooding of hydraulically interconnected mines.

Uncertainty is also associated with cross-border flows. A number of deposits are located in several countries and are independently developed. Information on the conditions for the development of drainage, depths, power of the separating pillars, speeds and levels of flooding of the liquidated mines is often not available. There are also abandoned mines in which vertical mine workings have not been preserved, through which you can make level measurements, take water samples or run markers.

6 Conclusion

1. Based on the study of the process of flooding of mines in several coal-mining regions of Russia, the basic conditions and factors for the formation of the groundwater regime of the liquidated mines are identified. The main natural conditions include: open fracturing (karst); complication of tectonic disturbances; the presence of zones of compression and tension; permeability of rocks filling tectonic disturbances; the presence of the introduction of "side rocks". The main technogenic conditions include: the amount of space worked out; three-dimensional configuration of the worked out space; the condition of the pillars; the presence of failures between the mines, as well as their throughput, depths of location and condition; the supported rate of drainage of underground and submersible drainage (if functioning); the number and power of the reservoir. The main natural factors in the formation of the regime include: precipitation regime; inflow from natural borders; collapse of the roof of the worked out space; crushing pillars by rock pressure; the variability of the coefficient of residual voidness as the mines flood; raskolmatatsiya crushed workings with increasing pressure gradients. The main technogenic factors, first of all, should include: the mode of water withdrawal (how much pumping equipment is turned on and with what frequency); transition from underground to submersible drainage; the functioning of hydraulically connected mines, where mining continues; change in mining technology.

2. A typology of uncertainties of the initial data on the state of the natural-technogenic system of the mine field has been developed, which critically affects the accuracy of hydrogeological forecasts of the regime of mine flooding. The basic uncertainties include: the number of mines in the hydraulically connected group; water conductivity of rocks after mining; conductivity of tectonic disturbances, especially with lithological variability of the section; insufficient information content of the observed rate of level rise in the presence of a system of hydraulically connected mines; the presence of cross-border flows between mines in different states; the presence of abandoned mines, the lack of information on the boundaries of mining allotments and the presence of hydraulic connections for mines with a very long history of operation; lack of information on the condition of pillars and hydraulic connections; inaccuracy of information on the volumes extracted from the operation of groundwater.
3. The concept of a compensatory groundwater regime, which is formed during the flooding of mines, was first introduced. The classical laws of this regime are: a decrease in the influence of intra-annual dynamics due to the infiltration supply of groundwater with depth; the dependence of long-term dynamics both on depth to groundwater level and on the geological structure of the territory; a decrease in the rate of level rise with a decrease in depth from the surface of the earth; local slowdown of the lifting speed when reaching the worked out horizon; temporary decrease in the level when pushing pillars or collapsed rocks and filling new voids with water; high synchronization of the rise of levels in hydraulically connected mines after water overcomes the level of hydraulic connection.

References

1. Mironenko VA (1976) *Gidrogeologicheskiye issledovaniya v gornom dele* [Hydrogeological research in mining.]. Pod obshch. red. dokt. geol.-mineral. nauk Nedra, 352 s
2. Batrak GI (2017) *Chislennyye gidrogeologicheskiye prognozy na osnove rezhimnykh ryadov nablyudeniya, obrabotannykh s ispol'zovaniyem apparata neyronnykh setey* [Numerical hydrogeological forecasts based on regime series of observations processed using the neural network apparatus]. *Monitoring. Nauka i tekhnologii.* – *Monitoring. Sci Technol* 4:30–377
3. Galitskaya IV, Batrak GI (2015) *Obosnovaniye printsipov monitoringa podzemnykh vod pri upravlenii riskom na territoriyakh ekologopasnykh predpriyatiy* [Justification of the principles of groundwater monitoring in risk management in the territories of environmentally hazardous enterprises]. *Monitoring. Nauka i tekhnologii.* – *Monitoring. Sci Technol* 4:21–27

Factor Modeling of Mass Transfer of Pollutants in the Areas of Hydrogeological Windows



Irina Galitskaya and Lubov Gomanuk

1 Introduction

Significant anthropogenic contamination of groundwater is one of the most pressing problems that our world faces today and scientists of many countries actively research the various aspects of this problem.

Currently the study of confined aquifer contamination is very relevant in the areas of hydrogeological windows location “where continuity of separating low-permeability deposits is disturbed and their permeability is relatively high” [1, 2]. It is here that contaminants can enter speedily from shallow into more deep aquifers.

Numerous publications have been devoted to the study of the hydrogeological windows role in groundwater contamination (for example, the study of groundwater quality in the areas of increased permeability in the Tobolskii artesian basin [3], petroleum products migration through hydrogeological windows [4], groundwater chemistry change in the mining area in Upper Silesia [5]). Studies related to the mapping of hydrogeological windows have been conducted in Sergeev Institute of Environmental Geoscience, Russian Academy of Sciences (IEG RAS) since 2008. In 2013–2014, a research group of IEG RAS has developed “Map of the Boundaries of Hydrogeological Windows” in some districts of the city at a scale of 1 : 10000 [1]. This map was compiled for the first time by an original method, combining large-scale mapping of the geological structure, hydrogeological and structural-tectonic conditions, groundwater flow calculations, and the analysis of groundwater level and chemistry. The map was based on a large body of data obtained from official sources with the application of modern computer technologies. The integrated approach used in this study allowed identify, map and compare the hydrogeological windows in terms of the filtration time of the pollutants from the

I. Galitskaya (✉) · L. Gomanuk
IEG RAS, Moscow, Russia

© The Author(s), under exclusive license to Springer Nature
Switzerland AG 2021

V. Svalova (ed.), *Heat-Mass Transfer and Geodynamics of the Lithosphere*,
Innovation and Discovery in Russian Science and Engineering,
https://doi.org/10.1007/978-3-030-63571-8_13

199

above-Jurassic to the Podol'sko-Myachkovskii aquifer, which is of strategic significance for drinking water supply.

The purpose of our research was to study the distinctive features of groundwater chemistry of the target Podol'sko-Myachkovskii aquifer in Moscow in the sites of hydrogeological windows. The choice of the study object is determined by the following. Firstly, the Podol'sko-Myachkovskii aquifer is the most important reserve source of drinking water supply in the capital, and secondly, the presence of hydrogeological windows can have a considerable significance for groundwater quality for this aquifer.

The main tasks were: (1) the research of the spatial distribution of contaminants concentrations in the overlying above-Jurassic and the target Podol'sko-Myachkovskii aquifers, (2) the choice of the elements – indicators of the contamination, (3) the construction of schemes based on combining of the schemes of the contaminants distribution and the map of the boundaries of hydrogeological windows, (4) to receive the background concentration of the chemical components of concern, (5) to study the distinctive features of groundwater chemistry of the target aquifer in Moscow in the areas of hydrogeological windows, (6) to specify the semi-variogram type when kriging and identify the features of the chemical composition of groundwater with the use of factor analysis.

The research is carried out within the framework of the project of the Russian Foundation for Basic Research (RFBR) № 17-05-01016.

2 Geological and Hydrogeological Setting

The geology of the area is heterogeneous. The geological conditions are represented by two different types of rocks: Precambrian crystalline rocks of the basement and Paleozoic, Mesozoic and Cenozoic sedimentary cover rocks. The total thickness of the sedimentary cover rocks is about 1000 m. Due to geological processes of erosion and denudation, the Triassic and Dyas rocks were washed out and are not represented in the Moscow area. Paleozoic sedimentary rocks are represented by Devonian limestones, clays and sandstones; Carboniferous limestones and Jurassic clays. Cretaceous rocks of the Mesozoic, portrayed on elevations of Moscow, are similarly absent in the geological section of the disposal fields area. Quaternary rocks are mostly represented by the Moscow River deposits. The variability of geology is due to the existence of a network of buried erosion troughs in bedrocks of Carboniferous and Jurassic, filled with sand–clay Quaternary deposits [1, 2]. The geology and the hydrogeological structure of the stratum that overlays the main Podol'sko-Myachkovskii aquifer varies depending on the presence and depth of ancient erosion troughs (Fig. 1).

Hydrogeological conditions of the city area shows up to 10 and more aquifers in the zone of active water exchange. In this interval, it is common to identify a higher waterbearing stratum in sands, clays, and other deposits of Quaternary and Mesozoic and a lower stratum in carbonate rocks and clays of Carboniferous [2]. At the major

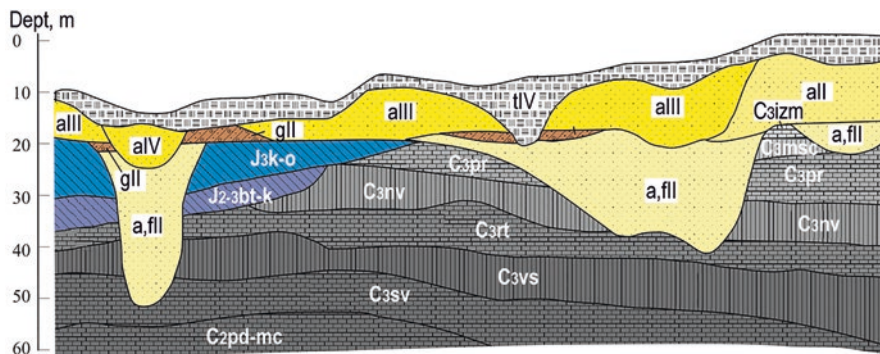


Fig. 1 Geological structure of the strata separating the above-Jurassic and Podol'sko-Myachkovskii aquifers

portion of the territory, except for the valleys of the Moskva River and its tributaries, the upper and lower strata are separated by low permeability Middle and Upper Jurassic (“Jurassic”) clays, which serve as a regional aquitard. In the upper stratum, in the zone of occurrence of moskovskaya and donskaya moraines, the aquifers and the low permeability deposits that separate them are combined into the above_moraine (intermoraine) aquifer system, while the entire water bearing stratum overlaying the “Jurassic” clays is combined into the “above – Jurassic” aquifer system. The above -Jurassic aquifer system is ubiquitous; it is represented most fully on the right bank side of the Moskva River, where it consists of 5 and more aquifers in Quaternary (alluvial, fluvio-glacial), Cretaceous and Upper Jurassic deposits. In the floodplain of the Moskva River and its tributaries, the above – Jurassic aquifer system contains a single aquifer in alluvial deposits, immediately overlaying the Carboniferous deposits. In the places where there is no “above – moraine” aquifer system, the above – Jurassic aquifer system is the first from the surface; those systems show close hydraulic interaction in the rest of the territory.

According to the “Map of the Boundaries of Hydrogeological Windows” [2] hydrogeological windows of different orders were defined based on the results of the vertical filtration time calculation for contaminants, migrating from the above – Jurassic aquifer to the deeper Podol'sko-Myachkovskii aquifer and the lifetime of drinking water supply wells: I – <400 days (survival time of pathogenic microorganisms in groundwater), II – <1000 days (half-life of oil products), III – 3–15 years (decomposition time of more than 60 organic compounds and tritium half-life), IV – 15–25 years (design lifetime of drinking water supply wells), V – 25–50 years (actual lifetime of drinking water supply wells), VI – 50–100 years (characteristic migration time, considering the sorption retention of heavy metals, ammonium ions, radionuclides (cesium and strontium), and nitrates (with denitrification taken into account) (Fig. 2).

In addition, according to tectonic features the potential hydrogeological windows have been identified, which are areas associated with zones of intersection of lineaments, tears, geodynamically active zones and other structural elements where the permeability of rocks can be increased due to increased fracturing.

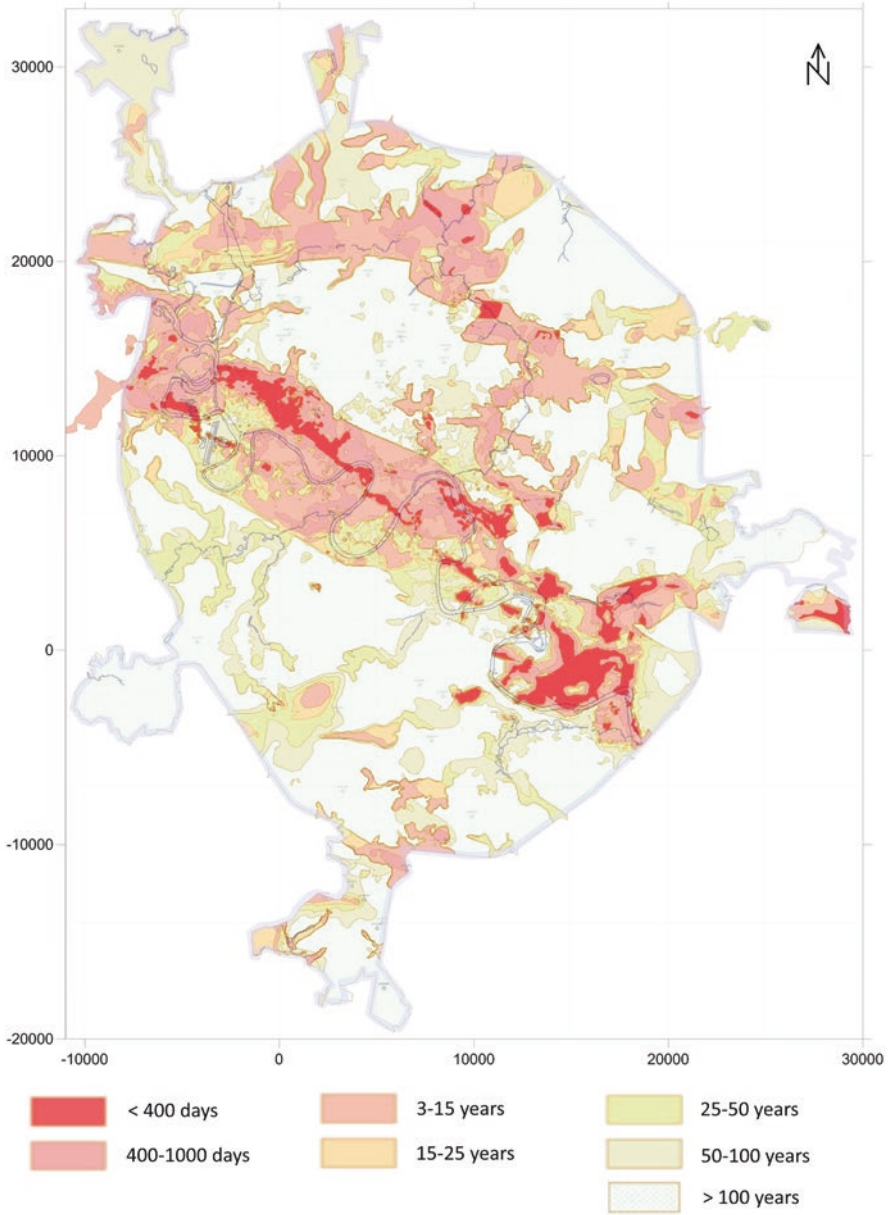


Fig. 2 Schematic map of the hydrogeological windows

3 Materials and Methods

Studying the hydrogeological windows impact on groundwater contamination in the Podol'sko – Myachkovskii aquifer consisted in analyzing the water chemistry data of the above – Jurassic and Podol'sko – Myachkovskii aquifers; choice of the elements – indicators of groundwater contamination on the basis of the study on the water chemistry genesis in the above-Jurassic aquifer; construction and analysis of the elements – indicators distribution schemes in the above – Jurassic and Podol'sko – Myachkovskii aquifers and their comparison with the “Map of the Boundaries of Hydrogeological Windows”.

When assessing the degree of the natural groundwater chemistry change because of anthropogenic activities, the data on background chemical elements concentrations were used, the assessment of groundwater contamination was performed by using the values of maximum permissible concentrations for drinking water. When constructing the schemes of contaminants – indicators distribution the software package “Surfer” was used, the most acceptable result (for a given sampling network) was obtained by Kriging method.

The information about groundwater chemistry from 52 monitoring wells in the above-Jurassic aquifer and 210 wells in the Podol'sko-Myachkovskii aquifer during 2006–2008 was used when conducting these researches. Groundwater chemistry data were obtained from official sources. If evaluating background concentrations the analysis of the data sample on the distribution was carried out for all selected element – indicators. Background concentrations were quantified by statistical processing of geochemical sampling data of specific geological objects within homogeneous areas that are remote from obvious anomalies. The contents of the elements at each individual test point in the background areas are considered as random variables obeying the normal or lognormal distribution law, since their fluctuations are caused by the simultaneous and independent influence of a large number of different causes. The value of the background concentration and its standard deviation are the most important parameters of the local hydrogeochemical background.

Statistical processing was carried out using SPSS® software: (a) for the entire data sample as a single data set, (b) for the data sample rejected in accordance with the “ 3σ ” rule (rejection of large values). To refute the hypothesis of normal distribution, the Kolmogorov-Smirnov (or chi-squared) test was used. In order to “remove” the influence of various factors, histograms of the distribution of the natural logarithms of the original values were plotted. The approach was considered on the example of the main indicator element – chloride ion. When the data interpolation by kriging the exponential theoretical variogram model was used. Detailed comparison of the experimental variograms with the theoretical ones was carried out. The principal component analysis (PCA) was applied to evaluate the main factors controlling groundwater chemistry in the sites of hydrogeological windows and outside the windows.

4 Results

4.1 Groundwater Chemistry

Analysis of the groundwater in the above – Jurassic aquifer showed that the natural chemical composition has been substantially disturbed. The significant transformation of the anionic type of groundwater from hydrocarbonate to chloride occurred under the influence of the technogenic factor in the most study sites (Figs. 3 and 4). The cationic type of groundwater at several sites has changed – from calcium to sodium and even ammonium. Groundwater showed the following concentrations (Table 1).

Exceeding the maximum permissible values was recorded for a wide range of components: chlorides, sodium, ammonium, nitrates, oil products, iron, and heavy metals. The highest levels of groundwater contamination were observed for oil products, manganese and, in particular, for iron. Elevated concentrations of chloride, sulfate, ammonium, nitrate, oil products are associated with infiltration of contaminated sewage and surface runoff, whereas water contamination by iron and manganese is due mainly to interactions in the water-rock system.

The results of studying the groundwater chemistry in the Podol'sko-Myachkovskii aquifer showed that the chemical composition has been insignificantly disturbed by technogenic processes. The natural interactions in the water-rock system form hydrocarbonate and sulfate–hydrocarbonate water of natural genesis. Chloride–hydrocarbonate groundwater of natural–technogenic genesis are less common, confined to the identified potential hydrogeological windows of the 3rd type, located within the Moskvoretskaya geodynamically active zone. The concentrations of technogenic components are much less than the concentrations in the above-Jurassic aquifer (Table 1).

Indicators of contamination can serve components primarily of technogenic origin – ammonium, nitrates, oil products, phenols, surfactants, as well as chloride ion, significantly higher concentrations of which, compared to the background, also have anthropogenic genesis. As the main indicator of contamination, it is advisable

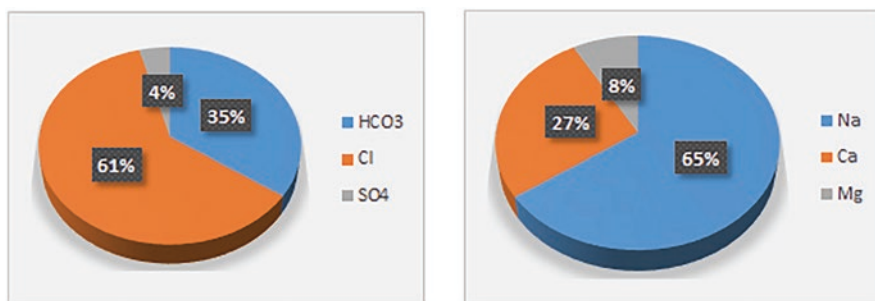


Fig. 3 Anionic and cationic types of groundwater (2007)

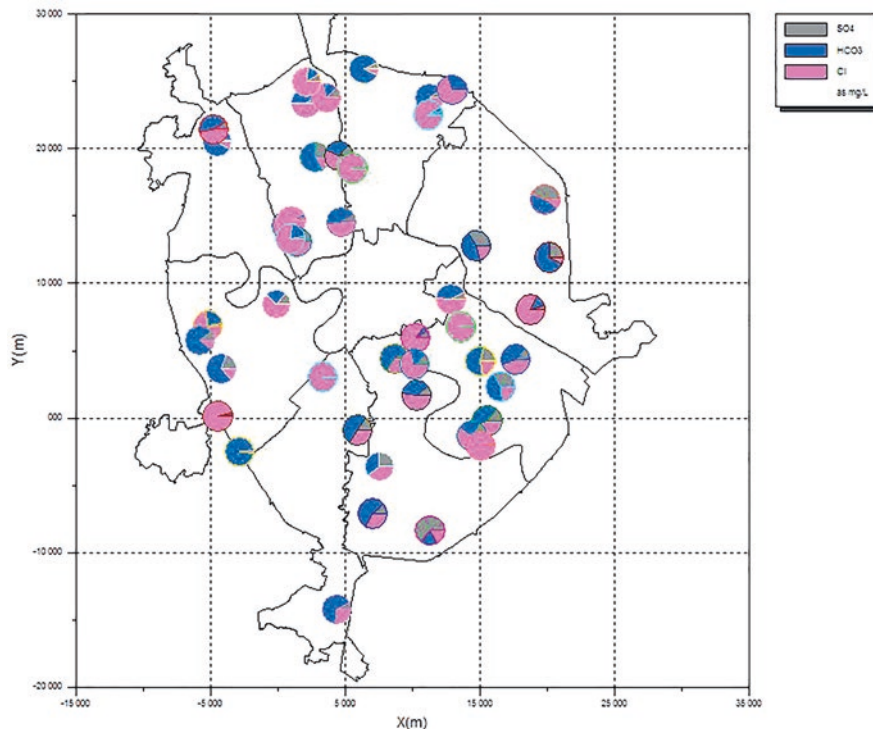


Fig. 4 Scheme of groundwater anionic types distribution

Table 1 Concentration of chemical elements in the above – Jurassic and Podol’sko-Myachkovskii aquifers

Element	Concentration, mg/L above – Jurassic aquifer	Concentration, mg/L Podol’sko-Myachkovskii aquifer
Chloride	0.5–12259	<0.05–293.0
Sulfate	0,1–748.9	<0.01–440.0
Nitrate	0.04–83.85	<0.01–37.2
Sodium	0.2–7778	4.4–1069.0
Ammonium	0.05–236	<0.05–183.0
Calcium	0.5–1900	3.2–250.5
Magnesium	0.27–350	0.01–141.0
Oil products	0.005–53.0	<0.005–113.0
Iron	01–1693	<0.01–14.2
Manganese	0.001–22.9	

to use chloride ion, which, unlike other components, is not sorbed by rocks, practically does not undergo physical and chemical transformations, and is characterized by a fairly stable character of the concentration change in the study area.

Other components of technogenic genesis – oil products, phenols, surfactants, nitrogen compounds, can be used as additional indicators to obtain a more complete picture of the influence of the flow of polluted waters from the above – Jurassic to contamination of the Podol'sko-Myachkovskii aquifer and to elucidate the possibility of using the chemical composition of groundwater as hydrogeochemical sign of the hydrogeological windows [availability](#).

4.2 *The Choice of the Elements – Indicators of Groundwater Contamination and Assessment of their Distribution in the Sites of the Hydrogeological Windows*

The determination of the hydrogeochemical background in the territory of Moscow is complicated by impact of both natural and anthropogenic factors. One should take into account that in the study territory the range of technogenic load in various sites is very significant. The content of chlorides in the aquifers under consideration is primarily due to the entering of anti-icing reagents (CaCl_2) from the road routes to the above-Jurassic aquifer and then to the Podol'sko-Myachkovskii aquifer in the sites of erosion or disturbed structure of the overlying Jurassic deposits.

The Above-Jurassic Aquifer The histogram constructed from the initial data had the form of lognormal distribution (Fig. 5a). The histogram without values exceeding the “mean $\pm 3\sigma$ ” contained 91 measurements out of 103, i.e. 12% of the sample was rejected. The range has decreased: values ranged from 2.8 to 516 mg/l. The distribution type is lognormal. The histogram of the distribution of logarithms of chloride content confirmed the lognormal type of distribution (Fig. 5b). The normal nature of the distribution is typical only for samples in which the concentration of chlorides does not exceed 120 mg/l (Fig. 6a). In general, the studied pollutants

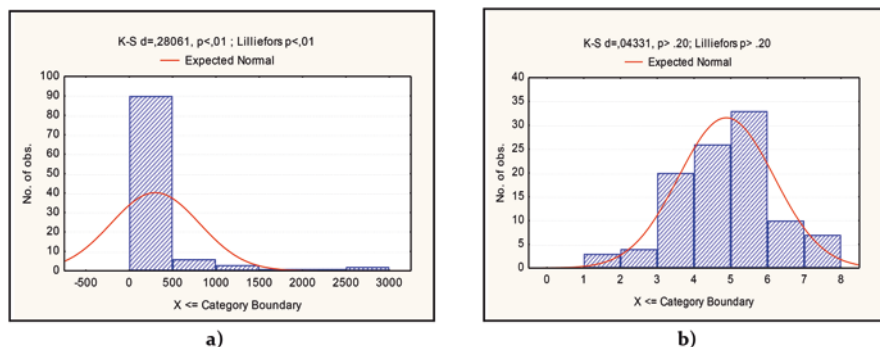


Fig. 5 (a) Distribution of chloride-ion in the above-Jurassic aquifer (entire simple, lognormal distribution) (b) Distribution of the natural logarithms of chloride-ion in the above-Jurassic aquifer (without values, exceeding “mean $\pm 3\sigma$ ” (lognormal distribution)

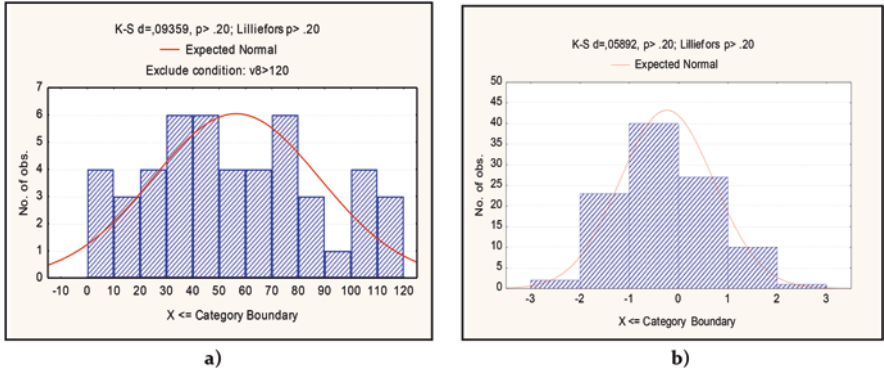


Fig. 6 (a) Distribution of chloride-ion in the above-Jurassic aquifer (concentration up to 120 mg/l, normal distribution) (b) Distribution of the natural logarithms of oil products in the above-Jurassic aquifer (entire simple, lognormal distribution)

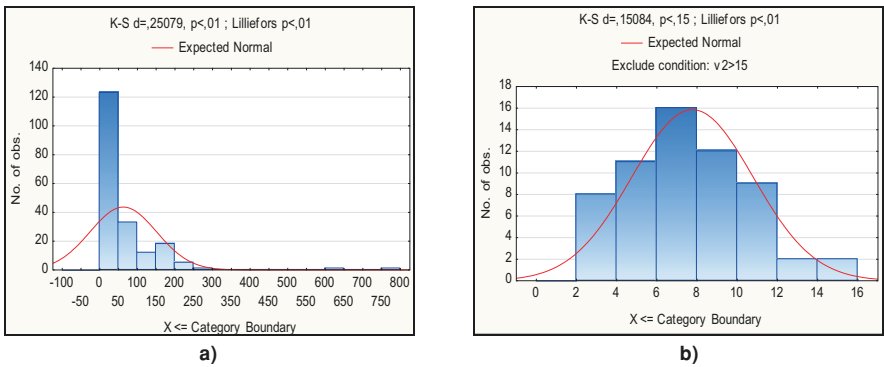


Fig. 7 Distribution of chloride-ion in the Podol'sko-Myachkovskii aquifer (a) entire simple, (b) concentration up to 15 mg/l

(chlorides, sodium, calcium, oil products (Fig. 6b), iron, manganese, and permanganate oxidation) are lognormal distributed.

Podol'sko-Myachkovskii Aquifer The database of chloride-ion concentration in the Podol'sko-Myachkovskii aquifer in the territory of Moscow for 2006–2008 contains 194 samples. The histogram of the distribution of chlorides, constructed over the entire sample, shows a lognormal distribution (Fig. 7a). However, based on the type of the normalized graph, it can be concluded that in the area of small values there is a site that is close to a straight line. This site is consistent with the law of normal distribution, and also corresponds to the natural background. The distribution histogram for the samples with concentrations of chloride-ion up to 15 mg/l covers a third of the entire series – 60 values (Fig. 7b). These samples were taken from wells located in the northern, northeastern, southern and southwestern parts of

the city, and belong to the areas, where the Podol'sko-Myachkovskii aquifer is reliably protected by Jurassic clays. The histograms of the distribution for the following two ranges of values: from 15 to 100 mg/l (96 values) and from 100 to 260 mg/l (36 values) are presented in Fig. 8a, b. Histograms of distribution have also been constructed for other components. In most cases, compliance with the normal or log-normal distribution was observed.

When constructing of the spatial distribution schemes for the concentrations of contaminants (Figs. 9 and 10), the linear or exponential semivariograms were used, but entire compliance theoretical variogram model was not achieved. When searching for spatial correlation using a semivariogram, difficulties arose due to the presence of the limit values. The construction of the semivariogram without a limiting value showed that the experimental and theoretical semivariograms coincide in the best way when taking into account the nugget effect and the wave effect. The semivariogram model obtained in this way was used to construct the spatial distribution schemes for the concentrations of the main indicator component – chloride ion (Fig. 11). However it should be noted that the distribution of components in whole is similar the distribution showed in Fig. 9.

The distribution of the concentration of elements – indicators in groundwater of the Podol'sko-Myachkovskii aquifer shows that higher concentrations of chloride ion (Fig. 9), oil products, nitrate ion and ammonium ion correlate with the occurrence areas of hydrogeological windows in the valleys of the Yauza and Moskva rivers. The highest concentrations of the contamination indicator were identified in the areas of hydrogeological windows of the I and II orders, (mg/L): chloride ion, up to 183–293; nitrate ion, up to 28.4–37.2; oil products, up to 0.113; phenols, up to 0.01; SAS, up to 0.135; and ammonium, up to 183. The most clearly the effect of hydrogeological windows on groundwater contamination in the Podol'sko-Myachkovskii aquifer can be seen in the scheme of chloride ion distribution (Fig. 11).

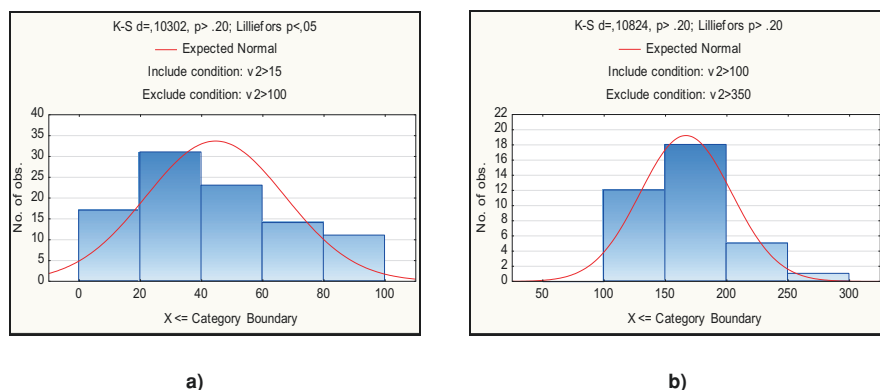


Fig. 8 Distribution of chloride-ion in the Podol'sko-Myachkovskii aquifer (a) concentration from 15 up to 100 mg/l, (b) concentration from 100 up to 260 mg/l

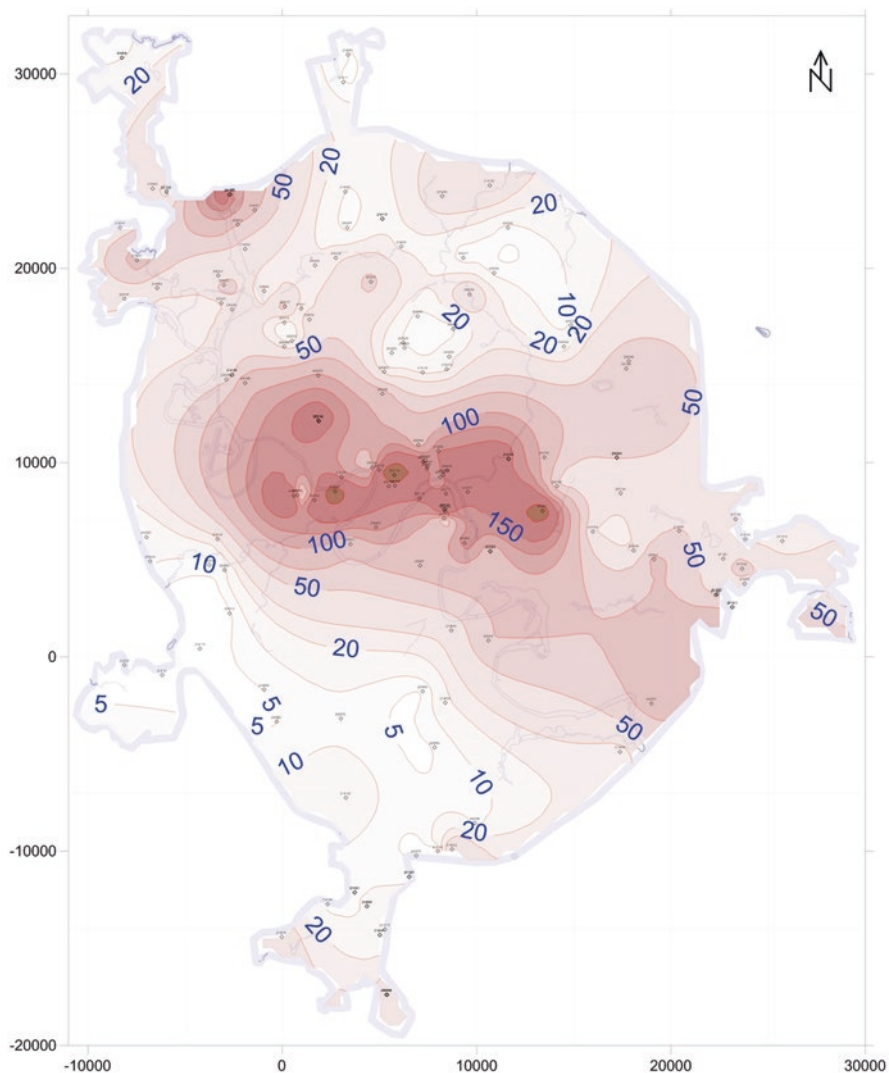


Fig. 9 Schematic map of the distribution of chloride ion in groundwater of the Podol'sko-Myachkovskii aquifer, mg/L (with using of the linear semivariogram)

Hydrogeological windows of the first order are among the most dangerous. In these areas there are no weakly permeable deposits separating the Podol'sko-Myachkovskii and the above – Jurassic aquifers, and where the aquifers form a single aquifer. In this stratum, contamination of the Podol'sko-Myachkovskii aquifer occurs due to the mechanisms of rapid mixing of contaminated groundwater of the above – Jurassic aquifer and pure groundwater of the Podol'sko-Myachkovskii aquifer (Fig. 12).

The average values of groundwater contamination indicators such as Cl^- , Na^+ , Ca^{2+} , Mg^{2+} , NH_4^+ , SO_4^{2-} , NO_3^- , NO_2^- and oil products, were determined when processing data of groundwater chemical analyses at the sites of hydrogeological windows of I–VI orders and the sites of the hydrogeological windows absence. The highest average values of indicators concentrations were found at the sites of the hydrogeological windows of the second order. In general, trend of the average values decreasing with increasing the order of hydrogeological window, i.e. with increasing time the vertical filtration of the contaminants from the above – Jurassic to the Podol'sko-Myachkovskii aquifer (Table 2).

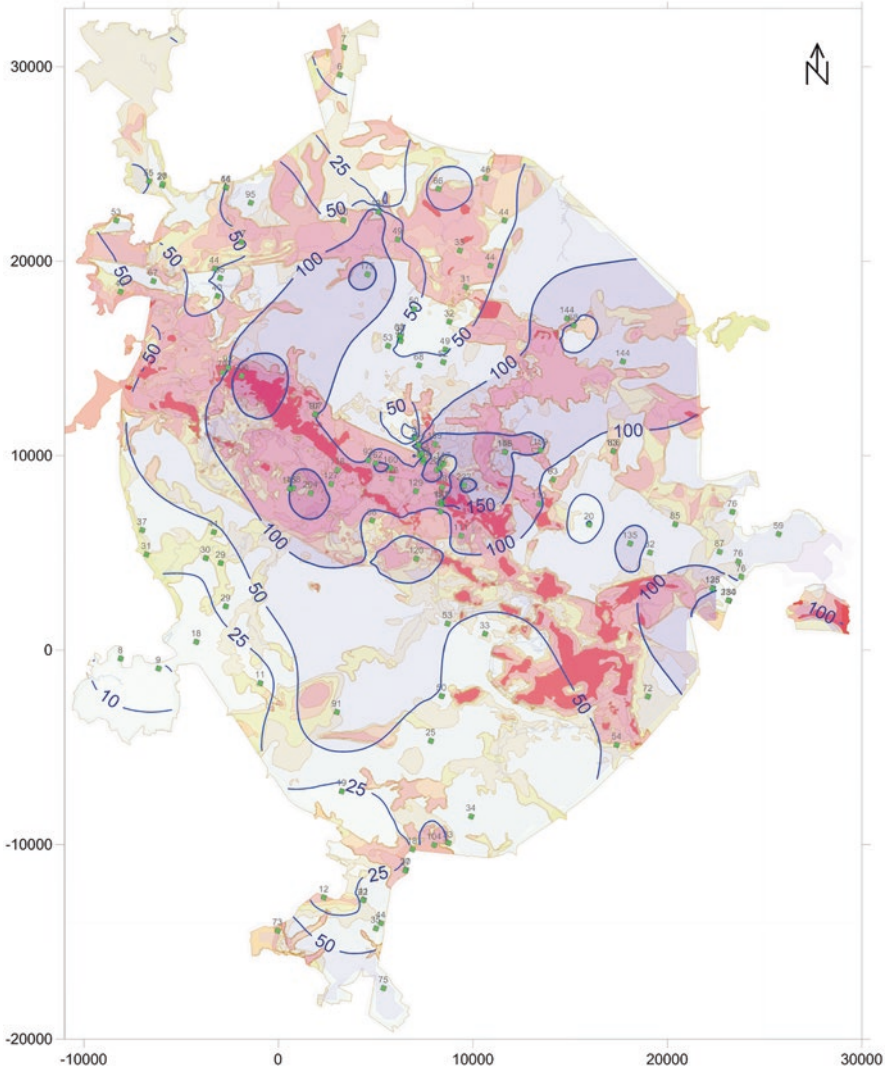


Fig. 10 Schematic map of the distribution of (a) sulfate ion and (b) oil products in groundwater of the Podol'sko-Myachkovskii aquifer, mg/L

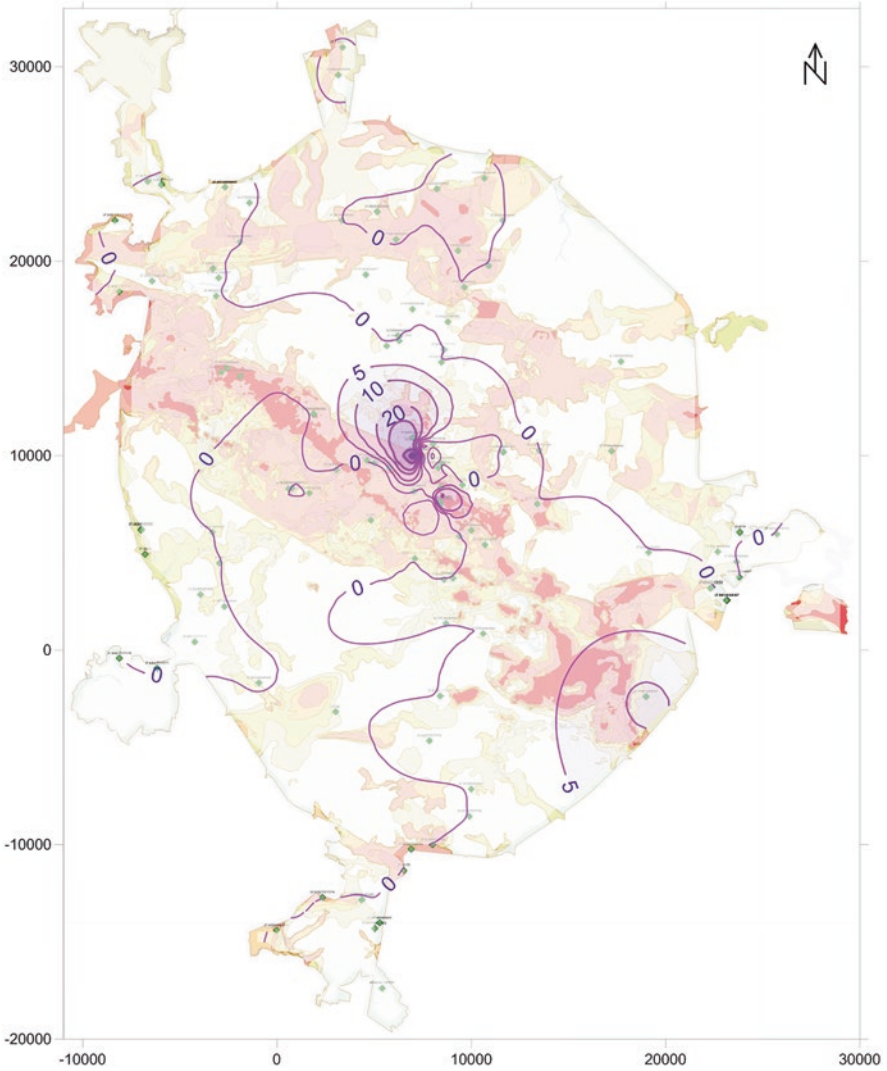


Fig. 10 (continued)

4.3 Results of Principal Component Analysis

The principal component analysis (PCA) was applied to evaluate the main factors, influencing groundwater chemistry in the sites of the hydrogeological windows of different orders and also outside the windows. To estimate the distributions, generalized statistical characteristics of the samples were previously obtained. To simplify the interpretation of factors, the varimax method was used, which minimizes the number of variables with high loads on each factor. Since the method is subject

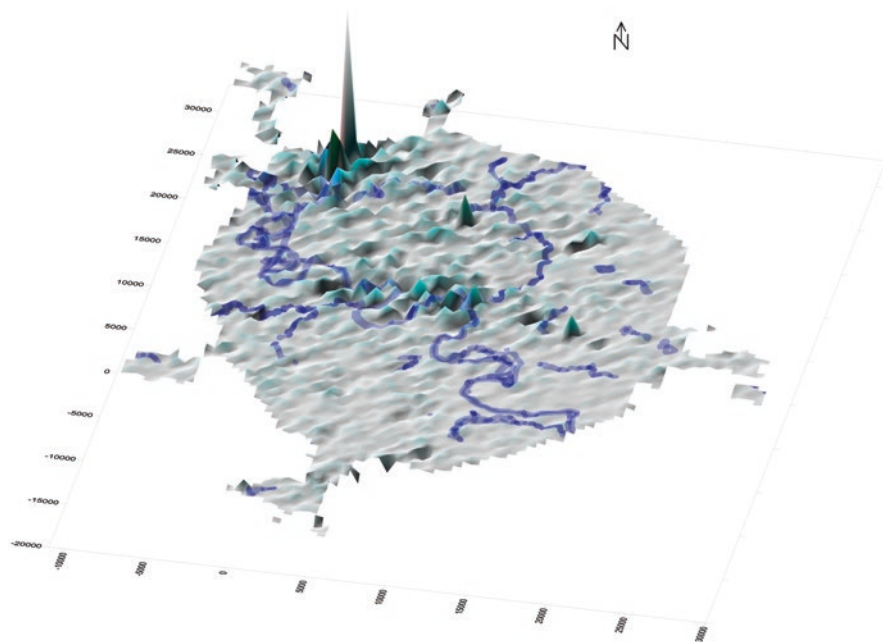


Fig. 11 Schematic map of the distribution of chloride ion in groundwater of the Podol'sko-Myachkovskii aquifer, mg/L (with using of variograms of the nugget effect and the wave effect)

to normal distribution constraints such as the absence of strong outliers, which can significantly distort the real relationships between groundwater components, two samples with maximum values in the northern part of the territory were ignored.

Hydrogeological Window of the II Order (Time of Vertical Filtration Is Less than 1000 Days) The variables Cl^- and Ca^{2+} strongly correlated with factor 1, the correlation values were 0.920 and 0.820, respectively (Table 3). All other variables were significantly (> 0.8) correlated with only one factor: the variable NH_4^+ – with factor 2 (0.975), the variable NO_2^- – with factor 3 (0.961), etc. The first factor included variables associated with the use of anti-icing agent – calcium chloride. The second and third factors determined the variability of ammonium nitrogen and nitrites contents, respectively, they belong to the group of anthropogenic factors characterizing the input of waters contaminated by municipal effluents.

Hydrogeological Window of the III Order (the Vertical Filtration Time Is Less than 15 Years) According to the Total Variation Explained table, three factors had values greater than one. The first factor accounted for 40.563% of the total variance, the second factor – for 5.114% and the third factor – for 10.267%. The variables NO_2^- (correlation value – 0.989), oil products (0.989), Na^+ (0.983), Mg^{2+} (0.951), NH_4^+ (0.936) correlated with factor 1 (Table 4). Only Cl^- (0.926), strongly correlates factor 2 and only Ca^{2+} (0.915) – with factor 3. The first factor combines NO_2^- ,

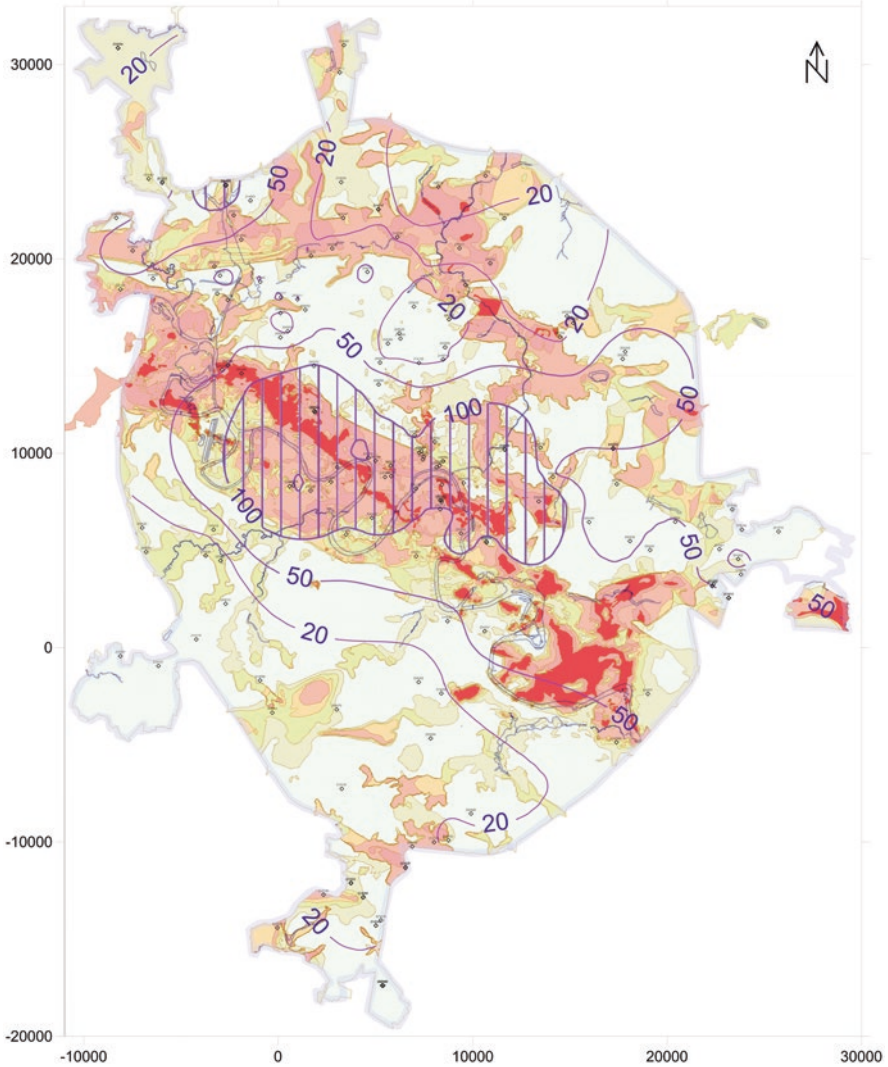


Fig. 12 Synthetic map of the hydrogeological windows and the distribution of chloride ion in the Podol'sko-Myachkovskii aquifer, mg/L

Na^+ , Mg^{2+} , NH_4^+ , oil products it can be interpreted as the predominant influence of technogenic factor. The second factor determines the variability of the content of Cl^- , it refers to anthropogenic factors, characterizing the influence of anti-icing agents. The third factor determines the variability of the content of Ca^{2+} , the lack of connection with Cl^- allows us to attribute it to the natural factors characterizing the dissolution of water-bearing carbonate rocks.

Table 2 Average values of groundwater contamination indicators

The order of the window	Cl ⁻	Na ⁺	Ca ²⁺	Mg ²⁺	NH ₄ ⁺	Fe _{o.oil}	SO ₄ ²⁻	Oil products	NO ₃ ⁻	NO ₂ ⁻
I	65.6	19.25	85.5	32.50	0.47	2.73	94.17	0.13	1.35	0.09
II	122.3	100.4	96.8	38.5	7.5	0.9	92.0	1.7	6.5	0.2
III	65.5	83.17	91.4	43.74	6.35	0.96	70.15	4.72	2.02	0.79
IV	100.2	35.47	75.9	36.45	0.51	0.96	88.59	0.01	2.49	0.05
V	35.4	33.2	77.2	34.36	0.87	1.39	56.16	0.01	1.14	0.03
VI	38.8	31.8	58.4	21.6	2.5	0.7	45.4	1.3	1.2	0.0
Without a window	38.8	41.1	85.3	38.6	1.6	1.1	59.9	0.5	0.9	0.2

Table 3 Factor loadings on the elements: (a) window 2 (time of vertical filtration – less than 1000 days)

Component	Factor 1	Factor 2	Factor 3	Factor 4
Cl ⁻	,920	-,003	-,088	,095
Ca ²⁺	,870	,199	-,151	,020
NH ₄ ⁺	,108	,975	-,027	-,055
NO ₂ ⁻	-,152	-,028	,961	-,014
Oil products	,077	-,065	-,014	,923
Fe ^{2+,3+}	,206	-,024	-,043	,259
Mg ²⁺	-,154	-,176	,221	-,238
SO ₄ ²⁻	,379	-,003	,157	,129
NO ₃ ⁻	,348	,149	-,056	,095

Hydrogeological Window of the IV Order (the Vertical Filtration Time Is Less than 25 Years) Five proper factors had the values exceeding one. The first factor explained 35.742% of the total variance, the second factor – 17.475%, the third factor – 15.405%. The variables Cl⁻ (correlation value – 0.951) and SO₄²⁻ (0.562) correlated with the first factor (Table 5). The variable Na⁺ (0.761) correlated with the second factor, the variables NO₂⁻ (0.920) and SO₄²⁻ (0.694) – with the third. The first factor characterizes the influence of anti-icing agents. Apparently, the second factor that determines the variability of Na⁺ content, is similar to the previous one. The third factor determines the variability of the content of NO₂⁻, SO₄²⁻, NH₄⁺, it should be attributed to man-made factors and can be explained by the composition of wastewater leaks.

Hydrogeological Window of the V Order (the Vertical Filtration Time Is Less than 50 Years) Three factors had values greater than one. The first factor explains 39.456% of the total variance, the second factor – 21.785% and the third factor – 14.146%. The variables SO₄²⁻ (0.956), Na⁺ (0.943), Cl⁻ (0.729), Ca²⁺ (0.698) correlated with factor 1, variable Mg²⁺ (0.943) – only with factor 2, variable NO₃⁻ (0.965) – only with factor 3. The first factor combines SO₄²⁻, Na⁺, Cl⁻, Ca²⁺. It seems that such association of chemical elements reflects both the influence of natu-

Table 4 Factor loadings on the elements: (a) window 3 (time of vertical filtration – less than 15 years)

Component	Factor 1	Factor 2	Factor 3	Factor 4
NO ₂ ⁻	,989	-,020	,014	-,069
Oil products	,989	-,009	,002	-,018
Na ⁺	,983	,058	,073	,004
Mg ²⁺	,951	,061	-,031	-,106
NH ₄ ⁺	,936	-,007	-,037	,004
Cl ⁻	,017	,926	,195	,193
Ca ²⁺	,001	,212	,915	,184
SO ₄ ²⁻	-,134	,205	,180	,923
Fe ^{2+,3+}	-,055	,030	-,015	,126

Table 5 Factor loadings on the elements: (a) window 4 (time of vertical filtration – less than 25 years)

Component	Factor 1	Factor 2	Factor 3	Factor 4
SO ₄ ²⁻	,956	,089	,205	-,064
Na ⁺	,943	,203	,062	-,038
Cl ⁻	,729	-,093	,181	-,100
Ca ²⁺	,698	,325	-,196	-,031
Mg ²⁺	,210	,943	-,138	,190
NO ₃ ⁻	,168	-,132	,965	-,067
Fe ^{2+,3+}	-,090	,163	-,063	,977
NO ₂ ⁻	,165	,070	-,042	,015
NH ₄ ⁺	-,050	,041	-,117	,077

ral processes (dissolution of gypsum interlayers in carbonate rocks, and the influence of anti-icing agents–sodium and calcium chlorides). The second factor determines the variability of Mg²⁺ concentration. Given the relatively high correlation coefficient Ca²⁺ (0.325) and the lack of connection with Cl⁻, it should be attributed to natural factors characterizing the dissolution of carbonate rocks. The third factor determines the variability of NO₃⁻ concentration, it belongs to the anthropogenic factors group, characterizing the infiltration of water contaminated by municipal effluents.

Hydrogeological Window of the VI Order (the vertical Filtration Time Is Less than 100 Years)

As in the previous case three factors had the values greater than one. The first factor explains 41.044% of the total variance, the second factor – 18.495% and the third factor – 13.632%. The variables Ca²⁺ (0.889) and Mg²⁺ – (0.889) correlate with factor 1, Cl⁻ (0.929) and Na⁺ (0.652) – with factor 2, only NH₄⁺ (0.933) – with factor 3 (Table 6). The first factor combines Ca²⁺, Mg²⁺, it can be interpreted as the influence of a natural factor – the dissolution of water-bearing rocks, that determines the formation of calcium, magnesium-calcium and calcium-magnesium hydrocarbonate groundwater in the territory under consideration. The second factor determines the variability of the content of Cl⁻, Na⁺, it reflects the

influence of anti-icing agents. The third factor determines the variability of NH_4^+ content, it belongs to the group of anthropogenic factors, characterizing the flow of water contaminated by municipal effluents.

The Territory of the Hydrogeological Windows Absence Three eigen values have values greater than one. The first factor explains 28.941% of the total variance, the second factor 21.368% and the third factor 12.548%. Factor 1 is correlated with NH_4^+ (0.978), Na^+ (0.948), factor 2 – Cl^- (0.930), Ca^{2+} (0.404), factor 3 – SO_4^{2-} (0.950). The first factor combines NH_4^+ , Na^+ , it can be interpreted as technogenic. The high factor load of Cl^- and Ca^{2+} in the second factor indicates the influence of anti-icing agents. The third factor determines the variability of SO_4^{2-} content. Taking into account that the next correlation value belongs to Ca^{2+} (0.238), it can be explained by the influence of natural processes (dissolution of gypsum interlayers in carbonate rocks).

The results of research allowed one to reveal a complex linear correlation between the concentrations of the contaminants and to identify the main factors of groundwater chemistry formation: the anthropogenic factor – percolation the water, contaminated with anti-icing agents or municipal wastewater, and the natural factor – dissolution of water-bearing carbonate rocks and gypsum layers in carbonate rocks. However, in some cases it is difficult to unambiguously determine whether a given factor is technogenic or natural. This fact is determined by a rather wide list of substances having both natural and technogenic origin, for example, calcium, magnesium, sulfate ion.

When performing PCA it was assumed that in areas outside the hydrogeological windows the natural factor would be decisive and the anthropogenic factor would be minimal. As the given results showed this assumption did not confirmed. Probably in the sites out of the windows the influence of the anthropogenic factor was caused by the lateral migration of pollutants from the areas of hydrogeological windows located upstream. More detailed studies are planned at the next stage.

Table 6 Factor loadings on the elements: (a) window 6 (time of vertical filtration – less than 100 years)

Component	Factor 1	Factor 2	Factor 3	Factor 4
Ca^{2+}	,889	,091	,263	–,092
Mg^{2+}	,889	,056	,162	–,190
Cl^-	,041	,929	,134	,133
Na^+	,182	,652	,302	–,037
NH_4^+	,289	,181	,933	–,022
NO_2^-	–,169	,095	–,021	,978
$\text{Fe}^{2+, 3+}$	–,004	,006	,058	,003
SO_4^{2-}	,304	,236	–,004	–,055
NO_3^-	,239	,403	,007	,084

5 Conclusions

Minimizing the adverse effect on the Podol'sko-Myachkovskii aquifer as the main reserve source of drinking water appears to be one of the major problems in Moscow urban planning. The Podol'sko-Myachkovskii aquifer is the most vulnerable to contamination at the sites of hydrogeological windows. It is here due to the high discontinuity and permeability in the separating layer the most fast contaminant transport from the polluted above-Jurassic aquifer to deep aquifers occurs.

The results of this study lead to the conclusion that the hydrogeological windows effect on the groundwater chemistry in the Podol'sko-Myachkovskii aquifer. Elevated concentrations of chlorides, nitrates, oil products, ammonium were characteristic for the areas of hydrogeological windows in the valleys of the rivers Yauza and Moscow, allocated according to geological structure, hydrogeological and tectonic conditions. Therefore, the hydrogeochemical criteria, notwithstanding the objective restrictions of applications, can be used to identify hydrogeological windows in the zones of higher permeability and lower thickness of low-permeability Jurassic clays. The accuracy of the method can be improved by the introduction of hydrogeological monitoring in the zones of both identified and potential hydrogeological windows, the data on which are insufficient now.

The system of measures for the preservation of the groundwater drinking quality should involve the identification of areas most vulnerable in terms of contamination penetration into them, the inventory of potential pollution sources, the assessment of groundwater pollution, and the development of special regulations on the economic activities in such areas. Of greatest importance is the development of environmental regulations on the use of the zones of hydrogeological windows, primarily, the most hazardous and unprotected hydrogeological windows of the I and II orders. For these areas, it should be recommended to remove industrial plants or modernize underground services, treatment facilities, etc.; eliminate landfills and technogenic soil dumps, modernize the sewage networks in residential areas, reduce motor transport emissions by introducing special types of fuel and electric transport; modernize road storm-water drains; introduce groundwater monitoring with obligatory allocation of observation wells at ecologically hazardous facilities; prohibit the construction of new industrial facilities (except for the critical life-supporting facilities), petrol stations, auto washing, etc. The possibility to allocate a potential groundwater pollution source in zones of hydrogeological windows must be substantiated by the results of forecasting groundwater pollution in the Podol'sko-Myachkovskii aquifer by numerical simulation of groundwater flow.

References

1. Pozdniakova IA, Kozhevnikova IA, Kostikova IA, Toms LS (2013) Groundwater interaction assessment based on the large-scale mapping of geological and hydrogeological conditions in Moscow. *Water Resour* 40(7):695–705

2. Pozdnyakova IA, Galitskaya IV, Mironov OK, Kostikova IA, Dorozhko AL, Batrak GI, Matveeva LA, Fesel KI (2016) Identification of hydrogeological windows based on large-scale mapping of the geological and hydrogeological conditions in Moscow. *Water Resour* 43(7):1012–1022
3. Vsevolodzkaya MA, Galitskaya IV (1980) Estimation of mass transfer in marine genesis clay under seepage. Materials of conference of Chemical society GDR. Dresden Technological University, pp 80–85
4. Aivars S, Romans J et al (2000) Modelling of groundwater flow dynamics and contamination transport processes at the Vilnius oil storage area. *Tracers and Modelling in Hydrogeology: TraM'2000*, No. 262, pp 97–102
5. Rozkowski A (1993) Impact of mining on the groundwater chemistry in the Upper Silesian Coal Basin (Poland). *Mine Water Environ* 12(Annual issue):95–106

Hydraulic Fracture Problem for Poroelastic Medium with Double Porosity



Andrej Karakin

1 Introduction

The known Biot's model [1] describes the poroelastic medium with usual porosity. The expressions for their medium constants are obtained in [1–3] from the thermodynamics understanding. The Aifantis's equations [4] generalize the Biot's equations for the medium with double porosity. But these equations too general and cumbersome. The monographers [5, 6] include the general principles of poroelastic medium mechanics and thermodynamics.

The thermodynamic approach vouches for concordance these results. But it is not suitable for various generalizations when the form of constitutive equations is determined from some complementary understanding. Due to this reason the monographer [7] suggests some heuristic method to construct the porous medium model with double porosity (with cracks and pores). There is no general method for such models and some special approach is required.

In this work we consider the hydrofracture in the medium with double porosity based on general principles proposed in [1–6]. There are two stages to solve this problem. Firstly we consider the medium model with double porosity. At the second stage we took the equilibrium hydrofracture under a constant pressure as an example. It moves under pumping down mud.

A specification of the many factor hydrofracture is to include itself many physical phenomena. The main idea of this model with complex phenomena is related with the incomplete coupling principle [8–10]. This essence is to reduce the solution of complex coupled problem, representing the motion in the fracture, to the

A. Karakin (✉)

Keldysh Institute of Applied Mathematics RAS, Moscow, Russia

e-mail: avkarakin@jandex.ru

© The Author(s), under exclusive license to Springer Nature
Switzerland AG 2021

V. Svalova (ed.), *Heat-Mass Transfer and Geodynamics of the Lithosphere*,
Innovation and Discovery in Russian Science and Engineering,
https://doi.org/10.1007/978-3-030-63571-8_14

219

sequential solution of three incompletely coupled simple problems. In fact on every stage one solves one the independent problem. In fact the solution on a previous stage is a known quantity. To implement this idea one divides the solution in the external region to the two components – elastic and percolating. The percolating component is a thin layer around the fracture the same as in the models with a simple porosity.

In [11] the flat hydrofracture problem was solved outright disregarding the incomplete coupling principle. The problem was tackled with standard general method disregarding the given principle with the help of the singular integral equation for two particular cases. The general method has own shortcomings related with an artificial hypothesis. In given case it related with the mechanism of a liquid leakage from crack into the poroelastic medium. The Newtonian liquid is pumped into a fracture at a constant velocity. A flow in the crack is governed by the lubricant approximation of the hydrodynamic equations. The liquid leakage from a crack into the poroelastic medium is described with one-dimension approximation of the parabolic diffusion equation. This equation is postulated (not reduced!) following to an intuitive consideration. As a result, author failed to attend some term in an equation and violated the law of conservation mass at the boundary crack in this work. The ultimate solution distinguishes from the analogous solution, obtained by a correct method in [8–10].

In this work we investigate a particular variant of the model with double porosity and heterogeneous pressure, supposed in [7]. In this model the cracks and pores are separately and filled up with the same fluid. The fluid and matrix substances are elastic compressed. The pore and fracture systems have different scale and that is why they are divided in the space. There is the fluid flow between them, but the force interaction is absent.

We consider the initial stage of an evolution only – the toughness-dominated regime. It is reduced to investigation of simple single problems in the porous media with usual porosity. In the main region the media is elastic with undrained volume elasticity module. In the boundary layer the double porosity effects are not significant. We describe this layer with help of model with usual porosity distinguished from porosity in the main region.

As it is easy to see the Aifantis's theory is more general, but it includes an unwarrantable complex consideration. In this meaning the Barenblatt's particular medium model [7] is more reasonable and real. Never the less as a matter of fact his approach is heuristic and it is not guided by a correct output from the initial equations. In our case its simplified model is deduced sufficiently rigorous. The crack movement model in this medium is an illustrative example.

2 Statement of the Problem and Its Solution

We consider the movement of the equilibrium hydrofracture in the weightless isotropic heterogeneous media with double porosity. A fracture moves along the horizontal axis x_1 in the two-dimensional space $\Omega : (x_1, x_2)$ under the action of pumped down liquid through a borehole in the state of heterogeneous pressure p_c .

The mechanic equations of poroelasticity with double porosity take place out of a hydrofracture. The pores and cracks is filled up with the one-phase incompressible liquid. Let us write out the equations of poroelasticity with double porosity [4] and Aifantis's equations, generalized the known expressions of Biot and Terzaghi,

$$\begin{aligned}
 \Omega: \quad \nabla \cdot \hat{\sigma} &= 0, \hat{\sigma} = \hat{\sigma}^{ef} - \alpha^{(p)} p^{(p)} \hat{I} - p^{(j)} \alpha^{(j)} \hat{I}, \hat{I} \equiv \{\delta_{ij}\}, & \text{a)} \\
 \hat{\sigma}^{ef} &= 2\mu \hat{\varepsilon} + \lambda \theta \hat{I}, \theta \equiv \hat{\varepsilon} : \hat{I}, K = \lambda + \frac{2}{3}\mu, f = f^{(p)} + f^{(j)}, & \text{b)} \\
 \nabla p^{(p)} &= -\frac{\eta}{k^{(p)}} \mathbf{s}^{(p)}, \nabla p^{(j)} = -\frac{\eta}{k^{(j)}} \mathbf{s}^{(j)}, & \text{c)} \\
 \hat{\varepsilon} &= \frac{1}{2} \left\{ \frac{\partial u_i}{\partial x_j} + \frac{\partial u_j}{\partial x_i} \right\}, \frac{\partial}{\partial t} (\rho^{(f)} f^{(p)}) + \nabla \cdot (\rho^{(f)} f^{(p)} \mathbf{w}^{(p)}) = -Q & \text{d)} \quad (1) \\
 \frac{\partial}{\partial t} (\rho^{(f)} f^{(j)}) + \nabla \cdot (\rho^{(f)} f^{(j)} \mathbf{w}^{(j)}) &= Q, \rho = (1-f)\rho^{(s)} + f\rho^{(f)}, & \text{e)} \\
 \frac{\partial}{\partial t} [(1-f)\rho^{(s)}] + \nabla \cdot [(1-f)\rho^{(s)} \mathbf{w}^{(s)}] &= 0, p^{(s)} = K^{(s)} \frac{\Delta \rho^{(s)}}{\rho^{(s)}}, & \text{f)} \\
 p^{(f)} &= K^{(f)} \frac{\Delta \rho^{(f)}}{\rho^{(f)}}, \Delta \rho^{(s)} \equiv \rho^{(s)} - \rho_0^{(s)}, \Delta \rho^{(f)} \equiv \rho^{(f)} - \rho_0^{(f)} & \text{g)}
 \end{aligned}$$

where $\hat{\sigma}$ and $\hat{\sigma}^{ef}$ are tensors of the total and effective stresses; \hat{I} is a unit tensor; $p^{(p)}$ and $p^{(j)}$ denote the pore and crack pressure components correspondingly; $\hat{\varepsilon}$ is a small strain tensor; θ is the bulk compression of the medium; $\alpha^{(p)}$ и $\alpha^{(j)}$ – are the coefficients ahead the pore and fracture pressures introduced by Aifantis; \mathbf{u} , \mathbf{w} are the displacement and velocity of the porous medium; $\mathbf{s}^{(p)} \equiv f(\mathbf{w}^{(p)} - \mathbf{w})$, $\mathbf{s}^{(j)} \equiv f(\mathbf{w}^{(j)} - \mathbf{w})$ denote the filtration rate of the pores and cracks; $\mathbf{w}^{(p)}$, $\mathbf{w}^{(j)}$ – are the absolute velocity of the pores and cracks; ρ , $\rho^{(s)}$, $\rho^{(f)}$ are the densities of the two-phase medium, as well as of the matrix and fluid phases; λ , μ are the Lamé coefficients; K is the drainage modulus of the bulk; f is the porosity; k and η are the coefficients of fluid permeability and fluid viscosity which are assumed to be constant; $p^{(s)}$ is the pressure in the matrix phase; $K^{(s)}$ and $K^{(f)}$ are the bulk modules of the matrix and fluid phases. The symbol Δ denotes the deviation of a given quantity from an equilibrium state (i.e., from a state of rest or from a background state), which is designated by the subscript zero.

Every crack is surrounded with small pores, which must be averaged and we can consider this medium as elastic one with some effective modulus $K^{(p)}$. Let us denote the effective volume modulus of average medium as K and carry out the mental experiment to determine some substance parameters according to [2, 5, 6]. In the elementary volume there are pores, only but there are no cracks. There is a change with water between them but the power interaction is absent. After that let us consider the jointing medium immersing into the effective homogeneous media. Then the known expressions take place after an obvious consideration

$$\alpha^{(p)} = 1 - \frac{K^{(p)}}{K^{(s)}}, \alpha^{(j)} = 1 - \frac{K}{K^{(p)}}, K^{(p)}\theta^{(p)} = -p^{(p)}. \tag{2}$$

The fluid content ξ generalizes an analogous concept in the Biot’s model on the medium with double porosity. Let us remember that at $\xi = 0$ a filtration through the elementary volume boundary is absent. At the same time this quantity can be changing with a time because of the elementary volume deformations. The both its components $\xi^{(p)}$ and $\xi^{(j)}$ have an analogous meaning. It is significant that the crack specific volume is small, the pores are impermeable, and they are deformed together with an elastic medium. Never the less a change between pores and cracks takes a place under the condition that a filtration is absent through outer boundaries. In the averaging procedure the crack component $\xi^{(j)}$ means the pores existence in form of some averaging medium by some stage. Its density is denoted as $\rho^{(j)}$. In view of accepted simplifications fluid content for every components is given with the expressions

$$\xi^{(p)} = \frac{1}{\rho_0^{(f)}} \Delta \left(f^{(p)} \rho^{(f)} \right), \xi^{(j)} = \frac{1}{\rho_0^{(f)}} \Delta \left(f^{(j)} \tilde{\rho}^{(f)} \right).$$

Both components $\xi^{(p)}$ and $\xi^{(j)}$ are non-observed values and they must be leave out of the final expressions. Because of cracks and pores have the different scales and distinguish with their geometric forms, there is not interaction between them and itself quantities are additive:

$$\xi = \xi^{(p)} + \xi^{(j)}, f = f^{(p)} + f^{(j)}, f_0 = f_0^{(p)} + f_0^{(j)}, \theta = \left(\theta^{(p)} + \theta^{(j)} \right). \tag{3}$$

We suppose the next simplification [6]. The summary cracks volume is small, their permeability is huge in comparison with pores permeability:

$$\begin{aligned} \nabla \xi^{(p)} \ll \nabla \xi^{(j)}, \frac{\partial \xi^{(p)}}{\partial t} \gg \frac{\partial \xi^{(j)}}{\partial t}, \nabla \theta^{(p)} \ll \nabla \theta^{(j)}, \frac{\partial \theta^{(p)}}{\partial t} \gg \frac{\partial \theta^{(j)}}{\partial t}, \quad \text{a)} \\ k^{(p)} \ll k^{(j)}, f \ll 1, s^{(p)} \ll s^{(j)} \equiv s, f^{(j)} \ll f^{(p)} = f. \quad \text{b)} \end{aligned} \tag{4}$$

The expressions (4) mean that in the fracture space a filtration is possible but a fluid accumulation is not possible. In the pores space a filtration is not possible. But a fluid accumulation is possible in the elementary volume as a consequence of the “interphase” crossflow, if one considers both pores spaces as different phases. In reality they are the same phase. A fluid flow between phases Q is describes with the zero dimension of Darcy’s low. These assumptions are the main point of the Barenblatt’s theory [7]. They simplify the general Aifantis’s equations [4] considerably:

$$\begin{aligned} \nabla p^{(j)} &= -\frac{\eta^{(f)}}{k^{(j)}} \mathbf{s}^{(j)}, & \text{a)} \\ \mathbf{s}^{(p)} &= 0, & \text{b)} \\ Q &= \frac{\rho^{(f)}}{\eta} \chi (p^{(p)} - p^{(j)}). & \text{c)} \end{aligned} \quad (5)$$

At these assumptions and on account of the inequality (4) the equation of phases continuity (1c, d) takes a form [6]

$$\begin{aligned} \nabla \cdot (\rho^{(f)} \mathbf{s}^{(j)}) &= Q \text{ or } \nabla \cdot \mathbf{s}^{(j)} = \frac{Q}{\rho^{(f)}}, & \text{a)} \\ \frac{\partial}{\partial t} (\rho^{(f)} f^{(p)}) &= -Q. & \text{b)} \end{aligned} \quad (6)$$

Following to the Rice’s thermodynamic considerations [3] and analogous argumentation [5, 6], we present the expressions for the components of the fluid content ξ through the observed quantities

$$\begin{aligned} \xi^{(p)} &= \alpha^{(p)} \left(\theta^{(p)} + \frac{\alpha^{(p)} p^{(p)}}{K_u - K} \right), & \text{a)} \\ \xi^{(j)} &= \alpha^{(j)} \left(\theta^{(j)} + \frac{\alpha^{(j)} p^{(j)}}{K_u - K} \right). & \text{b)} \end{aligned} \quad (7)$$

Let us transform the constitutive equations (1) to a standard form. We receive the known Aifantis’s equations [4], which generalize the analogous Biot’s equations for poroelastic media. In particular we have the dynamic equations

$$\mu \nabla^2 \mathbf{u} + (\lambda + \mu) \nabla \theta - \alpha^{(j)} \nabla p^{(j)} - \alpha^{(p)} \nabla p^{(p)} = 0. \quad (8a)$$

Applying the divergence operation to this expression we have

$$(\lambda + 2\mu) \nabla^2 \theta - \alpha^{(j)} \nabla^2 p^{(j)} - \alpha^{(p)} \nabla^2 p^{(p)} = 0. \quad (8b)$$

From definition ξ (and its components $\xi^{(p)}$ and $\xi^{(j)}$) one receives the next fact. At undrainage deformation of an elementary volume the poroelastic medium is deformed as the effective homogeneous elastic medium under a percolation absence through its boundaries. As a result the second expression (1a) and expression (8a) take a form at given condition

$$\begin{aligned} \hat{\sigma} &= 2\mu\hat{\varepsilon} + \lambda_u\theta\hat{I}, & \text{a)} \\ \mu\nabla^2\mathbf{u} + (\lambda_u + \mu)\nabla\theta &= 0, K_u = \lambda_u + \frac{2}{3}\mu. & \text{b)} \end{aligned} \quad (9)$$

Under drainage deformation one must add to the expression (9a) the proportional to $\xi^{(p)}$ and $\xi^{(j)}$ terms. However a medium drainage takes place through cracks only. That is why the component $\xi^{(p)}$ must be excluded and the first expressions (7a) and (3) take a form

$$\xi^{(p)} = \theta^{(p)} + \frac{\alpha^{(p)}p^{(p)}}{K_u - K} = 0, \xi = \xi^{(j)}. \quad (10)$$

The given expressions mean that the pore component of fluid pressure is determined with the skeleton elastic deformation only. The pores drainage and their connection with fractures have a small influence on the stress state of a poroelastic medium. They influence on the fluid mode only. The percolation properties of a medium and related with them deformations are determined with its jointing entirely. The pores have an influence on the stress state indirectly and through expression (5c) only. The next considerations repeat the known result of papers [5, 6] which can be applied to the medium with the double porosity. The constitutive equations and balance expressions in the form (9) and under drainage mode take a form

$$\begin{aligned} \hat{\sigma} &= 2\mu\hat{\varepsilon} + \lambda_u\theta\hat{I} - \frac{(\lambda_u - \lambda)}{\alpha^{(p)}}\xi\hat{I}, & \text{a)} \\ \mu\nabla^2\mathbf{u} + (\lambda_u + \mu)\nabla\theta - \frac{(\lambda_u - \lambda)}{\alpha^{(p)}}\nabla\xi &= 0, K_u = \lambda_u + \frac{2}{3}\mu & \text{b)} \end{aligned} \quad (11)$$

The general movement equations of medium with the double porosity (11), (5) should be supplemented with a concrete problem. In this case we take into account a hydrofracture.

3 Crack of Hydrofracture

This crack is the line of destruction Γ_{in} in the outer space Ω . Its length is $2L(t)$. It has a small but finite thickness $H(x_1, x_2, t)$ ($H \ll L$). The space into it is the inner region Ω_{in} which has the external boundaries Γ^\pm . This region spreads along horizontal axis $x_2 = 0$ and is located within limits $-H < x_2 < H$, where $2H$ is the crack thickness which depend on the time and longitudinal axis. The fluid flows in the crack through a borehole, which looks as a local inflow, and run out in the external region through the horizontal boundaries. The system “fracture – surrounding rock” is symmetric about the vertical and horizontal axes.

The external and internal problems of a hydraulic fracture include the small parameter

$$\varepsilon_1(t) = \frac{H(0, 0, t)}{L(t)}, \tag{12}$$

which has meaning of the elastic strain in the external region, and $H(0, 0, t)$ is a maximal fracture opening. In the external region the series expansion by this parameter means a linearization of the dynamic system equations. The hydrostatic equations take place inside the cavity of a fracture. This parameter is changed as needed with fracturing. The magnitude of the other quantities are changed correspondingly. We consider the state in a fixed time moment.

In the external problem the hydrodynamic fluid pressure in a fracture p_c is considered as given on the inner boundary Γ_{in} . In the inner problem it is a given homogeneous value. From point of the inner problem there are two fracture boundaries – upper and lower which denoted as Γ^\pm correspondingly. On these boundaries the boundary conditions are defined for stress in the external region and the continuity condition for displacement \mathbf{u} and velocity \mathbf{w} :

$$\begin{aligned} \Gamma_{in} : \mathbf{n} \cdot \hat{\sigma} \cdot \mathbf{n} &= -p_c, \mathbf{m} \cdot \hat{\sigma} \cdot \mathbf{n} = 0, & \text{a)} \\ \Gamma^\pm : p^f &= p_c, & \text{b)} \\ \Gamma^\pm : [\mathbf{u}] &= 0, [\mathbf{w}] = 0. & \text{c)} \end{aligned} \tag{13}$$

At infinity the perturbations are extinguished

$$\hat{\sigma} \rightarrow 0, \mathbf{s} \rightarrow 0, \nabla \cdot \mathbf{p}^f \rightarrow 0 \text{ by } (x_1^2 + x_2^2) \rightarrow \infty. \tag{14}$$

Also an initial value of the pore pressure is given

$$p^f = 0 \text{ by } t = 0. \tag{15}$$

An initial value of the pore pressure in the final solution is absent, because of we consider the situation at $t > 0$ only. Never the less it is reasonable to accept its some reasonable value to avoid the singularity in the initial point.

Let us consider the equilibrium condition of a rupture in the vicinity of the hydrofracture beak ignoring the crack and pore influence on the rock strength. In this vicinity we state the cylindrical coordinate system (r, φ) and write out the main members of an asymptotic formulae for the tensile fracture [12]:

$$\begin{aligned}\hat{\sigma}_x &= (K_1 / \sqrt{2\pi r}) \cos(\varphi/2) \left[1 - \sin(\varphi/2) \sin\left(\frac{3}{2}\varphi\right) \right], \\ \sigma_y &= (K_1 / \sqrt{2\pi r}) \cos(\varphi/2) \left[1 + \sin(\varphi/2) \sin\left(\frac{3}{2}\varphi\right) \right], \\ \tau_{xy} &= (K_1 / \sqrt{2\pi r}) \sin(\varphi/2) \cos(\varphi/2) \cos\left(\frac{3}{2}\varphi\right), \\ u_x &= (K_1 / \mu) \sqrt{2\pi r} \cos(\varphi/2) \left[(1 - 2\sigma) + \sin^2(\varphi/2) \right], \\ u_y &= (K_1 / \mu) \sqrt{2\pi r} \sin(\varphi/2) \left[2 - 2\sigma - \cos^2(\varphi/2) \right].\end{aligned}\tag{16}$$

Here $\hat{\sigma}_i$ ($i = x, y$), τ_{xy} are the principal and shear stress components, σ is the Poisson's ratio. Let us point the coordinate axes according to the central crack surface. From these formulae the expression for fracture profile in the vicinity of its tip is

$$H = \frac{K'_1}{E'} \sqrt{L - x_1} \quad \text{for } 8L - x_1 \ll L, E' = \frac{E}{\pi(1 - \sigma^2)}, K'_1 = \frac{4\sqrt{2}K_1}{\pi\sqrt{\pi}}.\tag{17}$$

We consider the equilibrium fracture state, which obeys to Irwin's criterion for brittle rupture

$$K_1 = K_c.\tag{18}$$

The main problem is to construct the hydraulic fracture model with a double porosity. At the boundary conditions adopted above the hydraulic fracture have some specification according the classic literature [8–10]. The main point is that the poroelastic medium is divided into two regions – the outside one and the boundary layer. The outside region is elastic with an undrainage modulus of elasticity. The one-dimension boundary layer allows some simplifications.

It is reasonable to admit that an analogous situation appears in the porous medium with a double porosity. Just as in citing papers the outside region is elastic with the non-drainage modulus of elasticity. The thin boundary layer with the specific properties arises near a fracture. The medium in this layer come into degeneracy and become jointing only without pore component (which actually has no time to form).

This situation would possible because of we selected the simplest toughness-dominated regime, which appears at the initial stage of the evolution fracture. It

describes with Irwin's criterion (18) in the crack tip. Both solution areas – outer region and boundary layer – are reduced to the known flat solutions for the usual poroelastic medium with a single porosity.

4 Boundary Layer in Hydrofracture

In this section the main aim is movement in a boundary layer at the initial evolution stage. That is why we override the redundant indexes and use the vocabulary and denominations for a usual poroelastic medium with the single pore system. In this relation following papers [8–10] let us decompose all magnitudes on the constituents:

$$\begin{aligned} \mathbf{u} &= \mathbf{u}^{(0)} + \mathbf{u}^{(1)}, p^f = p^{(0)} + p^{(1)}, \xi = \xi^{(0)} + \xi^{(1)}, \mathbf{u}^{(0)} = \nabla \Phi^{(0)}, \\ \mathbf{s} &= \mathbf{s}^{(0)} + \mathbf{s}^{(1)}, p^{(0)} \equiv p. \end{aligned} \quad (19)$$

One constituent (with upper index (0)) is potential and another one (with upper index (1)) is elastic only. These constituents have a simple physical meaning, related with magnitude ξ . The zero constituent corresponds a fluid replacement through the elementary volume boundary. It enters in the percolation equation in the fracture space. The first constituent is related with media displacement without a percolation, i.e. it is described with the usual elasticity theory.

Potential $\Phi^{(0)}$ obeys to the Poisson's equation and boundary condition

$$\Gamma_{\text{int}} : \nabla^2 \Phi^{(0)} = \theta^{(0)}, \mathbf{n} \cdot \nabla \Phi^{(0)} = 0, \quad (20)$$

which eliminates the arbitrariness in a displacement division into components.

Let us set the decomposition (19) in the equation (11). Taking into account above mentioned we receive the movement equation for every component:

$$\left(\frac{\partial}{\partial t} - \kappa_p \nabla^2 \right) \xi^{(0)} = 0, \kappa_p = \frac{k(K_u - K) \left(K + \frac{4}{3} \mu \right)}{\eta \alpha_e^2 \left(K_u + \frac{4}{3} \mu \right)}, \quad \text{a)}$$

$$(\lambda_u + 2\mu) \nabla \theta^{(0)} - \frac{(K_u - K)}{\alpha_e} \nabla \xi^{(0)} = 0, \xi^{(0)} = \xi = \frac{\alpha_e^2 p^{(0)}}{K_u - K} + \alpha_e \theta^{(0)}, \quad \text{b)} \quad (21)$$

$$\mu \nabla^2 \mathbf{u}^{(1)} + (\lambda_u + \mu) \nabla \theta^{(1)} = 0, \xi^{(1)} = \frac{\alpha_e^2 p^{(1)}}{K_u - K} + \alpha_e \theta^{(1)} \equiv 0. \quad \text{c)}$$

It is necessary to mark that the undrainage mode of an elastic component does not mean a fluid movement absence. The fact is that the fluid transfer through a

boundary of an elementary volume is impossible (it agrees with value $\xi = \xi^{(1)}$). As much as crack can move, the mutual fluid transition in the boundary layer takes place (from cracks into pores and backwards). In this case the nontrivial equations of a double porosity theory take place.

Never the less on the initial stage crack evolution (that we constrain ourselves) the elastic constituent in the boundary layer is absent. Due to this reason the movement equations are simplified essentially. In particular the elastic equation component (21c) is simplified and the penetration equation component is degenerated.

Let us transform these equations following to the citing above known considerations. Then we can receive the next expressions

$$\begin{aligned} \left(K_u + \frac{4}{3}\mu \right) \theta^{(0)} - \frac{(K_u - K)}{\alpha_e} \xi^{(0)} = 0, \alpha_e p^{(0)} = \left(K + \frac{4}{3}\mu \right) \theta^{(0)}, \quad \text{a)} \\ \xi^{(0)} = \alpha_e^2 \left[\frac{1}{K + \frac{4}{3}\mu} + \frac{1}{(K_u - K)} \right] p^{(0)}, \quad \text{b)} \quad (22) \\ \nabla^2 p^{(1)} = \nabla^2 \theta^{(1)} = 0, \theta^{(1)} = -\frac{\alpha_e p^{(1)}}{K_u - K}. \quad \text{c)} \end{aligned}$$

Hence the system (22) is reduced to the analogous system for the usual poroelastic medium. To solve this problem in the main poroelastic region one should to solve the classic elastic theory problem for equations (21c) with the corresponding boundary conditions and addition conditions (22c). In the boundary layer the equations (21a), (22a) are accomplished. Some of them are the algebra expressions in fact. Let us transform (21a) considering (22b)

$$\left(\frac{\partial}{\partial t} - \kappa_p \nabla^2 \right) p^{(0)} = 0. \quad (23)$$

Also taking into account (22c) and boundary condition (13b) we receive the boundary condition for this equation

$$\Gamma^\pm : p^{(0)} = p_c - p^{(1)} = p_c + \frac{K_u - K}{\alpha_e} \theta^{(1)} \equiv \tilde{p}^{(0)}. \quad (24)$$

The boundary layer in the medium with double porosity is a result of the difference between fluid velocity in the crack and in the porous medium. For simplicity let us go to the nondimensional values $(x_1, x_2) \rightarrow (x, y)$. In this case one can stretch the vertical coordinate in the equation (23) near boundary

$$y \rightarrow z = \frac{y}{\varepsilon_2}. \tag{25}$$

Consider the fact that an initial value for the perturbation in a boundary layer moves together with the crack tip. In every point of a fracture with coordinate x the time of water entry from a fracture into the environment is counted off from moment $t_0(x)$ – a tip arrival time in this point. From this time the boundary layer starts to increase. The function $t_0(x)$ can be received from a solution of the corresponding problem.

That is why let us introduce two times – the own time t' for every point of crack surface and “laboratory” time t , which is counted out from the crack arrival. They are related with the ratio

$$t'(x,t) = t - t^0(x). \tag{26}$$

Let us transform (23) with help of (25) and (26). Neglecting it’s small members in result we obtain the boundary problem for a filtration component

$$\left(\frac{\partial}{\partial t'} - \frac{\partial^2}{\partial z^2} \right) p^{(0)}(z,t') = 0. \tag{27}$$

There is only the own one time in this equation. Also, we have the boundary and asymptotic conditions for (27)

$$\begin{aligned} p^{(0)} &= p^{(0)}(x,t') \text{ at } z \rightarrow 0, & \text{a)} \\ p^{(0)} &\rightarrow 0 \text{ at } z \rightarrow \infty. p^{(0)} \rightarrow 0 \text{ at } z \rightarrow \infty. & \text{b)} \end{aligned} \tag{28}$$

The problem (27), (28) is determined in the boundary layer. One can receive the analytical solution

$$p^{(0)} = p^{(0)}(x) \operatorname{erfc} \left(\frac{z}{\sqrt{4t'}} \right) = p^{(0)}(x) \left(1 - \frac{2}{\sqrt{\pi}} \int_0^{\frac{z}{\sqrt{4t'}}} e^{-\xi^2} d\xi \right). \tag{29}$$

It is the final phase of solution for the given statement. The analogous solution (type of (29)) is represented in [8–10] in flat and cylindrical symmetric variants. The main distinguish is related with a substance. Here we considered the poroelastic medium with double porosity.

5 Conclusion

Barenblatt [6] was the first who supposed the simplified model with the double porosity. However in [6] there is no correct investigation of the medium with poroelastic properties. In contrast, this work provides a correct solution of the problem about crack propagation in the poroelastic medium for the first time. The elastic component of a problem in the outer region is described with the usual elasticity equations with an undrainage modulus. In the boundary layer there is the one dimension parabolic equation with natural boundary conditions (23), (27).

It is supposed that the small viscosity liquid is pumped down in a fracture. With all this the water penetrates a poroelastic medium. The special method to decompose the main problem on set of simple incompletely related problems [8–10] was used in this model. This phenomenon touches not only a poroelasticity process in the bearing strata but also the law of fracture motion including the boundary layer about it. A splitting of the initial equation system on two equation groups is the substance element of this procedure.

The incomplete coupling principle admits using the various generations of this problem effectively, for example related with the nonisothermal mode or physical chemistry phenomena in the thin boundary layer along a crack. The usual approach using complex integro-differential equations does not allow such possibility.

Acknowledgments This work was supported by the Russian Science Foundation, project № 15-11-00021.

References

1. Biot MA (1962) Mechanics of deformation and propagation in porous media. *J Appl Phys* 33(4):1482–1498
2. Gassmann F (1956) *Über die Elastizität poröser Medien*. Mitteilungen aus dem, vol 17. Institute für Geophysik, Zurich, pp 1–23
3. Rice J (1980) The mechanics of earthquake rupture. In: *Physics of the Earth's interior*. Amsterdam.
4. Wilson RK, Aifantis EC (1982) On the theory of consolidation with double porosity. *Int J Eng* 20(9):1009–1035
5. Detournay E, Cheng AH-D (1993) Fundamentals of poroelasticity. Chapter 5. In: Fairhurst C (ed) *Comprehensive rock engineering: principles, practice and projects*. Analysis and design method, vol. II. Pergamon Press, pp 113–171
6. Coussy O (2004) *Poromechanics*. Wiley, p 298
7. Barenblatt GI, Entov VM, Rizhik VM (1984) *Fluid and gas movement in the nature beds*. Nedra, Moscow, p 208
8. Karakin AV (2006) Hydraulic fracturing in the crust. *Izv Phys Solid Earth* 42:652–657. <https://doi.org/10.1134/S1069351306080039>
9. Karakin AV, Ramasanov MM, Borisov VE (2017) Incompletely coupled equation of hydraulic fracturing. *Math Models Comput Simul* 29(6):115–134. <https://doi.org/10.1134/S2070048218010076>

10. Karakin AV, Ramasanov MM, Borisov VE, Men'shov IS, Savenkov EB (2017) Self-similar solution of a hydraulic fracture problem for a poroelastic medium. *Math Models Computer Simul* 29(4):59–74. <https://doi.org/10.1134/S2070048217060060>
11. Adachi JI, Detournay E (2008) Plane strain propagation of a hydraulic fracture in permeable rock. *Eng Fract Mech* 75:4666–4694. <https://doi.org/10.1016/j.engfracmech.2008.04.006>
12. Muskhelishvili NI (1966) Some basic problems of the mathematical theory of elasticity. Nauka, Moscow, p 707

Incompletely Coupled Equations of Hydraulic Fracturing in Poroelastic Medium



Andrey V. Karakin and Mukamay M. Ramazanov

1 Introduction

Currently, the fluid-driven fracturing of an oil and gas reservoir (hydrofracture, HF) is one of the most popular methods of increasing oil recovery and it plays an important role in hydrocarbon production technologies. This process consists of creating an extended large-scale fracture in an oil and gas reservoir by injecting fluid into it. The analysis of this process, therefore, requires a self-consistent description of the mechanical and flow processes in the reservoir, the flow of the fluid in the fracture, and the actual propagation of the fracture.

Hydro-driven cracks are also naturally occurring phenomena resulting from the migration of aqueous solutions in the crust. A magmatic fracture can only be caused by natural phenomena, which cannot be controlled or investigated by instrumental methods used in hydraulic fracturing. In addition, the parameters of the magma fracture are significantly different from the parameters of hydraulic fracturing. Nevertheless, the simplification of the boundary-value problem associated with the splitting of equations proves useful in this case, too. It allows us to perform more profound investigations into the core of the multifactor physical processes by analytical and geological methods. For the sake of simplicity, we will only talk about hydraulic fracturing, while also having in mind the possible application of the method to the phenomena of a magmatic fracture.

We investigated both the dynamics of the fluid in a fracture itself and the stress state and flow in the poroelastic environment (formation) with the fracture. The

A. V. Karakin (✉)

Keldysh Institute of Applied Mathematics, Russian Academy of Sciences, Moscow, Russia

M. M. Ramazanov

Institute for Geothermal Research, Dagestan Scientific Center, Russian Academy of Sciences, Makhachkala, Russia

coupled external and internal problems are considered. In the outer region, the poroelastic medium is assumed to be homogeneous and isotropic and disturbances are damped at infinity. The fractures are assumed to be equilibrium.

The complexity of the HF processes and their simulation is due to the fact that the fracture propagation mode can significantly change during its development. At the initial stage of fracture propagation, the main energy of motion is spent on destroying the rock. At the stage of the mature development of the fracture, the energy dissipation per unit time in the viscous layer inside the fracture may significantly exceed the energy dissipated at the tip of the fracture. This requires significant changes in the type of model and the methods for its description which results in the so-called toughness model and viscosity dominated one respectively [1, 3–9]. In practice, the relatively specific role of these factors can vary depending on the change in the mode of the fracture motion. In a direct numerical calculation, it is very difficult to trace the dominant factor (not just in the fracture itself).

Due to specifics of HF dynamics, most of the applied software packages use simplified models [2] created in the middle of the last century. The later models [1, 3–9] are more accurate but their computational speed is not sufficiently high for commercial use. The problem is further aggravated by the difficulty in controlling errors in the numerical model, which can be purely computational or caused by the model's inaccuracy.

In many HF models there is a region (the so-called lag) near the tip of the fracture, which is free from the fluid injected into the fracture. If the host medium is purely elastic, the lag is filled only with air or gas. In a poroelastic medium, the lag can be filled with a liquid of different properties in comparison with the injected fluid. The latter is considered in [8], and it is also shown that the lag exerts a perceptible influence only on its nearest neighborhood. Therefore, for simplicity, we neglect the existence of the lag in our study.

There are relatively few HF models with poroelastic background media. Usually, they only study some aspects related to the poroelastic properties of the medium. For instance, [9] considers the generalization of the Khristianovich–Zhel'tov–Geertsma–De Klerk (KGD) model for the case of a poroelastic environment. It assumes that the disturbance created in a poroelastic medium by a fracture only extends to a narrow conical region (boundary layer) adjacent to the fracture. This form of perturbation (resembling the shock wave following a rocket) is due to the fact that the characteristic time of disturbances in a poroelastic medium is much greater than the characteristic time of the fracture motion. Based on the specifics of the parabolic equation and proceeding from purely dimensional considerations, it is easy to obtain the parameters of the boundary layer. The fluid flow from the fracture is determined by the reverse root dependence on time. The paper [9] does not take into account that there is also a perturbation in the boundary layer due to the imbalance dynamic processes in the poroelastic medium and in the fracture (in addition to the shock wave).

The study [4] is also of interest. It considers a crack in a poroelastic medium based on modern models. The fluid flow from a fracture into the poroelastic medium is regarded based on some “obvious” qualitative considerations. It is presumed that

this leakage is actually postulated as an inverse root dependence on time. This may seem quite obvious if we take into account the boundary layer near the surface of the crack and the one-dimensional nature of the flow in this layer. The described simplified models are basically unsuitable for the analysis of numerous important applied problems, for example, the development of a fracture under the reorientation of reservoir stress fields due to the injection and extraction of the formation fluid, as well as for the analysis of the multiple HF cracks development in horizontal wells.

In this paper, we use an approach based on resolving the original solution into its components [10]. It does not imply any priori assumptions about the form of the solution. The inverse root dependence in the present paper arises as a result of the correct approach and coincides with the term presented in [4]. However, the study [4] fails to allow for the additional term brought about by the discrepancy between the elastic and flow components. Evidently, the “obvious” intuitive considerations are hardly able to predict the existence of an additional term. It can be attributed to the fact that in the elastic component there are own fluid flows associated with the compression of a poroelastic medium in the absence of a global fluid transfer. Importantly, this additional term cannot be represented by reverse root dependence. Even if it is small in some cases, it does not seem entirely reasonable to leave it out of consideration. The chemical and physicochemical processes at the crack boundary proceed quite differently in models with and without allowance for this term.

Phenomena in the poroelastic medium remain analogous phenomena in the elastic medium [11] in many respects. Never the less the poroelastic medium has its own specific aspects. So, the analytical investigation of the HF model with a poroelastic medium appears to be highly relevant. Its purpose is to avoid the difficulties and to facilitate the verification of the numerical calculations. It seems to be reasonable transforming the original HF model to such a simple form, which makes it possible to single out certain aspects and study them separately. This means the possibility of reducing the coupled problem to a system of uncoupled components. Formally, this is not possible because the problem type cannot be changed without violating physical principles. However, this difficulty can be circumvented by applying the principle of incomplete coupling [10], which solves this problem.

This principle is that using identical transformations and natural simplifications (which do not limit the generality of the problem formulation) to reduce the coupled problem to sequential stages of solving the known problems of mathematical physics. Actually, at each stage an independent problem is solved, and the solution obtained at the previous stage enters the right-hand side of the solution as a known quantity. This approach allows us to save significant computing resources and effectively investigate every aspect of this problem, including special areas (for example, the tip of a fracture) and the change in the evolution modes of a fracture. In contrast to the cited works, we present a sufficiently rigorous solution of the problem on a fracture in a poroelastic medium free from simplifications and hypotheses.

The principle of incomplete coupling enables the use of ready-made algorithms or their slight modifications. It also makes it possible to manipulate individual blocks of the program both for debugging the codes and for investigating the

corresponding physical processes. In the future, the qualitative simplification of the numerical methods for solving HF problems can help to create a new generation of effective algorithms. Computationally, the principle of incomplete coupling can serve as a basis for the creation of new physics-based precondition to develop effective algorithms for solving the equations of a completely coupled problem of poroelasticity applied to the fracture.

2 Formulation of the External Problem

We consider the change in the state of a poroelastic medium in a three-dimensional space Ω due to a horizontal crack growing inside it. Let x_3 be the vertical coordinate of the Cartesian coordinate system $\mathbf{x} = \{x_1, x_2, x_3\}$. We assume that a weightless porous medium is homogeneous and isotropic and the pores are completely filled with a single-phase low-compressible liquid. We confine ourselves to isothermal quasistationary (i.e. inertialess) poroelastic processes, which are described by the Biot equations in their modern formulation [12–14], i.e.

$$\Omega : \nabla \cdot \boldsymbol{\sigma} = 0, \boldsymbol{\sigma} = \boldsymbol{\sigma}^{ef} - \alpha_e p^f \mathbf{I}, \rho = (1-f)\rho^s + f\rho^f, \mathbf{I} \equiv \{\delta_{ij}\} \quad (1a)$$

$$\hat{\boldsymbol{\sigma}}^{ef} = 2\mu\hat{\boldsymbol{\varepsilon}} + \lambda\theta\hat{\mathbf{I}} \quad \theta \equiv \hat{\boldsymbol{\varepsilon}} : \hat{\mathbf{I}}, K = \lambda + \frac{2}{3}\mu, \quad (1b)$$

$$\nabla p^f = -\frac{\eta}{k}\mathbf{s}, \quad \hat{\boldsymbol{\varepsilon}} \equiv \{\varepsilon_{ij}\} = \frac{1}{2} \left\{ \frac{\partial u_i}{\partial x_j} + \frac{\partial u_j}{\partial x_i} \right\}, \quad (1c)$$

$$\frac{\partial}{\partial t} [(1-f)\rho^s] + \nabla \cdot [(1-f)\rho^s \mathbf{w}^s] = 0, \quad \frac{\partial}{\partial t} (\rho^f f) + \nabla \cdot (\rho^f f \mathbf{w}^f) = 0, \quad (1d)$$

$$p^s = K^s \frac{\Delta p^s}{\rho^s}, \quad p^f = K^f \frac{\Delta p^f}{\rho^f}, \quad \Delta p^s \equiv p^s - p_0^s, \Delta p^f \equiv p^f - p_0^f, \quad (1e)$$

where $\hat{\boldsymbol{\sigma}}$ and $\hat{\boldsymbol{\sigma}}^{ef}$ are tensors of the total and effective stresses; $\hat{\mathbf{I}}$ is a unit tensor; p^f denotes the pore pressure; $\hat{\boldsymbol{\varepsilon}}$ is a small-strain tensor; θ is the bulk compression of the medium; α_e is the coefficient ahead of the pressure introduced by Biot; \mathbf{u} , \mathbf{w} are the displacement and velocity of the porous medium; $\mathbf{s} \equiv f(\mathbf{w}^f - \mathbf{w})$ denotes the filtration rate; \mathbf{w}^f is the fluid phase velocity; ρ , ρ^s , ρ^f are the densities of the two-phase medium, as well as of the matrix and fluid phases; λ , μ are the Lamé coefficients; K is the drainage modulus of the bulk; f is the porosity; k and η are the coefficients of fluid permeability and fluid viscosity which are assumed to be constant; p^s is the pressure in the matrix phase; K^s and K^f are the bulk modules of the matrix and fluid

phases. The symbol Δ denotes the deviation of a given quantity from an equilibrium state (i.e., from a state of rest or from a background state), which is designated by the subscript zero.

In the outer space Ω , the crack is the surface of fracturing Γ_{int} . In the plane variant, the crack length is $2L$, and in the three-dimensional space the fracture surface has two sizes $2L_1$ and $2L_2$ with the characteristic value $2L$. Nevertheless, the crack has a small but finite thickness $H(x_1, x_2, t)$ ($H < L$) and the space inside it will be called the internal region Ω_{int} . It extends along the horizontal plane $x_3 = 0$ and lies within $-H < x_3 < H$, where $2H$ is the crack's opening (thickness) depending on the longitudinal coordinates and time. The liquid enters the fracture through the well, which in this approximation can be regarded as a concentrated source, and flows out of it into the outer region through the horizontal boundaries. The fracture – environment system itself is symmetrical about the vertical coordinate.

The HF fracture is characterized by a set of small parameters. Both the external and internal problems contain a small parameter $\varepsilon_1(t) = H(0, 0, t)/L(t)$, which is of the order of elastic deformation magnitude in the outer region. In the external problem, the expansion with respect to the small parameter implies linearizing the equations of motion. Inside the cavity we use the approximation of the lubricating layer for the equations of hydrodynamics in the absence of inertial terms. It is characterized by the same small parameter. As the fracture grows, this parameter can change accompanied by the respective change in the scale of the other quantities. Therefore, it is reasonable to use the limiting value of this parameter (as well as the other ones). This is denoted by an asterisk and corresponds to the maximum size of the crack, i.e.,

$$\varepsilon_1 = \theta^* = \frac{H^*}{L^*}, \text{ where } H^* = H_{\text{max}}, L^* = L_{\text{max}} \tag{2}$$

Here $H_{\text{max}}, L_{\text{max}}$ are the maximum values of the quantities H and L .

In the external problem, the flowing pressure of the fluid in the fracture p_c is assumed to be set at the boundary Γ_{int} and in the internal problem it is the sought quantity. From the viewpoint of the internal problem, there are two boundary surfaces of the fracture, the upper and lower ones, denoted, respectively, as Γ_{int}^\pm . At these boundaries, the boundary conditions are given for the strains in the outer region and continuity conditions for displacement \mathbf{u} and velocity \mathbf{w} :

$$\Gamma_{\text{int}}^\pm : \mathbf{n} \cdot \hat{\boldsymbol{\sigma}} \cdot \mathbf{n} = -p_c, \mathbf{m}^{(i)} \cdot \hat{\boldsymbol{\sigma}} \cdot \mathbf{n} = 0, (i = 1, 2), \tag{3a}$$

$$p^f = p_c, \tag{3b}$$

$$[\mathbf{u}] = 0, [\mathbf{w}] = 0, \tag{3c}$$

where \mathbf{n} and $\mathbf{m}^{(i)}$ are normal and tangent (orthogonal) unit vectors, respectively. The brackets denote the jump in the values at both boundaries Γ_{int}^\pm . The first condition

in (3c) in effect determines the opening of the crack and the second one is the fluid no-slip condition for the internal problem.

At infinity, the perturbations are damped, i.e.,

$$\hat{\sigma} \rightarrow 0, \mathbf{s} \rightarrow 0, \nabla \cdot \mathbf{p}^f \rightarrow 0 \text{ at } (x_1^2 + x_2^2 + x_3^2) \rightarrow \infty. \tag{4}$$

We also set the initial value of the pore pressure, i.e.,

$$p^f = 0 \text{ at } t = 0. \tag{5}$$

In the neighborhood of the fracture tip, the flat approximation can be used if a vertical section is drawn perpendicularly to the fracture boundary. In this plane, a cylindrical coordinate system is used and we obtain asymptotic formulas for normal fractures under the conditions of plane deformation equation reference goes here [11], i.e.,

$$\begin{aligned} \sigma_x &= (K_1 / \sqrt{2\pi r}) \cos(\varphi / 2) \left[1 - \sin(\varphi / 2) \sin\left(\frac{3}{2}\varphi\right) \right] + f_x(r, \varphi), \\ \sigma_y &= (K_1 / \sqrt{2\pi r}) \cos(\varphi / 2) \left[1 + \sin(\varphi / 2) \sin\left(\frac{3}{2}\varphi\right) \right] + f_y(r, \varphi), \\ \tau_{xy} &= (K_1 / \sqrt{2\pi r}) \sin(\varphi / 2) \cos(\varphi / 2) \cos\left(\frac{3}{2}\varphi\right) + f_{xy}(r, \varphi), \\ u_x &= (K_1 / \mu) \sqrt{2\pi r} \cos(\varphi / 2) \left[1 - 2\sigma + \sin^2(\varphi / 2) \right], \\ u_y &= (K_1 / \mu) \sqrt{2\pi r} \sin(\varphi / 2) \left[2 - 2\sigma - \cos^2(\varphi / 2) \right]. \end{aligned} \tag{6}$$

Here, K_1 is the stress intensity factor and σ is Poisson’s ratio, through $f(r, \varphi)$ with different indexed designate regular parts of the strain tensor components.

These formulas yield the following expression for the fracture profile in the vicinity of its tip if the coordinate axes are oriented according to the section:

$$H = \frac{K_1'}{E'} \sqrt{L - x_1} \text{ at } L - x_1 \ll L, E' = \frac{E}{\pi(1 - \sigma^2)}, K_1' = \frac{4\sqrt{2}K_1}{\pi\sqrt{\pi}}. \tag{7}$$

We consider an equilibrium state of the fracture obeying the Irwin criterion of brittle failure

$$K_1 = K_{IC}. \tag{8}$$

Here, K_{IC} is the fracture toughness (fracture viscosity) characterizing the material resistance to fracturing.

We introduce a quantity ξ (which is called the relative content of the fluid) and the so-called no drainage elasticity modulus K_u by the following formulas [12, 13]:

$$\xi \equiv \frac{1}{\rho_0^f} \Delta(f \rho^f) + f_0 \theta, \frac{\alpha_e^2}{K_u - K} = \frac{(\alpha_e - f_0)}{K^s} + \frac{f_0}{K^f},$$

$$K_u - K = \lambda_u - \lambda, K_u = \lambda_u + \frac{2}{3} \mu, \alpha_e = 1 - \frac{K}{K_s}.$$

The quantity ξ is related to pore pressure, volumetric compression, and elastic moduli by the correlation

$$\xi = \frac{\alpha_e^2 p^f}{K_u - K} + \alpha_e \theta. \tag{9a}$$

Then the continuity equation for the fluid phase (1d) can be written in the equivalent form as

$$\frac{\partial \xi}{\partial t} + \nabla \cdot \mathbf{s} = 0. \tag{9b}$$

As it is known [10, 12–14], proceeding from (9) and the equations of motion, the following piezoconductivity equation can be derived for the quantity ξ :

$$\left(\frac{\partial}{\partial t} - \kappa_p \nabla^2 \right) \xi = 0, \tag{10a}$$

where

$$\kappa_p = \frac{k(K_u - K) \left(K + \frac{4}{3} \mu \right)}{\eta \alpha_e^2 \left(K_u + \frac{4}{3} \mu \right)}. \tag{10b}$$

The equations of motion of the poroelastic medium (1) can be expressed in terms of displacements in two equivalent forms:

$$\mu \nabla^2 \mathbf{u} + (\lambda + \mu) \nabla \theta - \alpha_e \nabla p^f = 0, \tag{11a}$$

$$\mu \nabla^2 \mathbf{u} + (\lambda_u + \mu) \nabla \theta - \frac{\lambda_u - \lambda}{\alpha_e} \nabla \xi = 0. \tag{11b}$$

Subject to $p^f = 0$, Eq. (11a) is a description of drainage mode and Eq. (11b) under $\xi = 0$ describes the non-drainage mode of motion in a poroelastic medium.

As a result of the assumptions made, the boundary condition (3a) takes a simpler form:

$$\Gamma_{\text{int}} : \sigma_{33}|_{x_3=0} = -p_c, \sigma_{i3}|_{x_3=0} = 0. \quad (12)$$

The solution of the poroelasticity problem for the outer region can be represented by the well-known integral expression in terms of Green's function [13, 14]:

$$\Gamma_{\text{int}} : \sigma_{33}|_{x_3=0} = -p_c = - \int_{-\infty}^t dt' \int_{\Omega} \gamma(\mathbf{x}' - \mathbf{x}, t - t') H(\mathbf{x}') d\mathbf{x}'. \quad (13)$$

The last expression shows that a poroelastic medium has memory properties associated with filtering processes. In other words, Green's function $\gamma(\mathbf{x}' - \mathbf{x}, t - t')$ includes the time dependence.

In the general case, the equation of water motion inside a crack takes the form of "lubrication layer" equation

$$\frac{\partial H}{\partial t} - \frac{1}{3\eta} \nabla \cdot (H^3 \nabla p_c) = -Q_L + \frac{1}{2} Q(t) \delta(\mathbf{x} - \mathbf{x}_0). \quad (14)$$

Here $Q(t)$ is a fluid flow that enters the fracture through the well, Q_L is a fluid stream from the fracture in the surrounding medium through its walls.

3 Splitting up the External Problem

In this section, we consider the external problem in the space Ω with a cut Γ_{int} in it, which has no internal structure. The implementation of the principle of incomplete coupling begins with the expansion of the displacement in the outer region into two components. Following [12, 13, 15], we set.

$$\mathbf{u} = \mathbf{u}^{(0)} + \mathbf{u}^{(1)}, \quad p^f = p^{(0)} + p^{(1)}, \quad \xi = \xi^{(0)} + \xi^{(1)}, \quad \mathbf{u}^{(0)} = \nabla \Phi^{(0)}, \quad \mathbf{s} = \mathbf{s}^{(0)} + \mathbf{s}^{(1)} \quad (15)$$

so that one of them $u^{(0)}$ is potential and the other one $u^{(1)}$ corresponds to displacements in the absence of flow.

The potential $\Phi^{(0)}$ satisfies the Poisson equation and the boundary condition

$$\nabla^2 \Phi^{(0)} = \theta^{(0)}, \quad (16a)$$

$$\Gamma_{\text{int}} : \mathbf{n} \cdot \nabla \Phi^{(0)} = 0. \quad (16b)$$

$$\bar{\Gamma}_\infty : \bar{\Phi}^{(0)} = 0. \tag{16c}$$

The boundary condition (16b) eliminates the arbitrariness in splitting the displacement into components.

The substitution of the expansion (15) into Eqs. (10a) and (11b) yields the equations of motion for each component, i.e.,

$$\left(\frac{\partial}{\partial t} - \kappa_p \nabla^2 \right) \xi^{(0)} = 0, \tag{17a}$$

$$(\lambda_u + 2\mu) \nabla \theta^{(0)} - \frac{(K_u - K)}{\alpha_e} \nabla \xi^{(0)} = 0, \xi^{(0)} = \xi = \frac{\alpha_e^2 p^{(0)}}{K_u - K} + \alpha_e \theta^{(0)}, \tag{17b}$$

$$\mu \nabla^2 \mathbf{u}^{(1)} + (\lambda_u + \mu) \nabla \theta^{(1)} = 0, \xi^{(1)} = \frac{\alpha_e^2 p^{(1)}}{K_u - K} + \alpha_e \theta^{(1)} \equiv 0. \tag{17c}$$

The non-drainage mode of the elastic component by no means implies the absence of flow. The gradient $p^{(1)}$ and the filtration rate $\mathbf{s}^{(1)}$ according to (17c) differ from zero and are closely related to the volumetric strain of the matrix. The non-drainage mode essence is that there is no fluid transfer, $\xi^{(1)}$, through the boundaries of the elementary volume even in the presence of flow inside it.

Now we transform these equations. We perform the divergence operation on Eq. (17c) and integrate the first Eq. (17b). Without loss of generality, we set the integration constant in the last equation to zero. The combination of these expressions yields coupled relations between these quantities:

$$\left(K_u + \frac{4}{3} \mu \right) \theta^{(0)} - \frac{(K_u - K)}{\alpha_e} \xi^{(0)} = 0, \alpha_e p^{(0)} = \left(K + \frac{4}{3} \mu \right) \theta^{(0)},$$

$$\xi^{(0)} = \alpha_e^2 \left[\frac{1}{K + \frac{4}{3} \mu} + \frac{1}{(K_u - K)} \right] p^{(0)}, \tag{18a}$$

$$\nabla^2 p^{(1)} = \nabla^2 \theta^{(1)} = 0, \theta^{(1)} = - \frac{\alpha_e p^{(1)}}{K_u - K}. \tag{18b}$$

The quantities $\theta^{(\alpha)}$ and $p^{(\alpha)}$ ($\alpha = 0, 1$) are not independent but these dependencies vary for different components. For this reason, splitting the equations of poroelasticity into components is not a trivial procedure.

As a result of the relation (18a), the piezoconductivity Eq. (16a) is simplified as follows:

$$\left(\frac{\partial}{\partial t} - \kappa_p \nabla^2 \right) p^{(0)} = 0. \quad (19)$$

Taking into account the boundary condition (3b), and (18b), we obtain.

$$\Gamma_{\text{int}} : p^{(0)} = p_c - p^{(1)} = p_c + \frac{K_u - K}{\alpha_e} \theta^{(1)} \equiv \tilde{P}^{(0)}. \quad (20)$$

Here, we introduce a new quantity, $p^{(1)}$, which is the value of the flow component of the pore pressure at the boundary. It is determined by the elastic deformations of the matrix and by the pressure in the fracture.

The expression written out for the total stress tensor is.

$$\hat{\sigma} = \hat{\sigma}^{(0)} + \hat{\sigma}^{(1)}, \text{ where } \hat{\sigma}^{(0)} = 2\mu \left(\nabla \otimes \nabla \Phi^{(0)} - \theta^{(0)} \hat{I} \right) - \alpha_e p^{(0)} \hat{I},$$

$$\hat{\sigma}^{(1)} = 2\mu \hat{\varepsilon}^{(1)} + \lambda_u \theta^{(1)} \hat{I} - \alpha_e p^{(1)} \hat{I}.$$

We also transform the boundary conditions (3a) taking into account the geometry of the fracture:

$$\Gamma_{\text{int}} : \mathbf{n} \cdot \hat{\sigma}^{(1)} \cdot \mathbf{n} = -p_c - 2\mu \left(\frac{\partial^2 \Phi^{(0)}}{\partial x_3^2} - \theta^{(0)} \right), \quad (21a)$$

$$\mathbf{m}^{(i)} \cdot \hat{\sigma}^{(1)} \cdot \mathbf{n} = -2\mu \frac{\partial^2 \Phi^{(0)}}{\partial x_i \partial x_3}, i = 1, 2. \quad (21b)$$

Equation (16a) is transformed using second relation (18a):

$$\nabla^2 \Phi^{(0)} = \frac{\alpha_e p^{(0)}}{\left(K + \frac{4}{3} \mu \right)}. \quad (22)$$

Note that the boundary conditions for the pore pressure (20) and for stresses (21) include both components of these fields, which necessitates solving the coupled problem. At the same time, we are searching for the possibility to solve uncoupled

problems in a certain sequence, i.e., to pass to the procedure of incomplete coupling. The idea of this work is to attain this using the specific features of the HF model. The meaning of transformation (15) is that the equations of the potential (zero) component include all flow effects, and the first component represents the equations of elasticity theory without flow. This significantly simplifies the initial poroelasticity equations within the incomplete coupling scheme.

In this respect, we apply auxiliary arguments for simplicity and without loss of generality based only on a two-dimensional model. Let the fracture be an elliptic cavity with major and minor semiaxes a and b , respectively. Near the contour of the elliptic hole, under specified tensile stresses σ_{33} at infinity, we have a complex expression for displacements [16]:

$$2\mu(u_1 + iu_3) = -\sigma_{33}(1 - 2\sigma)x_1 + i2\sigma_{33}(1 - \sigma)\left(\frac{a}{b}\right)x_3. \tag{23}$$

In (23) we pass to the opening mode crack assuming $a = L, b \rightarrow 0$. This formula provides a good description of the fracture’s vicinity everywhere except at its tips where there are singularities as in (6). From this expression, the vertical displacements and strains near the crack boundary are much larger than their horizontal components. This means that on the right-hand side of both formulas (21), the horizontal derivatives are negligible in comparison with the vertical derivatives. As a result, these formulas are simplified, i.e.,

$$\Gamma_{\text{int}} : \mathbf{n} \cdot \hat{\boldsymbol{\sigma}}^{(1)} \cdot \mathbf{n} = \mathbf{n} \cdot \hat{\boldsymbol{\sigma}} \cdot \mathbf{n} = -p_c, \mathbf{m} \cdot \hat{\boldsymbol{\sigma}}^{(1)} \cdot \mathbf{n} = \mathbf{m} \cdot \hat{\boldsymbol{\sigma}} \cdot \mathbf{n} = 0. \tag{24}$$

After these transformations, time is included in the boundary-value problem for the elastic component only as a parameter. As a result, the boundary condition (24) for the elastic component is simplified taking into account (13):

$$\Gamma_{\text{int}} : -p_c = \sigma_{33}^{(1)}\Big|_{x_3=0} = \sigma_{33}\Big|_{x_3=0} = -\int_{\Omega} \gamma(\mathbf{x}' - \mathbf{x})H(\mathbf{x}')d\mathbf{x}'. \tag{25}$$

Due to the dynamic boundary conditions (25), the elastic component of the external problem is related to the internal problem only in terms of the quantities H and p_c . The first one characterizes elastic strains in the outer region, the second one is the pressure in the fracture, and the flow component of the external problem does not belong to the kernel of the integral expression (25). It can be assumed to be specified and known. This kernel includes the drainage bulk elasticity modulus, which effectively allows for the saturated porous structure of the medium. The kinematic conditions (3c) include both the elastic and flow components of the outer region. The boundary condition (16b) excludes the filtration component.

4 Self-Similar Solution

4.1 Transition to Dimensionless Variables

The procedure for the transition to dimensionless quantities in the system of split Eqs. (16)–(22) should be carried out separately for the filtration and elastic components, and also for the inner area of the fracture taking into account the coordination of the characteristic scales of the elastic and filtration components [17, 18]. We seek the solution of the split system in a self-similar form, i.e.,

$$\begin{aligned}
 t = T\tau, \mathbf{y} &= \frac{\mathbf{x}}{L(\tau)}, H(\mathbf{x}, t) = \varepsilon(\tau)L(\tau)\tilde{h}(\mathbf{y}), L(\tau) = L_0\sqrt{\tau}, \varepsilon(\tau) = \varepsilon_0\tau^\beta, \\
 u_i^{(1)}(\mathbf{x}, t) &= \varepsilon(\tau)L(\tau)\tilde{u}_i^{(1)}(\mathbf{y}), u_i^{(0)}(\mathbf{x}, t) = \varepsilon(\tau)L(\tau)\tilde{u}_i^{(0)}(\mathbf{y}), \\
 \hat{\varepsilon}^{(1)}(\mathbf{x}, t) &= \varepsilon(\tau)\hat{\varepsilon}^{(1)}(\mathbf{y}), \theta^{(1)}(\mathbf{x}, t) = \varepsilon(\tau)\tilde{\theta}^{(1)}(\mathbf{y}), \\
 p^{(1)}(\mathbf{x}, t) &= \frac{\varepsilon(\tau)E_u}{(1-\sigma_u^2)}\tilde{p}^{(1)}(\mathbf{y}), p^{(0)}(\mathbf{x}, t) = \frac{\varepsilon(\tau)E_u}{(1-\sigma_u^2)}\tilde{p}^{(0)}(\mathbf{y}), \\
 \hat{\sigma}^{(1)}(\mathbf{x}, t) &= \frac{\varepsilon(\tau)E_u\hat{\sigma}(\mathbf{y})}{(1-\sigma_u^2)}, p_c(\mathbf{x}, t) = \frac{\varepsilon(\tau)E_u\tilde{p}_c(\mathbf{y})}{(1-\sigma_u^2)}, \\
 Q &= Q_0q(\tau), Q_L = Q_0q_L(\mathbf{x}, t), q_L(\mathbf{x}, t) = -\frac{k\varepsilon(\tau)L(\tau)E_u}{\eta(1-\sigma_u^2)L_0^2}\tilde{q}_L(\mathbf{y}), \\
 \tilde{\mu} &= \frac{\mu(1-\sigma_u^2)}{E_u}, \tilde{\lambda}_u = \frac{\lambda_u(1-\sigma_u^2)}{E_u},
 \end{aligned} \tag{26}$$

where the tilde superscript denotes the respective dimensionless quantities, T is the time scale.

The physical meaning of expansion (15) and transformation (26) associated with it is that the elastic component behaves as a purely elastic medium with nondrainage moduli. The formal allowance for this fact significantly simplifies the calculations. By substituting (26) into (17c), we obtain the corresponding equation for dimensionless displacements, i.e.,

$$\tilde{\mu} \nabla^2 \tilde{\mathbf{u}}^{(1)} + \left(\tilde{\lambda}_u + \tilde{\mu} \right) \nabla \tilde{\theta}^{(1)} = 0. \tag{27}$$

We also represent the dimensionless form of the boundary conditions for stresses on the surface of the fracture.

$$\mathbf{n} \cdot \hat{\boldsymbol{\sigma}}^{(1)} \cdot \mathbf{n} = -p_c, \mathbf{m}^{(\alpha)} \cdot \hat{\boldsymbol{\sigma}}^{(1)} \cdot \mathbf{n} = \mathbf{m}^{(\alpha)} \cdot \hat{\boldsymbol{\sigma}} \cdot \mathbf{n} = 0, \tag{28a}$$

and asymptotic at infinity

$$\hat{\boldsymbol{\sigma}}^{(1)} = 0, \tilde{\mathbf{u}}^{(1)} = 0. \tag{28b}$$

Since these relations do not include time derivatives, they retain their form also after transformation (26). This does not hold for equations including the partial time derivative. Thus, the piezoconductivity Eq. (19) assumes the form.

$$\left[\beta \tilde{p}^{(0)} - \frac{1}{2} \mathbf{y} \cdot \tilde{\nabla} \tilde{p}^{(0)} \right] - \varepsilon_p \nabla^2 \tilde{p}^{(0)} = 0, \varepsilon_p = \frac{\kappa_p T}{L_0^2}. \tag{29}$$

Equation (29) does not depend on time. Similarly, we can transform the equation of motion inside the crack (14), i.e.,

$$\left(\beta + \frac{1}{2} \right) \tilde{h} - \frac{1}{2} \mathbf{y} \cdot \tilde{\nabla} \tilde{h} - N_2 \tilde{\nabla} \left(\tilde{h}^3 \tilde{\nabla} \tilde{p}_c \right) = -N_1 \tilde{q}_L + q_0 \delta(\mathbf{y}), \tag{30a}$$

where the following dimensionless quantities are introduced:

$$N_1 = \frac{k E_u T}{(1 - \sigma_u^2) \eta L_0^2}, N_2 = \frac{\varepsilon^3 T \tau E_u}{3 \eta (1 - \sigma_u^2)}. \tag{30b}$$

The second expression (18b) is also transformed into the dimensionless form.

$$\tilde{p}^{(1)} = -A \tilde{\theta}^{(1)}, \text{ where } A = \frac{(K_u - K)(1 - \sigma_u^2)}{3 \alpha_c K_u (1 - 2 \sigma_u)}. \tag{31}$$

In the integral form, Eq. (30a) is.

$$\left(\beta + \frac{2 + \alpha}{2} \right) \int_{\Gamma_{\text{int}}} \tilde{h} d\tilde{s} = \tilde{q}_0 - N_1 \int_{\Gamma_{\text{int}}} \tilde{q}_L d\tilde{s}, \tilde{q}_0 \equiv \frac{QT\tau}{2 \varepsilon L^{2+\alpha}}. \tag{32}$$

Here, the values of the parameter α are set by the plane ($\alpha = 0$) and three-dimensional ($\alpha = 1$) cases, respectively. In (32), all three terms are time-independent. Using this relation we find the quantity $q(\tau)$, determined in (26):

$$\tilde{q}(\tau) = \frac{2\varepsilon L^{2+\alpha}}{Q_0 T \tau} \tilde{q}_0. \quad (33)$$

The asymptotic expression for the stress components near the edge of the normal hydraulic fracture is completely determined by the parameter K_I , which is called the stress intensity factor [11]. In the case of an unbounded medium, it depends on the applied loads and the shape of the crack.

The sought solution is characterized by the parameter of self-similarity β and parameter ε_0 , which determines the characteristic scale of the medium deformation. These parameters are given by the following equations:

$$K_I = K_{IC}, \quad (34a)$$

$$\frac{4\sqrt{2}(1-\sigma_u^2)K_{IC}}{\varepsilon E_u \sqrt{\pi L}} = 1. \quad (34b)$$

Here, the first equation is the Irwin condition defining the fracture development, where K_{IC} is the material constant. From this equation, the parameter β is obtained making the left-hand side time independent. As a result, it can be shown [10] that $\beta = -1/4$. Equation (34b) is the normalization condition which makes it possible to find $\varepsilon = \varepsilon_0$ in such a way as to ensure that the dimensionless crack opening, together with the normalized medium deformation, might be of the order of unity.

4.2 Condition of Self-Similarity

Almost all correlations (30)–(32), excluding (30a), allow separating the time and space variables, i.e., transition to a self-similar form. For these expressions, we need either to make certain simplifications or to restrict ourselves to some particular cases. It is possible two limiting cases.

$$N_2 \rightarrow \infty, N_1 / N_2 \ll 1. \quad (35)$$

Equation (30a) describes the balance of the fluid mass inside and outside the fracture. The second relation (35) means that the fluid flow from the crack into the outer area is small. At the same time, the first correlation (35) indicates that the pressure in the crack is homogeneous and depends on time only. This is the simplest variant which we assume in the paper.

Then, using correlation (34), we obtain all the parameters that explicitly or implicitly appear in (26), i.e.,

$$L_0 = \left[\frac{Q_0 T}{B} \left(\frac{\sqrt{\pi} E_u}{4\sqrt{2}K_1(1-\sigma_u^2)} \right) \right]^{\frac{2}{2(\alpha+2)-1}}, \varepsilon = \varepsilon_0 \tau^{-1/4}, q = \tau^{\frac{2\alpha-1}{4}}, \tag{36}$$

$$\varepsilon_0 = \left[\frac{(1-\sigma_u^2)^{2(\alpha+2)}}{E_u^{2(\alpha+2)} Q_0 T} B \left(\frac{4\sqrt{2}K_1}{\sqrt{\pi}} \right)^{2(\alpha+2)} \right]^{\frac{1}{2(\alpha+2)-1}},$$

$$B = \frac{2(2+\alpha)-1}{2} \int_{\Gamma_{int}} \tilde{h} d\tilde{s} + 2N_1 \int_{\Gamma_{int}} \tilde{q}_L d\tilde{s}.$$

Equalities (26), (31), and (36) yield the time dependence of the scales for the sought quantities.

4.3 The Final Form of the Equations

For the amplitudes of the elastic component depending only on the self-similar coordinates, we have the following dimensionless problem:

$$\tilde{\mu} \tilde{\nabla}^2 \tilde{\mathbf{u}}^{(1)} + \left(\tilde{\lambda}_u + \tilde{\mu} \right) \tilde{\nabla} \tilde{\theta}^{(1)} = 0 \tag{37}$$

with boundary conditions.

$$\tilde{\Gamma}_{int} : \tilde{\mathbf{n}} \cdot \hat{\tilde{\sigma}}^{(1)} \cdot \tilde{\mathbf{n}} = -p_c, \mathbf{m}^{(\alpha)} \cdot \hat{\tilde{\sigma}}^{(1)} \cdot \tilde{\mathbf{n}} = 0, \tag{38a}$$

$$\tilde{\Gamma}_{\infty} : \hat{\tilde{\sigma}}^{(1)} = 0. \tag{38b}$$

For the second (filtration) component, the piezoconductivity Eq. (19) takes the form

$$\left[\frac{1}{4} \tilde{p}^{(0)} + \frac{1}{2} \tilde{\mathbf{y}} \cdot \tilde{\nabla} \tilde{p}^{(0)} \right] + \varepsilon_p \tilde{\nabla}^2 \tilde{p}^{(0)} = 0 \tag{39}$$

with boundary conditions:

$$\tilde{\Gamma}_{\text{int}} : \tilde{p}^{(0)} = \tilde{p}_c + A\theta^{(1)}, \tag{40a}$$

$$\tilde{\Gamma}_{\infty} : \tilde{p}^{(0)} = 0. \tag{40b}$$

The relations of coupling (16a), (18a) with the boundary conditions (16b) and (16c) are written as follows:

$$\tilde{\nabla}^2 \tilde{\Phi}^{(0)} = F \tilde{p}^{(0)}, \quad F = \frac{\alpha_e E_u}{\left(K + \frac{4}{3}\mu\right)(1 - \sigma_u^2)}, \tag{41}$$

$$\tilde{\Gamma}_{\text{int}} : \mathbf{n} \cdot \tilde{\nabla} \tilde{\Phi}^{(0)} = 0, \tag{42a}$$

$$\tilde{\Gamma}_{\infty} : \tilde{\Phi}^{(0)} = 0. \tag{42b}$$

As a result, we have obtained a closed problem for a fracture in a three-dimensional space, which, generally speaking, must be solved numerically. However, in the particular case of a planar two-dimensional problem with the fracture shaped as a straight line segment $[-l(t), l(t)]$, an analytical solution can be obtained.

5 Plane Self-Similar Problem

Let us now consider a plane variant of this problem with a straight crack. This case involves the corresponding simplification of the boundary. It retains all the basic qualitative features of the three-dimensional version and at the same time makes it possible to obtain an analytical solution. The three-dimensional problem requires numerical calculations.

5.1 Elastic Component

We consider the plane (y_1, y_3) . In a planar self-similar problem, we are able to obtain an analytical solution in finite formulas. From the very beginning, we will use dimensionless variables preserving the notation of the previous section. Let the sought quantities be $\hat{\sigma}^{(1)}$, $\tilde{p}^{(0)}$, $\tilde{\nabla} \tilde{\Phi}^{(0)}$, $\tilde{h}(y_1)$. The other quantities are expressed through them. In the plane case, a complex representation for the elastic component can be used. We introduce the usual notation.

$$z = y_1 + iy_3, \tilde{u}_1^{(1)} + i\tilde{u}_3^{(1)} \equiv \tilde{u} + i\tilde{v},$$

and the standard complex potentials $\varphi(z)$ and $\psi(z)$. They can be transformed to a form adapted to the given problem [18]:

$$\varphi(z) = \frac{1}{2} Z_I, \psi(z) = -\frac{1}{2} z Z_I', Z_I' = \frac{dZ_I}{dz}, Z_I = \frac{dZ_I^0}{dz}. \tag{43}$$

Here, as always, the prime denotes a derivative with respect to a complex argument. Using representation (43), we write out the expressions for complex stresses and displacements.

$$\tilde{\sigma}_{11}^{(1)} = \text{Re } Z_I - y_3 \text{Im } Z_I', \tilde{\sigma}_{33}^{(1)} = \text{Re } Z_I + y_3 \text{Im } Z_I', \tilde{\sigma}_{13}^{(1)} = -y_3 \text{Re } Z_I',$$

$$2\tilde{\mu}\tilde{u} = (1 - 2\sigma_u) \text{Re } Z_I^0 - y_3 \text{Im } Z_I', 2\tilde{\mu}\tilde{v} = 2(1 - \sigma_u) \text{Im } Z_I^0 - y_3 \text{Re } Z_I'. \tag{44}$$

It should be recalled that in (44) all the quantities (including modules) are dimensionless. The solution of the boundary-value problem (37) (38) in the complex representation has the form.

$$Z_I = \frac{\tilde{p}_c}{\pi\sqrt{z^2 - 1}} \int_{-1}^1 \frac{\sqrt{1 - \xi^2}}{z - \xi} d\xi, \tilde{\theta}^{(1)} = \frac{1}{\tilde{\lambda}_u + \tilde{\mu}} \text{Re } Z_I, \frac{\partial \tilde{\theta}^{(1)}}{\partial y_3} = -\frac{1}{\tilde{\lambda}_u + \tilde{\mu}} \text{Im } Z_I'. \tag{45}$$

5.2 Filtration Component

Near the fracture, a thin boundary layer arises due to the fact that the crack propagation rate is much greater than the characteristic velocity of the piezoelectricity phenomenon in the poroelastic medium. We introduce in this layer an extended coordinate $\zeta = y_3 / \sqrt{2\varepsilon_p}$ and the function $\psi(\zeta)$, which is determined by the ratio.

$$\tilde{p}^{(0)} = \left(\tilde{p}_c + A\tilde{\theta}^{(1)} \right) \psi, A = \frac{(K_u - K)(1 - \sigma_u^2)}{3\alpha_e K_u (1 - 2\sigma_u)}. \tag{46}$$

In this layer, the double tilde denotes the boundary values of the quantities, which are functions only of the longitudinal coordinate. In (46), the quantity $\psi(\zeta)$ is a rapidly varying function of the extended coordinate ζ . After the substituting (46) into the piezoconductivity Eq. (19) and discarding the small terms, the subsequent simple transformations yield the ordinary differential equation

$$\psi'' + \zeta\psi' + \frac{1}{2}\psi = 0. \quad (47)$$

Here, the prime denotes a derivative of a fast variable ζ .

For the sought function, we have the boundary condition, which follows from (40a) and the damping conditions at infinity (40b), i.e.,

$$\psi|_{\zeta=0} = 1, \quad \psi|_{\zeta=\infty} = 0. \quad (48)$$

The boundary value problem (47) and (48) is solved numerically. In this case, we obtain $\psi'(0) = -0.479$. However, a comparison with the numerical calculations shows that the solution of this problem can be approximated quite satisfactorily by a simple analytic function

$$\psi(\zeta) = X(\zeta) \left(1 - \frac{\zeta}{2}\right), \quad (49)$$

where

$$X(\zeta) \equiv \begin{cases} 1, & \zeta \leq 2, \\ 0, & \zeta \geq 2. \end{cases}$$

Accordingly, the solution of the filtration problem in the boundary layer is written as

$$\tilde{p}^{(0)}(y_1, \zeta) = \left(\tilde{p}_c + A\tilde{\theta}^{(1)} \right) X(\zeta) \left(1 - \frac{\zeta}{2}\right). \quad (50)$$

The reason for representing the solution in form (46) is that we a priori seek an approximate solution precisely in this form. This makes it possible to simplify the coefficients of Eq. (47) and the boundary conditions (48). Moreover, this representation allows us to pass to an even simpler form, (49).

As should be expected, this solution does not actually depend on the longitudinal coordinate. Naturally, significant deviations from the simple dependence of the solution in form (50) only arise near the tip of the crack where the homogeneity of the solution along the horizontal coordinate is substantially violated. It is also possible to write out the expression for the dimensionless component of the fluid flow from the crack into the poroelastic medium

$$\tilde{q}_L(y_1) = -\frac{\psi'(0)}{\sqrt{2\varepsilon_p(1-y_1^2)}} \left(\tilde{p}_c + A\tilde{\theta}^{(1)} \right) + \frac{1}{\sqrt{1-y_1^2}} \left(\tilde{p}_c + A\tilde{\theta}^{(1)} \right) \frac{\partial \tilde{\theta}^{(1)}}{\partial y_3}. \tag{51}$$

Using the solution of (50) and formulas (41), we find expressions for the remaining values of the filtration component. In the dimensionless form, these formulas are as follows:

$$\tilde{\nabla}^2 \tilde{\Phi}^{(0)} = \tilde{\theta}^{(0)}, \tilde{p}^{(0)} = F\tilde{\theta}^{(0)}, F = \frac{\left(K + \frac{4}{3}\mu \right) (1 - \sigma_u^2)}{\alpha_e E_u}. \tag{52}$$

We perform the integral Fourier transform of Eq. (52) along the longitudinal coordinate y_1 :

$$\begin{aligned} \tilde{\Phi}^{(0)}(y_1, y_3) &= \frac{C}{\sqrt{2\pi}} \int_{-\infty}^{\infty} \tilde{\Phi}_k^{(0)}(k, y_3) e^{iky_1/\sqrt{2\varepsilon_p}} dk, \\ C &= \frac{2\varepsilon_2 \alpha_e E_u \tilde{p}_c}{\left(K + \frac{4}{3}\mu \right) (1 - \sigma_u^2)} \left(1 - \frac{K_u - K}{\alpha_e (\lambda_u + \mu)} \right), \end{aligned} \tag{53}$$

where

$$\tilde{\Phi}_k^{(0)}(k, y_3) = \frac{\sin k}{\sqrt{2\pi} k^3} \left[\frac{1 - \text{ch}2k}{|k|} e^{-|k|y_3/\sqrt{2\varepsilon_p}} - 2X \left(\frac{y_3}{\sqrt{2\varepsilon_p}} \right) \left[\left(1 - \frac{y_3}{2\sqrt{2\varepsilon_p}} \right) - \frac{1}{2k} \text{sh} \left(2k - \frac{y_3 k}{\sqrt{2\varepsilon_p}} \right) \right] \right]. \tag{54}$$

In deriving expressions (53) and (54), we used the well-known formula

$$\frac{1}{\pi} \int_{-\infty}^{\infty} \frac{\sin k}{k} e^{ikx} dk = \begin{cases} 1 & \text{at } |x| < 1, \\ 0 & \text{at } |x| > 1. \end{cases} \tag{55}$$

Here, the following point should be noted. Generally speaking, the improper integral represented by expressions (53) and (54), diverges at zero. Therefore, some transformations should be made to eliminate the divergent expressions. If we take in (53) the derivative with respect to y_1 under the integral sign, then the resulting integral converges. Therefore, without loss of generality, representation (53) can be written in the following form:

$$\tilde{\Phi}^{(0)}(y_1, y_3) = \frac{C}{\sqrt{2\pi}} \int_0^{y_3} \left(\int_{-\infty}^{\infty} \frac{\partial \tilde{\Phi}_k^{(0)}(k, \xi)}{\partial \xi} e^{iky_1/\sqrt{2\varepsilon_p}} dk \right) d\xi + \text{Const.} \quad (56)$$

In this expression, the improper integral converges and satisfies Eq. (52) if the sequence of operations is correct. In particular, the corresponding values satisfy the boundary conditions (40) and (42).

5.3 Internal Problem About a Fracture

The complex representation (43) with (44) and the solution (45) give it possible to determine the values inside the crack. Indeed, since the pressure in the fracture is uniform, these formulas, after simple calculations, yield expressions for the dimensionless quantities:

$$\tilde{h}(y_1) = \frac{4\tilde{p}_c}{\pi} \int_0^1 \ln \frac{\sqrt{1-y_1^2} + \sqrt{1-s^2}}{\sqrt{1-y_1^2} - \sqrt{1-s^2}} ds \text{ at } 0 < y_1 < 1. \quad (57a)$$

$$\tilde{h}(y_1) = \sqrt{1-y_1} \text{ at } \sqrt{1-y_1} \ll 1, p_c = \frac{1}{4\sqrt{2}}. \quad (57b)$$

6 Main Results

In this paper, a self-similar solution is obtained for HF crack in a poroelastic medium when condition (35) is satisfied. It implies that the pressure in the fracture itself is uniform. This solution has the following form.

The solution inside the crack is.

$$t = T\tau, H(x_1, t) = \varepsilon_0 L_0 \tau^{\frac{1}{4}} \tilde{h}(y_1), \mathbf{y} = \frac{\mathbf{x}}{L_0 \tau^{1/2}}, u_i^{(1)}(\mathbf{x}, t) = \varepsilon_0 L_0 \tau^{\frac{1}{4}} u_i^{(1)}(\mathbf{y}),$$

$$p_c(\mathbf{x}, t) = \frac{\varepsilon_0 \tau^{-\frac{1}{4}} E_u}{(1-\sigma_u^2)} \tilde{p}_c(\mathbf{y}), Q = Q_0 \tau^{-1/4}, q_L(x_1, t) = -\frac{\varepsilon_0 L_0 \tau^{-3/4}}{T} N_1 \tilde{q}_L(y_1),$$

$$\begin{aligned} \tilde{q}_L(x, t) &= \frac{\psi'(0)\tilde{p}_c}{\sqrt{2\varepsilon_p(1-y_1^2)}} \left(1 - \frac{K_u - K}{\alpha_e(\lambda_u + \mu)} \right) \tilde{h}(y_1) \\ &= \frac{4\tilde{p}_c}{\pi} \int_0^1 \ln \frac{\sqrt{1-y_1^2} + \sqrt{1-s^2}}{\sqrt{1-y_1^2} - \sqrt{1-s^2}} ds, \end{aligned} \tag{58}$$

$$B = \frac{3}{2} \int_s \tilde{h} d\tilde{s} + 2N_1 \int_s \tilde{q}_L d\tilde{s}, L_0 = \left[\frac{Q_0 T}{B} \left(\frac{\sqrt{\pi} E_u}{4\sqrt{2} K_1 (1-\sigma_u^2)} \right) \right]^{\frac{2}{3}},$$

$$\varepsilon_0 = \left[\frac{(1-\sigma_u^2)^4 B (4\sqrt{2} K_1)^4}{E_u^4 Q_0 T \sqrt{\pi}} \right]^{\frac{1}{3}}, N_1 = \frac{kE_u T}{(1-\sigma_u^2)\eta L_0^2}, \psi'(0) = -0.479, \tilde{p}_c = \frac{1}{4\sqrt{2}}.$$

The dynamics of the skeleton of the elastic component in the outer area is given by the following expressions:

$$t = T\tau, \mathbf{y} = \frac{\mathbf{x}}{L_0\tau^{1/2}}, z = y_1 + iy_3, Z_I(z, t) = \frac{\tilde{p}_c}{\pi\sqrt{z^2 - 1}} \int_{-1}^1 \frac{\sqrt{1-\xi^2}}{z-\xi} d\xi,$$

$$p^{(1)}(\mathbf{x}, t) = \frac{\varepsilon_0\tau^{-\frac{1}{4}} E_u}{(1-\sigma_u^2)} \tilde{p}^{(1)}(\mathbf{y}), \hat{\sigma}^{(1)}(\mathbf{x}, t) = \frac{\varepsilon_0\tau^{-\frac{1}{4}} E_u}{(1-\sigma_u^2)} \hat{\sigma}^{(1)}(\mathbf{y}), \hat{\varepsilon}^{(1)}(\mathbf{x}, t) = \varepsilon_0\tau^{-\frac{1}{4}} \hat{\varepsilon}^{(1)}(\mathbf{y}),$$

$$\hat{\sigma}^{(1)ef}(\mathbf{x}, t) = \frac{\varepsilon_0\tau^{-\frac{1}{4}} E_u}{(1-\sigma_u^2)} \hat{\sigma}^{(1)ef}(\mathbf{y}), \theta^{(1)}(\mathbf{x}, t) = \frac{\varepsilon_0\tau^{-1/4}}{\lambda_u + \mu} \operatorname{Re} Z_I, \frac{dZ_I^0}{d\tilde{z}} = Z_I,$$

$$\frac{\partial \hat{\theta}^{(1)}}{\partial y_3} = -\varepsilon_0\tau^{-3/4} \operatorname{Im} Z_I', p_f^{(1)} = -\frac{\varepsilon_0\tau^{-\frac{1}{4}} E_u \tilde{p}_c (K_u - K)}{\alpha_e(\lambda_u + \mu)(1-\sigma_u^2)} \operatorname{Re} Z_I, \tag{59}$$

$$\tilde{\sigma}_{11}(\mathbf{y}) = \operatorname{Re} Z_I - y_3 \operatorname{Im} Z_I', \tilde{\sigma}_{33}(\tilde{\mathbf{y}}) = \operatorname{Re} Z_I + y_3 \operatorname{Im} Z_I', \tilde{\sigma}_{13}(\mathbf{y}) = -y_3 \operatorname{Re} Z_I',$$

$$2\tilde{\mu}\tilde{u}_3^{(1)}(\mathbf{y}) = 2(1-\sigma_u) \operatorname{Im} Z_I^0 - y_3 \operatorname{Re} Z_I, 2\tilde{\mu}\tilde{u}_1^{(1)}(\mathbf{y}) = (1-2\sigma_u) \operatorname{Re} Z_I^0 - y_3 \operatorname{Im} Z_I.$$

In turn, the filtration component of the problem in the outer area is divided into two subcomponents: a skeleton subcomponent.

$$t = T\tau, \mathbf{y} = \frac{\mathbf{x}}{L_0\tau^{1/2}}, \mathbf{u}^{(0)}(x_1, x_3, t) = \nabla\Phi^{(0)}(x_1, x_3, t),$$

$$\Phi^{(0)}(x_1, x_3, t) = \frac{Ct^{3/4}}{\sqrt{2\pi}} \int_0^{y_3} \left(\int_{-\infty}^{\infty} \frac{\partial \tilde{\Phi}_k^{(0)}(k, \xi)}{\partial \xi} e^{ik y_1 / \sqrt{2\varepsilon_2}} dk \right) d\xi + \text{Const}, \tag{60}$$

$$\tilde{\Phi}_k^{(0)}(k, y_3) = \frac{\sin k}{\sqrt{2\pi}k^3} \left[\frac{1 - \text{ch}2k}{|k|} e^{-|k|y_3/\sqrt{2\varepsilon_p}} - 2X\left(\frac{y_3}{\sqrt{2\varepsilon_p}}\right) \left[\left(1 - \frac{y_3}{2\sqrt{2\varepsilon_p}}\right) - \frac{1}{2k} \text{sh} \left[k \left(2 - \frac{y_3}{\sqrt{2\varepsilon_p}}\right) \right] \right] \right],$$

$$C = \frac{2\varepsilon_p \alpha_e \tilde{p}_c}{\sqrt{\pi} \left(K + \frac{4}{3}\mu\right)} \left(1 - \frac{K_u - K}{\alpha_e(\lambda_u + \mu)}\right),$$

where $\tilde{\Phi}_k^{(0)}(k, y_3)$ is given by condition (54), and the fluid component

$$p^{(0)}(x_1, x_3, t) = \frac{\varepsilon_0 \tau^{-\frac{1}{4}} E_u \tilde{p}_c}{(1 - \sigma_u^2)} \left(1 - \frac{K_u - K}{\alpha_e(\lambda_u + \mu)}\right) X\left(\frac{y_3}{\sqrt{2\varepsilon_p}}\right) \left(1 - \frac{y_3}{\sqrt{2\varepsilon_p}}\right). \tag{61}$$

The formula for the outflow of the fluid from the crack $\tilde{q}_L(x_1, t)$ in (58) is very important. The first term in it represents the boundary layer near the crack associated with different rates of fluid processes inside and outside the fracture. The second term describes the outflow of the fluid from the crack due to the uniform volumetric compression of the medium. The processes near the crack are significantly affected by the elastic reaction of the porous medium to saturation with a fluid, which is proportional to the difference in the non drainage and drainage volume moduli. In addition, we should note that near the fracture edge the formula for $q_L(x_1, t)$ has a root singularity. This feature is also observed in the Carter model [19].

The Eqs. (58)–(61) include the terms proportional to $(K_u - K)$, which describe a change in the properties of rocks associated with their saturation with fluid. Under rapid (in comparison with the filtration in the outer area) crack propagation, the conditions for the development of fractures are significantly affected only by this change in the properties. At the same time, the fluid filtration itself does not affect this process in the first approximation. Such a complex combination of different factors requires a deeper study.

7 Conclusions

For HF fracture model, an incomplete coupling scheme consisting of three links (three steps) is shown to be implemented. It turns out that the splitting of the initial system of the HF crack equations into two components obeys the principle of

incomplete coupling, which affects not only the mechanics of poroelasticity in the host rocks but also the law of motion of the fracture itself.

The Eqs. (13) and (14) in the first approximation describes the motion of the fracture completely independently of the external environment and the flow processes in it. However, this is only an apparent independence. In fact, the elastic properties of the rock hosting the fracture are taken into account by the kernel of the integral ratio (25). This kernel indirectly depends on the state of the poroelastic medium through the nondrainage modulus of elasticity.

The elastic component of the solution in the outer region is described by Eqs. (17c), and (18b) with the boundary conditions (24). At the second step of the incomplete coupling scheme, the elasticity equations, jointly with the equation of motion of the fracture itself, form an independent system of equations. In the equations of poroelasticity, the quantities θ , and p^f are not independent. At the same time, these dependences are also different for different components. For this reason, the scheme for splitting the poroelasticity equations into components is not a trivial procedure.

The filtration component in the outer region, in turn, is divided into two groups of equations. The first one is described by Eqs. (17a), (17b), and (18a). It is connected with the bulk strains of the pore space induced by the external load on a poroelastic medium. The second group of equations is due to filtration processes, which eliminate the residual. It inevitably appears when the balance of forces and mass is disturbed during the interaction of both components.

The particular self-similar solution as an example of general problem is obtained with the numerical methods. This solution is too awkward and cumbersome for an investigation. One can see it in [20], which is devoted to the self-similar fracture in an elastic medium only. The solution is related with a numerical procedure and its investigations. The simple interpolation formula (49) was used for simplification of a solution procedure. It describes the numerical solution with an acceptable accuracy.

The effect of flow from the fracture into a poroelastic medium on the mode of the fracture motion is small for low-permeable rocks. However, in the general case, it is not small and should not be ignored. In the outer region, it is manifested in the boundary layer. When the HF technology is applied, a reservoir is exposed to the action of aggressive or heated liquid. Here the filtration effect can be controlled by adjusting the parameters of the boundary layer.

The principle of incomplete coupling enables independent numerical and analytical investigations of all components of the solution for the HF problem. This makes it possible to use the simplest known codes developed for a fracture model in a purely elastic medium for fluid motion in the fracture and for other auxiliary models.

Moreover, this principle is of a universal character. It will be fulfilled even if the fracture is in a nonequilibrium state, i.e., when the Irwin condition at the tip of the crack is not satisfied. In particular, the fracture can move irregularly, stop, and then move again, and at a certain stage, it can branch and turn into a system of fractures.

In a similar way, we can consider a system of interacting HF cracks connected hydrodynamically but not intersecting with each other. It is important that when implementing the splitting procedure, we introduce no additional simplifying physical restrictions into the model.

However, the principle of incomplete coupling also extends to the effects of the stimulating the reservoir. If hydraulic fracturing is used to stimulate the reservoir by a heated or aggressive liquid (for example, acid), then due to the specifics, including the structural features and dynamics of the HF crack, any similar problem can be split into two components. One of the components is a “pure” development of a totally unexposed fracture, and it has been considered above. This component does not depend on any impact. The second component is connected to the impact itself. It can formally be described as a small perturbation applied to a pure fracture. Moreover, the impact intensity is practically insignificant (within certain limits) in terms of the reverse effect on the pure fracture. The limit is understood as the applicability of the basic provisions of the HF model.

This conclusion entails far-reaching consequences. That is, the proposed procedure of incomplete coupling can reasonably be extended. The scheme of incomplete coupling considered in this paper only included three blocks, i.e., the fracture itself, elastic, and filtration components. As it is, another block can arise, which is associated with the exposure. It is based on the same principles as the previous three. This enables the construction of compact and effective computational packages with the performance many orders of magnitude greater than all existing ones. The practical significance of the obtained results is that they make it possible to create simple and efficient HF packages, which do not require high computational capacities.

In reality, the natural phenomenon of hydraulic fracturing can occur in two forms: the actual fracturing as a result of the groundwater migration and a magmatic fracturing. In each case, we cannot control these phenomena. However, the scheme for splitting the model equations into components may prove useful in studying these phenomena. The nature of splitting has a deep physical sense and is not related to the particular features of HF in oil reservoirs or to any special assumptions about the properties of hydraulic fracturing itself. Both hydro- and magmatic fracturing are closely connected with the processes of differentiation and concentration of the crustal matter and the emergence of ore deposits.

At present, we have practically no methods for mathematically modeling these processes based on well-posed problems. The known works on this subject are mostly qualitative and speculative in character. This is due to the extreme scarcity of factual material and the need to use indirect considerations and interpretations of observational data. This group of phenomena includes intrusions hardened millions of years ago and metamorphic transformations of rock caused by the natural migration of groundwater. In this respect, HF models, which are developed and refined to the smallest detail, can be very useful and relevant. The revealed general patterns can be used to develop mathematical models for similar natural processes.

The phenomenon of natural hydraulic fracturing in its active phase differs little from artificial HF except for the area adjacent to the well. The differences are mainly related to the composition of the fluid and the associated geochemical processes. Due to the specific nature of the splitting of the model equations, these differences have an auxiliary character and can easily be taken into account. For this reason, we believe this work to be of interest for geochemists studying the groundwater migration.

The processes of magma filtration in partially molten rocks are much slower than the motion of the fracture itself. Consequently, a boundary layer will inevitably arise near the fracture surfaces. Therefore, the study of metamorphic transformations at the boundaries of hardened magma fractures can provide very valuable information on the processes that took place in sill intrusions and dikes millions of years ago. Penetration of magmatic melt through the fracture boundaries can result in the differentiation and concentration of substance.

Advances in the geochemistry of magmatic processes may also have an influence on studying the hydrodynamics of aqueous suspensions. The forces of molecular interaction of the suspension particles (in mud solutions) are so small that their experimental investigation is difficult. No one has actually observed flocks in suspension. Their presence is simply inferred based on theoretical considerations. The processes in magmatic chambers are very slow, and the forces of viscous friction and molecular interaction in partially molten rocks are much greater than similar forces in an aqueous suspension. For this reason, the structures of flocks in magmatic chambers have time to harden and they keep to the present time that makes it possible their observation and study. Moreover, flocks can directly be observed in laboratory experiments with partially molten rocks [21, 22].

As an example, a self-similar problem about the fracture propagation in a poroelastic medium saturated with Newtonian fluid has been solved [18]. As far as we know, there is no analogous self-similar solution in the available scientific publications. It is assumed that a weakly compressible fluid is injected through a well into a reservoir inducing the development of a fracture. This is accompanied by the fluid leaking into a permeable poroelastic medium. In order to maintain the self-similar solution, the fluid's injection into the well must be assumed to obey to a certain temporal law. Using the method of the incomplete splitting of the external problem into two fields [17], we have obtained an analytical solution of the complete problem for the two-dimensional case when the pressure in the crack is uniform. It is shown that in this mode the strength properties of rocks play a greater role than the process of fluid filtration in them.

Acknowledgments This work was supported by the Russian Science Foundation, project № 15-11-00021.

References

1. Detournay E (2004) Propagation regimes of fluid-driven fractures in impermeable rocks. *Int J Geomech* 4(1):35–45
2. Fan Y, Economides MJ (1995) Fracture dimensions in Frack&Pack stimulation. Paper SPE 30469 presented at the 1995 annual technical conference and exhibition, Dallas, TX, 22–25 October 1995
3. Adachi JL, Detournay E (2002) Self-similar solution of a plane-strain fracture driven by a power-law fluid. *Int J Numer Anal Meth Geomech* 26:579–604
4. Adachi JL, Detournay E (2008) Plane strain propagation of a hydraulic fracture in a permeable rock. *Eng Fract Mech* 75:4666–4694
5. Adachi JL, Detournay E, Peirce AP (2010) Analysis of the classical pseudo-3D model for hydraulic fracture with equilibrium height growth across stress barriers. *Int J Rock Mech Min Sci* 47:625–639
6. Garagash D (2006) Propagation of a plane-strain hydraulic fracture with a fluid lag: early-time solution. *Int J Solids Struct* 43:5811–5835
7. Garagash D (2006) Plane-strain propagation of a fluid-driven fracture during injection and shut-in: asymptotics of large toughness. *Eng Fract Mech* 73:456–481
8. Detournay E, Garagash DI (2003) The near-tip region of a fluid-driven fracture propagating in a permeable elastic solid. *J Fluid Mech* 494:1–32
9. Bungler AP, Detournay E, Garagash DI (2005) Toughness-dominated hydraulic fracture with leak-off. *Int J Fract* 134:175–190
10. Karakin AV (2006) Incomplete coupling principle in the poroelastic models. *Math Model* 18(2):24–42
11. Muskhelishvili NI (1966) Some basic problems of mathematical theory of elasticity. Nauka, Moscow. (in Russian)
12. Biot MA (1956) Thermoelasticity and irreversible thermodynamics. *J Appl Phys* 27:240–253
13. Biot MA (1956) General solutions of the equations of elasticity and consolidation for a porous material. *J Appl Mech* 78:91–96
14. Detournay E, Cheng AH-D (1993) Fundamental of poroelasticity. In: Fairhurst C (ed) *Analysis and design methods. Comprehensive rock engineering: principles, practice and projects*, vol 2. Pergamon Press, New York, pp 113–171
15. Karakin AV, Kur'yanov Yu A, Pavlenkova NI (2003) Faults, fractured zones, and waveguides in the upper layers of the earth. VNIIGeosistem, Moscow. (in Russian)
16. Liebowitz H (ed) (1968) *Fracture: an advanced treatise, Mathematical fundamentals*, vol 2. Academic Press, New York
17. Karakin AV, Ramazanov MM, Borisov VE (2018) Incomplete coupling problem of hydraulic fracturing equations. *Math Models Comput Simul* 10(1):45–58
18. Ramazanov MM, Karakin AV, Borisov VE (2018) Analytical investigation of the dynamics of a hydraulic fracture using the principle of incomplete coupling. *Math Models Comput Simul* 10(3):322–332
19. Carter ED (1957) Optimum fluid characteristics for fracture extension. In: Howard GC, Fast CR (eds) *Drilling and production practices*. American Petroleum Institute, Tulsa, pp 261–270
20. Adachi JI, Detournay E, Carbonell RS (2002) Plane strain propagation of a fluid-driven fracture II: zero toughness self-similar solution. *Proc R Soc, London*
21. Kadik AA, Lebedev EB, Dorfman AM, Bagdasarov NS (1989) Simulating crystal-magma separation in a centrifuge. *Geochem Int* 26(8):39–47
22. Karakin AV, Pokatashkin PA (2014) Mechanism of density inversion formation in partially molten rocks. *Geochem Int* 52:22–32

Geomechanical Model for Large Scale Hydraulic Fracture Dynamics



E. B. Savenkov and V. E. Borisov

1 Introduction

Hydraulic fracturing (HF) is one of the most effective methods to increase oil and gas production from the reservoir field. The essence of the fracturing technology consists in pumping a special liquid into the oil reservoir to create an artificial crack with a length of ~100 m, height of ~10 m, and an average opening of 5–10 mm. As a result, an artificial channel is created that is connected with a well and has a large inflow area and a high permeability (by orders of magnitude greater than the one of the bulk medium). This provides a significant increase in inflow of the formation fluid to the well. Engineering aspects of technology are considered, e.g., in [1].

Currently used mathematical models of fracture dynamics are mostly “engineering”: they are based on two-dimensional formulations, *a priori* defined geometric models of fractures and rarely take into account geomechanical effects correctly, etc. (see, for example, [1–3]). The use of such mathematical models has long become standard engineering practice. However, a number of hydraulic fracture dynamics problems require the use of fully three-dimensional self-consistent formulations. First of all, such problems include the analysis of the fracture development in a substantially inhomogeneous stress field induced by the presence of neighboring technogenic (for example, multiple hydraulic fracturing on horizontal wells) or natural fractures, heterogeneous pressure fields generated by injection or production wells, *etc.* At the same time such self-consistent mathematical models should be practical enough to be handled with contemporary numerical techniques.

Physical and mathematical description of the crack dynamics during hydraulic fracturing process lead to the solution of complex multiphysics problem which includes the following groups of equations:

E. B. Savenkov (✉) · V. E. Borisov
KIAM RAS, Moscow, Russia

- a system of poroelasticity equations describing the evolution of stress-strain state of the formation and the fluid pressure fields during the development of the fracture;
- equations of fluid flow in the fracture;
- mechanical conditions for the fracture evolution which define direction of its development at each point of its front;
- dynamic interface conditions coupling pressure field in the fracture and in the formation defined on the lateral surfaces of the fracture as well as kinematic conditions relating the fracture opening and the displacement of the formation.

In this work we present a mathematical model for the analysis of hydraulic fracture propagation in fully 3D setting and accounting for all the major flow and geo-mechanical effects. It allows to describe consistently disturbances distribution of the stress field on a regional scale, taking into account the effects induced by porous media flow in the presence of production and injection wells; the presence of a fracture and its propagation, taking into account both regional and induced stress fields; fluid flow in the fracture. The model is suitable to analyze the effects of spontaneous fracture growth (“self-induced hydraulic fracturing”) on a spatial scale of an element (cell) of a waterflooding field pattern.

The reservoir state is described by non-isothermal Biot linear poroelastic model [4]. It should be noted that in general geological medium may exhibit plastic and/or viscoelastic properties on temporal and spatial scales associated with the hydraulic fracturing procedure. Taking such effects into account in the model will require a change in the “mechanical” part of the Biot model. It is a technical complication which doesn’t drastically change the structure of the mathematical model and the method of coupling the corresponding groups of equations. However, linearly elastic media models are often used for hydraulic fracturing analysis. This is due to the simplicity and robustness in estimation of the bulk parameters (elastic modules, Biot modules, *etc.*) in the case of a linear medium.

The fracture is assumed to be as an arbitrary sufficiently smooth surface with boundary [5]. The fracture flow is described by 2D lubrication Reynolds layer equation. The hydrodynamic model of the flow is supplemented by the energy balance equation and allows one to take into account non-isothermal effects.

Reservoir and fracture flow models are coupled by means of appropriate interface conditions defined at the fracture mid-surface. Fracture growth criteria based on Rice-Cherepanov J-integral in a vector form [6, 7] was used to describe fracture front propagation, taking into account the combined loading mode in the vicinity of the front.

Within this context we suggest a complex of numerical algorithms based on X-FEM/CPF method [8] suitable for the analysis of the hydraulic fracture dynamics problem. Some numerical results are presented which demonstrates applicability of developed models and techniques.

2 Geometry Model of Media and Fracture

The host medium is domain $\Omega \subset \mathbb{R}^3$ with a cut along the fracture mid-surface (see Fig. 1), which characteristic size is tens to hundreds meters (the scale of the water-flooding field pattern). The crack opening has an average value of the order of a few millimeters, the maximum is of the order of a few centimeters. For this reason, it does not make sense to account for a fracture as a three-dimensional object when considering poroelastic processes in the medium. Therefore, we will consider a fracture as of zero thickness with mid-surface being a smooth and simply-connected manifold $F : D_F \rightarrow \mathbb{R}^3$, $D_F \subset \mathbb{R}^2$, with a boundary (fracture front) ∂F . At the time moment t fracture mid-surface is denoted by F_t . The condition $F_{t_1} \subset F_{t_2}$ holds for any $t_{1,2}$ such that $t_1 \geq t_2$. At each time moment and point on $\gamma(t) = \partial F_t$ the fracture front velocity field is given by $\mathbf{v} = \mathbf{v}(\mathbf{x}, t)$ so the fracture extension is described by the equation

$$\dot{\mathbf{x}} = \mathbf{v}(\mathbf{x}, t), \quad \mathbf{x}|_{t=0} = \mathbf{x}_0 \in \gamma(0), \tag{1}$$

where velocity field $\mathbf{v} = \mathbf{v}(\mathbf{x}, t)$ is smooth enough function of point $\mathbf{x} \in \gamma(t)$ at each fixed time moment and a smooth function of time for each fixed (Lagrangian) point of the boundary.

3 Poroelastic Model for Host Medium

The main assumptions of the model are: the stress-strain state of the reservoir is based on a physically and geometrically linear model; the problem is considered in the non-isothermal setting with the temperature deviations from the initial state

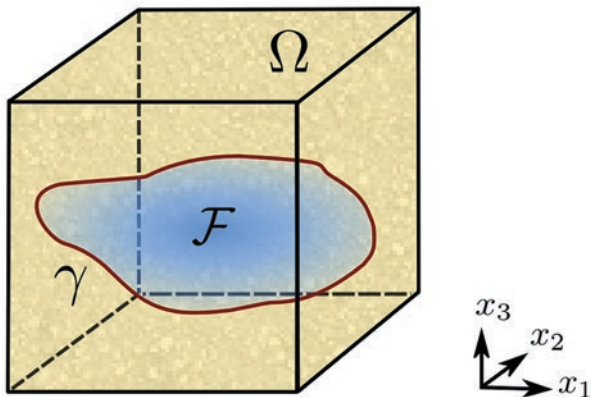


Fig. 1 General view of host medium and fracture

being small; reservoir fluid is a single phase and weakly compressible; dynamic effects (inertial forces) in the host medium can be neglected (that is, the process is quasi-equilibrium).

Mechanical equilibrium equations in the host medium are given by

$$\nabla \cdot \mathbf{T} + \rho \mathbf{g} = 0,$$

with $\rho = \rho(\mathbf{x})$ being an average density of fluid-saturated medium, \mathbf{g} being gravity acceleration, \mathbf{T} – Cauchy stress tensor. In the general anisotropic case and in the linear approximation the constitutive relations are given by [4] $\Delta \mathbf{T} = \mathbf{C} : \mathbf{E} - \mathbf{B} \Delta p - \mathbf{C} : \mathbf{A} \Delta \Theta$, $\Delta \varphi = \mathbf{B} : \mathbf{E} + \Delta p/N - 3\alpha_\varphi \Delta \Theta$. Here p is fluid pressure, $\mathbf{E} = [\nabla \otimes \mathbf{u} + (\nabla \otimes \mathbf{u})^T]/2$ – small deformation tensor, \mathbf{u} – displacements field, $\mathbf{C} = [C_{ijkl}]$ – symmetric tensor of elastic coefficients, $\mathbf{B} = [B_{ij}]$ – symmetric Biot tensor, $\mathbf{A} = [\alpha_{ij}]$ – symmetric thermal expansion coefficient tensor, Θ – temperature, φ – porosity, α_φ – thermal expansion coefficient of the pore volume, N – Biot coefficient that describes dependence of porosity on fluid pressure, $\Delta f = f - f_0$ for any variable f , $\rho = (1 - \varphi)\rho_s + \varphi\rho_f$, where $\rho_{s,f}$ is matrix and fluid density respectively.

During rock deformation, a change in the fluid volume occurs. This change is associated with both a change in the volume of the skeleton and a change in the volume of the pore volume due to the deformation of the skeleton. The relevant fluid mass conservation equation is given by

$$\frac{\partial m_f}{\partial t} + \nabla \cdot (\mathbf{w}_m) = q, \quad \mathbf{v} = \frac{\mathbf{w}_m}{\rho_f} = \mathbf{K} \cdot (-\nabla p + \rho_f \mathbf{g}), \quad (2)$$

where m_f is fluid mass in a unit volume of a saturated medium, $\mathbf{w}_m = \rho_f \mathbf{v}$ – mass flux density vector, \mathbf{v} – the filtration velocity determined by Darcy's law, \mathbf{K} – symmetric positively defined tensor of permeability coefficients, q – mass rate of inflow/outflow sources.

Assuming that the skeleton and the fluid are in a state of local thermodynamic equilibrium in the elementary volume of a saturated medium, the equation of the energy conservation law (in the absence of external energy sources) can be written in the form of

$$\frac{\partial e}{\partial t} + \nabla \cdot (h_f \mathbf{w}_m + \mathbf{q}_\Theta) = 0, \quad \mathbf{q}_\Theta = -\Lambda \nabla \Theta,$$

where h_f is fluid enthalpy, \mathbf{q}_Θ – heat flux vector (due to thermal conductivity effects), e – total internal energy of the saturated medium volume element, $e = \rho_s(1 - \varphi)e_s + \rho_f\varphi e_f$, Λ – symmetric positively defined thermal conductivity tensor, $e_{s,f}$ and $\rho_{f,s}$ are internal energies and densities of solid and fluid phases, respectively.

The above equations must be supplemented by constitutive relations. We assume that the deviations from the initial state are small and the fluid is weakly compressed:

$$\frac{\Delta \rho_f}{\rho_f^0} = \frac{\Delta p}{K_f} - 3\alpha_f \frac{\Delta \Theta}{\Theta_0}, \quad \Delta s_f = -3\alpha_f \frac{\Delta p}{\rho_f^0} + C_p \frac{\Delta \Theta}{\Theta_0},$$

where K_f is fluid bulk compression module, α_f fluid thermal expansion coefficient, s_f fluid entropy, C_p heat capacity at constant pressure, ρ_f^0 and Θ_0 are some reference values.

Taking into account the conditions of small changes in the properties of a saturated medium, it can be shown that

$$\Delta m_f = \rho_f^0 v_f, \quad v_f = \mathbf{B} : \Delta \mathbf{E} + \frac{1}{N} \Delta p - 3\alpha_\varphi \Delta \Theta,$$

where v_f is relative change of fluid volume in an elementary volume of a saturated medium.

The described equations must be supplemented with boundary conditions. In hydraulic fracture dynamics modelling the boundary conditions for pressure can be defined as Neumann homogeneous conditions providing zero fluid mass flow, or Dirichlet condition expressing the predefined pressure evolution as a function of time. The displacements of medium points on the outer domain boundary in reservoir conditions are typically unknown, for this reason the “mechanical” boundary conditions usually have the form of Neumann conditions which express a given value of normal stresses on the domain boundary.

4 Fracure Flow Model

We assume that the fluid propagates along the fracture, trying to fill its complete volume. Fracture opening w is a function of a point of the mid-surface F , $w = w(\mathbf{x})$, $\mathbf{x} \in F$. We assume that the opening is relatively small compared to the mid-surface curvature and its linear extents.

Lateral fracture surfaces $F^\pm = \mathbf{x} \mp \mathbf{n}(\mathbf{x})w(\mathbf{x})/2$ are located at a distance $w/2$ from F . Here $\mathbf{n}(\mathbf{x})$ is a unit normal to F at point \mathbf{x} directed to F^- (thus, $\mathbf{n}^+ = \mathbf{n}$, $\mathbf{n}^- = -\mathbf{n}$). Function w is smooth, nonnegative and equals vanishes on ∂F .

The equation of compressible fluid flow in a fracture has the form of Reynolds lubrication equation:

$$\frac{\partial \rho_f w}{\partial t} + \nabla_{\mathcal{F}} \cdot (\rho_f w \mathbf{v}_{\mathcal{F}}) = Q_f, \quad \mathbf{v}_{\mathcal{F}} = -D(\nabla_{\mathcal{F}} p_f - \rho_f \mathbf{g}_{\mathcal{F}}), \tag{3}$$

where $\mathbf{v}_{\mathcal{F}}$ is the velocity of fluid, D is an effective permeability, $\mathbf{g}_{\mathcal{F}}$ is the projection of the vector of gravity acceleration on the mid-surface of fracture, $\mathbf{g}_{\mathcal{F}} = (\mathbf{I} - \mathbf{n} \otimes \mathbf{n})\mathbf{g}$. In the case of a Newtonian fluid $D = w^2/(12\mu_f)$ with μ_f being dynamic viscosity of

fluid. In the general case of a non-Newtonian fluid $D = D(w, \nabla_{\mathbb{F}} p_f)$, see, for example, [9]. The symbol $\nabla_{\mathbb{F}}$ denotes the surface “nabla” (“del”) operator [10].

Source term Q_f can be represented as $Q_f = Q_f^m + Q_f^{out}$. In the latter the first term describes the inflow rate from the well to the fracture, the second one – the leakage of fluid into the poroelastic reservoir.

Equation (3) is considered in a bounded domain $\Omega_f = \Omega_f(t) \subset F$ with boundary (fluid front) $\partial\Omega_f(t)$. The appropriate boundary conditions are to be set at $\partial\Omega_f$.

In a number of practically important cases Eq. (3) can be supplemented by an equation describing the transfer of some passive component (for example, a “propant” which is a special calibrated “sand” intended to prevent fracture from “closing” in the case of sufficient pressure drop). The corresponding models are widely known (see, for example, [9, 11]) and practically do not change the structure of the model and the form of its equations. For this reason, they are not considered here.

If it is necessary to account for non-isothermal flow effects in the fracture, the fluid mass conservation equations are supplemented by the equation of energy balance. In the case of a weakly compressible fluid in a crack, the equation of energy conservation (three-dimensional) has the form (without taking into account external heat sources):

$$\frac{\partial}{\partial t}(\rho_f e) + \nabla \cdot (-\lambda_{\Theta} \nabla \Theta + \rho_f C \Theta \mathbf{v}_f) - \mathbf{D} : \mathbf{T} = 0, \quad (4)$$

where $\rho_f \Delta e = \rho_f C \Delta \Theta$ is a bulk density of fluid internal energy, λ_{Θ} is a fluid thermal conductivity, $\rho_f C$ – volumetric heat capacity of fluid. The last term in (4) describes the energy dissipation due to the work of viscous forces acting in the fluid.

Integration of Eq. (4) over the fracture opening in the range from $-w/2$ to $+w/2$ provides with:

$$\frac{\partial}{\partial t}(w \rho_f C \Theta_f) + \nabla_f \cdot (-w \lambda_f \nabla_f \Theta_f + w \rho_f C \Theta_f \mathbf{v}_f) - \mathcal{D} + q_{\Theta} = 0,$$

where Θ_f is the opening averaged temperature, \mathcal{D} is the dissipation due to the work of viscous forces, q_{Θ} is the heat flux through the side surfaces of the crack. Taking into account the assumptions about the structure of the flow in a thin lubricating layer (locally Poiseuille profile, small Reynolds numbers, small layer thickness), the expression for the dissipation can be written as $\mathcal{D} = (12\mu_f) / w \mathbf{v}_f^2$. For flows under consideration this quantity is usually small and can be neglected, that is, it can be considered $\mathcal{D} \equiv 0$.

5 Interface Conditions at the Fracture/Medium Boundary

Mid-surface F is a jump discontinuity for the variables that describe reservoir state and which are related by the interface conditions. These conditions couple the above considered independent groups of equations describing the state of a poroelastic medium and the fracture flow. The interface conditions include kinematic conditions and ones ensuring the continuity of the momentum, mass and energy fluxes.

Assume $\mathbf{x} \in F$ denotes a point on fracture middle surface \mathbf{x}^\pm are the corresponding points on the fracture faces F^\pm (see Fig. 2). The first group of interface conditions are kinematic conditions given by:

$$\begin{aligned} w(\mathbf{x}) &= (\mathbf{u}^+ - \mathbf{u}^-) \cdot \mathbf{n} = [\mathbf{u}] \cdot \mathbf{n} = [u_n], \quad u_n^\pm \\ &= \mathbf{u}^\pm \cdot \mathbf{n}, \quad [u_n] = u_n^+ - u_n^-, \quad \mathbf{u}^\pm = \mathbf{u}(\mathbf{x}^\pm). \end{aligned}$$

In the considered problem it is impossible to make natural *a priori* assumptions on the jump of the tangential components of the displacement field passing through the surface F , the value of this jump is unknown and is determined by the solution of the problem.

Dynamic interface conditions are given by:

$$\mathbf{T}^+ \cdot \mathbf{n}^+ = -p^* \mathbf{n}^+, \quad \mathbf{T}^- \cdot \mathbf{n}^- = -p^* \mathbf{n}^-.$$

Consider now interface conditions for the hydrodynamics part of problem. They can be given in different forms, depending on the assumptions imposed on the fracture flow.

In the first case fracture and medium are considered to be saturated with the same fluid that occupies entire volume of the fracture ($\Omega_f = F$), and the hydrodynamic contact between fracture and the medium is ideal. In that case at each point $\mathbf{x} \in F$ of the mid-surface the pressure on fracture faces are given by $p^+ = p^- = p_f$ with

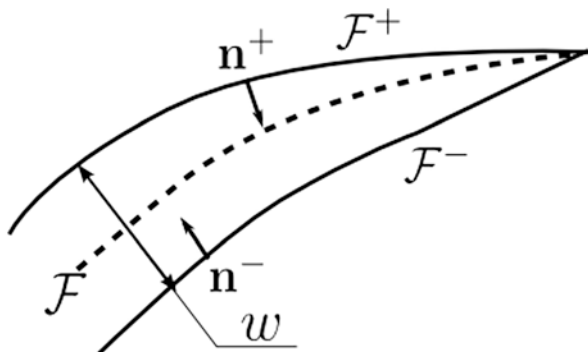


Fig. 2 Orientation of the lateral surfaces (shores) of the crack

$p^\pm = p(\mathbf{x}^\pm)$. The continuity of the material flux conditions with the corresponding expressions for the flow in the medium (2) and the form of Eq. (3), expressing the material balance in the fracture, have the form $Q_f = Q^+ + Q^-$, $Q^\pm = \mathbf{w}_m \cdot \mathbf{n}^\pm \Big|_{\mathbf{x}=\mathbf{x}^\pm}$ with p^* being defined as $p^*(\mathbf{x}) = p_f(\mathbf{x})$.

In the second case it is assumed that fluid in the fracture does not flow into the medium, i.e. the fracture volume is isolated. In this case it is natural to assume that $\Omega_f \subset F$, $\partial\Omega_f \cap \partial F = \emptyset$ (see Fig. 3). Interface conditions for the mass flux in domain Ω_f are given by $Q_f = 0$, $Q^\pm = 0$, $\mathbf{x} \in \Omega_f$. In other words, the interface conditions degenerate into the Neumann boundary conditions for the flow equation in the medium. In this case conditions for pressure in the medium cannot be formulated, and the fracture pressure is given by (3) with non-vanishing right-hand side Q_f with p^* defined as $p^*(\mathbf{x}) = p_f(\mathbf{x})$.

Interface conditions in the domain $F \setminus \Omega_f$ (“lag” domain) can be set in a different ways depending on whether the fracture faces are permeable or not for the fluid in the bulk. In the first case at points $\mathbf{x} \in F \setminus \Omega_f$ the relations $Q^\pm = 0$ and $p^*(\mathbf{x}) = 0$ are satisfied. In the second case it is natural to consider that fluid in porous media fills fracture (sub)domain $F \setminus \Omega_f$ without discontinuity in passing through the faces of the fracture, i.e. $[p] = 0$, $[Q] = 0$.

Finally, consider practically important case in which fluid doesn’t permeate medium, but contains a component, which can. Then it is usually assumed that the flows on the faces of the fracture are defined as functions of the fluid and bulk media properties, pressure fields in the fracture and its neighborhood. In the framework of the model under consideration, this leads to the conditions $Q_f = Q^+ + Q^-$, $Q^\pm = Q^\pm(p_f, p^\pm) = \mathbf{w}_m^\pm \cdot \mathbf{n}^\pm$. The last dependence can be given, for example, in accordance with the Carter leakage model or its generalizations [12].

Consider now energy balance conditions for the flow. We assume that at the points of the boundary F^\pm of the saturated poroelastic medium (the skeleton and the fluid) and the fluid in the crack are in a state of local thermal equilibrium, i.e.

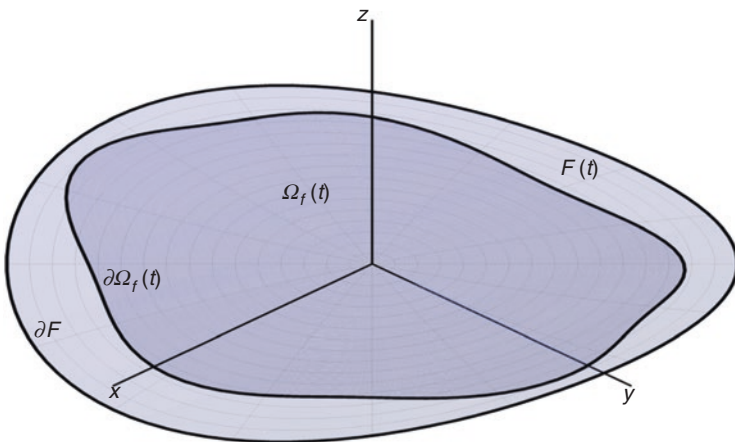


Fig. 3 Relative position of fracture mid-surface and fluid domain

$\Theta^\pm = \Theta_F$, or, equivalently, $[\Theta] = 0$, $\{\Theta\} = \Theta_F$. In the case when fluid does not leak from the fracture into the host medium, the continuity conditions for the energy flux read

$$q_\Theta = Q_\Theta^+ + Q_\Theta^-, \quad Q_\Theta^\pm = \mathbf{q}_\Theta^\pm \cdot \mathbf{n}^\pm, \quad \mathbf{m}^\pm = 0.$$

In the case a fluid leak occurs and is given by Q^\pm terms predefined in any suitable way, the continuity conditions for the energy flux read:

$$q_\Theta = Q_\Theta^+ + Q_\Theta^-, \quad Q_\Theta^\pm \equiv h_f Q^\pm = \left(h_f \mathbf{w}_m + \mathbf{q}_\Theta \right) \Big|_{\mathbf{x}=\mathbf{x}^\pm} \cdot \mathbf{n}^\pm.$$

The flow from the fracture into the host medium is assumed to be predefined. The temperature value is defined by the complete solution of the problem.

6 Fracture Front Boundary Conditions and Growth Criterion

During fluid injection in the fracture it starts to evolve. From mathematical point of view this corresponds to fracture mid-surface evolution. In what follows we assume that this evolution is quasi- equilibrium, i.e., at each time moment reservoir medium and fracture are in mechanical equilibrium. The latter conditions define not only stress state of the reservoir but also fracture configuration as a part of the solution of the complete coupled problem.

We assume that the fracture evolution can be described by linear elastic fracture mechanics using energy fracture growth criterion. In this approach a certain amount of the energy is assigned to a unit element of the fracture surface and is interpreted as an amount of energy which is needed to form it. Correspondently, fracture mid-surface evolution produce an energy flux related to the fracture front. This considerations lead to the concept of Cherepanov and Rice J -integral [8]. In the presented model we use vector valued J -integral [13] generalized to the poroelastic case in [6] together with the corresponding fracture growth criterion presented in [7].

Let us assume that at each point $\mathbf{x} \in \partial F_f$ a vector valued function $\mathbf{J} = \mathbf{J}(\mathbf{x})$ can be defined such that energy released during fracture propagation in the direction given by the unit vector \mathbf{l} ($\|\mathbf{l}\| = 1$) is equal to $J = \mathbf{J} \cdot \mathbf{l}$. In accordance to energy growth criterion fracture evolves in the direction which maximize value of J , $J = J_{\max} = J(\mathbf{l}_{\max})$. In the case when $J_{\max} \leq J_*$, where J_* is some critical value fracture growth does not occur. When $J_{\max} = J_*$ the fracture is in equilibrium. In the case when $J_{\max} > J_*$ fracture develops in an unstable way. Consequently, if the fracture growth occur, the growth direction is given by \mathbf{J} , i.e. one have $\mathbf{v} = \alpha \mathbf{J}$, $\alpha \geq 0$ in (1).

At the same moment, linear elastic fracture mechanics under quasi-equilibrium conditions does not provide a way to determine fracture growth velocity in the case $\alpha > 0$. Hence, (1) is a kind of “kinematic” equation and has to be supplemented by

equation which determines fracture front position under the given condition $J_{\max} \leq J_*$. This equation is nonlocal (both in space and time) and introduces dependency of the future fracture configuration on the history of the process, its current configuration, problem (fracture and reservoir) solution at the given time in the whole domain of the interest, boundary conditions, etc.

Let us now consider the case of fluid filled fracture. Let at each moment of time t one have $\Omega_f(t) \subset F$ and $\partial\Omega_f(t) \cap \partial F = \emptyset$. Hence, at each point of the fluid front it holds $w(\mathbf{x}) \geq w_0 > 0$, $\mathbf{x} \in \Gamma(t)$. Let \mathbf{n} be a unit normal to $\partial\Omega_f$ tangent to the fracture mid-surface, \mathbf{V} be the velocity of $\Gamma(t) = \partial\Omega_f(t)$, \mathbf{v}_F be the fluid particle velocity averaged over fracture opening, ρ_f be the fracture fluid density, Q_f be the external volumetric inflow rate, $q_f = Q_f/\rho_f$ – external mass flow rate. From (3) one has:

$$\int_{\Omega_f(t)} \frac{\partial \rho_f w}{\partial t} ds + \int_{\Gamma(t)} \rho_f w v_n d\gamma = \int_{\Omega_f(t)} Q_f ds, \quad v_n = \mathbf{v}_F \cdot \mathbf{n}|_{\Gamma(t)}. \quad (5)$$

In this case fluid velocity normal component V_n is equal to the normal component of the fracture front velocity v_n , i.e.

$$\lim_{\mathbf{x} \rightarrow \mathbf{x}_f} v_n = V_n = \frac{d\mathbf{x}_f}{dt} \cdot \mathbf{n} = \lim_{\mathbf{x} \rightarrow \mathbf{x}_f} \frac{\mathbf{q}_F \cdot \mathbf{n}}{\rho_f w}, \quad \mathbf{q}_F = \rho_f w \mathbf{v}_F, \quad \mathbf{x}_f \in \Gamma(t). \quad (6)$$

Equation (6) (called “speed equation”, see [14]) is quite obvious but nevertheless is of the fundamental nature and relates fluid front velocity to fluid particles velocity. The tangential component of fluid velocity usually can be neglected which leads to $\mathbf{V} = \mathbf{v}$. Note that Eq. (6) is fulfilled even in the case when fracture opening is vanishing at the fluid front (that is exactly why we use $\mathbf{x} \rightarrow \mathbf{x}_f$ and not $\mathbf{x} = \mathbf{x}_f$). Now let us discuss boundary conditions for Eq. (3) keeping (6) in mind.

The first option is to define Dirichlet boundary condition for fracture fluid pressure at the fluid front, $p_f(\mathbf{x}) = p_f^*(\mathbf{x})$, $\mathbf{x} \in \Gamma(t)$, with p_f^* being given function. In that case the fluid velocity at the front can be determined using (6). Temporal evolution of the fluid domain is described by equation similar to (1) with fluid front velocity defined by (6). The value of p_f^* at the point of the fluid front can be set to zero when reservoir fluid does not enter fracture (“empty” lag zone). Otherwise it is natural to set to be equal to the reservoir pressure at the given point.

The second option assumes that at each point of the fluid front its average particle velocity (or, which the same, the mass flux at the fluid front, see (6)) is defined. Temporal evolution of the fluid front is described in the same way as above. The fluid front velocity in that case can be defined in an arbitrary way the velocity value has to be in agreement with mass flux at the boundary at fracture opening at the fluid front in accordance with (6).

Let us note that the first option is more natural in the considered case. Also note that there are two fronts are present in the model: the fracture and the fluid one.

Let us now consider the case when fluid occupies complete fracture volume, i.e., the situation when two fronts - the fracture and the fluid ones, coincide. From

mathematical point of view such a case is the most complicated for the analysis. The reason is that, since fluid and fracture fronts coincides, opening is vanishing at the fluid front. Nevertheless the mass flux in (3) is finite since fluid front propagates with finite velocity. This leads to the singularity in the pressure field. The correct statement of the boundary conditions for fluid equations in fracture is nontrivial in this case. The “natural” form of boundary conditions is fluid front velocity which, in turn, is defined by fracture front velocity and fracture propagation criterion. Simultaneously, Eq. (6) can be considered not as definitive relation for fluid front velocity but rather as equation which relates fracture and fluid front velocities.

Finally let us note that (i) for practically important cases it is more important to account for lag itself but not for its precise value and (ii) consideration of lag is of the importance only in the relatively small neighborhood of the fluid front and at the initial stage of fracture development. This consideration usually allows to estimate lag values using some additional considerations or to set it to a small but fixed in time and space value (see, e.g., [14]).

7 Numerical Simulation Results

The mathematical model presented in the previous sections formed the basis of software for large scale hydraulic fractures dynamics. The core of developed computational algorithm is eXtended Finite Elements Method (X-FEM) [15, 16]. The method is based on the extension of a standard finite-element basis by special additional basis functions that allow one to correctly represent the discontinuous fields of the displacement, stresses and deformations on the middle surface of fracture. One important issue of the X-FEM method is an algorithm for fracture surface representation in a finite-dimensional problem, which should provide convenience of computation of all the necessary quantities in a view of the method implementation. In the contemporary variants of the X-FEM the most commonly used approach for fracture geometry representation is the level set method [17]. For the evolution of the level set functions the Hamilton-Jacobi type equations are used, see [18, 19].

In this paper we used an approach based on the method of the closest point (CP) projection to describe the geometry of a mid-surface. Algorithms to compute CP projector evolution during fracture growth are developed in [5]. In the context of fracture evolutions problems it is as general as the level set method, but it has a number of advantages when the boundary conditions on the lateral surfaces of a crack are determined by the solution of some equations (in our case, the lubricating layer equation). In addition, the method of closest point projection is currently a convenient tool for developing computational algorithms for solving equations on surfaces of arbitrary shape, see [20].

Thus, in this paper the CP projection method is used both to represent the fracture surface in X-FEM, and to solve the equation of the lubricating layer in the fracture. A description of the X-FEM /CP approach is presented in [8].

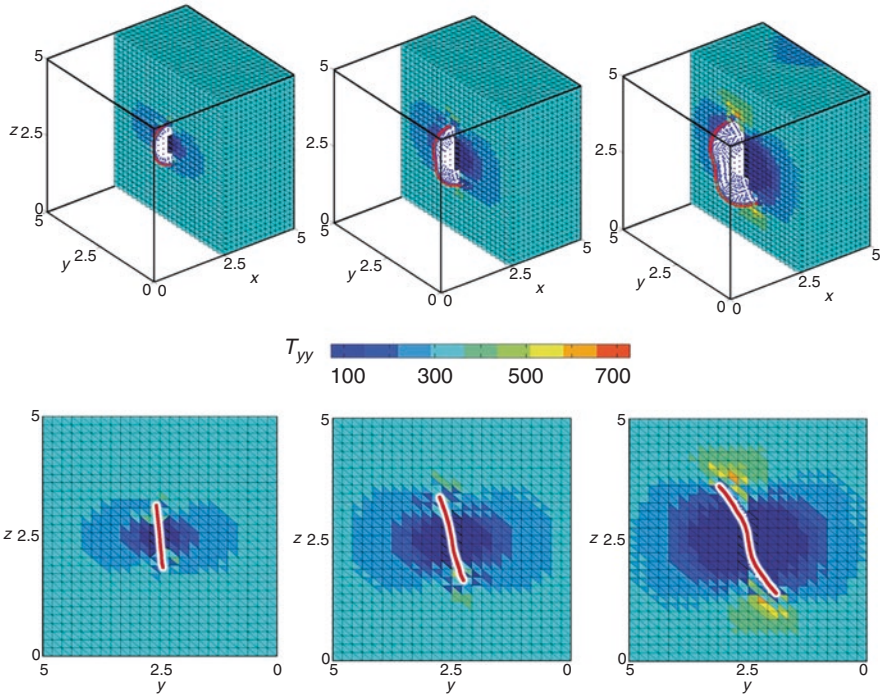


Fig. 4 The T_{yy} distribution of total stress field at different time moments. The red line denotes fracture mid-surface evolution

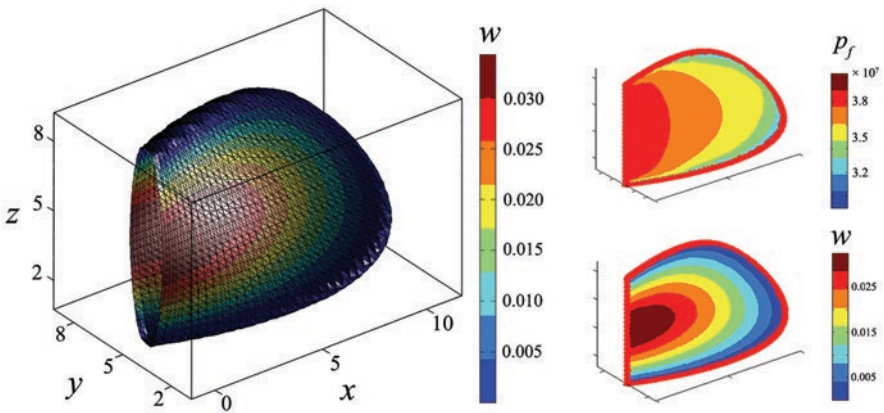


Fig. 5 Fracture opening on surface (left) and flow parameters on mid-surface (right)

We present below some simulations results that illustrate the applicability of the presented algorithms. On Fig. 4 an example of fracture mid-surface evolution and T_{yy} component of total stress field are shown for certain fracture configuration. On the left part of Fig. 5 fracture surface with corresponding opening field is presented, the right part of Fig. 5 shows fluid pressure (top) and fracture opening (bottom) on mid-surface.

References

1. Salimov VG, Ibragimov NG, Nasybullin AV, Salimov OV (2013) *Gidravlicheskii razryv karbonatnykh plastov* [Hydraulic fracturing of carbonate formations]. Neftyanoe khozyaistvo, Moscow
2. Economides MJ, Oligney RE, Valko P (2001) *Unified fracture design: bridging the gap between theory and practice* Alvin. Orsa Press, Texas
3. Economides MJ, Nolte KG (eds) (2000) *Reservoir stimulation*, 3rd edn. Wiley, West Sussex
4. Coussy O (2004) *Poromechanics*. Wiley, West Sussex
5. Ivanov AV, Savenkov EB (2017) Simulation and visualization of the dynamics of a surface with a movable boundary on a stationary unstructured mesh. *Sci Visual* 9(2):64–81
6. Ramazanov MM, Kritsky BV, Savenkov EB (2018) Formulation of J-integral for biot poroelastic medium. *J Eng Phys Thermophys* 91(6):1595–1602
7. Ramazanov M, Borisov V, Kritskiy B, Savenkov E (2018) Fracture growth criterion for poroelastic media. *AIP conference proceedings*, 2051, 020214
8. Savenkov EB, Borisov VE, Kritsky BV (2019) Utilization of closest point projection surface representation in extended finite element method. *Math Models Comput Simul.* (in press)
9. Adachi J, Siebrits E, Peirce A, Desroches J (2007) Computer simulation of hydraulic fractures. *Int J Rock Mech* 44:739–757
10. Dubrovin BA, Novikov SP, Fomenko AT (1986) *Sovremennaya geometriya. Metody i prilozheniya* [Modern geometry. Methods and applications], 2nd edn. Nauka, Moscow
11. Eskin D, Miller MJ (2008) A model of non-Newtonian slurry flow in a fracture. *Powder Technol* 182:313–322
12. Clifton RJ, Brown U, Wang J-J (1991) Modeling of poroelastic effects in hydraulic fracturing. *SPE Paper* 21871
13. Cherepanov GP (1979) *Mechanics of brittle fracture*. McGraw-Hill, New York
14. Linkov AM (2015) Particle velocity, speed equation and universal asymptotics for efficient modelling of hydraulic fracturing. *J Appl Math Mech* 79(1):54–63
15. Belytschko T, Black T (1999) Elastic crack growth in finite elements with minimal remeshing. *Int J Numer Methods Eng* 45:601–620
16. Moës N, Dolbow J, Belytschko T (1999) A finite element method for crack growth without remeshing. *Int J Num Methods Eng* 46:131–150
17. Stolarska M, Chopp D, Moës N, Belytschko T (2001) Modelling crack growth by level sets in the extended finite element method. *Int J Num Methods Eng* 51:943–960
18. Moës N, Gravouil A, Belytschko T (2002) Non-planar 3D crack growth by the extended finite element and level sets – part I: mechanical model. *Int J Num Methods Eng* 53:2549–2568
19. Gravouil A, Moës N, Belytschko T (2002) Non-planar 3D crack growth by the extended finite element and level sets – part II: level set update. *Int J Num Methods Eng* 53:2569–2586
20. Macdonald CB, Ruuth SJ (2009) The implicit closest point method for the numerical solution of partial differential equations on surfaces. *SIAM J Sci Comput* 31:4330–4350

Part IV
Fluid – Thermal Properties

Thermodynamic Properties of Geothermal Fluids from South Russia: Kayakent and Kizlyar Hot Sources



Ilmutdin M. Abdulagatov, Lala A. Akhmedova-Azizova, Rasul M. Aliev, and Gasan B. Badavov

Abstract Volumetric (density), acoustic (speed of sound), and transport (viscosity) properties of natural geothermal fluids from south Russia Geothermal Field have been measured over the temperature range from (278 to 343) K and at atmospheric pressure. The measurements were made using the Anton Paar DMA4500 densimeter and Stabinger SVM3000 viscometer for four geothermal fluid samples from the hot-wells. A sound-speed analyzer (Anton Paar DSA 5000 M) was used to measure the speed of sound and the density of the same geothermal samples. The combined expanded uncertainty of the density, viscosity, and speed of sound measurements at the 95% confidence level with a coverage factor of $k = 2$ is estimated to be – density: 0.0005% (for DMA 4500), 0.02% or $0.5 \text{ kg}\cdot\text{m}^{-3}$ (for the SVM 3000 viscodensimeter) and 0.01% (for the DSA 5000 M sound-speed analyzer); viscosity -0.35% (for SVM 3000); and speed of sound -0.1% (DSA 5000 M), respectively. Measured values of density and speed of sound were used to calculate other very important thermodynamic properties of the geothermal fluid samples. Measured values of density, viscosity, and speed of sound were used to develop correlation models which reproduced the measured values of density, viscosity, and speed of sound within 0.03%, 2.55%, and 0.06%, respectively. The measured properties at atmospheric pressure have been used as a reference values for prediction of high pressure properties.

Keywords South Russia · Republic of Dagestan · Geothermal fluids · Density · Vibrating tube densimeter · Speed of sound · Viscosity · Water

I. M. Abdulagatov (✉) · G. B. Badavov

Institute for Geothermal and Renewal Energy of the High Temperature Joint Institute of the Russian Academy of Sciences, Makhachkala, Russia

L. A. Akhmedova-Azizova

Azerbaijan Technical University, Baku, Azerbaijan

R. M. Aliev

Daghesten State Technical University, Makhachkala, Russia

© The Author(s), under exclusive license to Springer Nature Switzerland AG 2021

V. Svalova (ed.), *Heat-Mass Transfer and Geodynamics of the Lithosphere*, Innovation and Discovery in Russian Science and Engineering,

https://doi.org/10.1007/978-3-030-63571-8_17

1 Introduction

The Republic of Dagestan is located in the Southern part of the Russian Federation. It is a pioneer in the use of deep earth thermal potential in the former USSR. Dagestan has unique geothermal resources for the production of more than 2 billion kWh of electricity and more than five million Gcal of heat annually. The energy balance of the republic is extremely tense: up to 100% of solid fuel and up to 90% of natural gas are imported. Therefore, the geothermal energy utilization is especially important for power supply of its central and northern regions.

In Dagestan, the total amount of explored reserves of geothermal fluids in the Mesozoic sediments is 86 thousand m³/day when flowing, and 513 thousand m³/day when using the pumps. Thermal potential is equivalent to replacing 500 million cubic meters of natural gas or 575 thousand tons of reference fuel per year. The maximum amount of annual gas replacement reaches 1 billion cubic meters or 30% of regional gas consumption.

Currently, in the cities of Makhachkala, Kizlyar, and Izberbash, about 15 thousand cubic meters a day of thermal water with a temperature of 50–100 °C are used for heat supply and partly for greenhouses heating, as well as in balneology and for the production of mineral water. Volumes of replacement fuel do not exceed 20 thousand tons of reference fuel [24].

In order to enhance the efficiency of geothermal energy in the region, the accurate thermophysical characteristics of the geothermal fluids from various geothermal wells are required.

1.1 Key Thermodynamic Properties of Geothermal Fluids for Practical and Scientific Applications

Thermodynamic and transport property data of geothermal brines are needed for geothermal energy utilization devices. Geothermal energy production is directly related with thermophysical property data of geothermal fluids. Particularly, knowledge of the geothermal fluid properties is important in geothermal exploration and energy production, to establish optimal operations for the productions of geothermal brine fields. For example, the total heat content of geothermal fluid depends on the density, temperature, and heat capacity [66]. For the effective utilization of geothermal resources, a precise thermodynamic and transport properties data are required for the initial resource estimates, production and reservoir engineering study of the geothermal field, reservoir modeling, and binary geothermal power cycle optimization. Thermodynamic and transport properties (density, heat capacity, viscosity, thermal conductivity, *etc.*) of geothermal fluids determine the transfer of heat and mass by geothermal systems. The energy properties of the geothermal fluids may be extracted directly from the *PVT_x* properties of the geothermal fluid through standard thermodynamic approaches [38]. Available *PVT_x* properties of geothermal fluids are

not sufficient to meet the needs of the geothermal industry for complex solutions such as those found in geothermal reservoirs. Modeling geothermal wells (geothermal engineering, geothermal or reservoir installations) need accurate thermophysical property data [62, 71]. Thus, one of the key factors when planning the exploitation of geothermal resources is the availability of reliable data on thermodynamic and transport properties of geothermal brines. These data needed to properly estimate the likelihood of scaling and/or corrosion developing within the wells and surface installations, and to predict the commercial lifetime of the exploitation project. Also accurate thermophysical property data of the geothermal brines are prerequisite for chemical and reservoir modeling of geothermal brine systems (multiphase underground flows). Utilize geothermal sources as efficiently and economically as possible, and to ensure minimum disruption to the environment, modeling of geothermal systems and reservoirs is necessary. Modeling helps determine the natural (prior to exploration) state of a geothermal system and its behavior under exploration.

Initially geothermal fluids were modeled as pure water. Thermodynamic and transport properties of pure water are well-known (see IAPWS formulations for thermodynamic [74] and transport properties, viscosity [41] and thermal conductivity [42]). Thermophysical properties of geothermal fluids such as density, viscosity, heat capacity, and enthalpy play a fundamental role in mass and heat transfer in the Earth's interior. In order to provide numerical modelling of the heat and mass flow processes of geothermal fluids using concentration equations, definitions of the thermodynamic properties of density (ρ), viscosity (η), and enthalpy (H) of these fluids are required [32, 50, 55–57]. Viscosity is one of the key factors in fluid flow simulation (influencing the flow of reservoir fluids). Solution of the set of differential equations (equations of mass and energy conservation and linear momentum), which may be used to describe the transport of mass and heat in a porous media for mathematical simulations of the Earth's interior, considerably depends on thermodynamic properties of geothermal brines (density, enthalpy, and viscosity) as a function of temperature, pressure, and concentration of salt (minerals). Solving these sets of equations enables the determination of such quantities as T and P gradients at a point in the flow, and T , P , x profile in time and space [35, 36]. However, solving these equations requires knowledge of the thermodynamic properties of density, enthalpy, and viscosity of the geothermal fluids. To understand and control those processes, which used geothermal fluids, it is necessary to know their thermodynamic and transport properties, particularly density and viscosity as a function of temperature, pressure, and concentration. In the works [25, 26, 53] the authors described models of brines flows that require knowledge of the three key thermodynamic properties (density, viscosity, and enthalpy).

1.2 Review Previous Studies on Geothermal Brines Properties

Relatively little data has been published on the density and viscosity of natural geothermal brines. Most reported data only for binary or ternary aqueous salt solutions as a main component of geothermal brines (basically for synthetic geothermal

brines). Because of the scarcity of data for the density, dynamic viscosity, and enthalpy a different approach to the one used for these properties was adopted [31, 50, 55–57]. For example, Palliser and McKibbin [55–57] proposed correlation model for the viscosity of geothermal brine at $T < 1073$ K. The improvement of the estimation of brine properties such as density and viscosity are needed to use these in two- and three-dimensional simulations [55–57]. The model proposed by Potter and Haas [61] for geothermal brines predicts the density of geothermal brines and seawater within experimental uncertainty at a temperature of 423 K. Wahl [75] proposed following correlation for the density of geothermal brines.

$$\rho_b = \rho_{\text{H}_2\text{O}} + 0.73 \left[1 + 0.0000016(T - 273)^2 \right] w, \quad (1)$$

where w is the weight fraction of salt; $\rho_{\text{H}_2\text{O}}$ is the pure water density. As one can see from Eq. 1, geothermal brines density is linear function of salt concentration. The simplest way of determination of the thermodynamic properties of geothermal fluids is based on pure water properties, because pure water is the dominant constituent, therefore, governs the properties (thermodynamic behavior) of aqueous salt solutions and geothermal brines. Most reliable predictive models for aqueous salts solutions are representing their thermodynamic and transport properties relative to pure water. Using direct experimental thermodynamic data for the particular natural geothermal fluids allows minimize the errors arising from the empirical prediction data for geothermal brines models. Moreover, the brine composition can be changed during production. Thus, more direct measurements of the natural geothermal brines from various regions (wells) of the world with various concentrations of dissolved electrolytes are needed. This allows generalize the properties of various geothermal fluids from various geothermal fields (wells) with various solutes and to develop prediction models for geothermal brines with any chemical composition. Unfortunately, available theoretical models frequently cannot describe real systems such as those met in practice. For example, the accurate prediction of the thermodynamic and transport properties of complex multicomponent ionic aqueous solutions such as geothermal fluids is extremely difficult due to their complexity. In microscopic point of view the effect of individual ionic contributions to the properties of aqueous solution is depend on their structure (shape, size, ions environment, polarization orientation, ion mobility, etc.). Even for binary aqueous salt solution very difficult to accurately estimate the effect of ions on properties. Better predictive models can be developed based on reliable direct experimental information on thermodynamic and transport properties of natural geothermal brines. However, a literature survey reveals that very little information has been reported previously on the direct measurements of the density and viscosity of real (natural) multicomponent geothermal brines from various Geothermal Fields of the World.

In most cases, due to lack of the experimental thermodynamic data, the natural geothermal fluid is modeled as an aqueous salt (usually NaCl, KCl, CaCl₂, etc.) solutions. For example, Potter and Haas [61] indicated that geothermal fluids might be represented by the properties of aqueous NaCl solution as a model of the

geothermal brine. The geothermal fluid was modeled as an aqueous sodium chloride solution and functions for its density and viscosity are compared and applied to a model of the geothermal fluid cycle. Francke and Thorade [35] studied the sensitivity of the volumetric flow rate of a downhole pump in a geothermal production well on different density and viscosity functions during the startup and stationary operating phases. Used pure water or geothermal brine models (synthetic brines like binary or ternary aqueous salt solutions) properties lead to inaccuracies and impossible accurately estimate the effect all of the dissolved salts due to extremely complexities. The studies by Francke and Thorade [35] showed that the deviations between different density functions for geothermal brines are up to 52% of the volumetric flow rate. Presence of dissolved ions in water at various temperatures causes the reservoir flow properties to considerably deviate from those of pure water or model solution.

Since the number of different brines encountered is large, detailed measurements on all of them become impractical. The experimental study of the thermodynamic properties of each geothermal fluid would be a formidable task, and theoretical or semi-empirical models that would predicted the thermodynamic properties of complex geothermal brines would be useful. Consequently, the ability to predict the properties of brines from theories or models based on a few key aqueous electrolyte solutions is essential to the technical development of geothermal resources. The model brine not exactly matches the data for pure systems. Geothermal brine is a complex aqueous solution containing varying amounts of dissolved solids and gases. However, due to complexity of the interactions between the solvent (water) and solutes (salt ions) there is no theoretical guidance for the temperature, pressure, and concentration dependences of the thermodynamic properties of multicomponent geothermal brines. It is impossible accurately estimate the effect all of the dissolved salts due to extremely complexities intermolecular interaction between the salt ions, dissolved gases and water molecules and ion-ion interactions in the multicomponent aqueous solutions. Thus, its evaluation is based on the measured data only. Different predictive models were proposed by various authors [21, 25, 26, 28, 32, 35, 36, 46, 49, 51, 52, 54, 55, 58, 68] to represent the effect of temperature and concentration on the thermodynamic properties of geothermal fluids. All of these models based on thermodynamic properties of synthetic aqueous binary or ternary solutions, basically NaCl, since sodium chloride is the major solute in geothermal brines. Milsch et al. [51] studied density and viscosity of synthetic geothermal brines containing varying amounts (5 mol/kg NaCl and CaCl₂, and 4 mol/kg KCl) of dissolved NaCl, KCl, and CaCl₂ salts using Höppler-viscometer and a combination of volumetric and mass measurements for density. The systematic measurements with the three aqueous salt solutions yielded calibration of mixing rules, stoichiometrically weighting the individual viscosities measured at the total of the mixture for density and viscosity. The predictions when applied to a natural geothermal brine of specific chemical composition, showed good agreement with direct measurements performed with this geothermal fluid. The methods allow estimating the density and dynamic viscosity of a given geothermal fluid once the chemical composition has been determined. Further direct measurements of the

thermophysical properties of the natural geothermal brines with complex compositions are needed to confirm applicability and accuracy of the mixing rules.

Ershaghi et al. [34] reported viscosity data for synthetic brines consisting of NaCl, KCl, and CaCl₂ at concentrations from (0.99 to 16.667) wt. % and at temperatures up to 548 K. Measurements were made using a high-temperature capillary tube designed to operate up to a temperature of 588 K and a pressure of 14 MPa. From the use of the laboratory-derived data, a method is presented whereby the viscosity of geothermal brine may be estimated from knowledge of its composition. To quantitatively describe the thermodynamic and transport properties of geothermal fluids as a function of T , P , and x , the thermodynamic model (equation of state) or reference correlation model for transport properties are needed. Unfortunately, as was mentioned above, due to complexity physical chemical nature of the geothermal fluids, theory cannot accurately predict their thermodynamic properties needed for geothermal processes applications. The thermodynamic properties data for natural geothermal fluids are often missing and no equation of state for multicomponent aqueous salt solutions that valid in the wide T , P and x ranges. Inconsistence between existing theoretical models (equation of state) and experimental thermodynamic data for geothermal fluids is the result in difference and uncertainty in geochemical modeling.

The purpose of this study was to measure the density, speed of sound, and dynamic viscosity of four natural geothermal brines from Geothermal Filed of Dagestan (south Russia, Caspian seashore) and the effect of elevated temperatures (from 278 to 343 K) on these properties at various levels of dissolved ion concentrations. Another objective of the present study was to calculate other derived thermodynamic properties such as κ_S , κ_T , α_p , γ_V , ΔH , C_V , C_P , $\left(\frac{\partial H}{\partial P}\right)_T$, $\left(\frac{\partial U}{\partial V}\right)_T$ using the measured density and speed sound data. The correlation models for the density, viscosity, and speed of sound were also developed on bases of measured data. The reported in this work density, viscosity, and speed of sound data for the geothermal fluids at atmospheric pressure $P_0=0.101$ MPa as a function of temperature were used (see below Sect. 3.2) as reference values to predict their high pressures behavior.

2 Experimental

2.1 Geothermal Field Location and Wells Characteristics

The geothermal fluid samples for the present study come from geothermal wells Kayakent No.4, No.5 and Kizlyar No.6, No.17T (Dagestan, south Russia Geothermal Field, 42°24' N & 47°57'30'' E). The Geothermal Field is located in the southern part of Russia, approximately 50 miles to the south-west of capital city Makhachkala of Dagestan, near Caspian seashore (about 1 mile away from the seashore). The depths of the wells No.4, 5, 6, and 17T are 1767, 1437, 1330, and 1544 m, respectively. All wells acting in continuously run regime since 1948. The wellhead temperature T_{wh} is within (335 to 342) K, while the wellhead pressure is within from (0.08 to 0.20) MPa (see Figs. 1 and 2).

2.2 The Samples Description

As is well-known the thermophysical properties of geothermal fluids are affected by their chemical composition. Geothermal fluid is a brine solution as a result of it natural moving through the crust of the Earth. Geothermal fluids are responsible for mobility and transport of inorganic and organic solid and liquid phases and gaseous nonelectrolytes [20]. The composition of a particular well varies as a function of the total production time, the rate of flow, and the nature of the underlying sediments. Thus, the brine compositions will vary from well to well, depending on the depth of production and the temperature of the different parts of the reservoir [39] due to precipitation some component (phase-equilibrium behavior of brine). Therefore, chemical contents of the geothermal fluids from various wells are different and their properties will vary. In addition, studies conducted on the composition of dissolved ions in geothermal fluids indicate considerably variations from one area to other. In general, geothermal brines are chlorine rich, with elements Na, K, and Ca being the dominant ions.

The chemical compositions of the brine samples taken from the wells No.4, No.5, No.6, and No.17 T in the Kayakent and Kizlyar (Dagestan, south Russia)



Fig. 1 Geographical location of the geothermal area (geothermal wells location map) of Dagestan, (South Russia, near Caspian seashore) where the geothermal fluid sample comes from

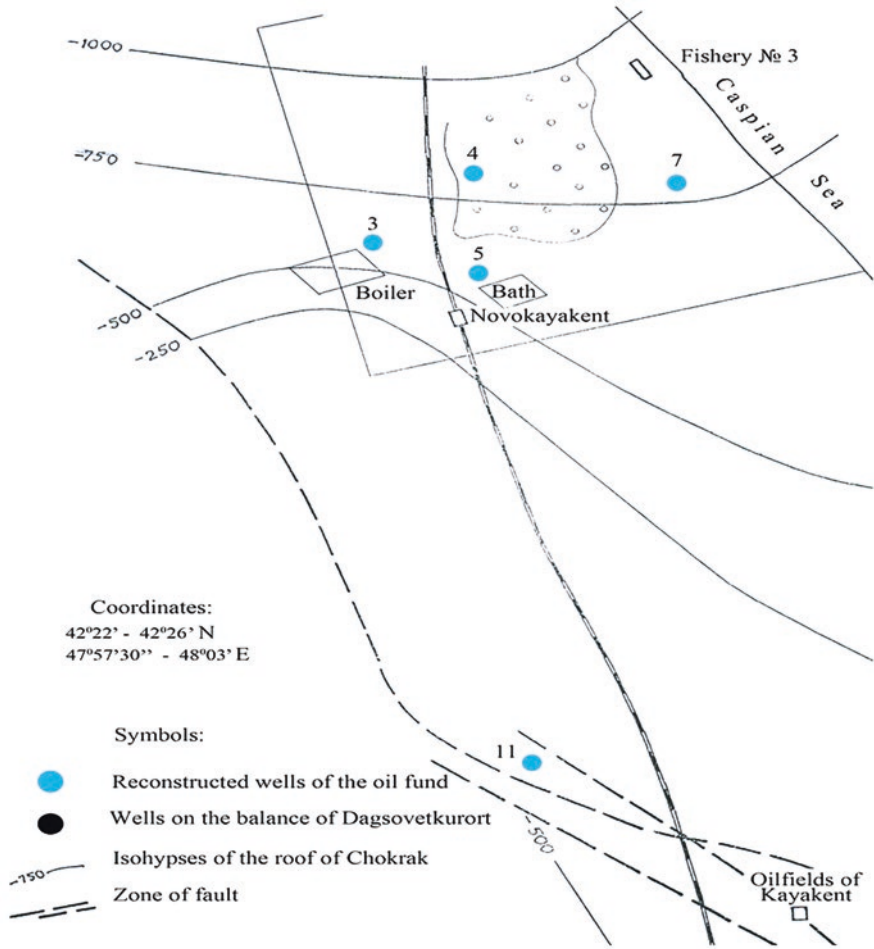


Fig. 2 Map of the Kayakent Geothermal Field (Dagestan, South Russia, near Caspian seashore) location (detailed view), indicating the details of the geothermal wells locations (No. 4 and No. 5)

Geothermal Field are presented in Table 1. A IRIS Intrepid II Optical Emission Spectrometer and Ion Chromatograph techniques were used to quantitative determination of the elemental composition (cations and anions) in the geothermal brine samples. Accuracy was 0.2% to 1.0%. The elements are ionized in the plasma flame of argon plasma and analyzed by a high resolution mass spectrometer.

As one can see from Table 1 the mineralization of the geothermal fluid samples from wells No.4, No.5, No.6, and No.17 T are 0.89 g/l, 1.07 g/l, 0.89 g/l, and 6.34 g/l, respectively. Based on the data from Table 1 the chemical composition distributions between the hot-wells are presented in Table 2. As one can note from Table 2, the main components of the present geothermal samples are: Wells No.4 and 5 (Kayakent)- sodium from (26 to 43)%, sulphate from (36 to 41)%, and sulfur

Table 1 Chemical compositions of the geothermal brines

Species	Sample – No 4 pH = 8.2 (mg/l)	Sample – No 5 pH = 8.2 (mg/l)	Sample – No 6 pH = 7.2 (mg/l)	Sample – No 17 T pH = 7.7 (mg/l)
Cations				
Al	<0.1	<0.1	<0.1	<0.1
As	<0.1	<0.1	<0.1	<0.1
B	2.2	2.2	6.8	8.9
Ba	<0.1	<0.1	0.2	0.5
Ca	56.7	1.2	8.3	50.7
Cd	<0.1	<0.1	<0.1	<0.1
Co	<0.1	<0.1	<0.1	<0.1
Cr	<0.1	<0.1	<0.1	<0.1
Cu	<0.1	<0.1	<0.1	<0.1
Fe	< 0.1	0.4	< 0.1	<0.1
Hg	<0.1	<0.1	<0.1	<0.1
K	11.2	3.4	9.27	71.7
Li	<0.1	<0.1	0.8	0.2
Mg	18.7	0.4	5.7	9.5
Mn	0.2	<0.1	<0.1	<0.1
Mo	<0.1	<0.1	<0.1	<0.1
Na	228	458	556	2410
Ni	<0.1	<0.1	<0.1	<0.1
P	<0.1	0.6	<0.1	<0.1
Pb	<0.1	<0.1	<0.1	<0.1
S	118	124	1.4	62.6
Sb	<0.1	<0.1	<0.1	<0.1
Se	1.3	<0.1	<0.1	1.6
Si	18.4	13.9	12.1	32.4
Sr	1.2	<0.1	0.5	3.4
Ti	<0.1	<0.1	<0.1	<0.1
T	<0.1	<0.1	<0.1	<0.1
V	<0.1	<0.1	<0.1	<0.1
Zn	<0.1	<0.1	0.1	0.1
Anions				
Chloride	67	68.5	280	3507
Nitrate	<0.1	<0.1	9.3	6.1
Sulfate	369.0	391.5	<0.1	175

about 12%; Wells No 6 and 17 T (Kizlyar) – sodium from (38 to 62)%, chlorine (31 to 55%). Therefore, the major mineral components in the geothermal fluid samples from No.4 and No.5 are (Na^+ and SO_4^{2-}), while for wells No.6 and 17 T are (Na^+ and Cl^-). The dissolved cations (SO_4^{2-}) and anions (Na^+) was found in significant quantities in samples No.4 and 5 (both wells located very close to each other, about 0.6

Table 2 Chemical composition distributions for geothermal fluid samples from the hot-wells (No.4, 5, 6, and 17 T)

Hot-wells number	No. 4	No. 5	No. 6	No.17 T
Sulphate	41.34%	36.71%	–	2.76%
Sodium	25.54%	42.94%	62.50%	38.00%
Sulfur	13.22%	11.60%	–	0.99%
Chlorine	7.50%	6.50%	31.50%	55.30%
Calcium	6.35%	0.11%	0.93%	0.80%
Magnesium & Silicon	2.10%	0.36%	1.36%	0.15%
Potassium	1.25%	0.32%	1.04%	1.13%
Nitrate	–	–	1.05%	–
Other components	2.70%	0.51%	0.98%	0.87%

mile), while more Na^+ and Cl^- was found in samples of No. 6 and No.17 T (these wells located close to each other).

The Na^+ content in the sample No.5 is almost two times higher than in No.4, although both wells located very close each other. The contents of the Ca^+ , Mg^+ , and K^+ are considerably higher in the sample No.4. The pH of the samples is 8.2 for No.4 and 5, (7.2 to 7.7) for No.6 and No.17 T. About (90 to 98)% gas content in the samples No.6 and 17 T is nitrogen, while in the samples No. 4 and 5 is about 43.75%. Carbon dioxide content in the samples No. 4 and 5 is 52.94% (methane is 2.1%). Small amount (0.6 to 6.5)% of carbon dioxide and (3.5 to 12)% of methane was found in the samples No. 6 and 17 T. The geothermal brine samples were collected at about (332 to 335) K, filtered to remove suspended solids. Filters with 2 micron pore size was used to remove suspended solids.

2.3 Density Measurements

Density of the geothermal fluid samples was measured with three different commercial instruments (Anton Paar DMA 4500, SVM 3000, and DSA 5000 M). Usually the temperature and pressure dependences of the parameters A and B in the working equation of the VTD apparatus are determined using the calibration procedures (see details [16–19]) with a minimum of two reference fluids such as water, air, nitrogen, benzene, and toluene whose PVT properties are well-known (REFPROP, [47] and should be performed very carefully. The accuracy of the method is limited by the calibration procedure and depends on the uncertainty of the properties of calibrating fluid. The temperature in the measuring cell, where located the U-tube, was controlled using a thermostat with an uncertainty ($k = 2$ and $\alpha = 95\%$ confidence level) of 10 mK and measured using the (ITS-90) PRT100 thermometer with an uncertainty of 0.03 K over the range from (288 to 373) K. This densimeter (DMA4500) allows for a highly precise density measurements in the wide measuring range from (0 to 3000) $\text{kg}\cdot\text{m}^{-3}$ and at temperatures from (273 to 363) K. The

combined expanded uncertainty of the density measurements at the 95% confidence level with a coverage factor of $k = 2$ is estimated to be $0.5 \text{ kg}\cdot\text{m}^{-3}$ (or about 0.005%). The repeatability of density and temperature measurements are $0.01 \text{ kg}\cdot\text{m}^{-3}$ and 0.01 K , respectively. This VTD has been successfully used previously in our earlier publications [16–19] to accurately measure the density of various fluids (ionic liquids, hydrocarbons, and their mixtures with alcohols, [16–19, 65]). During the oscillation of the U-tube, the sample shows the effect of damping of the oscillation, which is a function of the sample viscosity. Correction related with influence of the viscosity (Segovia et al. 2009) for the present geothermal fluid samples density is within $(0.03 \text{ to } 0.06) \text{ kg}\cdot\text{m}^{-3}$ or $(0.0035 \text{ to } 0.006)\%$. At temperatures above 343 K , we found that heating of the sample during the measurements causes the release of the dissolved gases. This is one of the reasons why in the present work we have measured the density, viscosity, and speed of sound at a limited temperature range (up to 343 K). Above the 343 K the intensity of the gas release is increasing. At moderate temperatures (below 343 K) the effect of gas release to the measured properties can be neglected. At temperatures below 343 K we did not find gas release in our samples (no warning messages from the instrument were observed). To study the effect of dissolved gases in the geothermal brine samples at high temperatures, the measurements at high pressures are needed.

2.4 Viscosity Measurements

The dynamic viscosity of the geothermal brines at atmospheric pressure were measured with an automated SVM 3000 Anton Paar rotational Stabinger viscometer-densimeter with a coaxial cylinder geometry [44, 45, 48, 69, 70]. The SVM 3000 viscodensimeter simultaneously measures the density (ρ), dynamic (η) and kinematic viscosities ($\nu = \eta/\rho$) over the range of $(217 \text{ to } 378) \text{ K}$ and in the viscosity range of $0.2 \text{ mPa}\cdot\text{s}$ to $20 \text{ Pa}\cdot\text{s}$ of liquids according to the ASTM D7042 standard. The SVM 3000 viscodensimeter uses Peltier elements for fast and efficient thermostability. The temperature uncertainty is 0.03 K . The precision of the dynamic viscosity measurements is $\pm 0.5\%$ (stated by the manufacturer uncertainty is 0.35%) and the absolute uncertainty of the density is $0.5 \text{ kg}\cdot\text{m}^{-3}$. Repeatability of the viscosity and density are 0.2% and $0.2 \text{ kg}\cdot\text{m}^{-3}$, respectively. Further details about the equipment and method can be found elsewhere [27, 73].

2.5 Speed of Sound Measurements

The speed of sound of the geothermal brines at atmospheric pressure was measured with a sound-speed analyzer DSA 5000 M (Anton Paar instrument). DSA 5000 M simultaneously determines the density and speed of sound of the sample.

The two-in-one instrument is equipped with a density cell and a sound velocity cell thus combining the proven Anton Paar oscillating U-tube method (see above Sect. 2.3) with a highly accurate measurement of sound velocity. Both cells are temperature-controlled by a built-in Peltier thermostat. The density and speed of sound measuring ranges are from (0 to 3000) $\text{kg}\cdot\text{m}^{-3}$ and from (1000 to 2000) $\text{m}\cdot\text{s}^{-1}$, respectively. The uncertainties (combined expanded uncertainty at the 95% confidence level with a coverage factor of $k = 2$) of the density and speed of sound measurements are 0.01% and 0.10%, with repeatabilities of 0.001 $\text{kg}\cdot\text{m}^{-3}$ and 0.10 $\text{m}\cdot\text{s}^{-1}$, respectively.

Combining of the density and speed of sound measurements in the DSA 5000 instruments makes it possible to determine the adiabatic compressibility, $\kappa_s = \frac{1}{c^2 \rho}$, where $k_s = -\frac{1}{V} \left(\frac{\partial V}{\partial P} \right)_s$.

3 Results and Discussion

Measurements of the density, speed of sound, and viscosity of the geothermal fluid samples from four hot-wells No.4, No.5, No.6, and No.17 T as a function of temperature at atmospheric pressure were performed at temperatures between (278 and 343) K. The experimental density, viscosity, and speed of sound results are presented in Table 3 and shown in Figs. 3, 4, 5, 6, 7 and 8 as a function of temperature together with pure water values calculated from the IAPWS formulations for the density [74] and viscosity [41]. As Fig. 3 demonstrate, ρ - T curves shows some curvature, just as observed for pure water behavior [74]. The difference between the present measured geothermal fluids densities and pure water values [74] are: No.4 – 0.12%; No.5 – 0.17%; No.6 – 0.2%; and for No.17 T – 57%, which are considerably higher than their experimental uncertainty. The measurements of the densities of geothermal fluids (the same samples) were made using three different Anton Paar instruments of DMA 4500, SVM 3000, and DSA 5000 M (vibrating-tube densimeter, VTD). The measured data from different instruments are agree each other within (0.01 to 0.02)% which close to their experimental uncertainties.

pure water values (solid lines) calculated from the IAPWS fundamental equation of state [74]. (a) – No.4; (b) – No.5; (c) – No.6; and (d) – No.17 T. Dashed lines are interpolated values

In general, the qualitative behavior of the present measured density, viscosity, and speed of sound data for all of the geothermal brine samples just like pure water temperature behavior. The same behavior has been observed also for reported data for binary and ternary aqueous salt solutions (see, for example, [3–5, 8, 12–15]). As Figs. 1, 2, and 3 demonstrate, geothermal fluid properties can be modeled as a few basic primary aqueous salt solutions (depending on the basic component of the geothermal brine) using appropriate mixing rules. The measured viscosities (Fig. 4) for all of the studied geothermal fluid samples drop rapidly with temperature increasing to (300 to 320) K. The rate of viscosity drop slows down at higher temperatures (above 320 K). The present viscosity data for the geothermal brines are

Table 3 Experimental values of density, viscosity, and speed of sound of the geothermal fluids as a function of temperature at atmospheric pressure

T/K	$\rho^a/\text{kg}\cdot\text{m}^{-3}$	T/K	$\rho^b/\text{kg}\cdot\text{m}^{-3}$	$\eta^b/\text{mPa}\cdot\text{s}$	T/K	$\rho^c/\text{kg}\cdot\text{m}^{-3}$	$c/\text{m}\cdot\text{s}^{-1}$
No. 4							
278.17	1001.2	278.15	1001.8	1.5025	278.15	1001.25	1428.88
283.15	1000.9	283.15	1001.1	1.2955	283.15	1000.97	1449.45
293.14	999.41	293.15	999.20	0.9929	293.15	999.45	1484.03
303.13	996.82	303.15	996.00	0.8124	303.15	996.88	1510.57
313.15	993.37	313.15	992.40	0.6719	313.15	993.42	1530.24
323.16	987.91	323.15	988.30	0.5653	323.15	989.22	1543.97
–	–	333.15	982.90	0.4824	333.15	983.80	1552.50
–	–	–	–	–	343.15	974.20	1556.44
No. 5							
278.15	1001.64	278.15	1002.60	1.5652	278.14	1001.78	1429.65
283.16	1001.34	283.15	1002.00	1.3659	283.11	1001.50	1450.70
293.16	999.80	293.15	999.90	1.1113	293.09	999.95	1485.35
303.12	997.23	303.15	996.70	0.8739	303.15	997.37	1511.19
313.13	993.77	313.15	993.73	0.7182	313.15	993.91	1530.85
323.14	989.53	323.15	989.54	0.5934	323.15	989.70	1544.55
–	–	333.15	984.81	0.4959	328.15	987.35	1549.43
–	–	–	–	–	333.15	984.85	1553.06
No. 6							
277.16	1001.8	277.15	1001.9	1.5944	278.42	1001.9	1431.26
283.16	1001.6	283.15	1001.7	1.4330	283.12	1001.7	1450.89
293.16	999.96	293.15	999.98	1.2142	283.15	1001.6	1451.05
303.13	997.39	303.15	997.61	0.8905	293.15	999.99	1484.98
313.15	993.89	313.15	993.85	0.7234	303.15	997.51	1511.46
323.14	989.74	323.15	989.82	0.6012	313.15	994.00	1531.08
333.13	984.82	333.15	984.59	0.5048	323.15	989.83	1544.77
–	–	343.15	979.35	0.4386	–	–	–
No. 17T							
277.17	1005.8	277.15	1006.2	1.5953	278.14	1006.0	1437.38
283.17	1005.5	283.15	1005.9	1.3394	283.14	1005.8	1457.92
293.15	1003.7	293.15	1003.5	1.0454	283.15	1005.7	1458.09
303.13	1001.0	303.15	1001.1	0.8663	293.15	1003.8	1492.06
313.13	997.53	313.15	997.59	0.7033	303.15	1001.1	1517.55
323.13	993.29	323.15	993.30	0.6034	313.15	997.62	1536.89
–	–	–	–	–	323.15	993.31	1550.33
–	–	–	–	–	333.09	988.07	1558.76
–	–	–	–	–	343.15	982.16	1562.50

^aDMA4500; ^bSVM3000; ^cDSA 5000 M; Standard uncertainties u are: (DMA4500) $u(T) = 0.01$ K; $u(\rho) = 0.00025\%$; (SVM3000) $u(T) = 0.005$ K; $u(\rho) = 0.01\%$; $u(\eta) = 0.17\%$; (DSA 5000 M) $u(\rho) = 0.005\%$ (or 0.002 $\text{kg}\cdot\text{m}^{-3}$); $u(c) = 0.05\%$ (or 0.5 $\text{m}\cdot\text{s}^{-1}$), (level of confidence = 95%)

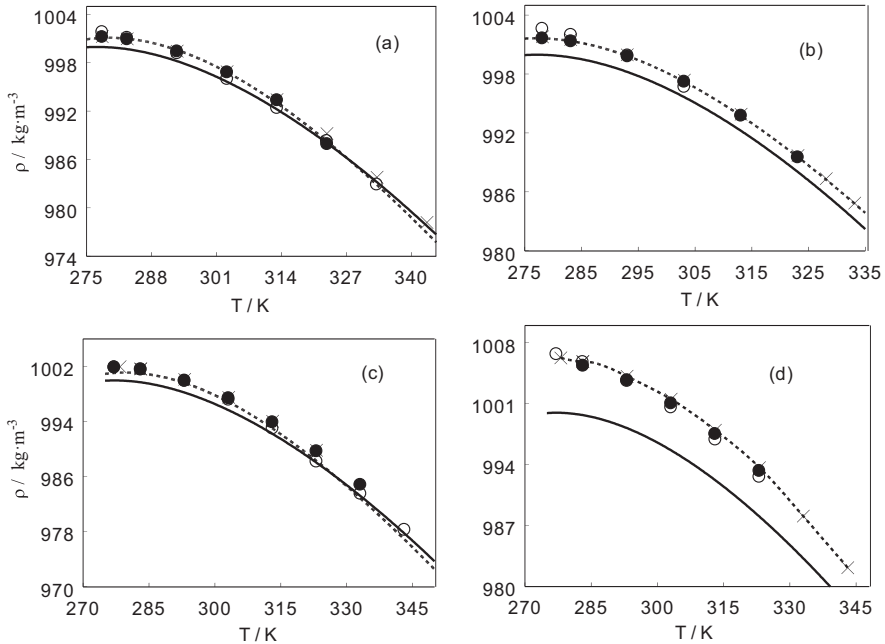


Fig. 3 Measured densities of geothermal fluids as a function of temperature at atmospheric pressure together with pure water values (solid lines) calculated from the IAPWS fundamental equation of state [74]. (a) – No.4; (b) – No.5; (c) – No.6; and (d) – No.17 T. ○, (measured with SVM 3000); ●, (measured with DMA 4500); ×, (measured with DSA 5000 M). Dashed lines are interpolated values

differing from those of pure water by 2.07% for No.4; by 7.61% for No.5; by 8.70% for No.6; and 5.41% for No.17 T, which are considerably higher than their experimental uncertainty. Figure 5 shows temperature behavior of the measured speed of sound in the geothermal fluid samples. The measured speed of sound data for geothermal fluids is differing from pure water values [74] within: No.4–0.12%; No.5–0.17%; No.6–0.2%; and for No.17 T–0.61%, which are higher than their experimental uncertainty. Viscosity is more sensitive to salt concentration than thermodynamic properties. As one can be note from Figs. 3 (d) to 3 (d), measured properties for geothermal fluid No.17 T are considerably deviate (by 0.57% for density, by 5.41% for the viscosity, and by 0.61% for speed of sound) from the values for pure water in compare with other geothermal samples. This is the result of the composition difference, *i.e.*, effect of high concentration of salt (2410 mg/l Na⁺; 175 mg/l SO₄²⁻; 3507 mg/l of Cl⁻¹) in the sample No.17 T.

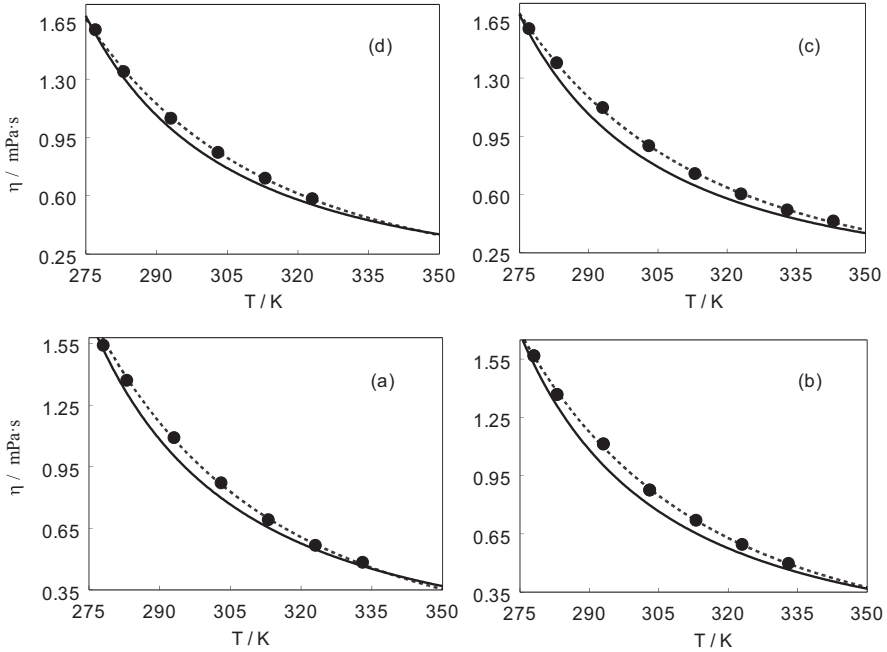


Fig. 4 Measured viscosities of geothermal fluids as a function of temperature at atmospheric pressure together with pure water values (solid lines) calculated from the IAPWS formulation [41]. (a) – No.4; (b) – No.5; (c) – No.6; and (d) – No.17 T. Dashed lines are calculated from Arrhenius-Andrade model Eq. 8

3.1 Correlation Model for Density, Viscosity, and Speed of Sound

Since a theory for thermodynamic (equation of state) and transport properties of multicomponent aqueous solutions is unavailable, its evaluation is empirical and based solely on experimental data. The present density, speed of sound, and viscosity data for the geothermal fluid samples were fitted to the correlation equations

$$\rho(T, c_i) = \rho_{H_2O}(T) \left(1 + \sum_n^{i=1} a_i c_i \right), \tag{2}$$

$$c(T, c_i) = c_{H_2O}(T) \left(1 + \sum_n^{i=1} d_i c_i \right), \tag{3}$$

$$\eta(T, c_i) = \eta_{H_2O}(T) \left(1 + \sum_n^{i=1} b_i c_i \right), \tag{4}$$

where $\rho_{H_2O}(T)$, $c_{H_2O}(T)$, and $\eta_{H_2O}(T)$ are the pure water density, speed of sound (IAPWS formulation, [74]), and viscosity (IAPWS formulation, [41]), respectively

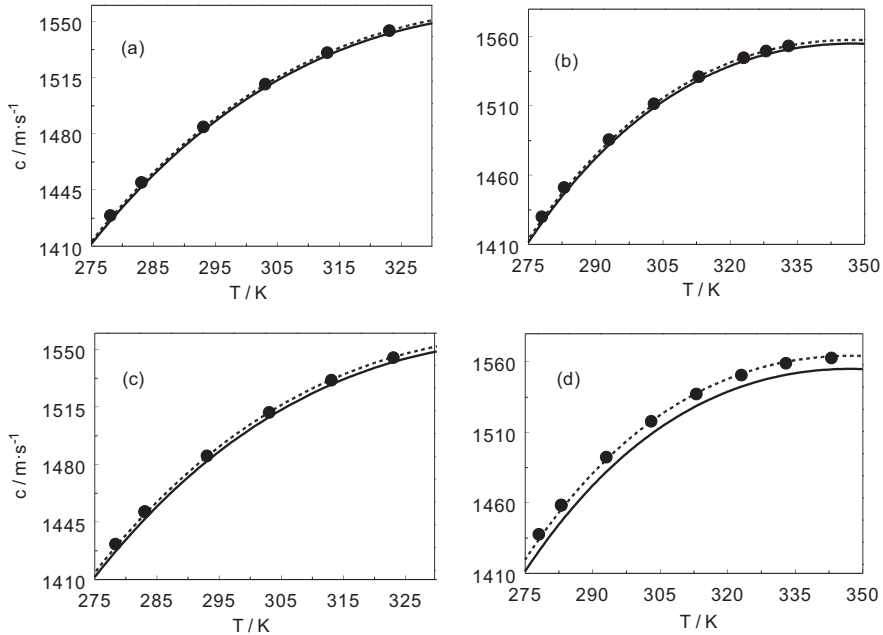


Fig. 5 Measured speed of sound of geothermal fluids as a function of temperature at atmospheric pressure together with

at a temperature T ; c_i is the concentration of ions (g/l); n is the number of the components; a_i , b_i , and d_i are the density, viscosity, and speed of sound coefficients (Riedel's characteristic constant of the ions) for each ion species and c_i is the concentration (g/l) of the i -th ion species. For the present geothermal fluid samples we selected 6 basic components (ion species): Na^+ , Ca^{2+} , Mg^{2+} , K^+ , SO_4^{2-} , and Cl^- . All of the measured data for the geothermal fluids were fitted to Eqs. 2 to 4. The derived values of fitting parameters a_i , b_i , and d_i are given in Table 4. The values of characteristic constant of the ions, a_i , b_i , and d_i , defined the contribution of each ions on the total experimental observed values of density, viscosity, and speed of sound. Riedel [63] has proposed the same correlation model for the thermal conductivity of multicomponent aqueous salt solutions. This relation for the thermal conductivity gives good prediction agreement (within 5%) with experimental data for many aqueous salt solutions [2, 10, 22, 23, 40]. Many authors examined the accuracy and predictive capability of the Riedel's model (see also review by [40]). The deviation statistics of the correlation Eqs. 2 to 4 are also presented in Table 4.

The values of density, speed of sound, and viscosity calculated from Eqs. 2 to 4 together with the present measured results are given in Figs. 6, 7 and 8. To confirm the accuracy and reliability of the developed correlation models 2 to 4, we have compared the predicted values of density and viscosity with the reported data for well-studied binary and ternary aqueous salt solutions. Figures 9 and 10 provide the

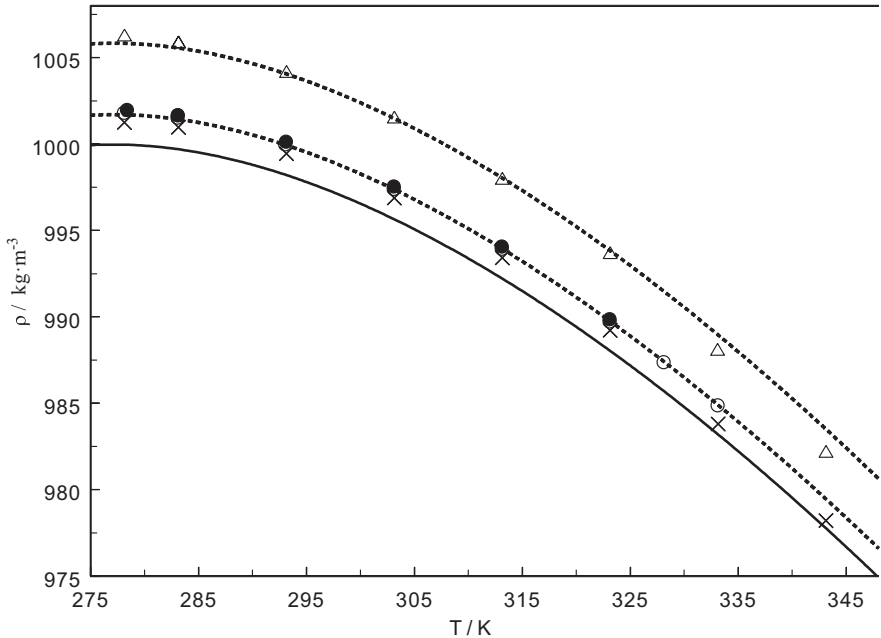


Fig. 6 Comparison of the measured densities of various geothermal fluids. Solid line is pure water values calculated from the IAPWS fundamental equation of state [74]. Dashed lines are predicted from the correlation model Eq. 2 for the samples No.5 and No.17 T. x –No. 4; o–No. 5; ●–No.6; and Δ–No.17 T

comparison between the predicted from Eqs. 2 and 4 values of density and viscosity with the measured values for selected binary and ternary aqueous salt solutions.

The differences between the measured and predicted values of density and viscosity are: Density-(0.01 to 0.30) % for H₂O + NaCl [64]; (0.18 to 0.33) % for H₂O + MgSO₄ [14, 15]; Viscosity-(3.6 to 5.1) % for H₂O + MgSO₄ [14, 15]; (4.0 to 6.9) % for H₂O + Na₂SO₄ [13]. These predictions for density and viscosity for binary and ternary aqueous salt solutions are acceptable for the present model. These equations can be used to calculate the density, speed of sound, and viscosity of any geothermal fluids with basic components of Na⁺, Ca⁺, Mg⁺, K⁺, SO₄²⁻, Cl⁻ and with concentrations within $c(\text{Na}^+) < 2.45 \text{ g/l}$; $c(\text{Ca}^+) < 0.06 \text{ g/l}$; $c(\text{Mg}^+) < 0.02 \text{ g/l}$; $c(\text{K}^+) < 0.012 \text{ g/l}$; $c(\text{SO}_4^{2-}) < 0.4 \text{ g/l}$; and $c(\text{Cl}^-) < 3.51 \text{ g/l}$. It is apparent that these correlation models cannot be used for geothermal fluid samples with the concentration of salts out of these ranges. In order to extend the models for the wide geothermal fluid samples with other compositions of the salt content, more experimental measurements for other natural geothermal fluids with various composition from various hot-wells are needed.

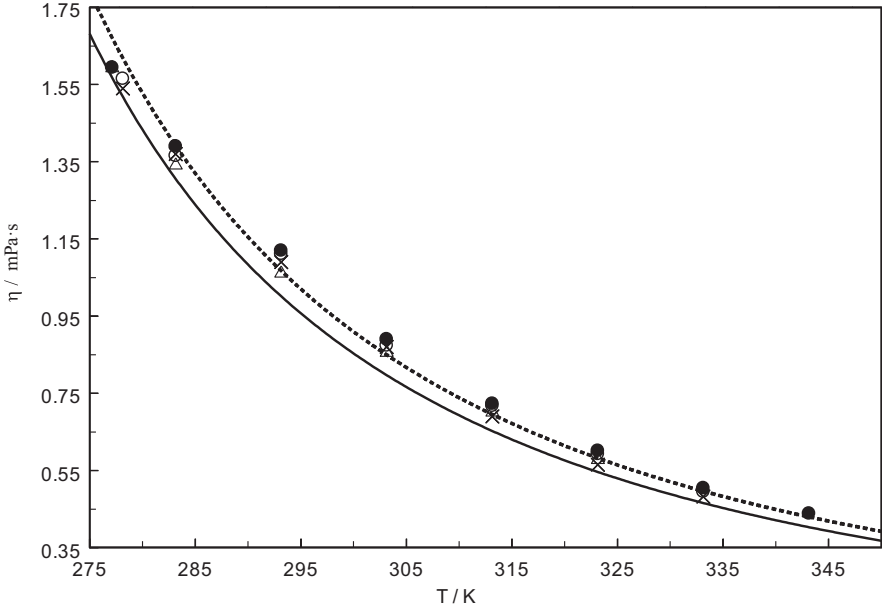


Fig. 7 Comparison of the measured viscosities of various geothermal fluids. Solid line is pure water values calculated from the IAPWS correlation [41]. × -No.4; ○-No. 5; ●-No.6; and Δ-No.17 T. Dashed line is calculated from the correlation model Eq. 4 for the sample No.6

3.2 High Pressure Prediction Models

[29, 30] proposed empirical predictive model for high pressure behavior of the thermal conductivity of aqueous salt solutions by multiplying the thermal conductivity of the salt solution at reference pressure, P_0 (usually at $P_0 = 0.101$ MPa) and any temperature T , by the ratio of the thermal conductivity of pure water at the desired pressure P to that at a known (reference) pressure, $P_0 = 0.101$ MPa and any T .

Thus, if the viscosity or other thermophysical properties (density, speed of sound, thermal conductivity, etc.) of the salt solution (or geothermal fluids) are known at the reference pressure (for example, $P_0 = 0.101$ MPa), the properties at any pressures (at which the property of pure water is known) may be calculated as.

$$\rho(P, T, c_i) = \rho(P_0, T, c_i) \left(\frac{\rho_{H_2O}(P, T)}{\rho_{H_2O}(P_0, T)} \right), \tag{5}$$

$$\eta(P, T, c_i) = \eta(P_0, T, c_i) \left(\frac{\eta_{H_2O}(P, T)}{\eta_{H_2O}(P_0, T)} \right), \tag{6}$$

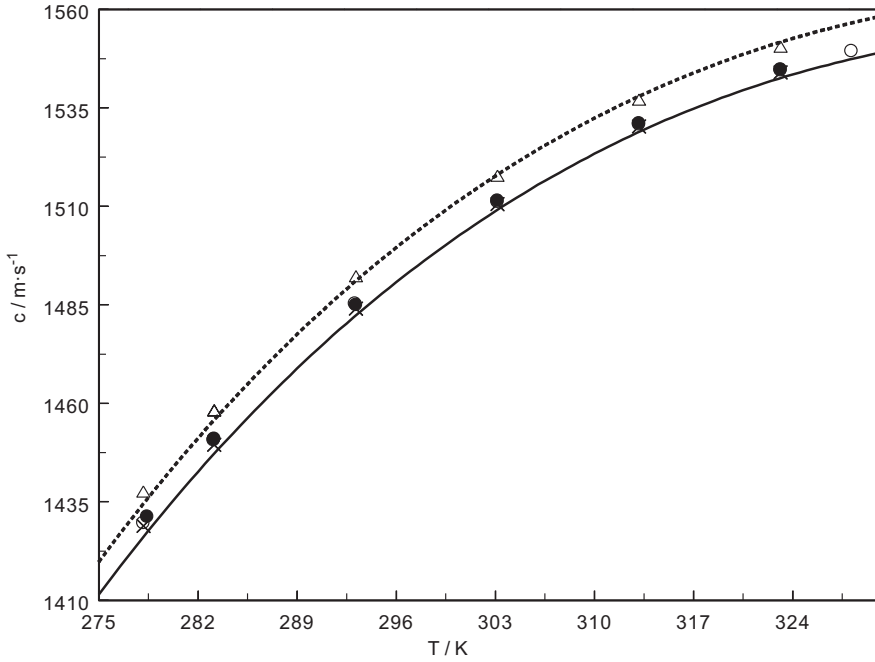


Fig. 8 Comparison of the measured speed of sound for various geothermal fluids. Solid line is pure water values calculated from the IAPWS fundamental equation of state [74]. ×-No.4; ○-No.5; ●-No.6; and Δ-No.17 T. Dashed line is calculated from correlation model Eq. 3 for the sample No.17 T

Table 4 Values of fitting coefficients (ion species characteristic constants) a_i, b_i , and d_i for density, viscosity, and speed of sound correlation models (Eqs. 2 to 4) for basic ion species in the geothermal fluid samples

Ions	$a_i / (l/g)$	$b_i / (l/g)$	$d_i / (l/g)$
Ca ⁺	0.082303	-3.038266	0.140139
K ⁺	-0.322627	-0.816218	-0.376991
Mg ⁺	-0.081951	7.611630	-0.186723
Na ⁺	0.005100	0.113502	0.008569
Cl ⁻¹	0.003773	-0.028713	0.002141
SO ₄ ⁻²	0.000421	0.037042	-0.003097
AAD	0.03%	2.55%	0.06%
St. dev	0.05%	2.51%	0.07%
Max. dev	0.11%	4.76%	0.20%

$$c(P, T, c_i) = c(P_0, T, c_i) \left(\frac{c_{H_2O}(P, T)}{c_{H_2O}(P_0, T)} \right), \tag{7}$$

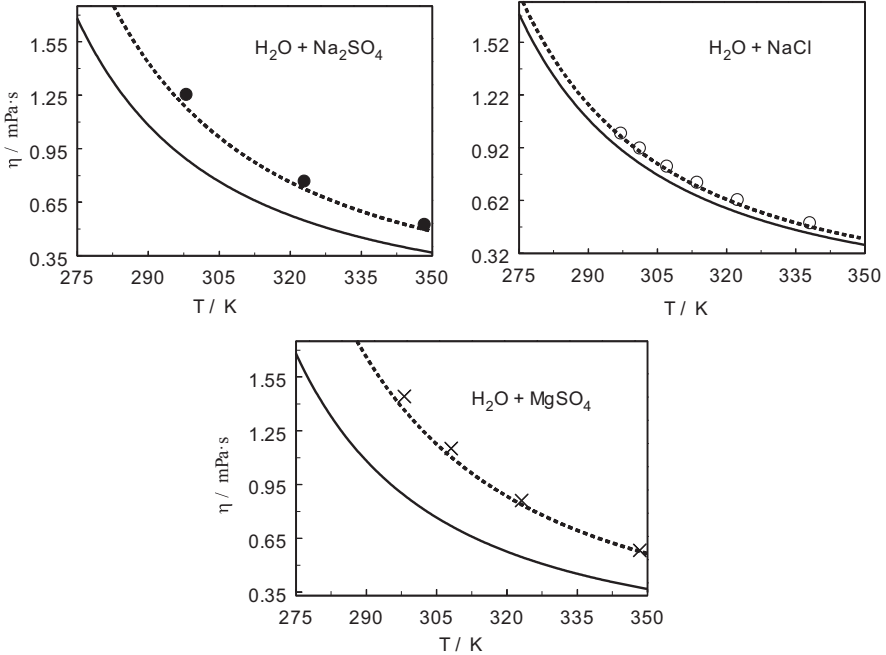


Fig. 9 Comparison of the measured viscosities for binary aqueous salt solutions with the values calculated from prediction model Eq. 4 (dashed lines). Solid line is pure water values calculated from the IAPWS formulation [41]. × – [8]; ○ – [43]; ● – Abdulagatov et al. 2006

where $\rho(P_0, T, c_i)$, $\eta(P_0, T, c_i)$, and $c(P_0, T, c_i)$ can be calculated from Eqs. 2 to 4 at $P_0 = 0.101$ MPa. The present measured values of the thermodynamic (density and speed of sound) and transport (viscosity) property of geothermal fluids at atmospheric pressure were used to predict their pressure dependences based on Eqs. 5 to 7. This technique has been successfully used and tested previously by many authors (see for example, [1, 10, 11, 29, 30]) to predict the thermal conductivity and other thermodynamic properties of different aqueous salt solutions. The predicted values of density, speed of sound, and viscosity of geothermal fluid No.17 T as a function of pressure are presented in Fig. 11. Unfortunately, there are no measured high – pressure density, speed of sound, and viscosity data for the present geothermal fluid samples to check the accuracy and reliability of the prediction.

For practical applications is very useful to use well-known theoretically based Arrhenius-Andrade type equation [33, 37, 72] for temperature dependence of viscosity for each measured geothermal fluid samples.

$$\eta(T) = e_0 \exp\left(\frac{e_1}{T}\right) \text{ or } \ln \eta(T) = \ln e_0 + \frac{e_1}{T}, \quad (8)$$

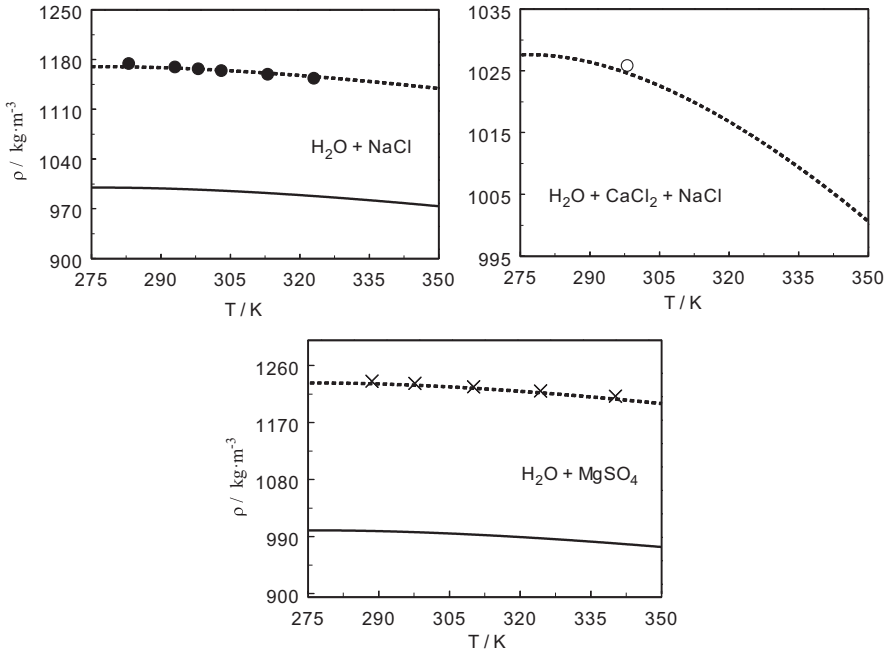


Fig. 10 Comparison of the measured densities for binary aqueous salt solutions with the values calculated from prediction model Eq. 2 (dashed lines). Solid lines are pure water values calculated from the IAPWS fundamental equation of state [74]. × – [8]; ○ – [76]; ● – [64]

where e_0 is the viscosity, $\eta = \eta_\infty$, at high temperature limit ($T \rightarrow \infty$), $e_1 = \varepsilon_a / R$, $\varepsilon_a = \Delta H$ is the flow activation energy (enthalpy of activation). Eq. 8 was theoretically confirmed by Eyring’s absolute rate theory [37]. This equation was successfully used previously to represent experimental viscosity data for aqueous salt solutions [6–8, 14, 15, 67]. The enthalpy of activation, $\Delta H / R$, can be directly calculated using experimental viscosity data for the geothermal fluids from the slope of the straight line of $\ln \eta \approx T^{-1}$. In this work, Eq. 8 was applied to the present viscosity data for the geothermal brine samples. The derived values of fitting parameters (e_0 and e_1) for the samples are presented in Table 5 together with the AAD between measured and calculated values of viscosity.

The present measured thermodynamic (density and speed of sound) properties of natural geothermal brines were used to calculate derived thermodynamic properties such as, $\kappa_S, \kappa_T, \alpha_p, \gamma_v, \Delta H, C_v, C_p, \left(\frac{\partial H}{\partial P}\right)_T, \left(\frac{\partial U}{\partial V}\right)_T$ on the bases of well-known thermodynamic relations (see Eqs. 9 to 10, Section 3.3, Supporting Information). The derived values of these properties are given in Tables S1 and S2. Thus, in Tables 3 and S1 and S2 we have all of the thermodynamic property data for four natural geothermal fluids at atmospheric pressure as a function of temperature. Unfortunately, there are no direct measured thermodynamic properties data for the geothermal fluids to check the accuracy and reliability of the derived properties. However, this

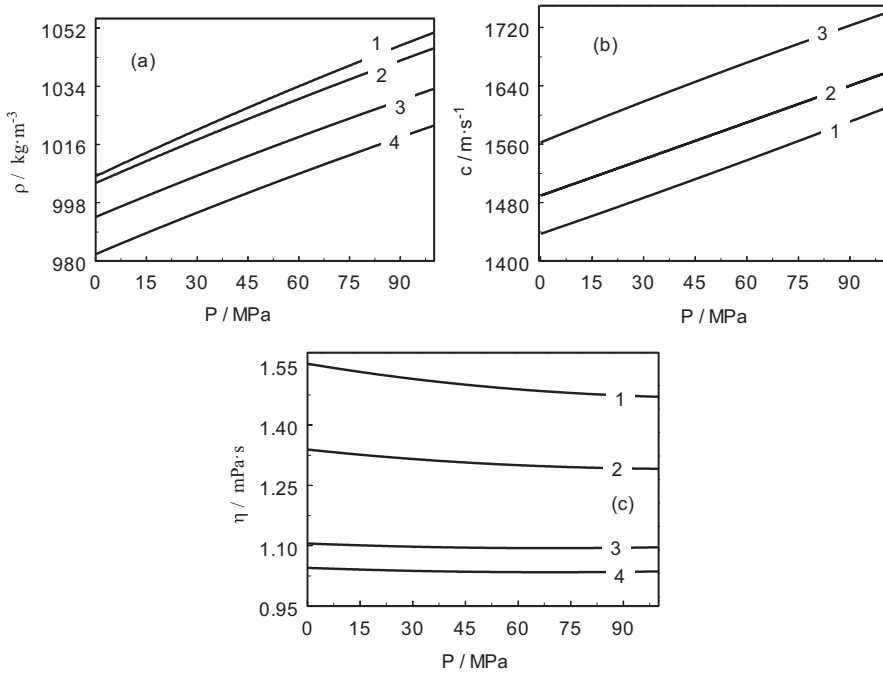


Fig. 11 Predicted from Eqs. 5 to 7 values of density (a), speed of sound (b), and viscosity (c) as a function of pressure at selected isotherms for geothermal fluid sample of No.17 T. 1–278 K; 2–293 K; 3–323 K; 4–343 K; and 5–283 K

Table 5 Values of fitting coefficients e_i for viscosity correlation models (Arrhenius-Andrade model) (Eq. 8)

Hot-wells number	No. 4	No. 5	No. 6	No. 17 T
e_0 / mPa·s	0.0011028	-0.0015025	0.0017503	0.0013858
e_1 / K	2019.476	1932.032	1889.824	1949.755
AAD / %	1.7	0.91	0.86	0.92

method of calculation of the thermodynamic properties has been examined previously for many other fluids (see for example, [9, 59, 60]).

4 Conclusions

The density, speed of sound, and viscosity of four natural geothermal fluid samples from Dagestan Geothermal Field (south Russia, Caspian seashore) have been measured with Anton Paar Instruments: densimeter DMA 4500; sound-speed analyzer (DSA 5000 M); and Schtanberg viscodensimeter (SVM3000), respectively.

Measurements were performed at temperatures from (278 to 343) K and at atmospheric pressure. The measured density, speed of sound, and viscosity data were used to develop correlation models (Riedel type model) to predict the properties for various concentrations of ion species and temperatures from (278 to 343) K. The models reproduced measured values of density, speed of sound, and viscosity of geothermal fluids within: Density: AAD = 0.03%; Speed of sound: AAD = 0.06%; and Viscosity: AAD = 2.55%. It was shown that, if the thermophysical properties of the geothermal fluids are known at reference pressure (for example, $P_0 = 0.101$ MPa) and any temperature, their properties at any pressures (at which this properties of pure water is known) and temperatures maybe calculated by multiplying the properties of the geothermal fluid at reference pressure, P_0 , and given temperature T , by the ratio of the this property of pure water at the desired pressure P to that at a known reference pressure, $P_0 = 0.101$ MPa and at any temperature. The measured values of density and speed of sound were used to calculate other derived thermodynamic properties such as κ_S , κ_T , α_p , γ_v , ΔH , C_v , C_p , $\left(\frac{\partial H}{\partial P}\right)_T$, and $\left(\frac{\partial U}{\partial V}\right)_T$.

Supporting Information

The Supporting Information is available free of charge on the ACS Publications website at DOI:

Derived values of thermodynamic properties such as κ_S , κ_T , α_p , γ_v , ΔH , C_v , C_p , $\left(\frac{\partial H}{\partial P}\right)_T$, and $\left(\frac{\partial U}{\partial V}\right)_T$ for geothermal fluids (nos. 4, 5, 6, and 17 T) (PDF).

Acknowledgments I.M.A. thanks the Applied Chemicals and Materials Division at the National Institute of Standards and Technology for the opportunity to work as a Guest Researcher at NIST during the course of this research.

Funding The authors thank Russian Found of Basic Research № 13-03-12078-oΦN-M and Russian Scientific Fund (№14-19-00749) for the financial support.

Notes The authors declare no competing financial interest.

References

1. Abdulgatov IM, Akhmedova-Azizova LA (2014) Thermal conductivity of aqueous CaCl₂ solutions at high temperatures and high pressures. *J Sol Chem* 43:421–444
2. Abdulgatov IM, Assael M (2009) Viscosity. In: Valyashko VM (ed) Hydrothermal properties of materials. Experimental data on aqueous phase equilibria and solution properties at elevated temperatures and pressures. John Wiley & Sons, London., Chapter 6, pp 249–270
3. Abdulgatov IM, Azizov ND (2003) PVTx measurements and partial molar volumes for aqueous Li₂SO₄ solutions at temperatures from 297 to 573 K and pressures up to 40 MPa. *Int J Thermophys* 24:1581–1610
4. Abdulgatov IM, Azizov ND (2004) Densities and apparent molar volumes of aqueous H₃BO₃ solutions at temperatures from 296 to 573 K and at pressures up to 48 MPa. *J Sol Chem* 33:1305–1331

5. Abdulagatov IM, Azizov ND (2005) Thermal conductivity and viscosity of the aqueous K_2SO_4 solutions at temperatures from 298 to 573 K and at pressures up to 30 MPa. *Int J Thermophys* 26:593–635
6. Abdulagatov IM, Azizov ND (2006a) Viscosity of aqueous $CaCl_2$ solutions at high temperatures and high pressures. *Fluid Phase Equilib* 240:204–219
7. Abdulagatov IM, Azizov ND (2006b) Densities, apparent and partial molar volumes of concentrated aqueous $LiCl$ solutions at high temperatures and high pressures. *Chem Geol* 230:22–41
8. Abdulagatov IM, Azizov ND (2007) Experimental study of the effect of temperature, pressure, and concentration on the viscosity of aqueous $SrCl_2$ solutions. *J Chem Eng Data* 52:841–850
9. Abdulagatov IM, Dvoryanchikov VI (1995) Thermodynamic properties of geothermal fluids. *Russian J Geochem* 5:612–620
10. Abdulagatov IM, Guseinov GG (2014) Thermal conductivity measurements of aqueous orthophosphoric acid solutions in the temperature range from (293 to 400) K and at pressures up to 15 MPa. *Int J Thermophys* 35:218–245
11. Abdulagatov IM, Magomedov UM (1998) Thermal conductivity of aqueous $ZnCl_2$ solutions at high temperatures and high pressures. *Ind Eng Chem Res* 37:4883–4888
12. Abdulagatov IM, Akhmedova-Azizova LA, Azizov ND (2004) Thermal conductivity of binary aqueous $NaBr$ and KBr and ternary $H_2O+NaBr+KBr$ solutions at temperatures from 294 to 577 K and pressures up to 40 MPa. *J Chem Eng Data* 49:1727–1737
13. Abdulagatov IM, Zeinalova AB, Azizov ND (2005) Viscosity of aqueous Na_2SO_4 solutions at temperatures from 298 to 573 K and at pressures up to 40 MPa. *Fluid Phase Equilib* 227:57–70
14. Abdulagatov IM, Azizov ND, Zeinalova AB (2007a) Density, apparent and partial molar volumes, and viscosity of aqueous Na_2CO_3 solutions at high temperatures and high pressures. *Z Phys Chem* 221:963–1000
15. Abdulagatov IM, Azizov ND, Zeinalova AB (2007b) Viscosities, densities, apparent and partial molar volumes of concentrated aqueous $MgSO_4$ solutions at high temperatures and high pressures. *Phys Chem Liq* 45:127–148
16. Abdulagatov IM, Tekin A, Safarov J, Shahverdiyev A, Hassel E (2008a) Densities, excess, apparent, and partial molar volumes of binary mixtures of ethanol+[BMIM][BF₄] as a function of temperature, pressure, and concentration. *Int J Thermophys* 29:505–533
17. Abdulagatov IM, Tekin A, Safarov J, Shahverdiyev A, Hassel E (2008b) Experimental densities and derived properties of liquid propan-1-ol at temperatures from 298 to 423 K and at pressures up to 40 MPa. *Fluid Phase Equilib* 268:21–33
18. Abdulagatov IM, Tekin A, Safarov J, Shahverdiyev A, Hassel E (2008c) Experimental study of the volumetric properties (density, apparent, partial, and excess molar volumes) of binary mixtures of Methanol+[BMIM][BF₄]. *J Chem Thermodyn* 40:1386–1401
19. Abdulagatov IM, Tekin A, Safarov J, Shahverdiyev A, Hassel E (2008d) High-pressure densities and derived volumetric properties (excess, apparent, and partial molar volumes) of binary mixtures of methanol+[BMIM][PF₆]. *J Sol Chem* 37:801–833
20. Ague JJ (2003) In: Rudnick RL (ed) *Fluid flow in the deep crust. Treatise of geochemistry, the crust, vol 3.* Elsevier, Amstrdam, pp 195–228
21. Alkan H, Babadagli T, Satman A (1995) The prediction of the PVT/Phase behavior of the geothermal fluid mixtures. *Proceeding of the World Geothermal Congress, IGA*, pp 1659–1665
22. Aseyev GG (1998) *Electrolytes. Properties of solutions. Methods for calculation of the multicomponent systems and experimental data on thermal conductivity and surface tension.* Begell-House, Inc., New-York
23. Aseyev GG, Zaytsev ID (1996) *Volumetric properties of electrolyte solutions. Estimation methods and experimental data.* Begell-House, Inc., New-York
24. Badavov GB, Belan SI (2015) Project of the republican target program “Utilization of renewable energy in the Republic of Dagestan until 2020”. *Proceedings of Round table: problems and prospects of using the potential of renewable energy in the region* (May 14, 2015), Makhachkala, ISER DSC RAS, pp 18–28

25. Battistelli A (2012) Improving the treatment of saline brines in EWASG for the simulation of hydrothermal systems. Proceedings of TOUGH Symp., Lawrence Berkeley Nat. Lab., Berkeley, California, pp 1–9
26. Battistelli A, Calore C, Pruess KA (1993) Fluid property module for the TOUGH2 simulator for saline brines with non-condensable gas. Proceedings of 18th Workshop on Geothermal Reservoir Engineering, Stanford University, pp 249–259
27. Carvalho PJ, Regueira T, Santos LMNBF, Fernández J, Coutinho JAP (2010) Effect of water on the viscosities and densities of 1-Butyl-3-methylimidazolium Dicyanamide and 1-Butyl-3-methylimidazolium Tricyanomethane at atmospheric pressure. *J Chem Eng Data* 55:645–652
28. Champel B (2006) Discrepancies in brine density databases at geothermal conditions. *Geothermics* 35:600–606
29. DiGuilio RM, Teja AS (1992) Thermal conductivity of aqueous salt solutions at high temperatures and high concentrations. *Ind Eng Chem Res* 31:1081–1085
30. DiGuilio RM, Lee RJ, Jeter SM, Teja AS (1990) Properties of lithium bromide–water solutions at high temperatures and concentrations-I. thermal conductivity. *ASHRAE Trans* 96:702–708
31. Dittman GL (1977) Calculation of brine properties, Lawrence Livermore Laboratory, Report UCID 17406
32. Dolejs D, Manning CE (2010) Thermodynamic model for mineral solubility in aqueous fluids: theory, calibration and application to model fluid-flow systems. *Geofluids* 10:20–40
33. Erday-Gruz T (1974) Transport phenomena in aqueous solutions. John Wiley & Sons Inc., New York
34. Ershaghi I, Abdassah D, Bonakdar MR, Ahmad S (1983) Estimation of geothermal brine viscosity. *J Pet Tech* 35:621–628
35. Francke H, Thorade M (2010) Density and viscosity of brine: an overview from a process engineers perspective. *Chem Erde, Geochem* 70:23–32
36. Francke H, Kraume M, Saadat A (2013) Thermal–hydraulic measurements and modelling of the brine circuit in a geothermal well. *Environ Earth Sci* 70:3481–3495
37. Glasstone S, Laidler K (1941) Eyring, *Theory of Rate Processes*. McGraw-Hill, New York
38. Haas JL Jr (1976) Physical properties of the coexisting phases and thermochemical properties of the H₂O component in boiling NaCl solutions: U.S. Geol. Survey Bull. 1421-A, 1421-B
39. Helgeson HC (1967) Solution chemistry and metamorphism. *Res Geochem PH*. Abelson (ed) 55:379–385
40. Horvath AL (1985) Handbook of aqueous electrolyte solutions. Physical properties, estimation methods and correlation methods. Ellis Horwood, West Sussex
41. Huber ML, Perkins RA, Laesecke A, Friend DG, Sengers JV, Assael MJ, Metaxa IN, Vogel E, Mares R, Miyagawa K (2009) New international formulation for the viscosity of H₂O. *J Phys Chem Ref Data* 38:101–125
42. Huber ML, Perkins RA, Friend DG, Sengers JV, Assael MJ, Metaxa IN, Miyagawa K, Hellmann R, Vogel E (2012) New international formulation for the thermal conductivity of H₂O. *J Phys Chem Ref Data* 41:033102-1–033102-23
43. Kestin J, Shankland IR (1984) Viscosity of aqueous NaCl solutions in the temperature range 25–200 °C and in the pressure range 0.1–30 MPa. *Int J Thermophys* 5:241–263
44. Kratky O, Leopold H, Stabinger H, (1980) DMA45 calculating digital density meter, instruction manual. Digital Densimeter of liquids and gases (Paar A, KG, A-8054, Graz, Austria), pp 1–12
45. Kroger D (2002/2003) Stabinger Viscometer. Petro Industry News, Annual Buyers Guide, 3 (4)
46. Lee KS (2000) Comparison of correlation equations for estimating brine properties under high pressure and temperature condition. *Geosystem Eng* 3:113–116
47. Lemmon EW, Huber ML, McLinden MO, (2010) *NIST Standard Reference Database 23, NIST Reference Fluid Thermodynamic and Transport Properties, REFPROP, version 9.0, Standard Reference Data Program, National Institute of Standards and Technology: Gaithersburg, MD*
48. Leopold H (1970) *Elektronik*, 297, 411–415
49. McCain WD Jr (1991) Reservoir fluid property correlations-State of Art. Society of Petroleum Eng. Res. Eng., May, pp 266–272

50. McKibbin R, McNabb A (1995) Mathematical modeling the phase boundaries and fluid properties of the system $H_2O+NaCl+CO_2$. In Proceedings of the 17th New Zealand Geothermal Workshop, University of Auckland, pp.255–262
51. Milsch H, Kallenberg B, Holzhauser J, Frick S, Blöcher G (2010) Mixing-rules of viscosity, electrical conductivity and density of NaCl, KCl, and $CaCl_2$ aqueous solutions derived from experiments. EGU2010-1584, EGU General Assambly-2010, Geophys. Research Abstract, 12
52. Muller PIN, Weare JH (1999) Model of geothermal brine chemistry. Final Report, Grant DE-FG07-93ID13247, pp 1–23
53. Oldenburg C, Pruess K, Lippmann M (1995) Heat and mass transfer in hypersaline geothermal systems. Proceeding of the World Geothermal Congress, IGA, pp 1647–1652
54. Ostermann RD, Paranjpe SG, Godbole SP, Kamath VA (1986) The effect of dissolved gas on geothermal brine viscosity. Proc. 56th Ann. Soc. Petrol. Eng. California Regional Meeting, pp 381–389
55. Palliser Ch (1998) A model for deep geothermal brines: State space description and thermodynamic properties. Ph.D. Thesis, Massey University
56. Palliser Ch, McKibbin R A (1998a) Model for deep geothermal brines, II: thermodynamic properties-density, Transport in Porous Medias, 33, 129–154
57. Palliser Ch, McKibbin R (1998b) A model for deep geothermal brines, III: thermodynamic properties-enthalpy and viscosity. Transport in Porous Medias, 33, 155–171
58. Piwinski AJ, Netherton R, Chan M (1977) Viscosity of brines from the Salton sea Geothermal Field, Imperial valley, California, Lawrence Livermore Laboratory, Report UCRL 52344, University of California
59. Polikhronidi NG, Abdulagatov IM, Batyrova RG, Stepanov GV, Ustuzhanin EE, Wu JT (2011) Experimental study of the thermodynamic properties of diethyl ether (DEE) at the saturation. Int J Thermophys 32:559–595
60. Polikhronidi NG, Batyrova RG, Abdulagatov IM, Magee JW, Wu JT (2014) Saturated and compressed liquid heat capacity at constant volume for 1-Hexyl-3-methylimidazolium bis[(trifluoromethyl)sulfonyl]imide. Phys Chem Liq 52:657–679
61. Potter RW, Haas JLJ (1977) A model for the calculation of the thermodynamic properties of geothermal fluids. Geothermal Res Counc Trans 1:243–244
62. Reindl J, Shen H, Bisiar T (2009) Reservoir engineering: An introduction and application to rico, Colorado, Geothermal Energy-MNGN598
63. Riedel L (1951) The heat conductivity of aqueous solutions of strong electrolytes. Chem Ing Tech 23:59–64
64. Rogers PSZ, Pitzer KS (1982) Volumetric properties of aqueous sodium chloride solutions. J Phys Chem Ref Data 11:15–81
65. Schmidt H, Stephan M, Safarov J, Kul I, Nocke J, Abdulagatov IM, Hassel E (2012) Thermophysical properties of 1-ethyl-3-methylimidazolium ethyl sulfate. J Chem Thermodyn 47:68–75
66. Schröder E, Thomauske K, Schmalzbauer J, Herberger S, Gebert C, Velevska M (2015) Design and test of a new calorimeter for online detection of geothermal water heat capacity. Geothermics 53:202–212
67. Segovia JJ, Fandiño O, López ER, Lugo L, Martín MC, Fernández J (2009) Automated densimetric system: measurements and uncertainties for compressed systems. J Chem Thermodyn 41:632–638
68. Spycher N, Pruess K (2011) A model for thermo physical properties of CO_2 -brine mixtures at elevated temperatures and pressures. In: Proc. 36th Workshop on Geothermal Reservoir Engineering, Stanford University, Stanford California, SGP-TR-191
69. Stabinger H (1994) Density measurement using modern oscillating transducers. Yorkshire Trading Standards Unit, Sheffield
70. Stabinger H, Kratky O, Leopold H (1967) Eine neue Präzisionsmethode zur Bestimmung der Dichte von Flüssigkeiten. Monatsh Chem 98:436–438

71. Stefánsson, A., Driesner, Th., Bénézech, P. (eds.) (2012). Thermodynamic of geothermal fluids, Mineralogical Society of America & Geochemical Society, Vol 76
72. Stokes RH, Mills R (1965) Viscosity of electrolytes and related properties. Pergamon Press, New York
73. Tariq M, Carvalho PJ, Coutinho JAP, Marrucho IM, Canongia Lopes JN, Rebelo LPN (2011) Viscosity of (C₂–C₁₄) 1-alkyl-3-methylimidazolium bis(trifluoromethylsulfonyl) amide ionic liquids in an extended temperature range. *Fluid Phase Equilib* 301:22–32
74. Wagner W, Pruß A (2002) New international formulation for the thermodynamic properties of ordinary water substance for general and scientific use. *J Phys Chem Ref Data* 31:387–535
75. Wahl EF (1977) Geothermal energy utilization. Wiley, New York
76. Zezin D, Driesner T, Sanchez-Valle C (2014) Volumetric properties of mixed electrolyte aqueous solutions at elevated temperatures and pressures. The systems CaCl₂-NaCl-H₂O and MgCl₂-NaCl-H₂O to 523.15, 70 MPa, and ionic strength from (0.1 to 18) mol•kg⁻¹. *J Chem Eng Data* 60(4):1181–1192

Thermodynamic Properties of Geothermal Fluids from South Russia: Izberbash and Ternair Hot Sources



Ilmutdin M. Abdulagatov, Gasan B. Badavov, Lala A. Akhmedova-Azizova, and Rasul M. Aliev

1 Introduction

The thermodynamic and transport properties of geothermal fluids are very important for determining the natural state of a geothermal system and its behavior under exploitation. Geothermal power plants use geothermal fluids as a resource and create waste residuals as part of the power generation process. Both the geofluid resource and waste stream are considered produced fluids. The chemical and physical nature of produced fluids can have a major impact on the geothermal power industry and influence the feasibility of power development, exploration approaches, plant design, operating practices, and reuse/disposal of residuals. Geothermal heat and power plants use hot geothermal fluids as a transport medium to extract thermal energy from the deep underground. A downhole pump in the production well lifts the brine up to the surface, where it is cooled in heat exchanger and reinjected subsequently (binary geothermal cycles). Knowledge of the thermophysical properties of geothermal brines is extremely important for determination of design characteristics and sizes of the downhole pump [55]. The flow characteristics (multiphase underground flows) of the brine in the well depends on their thermal properties, such as density and viscosity. The thermodynamic and transport property data of geothermal brines are also needed for geothermal energy utilization devices. Geothermal energy production operations require the ability to predict the

I. M. Abdulagatov (✉) · G. B. Badavov

Institute for Geothermal and Renewal Energy of the High Temperature Joint Institute of the Russian Academy of Sciences, Makhachkala, Russia

L. A. Akhmedova-Azizova

Azerbaijan Technical University, Baku, Azerbaijan

R. M. Aliev

Daghesten State Technical University, Makhachkala, Russia

© The Author(s), under exclusive license to Springer Nature Switzerland AG 2021

V. Svalova (ed.), *Heat-Mass Transfer and Geodynamics of the Lithosphere*, Innovation and Discovery in Russian Science and Engineering, https://doi.org/10.1007/978-3-030-63571-8_18

thermodynamic properties of the geothermal brines as a function of temperature, pressure, and concentration. Particularly, knowledge of the geothermal fluid properties is important in geothermal exploration and energy production, to establish optimal operations for the productions of geothermal brine fields. For example, the total heat content of geothermal fluid depends on the density, temperature, and heat capacity [57]. For the effective utilization of geothermal resources, a precise thermodynamic and transport properties data are required for the initial resource estimates, production and reservoir engineering study of the geothermal field, reservoir modeling, and power cycle optimization.

Thermodynamic and transport properties (density, heat capacity, viscosity, thermal conductivity, *etc.*) of geothermal fluids determine the transfer of heat and mass by geothermal systems. The energy properties of the geothermal fluids may be extracted directly from the $PVTx$ properties of the geothermal fluid through standard thermodynamic approaches [28, 29]. The available $PVTx$ properties of geothermal fluids are not sufficient to meet the needs of the geothermal industry for complex solutions such as those found in geothermal reservoirs. Modeling geothermal wells (geothermal engineering, geothermal or reservoir installations) need accurate thermophysical property data [53, 62]. Thus, one of the key factors when planning the exploitation of geothermal resources is the availability of reliable thermodynamic and transport properties data of geothermal brines. Initially geothermal fluids were modeled as pure water. Thermodynamic and transport properties of pure water are well-known (see IAPWS formulations for thermodynamic and transport properties, [32, 33, 66]). Used pure water or geothermal brine models (synthetic brines like binary or ternary aqueous salt solutions) properties leads to inaccuracies and impossible accurately estimate the effect all of the dissolved salts on the thermophysical properties due to extremely complexities. Also, the presence of the dissolved gases in geothermal fluids considerable influencing the thermodynamic properties. Due to pressure difference between underground and the near surface conditions (geothermal operations at 0.101 MPa), degassing occurs during geothermal energy production. Thermophysical properties of geothermal fluids such as density, viscosity, heat capacity, and enthalpy play a fundamental role in mass and heat transfer in the Earth's interior. In order to provide numerical modelling of the heat and mass flow processes in various geothermal energy generating (production) systems (reservoirs, pipe systems, power plants, binary geothermal cycles, heat-exchangers) definitions of the thermodynamic properties of density (ρ), viscosity (η), and enthalpy (H) of geothermal fluids as a function of temperature, pressure, and concentration are required [21, 42, 47–49]. Solution of the set of differential equations (equations of mass conservation, linear momentum, and energy conservation), which may be used to describe the transport of mass and heat in a porous media for mathematical simulations of the Earth's interior, considerably depends on thermodynamic properties of geothermal brines (density, enthalpy, and viscosity) as a function of temperature, pressure, and concentration of salt (minerals). Solving these sets of equations enables the determination of such quantities as temperature and pressure gradients at a point in the flow, and T, P, x profile in time and space [24, 25]. However, solving these equations requires knowledge of the thermodynamic

properties of density, enthalpy, and viscosity of the geothermal fluids. Since the measurements in this work were performed at atmospheric pressure, the present study is not considering the effect of dissolved gases on the thermophysical properties of geothermal brines. High pressure measurements or reliable high pressure predictive models are needed for heat and mass transfer phenomena study in Earth interior.

Viscosity and density are key factors in fluid flow simulation (influencing the flow of reservoir fluids). Relatively little data has been published on the viscosity of natural geothermal brines. Most reported data only for binary or ternary aqueous salt solutions (see review [7]) as a main component of geothermal brines (basically for synthetic geothermal brines). Adams and Bachu [9] reviewed various functions for the calculation of geothermal brine density and viscosity. Battistelli [14], Battistelli et al. [15], and Oldenburg et al. [45] also described models of brines flows that require knowledge of the three key thermodynamic properties (density, viscosity, and enthalpy). Because of the scarcity of data for the density, dynamic viscosity, and enthalpy a different approach to the one used for these properties was adopted [20, 42, 47, 48]. Potter and Haas [51] indicated that geothermal fluids might be represented by the properties of aqueous NaCl solution as a model of the geothermal brine. This model predicts the density of geothermal brines and seawater within experimental uncertainty at a temperature of 150 °C. The simplest way of determining of the thermodynamic properties of geothermal fluids is based on pure water properties, because pure water is the dominant constituent, therefore, governs the properties (thermodynamic behavior) of aqueous salt solutions and geothermal brines. Most reliable predictive models for aqueous salts solutions are representing their thermodynamic properties relative to pure water [2, 12, 13, 31, 67], because the behavior of the thermodynamic properties of geothermal brines also governs by the properties of pure water (see below Figs. 1, 2, 3, and 4).

Using direct experimental thermodynamic data for particular natural geothermal fluids allows minimize the errors arising from the empirical prediction data for geothermal brines models. Moreover, the brine composition can be changed during production. Thus, more direct measurements of the natural geothermal brines from various regions of the world with various concentrations of dissolved salts are needed. This allows generalize the properties of geothermal fluids from various geothermal fields (wells) with various solutes to develop prediction models for geothermal brines with any chemical composition. Unfortunately, available theoretical models frequently cannot describe real systems such as those met in practice. For example, the accurate prediction of the thermodynamic and transport properties of complex multicomponent ionic aqueous solutions such as geothermal fluids is extremely difficult due to complexity of the intermolecular interactions between water molecules and various types of salt ions. Better predictive models for practical applications can be developed based on reliable direct experimental information on thermodynamic and transport properties of natural geothermal brines. However, a literature survey reveals that very little information has been reported previously on the direct measurements of the density and viscosity of real (natural) multicomponent geothermal brines from various Geothermal Fields of the World.

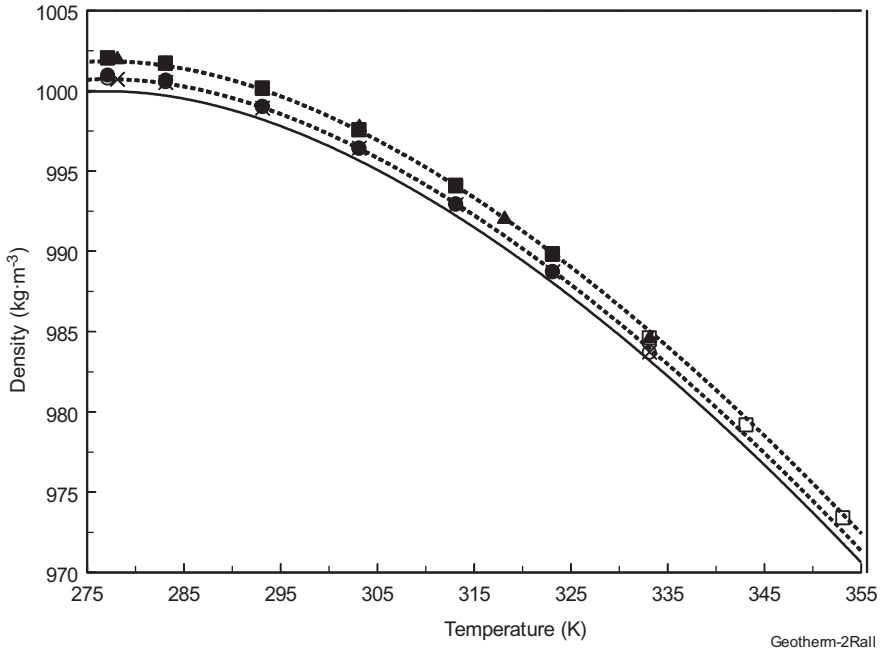
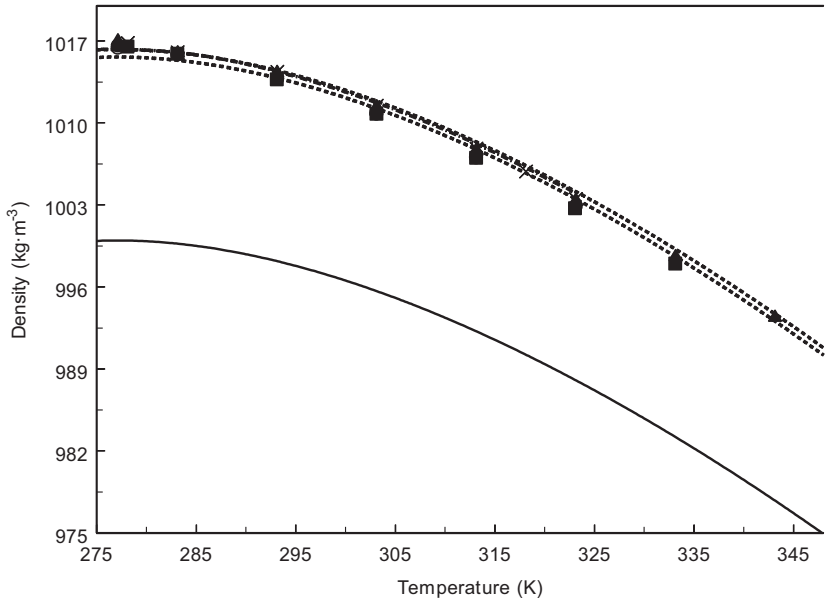


Fig. 1 Measured values of density of geothermal fluids together with the values for pure water calculated from IAPWS formulation. Solid line is pure water values calculated from the IAPWS fundamental equation of state [66]. Dashed lines are calculated from the correlation model Eq. (1) for the samples No. 68 and No. 129. \times -No. 68 (DSA); \circ -No. 68 (SVM); \bullet -No. 68 (DMA); \blacksquare -No. 129 (DMA); \square -No. 129 (DSA); \blacktriangle -No. 129 (DSA)

The experimental study of the thermodynamic properties of each geothermal fluid would, however, be a formidable task, and theoretical or semi-empirical models that would predicted the thermodynamic properties of complex geothermal brines would be useful.

Francke and Thorade [24] studied the sensitivity of the volumetric flow rate of a downhole pump in a geothermal production well on different density and viscosity functions during the startup and stationary operating phases. Used pure water or geothermal brine models (synthetic brines like binary or ternary aqueous salt solutions) properties leads to inaccuracies. The geothermal fluid was modeled as an aqueous sodium chloride solution and functions for its density and viscosity are compared and applied to a model of the geothermal fluid cycle (stationary model of a geothermal water loop). The study showed that the deviations between different density functions are up to 52% of the volumetric flow rate. Presence of dissolved ions in water at various temperatures causes the reservoir flow properties to considerably deviate from those of pure water or model solution.

Since the number of different brines encountered is large, detailed measurements on all of them become impractical. Consequently, the ability to predict the properties of brines from theories or models based on a few key aqueous electrolyte



Geotherm-2RailN129

Fig. 2 Measured values of density of geothermal fluids together with the values for pure water calculated from IAPWS formulation. Solid line is pure water values calculated from the IAPWS fundamental equation of state [66]. Dashed lines are calculated from the correlation model Eq. (1) for the samples No. 27T and No. 38T. Dashed-dotted line is calculated from the model by Rogers and Pitzer [54]. ○-No. 27T (SVM); ●-No. 27T (DMA); ■-No. 27T (DSA); ×-No. 38T (DSA); □-No. 38T (DMA); ▲-No. 38T (SVM)

solutions is essential to the technical development of geothermal resources. Unfortunately, there is no theoretical guidance for the temperature, pressure, and concentration dependences of the thermodynamic properties of multicomponent geothermal brines. Thus, its evaluation is based on the measured data only. Different predictive models were proposed by various authors [10, 15, 17, 21, 23, 24, 38, 41, 43, 44, 46–50, 59] to represent the effect of temperature, pressure, and concentration on the thermodynamic properties of geothermal fluids. All of these models based on thermodynamic properties of synthetic aqueous binary or ternary solutions, basically NaCl, since sodium chloride is the major solute in geothermal brines. Milsch et al. [43] studied density and viscosity of synthetic geothermal brines containing varying amounts (5 mol/kg NaCl and CaCl₂, and 4 mol/kg KCl) of dissolved NaCl, KCl, and CaCl₂ salts using Höppler-viscometer and a combination of volumetric and mass measurements for density. These systematic measurements with the three aqueous salt solutions yielded calibration of mixing rules, stoichiometrically weighting the individual viscosities measured at the total of the mixture for density and viscosity. The predictions when applied to a natural geothermal brine of specific chemical composition, showed good agreement with direct measurements performed with this geothermal fluid. The method allows estimate

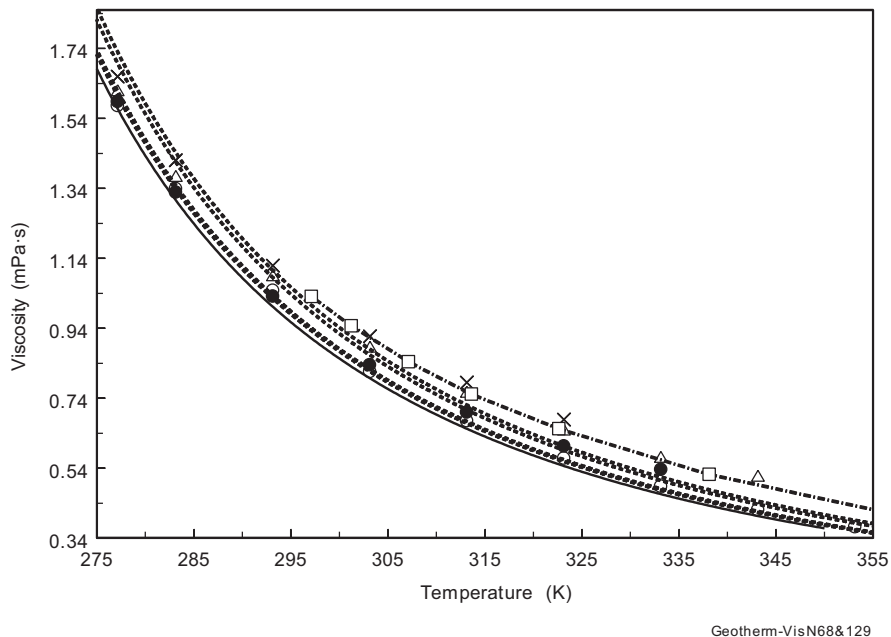


Fig. 3 Measured values of viscosity for geothermal fluids together with the values for pure water calculated from IAPWS formulation. Solid line is pure water values calculated from the IAPWS correlation [32]. Dashed lines are calculated from the correlation model Eq. (3). × –No. 27T; Δ–No. 38T; ○–No. 129; ●–No. 68; □– Kestin and Shankland [34] for H₂O + NaCl solution

the density and dynamic viscosity of a given geothermal fluid once the chemical composition has been determined. However, this model does not taking into account the effect of dissolved gases. Further direct measurements of the thermophysical properties of the natural geothermal brines with complex compositions are needed to confirm applicability and accuracy of the mixing rules developed by Milsch et al. [43]. Ershaghi et al. [23] reported viscosity data for synthetic brines consisting of sodium chloride, potassium chloride, and calcium chloride at concentrations from (0.99 to 16.667) wt.% and at temperatures up to 275 °C. Measurements were made using a high-temperature capillary tube designed to operate up to a temperature of 315 °C and a pressure of 14 MPa. From the use of the laboratory- derived data, a method is presented whereby the viscosity of geothermal brine may be estimated from knowledge of its composition. To quantitative describe the thermodynamic and transport properties of geothermal fluids as a function of T , P , and x , the thermodynamic model (equation of state) or reference correlation model for transport properties are needed. Unfortunately, as was mentioned above, due to complexity physical chemical nature of the geothermal fluids, theory cannot accurately predict their thermodynamic properties needed for geothermal processes applications. The thermodynamic properties data for natural geothermal fluids are often missing and no equation of state for multicomponent aqueous salt solutions that valid in the wide

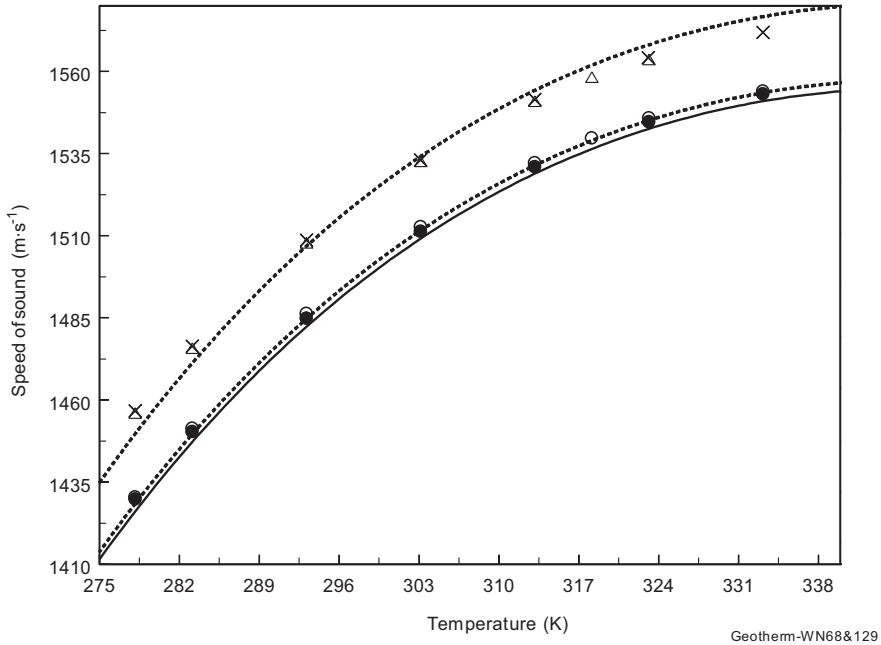


Fig. 4 Measured speed of sound for various geothermal fluids together with the values for pure water calculated from IAPWS formulation. Solid line is pure water values calculated from the IAPWS correlation [66]. Dashed lines are calculated from the correlation model Eq. (2). x-No. 27T; Δ-No. 38T; ○-No. 129; ●-No. 68

T, *P* and *x* ranges. Inconsistence between existing theoretical models (equation of state) and experimental thermodynamic data for geothermal fluids is the result in difference and uncertainty in geochemical modeling.

The purpose of this study was to measure the density, speed of sound, and dynamic viscosity of four natural geothermal brines from Geothermal Filed of Dagestan (south Russia, Caspian seashore) and the effect of elevated temperatures (from 277 to 353 K) on these properties at various levels of dissolved ion concentrations. Another objective of the present study was to calculate other derived thermodynamic properties such as adiabatic coefficient of bulk compressibility, coefficient of thermal expansion, thermal pressure coefficient, isothermal coefficient of bulk compressibility, isochoric heat capacity, isobaric heat capacity, enthalpy difference, partial pressure derivative of enthalpy, and partial derivatives of internal energy (internal pressure) using the measured density and speed sound data. The correlation models for the density, viscosity, and speed of sound were also developed on bases of measured data. The in this work reported density, viscosity, and speed of sound data for the geothermal fluids at atmospheric pressure $P_0 = 0.101$ MPa as a function of temperature were used as reference data to predict their high pressure behavior. In our recent publication [8] we have experimentally studied density, speed of sound, and viscosity of natural geothermal fluids from various geothermal

wells with different chemical compositions. This paper reports the continuation of study on thermodynamic and transport properties natural geothermal fluids at atmospheric pressure and temperatures to 353 K. These data were used as a reference data for high pressure and high temperature prediction. The present results are considerably expanding the available data base on thermophysical properties of geothermal fluids from various regions of the South Russia Geothermal Fields with various chemical compositions. A major research goal of the future study is to develop thermodynamic models for the geothermal brines that can treat a wide range of T , P , and x .

2 Geothermal Field Location and Wells Characteristics

The geothermal fluid samples for the present study come from geothermal wells Izberbash (No. 68 and 129), Ternair (No. 27T and No. 38T), located in south Russia Geothermal Field (Dagestan, Caspian seashore). The Izberbash geothermal wells (No. 68 and 129) are located approximately 38 miles to the south-west of capital city Makhachkala of Dagestan, near Caspian seashore (about 1 mile away from the seashore), at $42^{\circ}32' N$ & $47^{\circ}53' E$. The Ternair wells (No. 27T and No. 38T) are located in the north-east part of the capital city Makhachkala (at $42^{\circ}59' N$ & $47^{\circ}32' E$). The distance between the geothermal wells in Izberbash (No. 68 and 129) and Ternair (No. 27T and 38T) is about 40 miles. The wells (No. 27T and No. 38T) are closely located each other (the distance between them is about 1.25 miles), while distance between the wells (No. 68 and 129) is about 0.6 miles. This region is commonly known for its rich natural surface geothermal springs (about 24 wells). This indicates that a larger scale hydrothermal hot source may existing the subsurface. The depths of the wells No. 68, 129, 27T, and 38T are 1330, 1261, 2103, and 2060 m, respectively. All wells acting in continuously run regime since 1967. The wells characteristics are given in Table 1. The wellhead temperature T_{wh} is within (52 to 110) $^{\circ}C$, while the wellhead pressure is from (0.06 to 0.64) MPa. The hot geothermal brines produced from the wells have the potential for possible district-usage applications for surrounding communities.

Table 1 Characteristics of the geothermal wells^a

Well (No.)	Geological age	Date drilled	Depth (m)	Production horizon/ Perforated interval	Q (m ³ /h)	P_{wh} (MPa)	T_{wh} ($^{\circ}C$)
68	N ₁ ch	1967	1330	Chokrat /B	46	0.35	62
129	N ₁ ch	1979	1291	Chokrat /B	13	0.06	52
27 T	N ₁ ch	1997	2103	Chokrat /B ₂	104	0.90	98
38 T	N ₁ ch	1985	2060	Chokrat /B ₃	104	0.64	100

^a Q , wellhead brine flow rate; T_{wh} , wellhead temperature; P_{wh} , wellhead temperature

3 The Samples Description. Chemical Composition of the Geothermal Fluid Samples

Geothermal fluid is a brine solution as a result of its natural moving through the crust of the Earth. Geothermal fluids are responsible for mobility and transport of inorganic and organic solid and liquid phases and gaseous nonelectrolytes [11]. The chemical composition of geothermal fluids varies widely between and within geothermal fields, and in some cases, over time within the same geothermal well. The exact chemical makeup of the geothermal fluids can have significant implications for both the design and operation of a geothermal plant and its potential environmental impact. The composition of a particular well varies as a function of the total production time, the rate of flow, and the nature of the underlying sediments. Thus, the brine compositions will vary from well to well, depending on the depth of production and the temperature of the different parts of the reservoir [30].

Therefore, the properties of the geothermal fluids from various wells also are varying. The major chemical constituents of the geothermal samples include sodium (Na), chloride (Cl), bicarbonate (HCO_3), sulfate (SO_4), silica (SiO_2), calcium (Ca), and potassium (K). The chemical compositions of the brine samples taken from the Izberbash (No. 68 and 129) and Ternair (No. 27T and 38T) wells are presented in Table 2. An IRIS Intrepid II Optical Emission Spectrometer and Ion Chromatograph techniques were used to quantitative determination of the elemental composition (cations and anions) in the geothermal brine samples. The accuracy of the chemical composition measurements was 0.2–1.0%. As one can see from Table 2 the mineralization (total salt content) of the geothermal fluid samples from the wells No. 68, 129, 27T, and 38T are 1.65 g/l, 1.62 g/l, 15.35 g/l, and 15.81 g/l, respectively, *i.e.*, both (No. 68 and 129) and (No. 27T and 38T) have almost the same concentrations. The main components of the geothermal samples are (see Table 3) sulfate (45.4%), sodium (24%), sulfur (about 14.6%), chloride (9.2%), sodium (49.1%), and chlorine (48.1%). Although total mineralization of the samples (No. 68 and 129) is very close (about 1.63 g/l), the percentage contents of the various ions in the samples are completely different. For example, sample No. 68 contains 49.2 mg/l Ca^{+2} and 32.9 mg/l Mg^{+2} , while the contents of these ions in the sample No. 129 are about 2.3 mg/l and 1.3 mg/l, respectively (both wells located very close each other).

The mineralogical compositions of the samples from No. 27T to 38T are also very close each other (see Tables 2 and 3). Large difference in chemical compositions of the samples from wells (No. 68, 129) and (No. 27T, 38T) was observed (see Table 2). For example, as Table 2 shows, K^+ content in the sample (No. 27T) is almost 31 times higher than in the sample (No. 129), while Na^+ content in the sample (No. 38T) 19.3 times higher than in the sample (No. 68). The difference in Cl^- , S^+ , and B^+ content between the wells are within 44, 30, and 59 times, respectively. The wells (No. 68 and 129) are located about 40 miles southern of (No. 27T, 38T). The pH values for the geothermal fluids from various regions are roughly normally distributed around a median of 7.3, with the majority of values are between 5 and 10. For the present geothermal fluids the pH are 8.2 and 7.7 for samples (No. 27T

Table 2 Chemical composition of geothermal brines from Izberbash and Ternair geothermal wells

Species	Sample: No. 68 pH = 7.2	Sample: No. 129 pH = 7.2	Sample: No. 27T pH = 8.2	Sample: No. 38T pH= 7.7
	mg/l	mg/l	mg/l	mg/l
Cations				
All	<0.1	<0.1	<0.1	<0.1
As	<0.1	<0.1	<0.1	<0.1
B	1.2	2.4	59.3	59.8
Ba	<0.1	<0.1	1.7	2.0
Ca	49.2	2.8	73.6	72.6
Cd	<0.1	<0.1	<0.1	<0.1
Co	<0.1	<0.1	<0.1	<0.1
Cr	<0.1	<0.1	<0.1	<0.1
Cu	<0.1	<0.1	<0.1	<0.1
Fe	< 0.1	< 0.1	< 0.1	< 0.1
Hg	<0.1	<0.1	<0.1	<0.1
K	10.2	4.7	145	138
Li	0.2	0.1	2.2	2.1
Mg	32.9	1.3	28.5	29.6
Mn	<0.1	<0.1	<0.1	<0.1
Mo	<0.1	<0.1	<0.1	<0.1
Na	396	590	7540	7660
Ni	<0.1	<0.1	<0.1	<0.1
P	<0.1	0.2	<0.1	<0.1
Pb	<0.1	<0.1	<0.1	<0.1
S	240	211	39.8	34.2
Sb	<0.1	<0.1	<0.1	<0.1
Se	2.4	0.2	<0.1	<0.1
Si	13.8	12.3	29.4	28.1
Sr	1.1	0.1	6.7	6.8
Ti	<0.1	<0.1	<0.1	<0.1
Tl	<0.1	<0.1	<0.1	<0.1
V	<0.1	<0.1	<0.1	<0.1
Zn	<0.1	<0.1	<0.1	<0.1
Anions				
Chloride	152	176	7387	7689
Nitrate	<0.1	<0.1	<0.1	59.3
Sulfate	749	616	30.7	24.6
Total dissolved salt	1662.7	1830.0	15345.9	15808.0

Table 3 Mass percentage contents of main ions in the geothermal samples

Species	Sample: No. 68 (%)	Sample: No. 129 (%)	Sample: No. 27T (%)	Sample: No. 38T (%)
Sulfate	45.05	33.66	0.20	0.16
Sodium	23.82	32.24	49.13	48.46
Sulfur	14.43	11.53	0.26	0.22
Chlorine	9.14	9.62	48.14	48.64
Calcium	2.96	0.15	0.48	0.46
Magnesium	1.98	0.07	0.19	0.19
Silicon	0.83	0.67	0.19	0.18
Potassium	0.61	0.26	0.95	0.87
Boron	0.07	0.13	0.39	0.38
Other	<1.11	<11.67	<0.07	<0.44

and 38T), respectively and 7.2 for samples (No. 68 and 129). The major mineral components in the samples (No. 68 and 129, both wells located very close to each other, about 0.6 mile) are (Na^+ , SO_4^{2-} , Cl^- , and Ca^{+2}), while for (No. 27T and 38T, these wells located very close to each other, 1.25 miles) are (Na^+ , K^+ , Ca^{+2} and Cl^-).

Beside the dissolved solids, geothermal fluids contain some amount of dissolved gases (mostly N_2 , CH_4 , CO_2). The presence of the dissolved gases in geothermal fluids considerable influencing the thermodynamic properties, therefore, energy extraction processes. Due to pressure difference between the underground and the above ground (near surface, geothermal operations at 0.101 MPa) facility condition, degassing occurs during production. The average amount of dissolved gases in the geothermal fluid samples above ground (near surface, on the top of wells) are: $2.5 \text{ m}^3 \text{ (gas)/m}^3 \text{ (brine)}$ for (No. 27T), and $4.2 \text{ m}^3 \text{ (gas)/m}^3 \text{ (brine)}$ for (No. 38T). About (90 to 92) volume % gas content in the samples (No. 27T and 38T) is hydrocarbon gases, while in the samples (No. 68 and 129) N_2 content is about (95 to 98)%.

Carbon dioxide content in the samples (No. 68 and 129) is (4 to 5)%, while in the samples (No. 27T and 38T) is about (4.6 to 6.8)%. The contents of nitrogen and other rare gases in the samples from (No. 27T and 38T) are about (2.6 to 3.3)%. When the composition, temperature and pressure of the geothermal brine in the geological formation are changing, (during reservoir evolution, well production, energy extraction or injection processes), the fluids that were originally at formation condition come to a new P , T , and x conditions. As a result, some solid minerals can precipitate, dissolved gases released and heat lost. Almost all geothermal energy operations experience these phenomena. The geothermal brine samples were collected at about (52 to 110) °C, filtered to remove suspended solids. No salts precipitations were observed during the samples collecting and low temperature (at 277 K) measurements.

4 Experimental

The method (experimental details, the physical basis and theory of the method, procedures, uncertainty assessment) and apparatus have been described in our recent publication [8]. Only a brief review and essential information will be briefly given here.

4.1 Density Measurements

The densities of the natural geothermal fluids were measured as a function of temperature with three different Anton Paar commercial instruments (DMA 4500, SVM 3000, and DSA 5000M). The digital density analyzer in these instruments uses a U-shaped vibrating tube (VTD). The working principle of an oscillation-type densimeter is based on the law of harmonic oscillation, in which a U-tube is completely filled with the sample under study and subjected to an electromagnetic force. Density measurements with a VTD are based on the dependence of the period of oscillation of a unilaterally fixed U-tube on its mass.

The calibration procedure with a minimum of two reference fluids such as water, air, nitrogen, benzene, and toluene whose *PVT* properties are well-known [39] were used to determine the temperature dependence of the calibration parameters in the working equation. The temperature in the measuring cell, where located the U-tube, was controlled using a thermostat with an uncertainty ($k = 2$ and $\alpha = 95\%$ confidence level) of 10 mK and measured using the (ITS-90) PRT100 thermometer with an uncertainty 0.03 K over the range from (15 to 100) °C.

The densimeter (DMA 4500) allows for a highly precise density measurements in the wide measuring range from (0 to 3000) $\text{kg}\cdot\text{m}^{-3}$ and at temperatures from (273 to 363) K. The uncertainty of the density measurements is 0.5 $\text{kg}\cdot\text{m}^{-3}$ (or about 0.05%). The repeatability of density and temperature measurements are 0.01 $\text{kg}\cdot\text{m}^{-3}$ and 0.01 K, respectively. This VTD has been successfully used previously in our earlier publications to accurate measure of the density of various fluids (see also [56]). The correction related with influence of the viscosity of the samples is within (0.001 to 0.004)%. The total absolute uncertainty ($\text{kg}\cdot\text{m}^{-3}$) in density measurements caused by the viscosity effect can be approximately estimated as $\Delta\rho_b \approx 0.005\sqrt{\eta}$, where η is the viscosity of fluid in mPa·s. The correction for the present geothermal fluid samples is within from (0.03 to 0.06) $\text{kg}\cdot\text{m}^{-3}$ or (0.0035 to 0.006)%. Therefore, after correction the final uncertainty of the measured densities (including correction on the viscosity effect) is (0.503 to 0.506) $\text{kg}\cdot\text{m}^{-3}$ (or about 0.054 to 0.056%).

4.2 Viscosity Measurements

The dynamic viscosity of the natural geothermal fluids at atmospheric pressure were measured with an automated SVM 3000 Anton Paar rotational Stabinger viscodensimeter with a coaxial cylinder geometry. The SVM 3000 viscodensimeter simultaneously measures the dynamic viscosity and density of liquids according to the ASTM D7042 standard. The technique allows simultaneously density (ρ), dynamic (η), and kinematic viscosity ($\nu = \eta/\rho$) measurements over the range (217 to 378) K, and in the viscosity range of 0.2 mPa·s to 20 Pa·s. The details of the method widely described in the literature [35–37, 40, 60, 61]. The SVM 3000 viscodensimeter uses Peltier elements for fast and efficient thermostability. The temperature uncertainty is 0.03 K. The precision of the dynamic viscosity measurements is $\pm 0.5\%$ (stated by the manufacturer uncertainty is 0.35%) and the absolute uncertainty of the density is $0.5 \text{ kg}\cdot\text{m}^{-3}$. Repeatability of the viscosity and density are 0.2% and $0.2 \text{ kg}\cdot\text{m}^{-3}$, respectively. Further details about the equipment and method can be found elsewhere (see, for example, [16, 64]).

4.3 Speed of Sound Measurements

The speed of sound of the geofluids at atmospheric pressure was measured with a sound-speed analyzer DSA 5000 M (Anton Paar instrument). DSA 5000 M simultaneously determines the density of the sample. The density and speed of sound measuring ranges are from (0 to 3000) $\text{kg}\cdot\text{m}^{-3}$ and from (1000 to 2000) $\text{m}\cdot\text{s}^{-1}$, respectively. The uncertainties of the density and speed of sound measurements are 0.01% and 0.10%, with repeatabilities of $0.001 \text{ kg}\cdot\text{m}^{-3}$ and $0.10 \text{ m}\cdot\text{s}^{-1}$, respectively. Combining of the density and speed of sound measurements in the DSA 5000 instruments makes it possible to determine the adiabatic compressibility (see below,

Sect. 5.3), $\beta_s = \frac{1}{W^2 \rho}$. The two-in-one instrument is equipped with a density cell

and a sound velocity cell thus combining the proven Anton Paar oscillating U-tube method (see above Sect. 4.1) with a highly accurate measurement of sound velocity. Both cells are temperature-controlled by a built-in Peltier thermostat. The sample is introduced into the sound velocity-measuring cell that is bordered by an ultrasonic transmitter on the one side, by a receiver on the other side. The transmitter sends sound waves of a known period through the sample. The speed of sound can be calculated by determining of the period of received sound waves and by considering the distance between the transmitter and receiver.

Table 4 Experimental values of density, viscosity, and speed of sound as a function of temperature for geothermal fluids at atmospheric pressure^c

T (K)	ρ^a (kg·m ⁻³)	T (K)	ρ^b (kg·m ⁻³)	η^b (mPa·s)	T (K)	ρ^c (kg·m ⁻³)	W^c (m·s ⁻¹)
Izberbash (No. 68)							
277.16	1000.97	277.15	1000.78	1.588	278.15	1000.72	1429.79
283.16	1000.65	283.15	1000.55	1.328	283.15	1000.51	1450.32
293.17	999.00	293.15	999.01	1.032	293.15	998.91	1484.84
303.13	996.42	303.15	996.40	0.835	303.15	996.43	1511.31
313.13	992.94	313.15	992.92	0.700	313.15	992.91	1530.94
323.13	988.73	323.15	988.70	0.603	323.15	988.72	1544.64
		333.15	983.69	0.536	333.15	983.72	1553.12
Izberbash (No. 129)							
277.17	1002.02	277.15	1002.04	1.576	278.13	1002.01	1430.42
283.15	1001.71	283.15	1001.69	1.339	283.15	1001.74	1451.31
293.16	1000.13	293.15	1000.17	1.048	293.15	1000.10	1486.27
303.13	997.56	303.15	997.55	0.816	303.15	997.79	1512.68
313.13	994.10	313.15	994.05	0.676	313.15	994.02	1532.20
323.13	989.83	323.15	989.80	0.568	318.15	992.07	1539.74
		333.15	984.60	0.488	323.15	989.76	1545.85
		343.15	979.17	0.421	333.15	984.64	1553.97
		353.15	973.39	0.372			
Ternair (No. 27T)							
277.17	1016.60	277.15	1016.4	1.660	278.14	1016.50	1456.68
283.17	1015.82	283.15	1015.87	1.420	283.15	1015.89	1476.34
293.17	1013.75	293.15	1013.73	1.119	293.14	1013.70	1508.65
303.13	1010.80	303.15	1010.78	0.917	303.15	1010.76	1533.06
313.13	1007.06	313.15	1007.03	0.785	313.15	1007.01	1551.46
323.13	1002.84	323.15	1002.81	0.679	323.10	1002.70	1564.20
					333.15	997.98	1571.92
Ternair (No. 38T)							
277.16	1017.00	277.15	1017.08	1.618	278.14	1016.82	1455.79
283.17	1016.03	283.15	1016.05	1.373	283.15	1016.03	1475.53
293.16	1014.34	293.14	1014.38	1.089	293.15	1014.36	1507.58
303.13	1011.45	303.15	1011.43	0.885	303.15	1011.47	1532.40
313.13	1007.77	313.15	1007.73	0.756	313.15	1007.80	1550.72
–	–	323.15	1003.45	0.648	318.15	1005.85	1558.02
–	–	333.15	998.65	0.570	323.15	1003.50	1563.40
–	–	343.15	993.47	0.516	–	–	–

^aDMA 4500^bSVM 3000^cDSA 5000 M; Standard uncertainties u are: (DMA 4500) $u(T) = 0.01$ K; $u(\rho) = 0.00025\%$; (SVM 3000) $u(T) = 0.005$ K; $u(\rho) = 0.01\%$; $u(\eta) = 0.17\%$; (DSA 5000M) $u(\rho) = 0.005\%$ (or 0.002 kg·m⁻³); $u(W) = 0.005\%$ (or 0.05 m·s⁻¹)

5 Results and Discussion

Measurements of the density, speed of sound, and viscosity of the geothermal fluid samples from four hot-wells (No. 68, 129, 27T and 38T) as a function of temperature at atmospheric pressure were performed at temperatures between (277 and 353) K. The experimental density, viscosity, and speed of sound results are presented in Table 4 and shown in Figs. 1, 2, 3, and 4 as a function of temperature together with pure water values calculated from the IAPWS formulations for the density [66] and viscosity [32]. The measurements of the density of geothermal fluids (the same samples) were made using three different Anton Paar instruments of DMA 4500, SVM 3000, and DSA 5000 M (vibrating-tube densimeter, VTD). The measured data from different instruments agree with each other within (0.01 to 0.02)% which is close to their experimental uncertainties. In general, the qualitative behavior of the present measured density, viscosity, and speed of sound data for all of the studied geothermal brines very close to temperature behavior of pure water (see Figs. 1, 2, 3, and 4). The same behavior has been observed also for reported data of binary and ternary aqueous salt solutions (see, for example, [2–7]). In the present study we found that at low temperatures the deviation of the solution viscosity data from the water data is slightly lower than at high temperatures, especially for high salt concentrations samples. However, this is still within experimental uncertainty of the viscosity measurements. In the measured temperature range (from 277 to 353 K) the average difference between the present measured geothermal fluids densities and pure water values [66] are No. 68: (0.05 to 0.10)%; No. 129: (0.15 to 0.21)%; No. 27T: (1.47 to 1.64)%; and for No. 38T: (1.54 to 1.77)%, which are considerably higher than their experimental uncertainties, especially for wells 27T and 38T which mineralizations are large (almost 10 times higher than for wells No. 68 and 129). As one can see from Figs. 1, 2, 3, and 4 the measured values of properties (density, speed of sound, and viscosity) for samples from wells No. 68 and 129 are very close each other. The same results we found for the samples No. 27T and 38T. It is obviously, because the difference between the compositions of the samples from wells No. 68 and 129 (both very closely located, 0.6 miles) is small (total salt contents are 1.7 and 1.8 g/l, respectively, see also Tables 2 and 3). Also the location of the wells No. 27T and 38T is very close (1.25 miles) and the composition of the samples from the wells is very close (15.4 and 15.8 g/l, respectively, see also Tables 2 and 3). However, the difference of the salt concentrations between the samples from wells (No. 68, 129) and (No. 27, 38T) is considerable large. Thus, the property differences between the samples from (No. 68, 129) and (No. 27, 38T) are very large (see below).

The present viscosity data for the geothermal brines are differing from those of pure water by (1.3 to 13.1)% for No. 68; by (0.6 to 4.8)% for No. 129; by (5.6 to 19.5)% for No. 27T; and by (3.1 to 21.0)% for No. 38T, which are considerably higher than their experimental uncertainty. The measured speed of sound data for geothermal fluids is differing from pure water values [66] within (0.13 to 0.25)% for

No. 68; by (0.3 to 2.1)% for No. 129; by (1.33 to 1.97)% for No. 27T; and by (1.37 to 2.04)% for No. 38T, which are also much higher than the experimental uncertainty. Viscosity is more sensitive properties to salt concentration than thermodynamic properties (density and speed of sound). As one can be note, measured properties for geothermal fluids (No. 27T and 38T) are considerably (up to 1.77% for density, 21% for the viscosity, and 2.04% for speed of sound) deviate from the values for pure water than for geothermal samples from (No. 68 and 129). This is the result of the large composition difference between the samples (No. 27T and 38T, mineralization is about 15.5 g/l) and samples (No. 68 and 129, mineralization of 1.8 g/l). However, this effect depends not only on the total concentration of ions, but also on chemical nature of the ions, *i.e.*, type of chemical ion species in the brine. For example, the samples (No. 68 and 129 from the same Geothermal Fields, Izberbash) have almost the same mineralization of about 1.75 g/l, however concentration contents of ions (for example, Ca^{+2} , K^{+1} , Mg^{+2} , and Na^{+1} in the sample No. 68 are 49.2, 10.2, 33, and 396 mg/l), while the content of the same ions in the sample No. 129 are completely different 2.8, 4.7, 1.3, and 590 mg/l, respectively. Therefore, the properties of the samples No. 68 and 129 are also different. This is demonstrating how the chemical nature of the ion species is effecting on the measuring properties. Separation of the contribution of single ion species to the total measured properties in the multicomponent geothermal solutions is difficult, because the solution properties are defining not only by interaction between the water molecules and single ions, but also between the ion-ion interactions, which made the problem more complicate. The presence of various type ions in the solution considerable changes the effect of particular type ions on their properties. Therefore, prediction of the thermophysical properties of multicomponent aqueous solutions, like geothermal brine, based on empirical method and solely on reliable experimental data. Thus, the present experimental data for geothermal fluids can be used to develop new prediction methods and to test the available prediction techniques.

The distinct density, speed of sound, and viscosity contributions (single ion species contributions) to the total measured properties of the multicomponent geothermal solutions, can be separated and extracted from the present measured total thermophysical properties data. The measured properties are complex functions of temperature. The temperature dependence of the density, speed of sound, and viscosity is determined by many different contributions of ion species. The present accurate measurements of the temperature dependence of the total density, speed of sound, and viscosity for various geothermal fluid samples with various salt concentrations allow correctly estimate the contribution of the each single ion species and deeply understanding the physical and chemical nature and details of the temperature and concentration dependences of the measured properties (see below Sect. 5.1).

5.1 Correlation Models for Density, Viscosity, and Speed of Sound

Since there is no theory available for the thermodynamic (equation of state) and transport properties (temperature and concentration dependence correlation models) of multicomponent aqueous solutions, its evaluation is empirical and based solely on experimentally obtained data. Therefore, the present density, speed of sound, and viscosity data for the geothermal fluid samples were fitted to the correlation equations

$$\rho(T, x_i) = \rho_{H_2O}(T) \left(1 + \sum_n^{i=1} a_i x_i \right), \quad (1)$$

$$W(T, x_i) = W_{H_2O}(T) \left(1 + \sum_n^{i=1} c_i x_i \right), \quad (2)$$

$$\eta(T, x_i) = \eta_{H_2O}(T) \left(1 + \sum_n^{i=1} b_i x_i \right), \quad (3)$$

where $\rho_{H_2O}(T)$, $W_{H_2O}(T)$, and $\eta_{H_2O}(T)$ are the pure water density, speed of sound (IAPWS formulation, [66]), and viscosity (IAPWS formulation, [32]), respectively at a temperature T and at atmospheric pressure; x_i is the concentration of ions (g/l); n is the number of main components ($n = 9$); a_i , b_i , and c_i are the density, viscosity, and speed of sound coefficients (characteristic constant of the ions) for each ion species i . It is apparent that the empirical parameters a_i , b_i , and c_i are defined the contribution of each single ion species to total measured properties and allow separate the contribution of different species. For the present geothermal fluid samples we selected 6 main components (ions): Na^+ , Ca^{+2} , Mg^{+2} , K^+ , SO_4^{-2} , and Cl^{-1} . The effect of other ions on the measured properties is negligible small. Since the thermodynamic behavior of the geothermal fluids (binary and ternary aqueous salt solutions) governs by the properties of pure water (see Figs. 1, 2, 3, and 4), the

Table 5 Values of fitting coefficients a_i , b_i , and c_i for density, viscosity, and speed of sound correlation models Eqs. (1)–(3) for basic ions in the geothermal fluid samples (density)

Ions	a_i (density) (l/g)	b_i (viscosity) (l/g)	c_i (speed of sound) (l/g)
B^+	-0.385842	0.539016	-0.418696
Ca^{+2}	0.025925	-0.716700	0.066130
K^+	-0.005234	-0.986039	0.044718
Mg^{+2}	-0.046190	1.444916	-0.105018
Na^+	0.006454	0.017450	0.006028
S^+	0.006349	0.028139	0.008064
Si^+	-0.223142	-2.751235	-0.084065
Cl^{-1}	-0.000498	0.020534	-0.001379
SO_4^{-2}	0.000784	0.067295	-0.001405

Table 6 Deviation statistics between the measured and calculated from Eqs. (1)–(3) values of density, speed of sound, and viscosity

Deviations	Density	Speed of sound	Viscosity
AAD (%)	0.03	0.20	2.47
Bias (%)	−0.01	0.15	0.71
St.dev (%)	0.04	0.22	3.16
St.err (%)	0.01	0.06	0.65
Maxdev (%)	0.16	0.50	6.92

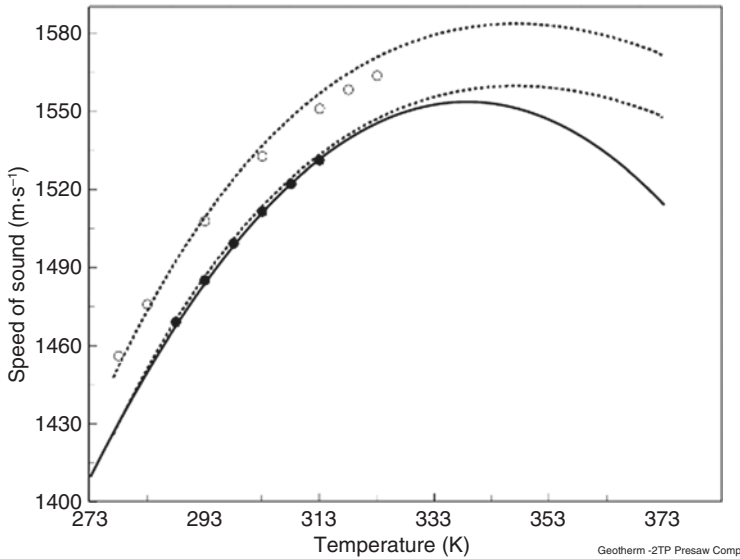


Fig. 5 Calculated from Eqs. (2) and (7) values of speed of sound for geothermal fluids (No. 68, full circles) and (No. 38T, open circles) together with the reported data by Golabiazar and Sadeghi [26] for H₂O + NaCl at atmospheric pressure. Dashed lines are predicted from Eq. (7). Solid line is calculate from Eq. (2). ○ - this work for geothermal fluid sample No. 38 T; ● -reported data by Golabiazar and Sadeghi [26] for H₂O + NaCl

temperature is not explicitly included in correlations (1) to (3), *i.e.*, the temperature dependence of the measured properties is determined through the pure water properties. All of the measured density, speed of sound, and viscosity data from Table 4 for the geothermal fluids together with the ions concentrations from Table 2 were fitted to Eqs. (1)–(3). The derived values of fitting parameters a_i , b_i , and c_i are given in Table 5. The values of characteristic constant of the ions, a_i , b_i , and, and, c_i , (or Riedel's characteristic constant of the ions) defined the contribution of each type ions on the total experimentally observed values of density, viscosity, and speed of sound. Riedel [52], Aseyev and Zaytsev [12], and Aseyev [13] have proposed the same correlation model for the thermal conductivity and other thermophysical properties of multicomponent aqueous salt solutions. This relation for the thermal conductivity gives good prediction agreement (within 5%) with the experimental data

for many aqueous salt solutions [2, 7]. Many authors checked the accuracy and predictive capability of the Riedel's model (see also review by [2, 3, 8, 31]). The deviation statistics between the measured and calculated values for density, speed of sound, and viscosity are given in Table 6. As Table 6 shows, these correlation Eqs. (1)–(3) reproduced the present density, speed of sound, and viscosity measurements for the geothermal brines within AAD = 0.03%, 0.20%, and 2.47%, respectively. The values of density, speed of sound, and viscosity calculated from Eqs. (1)–(3) together with the present measured results are presented in Figs. 1, 2, 3, and 4. To confirm the accuracy and reliability of the developed correlation models (1) to (3), we have compared the predicted values of the density and viscosity with the reported data for well-studied binary aqueous salt solutions. For example, the difference between the measured values of viscosity by Kestin and Shankland [34] and speed of sound data by Golabiazar and Sadeghi [26] and the present results calculated from Eqs. (2) and (3) for H₂O + NaCl solution are within 1.56% and 0.2%, respectively (see Figs. 3 and 5).

Developed correlation Eqs. (1)–(3) can be used to calculate the density, speed of sound, and viscosity of any geothermal fluids at atmospheric pressure with basic components of Na⁺, Ca⁺², K⁺, Mg⁺², B⁺, S⁺, Si⁺, SO₄⁻², Cl⁻¹ and with concentrations within $x(\text{Na}^+) < 7.7 \text{ g/l}$; $x(\text{Ca}^+) < 0.075 \text{ g/l}$; $x(\text{Mg}^+) < 0.033 \text{ g/l}$; $x(\text{K}^+) < 0.015 \text{ g/l}$; $x(\text{S}^+) < 0.24 \text{ g/l}$; $x(\text{B}^+) < 0.06 \text{ g/l}$; $x(\text{Si}^+) < 0.03 \text{ g/l}$; $x(\text{SO}_4^{-2}) < 0.75 \text{ g/l}$; and $x(\text{Cl}^{-1}) < 7.7 \text{ g/l}$. It is apparent that these correlation models cannot be used for geothermal fluid samples with the concentration of salt ions outside the experimental concentration ranges (see Table 2). More measurements for geothermal brines from various geothermal fields with various compositions are needed to develop accurate prediction models applicable for any natural geothermal fluids with a wide range of composition of salt ions. In order to extend the concentration and temperature ranges where the models (1) to (3) are valid and improve the accuracy of the experimental data representations, the next terms ($x_i^{0.5}$, x_i , $x_i^{1.5}$, x_i^2) in expansion Eqs. (1)–(3) can be used.

5.2 High Pressure Prediction Models

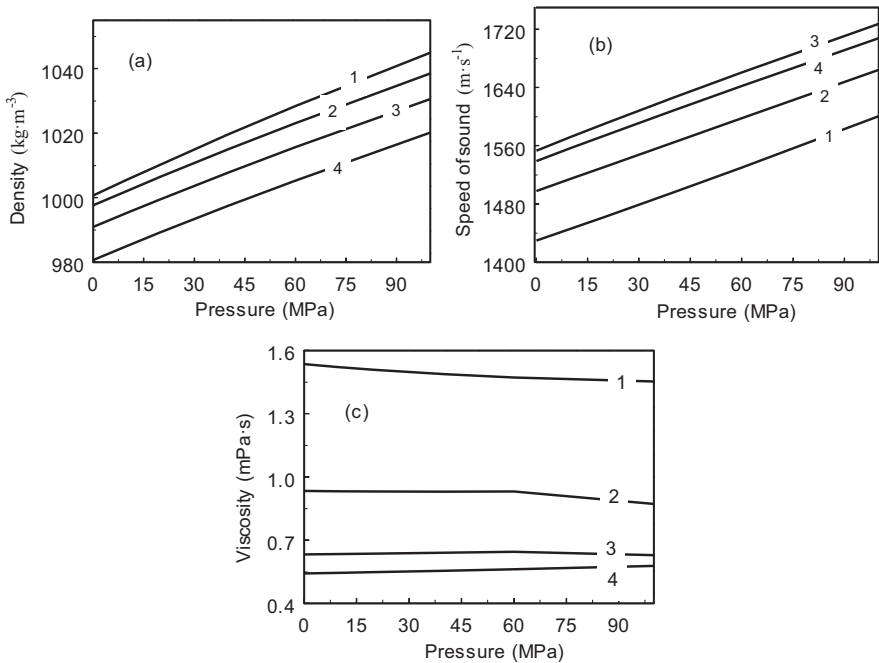
DiGuilio et al. [19] and DiGuilio and Teja [18] proposed empirical predictive equation for high pressure behavior of the thermal conductivity of aqueous salt solutions by multiplying the thermal conductivity of the salt solution at reference pressure, P_0 (usually at $P_0 = 0.101 \text{ MPa}$) and any temperature T , by the ratio of the thermal conductivity of pure water at the desired pressure P to that at a known (reference) pressure, $P_0 = 0.101 \text{ MPa}$ at the same temperature T . If the viscosity or other thermophysical properties (density, speed of sound, thermal conductivity, etc.) of the salt solution (or geothermal fluids) are known at the reference pressure (for example, $P_0 = 0.101 \text{ MPa}$) and any temperature T , the properties at any pressures (at which the property of pure water is known) may be calculated as

$$\rho(P, T, x_i) = \rho(P_0, T, x_i) \left(\frac{\rho_{H_2O}(P, T)}{\rho_{H_2O}(P_0, T)} \right)_{H_2O}, \tag{4}$$

$$\eta(P, T, x_i) = \eta(P_0, T, x_i) \left(\frac{\eta_{H_2O}(P, T)}{\eta_{H_2O}(P_0, T)} \right)_{H_2O}, \tag{5}$$

$$W(P, T, x_i) = W(P_0, T, x_i) \left(\frac{W_{H_2O}(P, T)}{W_{H_2O}(P_0, T)} \right)_{H_2O}, \tag{6}$$

where $\rho(P_0, T, x_i)$, $\eta(P_0, T, x_i)$, and $W(P_0, T, x_i)$ can be calculated from Eqs. (1)–(3) at $P_0 = 0.101$ MPa based on the present data. The present measured values of the thermodynamic (density and speed of sound) and transport (viscosity) property of geothermal fluids at atmospheric pressure were used to predict their pressure dependences based on Eqs. (4)–(6). The predicted values of density, speed of sound, and viscosity for geothermal fluids as a function of pressure and temperature are presented in Figs. 6 and 7 for various isobars and isotherms. This technique has been successfully used before and tested by many authors (see for example, [2, 18,



Geotherm-2Pressure

Fig. 6 Predicted, from Eqs. (4)–(6), values of density (a), speed of sound (b), and viscosity (c) as a function of pressure at selected isotherms for geothermal fluid sample of No. 68. 1–278 K; 2–298 K; 3–318 K; 4–338 K

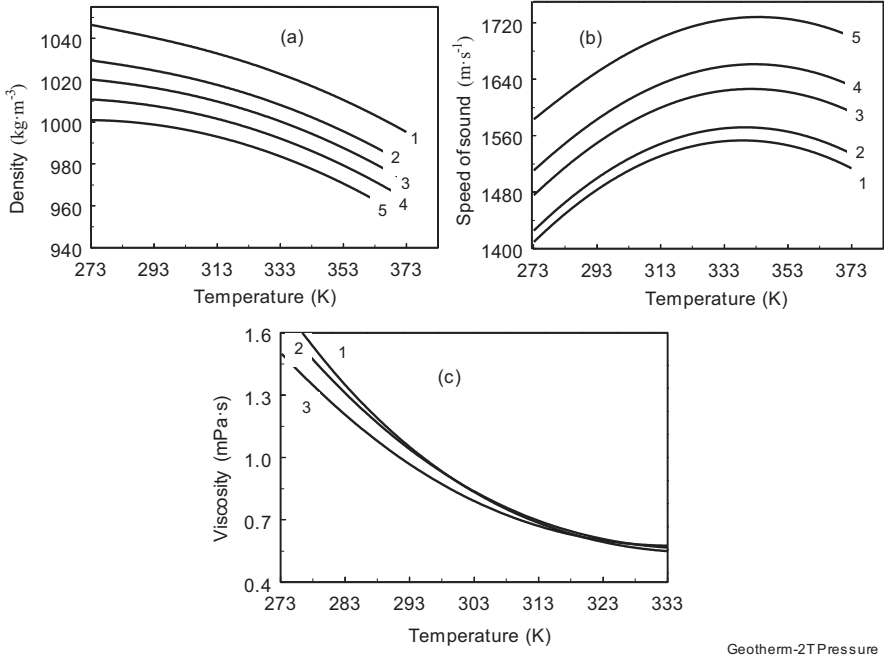


Fig. 7 Predicted, from Eqs. (4)–(6), values of density (a), speed of sound (b), and viscosity (c) as a function of temperature at selected isobars for geothermal fluid sample of No. 68. 1–0.101 MPa; 2–20 MPa; 3–40 MPa; 4–60 MPa; and 5–100 MPa

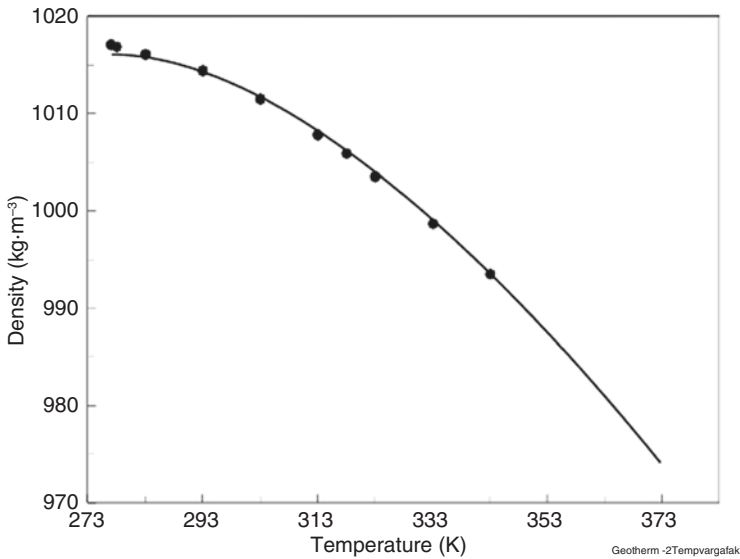


Fig. 8 Measured and predicted from Eq. (7) values of density for geothermal fluid No. 38T

19]) to predict the thermal conductivity and other thermodynamic properties of different aqueous salt solutions at high pressures and high temperatures. The same approach to predict the high temperature behavior of the aqueous solutions properties (thermal conductivity) based on the room temperature data for the solution and high temperature pure water data was developed by Vargaftik and Osminin [65] based on the relation.

$$Y(P_0, T, x_i) = Y(P_0, T_0, x_i) \left(\frac{Y_{H_2O}(P_0, T)}{Y_{H_2O}(P_0, T_0)} \right)_{H_2O}, \quad (7)$$

where $Y(P_0, T, x_i)$ is the selected values of thermophysical properties (density, speed of sound, viscosity, thermal conductivity, *etc.*) of salt solution at atmospheric pressure. Application of the relation (7) for the present measured densities of geothermal fluid (#38T) are depicted in Fig. 8. As can be note, the agreement between the present measurements and the predicted values of density is good enough (deviation AAD within 0.12%). Difference between the predicted from Eq. (4) values of density for H2O + NaCl at high pressures (at 20 MPa) and reported by Rogers and Pitzer [54] data is within AAD = 0.023% (see Fig. 9). Difference between the predicted values of viscosity at high pressures and measurements by Kestin and

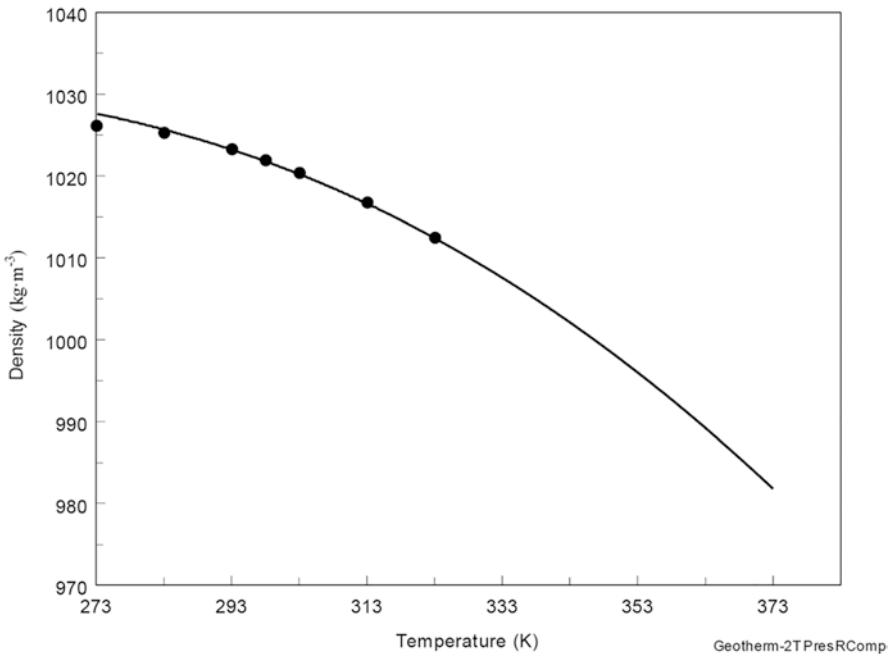


Fig. 9 Comparison predicted from Eq. (4) values of density at high pressure ($P = 20$ MPa) for geothermal fluids (No. 38T) with the measured values for H2O + NaCl solutions. Solid line is predicted from Eq. (4). Symbols are reported reference data by Rogers and Pitzer [54]

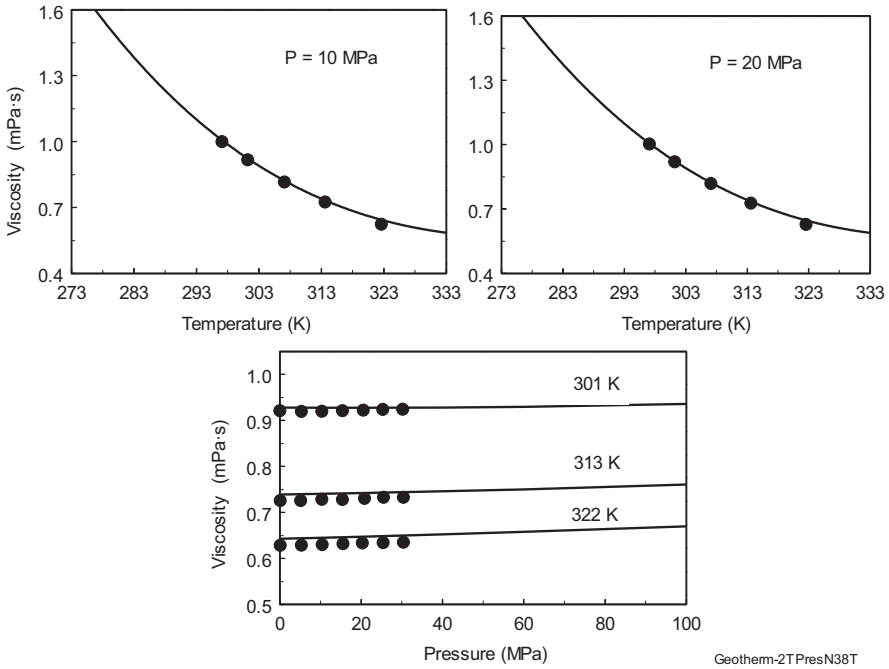


Fig. 10 Comparison predicted from Eq. (5) values of viscosity at high pressures for geothermal fluid (No. 38T) with measured values for H₂O + NaCl solutions by Kestin and Shankland [34]

Shankland [34] for H₂O + NaCl is within (1–2)% (see Fig. 10). Figure 10 demonstrate temperature dependence of viscosity of H₂O + NaCl solution calculated from Eq. (5) at selected pressures (10 and 20 MPa) using the present correlation model (3) together with the data by Kestin and Shankland [34]. This figure also shows pressure dependence of viscosity of the H₂O + NaCl solution for selected isotherms. The agreement is acceptable, although the measured values of viscosity are systematically lower than predicted values (above than the experimental uncertainty of 0.5%).

5.3 Derived Thermodynamic Properties of Geothermal Fluids

The measured values of density and speed of sound for the natural geothermal fluids were used to calculate other thermodynamic parameters such as, β_s , β_T , α_P , γ_V , ΔH , C_P , C_V , $\left(\frac{\partial H}{\partial P}\right)_T$, $\left(\frac{\partial U}{\partial V}\right)_T$. All of these thermodynamic properties were calculated using the well-known thermodynamic relations:

1. Adiabatic coefficient of bulk compressibility,

$$\beta_s = \frac{1}{W^2 \rho}; \quad (8)$$

where $\beta_s = -\frac{1}{V} \left(\frac{\partial V}{\partial P} \right)_s$ has been calculated using measured densities (ρ) and speed of sound data (W) from Table 4;

2. Coefficient of thermal expansion,

$$\alpha_p = -\frac{1}{\rho} \left(\frac{\partial \rho}{\partial T} \right)_p; \quad (9)$$

has been calculated using measured densities (ρ) as a function of temperature from Table 4;

3. Thermal pressure coefficient,

$$\gamma_v = \left(\frac{\partial P}{\partial T} \right)_v = \left(\frac{dP_s}{dT} \right) + \frac{1}{T} \frac{dT}{dV_s} \Delta C_v, \quad (10)$$

where ΔC_v is the one- and two-phase heat capacity difference, V_s is the specific volume at saturation, and P_s is the vapor pressure [1];

4. Isothermal coefficient of bulk compressibility,

$$\beta_T = \frac{\alpha_p}{\gamma_v}, \quad (11)$$

where $\beta_T = -\frac{1}{V} \left(\frac{\partial V}{\partial P} \right)_T$;

5. Isochoric heat capacity,

$$C_v = VT \alpha_p \gamma_v / (W^2 \rho \alpha_p / \gamma_v - 1), \quad (12)$$

where $V = 1/\rho$;

6. Isobaric heat capacity,

$$C_p = C_v W^2 \rho \alpha_p / \gamma_v; \quad (13)$$

7. Enthalpy difference,

$$\Delta H = H(T) - H(T_0) = \int_{T_0}^T C_p(T) dT, \quad (14)$$

has been calculated using derived C_p data;

8. Partial pressure derivative of enthalpy,

Table 7 Derived, from the present density and speed of sound measurements, values of thermodynamic properties of geothermal fluids^a

T (K)	$\beta_S \times 10^3$ (MPa ⁻¹)	$\alpha_P \times 10^3$ (K ⁻¹)	$\left(\frac{\partial H}{\partial P}\right)_T$ (cm ³ ·g ⁻¹)	$\left(\frac{\partial U}{\partial V}\right)_T$ (MPa)	$\beta_T \times 10^3$ (MPa ⁻¹)	γ_V (MPa·K ⁻¹)	C_V (kJ·kg ⁻¹ ·K ⁻¹)	C_P (kJ·kg ⁻¹ ·K ⁻¹)
Izberbas (No. 68)								
278.15	0.4888	0.0637	0.9816	36.12	0.4891	0.130233	4.259	4.262
283.15	0.4752	0.1089	0.9687	64.68	0.4760	0.228790	4.217	4.224
293.15	0.4541	0.1996	0.9425	127.95	0.4569	0.436804	4.163	4.188
303.15	0.4394	0.2908	0.9151	197.73	0.4455	0.652591	4.121	4.179
313.15	0.4297	0.3828	0.8864	271.85	0.4408	0.868439	4.080	4.185
323.15	0.4239	0.4758	0.8559	348.14	0.4415	1.077650	4.031	4.198
333.15	0.4214	0.5702	0.8235	424.47	0.4474	1.274407	3.990	4.236
Izberbash (No. 129)								
278.13	0.4878	0.0964	0.9712	54.82	0.4884	0.197475	4.282	4.288
283.15	0.4739	0.1356	0.9600	80.73	0.4752	0.285460	4.257	4.268
293.15	0.4526	0.2140	0.9372	137.52	0.4558	0.469468	4.209	4.238
303.15	0.4380	0.2929	0.9132	199.77	0.4442	0.659320	4.163	4.222
313.15	0.4285	0.3724	0.8887	265.60	0.4389	0.848470	4.110	4.209
318.15	0.4252	0.4125	0.8757	299.44	0.4381	0.941522	4.092	4.217
323.15	0.4228	0.4528	0.8625	333.50	0.4387	1.032340	4.070	4.223
333.15	0.4206	0.5344	0.8348	401.43	0.4434	1.205260	4.020	4.238
Ternair (No. 27T)								
278.14	0.4636	0.1382	0.9460	82.58	0.4648	0.297274	4.288	4.299
283.15	0.4516	0.1740	0.9359	108.48	0.4536	0.383488	4.244	4.262
293.14	0.4334	0.2456	0.9155	164.42	0.4376	0.561219	4.190	4.230
303.15	0.4210	0.3178	0.8940	224.95	0.4282	0.742359	4.141	4.212
313.15	0.4126	0.3907	0.8715	288.61	0.4238	0.921960	4.105	4.217
323.10	0.4076	0.4641	0.8478	353.53	0.4240	1.094500	4.065	4.229

T (K)	$\beta_s \times 10^3$ (MPa ⁻¹)	$\alpha_p \times 10^3$ (K ⁻¹)	$\left(\frac{\partial H}{\partial P}\right)_T$ (cm ³ ·g ⁻¹)	$\left(\frac{\partial U}{\partial V}\right)_T$ (MPa)	$\beta_T \times 10^3$ (MPa ⁻¹)	γ_V (MPa·K ⁻¹)	C_V (kJ·kg ⁻¹ ·K ⁻¹)	C_P (kJ·kg ⁻¹ ·K ⁻¹)
333.15	0.4055	0.5393	0.8220	419.24	0.4284	1.258700	4.012	4.239
Ternair (No. 38T)								
278.14	0.4640	0.1347	0.9466	80.42	0.4652	0.289510	4.307	4.318
283.15	0.4521	0.1692	0.9371	105.42	0.4539	0.372668	4.278	4.296
293.15	0.4338	0.2383	0.9170	159.51	0.4376	0.5444502	4.225	4.263
303.15	0.4210	0.3078	0.8964	218.08	0.4277	0.7197100	4.165	4.231
313.15	0.4126	0.3781	0.8748	279.68	0.4232	0.8934400	4.106	4.211
318.15	0.4096	0.4135	0.8634	311.31	0.4224	0.9788172	4.076	4.204
323.15	0.4077	0.4491	0.8519	342.88	0.4231	1.0613600	4.054	4.208

^aStandard uncertainties u are: $u(T) = 0.01$ K; $u(\beta_s) = 0.008\%$; $u(\alpha_p) = (0.05-0.10)\%$; $u(\beta_T) = (0.2-0.4)\%$; $u(C_V) = (2-3)\%$; $u(C_P) = (3-4)\%$

Table 8 Enthalpy difference, $\Delta H = H(T) - H_0(T_0)$, of geothermal fluids ($T_0 = 273.15 \text{ K}$)^a

$T \text{ (K)}$	$\Delta H \text{ (kJ}\cdot\text{kg}^{-1}\text{)}$	$T \text{ (K)}$	$\Delta H \text{ (kJ}\cdot\text{kg}^{-1}\text{)}$	$T \text{ (K)}$	$\Delta H \text{ (kJ}\cdot\text{kg}^{-1}\text{)}$	$T \text{ (K)}$	$\Delta H \text{ (kJ}\cdot\text{kg}^{-1}\text{)}$
Izberbas (No. 68)		Izberbas (No. 129)		Ternair (No. 27T)		Ternair (No. 38T)	
278.15	21.251	278.13	21.430	278.14	21.364	278.14	21.671
283.15	42.361	283.15	42.927	283.15	42.697	283.15	43.322
293.15	84.257	293.15	85.493	293.14	84.928	293.15	86.231
303.15	125.87	303.15	127.82	303.15	126.96	303.15	128.82
313.15	167.40	313.15	170.03	313.15	168.83	313.15	171.20
323.15	209.02	318.15	191.13	323.10	210.47	318.15	192.33
333.15	250.91	323.15	212.25	333.15	252.711	323.15	213.44
–	–	333.15	254.60	–	–	–	–

^aStandard uncertainties u are: $u(T) = 0.01 \text{ K}$; $u(\Delta H) = (2\text{--}4) \%$

$$\left(\frac{\partial H}{\partial P}\right)_T = V(1 - T\alpha_p), \tag{15}$$

9. Partial derivatives of internal energy (internal pressure),

$$\left(\frac{\partial U}{\partial V}\right)_T = -P_0 + T\gamma_v, \tag{16}$$

where $P_0 = 0.101 \text{ MPa}$.

Derived thermodynamic properties of geothermal fluids calculated using Eqs. (8)–(16) are given in Tables 7 and 8. Thus, in Tables 4, 7, and 8 we have all of the thermodynamically consistent property data as a function of temperature at atmospheric pressure for four natural geothermal fluids. Unfortunately, there are no direct measured thermodynamic properties data for the present geothermal fluids to check the accuracy and reliability of the derived properties. However, this method of calculation of the thermodynamic properties has been checked for many other fluids (see for example, [2]).

6 Conclusions

The density, speed of sound, and viscosity of four natural geothermal fluid samples from Dagestan Geothermal Field (south Russia, Caspian seashore) have been measured with Anton Paar Instruments: vibrating-tube densimeters (DMA 4500); sound-speed analyzer (DSA 5000 M); and Stabinger viscodensimeter (SVM 3000), respectively. Measurements were made at temperatures from (277 to 353) K and at atmospheric pressure. The temperature behavior of the density, speed of sound, and viscosity for geothermal fluids are just like pure water and other binary and ternary aqueous salt solutions. The average differences between the measured geothermal fluids density, speed of sound, and viscosity and pure water values (IAPWS

formulations, 2002 and 2009) are within (0.05 to 1.77)%, (0.13 to 2.04)%, and (0.6 to 21.0)%, respectively, which are much higher than their experimental uncertainties. The measured density, speed of sound, and viscosity data were used to develop correlation model (Riedel model) to predict the values of these properties for various concentrations of ions and temperatures from (277 to 353) K. The contribution (Riedel's characteristic constant of the ions) of the basic ions in the geothermal fluids (Ca^{+2} , K^{+1} , Mg^{+2} , Na^{+1} , B^{+1} , S^{+1} , Si^{+1} , SO^{-2} , and Cl^{-1}) to the total experimentally observed values of the density, viscosity, and speed of sound was estimated. The models reproduced measured values of density, speed of sound, and viscosity of geothermal fluids within: density: AAD = 0.03%; speed of sound: AAD = 0.20%; and viscosity: AAD = 2.47%. It was shown that if the thermophysical properties of geothermal fluid are known at reference pressure (for example, $P_0 = 0.101$ MPa) and any temperature, their properties at any high pressures (at which this properties of pure water is known) and temperatures maybe calculated by multiplying the properties of the geothermal fluid at reference state, P_0 , and given temperature, T , by the ratio of the this property of pure water at the desired pressure to that at a known reference pressure, $P_0 = 0.101$ MPa. The prediction of the values of density and viscosity from the model at high pressures for $\text{H}_2\text{O} + \text{NaCl}$ solutions agree with the data reported by Rogers and Pitzer [54] and Kestin and Shankland [34] within AAD = 0.023% and 1.5%, respectively. The measured values of viscosity at high pressures are systematically lower than predicted values (slightly higher than the experimental uncertainty of 0.5%). The measured values of density and speed of sound were also used to calculate other derived properties such as adiabatic coefficient of bulk compressibility, coefficient of thermal expansion, thermal pressure coefficient, isothermal coefficient of bulk compressibility, isochoric heat capacity, isobaric heat capacity, enthalpy difference, partial pressure derivative of enthalpy, and partial derivatives of internal energy (internal pressure). More measurements for geothermal brines from various geothermal fields with various compositions are needed to develop accurate prediction models applicable for any natural geothermal fluids with wide range of composition of salt.

References

1. Abdulagatov IM, Dvoryanchikov VI (1995) Thermodynamic properties of geothermal fluids. *Russ J Geochem* 5:612–620
2. Abdulagatov IM, Abdulagatov AI et al (2005a) Thermophysical properties of pure fluids and aqueous systems at high temperatures and high pressures. Begell House, Inc, New York
3. Abdulagatov IM, Zeinalova AB et al (2005b) Viscosity of aqueous Na_2SO_4 solutions at temperatures from 298 to 573 K and at pressures up to 40 MPa. *Fluid Phase Equilib* 227:57–70
4. Abdulagatov IM, Azizov ND (2005) Densities, apparent molar volumes, and viscosities of concentrated aqueous NaNO_3 solutions at temperatures from 298 to 607 K and at pressures up to 30 MPa. *J Solut Chem* 34:645–685
5. Abdulagatov IM, Azizov ND (2006) Densities, apparent and partial molar volumes of concentrated aqueous LiCl solutions at high temperatures and high pressures. *Chem Geol* 230:22–41

6. Abdulagatov IM et al (2007) Viscosities, densities, apparent and partial molar volumes of concentrated aqueous MgSO₄ solutions at high temperatures and high pressures. *Phys Chem Liq* 45:127–148
7. Abdulagatov IM, Assael M (2009) Chapter 6: viscosity. In: Valyashko VM (ed) *Hydrothermal properties of materials. Experimental data on aqueous phase equilibria and solution properties at elevated temperatures and pressures*. Wiley, London, pp 249–270
8. Abdulagatov IM, Akhmedova-Azizova LA, Aliev RM, Badavov GB (2016) Measurements of the density, speed of sound, viscosity and derived thermodynamic properties of geothermal fluids. *J Chem Eng Data* 61:234–246
9. Adams JJ, Bachu S (2002) Equations of states for basin geofluids: algorithm review and inter-comparison for brines. *Geofluids* 2:257–271
10. Alkan H, Babadagli T et al (1995) The prediction of the PVT/Phase behavior of the geothermal fluid mixtures. In: *Proceeding of the World Geothermal Congress, IGA*, pp 1659–1665
11. Ague JJ (2003) Fluid flow in the deep crust. In: Rudnick RL (ed) *Treatise of geochemistry, the crust, vol 3*. Elsevier, Amsterdam, pp 195–228
12. Aseyev GG, Zaytsev ID (1996) *Volumetric properties of electrolyte solutions. Estimation methods and experimental data*. Begell-House, Inc, New York
13. Aseyev GG (1998) *Electrolytes. Properties of solutions. Methods for calculation of the multicomponent systems and experimental data on thermal conductivity and surface tension*. Begell-House, Inc, New York
14. Battistelli A, Calore C et al (1993) A fluid property module for the TOUGH2 simulator for saline brines with non-condensable gas. In: *Proceedings 18th workshop on geothermal reservoir engineering*, Stanford University, pp 249–259
15. Battistelli A (2012) Improving the treatment of saline brines in EWASG for the simulation of hydrothermal systems. In: *Proceedings of the TOUGH symposium*, Lawrence Berkeley National Laboratory, Berkeley, pp 1–9
16. Carvalho PJ, Regueira T et al (2010) Effect of water on the viscosities and densities of 1-Butyl-3-methylimidazolium dicyanamide and 1-Butyl-3-methylimidazolium tricyanomethane at atmospheric pressure. *J Chem Eng Data* 55:645–652
17. Champel B (2006) Discrepancies in brine density databases at geothermal conditions. *Geothermics* 35:600–606
18. DiGuilio RM, Teja AS (1992) Thermal conductivity of aqueous salt solutions at high temperatures and high concentrations. *Ind Eng Chem Res* 31:1081–1085
19. DiGuilio RM, Lee RJ et al (1990) Properties of lithium bromide-water solutions at high temperatures and concentrations-I. Thermal conductivity. *ASHRAE Trans* 96:702–708
20. Dittman GL (1977) *Calculation of brine properties*, Lawrence Livermore Laboratory, Report UCID 17406
21. Dolejs D, Manning CE (2010) Thermodynamic model for mineral solubility in aqueous fluids: theory, calibration and application to model fluid-flow systems. *Geofluids* 10:20–40
22. Erday-Gruz T (1974) *Transport phenomena in aqueous solutions*. Wiley, New York
23. Ershaghi I, Abdassah D et al (1983) Estimation of geothermal brine viscosity. *J Pet Technol* 35:621–628
24. Francke H, Thorade M (2010) Density and viscosity of brine: an overview from a process engineers perspective. *Chem Erde, Geochem* 70:23–32
25. Francke H, Kraume M et al (2013) Thermal –hydraulic measurements and modelling of the brine circuit in a geothermal well. *Environ Earth Sci* 70:3481–3495
26. Golabiazar R, Sadeghi R (2014) Salt-effects in aqueous surface-active ionic liquid 1-dodecyl-3-methylimidazolium bromide solutions: volumetric and compressibility property changes and critical aggregation concentration shifts. *J Chem Thermodyn* 76:29–44
27. Glasstone S, Laidler K et al (1941) *Theory of rate processes*. McGraw-Hill, New York
28. Haas JL Jr (1976a) Physical properties of the coexisting phases and thermochemical properties of the H₂O component in boiling NaCl solutions. *U.S. Geological Survey Bulletin* 1421-A, 73 p

29. Haas JL Jr (1976b) Thermodynamic properties of the coexisting phases and thermochemical properties of the NaCl component in boiling NaCl solutions. U.S. Geological Survey Bulletin 1421-B, 71 p
30. Helgeson HC (1967) Solution chemistry and metamorphism. Res Geochem (PH Abelson ed) 55:379–385
31. Horvath AL (1985) Handbook of aqueous electrolyte solutions. Physical properties, estimation methods and correlation methods. Ellis Horwood, West Sussex
32. Huber ML, Perkins RA et al (2009) New international formulation for the viscosity of H₂O. J Phys Chem Ref Data 38:101–125
33. Huber ML, Perkins RA et al (2012) New international formulation for the thermal conductivity of H₂O. J Phys Chem Ref Data 41:033102-1–033102-23
34. Kestin J, Shankland IR (1984) Viscosity of aqueous NaCl solutions in the temperature range 25–200 °C and in the pressure range 0.1–30 MPa. Int J Thermophys 5:241–263
35. Kratky O, Leopold H et al (1969) Determination of density of liquids and gases to an accuracy of 10⁻⁶ g/cm³, with a sample volume of only 0.6 cm³. Z Angew Physiol 27:273–277
36. Kratky O, Leopold H et al (1980) DMA45 calculating digital density meter, instruction manual. Digital densimeter of liquids and gases (Paar A, KG, A-8054, Graz, Austria), pp 1–12
37. Kroger D (2002/2003) Stabinger viscometer. Petro Industry News, vol 3, issue 4, Annual Buyers Guide
38. Lee KS (2000) Comparison of correlation equations for estimating brine properties under high pressure and temperature condition. Geosyst Eng 3:113–116
39. Lemmon EW, Huber ML et al (2010) NIST standard reference database 23, NIST reference fluid thermodynamic and transport properties, REFPROP, version 9.0, standard reference data program, National Institute of Standards and Technology, Gaithersburg
40. Leopold H (1970) Digital density meter. Elektronik 297:411–415
41. McCain WD Jr (1991) Reservoir fluid property correlations-state of art. SPE Reserv Eng 6(2):266–272
42. McKibbin R, McNabb A (1995) Mathematical modeling the phase boundaries and fluid properties of the system H₂O+NaCl+CO₂. In: Proceedings of the 17th New Zealand Geothermal Workshop, University of Auckland, pp 255–262
43. Milsch H, Kallenberg B et al (2010) Mixing-rules of viscosity, electrical conductivity and density of NaCl, KCl, and CaCl₂ aqueous solutions derived from experiments. EGU2010–1584, EGU General Assembly-2010, Geophysical Research Abstracts, 12
44. Muller PIN, Weare JH (1999) Model of geothermal brine chemistry. Final report, Grant DE-FG07-93ID13247, pp 1–23
45. Oldenburg C, Pruess K et al (1995) Heat and mass transfer in hypersaline geothermal systems. In: Proceeding of the World Geothermal Congress, IGA, pp 1647–1652
46. Ostermann RD, Paranjpe SG et al (1986) The effect of dissolved gas on geothermal brine viscosity. In: Proceedings of the 56th annual society of petroleum engineers, California Regional Meeting, pp 381–389
47. Palliser C, McKibbin R (1998a) A model for deep geothermal brines, III: thermodynamic properties-enthalpy and viscosity. Trans Porous Media 33:155–171
48. Palliser C, McKibbin R (1998b) A model for deep geothermal brines, II: thermodynamic properties-density. Trans Porous Media 33:129–154
49. Palliser CH (1998) A model for deep geothermal brines: state space description and thermodynamic properties. PhD thesis, Massey University
50. Piwinski AJ, Netherton R et al (1977) Viscosity of brines from the Salton sea Geothermal Field, Imperial valley, California, Lawrence Livermore Laboratory, Report UCRL 52344, University of California, California
51. Potter RW, Haas JL Jr (1977) A model for the calculation of the thermodynamic properties of geothermal fluids. Geotherm Resour Counc Trans 1:243–244
52. Riedel L (1951) The heat conductivity of aqueous solutions of strong electrolytes. Chem Ing Tech 23:59–64

53. Reindl J, Shen H et al (2009) Reservoir engineering: an introduction and application to rigo, Colorado, Geothermal Energy-MNGN598
54. Rogers PSZ, Pitzer KS (1982) Volumetric properties of aqueous sodium chloride solutions. *J Phys Chem Ref Data* 11:15–81
55. Saadat A, Frick S et al (2008) Niedertemperaturstromerzeugung-systembetrachtung unter berücksichtigung des eigenbedarfs. In: Geothermische Technologien: Vom reservoir zur kilowattstunde; Tagung Potsdam, 27, und 28. Februar (2008)/VDI-Gesellschaft Energietechnik, VDI, pp 155–167
56. Schmidt H, Stephan M et al (2012) Thermophysical properties of 1-ethyl-3-methylimidazolium ethyl sulfate. *J Chem Thermodyn* 47:68–75
57. Schröder E, Thomauske K et al (2015) Design and test of a new calorimeter for online detection of geothermal water heat capacity. *Geothermics* 53:202–212
58. Segovia JJ, Fandiño O et al (2009) Automated densimetric system: measurements and uncertainties for compressed systems. *J Chem Thermodyn* 41:632–638
59. Spycher N, Pruess K (2011) A model for thermophysical properties of CO₂-brine mixtures at elevated temperatures and pressures. In: Proceedings of the 36th workshop on geothermal reservoir engineering, Stanford University, Stanford California, SGP-TR-191
60. Stabinger H, Kratky O et al (1967) Eine neue ra isionsmethode ur estim-mun der ichte von lu ssi keiten. *Monatsh Chem* 98:436–438
61. Stabinger H (1994) Density measurement using modern oscillating transducers. Yorkshire Trading Standards Unit, Sheffield
62. Stefánsson A, Driesner TH et al (eds) (2012) Thermodynamic of geothermal fluids, vol 76. Mineralogical Society of America & Geochemical Society, Chantilly
63. Stokes RH, Mills R (1965) Viscosity of electrolytes and related properties. Pergamon Press, New York
64. Tariq M, Carvalho PJ et al (2011) Viscosity of (C2–C14) 1-alkyl-3-methylimidazolium bis(trifluoromethylsulfonyl) amide ionic liquids in an extended temperature range. *Fluid Phase Equilib* 301:22–32
65. Vargaftik NB, Osminim YP (1956) Thermal conductivity of aqueous solutions of salts, acids and alkalis. *Teploenergetika* 7:11–15
66. Wagner W, Pruß A (2002) New international formulation for the thermodynamic properties of ordinary water substance for general and scientific use. *J Phys Chem Ref Data* 31:387–535
67. Wahl EF (1977) Geothermal energy utilization. Wiley, New York
68. Zezin D, Driesner TH et al (2014) Volumetric properties of mixed electrolyte aqueous solutions at elevated temperatures and pressures. The systems CaCl₂-NaCl-H₂O and MgCl₂-NaCl-H₂O to 523.15, 70 Ma, and ionic strength from (0.1 to 18) mol•k⁻¹. *J Chem Eng Data* (in press)

Part V
Geophysics and Geodynamics

ROSA Database and GIS Project: Accumulation of the World Largest Oil and Gas Deposits in Geological History



A. A. Odintsova, A. I. Rybkina, J. I. Nikolova, and A. A. Korolkova

The raw data is one of the necessary conditions for conducting such global study. Creating and support of verified databases is one of the priorities for the development of geoinformatics. A database provides the availability of reliable and comparable data as a prerequisite for effective analysis on issues affecting oil and gas industry.

However, before approaching the issue of elaborating the idea of creation a thematically oriented database, the authors solved a number of challenges related directly to the data – their search, collection, systematization, storage and management for the purpose of further analytical studies.

Since the emergence of the phenomenon of “Big Data” in the first decade of the new millennium a host of approaches to working with large amount of data have appeared. Data on disciplines of the natural sciences, including geology and geophysics, should be clearly classified as Big Data. In accordance with the definition, Big Data shall meet the following requirements of 4 V’s: volume, variety, velocity, veracity [21]. The volume of data on oil and gas fields presented in the framework of the project is slightly exceeded for Big Data, but the authors of this work took as a basis for the project implementation.

In our project the data is treated as a kind of strategic asset. Therefore, it is especially important to approve a number of principles that have organized a methodical

A. A. Odintsova (✉) · J. I. Nikolova · A. A. Korolkova
Geophysical Center of the Russian Academy of Sciences (GC RAS), Moscow, Russia
e-mail: a.odintsova@gcras.ru; j.zharkikh@gcras.ru; a.korolkova@gcras.ru

A. I. Rybkina
Geophysical Center of the Russian Academy of Sciences (GC RAS), Moscow, Russia
The Schmidt Institute of Physics of the Earth of the Russian Academy of Sciences (IPE RAS), Moscow, Russia
e-mail: a.rybkina@gcras.ru

process of extracting and systematizing the necessary data. One of the tools that allow it to organize is Systems Analysis. We used various methods and approaches of Systems Analysis to collect and integrate data, as well as to approve the structure of the ROSA database for further analytical studies.

Data collection and its further analysis will remain challenging in various aspects. Among a major barriers to data collection is low availability of data, due to the specific nature of the data and their secrecy, particularly in the case of Near and Middle East countries. Therefore, some fields of attribute tables of ROSA database appear insufficiently representative. Sometimes null values (empty fields) can be found in database.

Another challenge is data integration. Since the data comes from diverse sources (in Russian as well as other countries) in a variety of formats (textual and graphic material) and standards, special attention should be paid to converting data to the unified standard, because there is a significant number of differences between Russian and foreign terminology. One example is the classification of deposits according to their reserves. In the global oil and gas industry, the classifiers of the above indicators and their units of measure are significantly different. The following main classifications are: SPE-PRMS (Society of Petroleum Engineers and Petroleum Resources Management System, respectively), that takes into account not only the probability of finding oil and gas in the fields, but also the economic efficiency of extracting these reserves; it is used most often in audits and consulting; US Classification (Securities and Exchange Commission SEC Classification of the Securities Market Commission); American Association of Petroleum Geologist Classification, United Nations, etc. [2]. Thus, the principle of data unification is extremely important.

Another important issue is the data reliability. As many sources include contradictions, the data collection should be accurate and avoid invalid sources. For the verification propose ROSA database is linked to bibliographic summary that testify the reliability of obtained results and provide an efficient tool for its further analysis.

Consequently, data used in the ROSA project should have an appropriate systematization model, according to which the data should be compared from a single point of view for their further merging and harmonization.

The ROSA database requires a systems approach to overcome challenges listed above and at the same time meets the requirements of a specific scientific analytical research of the oil and gas industry worldwide development. A proper model should be established to provide a data comparison for its further matching and merging.

1 Building the Database

Scientific knowledge is much more than a simple compilation of data points. Among the key issues is the way we manage the data. The application of system analysis methods is the most effective tool that allows to systematize data for conducting

further extensive analytical study. In this way, to advance data analytical tools, the database is presented as multidimensional and multilevel.

In keeping with these principles in the first phase of the project a number of sub-projects were carried out in order to efficiently organize and compile a geospatial database. The database objects were the largest oil and gas fields in Russia and other countries in the twentieth and twenty-first centuries.

Adherence to the principles of the data work make the database as verified as possible due to a better control of the quality of data.

This article provides a comprehensive literature review covering over 500 open specialized Russian and foreign bibliographic sources: reference books on oil and gas fields; monographs; articles in specialized journals and books of abstracts of conferences; encyclopedias and dictionaries; reports of strategic research centers, specialized laboratories, ministries, commercial oil and gas companies; dissertations of experts in the oil and gas industry; materials of open Internet sources (sites of oil producing companies, academic profile dictionaries, etc.). As a result, an annotated bibliography was compiled. It consist of the separate thematic blocks linked to the corresponding bibliographic source that testify the reliability of obtained results and provide verification tool for its analysis [4–6, 8, 9, 14, 15, 17, 25].

To reflect the process of the oil and gas industry establishment and its development within twentieth and twenty-first centuries, the database attributive tables were constructed dividing all data into two blocks – static and dynamic.

Static data includes the characteristics of deposits that are constant over time: ID; Latitude & Longitude; Name; Location; Type of hydrocarbon resource; Exploration methods; Discovery date; Start of production; Type & Age of reservoir; Mass density; Operator; Reserves; Additional information; Keywords.

Dynamic data includes the parameters that are changing over time with an interval of 1 year: Extraction and Recovery methods; Technology & Features of extraction; Production.

The ROSA project went through several stages step-by-step of its development and each stage characterized by set of improvements and modifications.

The general structure of the ROSA database can be described as multidimensional and multilevel, and can be presented in three levels – ROSA 1.0, ROSA 2.0, ROSA 3.0 [19, 22].

The first information level ROSA 1.0 contains static and dynamic data on the largest oil and gas fields in Russia and other countries with reserves more than 1000 million tons of oil and 1000 m³ of gas, the search and commissioning of which fell on the twentieth century.

The second and third information levels ROSA 2.0 and ROSA 3.0 include the data on the largest strategically important hydrocarbon fields in Russia in the twentieth and twenty-first centuries. In total ROSA 2.0 includes 36 objects with reserves from 100 to 1000 million tons, and ROSA 3.0 includes 18 objects with reserves from 50 to 100 million tons.

The proposed block diagram represents the interaction of all levels of the ROSA database (Fig. 1). The principle of the inverted pyramid is applied since there is

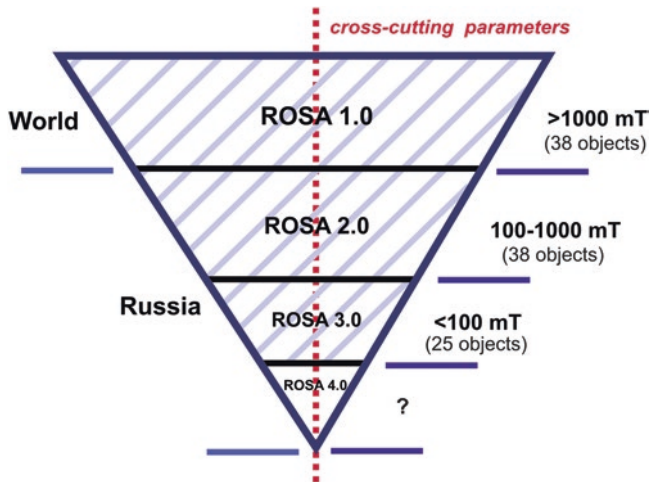


Fig. 1 Model for representing the structure of a multilevel ROSA database according to the principle of an inverted pyramid

gradual reduction of coverage and number of objects while the detail of the data is increased.

ROSA 1.0 includes the largest oil and gas fields in the world and at the level of ROSA 2.0–3.0 only deposits in the territory of the Russian Federation are considered. ROSA 4.0 contains more detailed and narrowly focused information where available. From the top of the pyramid, it provides the geographic coverage, as well as the volume of oil and gas in place. This principle is universal and can be additionally applied in other thematic databases. All levels can be analyzed independently or within a complete database using end-to-end parameters unified for all levels for a comparative analytical review.

Each object is characterized by unique and unified parameters. For example, the values of the fields “location”, “coordinates”, “identification number”, etc. are unique for each object. Other parameters of the attribute table, such as “collector type”, “exploration methods”, “mining technologies”, etc., are unified for all levels of the ROSA database. This, if necessary, it will allow to distribute the above-mentioned data to groups for further classification of deposits in the framework of conducting analytical studies.

Dynamic unit parameters (production methods; production technologies; technological features; well production rate), varying in 1-year increments for the ROSA 1.0 level, are also included in the ROSA 2.0 and ROSA 3.0 levels, but the way they are presented is somewhat different. Due to limited access to information, it is not always possible to track changes, for example, in the technologies used or in the level of production for a particular field. Another case is if the field was commissioned in the last few decades, and the attribute block table of the dynamic block is changed, for example, in steps of 1–2 years, while information for earlier fields may be available in steps of 5 or even 10 years. In view of this, all the necessary

information, which may change over time, is presented within one cell of the attribute table with a step that is most appropriate for each specific field.

Another tool with which the database is equipped is the availability of end-to-end parameters, which ensure efficient navigation within all blocks and levels, as well as facilitate the processing of a large amount of heterogeneous data in both numerical and text formats.

Thus, the ROSA database is a key element of the project and reflects all the information necessary for further analysis of industrial and economic transformation both within our country and in the world as a whole.

At the next stage of creating the database, the authors used a modern geographic information system ArcGIS [1]. It allows to present all deposits as a single world map with various backgrounds and provides the user with the opportunity to analyze the data with spatial algorithmic tools. To work and sort the deposits according to the desired parameters the built-in capabilities of the ArcGIS system analysis software package methods and algorithmic tools created by the authors are applied.

The preliminary datasets ROSA 1.0, ROSA 2.0 and ROSA 3.0 were exported to ArcMap in the form of tables containing the coordinates of the objects, as well as the accompanying attribute information. Next, the tables were converted into shapefiles of point objects using standard ArcGIS tools and added to the map as layers (Fig. 2). One of the base maps provided by ArcGIS, developed by National Geographic together with ESRI [16], was used as a substrate. The map contains information about administrative boundaries, cities, roads, superimposed on the relief and images of land cover. The global scale of the map is 1:144000. Also one

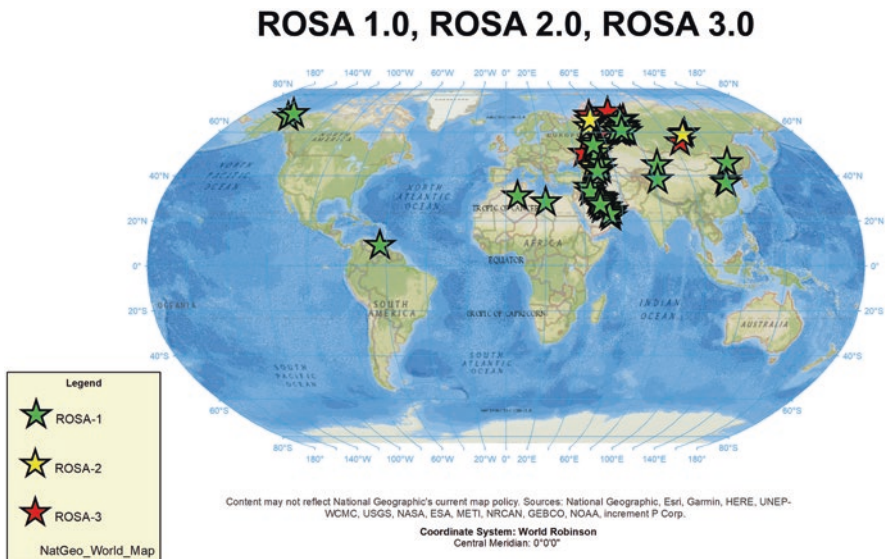


Fig. 2 ROSA database visualization in ArcGIS

of the main maps used as a base substrate is the World Imagery map, which represents satellite and aerial photographs with a resolution of 1 m or more in different parts of the world, as well as lower resolution satellite images for the whole world.

As mentioned above, for the analysis of the ROSA data, both the standard ArcGIS geoprocessing tools and the tools created by the authors were used. The first group of tools includes the following modules:

- 3D Analyst and Spatial Analyst, which contain sets of geoprocessing tools that allow to perform various operations for analyzing, managing and transforming data of surface models and three-dimensional vector data (Fig. 3);
- Spatial statistics, which enables the analysis of the spatial distribution, structures, processes and relationships.

For the exploration of the fields, the authors used geoprocessing tools included in the Cluster Analysis Toolbox, created in the Geophysical Center of the Russian Academy of Sciences. This set is designed to solve clustering problems and extract dense objects in the field of geospatial information analysis, in particular, in earth sciences, using the methods of discrete mathematical analysis (DMA) [11]. The “Clustering.tbx” script toolkit includes four DMA-based clustering algorithms: “Monolith”, “Roden-2”, “DPS” and “Modified DPS”, each of which represents script tool [18, 24].

In addition to studying geospatial data contained in the ROSA database, was also analyzed various thematic maps of the territory of Russia and the world. The following materials can be distinguished: Geological map of Russia 1:2500000 (VSEGEI) [7], Predictive-mineragenic map of Russia 1:2500000 (VSEGEI) [20], Mineragenic map of the Russian Federation and neighboring states 1:2500000 (Aerogeology) [13], Hydrocarbon resource map [12], CGMW [3] Bedrock and Structural geology (Fig. 4).

Creation of the web service for the further visualization of the database objects and its attributive field in the ArcGIS environment became the next step in the course of the project implementation. The database “Dynamics of the oil and gas industry development in the 20 century – the largest deposits of the world” (ROSA 1.0) is available online without installing specialized software. The user can select the base substrate for the data, change the design of the layer (for example, change the color and size of field symbols), view the attribute table for each layer or the attribute information of individual elements, display the elements that satisfy the specified users’ filters. The functions of measuring the area of the selected region, the distance between two points and determining the coordinates of the object are also available. If a user has an ArcGIS Online account, he can not only view the specified database, but also add additional data to the map from the Internet or from his PC (Fig. 5).

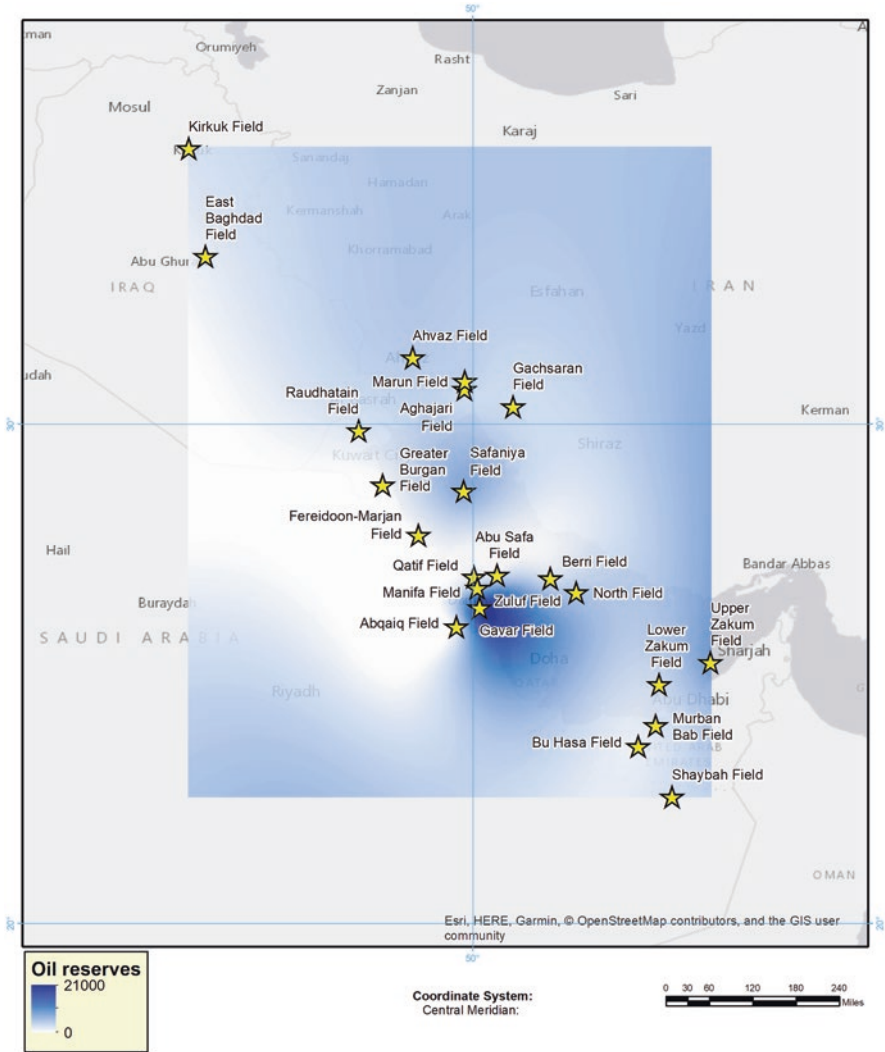


Fig. 3 Result of the implementation of Spline with Barriers tool naker 3D Analyst and Spatial Analyst for analysis of the distribution of oil resources in the Near and Middle East

2 Geology

One of the possible directions in further conduction analytical study based on the ROSA GIS Project is the overview of accumulations of the largest oil and gas deposits of the world with a view to examining geological history and identifying meaningful patterns.

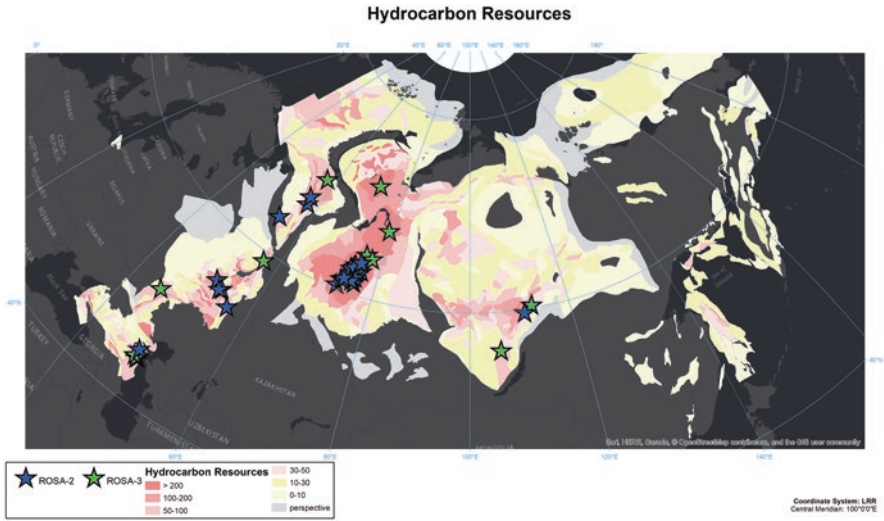


Fig. 4 ROSA 2.0 and ROSA 3.0 visualization on the hydrocarbon resource allocation map in ArcGIS. World Dark Grey Canvas Base is used as a base map

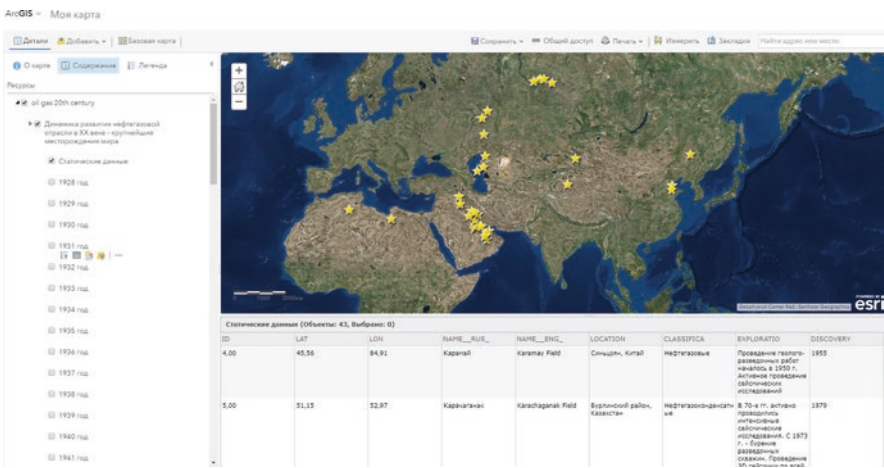


Fig. 5 Online visualization of the ROSA database using web service ArcGIS

Largest oil and gas fields are fairly widespread throughout the world, but their distribution across the countries is extremely uneven. The greatest concentration of deposits is in the countries of the Near and Middle East (Burgan, Safaniyah, Abqaiq, Ghawar, Gachsaran, etc.) as well as on the territory of Western Siberia of the Russian Federation (Samotlor, Priobskoye, Lyantorskoe, Fyodorovskoye, etc.).

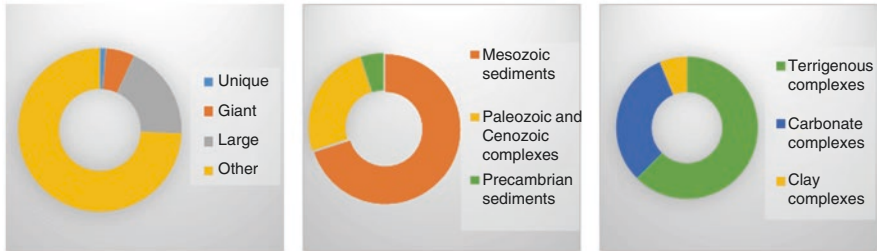


Fig. 6 (a) Ranking of the world's oil and gas provinces by known petroleum reserves. (b) Age of the reservoir rocks of the world's known petroleum reserves. (c) Types of reservoir rocks of the world's known petroleum reserves

There are about 160 oil provinces in the world, two of which belong to the category of unique, 9 – giant and about 30 – large. The unique are the pools of the Persian Gulf for oil and Western Siberia for gas [26] (Fig. 6a).

The giant provinces are Golf Coast, Mexican, Perm, Western Inner, North Sea-German, Sahara, Maracaib, West African, Volga-Ural. Their area is 300,000 – 2,000,000 km², sedimentary cover volume of 400,000 – 2,000,000 km³. They are confined mainly to platforms contain 25% of the largest and gigantic oil and gas fields of the whole world.

Large provinces have an area of 30–560,000 km², sedimentary cover volume – 100,000–1,500,000 km³, contain 15% of the largest deposits in the world. Giant deposits in their limits are absent [26].

Small provinces are located within the intermontane depressions, epiplatform orogens, small intraplant depressions, aulacogens, and grabens. Their areas are insignificant (5–200,000 km²), the volume of the sedimentary cover is relatively small (70–450,000 km³). In this group less than 10% of the largest deposits were found.

More than half of the initial hydrocarbon resources are located in the territories of young and ancient platforms (about 1/3), where they are associated with development areas, and not with dissociated or poorly dislocated sedimentary cover of increased (more than 1,0–1,5 km) thickness.

Hydrocarbon deposits are established in sediments from the Riphean to the Pliocene. Most (approximately 60–70%) of the initial total resources are confined to the Mesozoic sediments, Paleozoic and Cenozoic complexes have a smaller contribution, the share of Precambrian sediments is limited (Fig. 6b).

In each oil and gas basin, most of the resources are usually localized in relatively narrow mature intervals of the geological section. The majority of the resources (about 60%) are associated with terrigenous complexes, about a third with carbonate complexes, a small proportion with siliceous – clay complexes [26] (Fig. 6c).

Among the established traps in most regions the anticlinal traps are of primary importance. In a number of regions reefing, stratigraphic, and lithological, as well as salt dome tectonics, play an important role. Sub-thrust distribution of sedimentary complexes in the frame of the platforms are viewed as promising zones.

As mentioned above, after represented of the ROSA database objects on maps in ArcGIS system, two distinct clusters were formed. As we can trace, accumulations of hydrocarbons entry to the territory of the West Siberian and the Persian Gulf. These two provinces occupy a special position on the global map. West Siberian and the Persian Gulf provinces allocated in terms of area and the volume of the sedimentary cover and control most of the world's proven reserves of oil and gas. The West Siberian and Persian Gulf provinces characterized not only by the anomalously high hydrocarbon potential, but also by the significantly giant hydrocarbon deposits discovered in them, which ensure their uniqueness [23].

Comparative study of unique oil and gas provinces presented as a methodology used for a complex analytical review. Thus, for example, it allows to draft an assessment of the interaction important events in geological time – paleogeography conditions, evolution of flora and fauna, etc. It gives an opportunity to comprehensively approach the issue of investigating the character of territory development and highlight the main events of both the regional and global scales. Besides scientific research this way may be useful for carrying out various applications in order to assess the prospects of the territory.

Let us consider in more detail the geological history of the development of the two largest oil and gas provinces – the West Siberian and the Persian Gulf (Fig. 7).

West Siberian oil and gas province (area – approximately 2,000,000 km²) is one of the largest oil and gas provinces in the world, occupying most of the young epigercin plate and continuing within the Kara Sea shelf.

The West Siberian Plate began to develop in the Mesozoic era, in the Upper Jurassic period. At this time, the territory between the Urals and the Siberian platform descended, resulting in a huge sedimentary basin. Sea transgressions captured the West Siberian Plate more than once during its development. In the Lower Oligocene, the Plate was freed from the sea and turned into a huge lake-alluvial plain. Next uplift of the northern part of the plate occurs in the Late Oligocene and Neogene, and in the Quaternary period of the Cenozoic era the Plate descends again. The development of the Plate occurs in a way that resembles the process of oceanization and the development of bogs [26].

The foundation is heterogeneous: in the West it is Hercynian, in the north, in the center and east mostly Baikal, in some places more ancient, in the south – Salair, Caledonian, Hercynian in the south. It lies at depths of 2–3 to 5–10 km and more, and regionally plunges in the northern and northeastern directions. At the base of the sedimentary cover is a system of grabens consisting of T-J₁ sediments. Two complexes are distinguished: PZ-T with a capacity of up to 5 km, and J-N with a capacity of 7–8 km. Oil and gas bearing deposits are Paleozoic, Lower, Middle and Upper Jurassic, Lower and Upper Cretaceous. The entire geological section is characterized by a sharp predominance of terrigenous sandy-argillaceous sediments.

The regional cap rocks: Bazhenov clay Formation (J₃-K₁) and clay layers in the Cretaceous section. The oil-and-gas source rocks are considered to be siliceous-argillaceous rocks of the Bazhenov Formation (C_{organic} up to 10–12% or more), as well as a section of the lower Cretaceous [26].

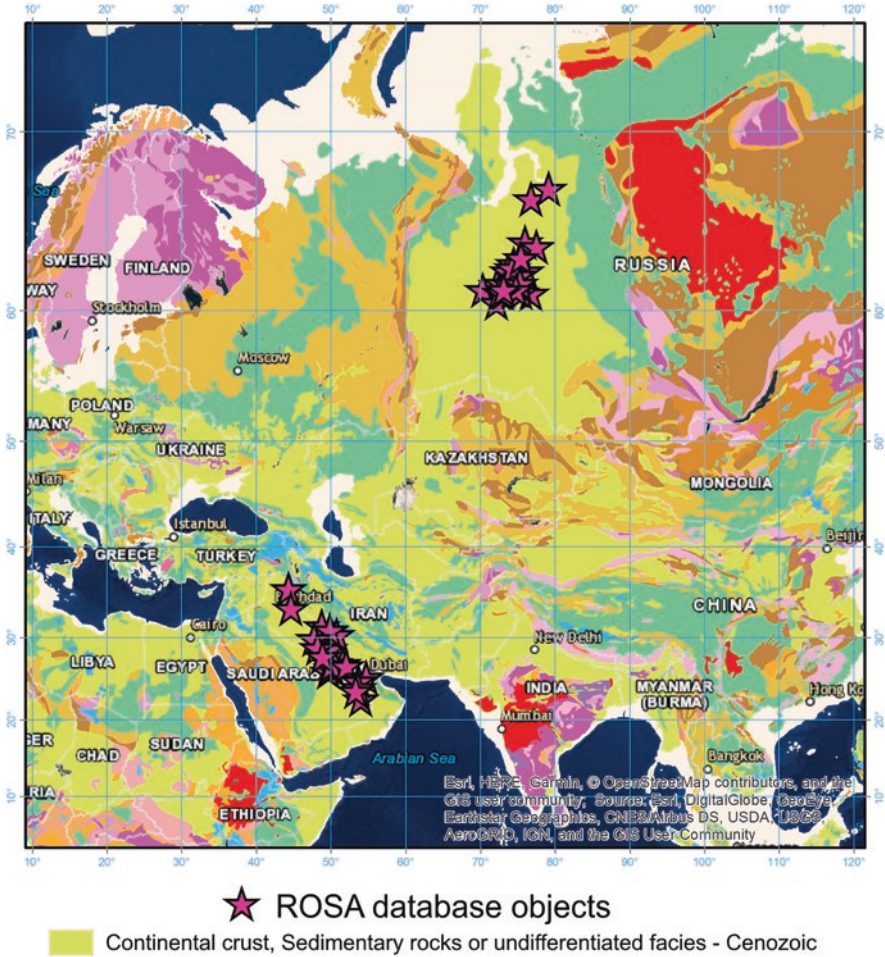


Fig. 7 Online visualization of the ROSA database using web service ArcGIS. The greatest concentration of deposits in the territory of the two largest oil and gas provinces – the West Siberian and the Persian Gulf

Anticlinal and lithological predominate among the traps. The main resources are enclosed in sediments of neocom and senoman; some of them are connected with other divisions of the Jurassic and Cretaceous. The province is characterized by unique reserves of resources and moderately average (middle) density. The deposits are concentrated in the fields, which are located to the central part of the West Siberian Plain and the south of the Kara Sea, not approaching the margins of oil and gas provinces closer than 150 km [26].

A number of giant oil (Samotlor, Priobskoye, etc.), gas and gas condensate (Yamburg, Urengoi, Fyodorovskoye, etc.) fields were discovered. Further prospects of the province are very high. Additional perspectives are associated with the devel-

opment of deep objects (Triassic and Paleozoic), and the Gydano-Yenisei Epibaikal basin.

The oil and gas **province of the Persian Gulf** is confined to a large asymmetric heterogeneous depression formed in the process of long-term sagging in the area of the junction of the African-Arabian platform with the Alpine-Himalayan mountain-folded belt.

The principal tectonic elements are the Arabian Plate and the Mesopotamia Foredeep, forming the platform and folded sides of the basin. The foundation is Archean-Proterozoic. The sedimentary cover is represented by sediments from the Vendian to Quaternary age with a maximum capacity of 10–12 km in the most arched part of the basin and a minimum of 2–2,5 km along its periphery (the areas adjacent to the Arabian-Nubian Shield) [26].

The Paleozoic section is mainly sandy-argillaceous. The Permian, Mesozoic, Paleogene, and Lower Miocene sediments are represented mainly by carbonate rocks. In the composition of Neogene-Quaternary sediments, terrigenous differences predominate, among which the salt-bearing strata of the Middle Miocene with a thickness of up to 1 km is distinguished. The main oil and gas complexes are Permian, Upper Jurassic, Lower Cretaceous, Upper Cretaceous and Oligocene-Lower Miocene. 3/4 of the proven oil reserves account for Mesozoic deposits, the main gas reserves are concentrated in the Permian and Cenozoic deposits [26].

Most of the oil and gas fields are concentrated on the eastern plunging of the Arabian Plate (Basra-Kuwaiti Depression, Gaza structural terrace, Rub-el-Kali Depression) and in the Mesopotamian Trough. In the Mesopotamian Trough, the accumulations of hydrocarbons are confined mainly to the Oligocene-Lower Miocene (Asmari Formation) and Upper Cretaceous (Bangestan Formation) limestones at a depth of 0,2–2,7 km. On the Arabian plate oil-bearing sands and sandstones of the lower Cretaceous (Zubair and Burgan Formations) and limestones of the Upper Jurassic (Arabic Formation) are at a depth of 1,3–3,2 km, Permian-age carbonate rocks are gas-bearing (Houf Formation) at a depth of 3–4,5 km [10, 26].

The main proven hydrocarbon reserves in the basin are concentrated in the depth interval of 1–3 km. The interval of 2–3 km contains a maximum of oil and gas reserves. At a depth of 3–5 km – the maximum gas reserves. The deposits of the structural type are mostly multi-layer. In the Mesopotamian Trough, the deposits are confined to large high-amplitude anticlinal folds stretched along the Zagros Folded System from northwest to southeast; on the Arabian Plate, they are mostly associated with local structures that complicate the lengthy forked uplifts of the submeridional strike. South of the latitude of the city of Basra, a significant part of the oil and gas deposits is confined to the structures of salt diapirism. The density of oil is 820–990 kg/m³, the average density of oil is 855–860 kg/m³, sulfur and high-sulfur (S 1–5%).

In this way, common features of these basins are large areas and volumes of sedimentary cover and their confined to platforms. Oil source rock are of MZ (Cretaceous) age. Both **West Siberian** and **Persian Gulf** contain about 50% of the largest and gigantic deposits of the world.

3 Conclusions

The way we store, set and manage the data is far more than only a tool for further investigations. For the last decades due to extremely growth of datasets it is formed as the separate scientific field – Data Science. This paper presents the authors methodology applied to oil and gas database and its development in twentieth century.

Further to this, the obtained results and applied mathematical tools allowed to reflect substantive regularities in combination with paleogeographic, geological and other data.

Thus, we have a full set of data development from its verification, validation and compilation to progressive analysis based on systems analysis. The presented methods are universal and could be applied in various dimensions and science studies.

Acknowledgments This work was conducted in the framework of budgetary funding of the Geophysical Center of RAS, adopted by the Ministry of Science and Higher Education of the Russian Federation.

This work employed facilities and data provided by the Shared Research Facility “Analytical Geomagnetic Data Center” of the Geophysical Center of RAS (<http://ckp.gcras.ru>).

References

1. ArcGIS 9. Russian Translation by DATA+. 2004. 124 p
2. BP Statistical Review of World Energy (2015). URL: <http://www.bp.com/content/dam/bp/pdf/energy-economics/statistical-review-2015/bp-statistical-review-of-world-energy-2015-full-report.pdf>
3. CGMW Bedrock and Structural geology. URL: <https://www.arcgis.com/home/item.html?id=b4e65a7f761940a08b41da71f0427ceb>. Accessed 11 Apr 2019
4. Cumo C (2014) Ghawar field (Saudi Arabia). In: Oil: a cultural and geographic encyclopedia of black gold, vol 1. ABC-Clio, Santa Barbara, pp 105–107
5. Facey W (1994) The story of the eastern province of Saudi Arabia. Stacey International, London, p 160
6. Fattah K, El-Katatney S, Dahab A (2011) Potential implementation of underbalanced drilling technique in Egyptian oil fields. J King Saud Univ – Eng Sci 23(1):49–66
7. Geological map of Russia and adjacent waters 1:2500000. <http://www.vsegei.ru/ru/info/gk-2500>. Accessed 10 Apr 2019
8. Geologiya nefi (Oil Geology) (1968) T. 2, kn. 2. Neftnyanye mestorozhdeniya zarubezhnyh stran (Oil fields of foreign countries)/Redaktsiya I.V. Vysotskogo. Nedra, Moscow, pp 804
9. Golf-Rakht T (1986) Fundamentals of oilfield geology and the development of fractured reservoirs. Nedra, Moscow, p 608
10. Guoyu L (2011) World atlas of oil and gas basins. Wiley, Hoboken, p 496
11. Gvishiani AD, Agayan SM, Bogoutdinov SR, Soloviev AA (2010) Diskretnyy matematicheskiy analiz i geologo-geofizicheskiye prilozheniya (Discrete mathematical analysis and geological and geophysical applications). Vestnik KRAUNZ Earth Sci 2(16):109–125
12. Hydrocarbon resource map. URL: <http://geology-gis.gcras.ru>. Accessed 11 Apr 2019
13. Mineragenic map of the Russian Federation and neighboring states 1:2500000. URL: <http://geology-gis.gcras.ru>. Accessed 11 Apr 2019
14. Mir nefi (World oil). URL: <http://www.mirnefti.ru/index.php?id=255>. Accessed 15 Jun 2017

15. Nahai L, Kimbell C (1963) The petroleum industry of Iran. U.S. Department of the Interior, Bureau of Mines, Washington, DC, p 112
16. National Geographic World Map. URL: <https://www.arcgis.com/home/item.html?id=b9b1b422198944fbbd5250b3241691b6>. Accessed 11 Apr 2019
17. Nehring R (1978) Giant oil fields and world oil resources [Report], Rand Corporation; R-2284-CIA. Rand, Santa-Monica
18. Nikolov BP, Zharkikh JI, Soloviev AA, Krasnoperov RI, Agayan SM (2015) Integration of data mining methods for earth science data analysis in GIS environment. *Russ J Earth Sci* 15(4):ES4004. <https://doi.org/10.2205/2015ES000559>
19. Odintsova A, Gvishiani A, Nakicenovic N, Rybkina A, Busch S, Nikolova J (2018) The world's largest oil and gas hydrocarbon deposits: ROSA database and GIS project development. *Russ J Earth Sci* 18:ES3002. <https://doi.org/10.2205/2018ES000621>
20. Predictive-mineragenic map of Russia and its continental shelf 1:2500000. URL: <http://www.vsegei.com/ru/info/atlas/prog-min>. Accessed 10 Apr 2019
21. Roberts FS (2016) What is Big Data and how has it changed? Book of Abstracts of the International Conference "Data intensive system analysis for geohazard studies", Sochi region, Mountain cluster, Russia, 18–21 July 2016, Edited by E. Kedrov, p. BS4002, GC RAS, Moscow
22. Rybkina AI, Odintsova AA, Gvishiani AD, Samokhina OO, Astapenkova AA (2016) Development of geospatial database on hydrocarbon extraction methods in the 20th century for large and super large oil and gas deposits in Russia and other countries. *Russ J Earth Sci* 16(6):ES6002. <https://doi.org/10.2005/2016ES000584>
23. Skorobogatov VA, Soloviev NN (2013) Sravnitelnyi analiz uslovii osadkonakopleniya v Zapadno-Sibirskom i Arabo-Persidskom megabasseinah (Comparative analysis of oil and gas accumulation conditions in West Siberian and Arab-Persian megabasins). *Vesti gazovoy nauki* № 5(16):43–52
24. Soloviev AA, Zharkikh JI, Krasnoperov RI, Nikolov BP, Agayan SM (2016) GIS-oriented solutions for advanced clustering analysis of geoscience data using ArcGIS platform. *Russ J Earth Sci* 16(6):ES6004. <https://doi.org/10.2205/2016ES000587>
25. Simmons MR (2006) *Twilight in the desert: the coming Saudi oil shock and the world economy*. Wiley, p. 464. ISBN: 978-0-471-79018-1
26. Vysotskiy IV, Vysotskiy VI, Olenin VB (1990) *Neftegazonosnye basseiny zarubezhnyh stran (Oil and gas basins of foreign countries)*. Nedra, Moscow, p 405

Lithosphere of the West Transbaikalian Sector of the Central Asian Fold Belt According to Electromagnetic Studies



Elena Pospeeva, Albert Duchkov, Vladimir Potapov, and Ludmila Sokolova

1 Introduction

Magnetotelluric soundings (MTS) performed along the Selenga River delta – Krasny Chikoy Village are a part of integrated geological – geophysical studies on the zone-block structure of the Earth crust in the South of the Eastern Siberia. MT sounding is one of the leading methods for obtaining information about the deep structure of the Earth. Currently, MT sounding is widely used in many regions of the world to solve a variety of problems – from territories minerogenic zoning to study the geodynamic condition of the lithosphere. The analysis of the first MTS works showed that the geoelectric characteristic of the Earth deep section is significantly different from the original apriori representations. Within the Earth crust and the upper mantle there is a differentiation of electrical properties and two layers of increased electrical conductivity. The lower one, located in the upper mantle, has a resistance in the first units of Ohm-m and usually coincides with the mantle waveguide – asthenosphere. Its formation is explained by the same reasons as the decrease in speed – the presence in this part of the upper mantle of partial melts in the amount of 1–5% [18, 43, 74]. According to the results of the “ELAS” program [91], mantle conductive layer is evident on the curves of deep MTS in all parts of the world. At the same time, the depth of its occurrence and the degree of severity vary markedly from region to region. The upper conductive layer, located in the section of the middle-lower Earth crust, was established due to its relatively shallow occurrence (15–37 km) and a significant increase in electrical conductivity. According to laboratory studies, the electrical resistivity of “dry” rocks typical of the consolidated crust decreases with a temperature from 10^7 to 10^{10} Ohm-m at

E. Pospeeva (✉) · A. Duchkov · V. Potapov · L. Sokolova
IPGG RAS, Novosibirsk, Russia
e-mail: pospeevaev@ipgg.sbras.ru

© The Author(s), under exclusive license to Springer Nature
Switzerland AG 2021

V. Svalova (ed.), *Heat-Mass Transfer and Geodynamics of the Lithosphere*,
Innovation and Discovery in Russian Science and Engineering,
https://doi.org/10.1007/978-3-030-63571-8_20

351

200 °C to 103–105 Ohm·m at 600 °C [62]. The nature of conductivity, the conditions and the mechanism of the crustal conductive layer formation are examined in detail in numerous literary sources, and it is currently not regarded as a geophysical anomaly, but as the inner element of the Earth hydrosphere [17, 36, 55, 64, 107–111]. The roof and the base of the top conductive layer in the different age structures are located at depths of corresponding to isotherms of 350–400 °C and 750–800 °C. The temperature range of 300–750 °C and the pressure range of 2.5–6 kbar cover the Earth crust granitometamorphic layer rocks from green shale to amphibolite facies inclusive. As the P-T parameters increase in a series of solid-phase metamorphic reactions, a gradual dehydration of rocks occurs with the release of the most part of the bound water and the formation of metamorphogenic solutions and supercritical fluids separated by a water critical point (374 °C) [36, 64]. A special role in the Earth crust conductive layer formation is given to the intergranular fluid phase [12, 36, 73]. The source of water generation is also the reduced mantle fluids oxidation processes [44, 51, 57, 63]. In most cases, in the same range of depths, deep seismic studies show zones of stratified lower crust and zones of increased absorption of seismic waves [36, 40, 86]. Absorption of elastic waves is associated with the presence of fluid in cracks and pores and its reaction during the passage of elastic waves in the medium [37, 38, 56].

A good correlation between the conductive layer roof depth and the heat flow value is established. Heat flow is one of the subsoil geodynamic (tectonomagmatic) activity indicators and carries important information about deep temperature regime, phase state, thermal inhomogeneities, thermodynamic conditions in the lithosphere, which largely determine its stress-strain condition and the intensity of tectonic and seismic processes. In tectonically stable regions with normal values of heat flow, the conducting layer roof is at greater depths (35–40 km) than in tectonically active structures (16–20 km) [1, 11, 33, 42, 54, 69]. The presence of conducting geoelectric inhomogeneities in the consolidated crust context, associated with the crushing zones of the latest faults or inhomogeneities of a large vertical length with high resistivity values, significantly complicates, and often makes it impossible to obtain information about the position of the crust conductive layer. In this case, geothermal studies are particularly important to assess the position of the conducting layer in the lithosphere. The results of magnetotelluric studies conducted in recent decades in large tectonic provinces, both in our country and abroad, revealed the relationship between the processes occurring in the earthquake zones and the parameters of the crust conductive layer. It is shown that the earthquake foci are localized mainly over the conducting layer or in its upper parts, in places where differences in the roof layer depths and an increase in its total electrical conductivity are noted.

MTS is also effective method in the isolation of fluid-saturated areas and zones of active faults in the Earth crust. The presence of deep faults is one of the characteristic features of the lithosphere, which during its active existence serve as fluid conductors. They form conducting channels that, crossing the high-resistance lithosphere, provide vertical redistribution of excess currents and are fixed in the magnetotelluric field in the form of conducting geoelectric inhomogeneities ($\rho < 5$ Ohm·m) with vertical and inclined lateral boundaries [11, 22, 50, 58, 76].

The aim of the present research was to study the deep electrical conductivity distribution features, reflecting the patterns of development and tectonic regime of the Western Transbaikalia on the profile of the Selenga river delta – Krasnyi Chikoi Village. This included the following tasks:

- determination of the Earth crust geoelectric structure main features of the Baikal (South-Eastern flank) and West Transbaikalia rift zones, and their relationship with the tectonic processes intensity;
- carrying out zoning of the study area by type of geoelectric cross section, paying particular attention to the study of key areas of transition territories from mountain ridges to the intermontane depressions;
- identification of disturbed crust areas associated with fault systems, active at the present stage of tectogenesis.

2 Geological Setting

The study area is located in the Western Transbaikalia segment of the Central Asian fold belt, whose structure formed as a result of Early Paleozoic accretion-collision events accompanied by the closure of the Paleo-Asian Ocean [19]. A consequence of these processes was the accretion of geodynamically different terranes (microcontinents, intraoceanic systems, and island arc systems to the marginal parts of the Siberian craton) [6, 14, 60, 61, 88, 112] and formation of collision belts along its margins [20, 27].

In the Late Paleozoic and Mesozoic, Western Transbaikalia was a region of within-plate magmatism resulting in the formation of large igneous provinces with batholith cores in the center (the Angara-Vitim and Hentiyn-Daurian) and rift zones on the periphery [39, 94, 101]. Batholiths are composed of granitoids varying widely in composition – from tonalities and plagiogranites to granosyenites and rare-metal granites dominated by normal granites [102]. Most of the granitoids of Western Transbaikalia of different types and different ages belong to the Angara-Vitim batholith, whose diversity of rocks reduces to two complex – Barguzin and Zaza [31, 45, 106]. The formation of granitoids of the Barguzin complex took place in two stages: quartz monzonites, monzo-syenites, and quartz syenites, and the rocks of the late (main) stage represent the rocks of the early stage by normal granites, which, according to [31, 46], are interspersed with allochthonous (predominant fraction) and autochthonous varieties. Both granite varieties correspond to different levels of batholith formation, separated by a depth interval of many kilometers and corresponding to the magma formation level (autochthonous granitoids) and the levels of intrusion of displaced (allochthonous) melts [45]. The time of formation of the Angara-Vitim batholith rocks was interpreted quite widely – from the Late Precambrian to the Late Paleozoic. Recently, clear evidence for the Late Paleozoic (Late Carboniferous – Early Permian) age of the batholith has been provided, and

many types of granitites identified as complexes of different ages were formed in interval of 340–270 million years [46, 47, 89, 99, 96, 102].

Granitoids of the Hentiyn-Daurian batholith (Fig. 1), varying widely in composition – from granodiorites to leucogranites, are widespread in the southeastern part of the study area. Granodiorites and leucocratic biotite granites dominate [84]. Gabbro and diorites are present in subordinate amounts, composing separate bodies corresponding to early phases of intrusion or forming unevenly distributed segregation in main-phase granodiorites corresponding to synplutonic intrusions of mafic magmas [98]. Small dike-like and boss-like bodies of leucogranites, including rare-metal lithium-fluoride, are the most recent in the batholith structure. The age of the Hentiyn-Daurian batholith, according to [98] is 230–195 Ma (Late Triassic–Early Jurassic).

The formation of batholiths is associated with the overlap of the North Asian continent with a number of hot spots of the Paleo-Asian ocean mantle and subsequent interaction between mantle plums and the lithosphere in the active continental margin setting [95, 98]. Mantle plumes initiated within-plate activity and contributed to the occurrence of rift splits and the formation of alkaline basic and alkaline

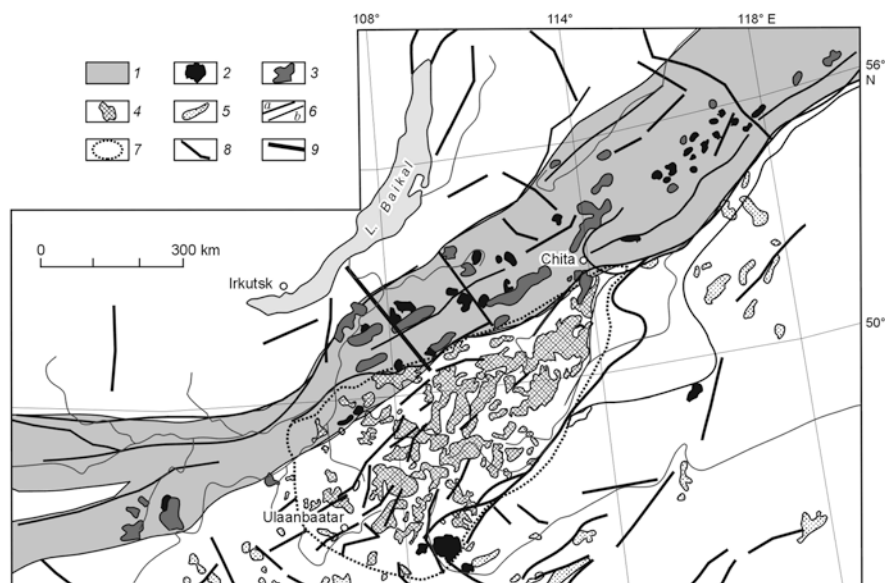


Fig. 1 Schematic of the position of the Northern Mongolia–Western Transbaikalia rift zone in the structure of the Early Mesozoic igneous area with the Hentiyn–Daurian batholith core in the center and rift zones on its periphery (Vorontsov A.A., Yarmolyuk V.V.) [94]. 1, Northern Mongolia–Western Transbaikalia rift zone; 2, alkaline granitoid massifs; 3, bimodal trachybasalt-comendite and trachybasalt magmatic associations; 4, 5, rocks of the zonal igneous area: 4, granitoids of the Hentiyn–Daurian batholith; 5, rift volcanic associations of the framing of the Hentiyn–Daurian batholith; 6, belt of major faults classified as a suture (a) and the boundaries of the Northern Mongolia–Western Transbaikalia rift zone (b); 7, boundaries of the Hentiyn–Daurian batholith; 8, faults; 9, MT profile

salic associations. The rifting zones located at the batholith margin are identified by zones of grabens and basins and their separating uplifts and horsts. The magmatism of these zones is determined by bimodal basalt-trachyte comendite (pantellirite) or substantially basalt (alkaline basaltoid) volcanic associations; intrusive rocks are dominated by alkaline syenites and granites, granosyenites, and leucogranites [94, 98].

One of the structures where Early Mesozoic within-plate magmatism was most intense is the Western Transbaikalia segment of the Northern Mongolia-Western Transbaikalia (NMWT) rift zone situated on the northern flank of the Hentiyn-Daurian regional igneous province. The Western Transbaikalia segment, within which a large part of the MT profile is located, extends from the confluence of the Selenga and Dzhida Rivers through the basin of the Uda, Tunga, and Khilok Rivers to the upper reaches of the Vitim River and has a length of over 800 km. Large volcanoplutonic structures up to 2000 km² in area formed within this zone in the Early Mesozoic. They consist of volcanic fields, trachybasalt and alkaline bimodal associations, alkaline granite and syenites massifs, and extend dyke fields associated with systems of longitudinal faults, grabens, and horsts [39, 94, 100]. The bimodal strata are composed of trachybasalt, comendite-pantellirite, trachyrhyolite-trachydacite, and trachyte of the volcanic Tsagan-Khurtei Formation [81, 93].

The further development of magmatism in the Mesozoic occurred almost continuously within both pre-existing and nearly formed grabens until the beginning of the Late Cretaceous, when the scale of volcanism decreased significantly [97]. Various, mostly highly alkaline, magmatic associations formed in these areas (grabens) at different stages of their development. A common feature of the magmatic associations of all stages is the absolute predominance of mafic rocks [95].

3 Estimation of the Thermal Regime of the Earth Crust

The thermal regime of the Earth crust is one of the main factors controlling the distribution of electrical conductivity in it and in particular the location of the crust conductive layer. The most reliable information about the temperature (T) of the Earth crust is given by the geothermal method based on the solution, in most cases, of the stationary heat equation for the Earth crust certain physical model and the measured value of the heat flow [85]. The model includes the Earth crust structure data, the change in the radiogenic heat generation intensity depth and thermal conductivity of rocks.

In the process of geothermal studies in southern Siberia (Altai-Sayan and Baikal folded zones), the depth temperature estimates for several tens of points were performed [85]. The results of calculations were analyzed to determine the effect of model parameters variations on the temperature values. It was found that the influence of the heat flow (HF) is always of the essence, and for temperatures less 900 °C it is crucial. In this case, for a fixed depth, there is a clear linear relationship between T and HF:

$$T = A HF + T_0 \left(T, T_0 = [^{\circ}C], HF = [mW / sq.m], A = [^{\circ}C sq.m / mW] \right).$$

In work [85, p. 149.] such dependences for depths of 5, 10, 20, 30, 40 and 50 km which have made the pallet allowing to estimate the folded areas crust temperature of southern Siberia on values of the measured heat flow are specified. This pallet is used in this work to estimate the T distribution at depths of 20 and 40 km along the analyzed MTS profile. T values were calculated using the following regression equations:

- (for a depth of 20 km) $T = 7,64 HF - 42$;
- (for a depth of 40 km) $T = 15,61 HF - 223$.

The T determination inaccuracy by these equations is 30–50 °C. It should be noted that similar pallets connecting HF and T values are constructed from other sets of geothermal information [26, 41, 65]. They are decorated differently, but the main indicators (range of parameters, T determination inaccuracies) correspond to each other.

To assess the thermal regime of the Earth crust in the MTS area, data on the heat flow distribution in a strip 100 km wide (± 50 km from the profile axis) along the profile are collected (see Fig. 2). The works [21, 25, 35] data were used. Within the selected band, geothermal measurements were performed on 50 wells with a depth of 100–400 m, located on 26 sites. The maximum values of heat flow (60–80 mW/sq. m) were recorded in the Eastern Baikal region in the band width of 20–40 km from the Eastern Baikal lake shore. The rest of the heat flow is noticeably less, about 50–55 mW/sq. m.

Shown in Fig. 2 average heat flow values are used to estimate the temperature in the Earth crust along the profile at depths of 20 and 40 km (Figs. 3 and 4) using the dependencies between T and HF at these depths.

At 20 km depth (see Fig. 3) the maximum values of T (400–600 °C) are predicted, as expected, in the Eastern Baikal region. At the same time, in the Northern part of the profile with a length of about 50 km, the temperature does not exceed 400–500 °C. To the South-West and North-East of this part of the profile T increases significantly. To the South of the Northern section the temperature is reduced and maintained mainly at the level of 350–380 °C.

At a depth of 40 km (see Fig. 4) in the Northern part of the profile temperature decreases rapidly from North to South from 1000 °C near Baikal lake to 700 °C. In the rest of the profile, the temperature is generally maintained at $(600 \pm 50) 0$ °C.

4 Magnetotelluric Soundings

Magnetotelluric soundings were performed at periods from 0.003 to 10,000 s using equipment produced by the Phoenix Geophysics Ltd. Canadian company. Five components (E_x , E_y , H_x , H_y , H_z) of the magnetotelluric field (MT field) were measured

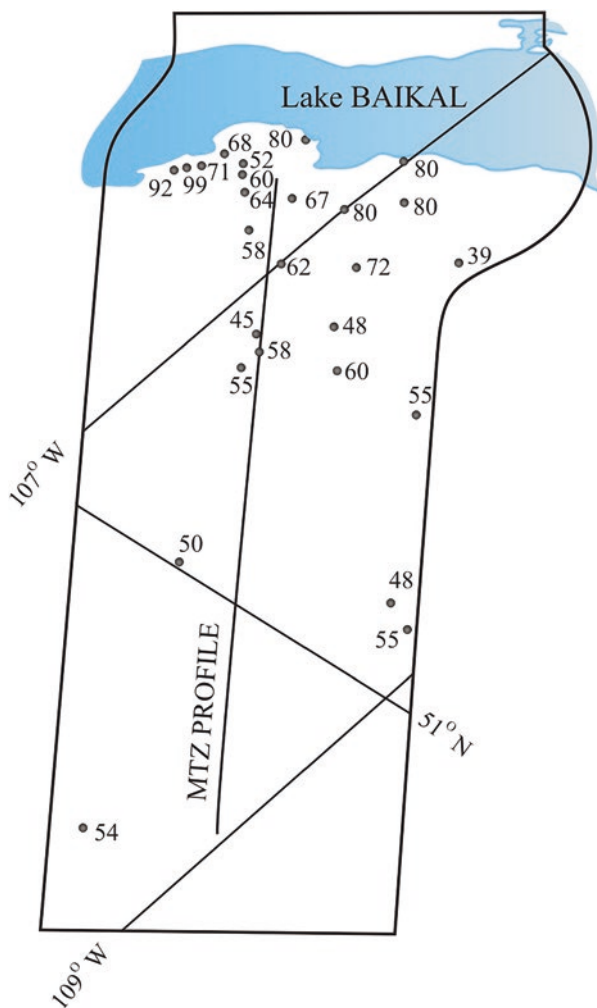


Fig. 2 Points and values of a heat flux (in mW/m^2) within a strip 100 km wide along the MTZ profile

with two MTU-5 measuring units. The observation step was 4–5 km. A cross-shaped array with an electric dipole length of 100 m was employed. Magnetotelluric field components were recorded for 19–22 h.

The field data were processed with the Phoenix Geophysics software, and 1-D and 2-D inversions of the experimental data were carried out using the WinGLink software. Qualitative and quantitative interpretations were performed according to the procedure described in detail in [22]. During qualitative interpretation, an analysis of magnetotelluric data was performed, showing that the study area is a northeast-trending regional two-dimensional structure:

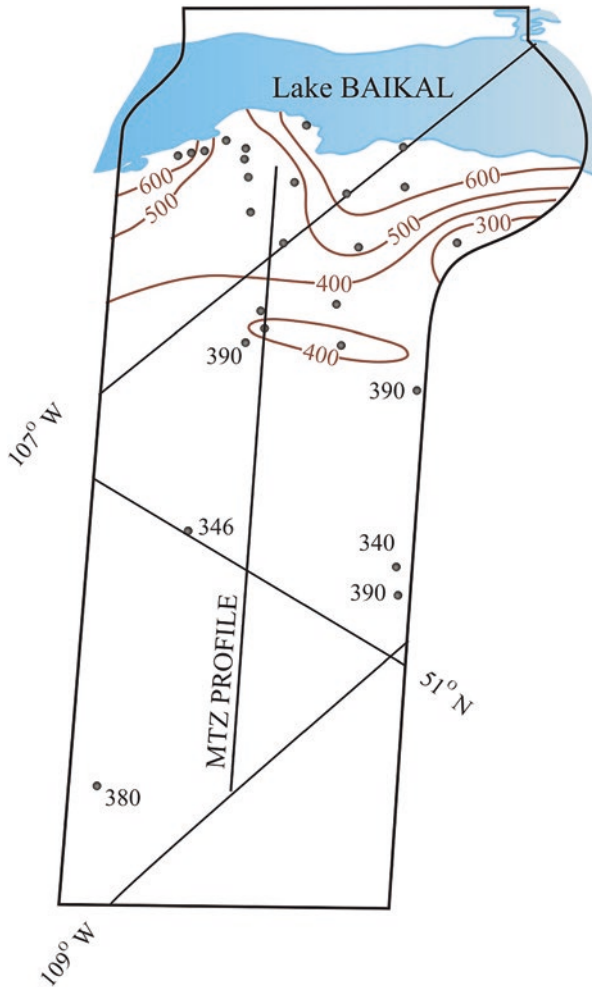


Fig. 3 Distribution of temperatures at a depth of 20 km along the MTZ profile. Points – points of assessment of T, numbers around points – values of T in °C

$$Nmt \gg \delta \rightarrow skew_s \leq \delta \rightarrow skew_B \leq \delta,$$

were Nmt is the heterogeneity parameter [9], and $skew_s$ is the skew parameter [83], and $skew_B$ is the phase-sensitive skew parameter [5]. The exception in the data set is the soundings across the Khamar-Daban Range, which is composed of a large granitoids massif and is a typical three-dimensional structure.

Deep rift faults predominantly have a northeast strike, coincident with the strike of regional structures. In places where they cross northwest- or roughly east-west-trending faults at a certain critical period, there is a rotation of the polar diagrams by 90° (Fig. 5) and in the $M = f(\sqrt{T})$ and $\theta = f(\sqrt{T})$ plots, there is a sudden change in

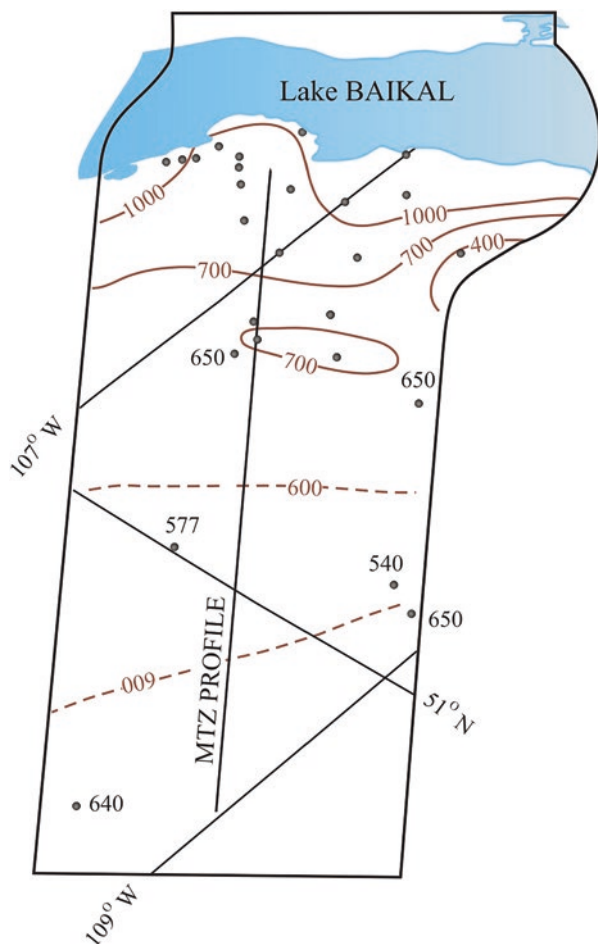


Fig. 4 Distribution of temperatures at a depth of 40 km along the MTZ profile. Points – points of assessment of T, numbers around points – values of T in °C

the values of θ by 90° and M becomes much smaller than 1. Here M is the ratio of the magnitudes of the longitudinal and transverse impedances, and θ is the angle between the positive X direction and the maximum impedance. Starting from this “critical” period, the branches of the curves are replaced (Z_{xy} by Z_{yx} , and φ_{xy} by φ_{yx}) in order that the curves of ρ_k correspond to the longitudinal and transverse directions of all the structures studied.

Another important objective of the MT studies was to identify distortions in the sounding curves associated with the horizontal heterogeneity of the section. Geologically, the study region belongs to the Barguzin igneous province – an extensive area of Late Paleozoic granitoids in Western Transbaikalia, where the electrical resistivity can reach more than 30,000 Ohm·m. Therefore, the distortions here are

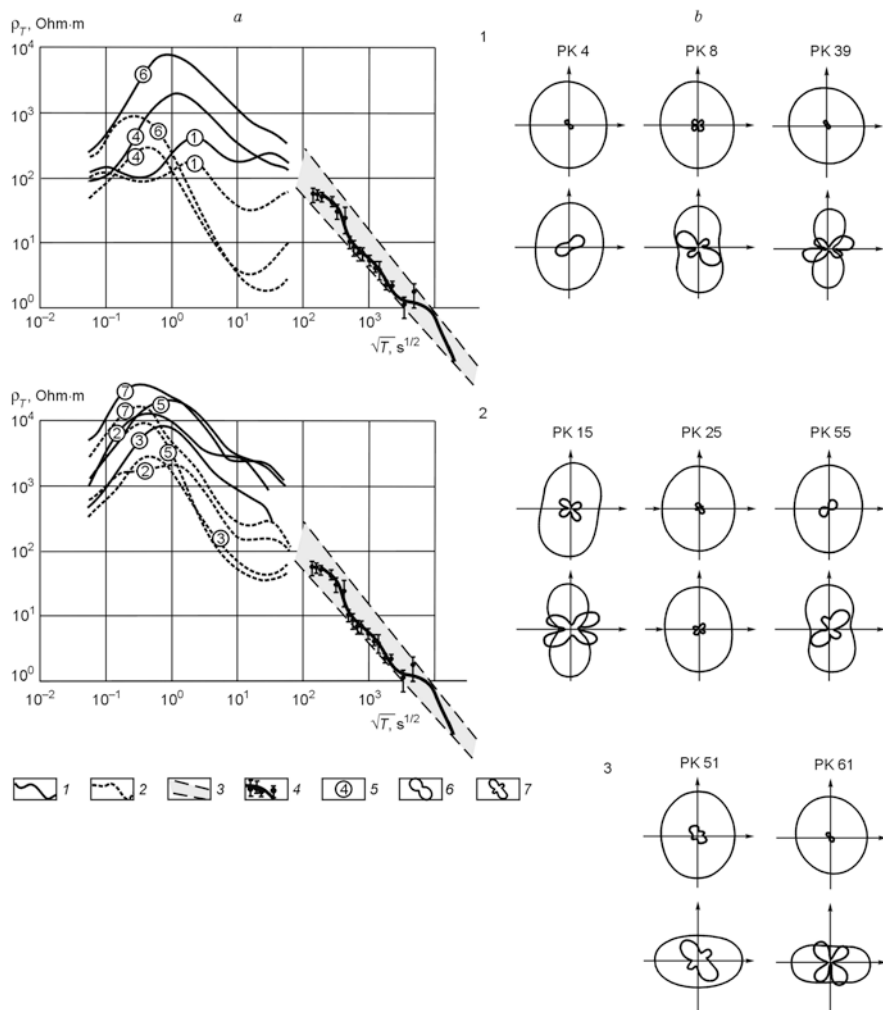


Fig. 5 (a) Semicharacteristic MT curves of the study area. (b) Typical polar diagrams of the impedance tensor: 1, within tectonic depressions; 2, within mountain ranges; 3, in fault zones. 1, transverse MT curves; 2, longitudinal MT curves; 3, GMV curve (Pospeev, 1979; Pospeev and Mikhalevskii, 1981); 4, lines bounding the region of experimental values of ρ_k ; 5, block numbers: 1, Selenga, 2, Khamar-Daban; 3, Tsagan-Daban; 4, Tugnui depression; 5, Zagan Range; 6, Khilok-Chikoi basin; 7, Malkhan Range; 6, principal polar diagrams of the impedance tensor; 7, additional polar diagrams of the impedance tensor

predominantly galvanic in nature. It is known that in the abstract two-dimensional model, only the transverse MT component experiences galvanic distortions manifested in a static shift of transverse apparent-resistivity curves [8]. However, in real geological setting, there is often a superposition quasi-dimensional structures and local three-dimensional subsurface heterogeneities, which distorts both MT

components, resulting in a static shift of both transverse and longitudinal curves. A certain reference is needed to identify the static shift and evaluate its magnitude. As such a reference we used a global magnetovariational (MV) sounding curve plotted from generalized data on global electromagnetic sounding [23]. Later, these data were revised in terms of mathematical statistics and interpretation based on the joint use of amplitude and phase MT curves [68, 70], making it possible to determine the boundaries of abrupt conductivity change in the global sounding curve. These boundaries are located at depths coincident with the phase-transition depths in the mantle inferred from geophysical and petrological data [72, 74, 104]. We evaluated our data exactly for this model of electrical conductivity distribution with depth.

Figure 5a shows the family of mean curves from different blocks of the investigation profile – rift basins (Fig. 5a, 1) and mountain ranges (Fig. 5a, 2). Within the basins, the ascending branches of transverse curves practically merge with the ascending branches of longitudinal curves, and their descending branches are shifted upward along the resistivity axis (Fig. 5a, 2). Longitudinal curves have well-defined lows, reflecting the presence of conductive zones (crustal conductive layer and conductive heterogeneities confined to fault zones) in the crust. Within the mountain ranges, a static shift of transverse curves is observed over the entire frequency range. Their descending branches are shifted relative to the MV curve by almost a decade. Because of strong galvanic screening, the sensitivity of the transverse MT component is too low to study the underlying section of the crust with low resistivity values, and information on this section can be derived only from the longitudinal MT component [8].

5 Results of the Investigations

The MT profile traverses blocks of the Western Transbaikalia segment of the Central Asian fold belt that differ in geoelectric structure, age, and the nature of underground processes (Fig. 6). The blocks correspond to northeast and roughly, east west trending granite-gneiss ranges and their separating intermontane basins.

The modern ranges of Transbaikalia are usually regarded as gentle anticlinal folds, and intermountain basins as synclinal basins. Their occurrence is associated with the Young-Cimmerian folding because Jurassic continental deposit accumulated in the already formed intermontane basins [15, 30, 32]. The correspondence of the modern topography of Western Transbaikalia to the main elements of its structure indicates a continuous restoration of disrupted tectonic forms by repeated movements of the Earth crust throughout the Neogene-Quaternary, when active uplift of mountain ranges and subsidence of intermontane basins took place [105].

The northwestern segment of the MT profile (sites 3–17) crosses the southwestern margin of the Bargusin igneous province within the boundary of the Angara-Vitim batholith and completely to the Baikal Rift Zone. The results of the study indicate the presence of two large blocks – Selenga and Khamar-Daban – in the crust of the study area (Fig. 7).

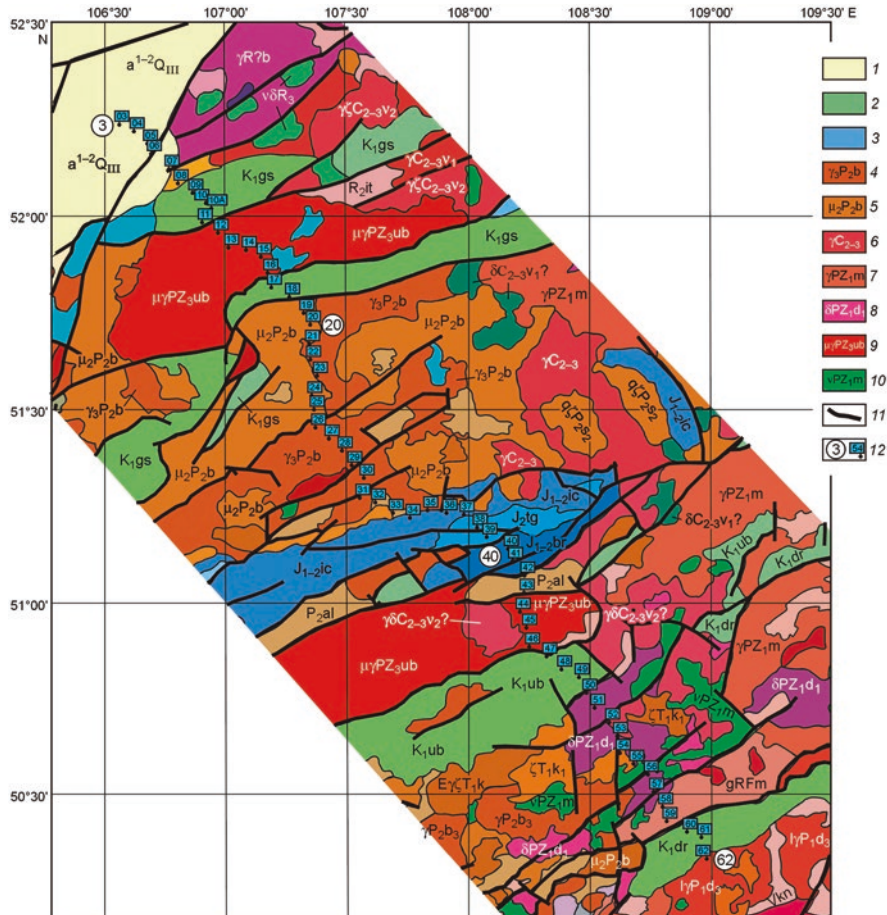


Fig. 6 Geological map of the MTS area compiled on the basis of geological maps of the Russian Federation, scale 1:1,000,000 (third generation): sheets N-48, M-48, N-49, M-49 (http://vsegei.ru/info/pub_ggk1000-3/). 1, Quaternary deposits; 2, Cretaceous deposits; 3, Jurassic deposits; Permian deposits: 4, 5, Bichurin gabbro–monzonite–granite complex; 6, Carbonaceous deposits, Daurian granodiorite complex; Paleozoic deposits: 7, Malkhan granite complex; 8, Dzhida diorite–granite–plagiogranite complex; 9, Ulan-Burga metamorphic complex; 10, Monostoi gabbro complex; 11, faults; 12, MT sites with numbers

5.1 The Selenga Block

The Selenga block (sites 3–11) includes the southern part of the Selenga River delta in the region of Cenozoic deposits overlying the moderately acidic granite massifs of the Barguzin complex and the overlain Selenga-Itantsy rift basin. The basin is composed of Jurassic and Cretaceous deposits, overlain by deposits of all epochs of the Quaternary Period. The sedimentary deposits are divided into three generalized

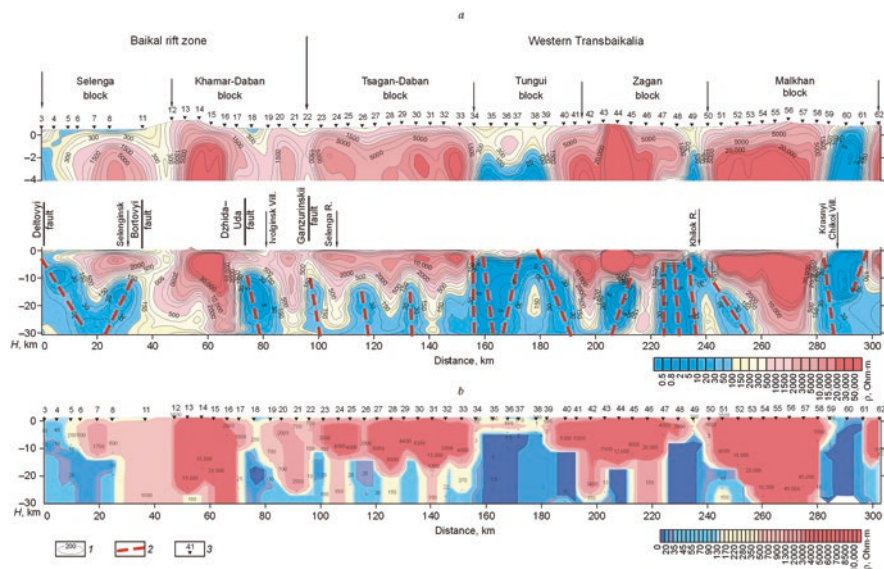


Fig. 7 Geoelectric section along the Selenga River delta–Krasnyi Chikoi Village profile. **(a)** From the results of inversion; **(b)** model; 1, resistivity isolines; 2, inferred deep faults; 3, magnetotelluric sounding

resistivity horizons, whose total thickness decreases in the southeast direction from 3500 to 300–500 m, in the Fofonovo crystalline bridge. The most subsiding part of the Fofonovo crystalline bridge is characterized by resistivity highs (above 2000 Ohm·m), which decrease to 150 Ohm·m with depth and are less than 30 Ohm·m at depths of 18,000–30,000 m.

A feature of the crustal section of the Selenga block is the presence of northeast- and northwest-trending deep rift faults, which determine the high fluid reworking of the crust and hence low resistivity. The Deltiviy and Bortoviy major deep faults are well-known rift-forming normal faults dipping toward the axis of the Baikal Rift [75, 80]. They appear in the geoelectric section (sites 3–4, sites 10–11) as low-resistivity zones with a pronounced dip of the lateral boundaries (Fig. 7). The boundary between the Selenga and Khamar-Daban blocks passed along the northeast-trending Bortoviy fault.

A fragment of a conductive layer with a resistivity of 5–10 Ohm·m is identified at of 8–16 km in the northwestern part of the block considered (sites 3–6) (Figs. 7 and 8). Inferring the parameters of the layer in other parts of the investigated profile is extremely difficult and impossible in cases due to the presence of anomalously low-resistivity zones and high-resistivity long vertically extended formations in the crust.

The conducting layer roof rise in the Selenga block to depths of 8–10 km, relative to 15–10 km, established in other parts of the Baikal rift zone [11, 66, 67, 71], is due to the increased tectonic activity of this Earth crust block. This conclusion is

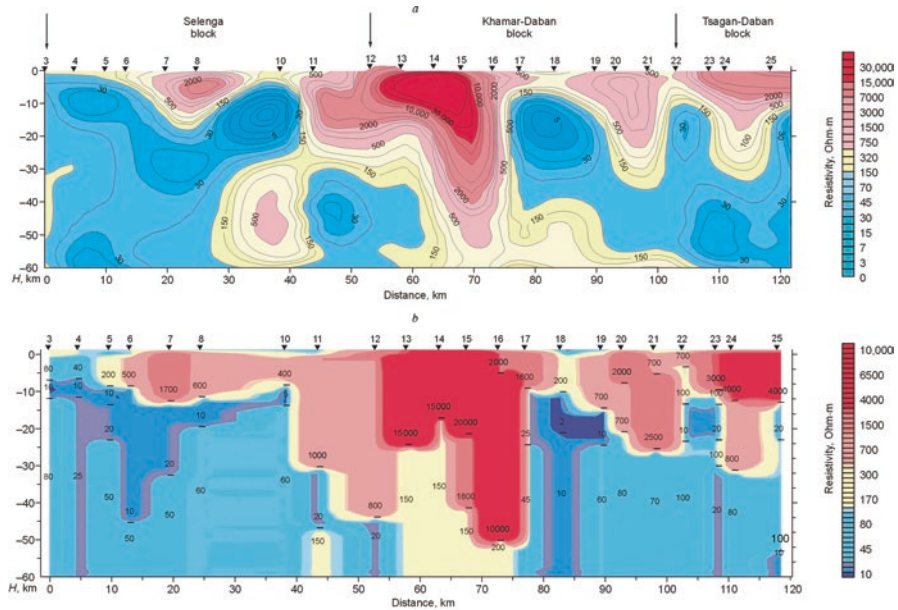


Fig. 8 Deep geoelectric section along a portion of the MT profile (sites 3–25). (a) From the results of inversion; (b) model. See Fig. 7 for the legend

consistent with the above geothermal data on the distribution of heat flow and temperatures at depths of 20 and 40 km in a 100-kilometer band along the MTS profile. Within the considered block there is an increase in the values of heat flow to 60–75 mW/sq. m, with a maximum of 80 mW/sq. m in the Selenga river delta (see Fig. 2). The temperatures at the calculated depths are 450 and 900 °C, which corresponds to the upper and lower limits of the crust conductive layer (see Figs. 7 and 8). According to seismological studies, earthquake foci of the Selenga focal zone are concentrated at the same depths [90]. In addition, at the North-Eastern end of the Selenga focal zone during the instrumental period of the last decade, a region of swarm seismicity not typical for this area was recorded. According to studies conducted by I.G. Kissin [36] fluids have a strong influence on the main conditions of the deformation process – the nature of the acting stresses and the strength properties of the medium. It is established that the earthquake foci are concentrated mainly over subhorizontal fluid-saturated bodies or in their upper parts, so the factors determining the seismic activity of the regions include the parameters of the crustal conducting layer. Raising the roof conductive layer to depths of 8–10 km is marked by many well-known focal zones of earthquakes: Altai (Altai, Shapshalsky, Danubian, South-Caspian, and many others). These data are consistent with the metamorphogenic model of the seismic zone proposed by I.G. Kissin [36]. According to this model, the metamorphic reaction of dehydration in one of the Earth crust blocks leads to additional stresses in the fault zone separating this block from the neighboring block, where such a process did not take place. Increased pore pressure (close to

lithostatic) leads to hydraulic fracturing and injection of high-pressure fluid into the fault zone, which serves as a trigger for an earthquake. The presence of deep faults is one of the characteristic features of the lithosphere, which during its active existence serve as fluid conductors. In essence, they are “through” channels penetrating into the lower crust and upper mantle, and lead to hypabyssal depths and even to the surface of the day alkaline-ultrabasic and carbonatite fluid-magmatic columns [34]. The strongest earthquakes are almost always confined to active faults. This is confirmed by experimental data indicating that the sudden rise of fluids in the fault zones initiates an earthquake [4]. In the magnetotelluric field, the zones of Earth crust disturbed areas are mapped by areas of low values of specific electrical resistance, which was shown, for example, for large interblock zones of fault type [7, 10, 50, 76].

The high permeability of the lithosphere of the Selenga block due to extensive disruption by active faults causes venting of their associated mantle fluids. The heat contained in the fluid at depth is completely transferred to rocks, i.e., is transformed to the conductive form of heat and mass transport as the fluids move to Earth surface [28]. The main features of the geothermal field of the Selenga block fit the conductive-convective model of the Baikal rift zone (BRZ) developed by Golubev [28]. According to this model, the positive thermal anomalies of the rift basins of the BRZ are caused by heat transport of the ascending branches of the regional hydrothermal convection cells (whose wide downward branches are located in water and heat removal zones on mountain ranges). This model easily satisfies the sustainability requirement. The formation of thermal anomalies of the BRZ from the thermal resources of its regional thermal field will take place under two conditions: the existence of groundwater-driving forces caused by the difference in groundwater level on ranges and in basins; permeability of faults in the crust, sustained by crust tension and recurrent earthquakes [28, 29].

5.2 *The Khamar-Daban Block*

The Khamar-Daban block (sites 12–17) includes three major structures: the eponymous mountain range, the Ivolga-Uda rift basin, and the Ganzurinskii Ridge. These structures are considered within a single block primarily because the latter two structures were insufficiently investigated in the present work. The second, more important reason. Is that based on the results of stress field studies and tectonic reconstructions, they belong to the Baikal rift zone [16, 48, 49, 77–80]. According to tectonic data [79, 80], this crustal block is characterized by three main types of dynamic setting: compression, left shear, and extension. Similar settings dominate in the central part of the Baikal Rift and associated with the Early Paleozoic (compression), Early Cenozoic (shear), and Late Cenozoic (extension) Stages of development of the crust of the Baikal region [80].

5.2.1 The Khamar-Daban Range

The Khamar-Daban Range (sites 12–17) is a structurally complex geoelectrical heterogeneity with high electrical resistivity. According to the distribution of geoelectrical parameters (thickness and resistivity), it is divided into three blocks: northwestern (sites 11–13), central (sites 14–15), and southeastern (sites 16–17) (Fig. 8). In the northwestern block, heterogeneity can be traced to a depth of 30–45 km and the resistivity is lower than 1000 Ohm·m. The central block is characterized by resistivity highs of 15,000–20,000 Ohm·m and a capacitance of about 25 km. In the southeastern block, significant variations in the geoelectric parameters are observed in both the vertical and the lateral direction. In the depth interval from 800 to 10,000 m, the resistivity values are 1600–2000 Ohm·m, increasing by almost an order of magnitude (10,000–20,000 Ohm·m) in the deep parts of the crustal section (10–50 km). In the area of influence of the Dzida-Uda deep fault, the thickness of high-resistivity formation is reduced to 10 km (Fig. 8).

The distribution of electrical resistivity within the Khamar-Daban Range is due to the compositional diversity of its constituent granitoids of different ages. Based on the age and composition, they belong to the Early Paleozoic S-type syncollisional formations [2, 3]. These are basically crustal formations originated from gneisses and schists of the Khamar-Daban metamorphic strata. The granitoids are mainly migmatites, plagiogranites, granite-gneisses, and Ka-Na granites. The Late Paleozoic igneous area of the Khamar-Daban Range is characterized by the development of sub-alkaline granitoids (monzodiorites, quartz syenites, and leucogranite) and intrusive subvolcanic rare-metal Li-F granites on its periphery. They are post-collisional formations and mark the transition to within-plate magmatism with manifestations of various geochemical rock types [2].

The low resistivity of the cross section lying below the high-resistivity rocks of the Khamar-Daban Range (100–150 Ohm·m) is due to the same processes as in the Selenga block discussed above, namely the high fluid reworking of the crustal section.

5.2.2 The Ivolga-Uda Basin

The Ivolga-Uda basin is a large Mesozoic structure extending from northwest to southeast and bounded by the Khamar-Daban and Ulan-Burgasy Ranges in the northwest and by the Ganzurinskii Ridge in the southeast. According to morphostructural features [24], it is a Transbaikalia type intermontane basin, with a characteristic smooth transition from the bottom of the foothills to the well-developed mountain frame. The southern margin of the basin is made up of Jurassic clastic deposits of the Galgatai Formations, and the central part is composed of the Lower Cretaceous Gusinoe Ozero argillo-arenaceous coal-bearing deposits. Continental margin molassoid deposits of the Sotnikov Formation are developed along its relatively steep northern boundary.

A determining factor in the modern morphostructure the Ivolga-Uda basin and its mountain frame is the structural continuity of roof-block movements and raptural deformations. The axial part of the mountain ranges rose faster than their margins, which led to the asymmetry of the “wings” of its frame with characteristic step-block structures bounded by faults. In the modern intracontinental rifting setting, there is an expansion of the basins due to their surrounding mountain ranges, as exemplified by the Ivolga-Uda basin and surrounding Khamar-Daban and Ganzurinskii Ranges. The results of this process are clearly seen in the geoelectric section (sites 17–20, Figs. 7 and 8). In the area of influence of the Dzhida-Uda rift fault adjacent to the steepest northern margin of the basin, there is a sharp uplift of the marginal part of the Khamar-Daban Range (from $-50,000$ to $-10,000$ m) and the resistivity decreases by almost an order of magnitude. In the area junction of the basin with the Ganzurinskii Ridge, the interval of the crustal section is characterized by values of 500–700 Ohm·m (Figs. 7 and 8). Within the ridge, composed of intrusive formations of the Dzhida complex [92], the resistivity varies from 2000 to 250 Ohm·m. The Ganzurinskii fault separating the Khamar-Daban and Tsagan-Daban blocks is the southeastern flank of the Baikal rift zone.

5.3 *The Tsagan-Daban Block*

The Tsagan-Daban block (sites 23–33), covering the territory of the eponymous mountain range, is located within the Western Transbaikalia segment of the Northern Mongolia-Western Transbaikalia (NMWT) rift zone and is an extensive area of granitoids magmatism. The granites are extremely diverse in composition: gneiss and alaskite granite, syenite, quartz diorite, granodiorite, alkaline aegerine-arfvedsonite and riebeckite granites, granite-porphyry, quartz porphyry, and acid volcanics.

A feature of this block is that it is dissected by recent regional deep faults (mainly northeast- and southwest-trending) into smaller blocks with identical structure characterized by a two-layer section of the Earth crust (Fig. 7). The upper part of the section in the depth range of 1000–15,000 m has the highest resistivity (2000–10,000 Ohm·m), with the maximum corresponding to the central part of the block. In the root parts of granitoids bodes, the resistivity is reduced to 500 Ohm·m. The lower part of the crustal section with a resistivity of 150 Ohm·m is complicated by a series of low-resistivity (below 30 Ohm·m) blocks, marking areas of neotectonic faults (Fig. 7).

The Tsagan-Daban block is bounded in the northwest and southeast by zones of regional long-lived northeast-trending faults (Fig. 7). According to [13, 14, 59], the Transbaikalia block structure formed as a result of activation of faults of this trend.

5.4 The Tugnui Block

The Tugnui block (sites 34–41) comprises one of the largest Mesozoic structures of the Western Transbaikalia – the Tugnui rift basin (graben). The basin is east-west trending, about 35–40 km wide, and stretches more than 140 km away from the lower reaches of the Khilok River in the west to the upper reaches of the Tugnui River in the east. Its northern and southern margins are the Tsagan-Daban and Zagan Ranges, respectively, made up of Precambrian Paleozoic rocks metamorphosed in the Late Mesozoic (Fig. 9).

The basin is mainly made up of Late Jurassic and Cretaceous volcanic and sedimentary strata, dominated by Middle Jurassic Ichetui Formation rocks. Along with dominating subalkaline basalts, they contain single beds and lenses of trachyte and trachydacite lavas and tuffs, interspersed with alkaline trachyriodacites and pantelirites [30, 32, 94]. The Ichetui Formation is underlain by the Berezovskaya Formation conglomerates. The overlying section consist of coal-bearing clastic

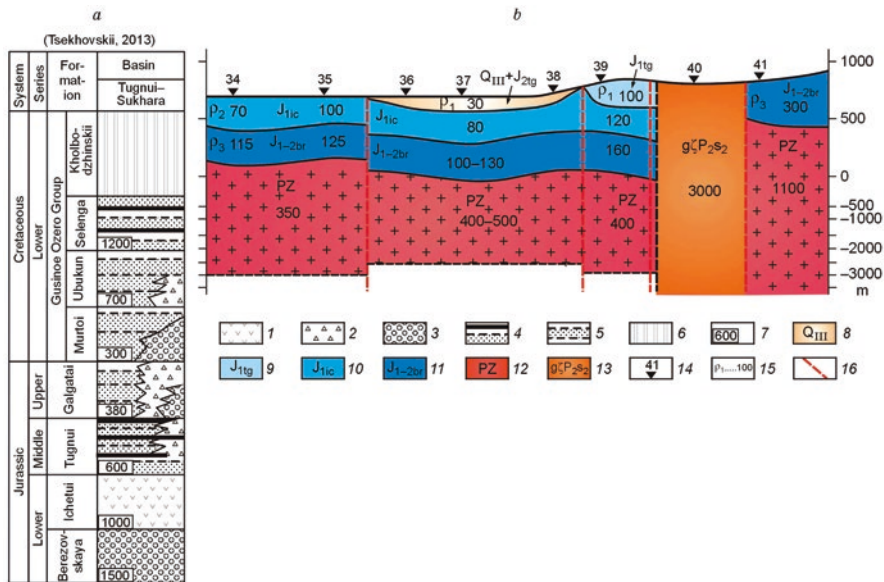


Fig. 9 (a) Schematic structure of the formations of the Jurassic–Cretaceous deposits of the Tugnui–Sukhara rift basin (Tsekhovskii Yu. G.) [87]; (b) geoelectric section of volcanic-sedimentary deposits of the Tugnui basin. 1, effusive rocks; 2, breccias with boulder lenses and rotten stone; 3, boulder conglomerate, conglomerate, and gravelstone; 4, interbedded sandstone, siltstone, and shale with coal beds; 5, interbedded sandstone, siltstone, and shale, often coal and sometimes weakly coal-bearing; 6, large interruptions in sedimentation; 7, numbers at the corner of the columns indicate the maximum thickness of deposits in meters; 8, Quaternary deposits; 9, Tugnui Formation; 10, Ichetui Formation; 11, Berezovskaya Formation; 12, basement; 13, granitoid intrusion of the Sogotin complex; 14, MT sites; 15, resistivity horizons and resistivity values in Ohm·m; 16, faults (from the 1:1,000,000 geological map of the Russian Federation, the third generation)

deposits of the Tugnui, Galgatai, Murtoi, and Selenga Formations, which accumulated until the Early Cretaceous [87].

The Lower and Middle Jurassic deposits of the Berezovskaya, Ichetui, and Tugnui Formations dominate the studied part of the Tugnui basin. The geoelectrical structure of the western and central parts of the basin (sites 34–39) is simple. Here the volcanic-sedimentary sequence is divided into three horizons (Fig. 9):

$$\rho_1 < \rho_2 < \rho_3.$$

The first horizon (ρ_1), represented by Quaternary and Middle Jurassic deposits of the Tugnui Formation stands out only in the central part of the basin (sites 36–39). Quaternary deposits pinch out in the direction of its both margins and are completely replaced the Tugnui Formation deposits in the vicinity of site 39 (Fig. 9). The second (ρ_2) and third (ρ_3) resistivity horizons, confined to the Ichetui and Berezovskaya Formation deposits, can be traced throughout the section and are characterized by laterally stable resistivity and thickness (Fig. 9). In the eastern part of the basin, bounded by a steep marginal bench, its disruption and erosion resulted in accumulation of coarse deposits of the Berezovskaya Formation with high resistivity (200–300 Ohm·m). Here the thickness of the sedimentary cover is reduced to 350–400 m, and the underlying section consists of ancient Paleozoic basement granitoids. In the area of site 40, the Berezovskaya Formation deposits are intruded by granitoids of the Late Permian Sogotin complex, represented by subalkaline granitoids, quartz syenite and syenite porphyry. Here the resistivity is 3000 Ohm·m (Fig. 9).

The basement of the Tugnui basin, made up of predominantly Paleozoic granitoids, has a complex block structure [15]. It is divided by tectonic faults of varying trend into different-sized blocks which have been displaced relative to each other by different magnitudes. Some of them, observed on the surface of the structure, cross the entire section of the basin deposits (Fig. 9). These tectonic disruptions, along with long-lived deep marginal faults improve the interaction of groundwater of various geological complexes and related hydrogeological structures [103]. These venting areas provide vertical and horizontal movement of groundwater due to changes in its chemical and gas composition, temperature, and salinity. These processes lead to a sharp decrease in the resistivity of the basin basement to 400–500 Ohm·m (Fig. 9).

The crustal section of the Tugnui block absolutely is dominated by low resistivities (10–30 Ohm·m). The exception is the depth range from –12,000 to –22,000 m near site 38, where they are increased to 150 Ohm·m and are in agreement with the resistivity level of the crustal section of neighboring blocks (Fig. 7).

The occurrence of high electrical conductivity in the crustal section of the block considered and the nature of its permeability are related to the structural evolution, magmatism, and general geodynamics of the Tugnui rift basin. It formed in an extensional setting caused by the rise of the mantle plume in the Tugnui-Konda system of long-lived deep faults [30, 94]. Rifting was accompanied by Late Jurassic bimodal and late Jurassic-early Early Cretaceous trachydacite-pantellirite volcanic

lava eruptions localized within the basin. The absence of similar products of magmatism outside the basin indicates that the system of effluent channels feeding magmatic activity was located directly under the basin and sustained throughout the subsequent geological history [94]. Highly permeable faulted areas of the Earth crust cause its saturation with fluids and gases, which, in turn, leads to the formation of a high-conductivity area. Subvertical zones with resistivity lows (<5 Ohm-m) are formed within the basin, which mark recent faults disrupting both margins of the basin and their feathering second-order faults (Fig. 7).

5.5 The Zagan Block

The Zagan block (sites 42–50) includes the eponymous range and the Khilok-Chikoi rift basin (included in the block because of insufficient MT data on this basin, sites 48 and 49) and considered as a complementary structure to the Zagan Range.

5.5.1 Zagansky Ridge

Zagansky ridge is a large (100×200 km) anticline structure of the North-Eastern stretch (granite-gneiss shaft), bounded from the North-West and South-East of the Tugnuisky and Khilok-Chikoisky Rift depressions (see Fig. 7). In the last time there was a different interpretation of the structure Zagansky ridge, where he and other granite-gneiss domes of the Transbaikal region are compared with the rifting gneiss-meanitime complexes of metamorphic cores of North America [82]. According to [82], it is composed of the Zagan metamorphic core complex and has a zonal structure consisting of a core zone and zone of brittle-plastic flow [52, 53, 82]. Most of the core is composed of various granitoids, including syenites and granosyenites, gneiss granites, medium-grained granites, and granodiorites. The core of the complex is flanked by a gently-dipping zone of dynamometamorphic formations (mylonites) marking the detachment zone. Dynamometamorphic formations are widespread mainly along volcanic-sedimentary sequences of Late Paleozoic and partly Early Mesozoic rocks [53]. The mylonites rocks vary in the degree of metamorphism and comprise protomylonites, mylonites, mylonites schists, blastomylonites, and pseudotachylites, and ultramylonites [52]. In addition, the slopes of the range contain Late Paleozoic- Mesozoic volcanic-sedimentary formations common in the associated basins: the Tugnui basin in the northwest and the Khilok-Chikoi basin in the southeast.

The zonal structure of the Zagan Range, with the variety of its compositional associations, is reflected in the resistivity distribution pattern. In general, the high resistivities characteristic of the upper crust of the block differ significantly in its central and marginal parts (Fig. 7). The central high-resistivity area (sites 43–46) corresponds to the rock spectrum of granite-metamorphic formations of the core. Here the resistivities are maintained at 12,000–20,000 Ohm-m over the entire range

of depths (from 600 to 15,000 m). They decrease to 4000–5000 Ohm-m. toward the margins and are 600–1000 Ohm-m in the range and the basins (Fig. 7). The marginal parts of the Zagan Range, comparable in resistivity, differ in vertical length. The eastern part of the range is the most elevated. In the western part, it is traced to depths to depths of 22,000 m and uplifts sharply to 15,000 m in the area of transition to the Tugnui basin.

The lower crust with a resistivity of 150 Ohm-m is disrupted by a series of sub-vertical conductive zones, associated with a system of longitudinal faults and marginal rift faults and range-associated basins (Fig. 7).

The formation of the Zagan metamorphic core complex and its complementary Tugnui and Khilok-Chikoi basins is related to rifting processes, which in Western Transbaikalia began with the occurrence of a mantle plume in the base of the region [52, 53, 82, 94]. Extension processes were accompanied by the formation of separate basins (grabens), including the Tugnui basin. Adjacent areas of the Earth crust, affected by enhanced heat flow, undergo anatexis and metamorphism, resulting in areas of increased plasticity. In the extensional setting, these plastic crust fragments contributed to the formation of a hollow detachment zone with a southeastern vergence, expressed as a mylonites zone [82]. The surface of the detachment zone restricted the access of mantle melts to the Tugnui basin and bulged up by the buoyant hot crustal mass of the Zagan Range. The Khilok-Chikoi basin formed above the steep branch of the detachment zone subsiding to the plume. This promoted the formation of a stable system of effluent channels under the basin and the displacement of sites of active magmatism into its area [94].

5.5.2 The Khilok-Chikoi Basin

The Khilok-Chikoi basin, like the Tugnui basin, extends roughly east-west over a distance of 150 km at a width of 20–30 km. The basin is made up of Cretaceous (Gusinoe Ozero Sequence and Khilok Formation) and Cenozoic volcanic and sedimentary strata. The Early Cretaceous Khilok Formation rocks (K_{1hl}) are dominant. They appear as almost continuous thick series of lava flows over the entire length of the basin.

A crustal role in the formation of the modern structure of the Khilok-Chikoi basin was played by marginal rift faults and transverse faults dissecting the basin and producing the distinct block structure of the basin (Fig. 10). The formation of steeply dipping faults is probably related to the period of isostatic buoyancy, i.e., with the establishment of the Zagan dome. According to geological features, this event occurred after the formation of shallow mylonites zones [82].

The Khilok-Chikoi basin appears in the geoelectric section as an area with a very low crust resistivity (≤ 5 –10 Ohm-m) (Fig. 7). Its marginal parts have subvertical zones with resistivity lows (5 Ohm-m or less), associated with marginal rift faults. Low resistivities of the basin basement (200–250 Ohm-m) are due to the venting of fracture-vein waters at the sites of intersection of marginal and meridional faults.

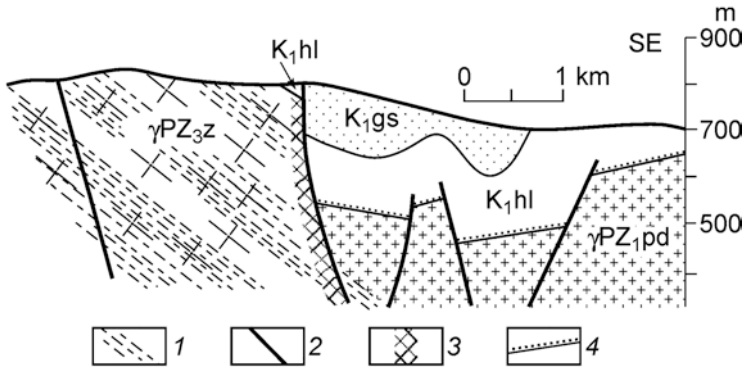


Fig. 10 Correlation between the Khilok–Chikoi basin and the Zagan Uplift. (Sklyarov E.V.) [82]. K1gs, Gusinoe Ozero Formation; K1hl, Khilok Formation; γ PZ_{3z}, Upper Paleozoic granitoids; γ PZ_{1pd}, Early Paleozoic granitoids; 1, mylonitization; 2, faults; 3, increased fracture zone; 4, thrust

5.6 The Malkhan Block

The Malkhan block (sites 51–62) is located within the southeastern flank of the MT profile and includes the Malkhan range and the Chikoi basin; the basin is not identified as a separate block because of a lack of sufficient MT data on it.

5.6.1 Malkhan Range

Within the Malkhan Range (sites 50–59), almost the entire crustal section, explored to depths of 30,000 m is characterized by high resistivity, which ranges from 5000 to 45,000 Ohm·m (Fig. 7). The high resistivity is due to the extensive development of various igneous complexes throughout the crustal section. These are primarily granitoids differing in composition and structure, including granitoids of the Malkhan metamorphic core complex, whose central part is composed of Early and Middle Paleozoic granitoids interspersed with metamorphic xenoliths. A special feature this complex is the much wider occurrence of diorite rocks [82]. The outer zone, facing the Early Cretaceous Chikoi basin, is composed of Middle Paleozoic foliated granites and Early Cambrian and Carboniferous metamorphic sedimentary and volcanic deposits. A significant part of these deposits is dynamically metamorphosed in a wide fault zone gently dipping to the southeast [82, 94].

The granitoids fields are extensively penetrated by mafic intrusions of rocks of the Lower Paleozoic Monostoi gabbroic complex. The rocks of this complex (gabbro, gabbro-diorite and diorite) contribute significantly to the formation of the high-resistivity region of the central part of the Malkhan Range. Here the resistivity varies between 12,000 and 45,000 Ohm·m. Resistivity highs correspond to outcrops of mafic intrusions. On the margins of the range, the resistivity is reduced to

5000–8000 Ohm-m, and in the areas of transition to the Khilok-Chikoi and Chikoi basins, it is 500–1500 Ohm-m (Fig. 7).

5.6.2 Chikoi Basin

The Chikoi basin, like the Tugnui and Khilok-Chikoi basins discussed above, is a Transbaikalia type basin formed in an extensional setting in a system of long-lived deep faults [15, 30, 94]. It is roughly east-west trending and extends over a distance of about 130 km with of 1–2 to 8 km. The basin is bounded in the north by the Malkhan Range and in the south by the spurs of the Asian, Uletntui, and Mergen Ranges (Fig. 7). Geologically, it is a sedimentation basin filled with Early Cretaceous terrigenous rocks with a total thickness of 700–1600 m. It originated in the Mesozoic and developed during the Neogene-Quaternary under the influence of neotectonic movements in the south of the Khilok-Vitim structural-faces zone.

Low resistivity values from 3–5 to 30–50 Ohm-m were measured virtually throughout the crustal section within the Chikoi basin. This is due not only to its deep structure but also to the insufficient exploration of this region. The profile traversed the basin only at two sites (60 and 61) in the marginal fault zone, which did not allow us to estimate the upper crust. In the geoelectric section, the Chikoi basins corresponds to a low-resistivity region complicated by subvertical conductive zones (less than 5 Ohm-m) related to marginal rift faults (Fig. 7). The southeast termination of the Malkhan block (and, in general, the entire investigated profile) are the high-impedance (10,000 Ohm-m) formations of the Chikoi Mountains.

6 Conclusions

The study area has a complex geological-tectonic structure produced by extensive rifting, leading to the formation of large crustal blocks, and by intense magmatic fluid activity along deep fault zones. These processes are manifested in the deep electrical conductivity and heat flow distribution as follows.

1. Significantly less tectonic activity of the West Transbaikal rift zone, compared with the Baikal region of modern rift formation, was reflected in the contrast of the resistivity distribution and heat flow values in the North-Western and South-Eastern parts of the studied profile. The high permeability of the lithosphere of the Baikal rift zone due to the strong disturbance by deep faults of the Cenozoic stage of activation, causes the unloading of endogenous fluids and provides additional heat transfer. The maximum values of heat flow are observed in the North-Western part of the profile (Eastern Baikal region) and are 60–99 mW/sq. m. In the rest of the territory they are much smaller – about 50–55 mW/sq. m. Areas with maximum destruction of the Earth crust and, consequently, increased permeability to fluids and heat flow are characterized by extensive minima of

electrical resistivity (Selenga block). The increased tectonic activity of the Selenga block is evidenced by the crust conductive layer parameters (the depth of the upper edge and the specific electrical resistance) and the increased values of the heat flow, which are: 8–10 km; 10 Ohm-m, 65–80 mW/sq. m, respectively. The depth of the roof and the sole layer is in accordance with the temperature distribution in this range of the crust.

2. For both parts of the profile is characterized by a combination of structures with different types of geoelectric section – mountain ranges and intermountain depressions, with their separating zones of long-lived deep faults. Ranges represent a complex of geoelectric inhomogeneity with a double-layered section of Earth crust. The upper part of the section, represented by different age and composition of granitoids, is characterized by high values of electrical resistivity. They are distributed in descending orders from the central parts of the ridges to the edge. A sharp decrease in the ER values in the underlying section of the crust is largely due not to the material composition of the rocks, but to its high permeability to fluids and gases, due to intensive disturbance by regional fault zones. The exception is the Malkhan ridge, within which the entire studied section of the Earth crust is characterized by high values of resistivity, the determining factor of which is the wide development within the Earth crust and the top of the main composition magmatism mantle.
3. Intermountain depressions are large Mesozoic riftogenic structures, the formation of which occurred in the mode of stretching in the system of long-lived deep faults. According to morphostructural features, they belong to the intermountain basins of the “transbaikal” type with a characteristic smooth transition from the bottom in the foothills to a well-developed mountain frame. In the conditions of the latest intracontinental riftogenesis there is an absorption of the mountain hills by the growing depressions, which in this case are the most active elements of the morphostructure. The results of this process are clearly manifested in the geoelectric section, where the cavities correspond to the Earth crust blocks with low resistivity values, complicated by subvertical conducting zones associated with onboard rift faults.
4. The regional deep faults separating blocks of different sizes appear in the geoelectric as distinct subvertical zones with resistivity lows. The deeps of their lateral boundaries coincide with the position of the fault planes determined from geological structure data on the surface (Boartovoi, Dzhida-Uda, and Ganzurin). The conductive zones within the Tsagan-Daban block mark recent fault zones.

References

1. Adam A (1987) Are there two types of conductivity anomaly (CA) caused by fluid in the crust? *Phys Earth Planet Inter* 45:209–215
2. Antipin VS, Goralcheva NV (2013) Evolution of the Paleozoic granitoids magmatism in the Baikal region: from collisional gneiss granites to within-plate rare-metal granites [in

- Russian]. In: Proceedings of the science conference granitoids: conditions of formation and mineralization, Kiev, May 27 – Jun 1, 2013, Kiev, pp 14
3. Antipin VS, Gorlacheva NV, Makrygina VA (2014) Geochemistry of Early Paleozoic granitoids of the Baikal region and their geodynamic setting exemplified by Khamar-Daban Range and Olkhon Island. *Geol Geofiz (Russ Geol Geophys)* 55(92):228–243 (177–189)
 4. Aptikayev SF (1995) Structure of the microlarge-scale seismic field [in Russian]. Candidate (Phys.-Mat.) Dissertation, Moscow
 5. Bahr K (1988) Interpretation of magneto telluric impedance tensor: regional induction and local telluric distortion. *J Geophys* 62:119–127
 6. Belichenko VG, Geletii NK, Barach IG (2006) Barguzin microcontinent (Baikal mountain area): the problem of outlining. *Russ Geol Geophys (Geol Geofiz)* 47(10):1035–1045 (1049–1059)
 7. Ben-Zion Y, Sammis CG (2003) Characterization of fault zones. *Pure Appl Geophys* 160(304):677–715
 8. Berdichevskii MN, Dmitriev VI (2009) Models and methods of magnetotelluric studies [in Russian]. Nauchnyi Mir, Moscow
 9. Berdichevskii MN, Dmitriev VI, Novikov DB, Pastutsan VV (1997) Analysis and interpretation of magnetotelluric data [in Russian]. Dialog-MGU, Moscow
 10. Berdichevskii MN, Borisov VP, Golubtsova NS, Ingerov AI, Konovalova YF, Kulikov AV, Solodilov IN, Chernyavsky GA, Chpak IP (1996) Experience of interpretation of these MT-soundings in mountains of Lesser Caucasus [in Russian]. *Fizika Zemli* 4:99–117
 11. Berdichevskii MN, Vany'an LV, Koshurnikov AV (1999) Magnetotelluric sounding in the Baikal rift zone [in Russian]. *Fizika Zemli* 10:17–35
 12. Brown JM, Shankland TJ (1981) Thermodynamic parameters in the Earth as determined from seismic profiles. *Geophys J Int* 66:579–596
 13. Bulgatov AN, Bulnaev KB, Ochirov TO, Turunkhaev VI (1978) Tectonic faults of Transbaikalia [in Russian]. Nauka, Novosibirsk
 14. Bulgatov AN, Gordienko IV, Zaitsev PF, Turunkhaev VI (2004) Geodynamic Map of the Baikal Region and Adjacent Territories. Scale 1:2,000,000. CDROM. Geological Institute of the Russian Academy of Sciences, Ulan-Ude
 15. Bulnaev KV (2006) The formation of Transbaikalia type basins [in Russian]. *Tikhokeanskaya Geol* 25(1):18–30
 16. Delvaux D, Mous R, Stapel G, Petit C, Levi K, Miroshnichenko A, Ruzhich V, San'kov V (1997) Paleostress reconstruction and geodynamics of the Baikal region, Central Asia. Part II: Cenozoic rifting. *Tectonophysics* 282(104):1–38. [https://doi.org/10.1016/S0040-1951\(97\)00210-2](https://doi.org/10.1016/S0040-1951(97)00210-2)
 17. Derpogolts VF (1963) The principles of the integrated natural classification of natural waters of the Earth [in Russian]. *Soviet Geol* 5:7–18
 18. Dobretsov NL (1981) Global petrologic processes [in Russian]. Nauka, Moscow
 19. Dobretsov NL, Buslov MN (2007) Late Cambrian-Ordovician tectonics and geodynamics of Central Asia. *Russ Geol Geophys (Geol Geofiz)* 48(1):71–82 (93–108)
 20. Donskaya TV, Sklyarov EV, Gladkochub DP, Mazukabzov Am, Sal'nikova EV, Kovach VV, Yakovleva SZ, Berezhnaya NG (2000) The Baikal collisional metamorphic belt [in Russian]. *Dokl Earth Sci* 374(7):1075–1079
 21. Duchkov AD, Sokolova LS, Ayunov DE (2004) Geothermal Atlas of Siberia [in Russian]. In: The structure and evolution of the geosphere: proceedings of the international science symposium, Khabarovsk, September 23–26, 2003. FEB RAS, Khabarovsk, pp 45–56
 22. Epov MI, Pospeeva EV, Vitte LV (2012) Crust structure and composition in the southern Siberian craton (influence zone of Baikal rifting) from magnetotelluric data. *Russ Geol Geophys (Geol Geofiz)* 53(3):293–306 (380–398)
 23. Fainberg EB, Fiskina MV, Rotanova NM (1977) Experimental data on the global electromagnetic sounding of the Earth. In: Spatiotemporal structure of the geomagnetic field [in Russian]. Nauka, Moscow, pp 102–113

24. Florensov NA (1960) Mesozoic and Cenozoic depressions of the Baikal Region [in Russian]. Izd. AN SSSR, Moscow, Leningrad
25. Geothermal Atlas of Siberia and Far East (2009–2015) (Internet resource)/A.D. Duchkov, M.N. Zheleznyak, D.E. Ayunov, O.V. Veselov, L.S. Sokolova, S.A. Kazantsev, P. Yu. Gornov, N.N. Dobretsov, I.I. Boldyrev, D.V. Pchel'nikov, A.N. Dobretsov <http://maps.nrcgit.ru/geoterm>
26. Hasterok D, Chapman DS (2007) Continental thermal isostasy: 1. Methods and sensitivity. *J Geophys Res* 112:B06414. <https://doi.org/10.1029/2006JB004663>
27. Gladkochub DP, Donskaya TV, Fedorovskii VS, Mazukabzov AM, Larionov AN, Sergeev SA (2010) The Olkhon metamorphic terrain in the Baikal region: an early Paleozoic collage of Neoproterozoic active margin fragments. *Russ Geol Geophys (Geol Geofiz)* 51(5):447–460 (571–588)
28. Golubev VA (2007) Conductive and convective heat transport in the Baikal Rift zone [in Russian]. *Akademicheskoe Izd. "Geo"*, Novosibirsk
29. Golubev VA (2009) Geophysical data confirming lack of Late Cenozoic mantle intrusions in the Earth crust under the Baikal Depression [in Russian]. *Dokl Earth Sci* 426(94):623–627
30. Gordienko IV, Klimuk VS (1995) Bimodal volcanism of the Tugnui Rift Depression (Transbaikalia). *Geol Geofiz (Russ Geol Geophys)* 36(95):23–37 (22–36)
31. Gordienko IV, Andreev GV, Kuznetsov AN (1978) Paleozoic igneous formations in the Sayan-Baikalia mountainous area [in Russian]. Nauka, Moscow
32. Gordienko IV, Bayanov VD, Klimuk VS, Ponomarchuk VA, Travin AV (1999) The composition and $^{39}\text{Ar}/^{40}\text{Ar}$ age of volcanogenic rocks of the Chikoi-Khilok rift Valley in Transbaikalia. *Geol Geofiz (Russ Geol Geophys)* 40(4):583–591 (566–575)
33. Jones AG (1981) On a type classification of lowers under Precambrian regions. *J Geophys* 49:226–233
34. Kadik AA (2006) Fluids as reflection of the oxidation-reduction mode in a cloak: the investigations for geophysical properties of deep substance. *Fluids and geodynamics* [in Russian]. Nauka, Moscow
35. Catalog of data on the heat flux of Siberia (1985) [in Russian] Novosibirsk, IGG SB AS USSR
36. Kissin IG (2009) Fluids in the earth in the crust: geophysical and tectonic aspects [in Russian]. Nauka, Moscow
37. Kobranova VN (1986) Petrophysics [in Russian]. Nedra, Moscow
38. Kopnichev YF, Sokolova IN (2000) Space-time variations of absorption S – waves in the ochfgovykh zones of strong earthquakes [in Russian]. *Fizika Zemli* 7:35–47
39. Kovalenko VI, Yarmolyuk VV, Sal'nikova EV, Budnikov SV, Kovach VP, Kotov AB, Ponomarchuk VA, Kozlov VD, Vladykin NV (2003) Sources of igneous rocks and genesis of the Early Mesozoic tectonomagmatic area of the Mongolia-Transbaikalia magmatic region: 1. Geology and isotopic geochronology. *Petrologiya* 11(2):164–178; Koval PV (1998) Regional geochemical analysis of granitoids [in Russian]. Izd. SO RANX. NITs OIGGM, Novosibirsk
40. Krasnopevceva GV (1985) A modern view of the seismic model of the continental crust [in Russian]. *VJEMS*, Moscow
41. Kutas RI (1986) Thermal model of the continental lithosphere. *Geofizicheskij Zh* 8(1):19–27
42. Kovtun AA, Vagin SA, Vardanyants IL, Legen'kova NP, Smirnov CCCC, Yu M, Uspenskii NI (2004) Structure of the Karelian region from resistivity sounding data. In: Sharov NV (ed) Deep structure and seismicity of the Karelian region and its framing [in Russian]. Karelian Research Centre of RAS, Petrozavodsk, pp 120–150
43. Lebedev EB, Hitarov NI (1979) Physical properties of magmatic fusions [in Russian]. Nauka, Moscow
44. Letnikov FA (2000) Deep earth fluids. In: Russian science: facets of creativity at the Tern of the century [in Russian]. Nauchnyi Mir, Moscow, pp 333–340
45. Litvinovsky BA, Zanzilevich AN, Alakshin AM, Podladchikov YU (1992) Angara-Vitim Batholith, the largest Granitoid Pluton [in Russian]. NITs OIGGM SO RAN, Novosibirsk

46. Litvinovsky BA, Posokhov VF, Zanzilevich AN (1999) New Rb-Sr data. *Geol Geofiz (Russ Geol Geophys)* 40(5):694–702 (677–685)
47. Litvinovsky BA, Yarmolyuk VV, Vorontsov AG, Zhuravlev DZ, Posokhov VF, Sandimirova GP, Kuz'min DV (2001) Late Triassic stage of formation of the Mongolo-Transbaikalian alkaline-granitoid province: data of isotope-geochemical studies. *Geol Geofiz (Russ Geol Geophys)* 42(3):445–456 (433–444)
48. Levi KG, Arzhannikova AV, Buddo VY, Kirillov PG, Lukhnev AV, Miroshnichenko AI, Ruzhich VV, San'kov VA (1997) Modern geodynamics of the Baikal rift [in Russian]. *Razvedka i Okhrana Nedra* 1:10–20
49. Logachev NA (ed) (1984) The geology and seismicity of the BAM zone. Vol. 3: neotectonics [in Russian]. Nauka, Novosibirsk
50. Maercklin N, Bedrosian PA, Haberland C, Ritter O, Ryberg T, Weber M, Weckmann U (2005) Characterizing a large shear-zone with seismic and magnetotelluric methods: the case of the Dead Sea transform. *Geophys Res Lett* 32(15):L15303
51. Marakushev AA, Perchuk LL (1971) Origin and evolution of transmigmatic and metamorphic fluids. In: Abstracts of international geochemical congress. International Association of Geochemistry and Cosmochemistry, Moscow [in Russian], vol 2, pp 513–514
52. Mazukabzov AM, Sklyarov EV (1995) Mylonites of the Zagan metamorphic core (Western Transbaikalia). In: RFBR in Siberia (the crust and mantle) [in Russian]. Irkutsk, vol 1, pp 94–96
53. Mazukabzov AM, Sklyarov EV, Donskaya TV, Gladkochub DL, Fedorovskii VS (2011) Metamorphic core complexes of Transbaikalia: review [in Russian]. *Geodinamika Tectonofizika* 2(2):95–125
54. Moroz YF, Laguta NA, Moroz TA (2008) Magnetotelluric sounding of Kamchatka. *Vulkanologiya i Seismologiya* [in Russian], No. 2. March–April, pp 97–109
55. Nesbitt BE (1993) Electrical resistivities of crustal fluids. *J Geophys Res* 98 (NB3):4301–4310
56. Nevskij MV, Fokin OS, Riznichenko OJU (1994) P-wave attenuation in the Earth crust and the deformation process [in Russian]. *Dinamicheskie processy v geofizicheskoy srede*. Nauka, Moscow, pp 185–209
57. Nikol'skii NS (1987) Fluid regime of endogenous mineralization [in Russian]. Nauka, Moscow
58. Novikov IS, Pospeeva EV (2017) Neotectonics of eastern Gorny Altai: evidence from magnetotelluric data. *Russ Geol Geophys* 58(7):769–777
59. Ochirov TO (1976) Block tectonics of Transbaikalia [in Russian]. Nauka, Novosibirsk
60. Parfenov LM, Bulgatov AN, Gordienko IV (1996) Terranes and formation of Transbaikalian orogenic belts [in Russian]. *Tikhookeanskaya Geol* 15(4):3–15
61. Parfenov LM, Berzin NA, Khanchuk AI, Badrach G, Belichenko VG, Bulgatov AN, Dril' SI, Kirillova GL, Kuz'min MI, Nokleberg WJ, Prokop'ev AV, Timofeev VF, Tomurtogoo O, Yan H (2003) A model for the formation of orogenic belts in Central and Northeastern Asia [in Russian]. *Tikhookeanskaya Geol* 22(6):7–41
62. Parkhomenko EI (1989) Geoelectric properties of minerals and rocks with high pressures and temperatures [in Russian]. Nauka, Moscow
63. Perchuk LP (2000) Fluids in the lower crust and upper mantle of the Earth [in Russian]. *Vestnik Mosk Univ Ser 4 Geologiya* 4:25–39
64. Pokrovskii AV (2006) On the endogenous component of the water cycle on the Earth [in Russian]. *Vestnik Baltiiskogo Federal'nogo Universiteta im I Kanta* 7:46–56
65. Pollack YN, Chapman DS (1977) On the regional variation of heat flow, geotherms and lithospheric thickness. *Tectonophysics* 38:279–296
66. Popov AM (1977) Deep layers of increased electrical conductivity from magnetotelluric sounding data. In: Essays on the deep structure of the Baikal Rift [in Russian]. Nauka, Novosibirsk, pp 99–115
67. Popov AM (1990) A deep geophysics study in the Baikal region [in Russian]. *PAGEOPH* 34(4):675–587

68. Pospeev VI (1979) Results of statistical analysis of experimental data on global magnetotelluric sounding. In: *Methods and results of geophysical studies in East Siberia* [in Russian]. Irkutsk, pp 46–52
69. Pospeev VI, Mikhalevskii VI (1975) MTS studies in the south of the Siberian platform and the Baikal rift zone. In: *Studies of the thermal and electromagnetic fields in the USSR* [in Russian]. Nauka, Moscow, pp 121–127
70. Pospeev VI, Mikhalevskii VI (1981) Electromagnetic data on the asthenosphere in regions of the Siberian platform [in Russian]. *Geol Geofiz (Sov Geol Geophys)* 22(1):153–157 (128–132)
71. Pospeev VI, Vany'an LV, Gornostaev VP (1978) Deep electrical conductivity in the Baikal and Pacific rift zones. In: *All-union workshop on electromagnetic sounding* [in Russian]. Mosk. Gos. Univ, Moscow, pp 45–51
72. Pusharovskii YM, Pusharovskii DYU (2010) *Geology of the earth mantle* [in Russian]. GEOS, Moscow
73. Ringwood AE (1975) *Composition and petrology of the earth mantle*. McGraw-Hill, New York
74. Ringwood AE (1981) *Composition and petrology of the earth mantle*. Mir, Moscow
75. Ryazanov IN, Tat'kov GI, Kolomiets VI, Nefed'ev MA, Chebakov GI (2004) Regional stress field and seismotectonics of the Ust'-Selenga basin. In: *Evolution of tectonic processes in the earth history* [in Russian]. Izd. SO RAN, Filial "Geo", Novosibirsk, vol 2, pp 106–109
76. Unsworth MJ, Bedrosian PA (2004) On the geoelectric structure of major strike-slip faults and shear zones. *Earth Planets Space* 56(12):1177–1184
77. Seminsky KZH (1994) Principles and steps of special fracture-based mapping of a fault-block structure. *Geol Geofiz (Russ Geol Geophys)* 9:112–130 (94–112)
78. Seminsky KZH (2003) Internal structure of continental fault zones: tectophysical aspect [in Russian]. Izd. SO RAN, Filial "Geo", Novosibirsk
79. Seminsky KZH (2009) Major factors of evolution of basins and faults in the Baikal rift zone: tectonophysical analysis. *Geotectonics* 43(6):489–500. <https://doi.org/10.1134/S001685210906003X>
80. Seminsky KZ, Kozhevnikov NO, Cheremnykh AV, Pospeeva EV, Bobrov AA, Olenchenko VV, Tugarina MA, Potapov VV, Zaripov PM, Cheremnykh AS (2013) Interblock zones in the Earth crust of the south of East Siberia: Tectonophysical interpretation of geological and geophysical data [in Russian]. *Geodinamika Tektonofizika* 4(3):203–278
81. Shergina YP, Murina GM, Kozubova GA, Lebedeva VP (1979) Age and some genetic features of the Kunalei complex rocks in Western Transbaikalia from Rb-Sr data [in Russian]. *Dokl Akad Nauka SSSR* 246(5):1199–1202
82. Sklyarov EV, Mazukabzov AM, Mel'nikov AI (1997) Cordilleran metamorphic core complexes [in Russian]. Izd. SO RAN, NITs OIGGM, Novosibirsk
83. Swift CM (1967) A magnetotelluric investigation of an electrical conductivity anomaly in the Southwestern United States. Dissertation MIT, Cambridge
84. *The Mesozoic and Cenozoic Tectonics and Magmatism of Mongolia* [in Russian] (1975) Nauka, Moscow
85. *Thermal field bowels of Siberia* [in Russian] (1987) Novosibirsk, Nauka
86. Trapeznikov YA, Andreyeva EV, Batalev VY (1997) Magnetotelluric soundings in mountains of the Kyrgyz Tien Shan [in Russian]. *Fizika Zemli* 7:3–20
87. Tsekhovskii YG (2013) Sedimentology and volcanogenic-sedimentary formations in the Mesozoic and Cenozoic continental rift basins of the Baikal region and southern Mongolia [in Russian]. *Litol Pol Iskop* 2:145–186
88. Tsygankov AA (2005) Magmatic evolution of the Baikal-Muya Volcanoplutonic Belt in the Late Precambrian [in Russian]. Izd. SO RAN, Novosibirsk
89. Tsygankov AA, Mutukov DI, Berezhnaya NG, Larionov AN, Posokhov VF, Tsyrenov BTS, Khromov AA, Sergeev SA (2007) Late Paleozoic granitoids of western Transbaikalia:

- magma sources and stages of formation. *Russ Geol Geophys (Geol Geofiz)* 48(1):120–140 (156–180)
90. Tubanov CA, Tat'kov GI, Suvorov VD (2007) Seismicity of Central Baikal according to the local observation network [in Russian]. *Problemy sovremennoj sejsmologii i geodinamiki Central'noj i Vostochnoj Azii*. Irkutsk, vol 2, pp 179–181
 91. Van'jan LL, Gordienko VV Study of the asthenosphere [in Russian]. ELAS Project [in Russian]. *Vestnik Akademii Nauk SSSR*. № 9, pp 54–61
 92. Viktorova NV (2001) Geochemistry, mineralogy, and petrography of the Dzhida intrusive complex [in Russian]. In: *Geology, prospecting, and exploration of mineral deposits and geophysical methods. Selected papers of a scientific and technical conference (Irkutsk, April 12–1115, 2001)*. Izd. IRGTU, Irkutsk, Part 2, pp 44–59
 93. Vorontsov AA, Yarmolyuk VV (2004) Northern Mongolia-Western Transbaikalia polychromous rift system (stages of formation, magmatism, melt sources, geodynamics) [in Russian]. *Lithosphere* 3:17–32
 94. Vorontsov AA, Yarmolyuk VV (2007) The evolution of volcanism in the Tugnui-Khilok sector of the Western Transbaikalia rift area in the Late Mesozoic and Cenozoic [in Russian]. *Vulkanol Seismol* 4:3–29
 95. Vorontsov AA, Yarmolyuk VV, Baikin DG (2004) Structure and composition of the Early Mesozoic volcanic series of the Tsagan-Khurtei Graben (Western Transbaikalia): geological, geochemical, and isotopic data [in Russian]. *Geokhimiya* 11:1186–1202
 96. Vorontsov AA, Yarmolyuk VV, Lykhin DA, Dril' SI, Tatarnikov SA, Sandimirova GP (2007) Sources of magmatism and the geodynamics of formation of the Early Mesozoic Northern Mongolia-Western Transbaikalia Rift Zone [in Russian]. *Petrologiya* 15(1):37–60
 97. Yarmolyuk VV, Ivanov VG (2000) Magmatism and geodynamics of Western Transbaikalia in the Late Mesozoic and Cenozoic [in Russian]. *Geotektonika* 2:43–64
 98. Yarmolyuk VV, Kovalenko VI (2003) Batholiths and geodynamics of batholith formation in the Central Asian fold belt. *Geol Geofiz (Russ Geol Geophys)* 44(12):1305–1320. (1260-1274)
 99. Yarmolyuk VV, Budnikov SV, Kovalenko VI, Antipin VS, Goreglyad AV, Sal'nikova EB, Kotov AB, Kozakov IA, Kovach VP, Yakovleva ZS, Berezhnaya NG (1997) Geochronology and geodynamic position of the Angara-Vitim batholith [in Russian]. *Petrologiya* 5(5):451–466
 100. Yarmolyuk VV, Litvinovsky BA, Kovalenko VI, Jang BM, Zanvilevich AN, Vorontsov AA, Zhuravlev DZ, Posokhov VF, Kuz'min DV, Sandimirova GP (2001) Steps of formation and sources of alkaline-granitoid magmatism in the Northern Mongolia-Transbaikalia Rift Belt in the Permian and Triassic [in Russian]. *Petrologiya* 9(4):3351–3380
 101. Yarmolyuk VV, Kovalenko VI, Sal'nikova EB, Budnikov SV, Kovach VP, Kotov AB, Ponomarchuk VA (2002) Tectonomagmatic zoning, magmatic sources, and geodynamics of the Early Mesozoic Mongolia-Transbaikalia area [in Russian]. *Geotektonika* 4:42–63
 102. Yarmolyuk VV, Kovalenko VI, Sal'nikova EB (2003) Sources of igneous rocks and genesis of the Early Mesozoic tectomagmatic area of the Mongolia-Transbaikalia magmatic region [in Russian]. *Petrol Geokhimiya* 11(3):227–254
 103. Yas'ko VG (1982) Groundwater of intermontane depressions in Transbaikalia [in Russian]. Nauka, Novosibirsk
 104. Zharkov VN (1983) Interior structure of the earth and planets [in Russian]. Nauka, Moscow
 105. Zhavaronkin OV (2007) Morphostructure and neotectonic of the South of Western Transbaikalia [in Russian]. Candidate (Geol.-Mineral.) Dissertation, Saratov
 106. Zanvilevich AN, Litvinovsky BM, Andreev GV (1985) Mongolia-Transbaikalia Province of Alkaline and Peralkaline Granitoids [in Russian]. Nauka, Moscow
 107. Zverev VP (1982) A role of underground waters in migration of chemical elements [in Russian]. Nauka, Moscow
 108. Zverev VP (1999) Mass flows of the underground hydrosphere [in Russian]. Nauka, Moscow

109. Zverev VP (1982) A role of underground waters in migration of chemical elements [in Russian]. Nauka, Moscow
110. Zverev VP (2007) Groundwaters of earth crust and geological processes [in Russian]. Nauchniy mir, Moscow
111. Zverev VP (2011) Underground hydrosphere. Problems of fundamental hydrogeology [in Russian]. Nauchniy mir, Moscow
112. Zonenshain LP, Kuz'min MI, Natapov LM (1990) Tectonic of lithospheric plates in the territory of the USSR [in Russian], vol 2. Nedra, Moscow

Caucasian-Arabian Segment of Alpine-Himalayan Convergence: An Example of Continental Collision Above Mantle Plume



Evgenii V. Sharkov and Vladimir A. Lebedev

1 Introduction

The Caucasian-Arabian segment of the huge Cenozoic Alpine-Himalayan continental collision zone (belt) is located in its center, between Alpine and Himalayan parts of the belt (Fig. 1). The segment consists of two domains: the NW-SE-striking Greater Caucasus (GC) at the north and the Caucasian-Arabian Syntaxis (CAS) at the south. The Greater Caucasus is represented the south margin of the Eurasian plate (East-European Craton in this case), uplifted along the Main Caucasian Fault (MCF) ([15, 26], etc.). The latter is a part of modern super-regional deep-seated fault which stretches out from Kopetdag through Caspian Sea, Caucasus and Crimea. This megafault separates areas of Alpine convergence from Eurasian plate *sensu stricto* [24]. Very likely, that its further continuation is the Tornquist-Teisseyre Fault Zone (Trans-European Suture Zone) which divides East-European craton between Variscides and Alpides [1].

The CAS includes arc-like tectonic domains of the Lesser Caucasus and Eastern Anatolia which form transitional folded-thrusted belt (foreland) between Eurasian and Arabian plates, i.e. between the MCF in the north and Bitlis-Zagros Fault (BZF) in the south. A large NS-trending positive isostatic anomaly is characterized for CAS, which assumes presence of a mantle plume head beneath it which conforms with existence of modern plume-related volcanics here [24]. So, discussed below case, very likely, represents an example of continental convergence above a mantle plume head, and this work is devoted to geological-petrological features of such convergence.

E. V. Sharkov (✉) · V. A. Lebedev

Institute of Geology of Ore Deposits, Petrography, Mineralogy and Geochemistry RAS,
Moscow, Russia

e-mail: sharkov@igem.ru; lebedev@igem.ru

© The Author(s), under exclusive license to Springer Nature
Switzerland AG 2021

V. Svalova (ed.), *Heat-Mass Transfer and Geodynamics of the Lithosphere*,
Innovation and Discovery in Russian Science and Engineering,
https://doi.org/10.1007/978-3-030-63571-8_21

381

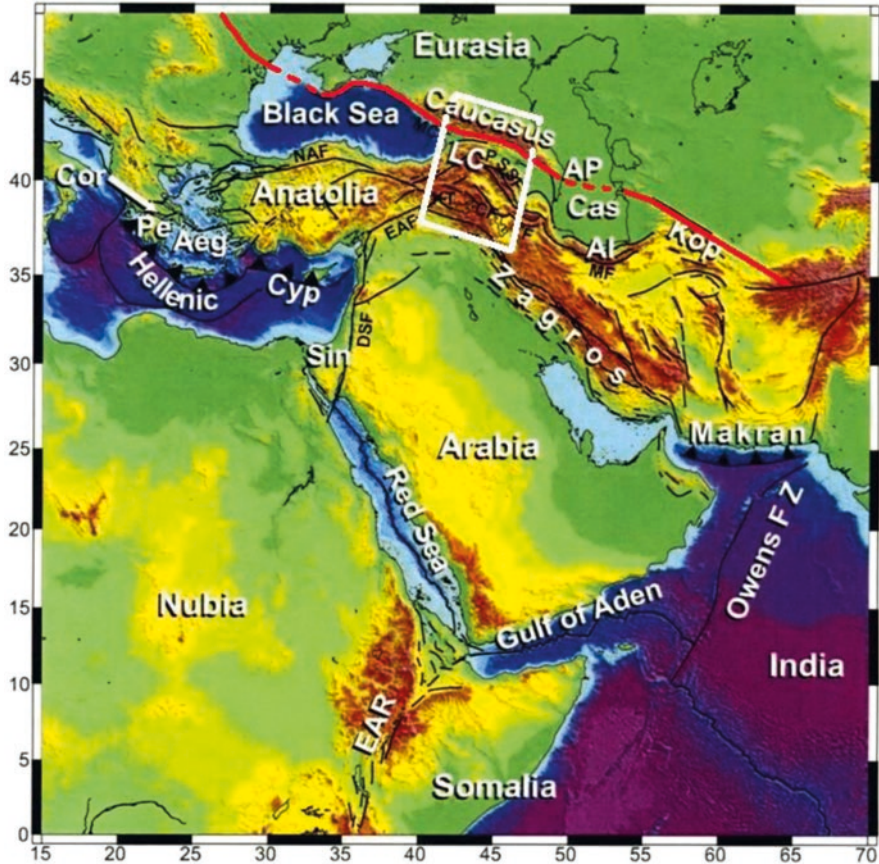


Fig. 1 Location of the Caucasian-Arabian part of the Alpine-Himalayan Convergence with the use of the scheme from [21]. Red line – the Kopetdag-Caucasus-Trans-European Suture megafault (see text)

2 Geological, Petrological and Geophysical Data

2.1 Geological Features

The modern (Alpine) structure of the Caucasus is formed by NS horizontal compression generated by interaction of two plates: the Arabian indenter and the East European Craton. In the late Cenozoic this plate interaction resulted in the transverse shortening of the CAS up to 400 km, mainly at the expense of the territory south to the Main Caucasian Fault (MCF) [2, 15]. Many scientists believe that the MCF is due to the overthrust or underthrust of the Transcaucasian massif under the Greater Caucasus, e.g. Khain [11], Saintot et al. [23], Forte et al. [8], Mosar et al. [17]; etc. However, direct geological observations suggest the linear shape of the

fault, as well as rather steeply dipping imbricate structures and/or reverse faults. In addition, geophysical data suggest a steep or vertical angle of the MCF up to depths of 70–80 km ([15, 22, 25], etc.). So, we accept that the MCF is a reverse fault with a large rate of vertical displacement and minimal horizontal displacement.

In this case, the shortening south of the MCF could result from a lateral “diffuence” or “spreading” of lithospheric material under the push of the Arabian indenter in two opposite directions away from the GC in front of the rigid East European Craton (Fig. 1). More evidence for this comes from geological [12] and GPS data from the zone of the Africa-Arabia-Eurasia continental collision [20]. We suggest that the convergence of Arabia and Eurasia resulted in lithosphere shortening and bi-lateral transportation of excessive lithosphere material, i.e., its “diffuence” both to the south-west and south-east the CAS, which formed the tectonic sheets of the eastern Asia Minor Peninsula and Zagros Mountains, respectively (Fig. 2). Obviously, the removal of a significant part of the basement in front of the MCF can be responsible for the difference between the structures of the northern and southern Caucasian domains.

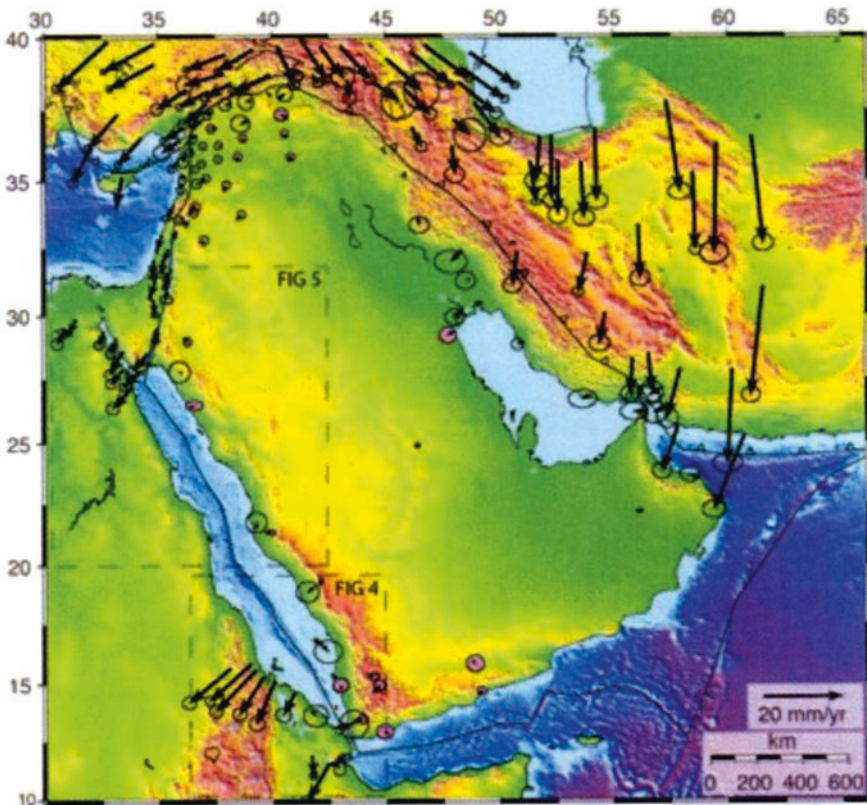


Fig. 2 Diffuence of material of Arabian plate in front of rigid East-European Craton [18]

2.2 Deep-Seated Structure of the Region

Arabian-Caucasus Syntaxis is characterized by high seismicity. Shallow focuses sharply predominate and very rare relatively deep earthquake (up to 120–140 km) found mainly on north-east of region, aside of the area of modern magmatism [24]. The seismic data available do not reveal subduction zone beneath the Greater Caucasus, although some earthquake's hypocentral depths can reach 175 km ([9]). While, beneath transitional fold and thrust zone between north margin of Arabian plate (BZF) and the Greater Caucasus north-directed seismic zones occurred which are traced up to 50–70 km depth. Judging on seismic data, descending tongue-like ledges of crustal material pushed into the mantle plume head [24]. They look like possibly peculiar “embryonic” subduction zones, where crustal material involves in descending currents (Fig.3). From such viewpoint mention above shortening of the CAS (~400 km) was due to two major mechanisms: (1) the south-directed tectonic “diffluence” of crustal material apart from the Arabian indenter, in front of the East European Craton, and (2) involving another part of crustal material in the north-directed descending flows of such material beneath the folded-thrusted belt.

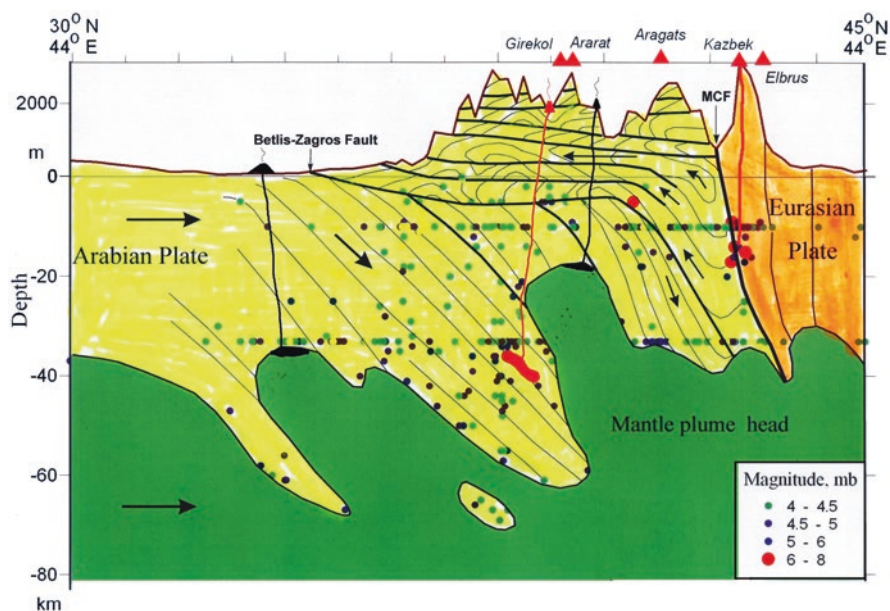


Fig. 3 Schematic structure of zone of Arabian-Eurasian convergence and magma-forming processes beneath it

2.3 *Modern Volcanism*

The CAS includes Neogene-Quaternary volcanic belt, which is extended from Eastern Anatolia via the Lesser Caucasus up to the Great Caucasus. The belt is composed by two types of volcanics: (1) extensive plateau basalts possessing geochemical characteristics of intra-plate (plume-related) rocks, and (2) calc-alkaline volcanics, which are petrologically and geochemically close to those formed in a suprasubduction setting (Fig. 3). Isotopic-geochemical data evidence that both types of magmatism contaminated by each other material ([13, 14, 18, 19], etc.). So, two independent types of magmatism are developed in zone of Arabian-Eurasian collision, i.e. specific type of “mixed” magmatism occurred here.

Mentioned above positive isostatic anomaly in fold-thrusted zone can evidence about presence of a mantle plume beneath the CAS. It is in a good agreement with existence of flood basalts here, which are considered to adiabatic melting of local ledges on the plume head. In other words we suggest that calc-alkaline volcanics, apparently, derived from “embryonic” subduction zones. Fragments of these rocks, represented by heavy garnet granulites and eclogites, can, very likely, sink into hot plume head material and dissolve in it. As a result, newly-formed plume-derived magmas of basaltic plateaus were contaminated by crustal material. Calc-alkaline melts, in own turn, can be partly contaminated by mantle-derived magmas in such dynamic occurrence.

Magmatism, very probably, appeared as a result of two kinds of independent processes: (1) adiabatic melting in the upper parts of ledges on the mantle plume’s surface, generated flood basalts, and (2) calc-alkaline melts occurred in the “embryonic subduction zones” between them due to intense high pressure heat-generated deformations of continental crust in the zone of plates collision. We suggest that fragments of these rocks, represented by heavy garnet granulites and eclogites, can sink into hot plume head material and dissolve in it. As a result, newly-formed plume-derived magmas of basaltic plateaus were contaminated by crustal material. Calc-alkaline melts, in its turn, can be partly contaminated by mantle-derived magmas in such dynamic occurrence.

3 Discussion

Zone of Arabian-Eurasian convergence is located on the north termination of large belt of Cenozoic basaltic plateaus which develops along all west margin of Arabian Plate (Afro-Arabian LIP [6, 7, 28], and stretch out like an “arm” from Afar Hot Spot (Fig. 4). Because such type of magmatism is considered with adiabatic melting of the mantle plume matter, we suggest that this belt reflect morphology of the crest of a large mantle plume head and basaltic volcanism outlines its contour in projection to the surface. So, the plume head has elongated shape here (~3500 km long at 300–400 km wide) and goes from Gulf of Aden up to the Greater Caucasus. It looks



Fig. 4 Distribution of the modern plume-related volcanism in the Afro-Arabian LIP up to the Greater Caucasus. Black line – contour of projection of proposed mantle plume head to the surface. The fields painted by black represent the areas of young volcanic activity (composed by V. Lebedev)

The largest Quaternary volcanoes: A Ararat, Ar Aragats, CMW Caucasian Mineral Waters, E Elbrus, Er Ercies, K Kazbek, N Nemrut, S Savalan, Sa Sahand, Su Suphan, T Tendürek

like sublithospheric flow in the mantle which gradually moves from Afar via Arabia to the north ([27]; Sharkov, Lebedev 2017). According to [27], variations in a rate of this flow in different epochs are from 4 to 12 cm/yr., about 8 cm/yr. on average.

Judging on aforementioned geological, petrological, geochronological and geophysical data, magmatism CAS, in essence, is a part of Afro-Arabian LIP, which developed above the northern termination of the same Afro-Arabian mantle plume but already evolved under specific dynamic conditions of the collision zone.

According to the seismic tomography data [27], this plume is generated at the core-mantle boundary, ascend throughout the mantle and at depths of 70–100 km its head begins spread in the north direction (Fig. 5). Judging on aforementioned geological, petrological, geochronological and geophysical data, magmatism CAS, in essence, is a part of Afro-Arabian LIP, which developed above the northern termination of the same Afro-Arabian mantle plume but already evolved under specific conditions of collision zone. We suggest that northern end of plume-related sublithospheric (within-lithospheric) mantle flow from Afar finally reached the already existed southern tectonic border of the East European Craton, partly “dives” under it and lifts its margin, forming the Greater Caucasus Range. So, situation in this case was reverse to hot-spot: hot plume material flowed beneath stable lithosphere instead of lithospheric plate shift above stable hot-spot.

The beginning of igneous activity in this volcanic belt is in concordance with the first stages of spreading of the Red Sea (~30 Ma; [4]) and its activity has continued till historical time. On the basis of incompatible trace element content, the volcanic activity in Syria can be divided into two stages: the first lasting from ~26 to ~6 Ma and the second from ~6–5 Ma to historical times [16, 28]. This temporal change in composition of magmas is related to major tectonic re-organization of the region occurred during upper Miocene and dates for beginning of Arabia-Eurasia collision. Very probably that a new portion of fresh material arrived to the plume head, which was allowed to the plume head continue its motion to the north. From these data follow that the Afro-Arabian mantle plume exists already 30 Myr and periodically was supplied with pulses of fresh plume material which provided stable composi-

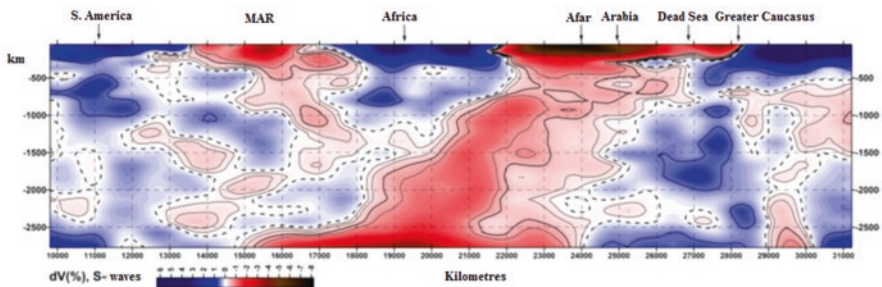


Fig. 5 Section δV of NGRAND seismic tomographic model [3, 10] based on S -waves from mantle roof to its base from western coast of South America across Atlantic Ocean, Africa, and Arabia to East European Platform. Zero isoline is shown by dotted line. After [27]

tion of basaltic lava on all distance of the “arm”. Basaltic plateaus, which trace a crest of this flow, very likely, mark location of “fingers” (local plumes) at its surface.

The CAS is located at the north termination of this belt. Judging on geophysical and petrological data, the north continuation of the Afro-Arabian mantle plume “dive” under the Main Caucasus Fault [24]. It was led to lifting of the Greater Caucasus and provided appearance of the Caucasian Mineral Vody igneous complex as well as Elbrus and Kazbek volcanoes. Pb-isotopic data evidence about presence of material of the Afar Hot Spot in the Elbrus’s volcanics [5]. The deepest earthquakes beneath the GC are, probably, considered with dynamic processes below Afar-Caucasus mantle flow.

4 Conclusions

1. The Caucasian-Arabian segment of the huge Cenozoic Alpine-Himalayan collision belt consists of two domains: the NW-SE striking Greater Caucasus (GC) at the north and the Caucasian-Arabian Syntaxis (CAS) at the south. GC, in essence, represent uplifted along the Main Caucasian Fault southern margin of the East-European Craton, whereas CAS includes tectonic domains of the Lesser Caucasus and Eastern Anatolia; it is characterized by large NS-trending positive isostatic anomaly, which suggests presence of a mantle plume head beneath it.
2. The Alpine (late Cenozoic) structure of the Caucasus formed by NS horizontal compression generated by interaction of two plates: the Arabian indenter and the Eurasian Plate (East-European Craton in this case). GS, in essence, represent southern margin of the East European Craton, uplifted along the Main Caucasian Fault (MCF), whereas the CAS includes tectonic structures of the Lesser Caucasus and Eastern Anatoly, which form transitional which resulted in appearance of transitional vast fold-thrusted belt. Its formation accompanied by transverse shortening of territory up to 400 km, mainly at the expense of the CAS.
3. Subduction zone, as such, is absent beneath the GC. However, some north-directed seismic zones occurred beneath transitional fold-thrusted zone between Arabian plate (Bitlis-Zagros Fault) and the MCF, which trace up to 50–70 km depth and look like possibly peculiar “embryonic” subduction zones. We assume that mention above shortening occurred due: (1) the tectonic “difffluence” of crustal material apart from the Arabian indenter, in front of the East European Craton, and (2) involving another part of crustal material in descending flows.
4. The CAS includes the Neogene-Quaternary volcanic belt, which is extended from Eastern Anatolia to the Lesser Caucasus and farther to the Greater Caucasus. The belt is dominated by two types of volcanic rocks: (1) extensive basalt plateaus possessing geochemical characteristics of plume-related rocks, and (2) calc-alkaline volcanics, which origin we considered with “embryonic” subduction zones; their origin we consider with “embryonic” subduction-like structures.

5. The Caucasian-Arabian segment of the Alpine-Himalayan convergence zone is located at the north termination of the Afro-Arabian LIP and has developed in specific tectonic conditions of continental collision above modern mantle plume.

The authors declare that the chapter has no conflict of interests.

References

1. Artemieva IM, Thybo H, Kaban MK (2006) Deep Europe today: geophysical synthesis of the upper mantle structure and lithospheric processes over 3.5 Ga. In: Gee DG, Stephenson RA (eds) *European lithosphere dynamics*, vol 32. Geological Society of London Memoir, pp 11–42
2. Bazhenov ML, Burtman VS (1990) Structural arcs of Alpine Belt (Carpatian, Caucasus, Pamir). Nauka Publications, Moscow, p 167. (in Russian)
3. Becker TW, Boschi L (2002) A comparison of tomographic and geodynamic mantle models. *Geochem Geophys Geosyst* 3. <https://doi.org/10.1029/2001GC000168>
4. Camp VE, Roobol MJ (1989) The Arabian continental alkali basalt province. *Geol Soc Amer Bull* 101:71–95
5. Chugaev FV, Chernyshev IV, Lebedev VA, Eremina AV (2013) Isotopic composition of plumbum and origin of Quaternary lavas of Elbrus volcano (greater Caucasus, Russia): data of high-precisions MC-ICP-MS method. *Petrology* 21:16–27
6. Eppelbaum LV, Katz YI (2017) A new regard on the tectonic map of the Arabian-African region inferred from the satellite gravity analysis. *Acta Geophys* 65:607–626
7. Ernst RE (2014) *Large Igneous Provinces*. Cambridge University Press, Cambridge
8. Forte AM, Cowgill E, Bernardin T, Kreylos O, Hamann B (2010) Late Cenozoic deformation of the Kura fold-thrust belt, Southern Greater Caucasus. *GSA Bull* 122(3/4):465–486. <https://doi.org/10.1130/B26464.1>
9. Godoladze T, Sandvol EA, Mackey KG et al (2018) The Caucasian seismic network (CNET): seismic structure of the Caucasus. *Geophys Res Abstracts* 20:EGU2018-19744. EGU General Assembly 2018
10. Grand SP, van der Hilst RD, Widiyantoro S (1997) Global seismic tomography: a snapshot of convection in the earth. *GSA Today* 7(4):1–7
11. Khain VE (1984) *Regional Geotectonics. Alpien-Mediterranean Belt*. Moscow, Nedra, 344 p. (in Russian with English abstract)
12. Kopp ML (2007) Late alpine collisional structure of Caucasus region. In: Leonov YG (ed) *Alpine history of the great Caucasus*. GEOS, Moscow, pp 285–316. (in Russian)
13. Lebedev VA, Chernyshev IV, Sharkov EV (2011) Geochronological scale and evolution of late Cenozoic magmatism within Caucasian segment of the Alpine Belt. *Dokl Earth Sci* 441(2):1656–1660
14. Lebedev VA, Sharkov EV, Unal E, Keskin M (2016) Late Pleistocene Tendurek volcano (eastern Anatolia, Turkey): II. Geochemistry and Petrogenesis of the rocks. *Petrology* 24(3):234–270
15. Leonov YG (2007) Cimmerian and late alpine tectonics of the greater Caucasus. In: Leonov YG (ed) *Alpine history of the great Caucasus*. GEOS, Moscow, pp 317–340. (in Russian)
16. Lustrino M, Sharkov E (2006) Neogene volcanic activity of western Syria and its relationship with Arabian plate kinematics. *J Geodynamics* 42:115–139
17. Mosar J, Mauvilly J, Enna N et al (2018) The greater Caucasus: a new tectonic map! *Geophys Res Abstracts* 20:EGU2018-7934. EGU General Assembly 2018

18. Oyan V, Keskin M, Lebedev VA, Chugaev AV, Sharkov EV, Ünal E (2017) Petrology and geochemistry of the quaternary mafic volcanism in the north-eastern branch of Lake Van, Eastern Anatolian collision zone, Turkey. *J Petrology* 58(9):1701–1728
19. Pearce JA, Bender JF, De Long SE, Kidd WSF, Low PJ, Guner Y, Saroglu F, Yilmaz F, Moorbath S, Mitchell JG (1990) Genesis of collision volcanism in Eastern Anatoly, Turkey. *J. Volcan. Geotherm. Res.* 44:189–229
20. Reilinger R, McClusky S (2011) Nubia-Arabia-Eurasia plate motions and the dynamics of Mediterranean and Middle East tectonics. *Geophys J Int* 186:971–979
21. Reilinger R, McClusky S, Vernant P, Lawrence S, Ergintav S, Cakmak R, Ozener H, Kadirov F, Guliev I, Stepanyan R, Nadariya M, Hahubia G, Mahmoud S, Sakr K, ArRajehi A, Paradissis D, Al-Aydrus A, Prilepin M, Guseva T, Evren E, Dmitrotsa A, Filikov V, Gomez F, Al-Ghazzi R, Karam G (2006) GPS constraints on continental deformation in the Africa-Arabia-Eurasia continental collision zone and implications for the dynamics of plate interactions. *J Geophys Res* 111:B05411
22. Rogozhin EA, Gorbatikov AV, Stepanova MY, Ovsyuchenko AN, Kharazova YV, Andreeva NV (2015) Structure and modern geodynamics of the greater Caucasus in the light of new data on its deep-seated structure. *Geotectonics* 2:36–49
23. Saintot A, Brunet M-F, Yakovlev F, Sebrier M, Stephenson R, Ershov A, Chalot-Prat F, McCann T (2006) The Mesozoic-Cenozoic tectonic evolution of the great Caucasus. In: Gee DG, Stephenson RA (eds) *European lithosphere dynamics*, vol 32. Geological Society of London Memoir, pp 129–145
24. Sharkov E, Lebedev V, Chugaev A, Zabarinskaya L, Rodnikov A, Sergeeva N, Safonova I (2015) The Caucasian-Arabian segment of the alpine-Himalayan collisional belt: geology, volcanism and neotectonics. *Geosci Front* 6:513–522
25. Shempelev AG, Prutsky NI, Kukhmazov SU Materials of geophysical investigation along Near-Elbrus profile (volcano Elbrus-Caucasian Mineral Waters). In: *Tectonics of the Earth's crust and mantle. Proceedings of XXXVIII Tectonic Meeting. GEOS, Moscow*, pp. 361–365 (in Russian)
26. Somin ML (2007) Main features of structure of the pre-alpine basement of great Caucasus. In: Leonov YG (ed) *Alpine history of the great Caucasus. GEOS, Moscow*, pp 15–38. (in Russian)
27. Trifonov VG, Sokolov SY (2017) Sublithospheric flows in the mantle. *Geotectonics* 51(6):535–548
28. Trifonov VG, Dodonov AE, Sharkov EV, Golovin DI, Chernyshev IV, Lebedev VA, Ivanova TP, Bachmanov DM, Rukieh M, Ammar O, Minini H, Al Kafri A-M, Ali O (2011) New data on the late Cenozoic basaltic volcanism in Syria, applied to its origin. *J Volcan Geotherm Res* 199:177–192

Geothermics and Seismicity of the Caucasus Region and the Inverse Problem of Geodynamics



Valentina Svalova

1 Introduction

The origin and evolution of geological structures could be a clue for understanding the crust-mantle interaction. For a simulation of the evolution of geological processes and geological structures in connection with deep mantle movements, all possible geological-geophysical data were combined and analysed and the mechanical-mathematical models were used. In making analytical decision, it is possible to find the critical parameters of the problem. After defining boundary conditions on the uppermost surface, it is possible to make some conclusions about deep movements in the lithosphere [8, 11, 12, 15, 21].

One of the most interesting problems arising in the mechanical-mathematical modelling of the formation and evolution of geological structures is the description of matter behaviour above a rising mantle plume and a mantle diapir. A super plume is associated with super structures, such as continents and oceans. A diapir is responsible for geological structures, such as basins, orogenes and others [1–3, 8–10, 13–18, 21].

During many years of geological modelling, many interesting problems were solved. But the interest in superplumes, plumes and diapir modelling only increases.

One of the reasons is that mantle upwelling is associated with tectono-magmatic activation and the geothermal regime of the lithosphere.

The problem of the relationship between heat flow and the age of the last tectonic event is not yet decided.

Additional stimuli for the investigation of diapirs is the development of seismotomography. The possibility to “see” a mantle plume increases the pressure to research different geological structures connected with plumes [3, 4, 7].

V. Svalova (✉)
IEG RAS, Moscow, Russia

2 Geodynamics of the Caucasus Region

Analysis of geological and geophysical data on the development of the Caucasus region within the Alpine-Himalayan belt leads to the conclusion that the Caucasus can be considered as one of the most stressed and geodynamically active segments of the global structure, characterized by increased heat flow, high seismicity, magmatism and volcanism [1, 5, 18, 20].

From the point of view of deep geodynamics, the Caucasus is one of the most active zones of collision of lithospheric plates, characterized by significant speeds of horizontal and vertical movements (Fig. 1) [1, 20].

The velocity field of the North Caucasus is characterized by horizontal displacement in the northeast direction at a speed of 26–28 mm/year. Relatively motionless Eurasia, a general compression of the region was revealed at a speed of 1–2 mm/year, which is the source of modern geological and seismic activity in the border region of the Caucasus and the East European platform.

Modern vertical movements of the North Caucasus region are characterized by small vertical movements of 2.5 mm/year in the lowland of Ossetia, the highest ascent rates for the region of about 3.5–4.5 mm/year in the mountainous part of the North Caucasus, and moderate steady rise of 2.9 mm/year in the northern part of the northern slope of Greater Caucasus [5].

According to geodynamic ideas, on the site of the Greater Caucasus 35 million years ago there was a deep-water basin about 200 km wide. With the gradual closure of its sides, they approached until a complete collision about 11 million years ago, after which the region began a constant uplift. During compression, the lithosphere material formed a mountain belt with a crust thickness of 45–50 km and a lithosphere thickness of up to 250 km. Later, 5–10 million years ago, the Greater Caucasus began to rise rapidly, and volcanoes Elbrus, Kazbek, and others arose on its axis [3]. Apparently, this is due to the rise of the asthenosphere due to compression and gravitational instability.

The structure of the Alpine zone includes individual sea depressions, sedimentary basins and mountain formations. Above the rising mantle diapirs on the Earth's

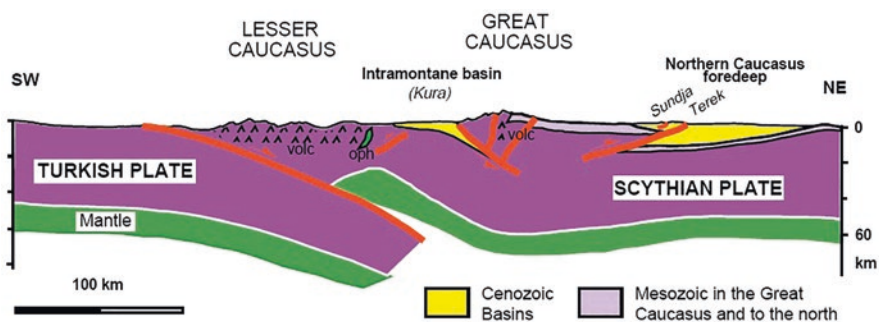


Fig. 1 Schematic cross section through Caucasus

surface, the structures of the arched uplift, sedimentary basin, or the outflow of basalts can form, depending on the stage of diapir uplift and its energy [8, 11, 12, 15, 21]. At the same time, compression zones are formed between the individual diapirs, leading to mountain building and thickening of the crust. So the depressions of the western sector of the Alpine-Himalayan belt (Alboran, Balearic, Tyrrhenian, Ligurian, Pannonian, Ionian, Black Sea, Pre-Caspian Depression, Middle and South Caspian) can be associated with rising mantle diapirs, and the Caucasus not only with the zone of collision of lithospheric plates but also with the zone of collision of lithosphere flows from two mantle diapirs beneath the hollows of the Black and Caspian Seas.

The complex stress-strain state of the lithosphere of the Caucasus is expressed in the presence of faults, fracturing of rocks, manifestation of magmatism and volcanism, high seismicity, increased heat flow, hydrothermal activity, and is also confirmed by seismic data and seismotomography.

3 Geothermy of the Caucasus Region

The value of the heat flux density is an indicator of the geodynamic activity of the structures of the lithosphere. Comparison of the heat flux density with the thickness of the Earth's crust gives mixed results. For individual blocks of the cortex, there is a direct connection of these parameters, for others, the inverse one. Feedback is more common when a thin crust corresponds to a high heat flux. This is explained by the removal of deep heat by the mantle diapir with the formation of a zone of extension and thinning of the crust. An example of a direct connection is the basin of the Black Sea with a thin earth crust. In this structure, low values of the heat flux (30–40 mW/m²) with a low power of the Earth's crust are noted [6, 19]. This may be explained by avalanche sedimentation and the more complex geodynamics of the structure.

Another situation with a high heat flux is observed in orogenic regions with a thick crust, for example, in the Himalayas, meganticlinoria of the Greater Caucasus, etc. The high heat flux here is due to the high geodynamic activity of the asthenosphere, manifested by magmatism and geothermal activity.

The Caucasus region is characterized by a complex and highly differentiated thermal field. Reduced flows correspond to foothill and intermountain troughs, elevated folded zones. The average heat flux for the folded region of the Caucasus is 78 mW/m² [6, 19].

The nature of the thermal field of the Caucasus region correlates well with the features of its geological structure and development history. Zones of folding and manifestations of young volcanism are distinguished by high heat fluxes. Piedmont and intermountain troughs correspond mainly to low heat fluxes. The structure of the sedimentary cover and the structure of the foundation have a significant effect on the nature of the thermal field.

4 Description of the Model

For simulation of the formation and evolution of geological structures, a roof and base surface of the lithosphere can be considered as the top and bottom boundaries of the simulation, where the boundary and initial conditions of a problem depend on a particular statement. Boundary conditions on the uppermost surface are much more reliable owing to the greater security of an authentic geological-geophysical material. The system JPS gives the information on the surface motion. The geologic data make an invaluable contribution to the representation of the relief motion.

The geothermal, geomagnetic, and gravitational fields give additional information about the formulation of boundary conditions on the Earth's surface. On one hand, the internal seismic boundaries in the stratified lithosphere monitor reference marks of simulation, and on the other hand, these boundaries are the outcome of simulation, when the suppositions about the previous system conditions result in a modern picture of a geologic pattern with the applicable geophysical fields.

The solution of inverse problem of geophysics, as it is known, is ill-defined problem. The forecasting of the internal constitution and plutonic characteristics of shells of the planet under the geophysical surface data is a complicated mathematical problem, influenced by the approach of different authors. The mechanical behaviour and transformation of matter at depth fundamentally determines the surface structure of geophysical fields.

So the rise of the molten mantle diapir, achievement of a level of buoyancy, and the cooling and crystallization of matter change temperatures, gravitational and magnetic fields. An analysis of the legitimacy of such connections is an indispensable stage of the geological-geophysical data and the outcomes of simulation. In this way, special concerns introduce the solution of an inverse geodynamical problem when under the geological-geophysical data on a surface it is possible to forecast the behaviour of matter at depth.

There are two standard ways to solve inverse problems – the regularization method, when the parameters of the solution of specific limitations are superimposed, and the approach method, when an inverse problem is decided by the solution of many direct problems.

The most interesting feature is the capability of the direct method to solve inverse problems of geodynamics when using reliable geological-geophysical surface data enables us to forecast behaviour of matter at depth in a unique manner.

Let us consider the behaviour of a layer of high-viscosity, incompressible fluid describing behaviour of matter of the lithosphere [8, 11, 12, 15, 21]. Let us the characteristic size of modelled patterns on lateral L considerably surpasses characteristic thickness of the layer h . Then using an equation of continuity and an approximated equation of the Navier-Stokes for enough slow motions in a thin layer, it is possible to obtain in a dimensionless form for a two-dimensional case [8, 11, 12, 15, 21]:

$$\begin{cases} \frac{\partial P}{\partial X} = \alpha \mu \frac{\partial^2 U}{\partial Z^2} \\ \frac{\partial P}{\partial Z} = -\rho \end{cases} \tag{1}$$

$$\frac{\partial U}{\partial X} + \frac{\partial W}{\partial Z} = 0 \tag{2}$$

$$\alpha = \frac{F}{R \left(\frac{h}{L}\right)^3}, F = \frac{u_0^2}{gL}, R = \frac{u_0 L \rho_0}{\mu_0} \tag{3}$$

Here P is pressure, U, W – velocities, F – Frude number, R – Reynolds number, ρ – density, μ – viscosity, ρ_0, μ_0, u_0 – scales of density, viscosity and velocity.

The forces on the high boundary are equal zero (free surface). Let the velocities U^*, W^* on the high boundary of simulation ζ^* are known. Then it is possible to find the velocity distribution and pressure in the layer:

$$P = \rho (\zeta^* - Z) \tag{4}$$

$$U = U^* + \frac{\rho}{2\alpha\mu} \frac{\partial \zeta^*}{\partial X} (\zeta^* - Z)^2 \tag{5}$$

$$W = W^* + \frac{\partial U^*}{\partial X} (\zeta^* - Z) + \frac{\rho}{2\alpha\mu} \left[\frac{\partial^2 \zeta^*}{\partial X^2} \frac{1}{3} (\zeta^* - Z)^3 + \left(\frac{\partial \zeta^*}{\partial X}\right)^2 (\zeta^* - Z)^2 \right] \tag{6}$$

On the high boundary, the kinematic condition of a free surface should also be executed. This means that points of a surface will not escape it during motion:

$$S \frac{\partial \zeta^*}{\partial t} + U^* \frac{\partial \zeta^*}{\partial X} - W^* = 0 \tag{7}$$

$$S = \frac{L}{u_0 t_0} \tag{8}$$

Here S is the Strukhal number. t_0 is the scale of time.

Similarly it is possible to consider the lower boundary of simulation as a surface where the points remain during the evolutionary process (the condition of non-penetration). Then, substituting velocities, we get an equation of movement for the lower boundary ζ :

$$S \frac{\partial \zeta_*}{\partial t} - W^* + U^* \frac{\partial \zeta_*}{\partial X} (\zeta^* - \zeta_*) + \frac{\rho}{2\alpha\mu} \left[\frac{\partial \zeta_*}{\partial X} \frac{\partial \zeta^*}{\partial X} (\zeta^* - \zeta_*)^2 - \frac{\partial^2 \zeta^*}{\partial X^2} \frac{1}{3} (\zeta^* - \zeta_*)^3 - \left(\frac{\partial \zeta^*}{\partial X} \right)^2 (\zeta^* - \zeta_*)^2 \right] = 0 \quad (9)$$

The given equation represents the direct solution of an inverse problem when a relief of the uppermost surface and velocities on it determine the geodynamics of the deep boundaries. A similar equation can be written for any material boundary at depth through which the flow of matter is absent.

5 The Analysis of the Obtained Solution

Thus, setting the motion of the upper surface, we have an equation of motion for the deep boundaries.

Some conclusions about the structure of deep motion on known speeds and relief of a surface can be made by analysing the velocity distribution at depth.

Let us consider some typical cases of formation and evolution of the geological structures.

5.1 Case 1. Sedimentary Basin Under Stretching Surface Conditions

Uppermost surface is concave, that is $\frac{\partial^2 \zeta^*}{\partial X^2} > 0$.

$\text{Sgn } U^* = \text{Sgn } X$.

Analysis shows that U increases with depth and with $\text{grad} \zeta^*$.

W describes rising flux at depth.

5.2 Case 2. Sedimentary Basin Under Pressing Surface Conditions

Uppermost surface is concave, that is $\frac{\partial^2 \zeta^*}{\partial X^2} > 0$.

$\text{Sgn } U^* = - \text{Sgn } X$.

Analysis shows that critical depth exists where horizontal pressing is changed by stretching:

$$\zeta_* = \zeta^* - \sqrt{-\frac{U^*}{\frac{\rho}{2\alpha\mu} \frac{\partial \zeta^*}{\partial X}}} \tag{10}$$

W can be positive or negative, depending on the relationship between task parameters. But in the center of the structure, W is positive (uprising).

In a stretching basin, the uprising flux at depth is more intensive.

5.3 Case 3. Orogene Under Stretching

Uppermost surface is convex, that is $\frac{\partial^2 \zeta^*}{\partial X^2} < 0$.

$\text{Sgn } U^* = \text{Sgn } X$.

Hence, a critical depth exists where stretching is changed by pressure:

$$\zeta_* = \zeta^* - \sqrt{-\frac{U^*}{\frac{\rho}{2\alpha\mu} \frac{\partial \zeta^*}{\partial X}}} \tag{11}$$

Analysis of W shows descending flux in the center of the structure at depth.

If stretching is intensive, the uprising flux can exist.

5.4 Case 4. Orogene Under Pressure

Uppermost surface is convex, that is $\frac{\partial^2 \zeta^*}{\partial X^2} < 0$.

$\text{Sgn } U^* = - \text{Sgn } X$.

In this case, pressure is in whole layer. Descending flux at depth exists with high probability.

Preliminary analysis shows that a stretching basin and an orogene under pressure are more stable structures than basin under pressure and orogene undergoing stretching.

It is possible to forecast deep movements in the lithosphere if the geodynamics of the uppermost surface are known. Complex interpretation of geological-geophysical data, together with mechanical-mathematical modelling, are effective instrument to explain the evolution of geological structure.

The collision of lithospheric plates is determined by the collision of deep asthenospheric flows. Plates move due to movements in the asthenosphere. The geodynamics of the collision zone of asthenospheric flows is determined by the ratio of the density, viscosity, and temperature of the layers of the lithosphere and

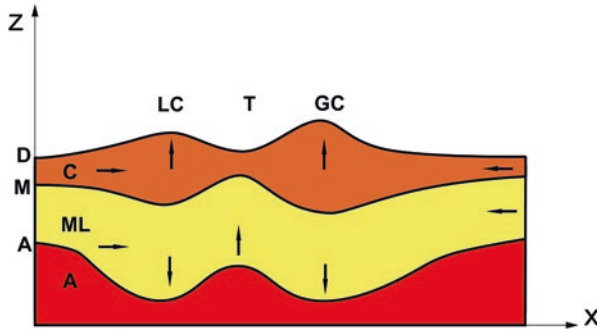


Fig. 2 Schematic cross-section of the Caucasus region on the base of mechanical-mathematical modeling

D upper surface, *M* Moho boundary, *A* asthenosphere surface, *C* crust, *ML* mantle lithosphere, *LC* Lesser Caucasus, *GC* Great Caucasus, *T* Caucasus Trough. Arrows – possible directions of the matter movements

asthenosphere. The same relations determine how intensively the lithosphere plate overlaps the rise of the asthenosphere and how fast the asthenosphere diapir rises in the collision zone, forming the structure of back-arc spreading or thickening of the asthenosphere and rise of the lithosphere. The complex geodynamic picture is determined by the ratio of geological and geophysical parameters and external limiting factors for speeds and motions on the spherical surface of the Earth and in its depths.

So, based on the analysis of the obtained relations for surface movements, we can speak of the presence of downward movements in the lithosphere with the immersion of the bottom of the lithosphere under mountain structures, which can be the case in the Caucasus.

Thus, in the Caucasus region, at the bottom of the lithosphere, downward flows of matter and subsidence of the lithosphere must exist (Fig. 2).

It is interesting to compare the results of mechanical-mathematical modeling with the data of geological and geodynamic reconstruction and seismotomography (Fig. 3) [4].

6 Conclusions

Schematic cross-section of the Caucasus region on the base of mechanical-mathematical modeling.

D – upper surface, *M* – Moho boundary, *A* – asthenosphere surface, *C* – crust, *ML* – mantle lithosphere, *L* – Lesser Caucasus, *G* – Grate Caucasus, – Caucasus Trough. Arrows – possible directions of the matter movements. Solution of the inverse problem of geodynamics by the direct method is proposed and developed. The first inverse problem of geodynamics is solved – the restoration of the velocity,

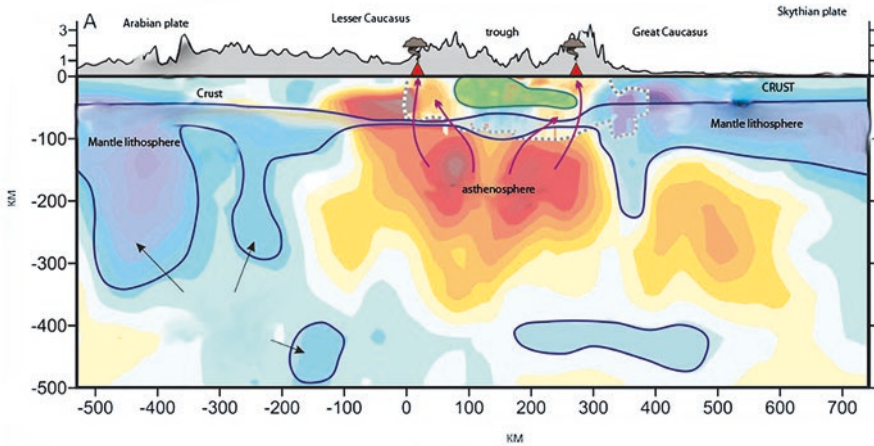


Fig. 3 Seismotomographic cross-section of the Caucasus region
 Lesser Caucasus, Great Caucasus, Caucasus Trough
 Red and yellow – asthenosphere, dark blue – mantle lithosphere, light blue – crust, green – higher density crust

pressure and stress fields at the depth of the lithosphere from the available data on the velocities on the day surface. The second inverse problem of geodynamics is posed and solved – the determination of the movement of boundaries at the depth of the lithosphere by the given movements of the day surface. The obtained solutions can be used to analyze deep geodynamic problems, and together with geothermal modeling, geological and geophysical methods and seismotomography can serve as a reliable tool for studying the deep geodynamics of geological structures and forecasting oil and gas potential.

It should be understood that geophysics and seismotomography give a deep section at present time, while mechanical and mathematical modeling allows us to study the evolution of the structure in dynamics. A comparative analysis of various approaches and solutions makes it possible to more reliably draw conclusions about the underlying mechanisms of movements and their manifestation on the Earth’s surface and substantiate the most probable reasons for the formation and evolution of various geological structures and processes.

There is no conflict of interests in the chapter.

Acknowledgments This work was supported by a grant from the Russian Science Foundation (project No. 19-47-02010, “Natural hazards and monitoring for research in Russia and India”) and research topics (No. 0142-2014-0027 “Development of the theory and methods of studying the latest tectonics and modern geodynamics of platform and orogenic territories in relation to the assessment of their safety”).

References

1. Gee DG, Zeyen HJ (eds) (1996) EUROPROBE 1996 – lithosphere dynamics: origin and evolution of continents. Uppsala University, Uppsala. 138 pp
2. Goncharov MA, Koronovskii NV, Svalova VB, Raznitsin YN (2015) The contribution of mantle diapirism to the formation of newly formed basins of the Mediterranean and the Caribbean and the surrounding centrifugal-vergent folded-overlapped orogens. *Geotectonics* 6:80–93
3. Khain VE, Lomize MG (2005) *Geotectonics with the basics of geodynamics*. KDU, Moscow. 560 pp
4. Koulakov I, Zabelina I, Amanatashvili I, Meskhia V (2012) Nature of orogenesis and volcanism in the Caucasus region based on results of regional tomography. *Solid Earth* 3:327–337
5. Milyukov VK, Mironov AP, Rogozhin EA, Steblov GM (2015) Estimates of the speeds of modern movements of the North Caucasus from GPS observations. *Geotectonics* 3:56–65
6. Moiseenko UI, Negrov OB (1993) Geothermal conditions of the North Caucasian seismic hazard zone. In: *Geothermy of seismic and non-seismic zones*. Science, Moscow, pp 32–40
7. Rogozhin EA, Gorbaticov AV, Stepanova MY, Ovsyuchenko AN, Andreeva NV, Kharazova YV (2015) The structure and modern geodynamics of the meganticlinorium of the Greater Caucasus in the light of new data on the deep structure. *Geotectonics* 2:36–49
8. Sharkov E, Svalova V (2011) Geological-geomechanical simulation of the late Cenozoic geodynamics in the alpine-Mediterranean mobile belt. In: *New frontiers in tectonic research – general problems, sedimentary basins and island arcs*. INTECH, Rijeka, pp 18–38
9. Sharkov EV, Svalova VB (1989) Intracontinental seas as a result of back-arc spreading with a collision of continental plates. *Rep USSR Acad Sci* 308(3):685–688
10. Sharkov EV, Svalova VB (1991) On the possibility of involving the continental lithosphere in the subduction process during back-arc spreading. *Izv. AN USSR, Ser. Geol. No. 12*, pp 118–131
11. Svalova VB (1992) Mechanical-mathematical models of the formation and evolution of sedimentary basins. *Sci Terre Ser Inf* 31:201–208
12. Svalova VB (1993) Mechanical-mathematical simulation of geological structures evolution. *Geoinformatics* 4(3):153–160
13. Svalova VB (1997) Thermomechanical modeling of geological structures formation and evolution on the base of geological-geophysical data. *Proceedings of the Third Annual Conference of the International Association for Mathematical Geology IAMG'97, Barcelona, Spain. Part 2*. pp 1049–1055
14. Svalova V (2002) Mechanical-mathematical modeling for the Earth's deep and surface structures interaction. *Proceedings of International Conference IAMG, Berlin*. 5 p
15. Svalova VB (2014) Mechano-mathematical modeling of the formation and evolution of geological structures in connection with deep mantle diapirism. *Monit Sci Technol* 3(20):38–42
16. Svalova VB, Sharkov EV (1991) Formation and evolution of back-arc basins of the alpine and Pacific belts (comparative analysis). *Pac Geol* 5:49–63
17. Svalova VB, Sharkov EV (1992) Geodynamics of the Baikal rift zone (petrological and geomechanical aspects). *Geol Geophys* 5:21–30
18. Svalova VB, Zaalishvili VB, Ganapathy GP, Nikolaev AV, Melkov D (2019) A landslide risk in mountain areas. *Geol S Russ* 9(2):109–127. <https://doi.org/10.23671/VNC.2019.2.31981>
19. The Global Heat Flow Database of the International Heat Flow Commission. <http://www.heat-flow.und.edu/>
20. Ulomov VI, Danilova TI, Medvedeva NS, Polyakova TP, Shumilina LS (2007) To the assessment of seismic hazard in the North Caucasus. *Phys Earth* 43(7):31–45
21. Zanemonetz (Svalova) VB, Kotelkin VD, Miasnikov VP (1974) On the dynamics of lithospheric movements. *Izvestia of the USSR Ac. Sci., Ser. Phys Earth* 5:43–54

Geothermics and Geodynamics of the Back-Arc Basins of the Alpine and Pacific Belts



Valentina Svalova

1 Introduction

An important technique applied in the studies of geological structures at different phases of evolution and analysis of velocity fields, stresses and temperatures in the sedimentary cover, crust and upper mantle in different tectonic environment is the construction of an adequate mechanical-mathematical model of the geological region evolution [16–23, 25, 32].

There are two different approaches to mathematical modeling of geological structures and processes. The first one is to apply complete system of mechanical equations that adequately describes formation and evolution of some or other tectonic structure and subsequent calculation of the obtained equations under required boundary and initial conditions with high-capacity computers.

The second one is the maximum possible simplification of the obtained system of equations allowing for analytical decision of the problem with subsequent semi quantitative conclusions comparable with available geological-geophysical information. Optimal solution of geotechnical problems based on mechanical-mathematical modeling combines the advantages of each of above methods.

It is possible to describe some characteristic features of geological structures evolution above upwelling mantle diaper. For such analysis the mechanical-mathematical models of high viscous fluid can be used. The models are investigated on the base of geological structures of Alpine and Pacific belts.

V. Svalova (✉)
IEG RAS, Moscow, Russia

© The Author(s), under exclusive license to Springer Nature
Switzerland AG 2021

V. Svalova (ed.), *Heat-Mass Transfer and Geodynamics of the Lithosphere*,
Innovation and Discovery in Russian Science and Engineering,
https://doi.org/10.1007/978-3-030-63571-8_23

401

2 Alpine and Pacific Belts Geological-Geophysical Features

Alpine belt is connected with collision of continental plates (Arabian-African and Euroasian plates) and Pacific belt is connected with collision of oceanic and continental plates (Pacific and Euroasian plates), but they have many common features [2, 6, 7, 10, 11, 13, 15–17, 24, 27, 28, 30, 31]. Structures of Alpine and Pacific belts include back-arc basins, sea depressions, sedimentary basins, orogens (Fig. 1) [17]. Seas and depressions are characterized by thin crust and mostly high heat flow (Table 1) [1, 2, 8, 9, 10, 12, 13, 27–29]. Structures are characterized by active magmatism and basalt volcanism with xenoliths of asthenospheric matter. So geological-geophysical data give possibility to link these structures with upwelling of mantle diapirs [1–5, 7, 8, 10, 11, 14, 17, 26, 30]. Above rising mantle diapirs on the upper surface the structures of swell, deep basin or basalt flooding can arise depending on energy and upwelling stage of the diapirs. Between diapirs the structures of orogens and thickening of crust arise.

So the depressions of the Western sector of Alpine-Himalayan belt can be explained by mantle diapirs upwelling, and the Caucasus structure is connected not only with zone of the lithosphere plates collision, but also with collision of asthenosphere fluxes from mantle diapirs under Black and Caspian seas. It is interesting and important to analyze and explain origin and evolution of these structures on the base of mechanical-mathematical modeling.

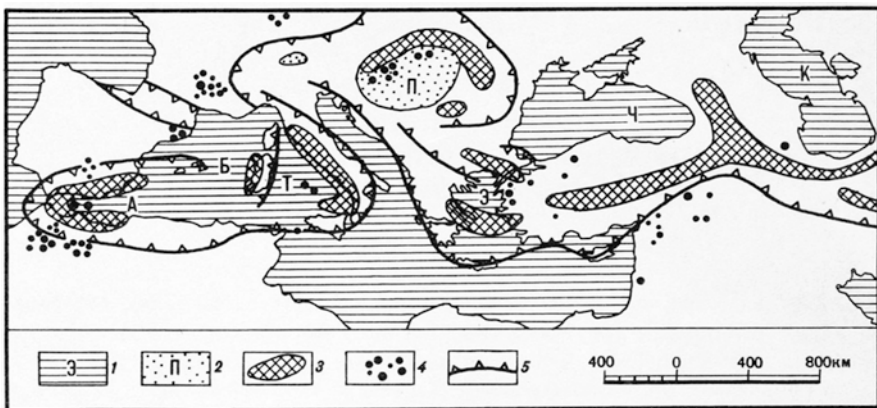


Fig. 1 Structure of Western sector of Alpine-Himalayan belt. 1 – seas (A – Alboran sea, Б – Balearic sea, К – Caspian sea, Т – Tyrrhenian sea, Ч – Black sea, Э – Aegean sea). 2 – Pannonian Depression. 3 – volcanic arcs. 4 – areals of basalt volcanism. 5 – frontal zones of napping structures

Table 1 Geological-geophysical data for Alpine and Pacific belts

Structure	Thickness of sedimentary cover (km)	Thickness of crystal crust (km) in depression (numerator) in frame (denominator)	Heat flow (mW/m ²)
1. Tyrrhenian sea	6	16/45	30–160
2. Aegean sea	3	15/23	100
3. Black sea	16	15/45	30–35
4. Pre-Caspian depression	24	12/40	40
5. South-Caspian depression	20	12/45	40–50
6. Ionian sea (South)	12	10/35	30–40
7. Ionian sea (North)	8	10/30	50–70
8. Balearic sea	8	10/40	50
9. Levant sea	6	8/30	30
10. Pannonian depression	9	18/27	90
11. Aleutian depression	5	10/26	60–80
12. Okhotsk sea	4	8/20	100
13. Sea of Japan	2	12/29	100–120
14. Philippines sea	2	6/13	60

3 Description of the Model

In order to get approximation system of mechanical equations by means of analyzing order of respective values in these equations it is unavoidable to separate small parameters of the problem which can be used for the decomposition.

Numerous geological structures are characterized by rather gentle occurrence of layers and significant elevation of horizontal regional scale *L* over vertical scale *h* of typical thickness. This allows to introduce small parameter *h/L* into analysis of the problem. The second small parameter of the problem *F/R*, *F* – Frude number, *R* – Reynolds number, arises while analyzing rheological behavior of matter in the layers [19, 20, 23, 32].

Slow lithospheric deformations will be simulated by models of viscous flow in multi-layered, incompressible, high-viscosity Newtonian fluid, using Navier-Stocks Eq. (1) and discontinuity Eq. (2):

$$d\mathbf{v} / dt = \mathbf{F} - (1 / \rho) grad p + (\mu / \rho) \Delta \mathbf{v} \tag{1}$$

$$div \mathbf{v} = 0 \tag{2}$$

\mathbf{v} – velocity vector, \mathbf{F} – force of gravity, p – pressure, ρ – density, μ – viscosity, t – time.

Let us introduce dimensionless values for coordinates, velocities and pressure X, Y, Z, U, V, W, P :

$$x = LX, y = LY, z = hZ, u = u_0 U, v = u_0 V, w = u_0 (h/L) W, p = \rho_0 ghP. \quad (3)$$

ρ_0, u_0 – characteristic scales of density and velocity.

Then it is possible to get dimensionless form of Navier-Stocks equation and discontinuity equation for slow movements in thin layers for 2-dimension case:

$$\begin{cases} \frac{\partial P}{\partial X} = \alpha \mu \frac{\partial^2 U}{\partial Z^2} \\ \frac{\partial P}{\partial Z} = -\rho \end{cases} \quad (4)$$

$$\frac{\partial U}{\partial X} + \frac{\partial W}{\partial Z} = 0 \quad (5)$$

$$\alpha = \frac{F}{R \left(\frac{h}{L}\right)^3}, F = \frac{u_0^2}{gL}, R = \frac{u_0 L \rho_0}{\mu_0} \quad (6)$$

F – Frude number, R – Reynolds number, ρ_0, μ_0, u_0 – characteristic scales of density, viscosity and velocity.

The forces on the high boundary are equal zero (free surface). Then it is possible to find pressure and velocities in the layers [23, 32].

On the high boundary ζ^* , the kinematic condition of a free surface should also be executed (7). This means that points of a surface will not escape it during motion:

$$S \frac{\partial \zeta^*}{\partial t} + U^* \frac{\partial \zeta^*}{\partial X} - W^* = 0 \quad (7)$$

$$S = \frac{L}{u_0 t_0} \quad (8)$$

S is the Strukhal number. t_0 is the scale of time.

Similarly it is possible to consider Moho boundary as a surface where the points remain during the evolutionary process (the condition of non-penetration). Then, substituting velocities, we get an equation of movement for any non-penetrated boundary .

Depth of a surface of asthenosphere under Alpine belt changes from 30 km in the centre of Tyrrhenian sea up to 70–100 km in depressions of East Mediterranean, strongly changing on lateral. The characteristic size of depressions reaches 500–1000 km and more, distance between them of 1000–1500 km.

From here a choice of characteristic parameters of a problem: $h_3 \sim 10$ km thickness of crust, $h_2 \sim 100$ km – thickness of mantle lithosphere, $L \sim 1000$ km – horizontal scale, $\varepsilon = h_3/L = 10^{-2}$ -small parameter.

Decomposing velocities and pressure on $\sqrt{\varepsilon}$, it is possible to receive in zero approximation the equation of upper surface ζ_3 and Moho surface ζ_2 dynamics depending on velocities of the mantle diapir surface ζ_1 $U_0, W_0|_{\zeta_1}$:

$$\begin{cases} \frac{\partial^2 \zeta_3}{\partial X^2} = \beta \left[h_2 \frac{\partial U_0}{\partial X} - W_0 \right] \\ S \frac{\partial \zeta_2}{\partial t} + U_0 \frac{\partial \zeta_2}{\partial X} + \alpha \left[h_2 \frac{\partial U_0}{\partial X} - W_0 \right] = 0 \end{cases} \quad (9)$$

$$\alpha = \frac{(h_3)^3}{(h_3)^3 + \frac{\mu_3}{\mu_2} (h_2)^3}, \beta = \frac{1}{\frac{\rho_3}{3} \left[\frac{(h_3)^3}{\mu_3} + \frac{(h_2)^3}{\mu_2} \right]}$$

$S = \frac{L}{u_0 t_0}$ – Strukhal number, u_0 – characteristic velocity of the lithosphere matter, t_0 – characteristic time of considered processes, μ_i – viscosity, ρ_i – density in layers.

Let’s set a field of velocities and morphology of border ζ_1 as:

$$U_0 = a \operatorname{th} kX, \zeta_1(X,t) = -\gamma \operatorname{sh}^2 kX - (h_2 + h_3) + \frac{D}{S} t \quad (10)$$

Where k , a characterize intensity of spreading: k -in the centre of structure, a – far from the centre; γ – allows to vary the form of rising diapir; $D = S \frac{\partial \zeta_1}{\partial t}$ – the given velocity of rising diapir (Fig. 2).

The given field of velocities well reflects the basic features of a considered class of movements: rise of the asphenosphere diapir, spreading above it and lowering of substance on sufficient distance from the centre. Quantitative conformity at comparison with the available geological-geophysical data is reached with the help of a variation of factors in a modeling field of velocities and their change during considered process at preservation of the general structure of movements. From the decision of system (4, 5, 7) it is possible to receive for big t :

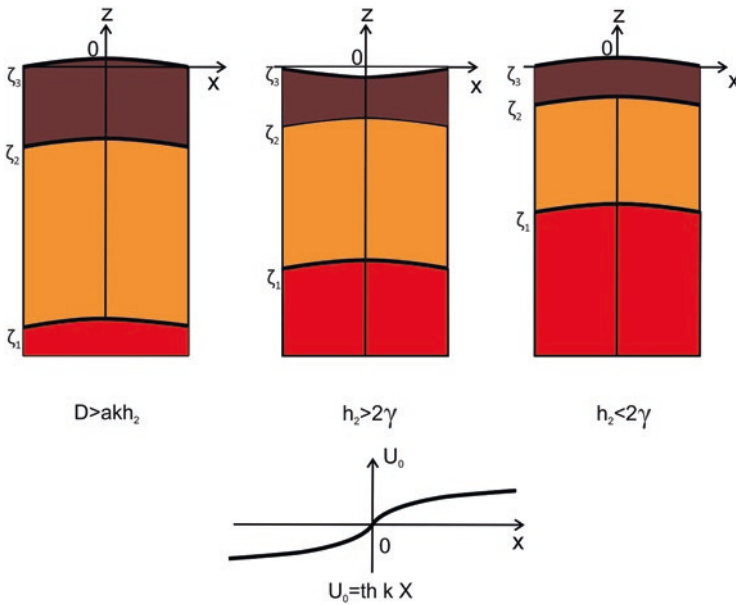


Fig. 2 Characteristic section of layers of crust and mantle lithosphere above asthenosphere diaphragm upwelling without lateral restriction of movement. $U_0 = a \text{ th } kX$

$$\begin{cases} \zeta_2 = -h_3 - \alpha\gamma \operatorname{sh}^2 kX + \alpha h_2 \ln(\operatorname{ch} kX) + \alpha(D - h_2 ak) \frac{t}{S} \\ \zeta_3 = \beta \left[\frac{h_2 a}{k} \ln(\operatorname{ch} kX) + \frac{\gamma a}{(2k)^2} \operatorname{ch} 2kX - \left(\frac{\gamma a + D}{2} \right) X^2 \right] + C_1(t) \end{cases} \quad (11)$$

$C_1(t)$ is defined from balance of mass.

The analysis of the received expressions shows, that there is a critical depth of upwelling of mantle diaphragm $h_2 = 2\gamma$ when the characteristic form of the lithosphere layers changes. If $h_2 > 2\gamma$ there is a deflection of a surface of the base in the centre of spreading, that really takes place in considered back-arc seas. If $h_2 < 2\gamma$ (depth of diaphragm is small) or speed of its rise is essential ($D > h_2 ak$) the diaphragm surface corresponds to rise of Moho surface (Fig. 2).

When on periphery of basin there are the conditions interfering free spreading of the lithosphere of region, for example, caused by collision of the Arabian-African and Euroasian plates, the field of velocities on the bottom border of layers can be modelled as:

$$U_0 = \frac{\operatorname{th} X}{\operatorname{ch}^2 X}, \quad \zeta_1 = -\operatorname{sh}^2 X - (h_2 + h_3) \quad (12)$$

For better presentation of result the coefficients in a modeling problem are omitted. Then:

$$\left\{ \begin{aligned} \zeta_3 &= -\frac{\beta h_2}{2} \frac{1}{\text{ch}^2 X} + \frac{\beta}{2} X^2 - \beta \ln(\text{ch} X) + C(t) \\ \zeta_2 &\cong -h_3 - \frac{\alpha h_2}{S} t - \alpha(1-2h_2)\text{sh}^2 X \\ &+ \alpha(1-2h_2)(\text{sh} X)^{\frac{2(h_2-1)}{1-2h_2}} \exp\left[\frac{2-3h_2}{1-2h_2}\left(\frac{t}{S} - \text{sh}^2 X\right)\right] \end{aligned} \right. \quad (13)$$

$C(t)$ is defined from balance of mass.

In this case there are two critical depths of a roof of the asthenosphere diapir at which the section of layers qualitatively changes the structure. At $h_2 > 2/3$ in the centre of structure the deflection is formed. At $1/2 < h_2 < 2/3$ Moho surface uprise in the center of structure, and at $h_2 < 1/2$ reflects morphology of diapir in the centre of spreading and forms concavity of the base on periphery of basin (Fig. 3).

The first type of velocities (2) can describe the initial stage of the structures development. The second type (3) describes the internal basins and seas structures.

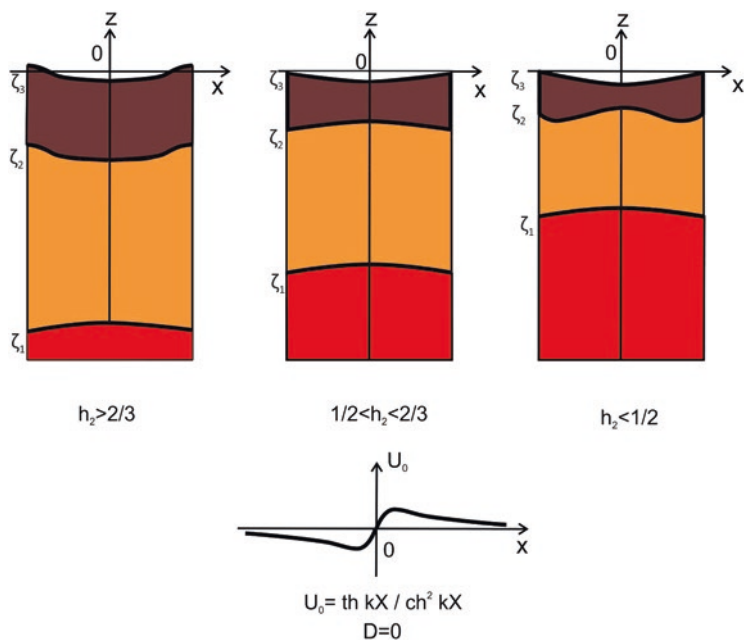


Fig. 3 Characteristic section of layers of crust and mantle lithosphere above asthenosphere diapir upwelling with lateral restriction of movement

4 Conclusions

Mechanical-mathematical modeling of the lithosphere evolution above rising asthenosphere diapir shows that during rising the swell structures forms on the upper surface and then deep depression arises. The deep depression formation does not demand big stretching in the layers of the lithosphere. The depth of depression is determined by velocity, depth and form of uprising diapir. The changing of swell structure by deep depression structure is confirmed by many geological factors: sedimentation regime characteristics, paleorivers direction change, evolution of paleodepthes of basins.

There is no conflict of interests in the chapter.

Acknowledgments This work was supported by a grant from the Russian Science Foundation (project No. 19-47-02010, “Natural hazards and monitoring for research in Russia and India”) and research topics (No. 0142-2014-0027 “Development of the theory and methods of studying the latest tectonics and modern geodynamics of platform and orogenic territories in relation to the assessment of their safety”).

References

1. Anderson DL, Dzevonsky AM (1984) Seismic tomography. In the World of Science. No. 12, pp 16–26
2. Bogdanov NA (1989) Geology of deep depressions of back-arc seas. Nedra, Moscow, p 221
3. Condie KC (2001) Mantle plumes and their record in earth history. Cambridge University Press, p 306
4. Davies GF (1999) Dynamic earth. Plates, plums and mantle convection. Cambridge University Press, p 458
5. Gee DG, Zeyen HJ (eds) (1996) EUROPROBE 1996 – lithosphere dynamics: origin and evolution of continents. Uppsala University, 138 pp
6. Goncharov MA, Koronovskii NV, Svalova VB, Raznitsin YN (2015) The contribution of mantle diapirism to the formation of newly formed basins of the Mediterranean and the Caribbean and the surrounding centrifugal-vergent folded-overlapped orogens. *Geotectonics* 6:80–93
7. Karig DS (1974) Evolution of arc systems in the Western Pacific. *An Rev Earth Planet Sci* 2:51–75
8. Khain VE, Lomize MG (2005) *Geotectonics with the basics of geodynamics*. M.: KDU, 560 pp
9. Koulakov I, Zabelina I, Amanatashvili I, Meskhia V (2012) Nature of orogenesis and volcanism in the Caucasus region based on results of regional tomography. *Solid Earth* 3:327–337
10. Malovitsky YP, Senin BV (1988) Pelagogenic depressions on modern and ancient continental margins. *Geotectonics* 1:11–23
11. Milyukov VK, Mironov AP, Rogozhin EA, Steblov GM (2015) Estimates of the speeds of modern movements of the North Caucasus from GPS observations. *Geotectonics* 3:56–65
12. Moiseenko UI, Negrov OB (1993) Geothermal conditions of the North Caucasian seismic hazard zone. In: *Geothermy of seismic and non-seismic zones*. Moscow, Science, p. 32–40
13. Nikolaev VG (1986) Pannonian basin. Moscow, Science, 120 pp
14. Ringwood AE, Irifune T (1988) Nature of 650 km seismic discontinuity: implication for mantle dynamics and differentiation. *Nature* 331(6152):131–134

15. Rogozhin EA, Gorbatikov AV, Stepanova MY, Ovsyuchenko AN, Andreeva NV, Kharazova VY (2015) The structure and modern geodynamics of the meganticlinorium of the greater Caucasus in the light of new data on the deep structure. *Geotectonics* 2:36–49
16. Sharkov E, Svalova V (2011) Geological-geomechanical simulation of the Late Cenozoic geodynamics in the Alpine-Mediterranean mobile belt. *New frontiers in tectonic research – general problems, sedimentary basins and Island arcs*. INTECH, Croatia, pp 18–38
17. Sharkov EV, Svalova VB (1989) Intracontinental seas as a result of back-arc spreading with a collision of continental plates. *Rep USSR Acad Sci* 308(3):685–688
18. Sharkov EV, Svalova VB (1991) On the possibility of involving the continental lithosphere in the subduction process during back-arc spreading. *Izv AN USSR Ser Geol* 12:118–131
19. Svalova VB (1992) Mechanical-mathematical models of the formation and evolution of sedimentary basins. *Sci de la Terre Ser Inf* 31:201–208
20. Svalova VB (1993) Mechanical-mathematical simulation of geological structures evolution. *Geoinformatics* 4(3):153–160
21. Svalova VB (1997) Thermomechanical modeling of geological structures formation and evolution on the base of geological-geophysical data. *Proceedings of the Third Annual Conference of the International Association for Mathematical Geology IAMG'97, Barcelona, Spain, Part 2*, pp 1049-1055
22. Svalova V (2002) Mechanical-mathematical modeling for the Earth's deep and surface structures interaction. In *Proceedings of international conference IAMG, Berlin*, 5 pp
23. Svalova VB (2014) Mechano-mathematical modeling of the formation and evolution of geological structures in connection with deep mantle diapirism. *Monitoring. Sci Technol* 3(20):38–42
24. Svalova VB, Sharkov EV (1991) Formation and evolution of back-arc basins of the alpine and Pacific belts (comparative analysis). *Pac Geol* 5:49–63
25. Svalova VB, Sharkov EV (1992) Geodynamics of the Baikal rift zone (petrological and geomechanical aspects). *Geol Geophys* 5:21–30
26. Svalova VB, Zaalishvili VB, Ganapathy GP, Nikolaev AV, Melkov D (2019) A landslide risk in mountain areas. *Geol South Russia* 9(2):109–127. <https://doi.org/10.23671/VNC.2019.2.31981>
27. *Tectonics of Mediterranean belt* (1980) Moscow, Science, 244 pp
28. Tamaki K (1988) Geological structure of the sea of Japan and its tectonic implications. *Bull Geol Surv Japan* 39(3):269–365
29. The Global Heat Flow Database of the International Heat Flow Commission. <http://www.heat-flow.und.edu/>
30. Ulomov VI, Danilova TI, Medvedeva NS, Polyakova TP, Shumilina LS (2007) To the assessment of seismic hazard in the North Caucasus. *Phys Earth* 7:31–45
31. Wyllie PI (1988) Magma genesis, plate tectonics, and chemical differentiation of the earth. *Rev Geophys* 26(3):370–404
32. Zanamonez (Svalova) VB, Kotelkin VD, Miasnikov VP (1974) On the dynamics of lithospheric movements. *Izvestia USSR Acad Sci Ser Phys Earth* 5:43–54

Structure and Dynamics of the Lithosphere for the Eurasia-Pacific Transition Zone



Ludmila P. Zabarinskaya, Nataliya A. Sergeyeva, Vladimir A. Rashidov, Mikhail V. Nisilevich, and Tamara A. Krylova

1 Introduction

The International Geotraverse Project led by Dr. A.G. Rodnikov (Geophysical Center of the Russian Academy of Sciences), was devoted to study of the deep structure and construction of the cross-sections through the tectonosphere including the lithosphere and the asthenosphere in the transition zone from the Eurasian continent to the Pacific Ocean. The Project was done in cooperation with Japanese geoscientists (led by Prof. S. Uyeda) and Chinese geoscientists (led by Prof. L. Guodong). The transition zone (Fig. 1) is an especially large region and is seismically very active. It is particularly important to study the deep structure of such regions, focusing on the areas beneath active volcanoes, the sedimentary basins, and the minerageny areas [22].

The Cenozoic was a period of major tectonic events that influenced the geological structure of the investigated region. Starting with the Paleogene tectonic processes took place here, accompanied by the formation of back-arc basins, rifts, strike slip faults, grabens and horsts, various types of deep faults caused by subduction processes when the Pacific Plate moved under the continent, as well as collision of lithospheric plates activated at that time. These processes were accompanied by volcanic eruptions, earthquakes, tectonic movements, causing destruction of the earth's crust. At the beginning of the Cenozoic, the collision between the Indian and Eurasian plates changed the structure of Southeast Asia and led to the transformation of the lithospheric plates in the transition zone. Later, the ongoing collision led

L. P. Zabarinskaya (✉) · N. A. Sergeyeva · M. V. Nisilevich · T. A. Krylova
Geophysical Center RAS, Moscow, Russia
e-mail: mila@wpcb.ru

V. A. Rashidov
Institute of Volcanology and Seismology FED RAS, Petropavlovsk-Kamchatsky, Russia

© The Author(s), under exclusive license to Springer Nature
Switzerland AG 2021

V. Svalova (ed.), *Heat-Mass Transfer and Geodynamics of the Lithosphere*,
Innovation and Discovery in Russian Science and Engineering,
https://doi.org/10.1007/978-3-030-63571-8_24

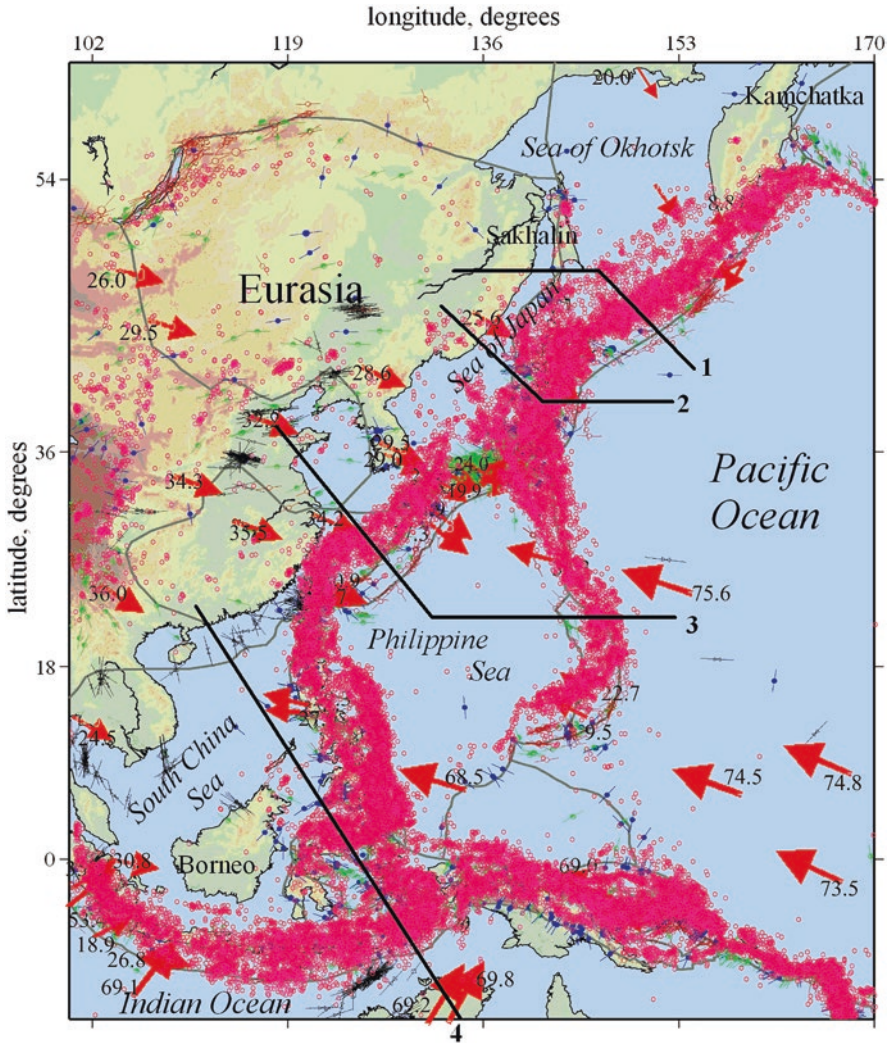


Fig. 1 The region of the transition zone from the Eurasian continent to the Pacific Ocean with spatial distribution of earthquakes with $M \geq 3.5$ for the period 1973–2011 (pink circles), and profiles of geotraverses (1 – Okhotsk Sea geotraverse; 2 – Japan Sea geotraverse; 3 – North China Plain–Philippine Sea geotraverse; 4 – South-China Sea geotraverse). Red arrows and adjacent numbers indicate the direction and velocity (mm/year) of plates movement. Black lines are plate boundaries

to the interaction of the Australia, Eurasia, and Pacific plates, which was also accompanied by volcanic activity and earthquakes, the disappearance of some volcanic arcs and the appearance of new ones, the formation of an asthenospheric layer in the upper mantle, in which the processes cause tectonic movements in the earth's crust.

Geodynamic models of the deep structure were created for the regions of the Okhotsk, Japan, Philippine, and South China seas located in the transition zone. Deep cross-sections of the crust and upper mantle were constructed on the basis of combined interpretation of the geological and geophysical data at the disposal of the Geophysical Center of the Russian Academy of Sciences.

It is established that the distinctive feature of the deep structure of the transition zone is the shallow depths of the asthenospheric layer in the upper mantle from which diapirs of a hot anomalous mantle material rise. The processes in the diapirs determine a formation of the earth's crust structures [25, 26]. The existence of the asthenosphere in the upper mantle of the transition zone is confirmed by tomographic studies [2, 5, 35]. The paper is focused on the deep structure of the Sea of Okhotsk located in the transition zone from Eurasian continent to the Pacific.

2 Tectonic Setting

The Okhotsk Sea region is a lithospheric plate in the transition zone from the Eurasian continent to the Pacific. The region is located in the contact zone of three lithospheric plates: Eurasian, North American and Pacific (Fig. 2). The Okhotsk Sea Plate is bounded by deep faults, for the major part strike-slip faults, and in the south-east it is bounded by a recent subduction zone that is the Benioff zone. Its basement is heterogeneous from the Paleozoic–Mesozoic crystalline rocks revealed in the continent, Sakhalin and Kamchatka to the Mesozoic–Cenozoic rocks in the Sea of Okhotsk. The plate was finally formed in the Late Cretaceous. In the Cenozoic it was overlapped with a cover of sedimentary and volcanogenic sedimentary deposits. The thickness of the crust is approximately 28–32 km decreasing to 24 km in the Deryugin basin and to 15 km beneath the Kuril Basin.

The Okhotsk Sea Plate belongs to intensely deformed structures as evidenced both by geological and geophysical data and the analysis of the recent crustal movements. The origin of the plate structure is determined by general geodynamic settings which were formed by the end of the Paleocene [7], and in this case, according to [8], the geometry of horizontal displacement vectors in general agrees with the assumption that the direction of velocities measured experimentally is related to the Pacific Plate effects. But it is likely that the deformation of the Okhotsk Sea Plate structures was also caused by the Eurasian continent moving eastwards with the Baikal rift development [32]. Structural dislocations inside the plate may be related to extensions in the Kuril Basin, Tatar Strait and Deryugin Basin caused by upwelling of the asthenosphere diapirs, which reached their peaks in the Miocene.

The sedimentary basins were formed in the conditions of the Okhotsk Sea crust destruction caused by rifting in the Cenozoic. It is assumed that extensional conditions started in the Paleocene but they were manifested most intensely in the Late Oligocene–Middle Miocene, which resulted in the formation of grabens, semi-grabens and pull-apart deep basins with oceanic and thin sub-continental crust [24].

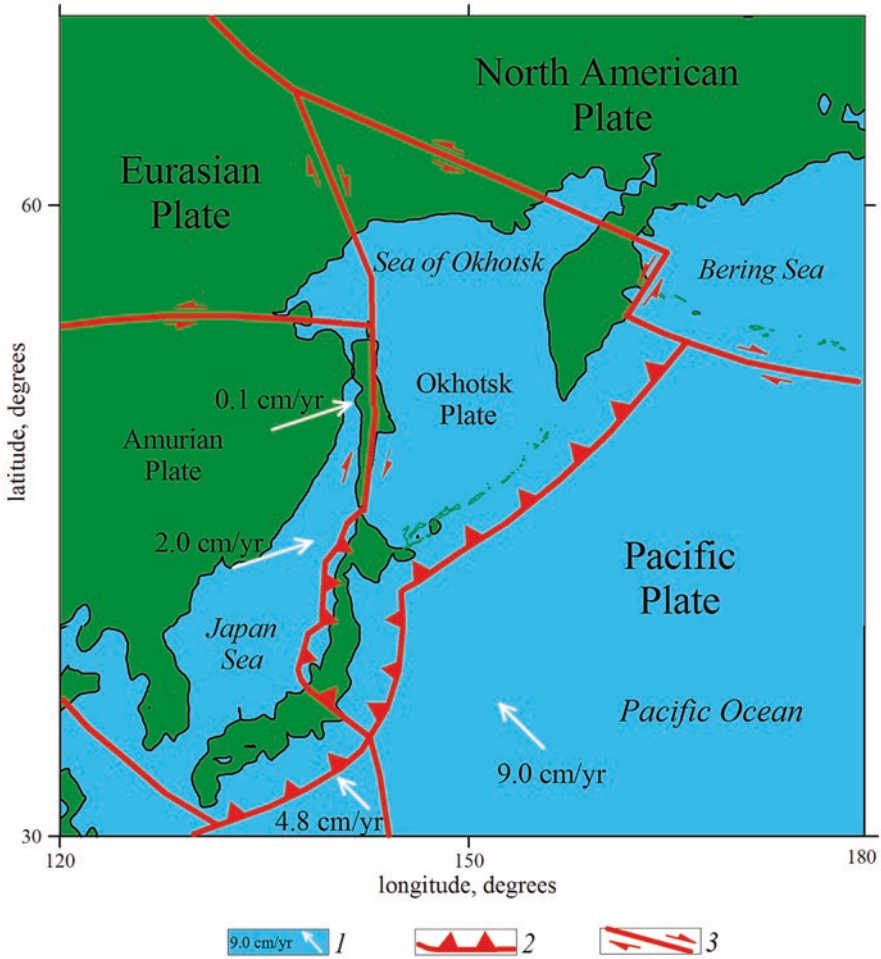


Fig. 2 Tectonic map of the Okhotsk Sea region. Based on the compilations of Biebow et al. [4], Kiratzi and Papazachos [13], Maruyama et al. [16], and Rodnikov et al. [25]. 1 – velocity of plate movement from GPS data; 2 – subduction zones; 3 – faults

In the Late Miocene and Pliocene, compression conditions were activated, which resulted in the formation of reversed faults, strike-slip faults and thrusts [4].

3 Heat Flow

In the Okhotsk Sea region the heat flow is high within the deep-sea basins and troughs and is relatively low in the continental structures of the Far East and the Kuril area of the Pacific (Fig. 3). The heat flow data come from an updated version

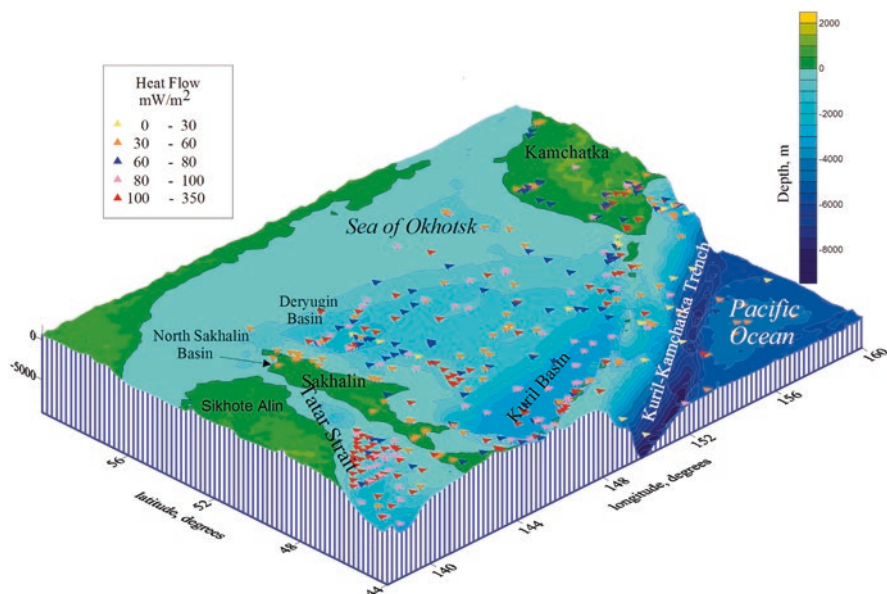


Fig. 3 3D surface view of the Okhotsk Sea region with distribution of the heat flow measuring points [18, 29]

of the global database of Pollack et al. [18] and were compiled from the literature and heat flow maps [29, 30, 33].

The heat flow variations for the Sikhote-Alin are only $39\text{--}56 \text{ mW}\cdot\text{m}^{-2}$. In the Kuril area adjacent to the Pacific, the heat flow mean values are about $52 \text{ mW}\cdot\text{m}^{-2}$. The lowest values are noted in the Kuril-Kamchatka deep-sea trench reaching the value of $22 \text{ mW}\cdot\text{m}^{-2}$. The heat flow mean values for the Kuril island arc are $118 \text{ mW}\cdot\text{m}^{-2}$ with the highest point reaching $790 \text{ mW}\cdot\text{m}^{-2}$ in the western part of the island arc. Heat flow mean values in Sakhalin amount to $76 \text{ mW}\cdot\text{m}^{-2}$. The high heat flow values are noted in Tatar Strait ($123\text{--}132 \text{ mW}\cdot\text{m}^{-2}$) and in the Deryugin basin where they reach $200 \text{ mW}\cdot\text{m}^{-2}$. Besides, the high heat flow values are established in the Kuril Basin of the Sea of Okhotsk, where they range from $346\text{--}354 \text{ mW}\cdot\text{m}^{-2}$ [24].

The temperature changes along the geophysical section through the Kuril Basin (Fig. 4) shows that the upper edge of the partial melting in the upper mantle, corresponding to the $1100 \text{ }^\circ\text{C}$ isotherm, is located at a depth of about 25 km. On the surface, the rift formations and eruptions of basalts are in accordance with the upwelling of the asthenosphere [26].

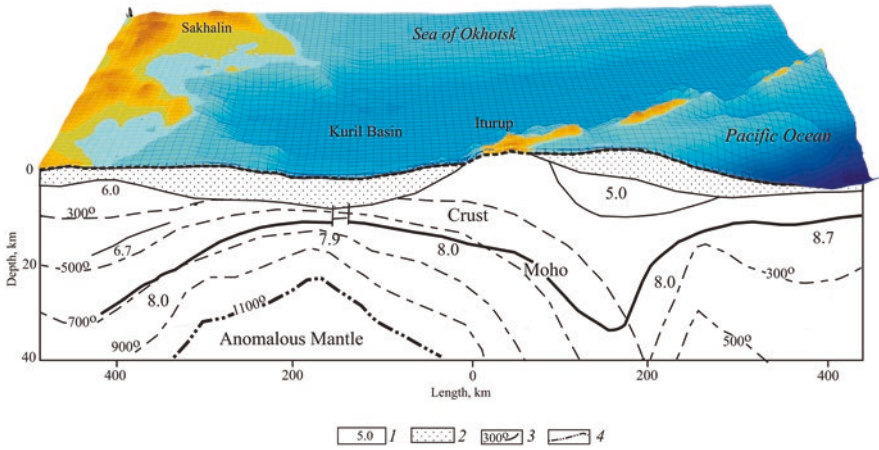


Fig. 4 Earth's internal temperature in the crust and upper mantle for Sakhalin, Kuril Basin, Kuril island arc, Kuril trench and west Pacific (crust and isotherms are given according to Rodnikov et al. [26]). 1 – seismic velocities, $\text{km}\cdot\text{s}^{-1}$; 2 – sedimentary layer; 3 – isotherms, $^{\circ}\text{C}$; 4 – isotherm of 1100°C

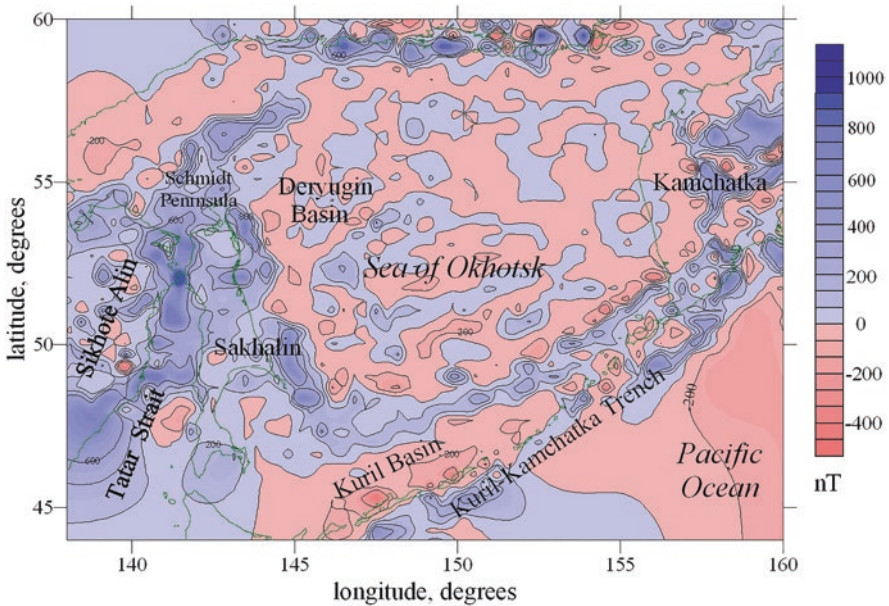


Fig. 5 Anomalous magnetic field of the Okhotsk Sea region [26]

4 Magnetic Field

Anomalous magnetic field of the Okhotsk Sea region (Fig. 5) is characterized by various orientation of the extension of anomalies having different configurations and values [24]. Magnetic field anomalies for the major part show linear northwestward and northeastward extension. Magnetic field of Sikhote Alin is positive anomalies extended along deep faults and reaching values from 300 to 600 nT, which are related to magmatic body masses. In Tatar Strait, a chain of individual maximums is distinguished, which approximately coincides with the axis of greatest depths of the strait. Generally, in Sakhalin, negative magnetic field is noted. Individual positive linear anomalies are related to intrusive and effusive basic and ultra-basic bodies. Along eastern Sakhalin in the Sea of Okhotsk, the East Sakhalin positive magnetic anomaly extends, which reaches values of 1200–1400 nT. This anomaly locates in the East Sakhalin ophiolite belt where ultrabasic and basic rocks are exposed in the Schmidt Peninsular and in the East Sakhalin mountains. This belt separates northern Sakhalin from the Deryugin Basin. The Deryugin and Kuril basins are characterized by weak negative anomalies with the amplitude of -200 nT, which are related to nonmagnetic sedimentary rocks composing the basins.

With approach to the Kuril Islands the magnetic field becomes differentiated and varying from -300 to $+400$ nT. A narrow zone of disturbed magnetic field with local positive and negative anomalies of individual volcanic constructions is consistent with volcanic structures in the Kuril island arc. Local positive anomalies and negative anomalies commonly associated with them are confined to submarine volcanoes. The northwest extension of the magnetic field anomalies is associated with deep faults breaking the Kuril island arc into separate blocks [24].

In the Northwest Pacific basin bordering the Kuril island arc, the systems of linear magnetic anomalies were revealed of the age ranging from 108 to 160 Ma. The continental slope anomalies of the deep-sea trench have the general northeastern extension, which is disturbed by transverse anomalous zones. In the southern area of the trench slope, the linear northeastern anomalies parallel to the trench axis look as if they continued band anomalies of the Pacific Plate but are less distinct [28].

5 Seismicity

The location of the Okhotsk Sea Plate in the contact zone of three lithospheric plates (Eurasian, North American and Pacific) caused high seismicity in its margins. In the active continental margin of the Far East a large number of earthquakes commonly occur (Fig. 6). It accounts for 80% of the total energy of earthquakes in North Eurasia [34]. The largest earthquakes that occurred in the last 10 years are Shikotan earthquake in southern Kurils of 1994 (magnitude $M = 8.4$ and the source depth is approximately 65 km), Neftegorsk earthquake in Sakhalin of 1995 ($M = 7$),

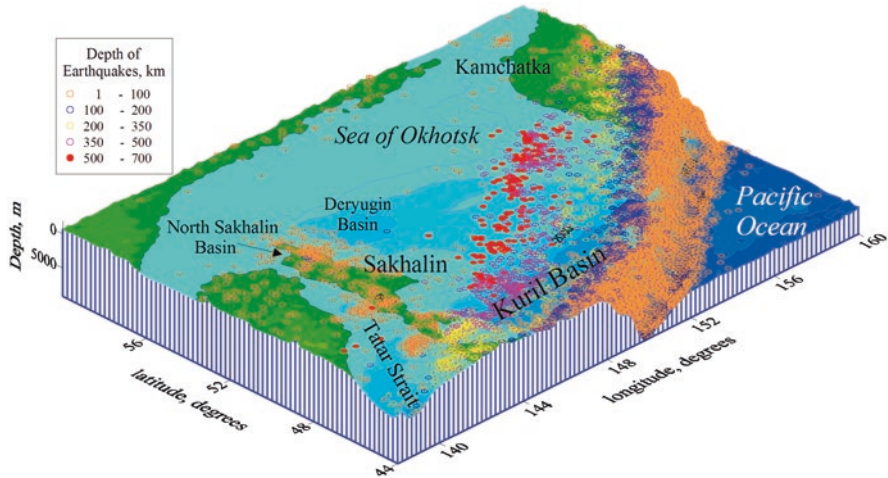


Fig. 6 3D surface view and seismicity 1964–2011 of the Okhotsk Sea region [14, 31]

Kronotskoe in eastern Kamchatka of 1997 ($M = 7.9$), and Okhotsk Sea earthquake of 2013 (moment magnitude $M = 8.3$ at depth of 609 km).

The highest seismic activity is noted along the Kuril island arc. The Pacific Plate subducts under the continent, forming a seismofocal zone, which is traced to the depth of 700 km. In the west, the Okhotsk Sea Plate is bounded by deep faults extending along Sakhalin. There the earthquakes for the major part are localized in the crust. In the Kuril island arc the majority of earthquakes are confined to depth up to 100–150 km and the maximum of seismic activity is at depths of approximately 30–40 km. At depths greater than 100–150 km seismic activity abruptly decreases, and a sharp fracture of focal zone is noted at depths of 200–300 km. The Sakhalin seismicity is associated with sub-meridian deep faults [24] bounding the Okhotsk Sea lithospheric plate and separating it from the Eurasian Plate. Plate movements relative to each other as well as spreading processes going on in the rift structure of Tatar Strait cause active seismicity. Earthquakes distribution along the cross-section is shown in Fig. 7.

6 Volcanism

The Kuril island arc is an area of intense recent volcanism manifestations. Different authors distinguish from 68 to 160 surface volcanoes. Twenty nine of them erupted in historic time and six are in the solfatarie stage. From different assessments, the number of submarine volcanoes varies from 96 to 104 [6, 9, 20]. In the opinion of V. A. Rashidov [21], reliable data on submarine volcanic activity manifestations in this region are lacking although data of various catalogues are available.

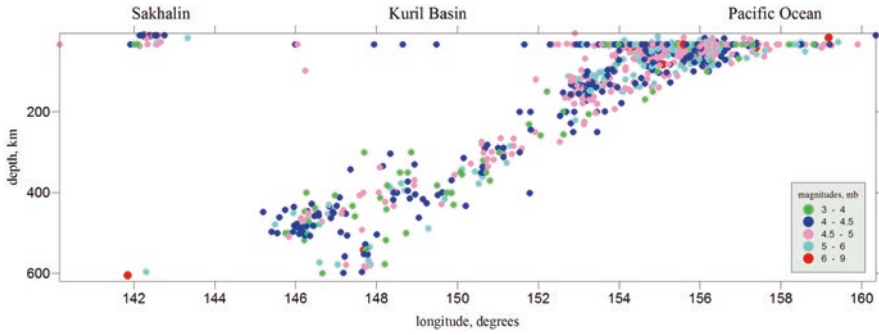


Fig. 7 Deep distribution of earthquake’s hypocenters along the profile with a width of 2 degrees. Profile coordinates: 53.0°N, 138.0°E; 53.0°N, 160.0°E

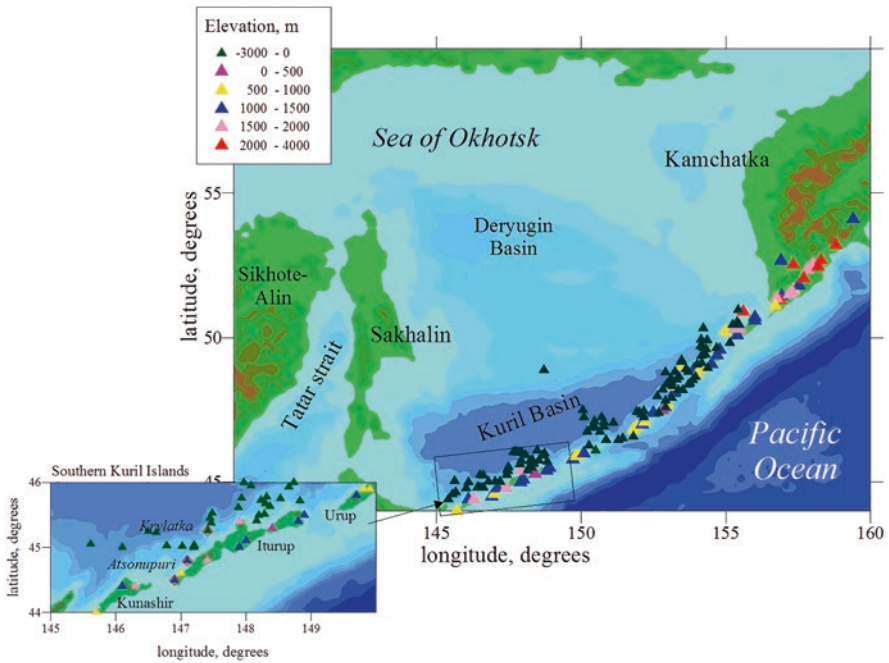


Fig. 8 Volcanoes of the Kuril Islands. Color triangles indicate surface volcanoes and black triangles indicate submarine volcanoes

Both surface and submarine volcanoes form volcanic chains oriented at different angles to the general strike of the Kuril island arc (Fig. 8). Surface and submarine volcanoes of the Kuril island arc are composed of rocks from basaltic to rhyolite composition. Normal and sub-alkali rocks are separated ranging from low-potassium to high-potassium series. Low titanium and magnesia contents and high aluminum hydrate content are characteristic of the Kuril island arc lavas [19].

About 40 large surface volcanic constructions and more than 160 minor volcanic cones are situated in the Iturup Island, across which the deep section runs. Nineteen surface volcanoes are Quaternary and in ten of them historic eruptions were noted beginning since 1778. Among submarine volcanoes, we find both table mounts (guyot) and point mounts [26]. The former seem to be encompassing Iturup Island and the latter are at a distance from the island. Depths above table mounts increase with distance from the island, which may testify to subsidence of the island arc slope on the Okhotsk Sea side towards the Kuril deep basin and may be related to its formation [19]. The structure of some volcanoes is discussed in the paper.

Submarine Volcano Krylatka Four expeditions were conducted on board the RV Vulkanolog during the 1980s to investigate the Krylatka submarine volcano located at 17 km to north-northwest of Iturup Island.

The flat summit of the volcano is at 300 m depth, the base is 14 by 22 km. The full height is 2900 m (including the sediment-covered base). The volcano is of pre-Holocene age. It is likely that the volcano formed near sea level. The last lava effusions occurred under water. Acoustic anomalies were recorded in water at the central part of the Krylatka summit in the depth range 210–250 m possibly providing evidence of the volcano's gas- and hydrothermal activity [21].

Volcano Atsonupuri (Fig. 9) is situated in the southern Iturup Island to which it is linked with an isthmus of height of 30 m [9]. It is a stratovolcano with the central



Fig. 9 Volcano Atsonupuri. (Photo by A.G. Rodnikov, 1963)

cone in caldera. The base diameter at sea-level is about 6 km. Absolute height is 1205 m. The crater dimensions are 400 × 600 m and the depth is approximately 150 m. In the eastern part of the cone a small area of flat atrio and remnants of soma crest are preserved. The size of soma is approximately 2 km. The height of soma crest is 900 m. The elevation of the central cone above the soma is approximately 300 m [9, 10, 3].

The predecessor of Atsonupuri was active in the late Pleistocene or early Holocene and once formed an island up to about 1.5 km high, which was later connected to Iturup Island by sediments. Atsonupuri erupted in 1812 and 1932 [10]. Both eruptions were small.

7 Deep Structure

The research of the deep structure was conducted along the geotraverse constructed on the basis of combined interpretation of geological and geophysical data (Fig. 10). Geotraverse crosses the Mesozoic structures of Sikhote Alin, rift structure of the Tatar Strait, the Cenozoic formations of Sakhalin, the Kuril Basin, volcanic Kuril Arc, Kuril-Kamchatka Trench and Pacific Ocean.

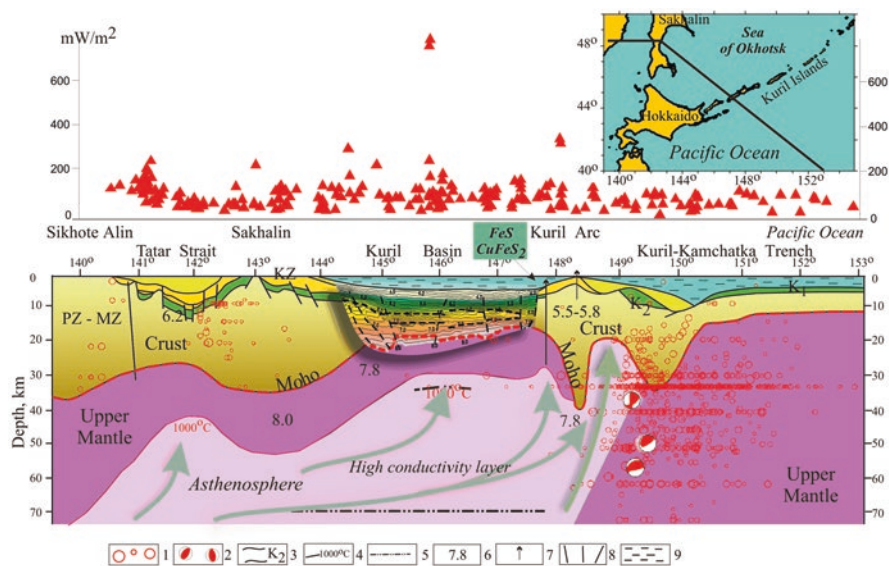


Fig. 10 Geotraverse of the Okhotsk Sea region [26]. In the top right the geotraverse position is shown. Below the distribution of measured values of the heat flow ($\text{mW}\cdot\text{m}^{-2}$) is shown along the profile. Flows in the asthenosphere correspond to hot mantle fluids. PZ Paleozoic, MZ Mesozoic, KZ Cenozoic, K2 Upper Cretaceous. 1 – earthquake hypocenters; 2 – focal mechanism; 3 – geological layers; 4 – isotherm, °C; 5 – high conductivity layer boundary; 6 – seismic wave velocities, $\text{km}\cdot\text{s}^{-1}$; 7 – volcanoes; 8 – water mass; 9 – faults

structures of the Kuril island arc, the Kuril Trench and the Mesozoic plate in the northwest basin of the Pacific. The profile length is about 2000 km and its depth reaches 100 km.

The thickness of the crust in the Okhotsk Sea varies from 35–40 km beneath Sakhalin and Kuril Islands to 10 km beneath the Kuril Basin. The crust is divided into the basement and sedimentary cover. The basement rocks are exposed in Sakhalin, Kamchatka, and Kuril island arc and were brought up from underwater elevations with dredge. The basement age ranges from the Paleozoic to the Mesozoic. The sedimentary basin comprises individual abysses where its thickness reaches 12 km. For the major part it is composed of sedimentary rocks and partially of volcanogenic sedimentary rocks of the Late Cretaceous–Cenozoic. In the Late Cretaceous, sedimentation went on in rifting-causing conditions and was accompanied by considerable volcanic activity. That resulted in the formation of deep-sea basins composed of volcanogenic-siliceous sediments gradually replaced with more shallow-water rocks up the section. Most sedimentary basins appeared in the Cenozoic. The deposits of this time as an unbroken cover overlapping the underlying formations contain almost all oil and gas complexes of the Sea of Okhotsk.

Tatar Strait is a large rift structure, which is approximately 50 km wide and 10 km deep [17]. It is composed of a thick bed up to 8–10 km of the Mesozoic–Cenozoic sedimentary formations. The rift is located between the Mesozoic structures of Sikhote Alin and West Sakhalin Mountains and is separated from them by deep faults. Sediments composing the trough are divided into four structural complexes separated from each other by regional stratigraphic disconformities and having different structural compositional and physical characteristics: Upper Cretaceous, Paleogene, Oligocene–Lower Miocene and Middle Miocene–Quaternary. The trough basement is granite-metamorphic layer with seismic boundary velocities in the range of 5.8–6.2 km•s⁻¹.

The formation of Tatar Strait rift structure is associated with the upwelling of the asthenosphere to the earth's crust [23]. The rift is the northern continuation of the spreading center located in the abyssal basin of the Sea of Japan, which was revealed from the studies of magnetic field anomalies profiles of the Sea of Japan. It is believed that spreading processes went on 25–15 Ma ago and were accompanied by basalt lavas eruptions [11, 16]. In the middle of the Oligocene the processes of the earth's crust extension started and finished in Tatar Strait in the Miocene as a result of rift formation accompanied by area basalt volcanism manifested in Moneronskiy rise located in the central part of Tatar Strait.

Sakhalin Island is a fragment of Eurasian continental margin separated from it by the Cenozoic rift structure of Tatar Strait. In this context, Paleozoic and Mesozoic–Early Paleogene structures widespread in Sikhote-Alin are traced on the island though they are considerably dislocated here by a system of faults drawn together and having north-south extension. The western Sakhalin is occupied by thick (up to 10 km) Cretaceous–Paleogene turbidites of the fore-arc trough of Sikhote-Alin volcanogenic belt and under them basement rocks like intensely dislocated Jurassic–

Neocomian and Paleozoic oceanic formations are buried. To the east, these rocks of ancient oceanic plates, which underwent intense greenschist, glaucophanitic and locally eclogitic metamorphism, form the submeridional zone of the East Sakhalin mountains bounded by faults from where it can be followed to the south of Sakhalin Island and farther to Hokkaido Island. The extreme east of Sakhalin Island is occupied by fragments of Campanian–Paleocene island arc and they together with fragments of Cretaceous oceanic plate are thrust on Sakhalin structures from the Okhotsk Sea Plate.

Basites-ultrabasites participating in the scaly-thrust structures and separated from Cretaceous oceanic crust (earlier had belonged to the Okhotsk Sea Plate), apparently create the linear magnetic anomaly along the eastern coast of Sakhalin Island. These ultrabasic rocks are apparently remnants of the Late Cretaceous–Early Paleogene zones of subduction. On deep seismic sounding profiles, listric faults sloping approximately at an angle of 15° and penetrating into the upper mantle from the sedimentary cover; discontinuities observed on the M-boundary surface, thickness variations of the crust upper layer, and existence of crust blocks with high values of seismic velocities are clearly distinguished [17].

Kuril Basin belongs to back-arc depressions. Thick (more than 4000 m) sedimentary beds overlie acoustic basement, which evidently is a volcanogenic sedimentary layer, and beneath it, the third layer of oceanic crust is observed with seismic velocities $6.4\text{--}6.8\text{ km}\cdot\text{s}^{-1}$ and thickness of 5 km in the middle of the basin. High heat flow is characteristic of the basin [30]. The acoustic basement is intensely rugged; scarps associated with faults are abundant on the slopes. From data obtained with the use of reflected wave method the sedimentary cover is subdivided into two complexes. The upper one, which is likely of Pliocene–Quaternary age, with a thickness of up to 800–1000 m is characterized by thin stratification. Sediments of the lower complex in the central part of the basin have thickness more than 3000 m and represent acoustically transparent layer.

According to seismic data, a rift or spreading structure is distinguished in the central part of the Kuril Basin [17]. This structure is pronounced in the upper sedimentary layers. Faults forming it penetrate into the upper mantle where zones of anomalous low velocity ($7.0\text{--}7.5\text{ km}\cdot\text{s}^{-1}$) are probably the asthenospheric diapir containing magma-formation sources.

The Marginal Trough is located between the outer and inner Kuril island arcs, contact with which occurs along the system of faults. The width of the trough is 45–60 km. It is composed of Neogene and Quaternary tuff-sedimentary formations. The thickness of the sediments in the axial zone exceeds 3 km, but seismic surveys have not traced the bottom of the sediments. The spread of volcanogenic rocks in sediment deposits is associated with rift formation, the structures of which are currently covered by sediments. The thickness of the crust under the trough is reduced to 20 km.

Northwest Pacific Basin according to geological and geophysical data has the most ancient crust in the region described (about 150 Ma) and is covered through by sedimentary cover of thickness 300–400 m. According to DSDP Holes 303 and 580, the cover is composed of diatom and radiolarian ooze and laminated clays enriched with Late Miocene–Quaternary ash overlying zeolitic pelagic clays, clayey nanosilt and siliceous rocks. At a depth of 211 m, those sediments are underlain by Lower Cretaceous pelagic zeolitic clays and in the bottom of the section with interlayers of flinty slate and nanoplankton limestone. At a depth of 284.75 m, sediments are underlain by pillow lavas of Jurassic and Cretaceous basalts of MORB type accumulated with the activity of spreading axes of different orientation [12]. The thickness of the crust is about 6–8 km.

The Upper Mantle beneath the Sea of Okhotsk is characterized by both horizontal and vertical heterogeneities. From seismic tomography data [2, 5], we note decreased values of seismic velocities in the upper mantle beneath the Sea of Okhotsk. In the Kuril Basin on the basis of electromagnetic research in the depth range of 30–65 km a layer of specific conductivity $0.3\text{--}0.5\text{ S}\cdot\text{m}^{-1}$ and integral conductivity of approximately 15,000 S is distinguished [15]. The nature of the layer is related to partial melting and its distribution is limited to the basin bounds. At a depth of 100 km, the second conductivity layer may be separated. Obtained results are in agreement with deep temperatures in the upper mantle, seismic research and other geophysical data [16].

The asthenosphere in the upper mantle is separated by various research methods: seismic, geothermal, electromagnetic. The upper boundary of the asthenosphere is assumed to be isothermal line of 1000–1200 °C. Under such temperatures the upper mantle rocks partially melt with account for deep fluid influence [24, 30]. The asthenosphere is located at a depth of 50–70 km in the upper mantle of the Sea of Okhotsk, and at a depth of approximately 100 km beneath the Northwestern Pacific Basin. The diapirs of partial melted matter depart from the asthenosphere. They reach a depth of 20–30 km beneath the sedimentary trough of Tatar Strait, Deryugin basin and Kuril Basin and cause the active tectonic regime, manifested in volcanic, seismic and hydrothermal activities.

Beneath the North Sakhalin sedimentary basin containing almost all oil and gas fields of Sakhalin, the asthenosphere is located at a depth of approximately 70 km. Besides, hydrocarbon deposits were noted above asthenospheric diapirs in the sedimentary basin of Tatar Strait and Deryugin Basin, and sulfide mineralization was revealed in Kuril Basin in submarine volcano peaks. Mantle fluids of asthenospheric diapirs determine the geodynamic evolution of sedimentary basins and the formation of hydrocarbon deposits in them (Fig. 11).

In Sakhalin, the asthenosphere conductivity layer occurs in the upper mantle beneath the whole island and Tatar Strait where it is noted at a depth of 80 km. Along the continent eastern margin in the upper mantle the junction is noted of the asthenosphere high-conductivity layers and the continent rigid high-resistance

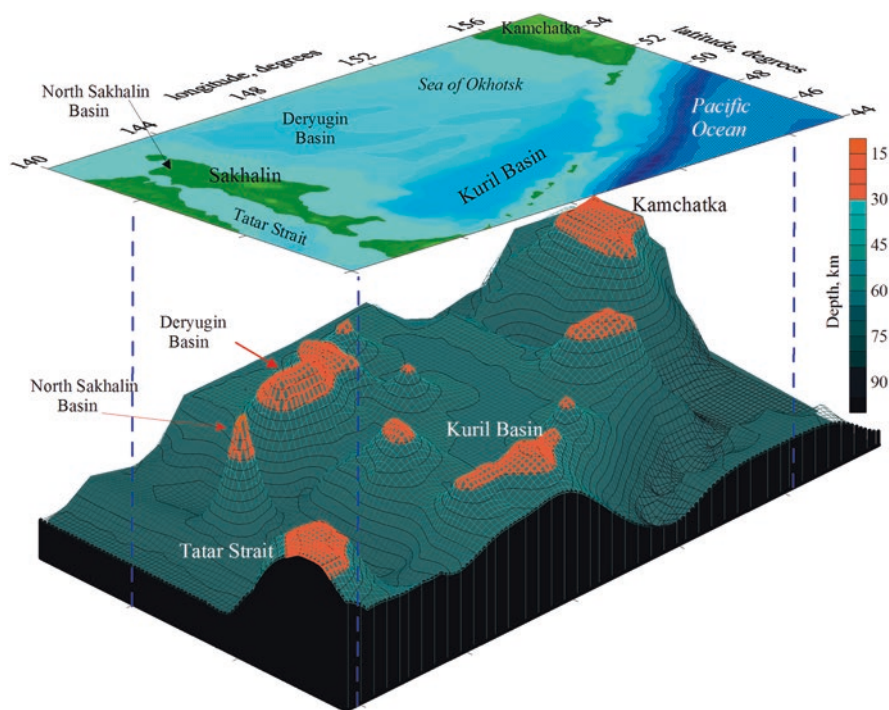


Fig. 11 3-D Model of lithosphere structure beneath the Sea of Okhotsk [26]. Bathymetry/topography of the Okhotsk Sea region is given at the top [27] and the asthenosphere beneath it (red color shows the area of magma formation)

upper mantle. Besides, beneath Sakhalin in the depth range of 300–500 km anomalous high-resistance areas are noted, which may be related to the cold subsiding plate of subduction zone occurring there.

Beneath South Kuril islands in the geotransverse area, the depth down to conductivity layer in the upper mantle is 60–80 km [1]. Geothermal observations corroborate the results of electromagnetic research. Highest temperatures are observed beneath Kuril Basin where partial melting area is located at a depth of approximately 25 km. Lowest values are noted beneath the deep trench [30]. On the sea-floor surface of Kuril Basin anomalous mantle rise corresponds to rift structures and basic magmatism. Deep temperatures in Moho boundary vary from 100 °C in the Pacific to 800 °C beneath Tatar Strait and Kuril Basin.

Thus maximum temperatures and minimum thickness of the lithosphere are characteristic of deep basins of the Okhotsk Sea. In axial areas of the structures the asthenospheric layer rises to 15 km; in the sides it subsides to depths of 40–50 km and beneath the Pacific it goes down to a depth of 100 km.

8 Conclusions

The combined interpretation of geological and geophysical data enables to reveal features of the high activity of modern geodynamic processes in the transition zone from the Eurasian continent to the Pacific Ocean. Systematic research was undertaken along deep cross-sections of the lithosphere in the transition zone across the Sea of Okhotsk, Sea of Japan, Philippine Sea and South China sea. The distinctive features that characterize the transition zone were established.

- The presence of an asthenospheric layer in the upper mantle and the rising of diapirs of a hot anomalous mantle material, which controlled the formation of the sedimentary basins in the marginal seas. There is an obvious correlation among the geological features, tectonomagmatic activity, and the structure of the upper mantle. The tectonic active regions, such as the island arcs and the rifts of the marginal seas, correlate with a thick, clearly expressed magma-generating asthenosphere.
- The asthenospheric rises are marked on the Earth's surface by rift formations and mainly tholeiitic magma flows. They reside in extension zones and develop in regions of a thinner lithosphere and high heat flow.
- The sedimentary basins are specific by their anomalous deep structure. Their formation is often associated with recent and ancient subduction zones. The sedimentary basins are characterized by:
 - active magmatism at the initial stage of formation;
 - high density of heat flow caused by uplifting of the asthenosphere in the crust;
 - localization of asthenosphere diapirs under the crust in the upper mantle;
 - asthenospheric diapirs are channels, along which hot mantle fluids from the asthenosphere penetrate into the sedimentary basins.

Acknowledgements This work was conducted in the framework of budgetary funding of the Geophysical Center of RAS, adopted by the Ministry of Science and Higher Education of the Russian Federation.

This article is written in memory of a joint multiyear and interesting work with our now deceased leader, Dr. Alexander G. Rodnikov (1937–2015).

References

1. Alperovich IM, Nikiforov VM, Usanova MI (1978) Magnitotelluricheskie issledovaniya na o. Iturup (Magnetotelluric research on Iturup Island). *Izvestiya AN SSSR. Fizika Zemli* 1:120–123
2. Anderson DL, Dziewonski AM (1984) Sejsmicheskaya tomografiya (Seismic tomography). *V Mire Nauki* 12:16–25
3. Aprodov VA (1982) *Vulkany (The Volcanoes)*. Mysl, Moskva

4. Biebow N, Ludmann T, Karp B, Kulinich R (eds) (2000) Cruise Reports: Komex V and VI, RV Professor Gagarinsky Cruise 26 and MV Marshal Gelovany Cruise 1. GEOMAR Report 88. Kiel
5. Bijwaard H, Spakman W, Engdahl ER (1998) Closing the gap between regional and global travel time tomography. *J Geoph Res* 103(B12):30055–30078
6. Bondarenko VI, Rashidov VA (2004) Novye dannye o morfologii podvodnyh vulkanicheskikh hrebtoy Gidrografa i Broutona (Kuril'skaya ostrovnaya duga) (New data regarding morphology of submarine volcanic ridges Gidrographov and Browton (Kuril island arc)). *Vestnik KRAUNC. Seriya Nauki o Zemle* 4:51–58
7. Filatova NI, Rodnikov AG (2006) Ohotomorskij geotravers: tektonomagmaticheskaya ehvoluciya kajnozojskikh struktur rastyazheniya v kontekste ih glubinnogo stroeniya (The Sea of Okhotsk geotraverse: Tectono-magmatic evolution of Cenozoic extension structures in the context of their deep structure). *Doklady RAN* 411(3):360–365
8. Gatinskiy YG, Rundkvist DV, Tyupkin YS (2005) Bokovye struktury i kinematika Vostochnoj i Centralnoj Azii po dannym GPS (Block structures and kinematics of East and Central Asia according to GPS). *Geotektonika* 5:3–19
9. Gorshkov GS (1967) Vulkanizm Kuril'skoj ostrovnnoj dugi (Volcanism of the Kuril island arc). Nauka, Moskva
10. Gushchenko II (1979) Izverzheniya vulkanov mira. Katalog (Volcanic eruptions of the world. Catalogue). Nauka, Moskva
11. Jolivet L, Shibuya H, Fournier M (1995) Paleomagnetic rotation and the Japan Sea opening. In: Taylor B, Natland J (eds) Active margins and marginal basins of the western Pacific, *Geophys Monogr*, vol 88. American Geophysical Union, Washington, DC, pp 355–369
12. Khain VE (2001) Tektonika kontinentov i okeanov (The tectonics of continents and oceans). Nauchnyi Mir, Moskva
13. Kiratzi A, Papazachos C (1996) Moment-tensor summation to derive the active crustal deformation in Japan. *B Seismol Soc Am* 86(3):821–831
14. Kondorskaya NV (ed) (1964–1997) Zemletryaseniya v SSSR, 1962–1991 (ezhegodniki) (The earthquakes in the USSR, 1962–1991 (annuals)). Nauka, Moskva
15. Lyapishev AM, Sychev PM, Semenov VY (1987) Struktura elektroprovodnosti verhnjej mantii Kuril'skoj kotloviny Ohotskogo morya (The structure of electrical conduction of the upper mantle of the Kuril Basin of the Sea of Okhotsk). *Tihookeanskaya Geologiya* 4:45–55
16. Maruyama S, Isozaki Y, Kimura G, Terabayashi M (1997) Paleogeographic maps of the Japanese Islands: plate tectonic synthesis from 750 Ma to the present. *Island Arc* 6(1):121–142
17. Piip VB, Rodnikov AG (2004) The Sea of Okhotsk crust from deep seismic sounding data. *Russian J Earth Sci.* <https://doi.org/10.2205/2003ES000140>
18. Pollak HN, Hurter SJ, Johnson JR (1991) The new global heat flow compilation. Michigan, Department of Geological Sciences, University of Michigan
19. Pushcharovskii YM (ed) (1992) Podvodnyj vulkanizm i zonalnost Kuril'skoj ostrovnnoj dugi (The submarine volcanism and zonality of Kuril island arc). Nauka, Moskva
20. Rashidov VA, Bondarenko VI (2003) Podvodnyj vulkanicheskij massiv Ehdelshtejna (Kuril'skaya ostrovnaya duga) (Submarine volcanic massif of Edelshtein (Kuril island arc)). *Vulkanologiya i Seismologiya* 1:3–13
21. Rashidov VA, Bondarenko VI (2004) Geofizicheskie issledovaniya podvodnogo vulkana Krylatka (Kuril'skaya ostrovnaya duga) (Geophysical investigations of submarine volcano Krylatka (Kuril island arc)). *Vulkanologiya i Seismologiya* 4:65–76
22. Rodnikov AG (1986) Mezhdunarodnyj proekt «Geotravers»: zadachi, problemy, perspektivy (International project “Geotraverse”: tasks, challenges, prospects). *Vestn Akad Nauk SSSR* 2:101–106
23. Rodnikov AG (1997) Deep structure of the sedimentary basins along the Okhotsk Sea Geotraverse. Extended abstracts book: 59th EAGE Conference and Technical Exhibition, Geneva, Switzerland, 26–30 May 1997. 2(D-022):1

24. Rodnikov AG, Tuezov IK, Kharakhinov VV (eds) (1996) *Struktura i dinamika litosfery i astenosfery Ohotomorskogo regiona* (Structure and dynamics of the lithosphere and asthenosphere of the Okhotsk Sea region). Nacional'nyj geofizicheskij komitet, Rossijskaya Akademiya Nauk, Moskva
25. Rodnikov AG, Sergejeva NA, Zabarinskaya LP (2001) Deep structure of the Eurasia-Pacific transition zone. *Russian J Earth Sci.* <https://doi.org/10.2205/2001ES000061>
26. Rodnikov AG, Zabarinskaya LP, Rashidov VA, Sergejeva NA (2014) Geodinamicheskie modeli glubinnogo stroeniya regionov prirodnyh katastrof aktivnyh kontinental'nyh okrain (Geodynamic models of the deep structure beneath the natural disaster regions of active continental margins). *Nauchnyj mir*, Moskva
27. Smith WHF, Sandwell DT (1997) Global seafloor topography from satellite altimetry and ship depth soundings. *Science* 277:1957–1962
28. Sergeev KF, Krasnyi ML (eds) (1987) *Geologo-geofizicheskij atlas Kurilo-Kamchatskoj ostrovnnoj sistemy* (Geological and geophysical atlas of Kuril-Kamchatka island system). Ministerstvo geologii SSSR, Vsesoyuznyj ordena Lenina nauchno-issledovatel'skij geologicheskij institut (VSEGEI), Leningrad
29. Smirnov YB (1986) *Geotermicheskaya karta Severnoj Evrazii i metody analiza termicheskoj struktury litosfery (poyasnitel'nyj-tekst)* (Geothermal map of northern Eurasia and methods of lithosphere geothermal structure analysis (explanatory text)). Geologicheskij institut AN SSSR, Moskva
30. Smirnov YB, Sugrobov VM (1980) *Zemnoj teplovoj potok v Kurilo-Kamchatskoj i Aleutskoj provincijah* (Earth heat flow in the Kuril-Kamchatka and Aleutian provinces). *Vulkanologiya i Sejsmologiya* 2:3–17
31. Starovoit OE (ed) (1997–2017) *Zemletryaseniya Severnoj Evrazii, 1992–2011 (ezhegodniki)* (Earthquakes of the Northern Eurasia, 1992–2011 (annuals)). Geofizicheskaya Sluzhba RAN, Obninsk
32. Tamaki K, Honza E (1985) Incipient subduction and obduction along the Eastern margin of the Japan Sea. *Tectonophysics* 119:381–406
33. Tuezov IK (1988) *Karta teplovogo potoka Tihogo okeana i prilegayushchih kontinentov* (Heat flow map of the Pacific ocean and adjacent continents). DVO AN SSSR, Khabarovsk
34. Yunga SL, Rogozhin EA (2000) *Sejsmichnost, mekhanizmy ochagov zemletryasenij i sejsmotektonicheskie deformacii v predelah aktivnyh blokov litosfery* (Seismicity, earthquake focal mechanisms and seismotectonic deformations within active blocks of the lithosphere). In: *Novejshaya tektonika, geodinamika i sejsmichnost Severnoj Evrazii* (Neotectonics, Geodynamics and Seismicity of North Eurasia). Probel, Moskva
35. Zhao D, Pirajno F, Dobretsov N, Liu L (2010) Mantle structure and dynamics under East Russia and adjacent regions. *Russ Geol Geophys* 51(9):1188–1203

Structural Geodynamic Zoning of Eastern European Platform – The Basis for Creating of Geothermal Model



Vladimir Makeev, Natalia Makarova, Valentina Svalova,
and Tatyana Sukhanova

1 Introduction

The structural-geodynamic zoning of platform areas based on the geodynamic principles of the superposition of heterogeneous stresses is an actual problem of modernity [1, 3–7, 9, 10]. In the process of geodynamic research were identified and typed deformation of the Earth's crust layers of the East European platform, taking into account the its primary stratification (Figs. 1, 2, 3, 4, and 5). From our point of view, such zoning can be considered as a basis for the development of a geothermal model of the platform lithosphere.

Irregularity of heat flow are considered as a result of superposition of heterogeneous endogenous factors localized at different levels of the lithosphere: in the deep layers of the Earth's crust, in the Moho discontinuity and the lithosphere base [8, 10]. On the basis of structural-geodynamic approach [5–7] the authors have identified geodynamic active centers (tectonic-magmatic hearth) and deformations (mantle uplift and down lift, thickening and thinning in the deep layers of the Earth's crust) at different hypsometric (topographic) levels, – which may be the cause of heat flow irregulars.

The research is devoted to the analysis of the surface of the mantle lithosphere (Mohorovich discontinuity, or Moho). On this surface, hypsometric centers of uplifts and down lift, relative lows and high were identified (Fig. 2). We have investigated the thickness (isopachytes, km) of the lower (estimated layer “basalt”), intermediate (estimated layer “diorite”) and upper (estimated layer “granite”) layers of the Earth's crust in the aspect of their deformations (Figs. 3, 4, and 5) [2, 3, 10].

V. Makeev (✉) · V. Svalova
Sergeev Institute of Environmental Geoscience of the RAS, Moscow, Russia

N. Makarova · T. Sukhanova
Geological Faculty, Moscow State University, Moscow, Russia

© The Author(s), under exclusive license to Springer Nature
Switzerland AG 2021

V. Svalova (ed.), *Heat-Mass Transfer and Geodynamics of the Lithosphere*,
Innovation and Discovery in Russian Science and Engineering,
https://doi.org/10.1007/978-3-030-63571-8_25

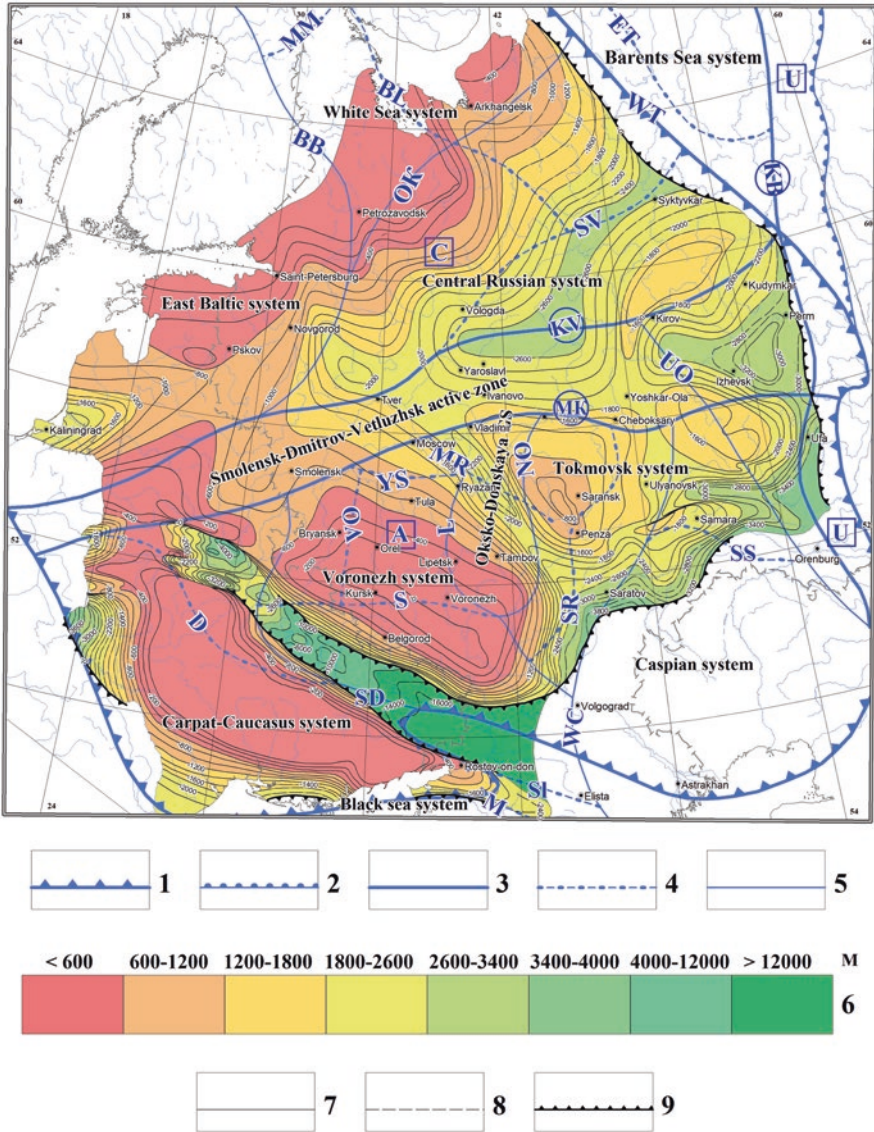


Fig. 1 The recent geodynamic systems of the Eastern European platform (EEP) [7], put on the deformations (strains) of the EEP crystalline basement

1 – borders of the Eastern European platform; 2 – borders of the Urals and the Caucasus orogens. *Geodynamic active zones*: 3 – pan-regional, 4 – regional, 5 – local. 6 – The surface of the crystalline basement (m): 7 – installed, 8 – assumed. 9 – The high gradient scarp of the crystalline basement. *Pan-regional geodynamic systems* (letters in squares): A – Alpine, C – Scandinavian, U – Ural. Shown on map – Smolensk-Dmitrov-Vetluzhsk geodynamic active zone. *Regional geodynamic systems*: Carpat-Caucasus, Tokmovsk, Black sea, Caspian, White Sea, Barents Sea, East Baltic, Voronezh, Central Russian (shown on the map). Oka-Don local geodynamic system (shown on the map)

Thinning and thickening of the layers were considered as deformations. These studies are based on the maps of deep layers, which were published by G. Krasnopevtseva and Yu. Shchukin in the year 2000 [2].

The evolution of structural forms from layer to layer and to the Earth's surface is traced. For all deformed layers is typical the geodynamics active centers, that are genetically related to each other. Such a center is the Central Caspian, manifested by the stability mantle uplift (Fig. 2). Above it reduced the thickness of all deep layers of the Earth's crust (Figs. 3, 4, and 5). Above the Central-Finland and the Karel-Finnish down lift (geodynamic centers) increase thickness of deep layers (Figs. 2, 3, 4, and 5). From the geodynamic centers stress propagate in different directions, causing the development of wave-like and curved deformations, grouped conformal around these centers. In general, they form geodynamic area: Central Caspian, Central-Finland, the Karel-Finnish and other. The boundaries of the area are active zones, in most cases manifested in the near-surface neotectonic structure.

2 Structural-Geodynamic Research of the Earth's Crust Layers

As a result of the typing are defined through areas (main areas), manifested in each layer and areas, manifested only in separate layers (local areas). In this regard, a special role belongs to the intermediate layer of the Earth's crust, which is considered as compensating for thickening and thinning, localized in the upper and lower layers.

Within main the areas are defined local structures. Their origin is associated with autonomous tectonic-magmatic processes. Thus, in the Earth's crust are established processes initiated by the influence of external sources, located on the borders of the East-European platform (tectonically active mountain areas), and the processes initiated by the influence of intra-platform sources (tectonic-magmatic centers or hearth).

Structural geodynamic research of the deep layers (Moho discontinuity, lower, intermediate and upper layers) allowed defining two types of deformations: (1) through (main type) and (2) localized in separate layers (local type). The selected deformations of the deep layers were compared with the near-surface neotectonic structures (upland and lowland), between which a geodynamic connection was established.



Fig. 1 (continued) *Geodynamic active zones* (GdAZ) (letters in circles): KB – Kamsk-Belsk, KV – Klinsk-Vyatsk, MK – Moskvoretsk-Kamsk. *The local geodynamic active zones (secondary)* (GdAZ): BB – Belomor-Baltic, BL – Belomorsk, VO – Verkhneoksk, ET – East-Timansk, D – Dnieper, WC – West-Caspian, WT – West-Timansk, L – Losevsk, MM – Murmansk, M – Manych, MR – Moskvoretsk-Ryazansk, NO – Nizhneoksk, OK – Onezhsk-Karpogorsk, S – Seimsk, SV – Sukhon-Vychegdsk, SD – Seversk-Donetsk, Sl – Salsk, SR – Sura, SS – Syzran-Samara, UO – Urzhum-Orenburgsk, YS – Yukhnov-Serpukhovsk

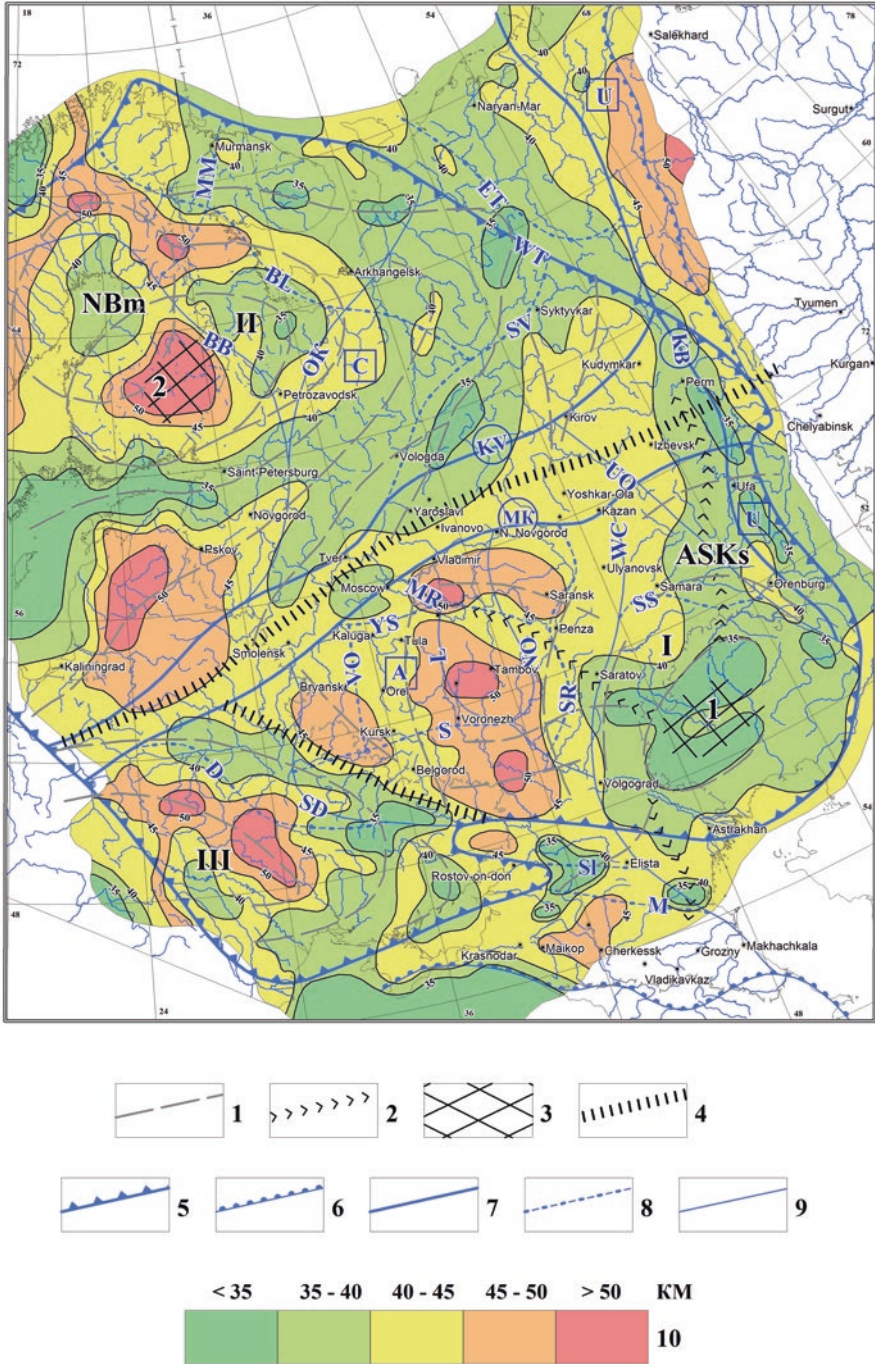


Fig. 2 Deformations (strains) of the Moho discontinuity

The geodynamic active areas – Caspian, Baltic, Central Russian and Pre-Dniester – respond to through main structures (deformations or strains) (Figs. 2 and 3). They occupy large areas, but despite the fact that they are manifested in all the deep layers, each of them has its own specificity.

Caspian Geodynamic Areas With a stable growth of the Central Caspian active center in the form of mantle uplift, the thickness of all layers tectonic is thinned up to wedging (from 10–5 km to zero). At the same time, an increase in the Earth's crust thickness from this uplift (35 km) to the periphery (50 km) is observed. From layer to layer, the total area of the Caspian area (region) is reduced and its orientation changes – from sublatitudinal to submeridional. Submeridional orientation is characteristic of the neotectonic structure expressed in deformations of the Earth's surface.

Baltic Geodynamic Areas In the Baltic areas the Central Finnish active center keeps its overall location in all layers. The active center is characterized by the tectonic down lift of the mantle lithosphere up to 50 km, and in the higher layers over it there are thickening (blowing) up to 20 km. The thickness of the lower layer from this center to the periphery decreases from 15–20 km to 10 and 5 km. Generally the thickness of the Earth's crust is reduced from this thickening (active center) to the periphery of from about 60–70 km to 30–40 km. The area of the Baltic area has a sustained sublatitudinal orientation in the Moho surface, as well as in the lower and upper layers. In the intermediate layer, the area configuration is sharply reduced and its orientation changes: it becomes submeridional.

Central Russian Geodynamic Areas The Central-Russian area with the Smolensk-Orel active center (tectonic stresses source) is located in the intermediate and upper layers of the Earth's crust (Figs. 4 and 5). In it there is the thinning of the intermediate layer up to 10 km and thickening of the top layer to 15–20 km.

Pre-Dniester Geodynamic Area The deformations (strains) of the Pre-Dniester area are expressed in all layers of the Earth's crust and the surface of Moho. In Moho its depth changes, and in layers changes their thickness from 5–10 km to 15–25 km. The total area of the Pre-Dniester area is kept from layer to layer, but the drawing wave-like and curved deformations is not always the same.



Fig. 2 (continued) 1 – axial lines of the relative lows and high of the Moho discontinuity; 2 – intermediate deformations (strains): topographic hollow and “nose” (structural terrace), 3 – geodynamic active centers (mantle uplift and down lift), 4 – geodynamic active zones – the boundaries of geodynamic areas

5 – borders of the Eastern European Platform; 6 – borders of the Caucasus and the Ural orogens. *Geodynamic active zones*: 7 – regional, 8 – local. 9 – the isoline of the Moho discontinuity (km), 10 – the depth scale of the Moho [2]. The Arabic data shows geodynamic active centers: 1 – Central Caspian and 2 – Central Finnish. *Structural-geodynamic areas*: I – Caspian, II – Baltic and III – Pre-Dniester. NBm – North-Bothnian mantle uplift, ASKs – All-Sirt-Kama intermediate structure

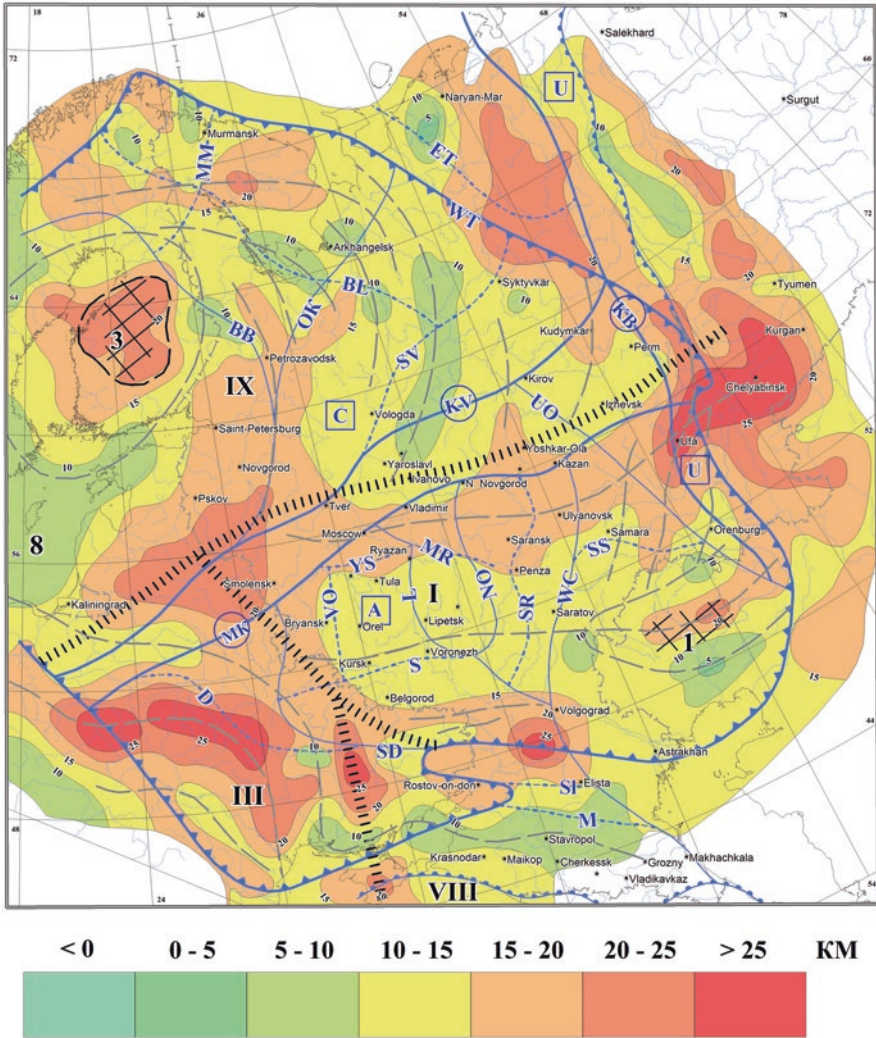


Fig. 3 Deformations of the lower (“basalt”) layer of the Earth’s crust
 Isolines with Arabic numbers – isopachytes (km) of the lower crust [2]
 Black dotted lines indicate thickening and thinning of the lower layer
 Structural-geodynamic areas: I – Caspian, III – Pre-Dniester, VIII – Pre-Caucasus, IX – Eastern Baltic. Geodynamic active centers: 3 – Karel-Finnish, 8 – Gotland

The Eastern Baltic, Onega-Norland, Norland, White Sea-Pre-Timanskaya and Pre-Caucasus deformation areas are manifested in separate layers of the Earth’s crust. They are located within the main (large) areas in different deep layers of the Earth’s crust.

Thus, the structure of the layers of the Earth’s crust changes under the influence of various causes. Deformation of any layer can be caused by the influence of

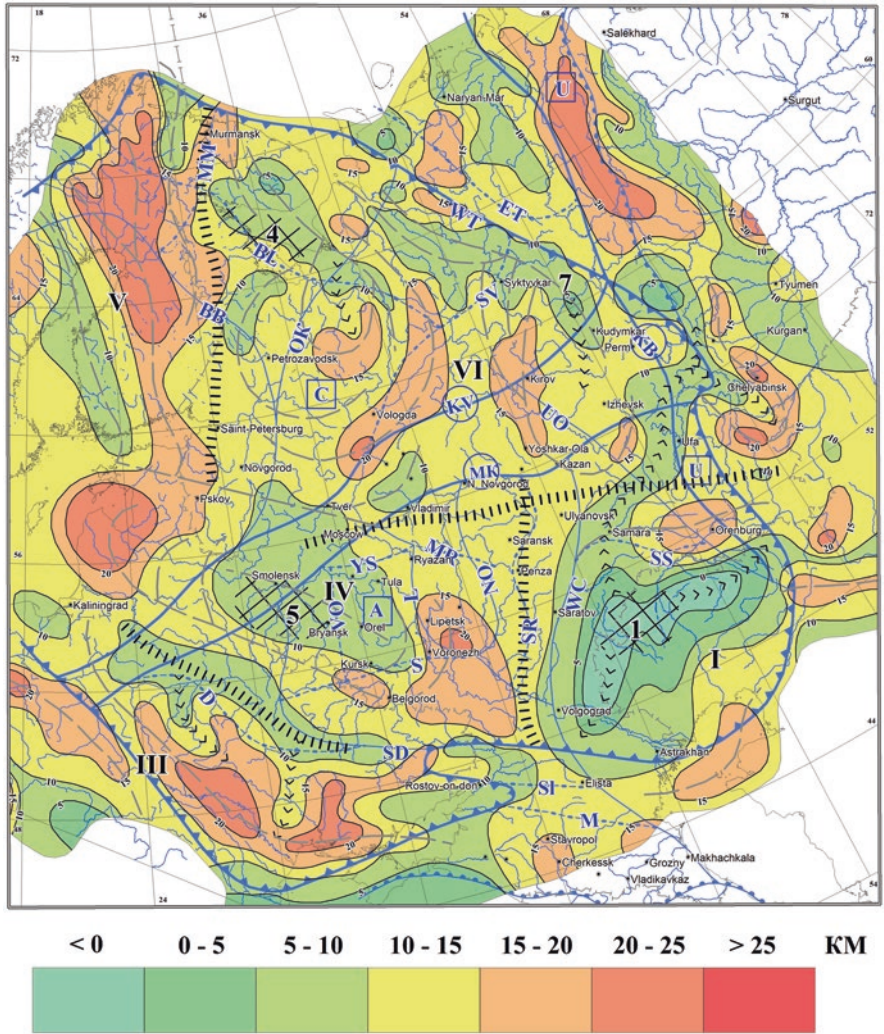


Fig. 4 Deformations of the intermediate (“diorite”) layer of the Earth’s crust
 Isolines with Arabic numbers – isopachytes (km) of the intermediate layer [2]
 Black dotted lines indicate thickening and thinning of the intermediate layer
 Structural-geodynamic areas: III – Pre-Dniester, IV – Central Russian, V – Norland, VI – Belomorsk-Pre-Timansk. Geodynamic active centers (hearth): 4 – Kandalaksha, 5 – Smolensk-Orlovsk, 7 – Pre-Timansk (assumed)

regional (plate tectonics) processes in the mantle lithosphere, and local (intra-platform) processes occurring in the Earth’s crust. The tectonic down lift and uplift of the lithosphere mantle cause the deformations manifested by thinning and thickening in the above lying layers. The tectonic down lift and uplift of the lithosphere mantle cause the deformations manifested by thinning and thickening in the above

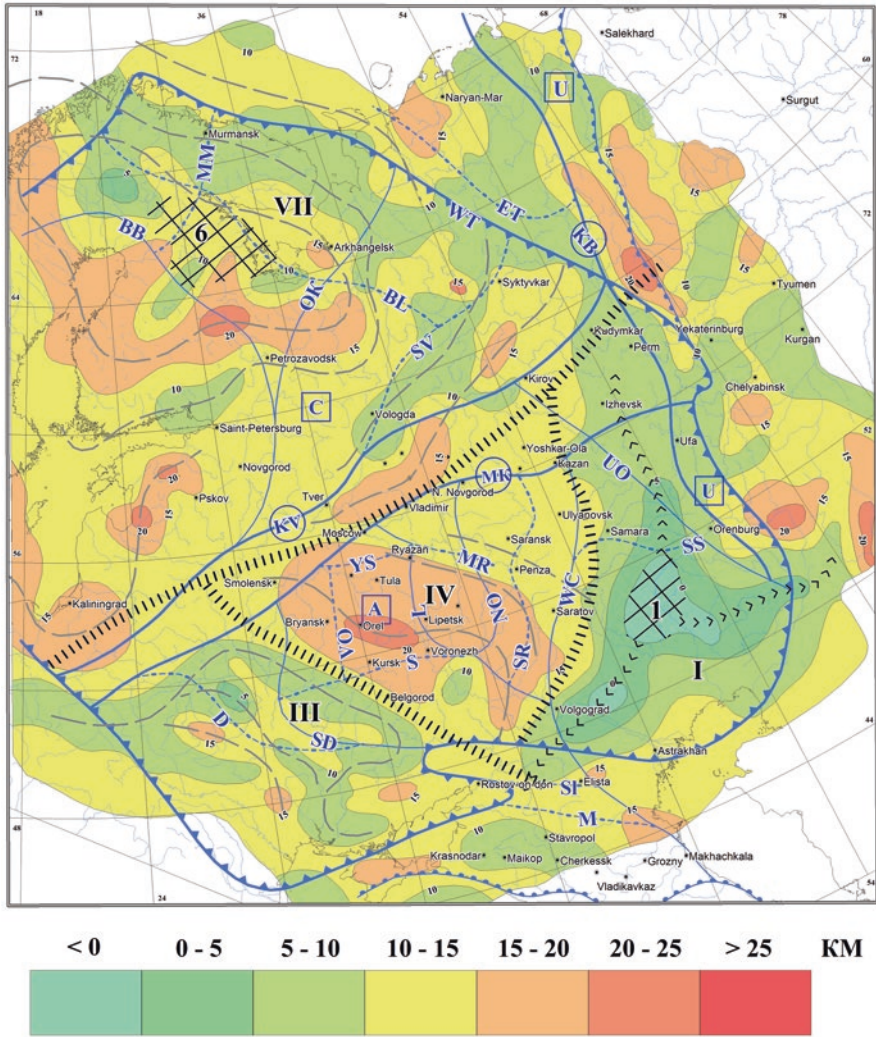


Fig. 5 Deformations of the upper (“granite”) layer of the Earth’s crust
 Isolines with Arabic numbers – isopachytes (km) of the upper layer [2]
 Black dotted lines indicate thickening and thinning of the upper layer
 Structural-geodynamic areas: III – Pre-Dniester, IV – Central-Russian, VII – Onega-Norland. 6 – Northern Norland geodynamic active center

lying layers. These deformations, in turn, can be centers or tectonic-magmatic hearth (sources of stresses) for the development of associated wave-like warping, which can extend laterally and vertically.

In this regard, it is possible to note the special role of the intermediate layer, which is considered as compensating thickening and thinning, localized in the upper and lower layers. The different structure of each layer of the Earth’s crust confirms

the known fact of tectonics delamination of the lithosphere by stresses and deformations (strains). At the same time, the observed through development of deformations from layer to layer in vertical direction or the expression of some of them in one or two deep layers indicates the subvertical tectonic separability of the Earth's crust.

3 Deep Layers of the Earth's Crust and Near-Surface Neotectonic Structures

Comparison of deformations of the deep layers with the near-surface neotectonic structures (upland and down land) indicates their geodynamic connection with each other. The large neotectonic Caspian lowland (depression) is expressed in uplift the surface of the mantle lithosphere and in all higher layers of the Earth's crust. A large neotectonic upland of the Fennoscandian shield is expressed in the downlift of the mantle lithosphere and in the thickening (bulges of the thickness) of the lower and upper layers. Small neotectonic structures, such as the Oka-Don lowland, Voronezh upland, etc., are expressed in separate deep layers. The Oka-Don lowland (trough) is expressed in the thinning of the upper layer, the Voronezh upland – in the thinning of the intermediate layer.

Pan-regional and regional geodynamical active zones inditified by deformations of the Earth's surface are also reflected in the structure of the deep layers. Thus, the Smolensk-Dmitrov-Vetluzhsk, West-Caspian zones are manifested in the form of borders between the deep geodynamics areas: Smolensk-Dmitrov-Vetluzhsk zone is located between the Caspian and the East-Baltic geodynamic areas, West-Caspian zone – between Caspian and Tokmovsk geodynamic areas. This correlation of near-surface neotectonic and deep structures may indicate the age of deep structures, most of which are obviously the neotectonics.

4 Conclusion

Thus, our research have confirmed the fact of horizontal and vertical tectonics delamination of the platform lithosphere by stresses and deformations at the neotectonic stage of its evolution. Regional (general) and local geodynamic centers located at different hypsometric levels of the lithosphere are sources of stresses and deformations (strains) and formation of geodynamic active zones. The superposition of different origin of the strains can be considered as the cause of the heat flow irregularity.

Acknowledgements This work was supported by the Basic Research Program of the Presidium of the Russian Academy of Sciences No. 19 “Fundamental problems of geological and geophysical studies of lithospheric processes” No. 13000/2215-1 of 04.19.2018.

References

1. Artyushkov EV (1993) Physical tectonics. Science, 456 p
2. Krasnopevtseva GV, Schukin YK (2000) Volumetric deep model of the Earth's crust of the East-European platform according to regional seismic data. Regional Geol Metallogeny 10:73–84. VSEGEI, Saint-Petersburg
3. Leonov MG (2008) Tectonics of consolidated crust. Science, 457 p
4. Leonov YG, Gushchenko OI, Kopp ML, Raststayev LM (2001) Connection of Late Cenozoic stresses and deformations in the Caucasus sector of the Alpine Belt and in its northern platform frame. Geotectonic 1:36–59
5. Makarov VI (1996) Regional specificity of the recent geodynamics of platform areas in connection with the assessment of their tectonics activity. Buried Volga Region and near-Caspian. Special edition number 13, pp 49–60
6. Makarov VI, Makarova NV, Nesmeyanov SA, Makeev VM, Dorozhko AL, Zaitsev AV (2006) The recent tectonics and geodynamics: the area of articulation of the East-European platform and the Scythian plate. Nauka, 206 p
7. Makarova NV, Makeev VM, Dorozhko AL, Sukhanova TV, Korobova IV (2017) Geodynamic systems and geodynamic active zones of the East-European platform. Bull Mosk Society of nature testers. Dep. Geol 91(4–5):9–25
8. Polyak BG, Khutorskoy MD (2018) Heat flow from earth's interior as indicator of deep processes. Georesources 20(4):366–376
9. Sim LA (2000) The impact of global tectogenesis on the recent stress state of European platforms. M.B. Gzowski and the development of tectonophysics. Science:326–350
10. Yudahin FN, Schukin YK, Makarov VI (2003) The deep structure and modern geodynamics processes in the lithosphere of the East-European platform. Ural Department of RAS, Yekaterinburg, 299 p

Part VI

Seismicity

Recognition of Strong Earthquake-Prone Areas with a Single Learning Class. Caucasus, $M \geq 6.0$



Boris Dzeboev, Boris Dzeranov, and Maxim Pasishnichenko

1 Introduction

Earthquake-prone areas recognition is an important part of seismic zoning. It is known that strong ($M \geq M_0$) earthquakes in the studied region, as a rule, do not occur throughout the entire territory. Starting from the 70s of the last century the training dichotomy algorithms are used to divide the territory into two non-intersecting areas, where the occurrence of a strong earthquake is possible and not [1–3]. The recognition algorithm with training on two classes firstly was used in 1972 in the Pamir and Tien Shan regions [4, 5]. The approach which was developed this way later was called EPA (Earthquake-Prone Areas recognition) [2], has been successfully used for more than four decades to recognize strong earthquake-prone areas in various mountainous countries [2, 3, 6]. A large amount of statistics was accumulated based on the research findings. Nowadays the EPA approach has become classic. Its creation dates back to the works of I.M. Gelfand, V.I. Keilis-Borok, F. Press, L. Knopov et al. [2, 4, 5, 7, 8].

In 2014, a posteriori independent verification of the recognition results obtained by the EPA method [3] was performed. This verification showed that 87% of the strong earthquakes occurring in the regions analyzed by the EPA method after the publication of the relevant works occurred in areas recognized as potentially high seismicity. At the same time, 30% of earthquakes occurred in the recognized high seismicity zones, where strong ($M \geq M_0$) seismic events have not occurred before.

As a pattern recognition problem, the EPA problem is interpreted as a dichotomy with training for a variety of objects that have a vector representation in space of

B. Dzeboev (✉) · M. Pasishnichenko · B. Dzeranov
Geophysical Center of the Russian Academy of Sciences (GC RAS),
Moscow, Russian Federation
e-mail: b.dzeboev@gcras.ru

© The Author(s), under exclusive license to Springer Nature
Switzerland AG 2021

V. Svalova (ed.), *Heat-Mass Transfer and Geodynamics of the Lithosphere*,
Innovation and Discovery in Russian Science and Engineering,
https://doi.org/10.1007/978-3-030-63571-8_26

441

geological and geophysical characteristics. In the algorithms of recognition used in the EPA approach, objects are represented by binary vectors obtained by coding procedures from real-valued or Boolean geological and geophysical parameters [2]. Recognition objects are determined on the basis of morphostructural zoning as nodes or intersections of morphostructural lineaments [2, 9].

The algorithms of dichotomy with training in EPA: “Cora-3”, “Subclasses”, “Hemming” are used to separate objects of recognition into high- and low-seismicity [2]. Their starting point is the formation of training samples of high- and low-seismicity classes that are the basis for algorithms training. It has to be noted that, when recognized by the EPA method [2], the problem is not only to determine potentially high seismicity morphostructural nodes or intersections of lineament axes but also to obtain a geological and geophysical description of such areas, i.e. identification of criteria for high seismicity of the considered region.

The algorithms “Cora-3”, “Subclasses”, “Hemming” [2] reveal the geological and geophysical characteristics which are typical for the high- and low seismicity classes. Then, the entire set of recognition objects is examined for the possession of these features. If there are such features then the exam objects are declared, respectively high or low-seismic. The set of objects recognized as high seismicity determines the strong earthquake-prone areas. It should be noted that the “Cora-3” algorithm [10] is the most frequently used algorithm in EPA.

As a result of recognition with training using algorithms mentioned above, the considered territory (in fact a finite set of recognition objects) is algorithmically divided into two non-intersecting parts: B – where a strong ($M \geq M_0$) earthquake can occur, and H – where the occurrence of such an earthquake is impossible. At the same time, the training set consists of two disjoint subsets: B_0 – training objects of high seismicity class B and H_0 – training objects of low seismicity class H [2, 11].

The training sample of the high-seismicity class includes objects, in the vicinity of which the epicenters of strong ($M \geq M_0$) earthquakes are known. This sample does not contain a priori errors [11].

The situation is different with the training sample of the low-seismicity class. As a rule in the EPA, it includes objects in the neighborhood of which earthquakes with a magnitude of only $M < M_0 - \delta$, $\delta > 0$ are known [11]. Moreover, δ turns out to be another fitting parameter. Classical EPA-dichotomy algorithms are symmetrically training on the two samples that are formed in this way.

In fact, the problem itself being the limitary recognition problem [12–14], a low seismicity training class contains potential errors. These are the objects that will go to the high seismic class as a result of solving the problem. Moreover, if such a transition does not occur, the recognition will give a trivial result. Thus, the low seismicity training class, in fact, is not a set of reference objects that cannot be connected with the strong earthquake-prone areas. The training samples of high- and low seismicity classes turn out to be unequal in the classical variant of the EPA approach [11], and this is ignored by the EPA procedure.

2 Method

Since the creation of the EPA method, the question of assessing the reliability of results obtained using algorithms in which training takes place on potentially intersecting training samples of different quality remains relevant. The authors created a new recognition algorithm “Barrier” [11], which does not have this drawback. Its fundamental difference from the algorithms used earlier in the EPA is that it is learned only from single training sample of a high seismicity class that does not contain deliberate classification errors. Authors hope that this will enhance the accuracy of the desired recognition of potentially high-seismicity zones.

The “Barrier” algorithm that is training from single high-seismic class generally speaking is not a dichotomy algorithm. However, it can be effectively used in the EPA method by replacing the classical dichotomy algorithms [2, 3]. The “Barrier” also divides the territory into two non-intersecting areas where respectively strong ($M \geq M_0$) earthquakes can occur or not [11].

The “Barrier” algorithm eliminates the situation when during the formation of a training sample it includes potentially high seismicity objects, which are deliberate errors. It is expected that an improvement in the quality of training will lead to an increase in the reliability of recognition. The purpose of the “Barrier” algorithm is to study the characteristics of the training sample of this single “pure” high-seismicity class and, on the basis of the gained knowledge to identify objects “similar” to the training objects. The latter are declared to be high seismicity by the “Barrier” algorithm.

In the language of set theory “Barrier” solves the problem of constructing in the finite set of objects its subset B , extending the only and reliable training class B_0 . For this purpose on every geological and geophysical characteristic, a measure of a difference between two arbitrary recognition objects is constructed. Thus a “barrier” separating these objects by the considered characteristic is found and quantified. This “barrier” plays the role of a metric on the initial set, which makes it possible to give an exact meaning to the concept of proximity to B_0 on the basis of a set of geological and geophysical characteristics. A detailed description of the mathematical construction of the algorithm is given in the paper [11].

To quantify the contribution of each used geological and geophysical characteristics to the formation of the desired subset of high seismicity objects, the construction of the “Barrier” algorithm was modified. The modification consists in the creation of computational blocks, which make it possible to evaluate both the average contribution of geological and geophysical characteristics, as well as their contribution through falling into the three “strongest” characteristics. It is logical that the new version of the algorithm is called “Barrier-3”. The construction of the algorithm is designed in such a way that the training objects in the final classification always fall into the high seismicity class [11]. In turn, when recognizing the dichotomy algorithms listed above, the objects of training of both high- and low seismicity classes, generally speaking, are not obliged to retain their belonging to the corresponding class [2].

3 Initial Data

Disjunctive nodes or intersections of the axes of morphostructural lineaments [2] are considered as recognition objects in the “Barrier-3” algorithm, as well as in the dichotomy algorithms used in EPA. They are distinguished by morphostructural zoning. It is done according to the classical technique formalized in the paper [9].

The choice of morphostructural lineament intersections as objects of recognition is based on their deep tectonic connection with strong earthquakes. Such a connection was noted already in 1972 [5] during EPA recognition in the Pamir and Tien Shan regions. Subsequently, the confinement of epicenters of strong earthquakes to the intersections of morphostructural lineaments was confirmed statistically [15].

Recognition in the EPA problem is performed on the basis of the vector representation of objects in the space of geological and geophysical characteristics. These characteristics must be a priori associated with the ability to characterize areas of high seismicity with their help. As a rule, geological and geophysical characteristics are used to reflect the contrast and intensity of the newest tectonic movements, the tectonic fragmentation degree in the vicinity of intersections, deep heterogeneity, etc.

Experience in the study of numerous regions by the EPA method has formed a list of frequently used for recognition geological and geophysical characteristics [2, 6]:

- maximum and minimum heights, their gradient and range;
- a combination of relief types;
- area of friable strata;
- the maximum and minimum values of the Bouguer anomaly, their range, and average value;
- the anomaly in free air;
- maximum and minimum values of the lithospheric magnetic anomaly and their range;
- the highest rank of lineament and the number of lineaments in the intersection and in the circle;
- minimal distance to lineaments of the first and second rank,

as well as other characteristics associated with the above.

This work is one of the first in which the values of lithospheric magnetic anomalies in the vicinity of an object are used to describe objects. For the first time, their significant informativity for strong earthquake-prone areas recognition was shown in the paper [6].

Before using one or another geological and geophysical characteristic, it is necessary to make sure that it is informative in the context of the recognition problem being solved. To do this, the possibility of separating high seismicity objects from low seismicity ones by this single characteristic should be evaluated. In the paper [6] a description of the methodology for such an evaluation for the EPA variant with two training classes: B_0 and H_0 is given. In this work method of evaluating informativity is modified for the case of one training class.

To reproduce the result and enhance its reliability, the values of the characteristics of recognition objects are calculated automatically using an intelligent GIS [16, 17], developed at the Geophysical Center of the Russian Academy of Sciences.

4 Earthquake-Prone Areas in the Caucasus. $M \geq 6.0$

In papers [6, 18–20], a scheme of morphostructural zoning of the Caucasus was constructed. The scheme highlights 237 intersections of the morphostructural lineament axes of three ranks (Fig. 1). An analysis of the occurrence of earthquake epicenters with $M \geq 6.0$ to the intersections of morphostructural lineaments was performed [6, 20]. The analysis showed that in the Caucasus, the epicenters of earthquakes with $M \geq 6.0$ are located in the vicinity of lineament intersections.

As in the “Barrier-3” algorithm in the present study, so in the “Cora-3” algorithm [6], 16 intersections of morphostructural lineaments were used as a training sample of the high seismicity class. In the 25-km vicinity of these intersections, the crustal earthquake epicenters with $M \geq 6.0$ for the period 1900–1992 are known. The intersections of lineaments in the vicinity of which are known the earthquake epicenters with $5.5 \leq M < 6.0$ since 1900 or the earthquake epicenters with $M \geq 6.0$ that occurred before 1900 were not included in the training material of the “Cora-3” algorithm and compiled examination material of the algorithm. There are 150 such

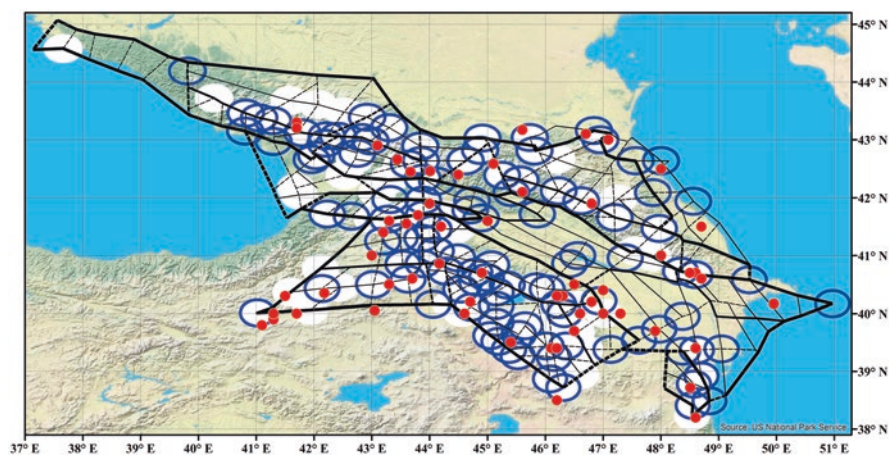


Fig. 1 Scheme of morphostructural zoning (thick lines – lineaments of the I rank, medium – II rank, thin – III rank, solid lines – longitudinal lineaments, dashed – transverse lineaments [20]), earthquake-prone zones with $M \geq 6.0$ (empty ellipses with blue borders – zones recognized by the “Barrier-3” algorithm, white ellipses – “Cora-3”, white ellipses with blue borders – both algorithms) and the epicenters of crustal earthquakes with $M \geq 6.0$ (from ancient times to 2018) in the Caucasus

intersections. The remaining 71 intersections made up the training material of the low seismicity class of the “Cora-3” algorithm.

Table 1 shows the initial list used for the recognition of geological and geophysical characteristics of objects in the Caucasus. According to the results of evaluating the informativeness of characteristics for the case of one training class, it was decided to use 11 characteristics in the “Barrier-3” algorithm (highlighted in bold in Table 1). According to the results of evaluating the informativeness of characteristics for two training classes, 14 characteristics were used in recognition by “Cora-3” algorithm [6] (highlighted in italic in Table 1). From Table 1 it is easy to notice that 8 characteristics were used in recognition by both algorithms. These are maximum (Hmax), minimum (Hmin) heights and their range (dH), combination of relief types (Top), area of Quaternary rocks (Q), number of lineaments in the vicinity of the intersection (NLC), distance to the closest lineament of rank II (R2) and the range of the Bouguer anomalies (dB).

In the Caucasus circles with a radius of 25 km were taken in the capacity of vicinity inside which the values of geological and geophysical characteristics were calculated. This is based on the threshold of magnitude ($M \geq 6.0$) of earthquakes which potential areas were recognized [6, 11, 20].

In Fig. 1 empty ellipses with blue borders show the result earthquake-prone areas recognition with $M \geq 6.0$ in the Caucasus, obtained using the “Barrier-3” algorithm. According to the results of recognition, 108 out of 237 considered recognition objects were assigned to the high seismicity set of lineament intersections. From the consideration of the recognition module by the “Barrier-3” algorithm as an EPA

Table 1 The initial list of geological and geophysical characteristics of recognition objects in the Caucasus

<i>Maximum height</i>	Hmax
<i>Minimum height</i>	Hmin
<i>The range of heights</i>	dH=Hmax-Hmin
Height gradient	dH/l
<i>The combination of relief types</i>	Top
<i>The area of Quaternary rocks</i>	Q
<i>The highest rank of lineament</i>	HR
<i>The number of lineaments at the intersection</i>	NL
<i>The distance to the nearest intersection</i>	Rint
<i>Number of lineaments in the neighborhood of the intersection</i>	NLC
<i>The distance to the nearest lineament of rank I</i>	R1
<i>The distance to the nearest lineament of rank II</i>	R2
<i>The maximum value of the Bouguer anomaly</i>	Bmax
<i>The minimum value of the Bouguer anomaly</i>	Bmin
<i>The range of the Bouguer anomaly values</i>	dB=Bmax-Bmin
<i>The maximum value of magnetic anomaly</i>	MOmax
<i>The minimum value of magnetic anomaly</i>	MOmin
<i>The range of the magnetic anomaly values</i>	MOdif=MOmax-MOmin

block [2], it follows that the set of ellipses shown in Fig. 1 (circles with a radius of 25 km) with the centers at the corresponding 108 lineament intersections are the desired earthquake-prone areas with $M \geq 6.0$ in the Caucasus. It should be noted that in addition to the 16 objects from the training set, 92 intersections of 221 that made up the examination material of algorithm were declared high seismicity.

Figure 2 shows histograms characterizing the contribution of the 11 geological and geophysical characteristics used to the recognition by the “Barrier-3” algorithm of a subset of lineament intersections in the vicinity of which earthquakes with

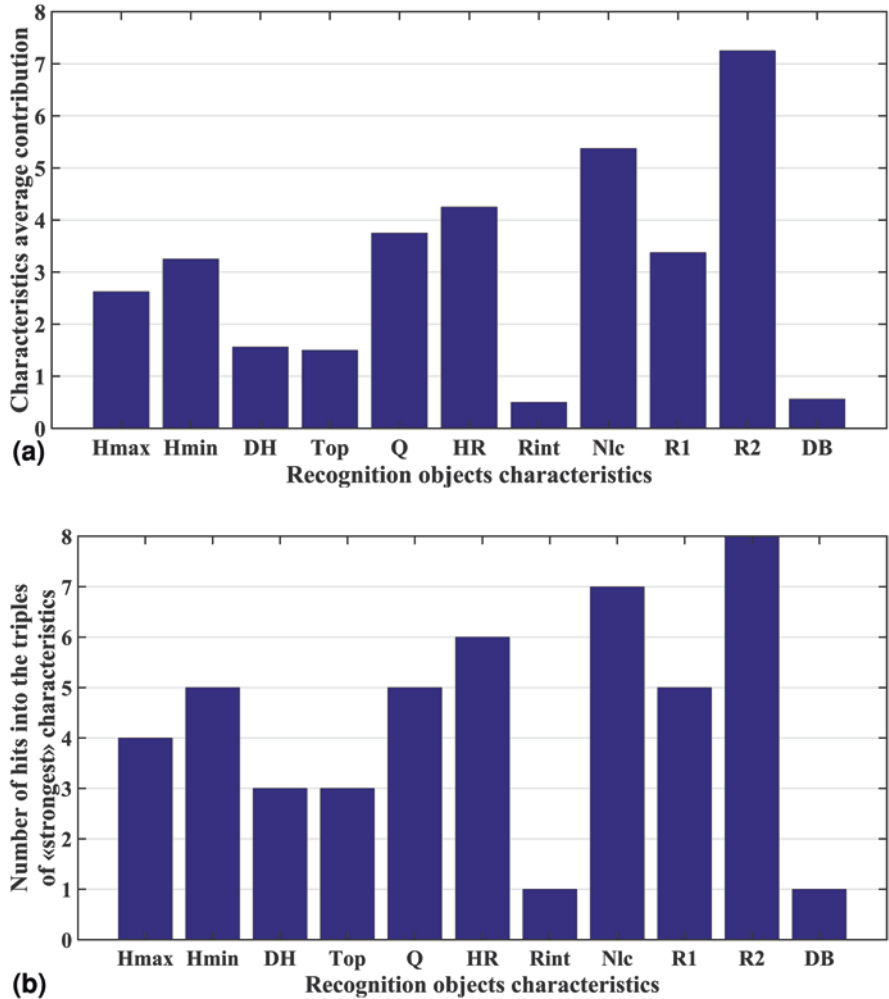


Fig. 2 Recognition of high-seismicity zones ($M \geq 6.0$) in the Caucasus using the “Barrier-3” algorithm: (a) the average contribution of 11 geological and geophysical characteristics used in recognition; (b) the contribution of the characteristics, expressed through their hit in the triples of the “strongest” characteristics

$M \geq 6.0$ are possible. The ordinate axis in Fig. 2a shows the average number of response characteristics during recognition, in Fig. 2b – the number of hits of the characteristics in triples of the “strongest” characteristics.

Figure 2 shows that when recognizing in the Caucasus by the “Barrier-3” algorithm, the greatest contribution to the formation of the desired high-seismicity set of objects is made by the characteristics responsible for the relief height (Hmax and Hmin), the area of the Quaternary rocks (Q), the highest rank of the lineament (HR), the number of lineaments in the neighborhood (NLC), as well as the distance to the nearest lineaments of the I (R1) and II (R2) ranks. Crossings of lineaments in the Caucasus, recognized by “Barrier-3” as hazardous for $M \geq 6.0$ against the background of the whole set of recognition objects in their neighborhood are characterized by large values of maximum and minimum heights (Hmax ≥ 2500 m and Hmin ≥ 600 m), not a large area of quaternary rocks ($Q \leq 30\%$), they are formed by three or more lineaments of the II or III ranks (NLC ≥ 3 , HR = 2 or HR = 3, R2 ≤ 30 km) and are located at relatively large distances from the I rank lineament ($0 < R1 \leq 50$ km). These signs are naturally interpreted as criteria for high seismicity in the Caucasus. From Fig. 2 we can see that the height range and combination of relief types also contribute to the formation of the final result.

White ellipses in Fig. 2 show the result of earthquake-prone areas recognition with $M \geq 6.0$ in the Caucasus, obtained using the “Cora-3” algorithm. This result was published in [6]. The “Cora-3” algorithm has recognized all 16 training objects of high seismicity class as hazardous. 22 intersections from a training sample of a low seismicity class and 69 objects among that were not included in the training sample and made up the examination material is classified as high-seismicity objects. As a result, the “Cora-3” algorithm recognized as hazardous 107 lineament intersections for a magnitude of $M \geq 6.0$ [6]. Practically all the intersections recognized as high seismicity by the “Cora-3” algorithm are associated with lineaments of the I-st and II-nd ranks. This suggests that seismic objects are located at the boundaries separating the largest blocks of the Earth’s crust of the Caucasus [20].

A comparative analysis of the recognition results by the “Barrier-3” and “Cora-3” algorithms was carried out. The Barrier-3 algorithm recognized 108 lineament intersections as high seismicity and “Cora-3” algorithm 107 lineament intersections. At the same time, 73 intersections are classified as hazardous for $M \geq 6.0$ by both algorithms. It has to be noted that both algorithms have recognized all 16 objects from the training sample of this class as high seismicity. The “Barrier-3” algorithm classified 24 of 71 objects of the training sample of the low seismicity class “Cora” as hazardous, the “Cora-3” algorithm – 22 objects. At the same time, 16 of them are classified as hazardous by both algorithms. It is obvious that 41 training objects of low seismicity class were recognized by both algorithms as not hazardous. Of the numerous recognition objects that were originally not related to the training samples of the “Cora”, the algorithms “Barrier-3” and “Cora-3” classified 95 intersections in the same and 55 in different ways.

Figure 1 shows that the differences in the recognition results by the “Barrier-3” and “Cora-3” algorithms are observed in the western part of the Central Caucasus,

on the Caspian Sea coast, and also in the south-west and southeast sectors of the considered morphostructural zoning scheme.

Analysis of Fig. 1 showed that all 17 epicenters of earthquakes with $M \geq 6.0$ that occurred during the period 1900–1992. And taking part in the formation of the training sample of the high seismicity class, are inside the zones recognized by both algorithms. Of the 42 epicenters of earthquakes with $M \geq 6.0$ that occurred before 1900, there are 7 and 8 epicenters outside the zones recognized by the “Barrier-3” and “Cora-3” algorithms, respectively. Half of these epicenters are located at insignificant distances from potentially high seismicity zones recognized by algorithms. We emphasize that, with a significant degree of probability, the coordinates of the earthquake epicenters that occurred before 1900 may be incorrect. Whereby the error may be in our favor or not. In the first case, we increase the reliability of the result. In the second, we lose nothing, because for these epicenters, the recognition result is a priori negative. Some of the epicenters located outside the recognized zones may actually be inside them. Moreover, only one of these earthquakes has a magnitude far exceeding 6.0, $-M = 7.8$. For all others $-6.0 \leq M \leq 6.5$. This means that some of the earthquakes may not be the subject of present research. It should also be noted that only 4 (6%) out of the 62 epicenters of earthquakes with $M \geq 6.0$ occurring since ancient times until 2018 are outside the union of the zones recognized by both algorithms.

After 1992, 3 earthquakes with $M \geq 6.0$ occurred in the studied region. Information about these earthquakes was never used in the formation of the training samples of the “Barrier-3” and “Cora-3” algorithms. An analysis of the location of their epicenters showed that within the high seismicity zones, recognized as by “Barrier-3” so by “Cora-3” algorithms there are two of the three epicenters of earthquakes. It has to be noted that the hypocenter of the earthquake that occurred in the Caspian Sea near the city of Baku outside zones recognized by both algorithms was according to one data, located in the crust, on others outside deeper. Thus, perhaps the epicenter of this earthquake is not an error of the first kind.

An analysis of the high seismicity criteria in the Caucasus identified by the “Barrier-3” algorithm in the present work and the “Cora-3” algorithm in [6] showed their sufficient proximity.

5 Conclusions

Replacing in the EPA method the dichotomy algorithm with the original “Barrier-3” algorithm is an attempt to open a new page in the development of this method [2]. According to [14], the problem of strong earthquake-prone areas recognition is a dynamic, liminary recognition problem. As shown in [13, 14], in liminary problems, there is only single reliable (“pure”) training class formed by objects with which strong earthquakes that have already occurred are associated. Moreover, as a result of recognition, objects from the low seismicity training class in the desired liminary classification may end up in a high-seismicity class.

The algorithm “Barrier-3” in its idea and construction more adequately than the dichotomy meets the formulation of the studied dynamic problem EPA [11]. The “Barrier-3” algorithm is training only on the single high-seismicity class that does not contain invariable errors only expands the training class B_0 . The “Cora-3” algorithm was created in 1966 by Bongard [10] to solve other non-dynamic applied dichotomy problems. Its routine application to the EPA problem turns out to be, generally speaking, less adequate due to the presence in it of training in a low seismicity class that contains prior classification errors.

Thus, it can be argued that the “Barrier-3” is currently the type of algorithm most suitable for solving the EPA problem in its classical dynamic-limitary formulation, belonging to Academicians of the Academy of Sciences of the USSR I.M. Gelfand, V.I. Keilis-Borok and academicians of the National Academy of Sciences of the USA F. Press, L. Knopov [7]. These results demonstrate on the example of the Caucasus that the quality of the result obtained is not inferior to that obtained earlier by the “Cora-3” algorithm [6].

The algorithm “Barrier-3” has proven itself in earthquake-prone areas recognition with single training class in the Caucasus [11]. This fact strengthens our assumptions that the earthquake-prone areas recognition of the strongest, strong and significant earthquakes on a single pure training class by expanding it is adequate to the formulation of the EPA problem. The use of “Barrier-3” does not fundamentally change the EPA recognition procedure [11] as the FCAZ method (Formalized Clustering And Zoning) [21–24] that was also developed in the Geophysical Center of the Russian Academy of Sciences does. In this case, only the recognition block with training changes. “Barrier-3” comes to the place of “Cora-3”, leaving the blocks of morpho-structural zoning and measurements of geological and geophysical parameters unchanged. Thus, the authors think that, in the classical EPA method, the pattern recognition block may vary: “Cora-3” \leftrightarrow “Barrier-3”. For the presence of good consistency of both options, we can talk about the high reliability of the result.

It should be noted that the independently obtained positive recognition variants by the “Barrier-3” and “Cora-3” algorithms make them control experiments for each other. Due to the close proximity of the results, these control experiments should be considered successful. This increases the reliability assessment of both the result of the EPA (“Cora-3”) and the EPA (“Barrier-3”).

Nowadays in the Geophysical Center of the Russian Academy of Sciences under the guidance of Academician A.D. Gvishiani is developing a project for the creation and evolving of a universal GIS-oriented database [25]. It contains solutions for a problem of strongest, strong and significant earthquake-prone areas recognition in various regions of the world that were obtained using the EPA (“Cora-3”), EPA (“Barrier-3”) and other methods [2, 3, 26]. Later this will make it possible to verify the universality of the variation of the pattern recognition block for other regions, where the EPA (“Cora-3”) recognition was previously successfully performed [3].

One possible interpretation of the joint recognition result by the “Barrier-3” and “Cora-3” algorithms can be its definition as a fuzzy set $\{W, \mu_{B_b, B_c}\}$ of lineament intersections, in the neighborhood of which strong earthquakes can occur in the considered region. The corresponding membership function of such a set will have the following form:

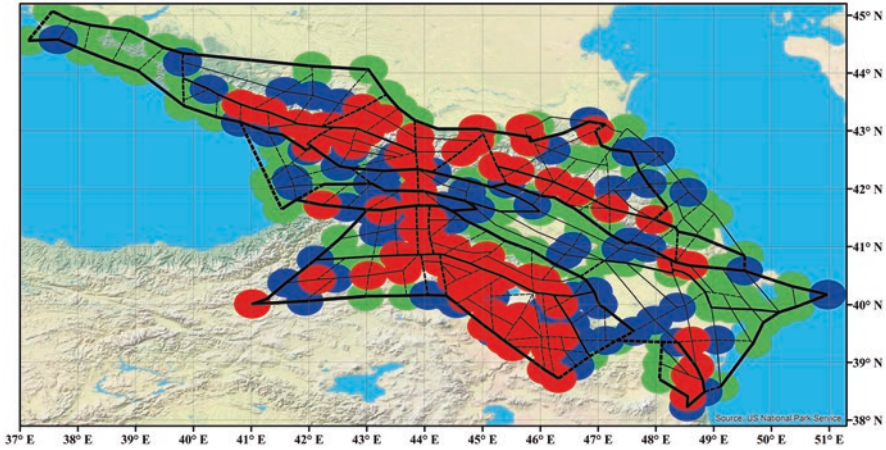


Fig. 3 Presentation of a joint recognition results in the Caucasus of earthquake-prone areas recognition with $M \geq 6.0$ by the “Barrier-3” and “Cora-3” algorithms as a fuzzy set of neighborhoods of lineament intersections. Red color shows neighborhoods of intersections with the membership function $\mu_{B_B, B_C} = 1$, blue $-\mu_{B_B, B_C} = 0.5$, green $-\mu_{B_B, B_C} = 0$

$$\mu_{B_B, B_C}(w) = \begin{cases} 1, & w \in B_B \cap B_C \\ 0.5, & w \in B_B \Delta B_C = (B_B \cup B_C) \setminus (B_B \cap B_C), \\ 0, & w \notin B_B \cup B_C \end{cases}$$

where $w \in W$ are the objects of recognition, and B_B, B_C are the intersections of the lineaments recognized as high seismicity by the algorithms “Barrier-3” and “Cora-3” respectively. Figure 3 shows an example of interpreting the results of earthquake-prone areas recognition with $M \geq 6.0$ in the Caucasus in the form of a fuzzy set.

The development of the “Barrier-3” algorithm can be considered as a new step in solving the problem of strong earthquake-prone areas recognition [2].

Acknowledgements The authors express particular gratitude to the Chief Scientist of the GC RAS, academician of RAS A.D. Gvishiani for helpful discussions and support, to the Chief Researcher of the IEPT RAS, corresponding member of RAS, A.I.A. Soloviev for the provided data on the scheme of morphostructural zoning of the studied region, to the Leading Researcher of the GC RAS N.A. Sergeeva for her active help in interpreting the recognition results.

References

1. Gvishiani AD, Kossobokov VG (1981) On foundations of the pattern recognition results applied to earthquake-prone areas. *Izv Acad Sci SSSR Fizika Zemli* 2:21–36
2. Gvishiani A, Gorshkov A, Rantsman E, Cisternas A, Soloviev A (1988) *Prognozirovanie mest zemletryasenii v regionakh umerennoi seismichnosti (Recognition of earthquake-prone areas in the regions of moderate seismicity)*. Nauka, Moscow

3. Soloviev AA, Gvishiani AD, Gorshkov AI, Dobrovolsky MN, Novikova OV (2014) Recognition of earthquake-prone areas: methodology and analysis of the results. *Izv Phys Solid Earth* 50(2):151–168. <https://doi.org/10.1134/S1069351314020116>
4. Gelfand IM, Guberman SA, Izvekova ML, Keilis-Borok VI, Rantsman EY (1973) Recognition of the locations of the probable occurrence of strong earthquakes. I. Pamir and Tien-Shan. In: Keilis-Borok VI (ed) *Vychislitel'naya seismologiya. Vyp. 6. Vychislitel'nye i statisticheskie metody interpretatsii seismicheskikh dannykh* (Computational seismology, vol. 6: computational and statistical methods for interpretation of seismic data). Nauka, Moscow, pp 107–133
5. Gelfand IM, Guberman SI, Izvekova ML, Keilis-Borok VI, Ranzman EJ (1972) Criteria of high seismicity, determined by pattern recognition. *Tectonophysics* 13:415–422
6. Soloviev AA, Gorshkov AI, Soloviev AA (2016) Application of the data on the lithospheric magnetic anomalies in the problem of recognizing the earthquake prone areas. *Izv Phys Solid Earth* 52(6):803–809. <https://doi.org/10.1134/S1069351316050141>
7. Gelfand IM, Guberman SA, Keilis-Borok VI, Knopoff L, Press F, Ranzman EY, Rotwain IM, Sadovsky AM (1976) Pattern recognition applied to earthquake epicenters in California. *Phys Earth Planet Inter* 11(3):227–283
8. Gelfand IM, Guberman SA, Zhidkov MP, Keilis-Borok VI, Rantsman EY, Rotwain IM (1974) Recognition of the locations of the probable occurrence of strong earthquakes. III. The case when the boundaries of the disjunctive knots are unknown. In: Keilis-Borok VI (ed) *Vychislitel'naya seismologiya. Vyp. 7. Mashinnyi analiz tsifrovyykh seismicheskikh dannykh* (Computational seismology, vol. 7: computer analysis of digital seismic data). Nauka, Moscow, pp 41–64
9. Alekseevskaya M, Gabrielov A, Gelfand I, Gvishiani A, Rantsman E (1977) Formal morphostructural zoning of mountain territories. *Geophysics* 42(2):227–233
10. Bongard MM, Vaintsvaig MN, Guberman SA, Izvekova ML, Smirnov MS (1966) Application of learning program for identifying oil-bearing layers. *Geol Geofiz* 2(6):15–29
11. Gvishiani AD, Agayan SM, Dzeboev BA, Belov IO (2017) Recognition of strong earthquake-prone areas with a single learning class. *Dokl Earth Sci* 474(Part 1):546–551. <https://doi.org/10.1134/S1028334X17050038>
12. Dubois J, Gvishiani A (1998) *Dynamic systems and dynamic classification problems in geophysical applications*. Springer. 256 p, Paris. <https://doi.org/10.1007/978-3-642-49951-7>
13. Gvishiani A, Dubois J (2002) *Artificial intelligence and dynamic systems for geophysical applications*. Springer, Paris. 350 p. <https://doi.org/10.1007/978-3-662-04933-4>
14. Gvishiani AD, Gurvich VA (1992) *Dinamicheskie zadachi klassifikatsii i vypukloe programirovanie v prilozheniyakh* (Dynamical problems of classification and convex programming: applications). Nauka, Moscow
15. Gvishiani AD, Soloviev AA (1981) On the concentration of major earthquakes round the interactions of morphostructural lineaments in South America. In: Keilis-Borok VI, Levshin AL (eds) *Vychislitel'naya seismologiya. Vyp. 13. Metody i algoritmy interpretatsii seismologicheskikh dannykh* (Computational seismology. Vol. 13: interpretation of seismological data: methods and algorithms). Allerton, New York, pp 42–48
16. Nikolov BP, Zharkikh JI, Soloviev AA, Krasnoperov RI, Agayan SM (2015) Integration of data mining methods for earth science data analysis in GIS environment. *Russ J Earth Sci* 15(4):ES4004. <https://doi.org/10.2205/2015ES000559>
17. Soloviev AA, Krasnoperov RI, Nikolov BP, Zharkikh JI, Agayan SM (2018) Web-oriented software system for analysis of spatial geophysical data using geoinformatics methods. *Izv Atmos Ocean Phys* 54(9):1312–1319. <https://doi.org/10.1134/S0001433818090360>
18. Gvishiani AD, Gorshkov AI, Kossobokov VG, Rantsman EY (1986) Morphostructures and locations of the earthquakes of Greater Caucasus. *Izv Akad Nauk SSSR Fiz Zemli* (9):45–55
19. Gvishiani AD, Gorshkov AI, Zhidkov MP, Rantsman EY, Trusov AV (1987) Recognition of the locations of probable occurrence of the strong earthquakes. XV. Morphostructural nodes of the Greater Caucasus, $M \geq 5.5$. In: Keilis-Borok VI (ed) *Vychislitel'naya seismologiya. Vyp. 20:*

- Chislenoe modelirovanie i analiz geofizicheskikh protsessov* (Computational seismology. Vol. 20: numerical simulation and analysis of geophysical processes). Nauka, Moscow, pp 136–148
20. Soloviev AA, Novikova OV, Gorshkov AI, Piotrovskaya EP (2013) Recognition of potential sources of strong earthquakes in the Caucasus region using GIS technologies. *Dokl Earth Sci* 450(2):658–660. <https://doi.org/10.1134/S1028334X13060159>
 21. Gvishiani A, Dzeboev B, Agayan S (2013) A new approach to recognition of the earthquake-prone areas in the Caucasus. *Izv Phys Solid Earth* 49(6):747–766. <https://doi.org/10.1134/S1069351313060049>
 22. Gvishiani AD, Dzeboev BA (2015) Assessment of seismic hazard in choosing of a radioactive waste disposal location. *Gornyi Zhurnal (Min J)* (10):39–43. <https://doi.org/10.17580/gzh.2015.10.07>
 23. Gvishiani AD, Dzeboev BA, Agayan SM (2016) FCAZm intelligent recognition system for locating areas prone to strong earthquakes in the Andean and Caucasian mountain belts. *Izv Phys Solid Earth* 52(4):461–491. <https://doi.org/10.1134/S1069351316040017>
 24. Gvishiani AD, Dzeboev BA, Sergeyeva NA, Rybkina AI (2017) Formalized clustering and the significant earthquake-prone areas in the Crimean Peninsula and Northwest Caucasus. *Izv Phys Solid Earth* 53(3):353–365. <https://doi.org/10.1134/S106935131703003X>
 25. Soloviev AA, Soloviev AA, Gvishiani AD, Nikolov BP, Nikolova YI (2018) GIS-oriented database on seismic hazard assessment for Caucasian and Crimean regions. *Izv Atmos Ocean Phys* 54(9):1363–1373. <https://doi.org/10.1134/S0001433818090505>
 26. Gvishiani A, Gorshkov A, Kossobokov V, Cisternas A, Philip H, Weber C (1987) Identification of seismically dangerous zones in the Pyrenees. *Ann Geophys Ser B-Terr Planet Phys* 5(6):681–690

Assessment of the Effect of Resonance Properties of Soils during Seismic Microzoning



M. D. Kaurkin, V. V. Romanov, and D. O. Andreev

1 Introduction

As is well-known, most of the territory of the Russian Federation can be attributed to aseismic. However, the southern regions of the country and the Far East are seismic hazardous; therefore, the assessment of seismic hazard is an urgent problem for these regions.

Seismic microzoning is the final step in assessing the seismicity of future construction sites. The task of seismic microzoning is to assess the influence of local conditions (soil, geomorphological, hydrogeological and geophysical) on possible seismic effects.

If the periods of natural vibrations of buildings and structures coincide with the periods of foundation vibrations, the latter are destroyed due to the phenomenon of seismic resonance – a significant increase in the amplitude of transverse seismic waves. Resonance phenomena also occur in extended waveguides of the earth crust (for example, in grabens), which capture the energy of earthquake waves and, without significant attenuation, propagate it over large distances in the horizontal direction.

According to the current regulatory documents, when calculating the seismicity and expected seismic effects, it is necessary to take into account the resonant effects that may occur in the studied soil mass. In turn, in practice, the evaluation of the resonance properties of soils is extremely rare, due to many factors. The main one is the atypical conditions for the appearance of resonance effects for most soil strata.

M. D. Kaurkin (✉) · D. O. Andreev
IEG RAS, Moscow, Russia

V. V. Romanov
National University of Oil and Gas «Gubkin University», Moscow, Russia

© The Author(s), under exclusive license to Springer Nature
Switzerland AG 2021

V. Svalova (ed.), *Heat-Mass Transfer and Geodynamics of the Lithosphere*,
Innovation and Discovery in Russian Science and Engineering,
https://doi.org/10.1007/978-3-030-63571-8_27

455

2 The Frequency Composition of Seismic Effects

Resonance effects in the soil stratum can occur as a result of the influence of various sources of seismic waves, such as railroad transport, vibration of large aggregates and mechanisms, industrial explosions, but the earthquake is considered the most intense. Earthquakes are characterized by various parameters: magnitude, peak acceleration, duration of oscillations and, what is more important for us, prevailing period.

In a research paper [1], the results of long-term studies of a large number of real earthquake records are presented, on the basis of which formulas for calculating the main parameters of earthquakes were obtained, including the prevailing acceleration period, which is calculated by the following formula [1]:

$$\lg T = 0.15M_s + 0.25 \lg R_{hyp} + C_1 - 1.9 \pm 0.2 \quad (1)$$

where R_{hyp} – hypocentral distance, and in the near zone and the focal zone, the value of T does not depend on the distance; coefficient $C_1 = -0.2$ for underthrusts, -0.1 for upthrows, 0.0 for shifts and 0.1 for faults.

If the period is known, the frequency can be calculated according to the trivial formula:

$$f = \frac{1}{T} \quad (2)$$

Thus, using formulas (1) and (2), it is possible to calculate the frequency composition of earthquakes of various magnitudes at different distances from the source. Graphically, the results of these calculations are presented below in the Figures (1, 2, 3, 4, and 5). Since in the formula (1) there is a coefficient of ± 0.2 , then the Figures (1, 2, 3, 4, and 5) show graphs for the maximum (+) and minimum (–) calculated values.

The results obtained clearly show that the prevailing frequency of earthquakes with different magnitudes is in the range of 0.4–10 Hz. This range will be further considered in determining the resonance properties of soils.

3 Resonance Properties of Soils

It should be recalled that resonance is the frequency-selective response of an oscillatory system to a periodic external influence, which manifests itself in a sharp increase in the amplitude of stationary oscillations when the frequency of the external influence coincides with certain values characteristic of this system.

Resonance phenomena occur when there is a uniform layer of sandy, clayey, or coarse-grained soils with a sand-clay aggregate content of more than 30% in the section, underlain by rocks, which are characterized by significantly higher seismic

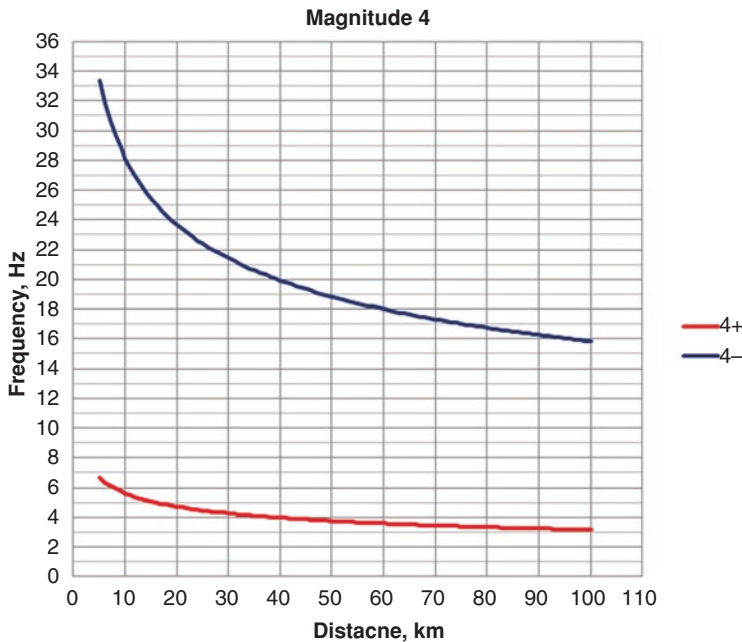


Fig. 1 The prevailing frequency range for an earthquake of magnitude 4

stiffness values in comparison with covering sediments. However, absolutely uniform thicknesses of dispersed soils are extremely rare, especially in the presence of technogenic deposits or coatings. In the presence of several homogeneous strata of dispersed soils, the contribution of resonance phenomena to the increment of seismic intensity is determined only by calculation methods.

The natural oscillation frequency of the layer is calculated by a simple formula [2, 8]:

$$f = \frac{V_s}{4H} \tag{3}$$

where V_s – shear wave velocity in a layer, and H – layer thickness.

With the use of the formula (3), the natural frequency of vibrations for formations of different thicknesses can be calculated. Figure 6 shows a graph of the dependences of the natural frequencies of the small formations oscillations on the shear wave velocity in them.

As can be seen in Fig. 6, layers with a thickness of 2.5–5 m fall into the studied frequency range, while the shear wave velocities in these layers are in the range from 100 to 225 m/s, such velocities are characteristic of weak soils usually lying in the upper part of the section.

Using formula (3) to calculate higher power layers or a mass consisting of a combination of low power layers, one can obtain the following results (Fig. 7).

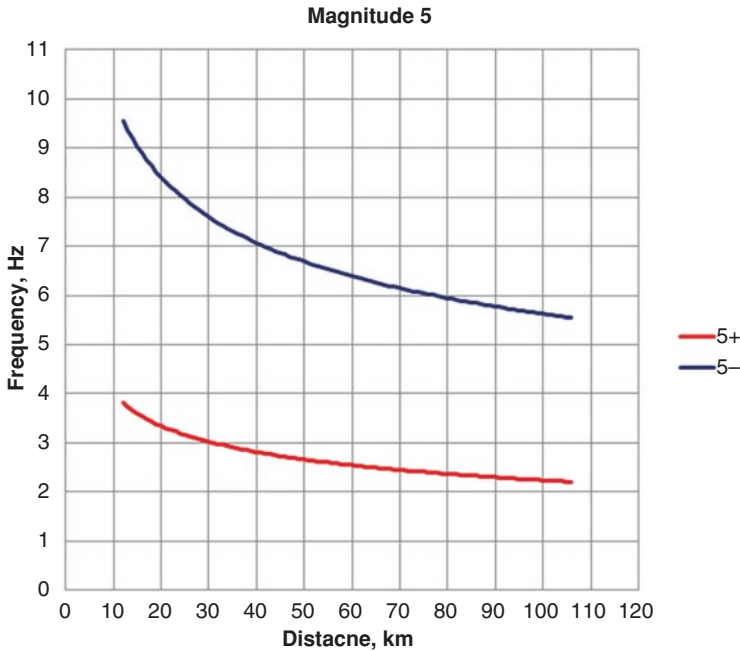


Fig. 2 The prevailing frequency range for an earthquake of magnitude 5

When comparing Figs. 6 and 7, it can be seen that in the latter the range of shear wave velocities is much larger (from 100 to 1200 m/s), which in turn proves that resonance effects can occur in separate layers of small power, so and in large masses of rocks.

4 Modeling the Effect of Resonance in a Program NERA

The NERA program (Nonlinear Earthquake site Response Analyzes of Layered Soil deposits), was developed by J. P. Bardet and T. Tobita [9] and is widely used for calculating seismic impacts, including for objects of increased level of responsibility [2, 3, 8]. The instructions for the NERA program [9] and one of the authors' works [4] describe the calculation methodology, so we will not dwell on a detailed description of all the nuances of the program.

In the beginning, consider the simplest example. As a seismic-geological model, we take an arbitrary mass consisting of ten layers that lie on a rocky base (Table 1).

As can be seen in Table 1, the program itself calculates the Fundamental period of a given mass of layers. Knowing the period, you can get the value of the frequency at which resonance is possible, it will be approximately 4.76 Hz.

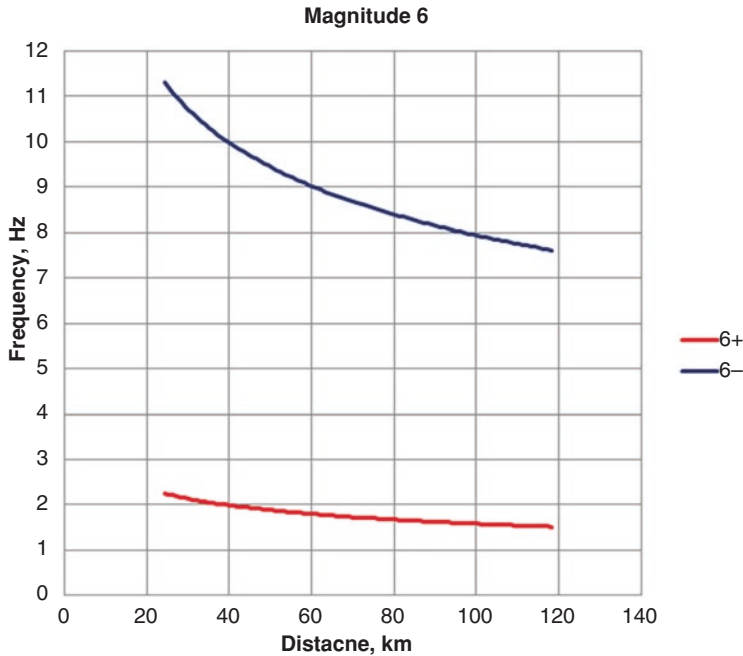


Fig. 3 The prevailing frequency range for an earthquake of magnitude 6

When modeling the process of seismic waves propagation through a soil-geological medium, an initial signal is required in the form of an accelerogram at the level of the so-called elastic half-space, which is usually taken as a rock roof. As the initial seismic impact, we take an accelerogram, the shape of which is set by a sinusoid with a frequency of 4.76 Hz (Fig. 8).

The results of calculations carried out in the NERA program are shown below.

When comparing the initial (Fig. 8) and calculated accelerograms (Fig. 9), then on the latter it can be seen a sharp increase in amplitude almost three times (0.267). In addition, the calculated spectrum of the reaction (Fig. 10) contains a pronounced peak at a period of 0.21 s, which coincides with the Fundamental period of the layer mass. The above results show the effect of the resonance effect in the calculation of seismic effects.

If we turn to the building codes and rules of the Russian Federation [5–8], then the results obtained above can be interpreted as follows. The magnitude of the amplitude of the initial accelerogram (Fig. 8) corresponds to an earthquake with an intensity of 7 points; as a result of the calculations, an accelerogram with a peak acceleration of 0.267 g was obtained, which in turn corresponds to a seismic event with an intensity of 8.3 points. Thus, in the considered example, the seismic intensity increased by 1.3 points.

Now we will consider the seismic-geological model (Table 2), which is typical for foothill and mountainous regions (the territory of the Urals, the Caucasus, the

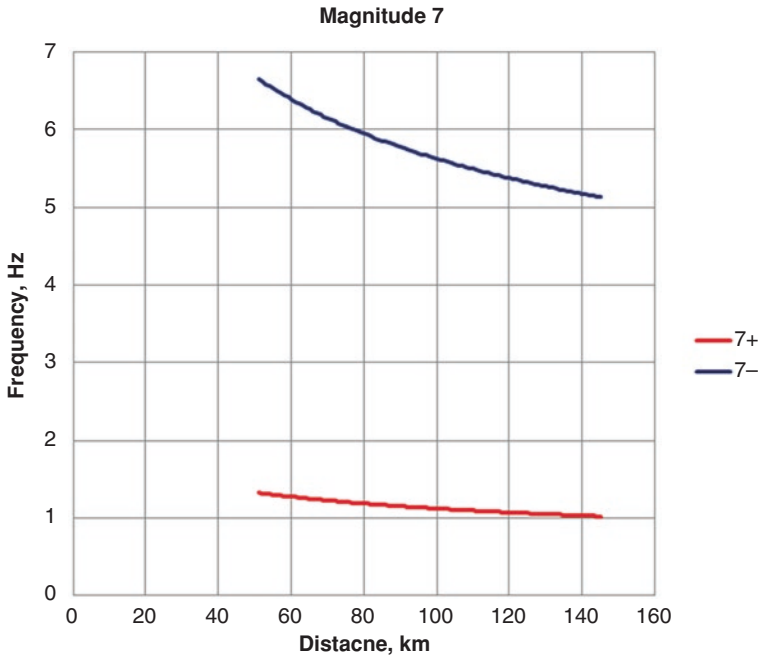


Fig. 4 The prevailing frequency range for an earthquake of magnitude 7

Republic of Sakha, etc.). The thickness of dispersed soils with a low thickness with low shear wave velocities lies on a rocky or semi-rock base. In addition, such areas are characterized by high seismicity.

Table 2 shows the real seismological model of the site located in the middle Urals.

As a seismic impact, a local earthquake was chosen directly below the area of magnitude $M = 4$ and the location of the hypocenter at a depth of 10 km. The main characteristics of the seismic action necessary for synthesizing accelerograms were calculated using the formulas given in the monograph [1].

In the near zone, the PGA value is calculated by the equation [1]:

$$\lg PGA \left(\frac{m}{s} \right) = 0.209M_s - 0.633 \lg R - 0.156 \tag{4}$$

where R – the shortest distance to the fault surface in km. Acceleration values should not exceed PGA_0 . In the near zone, accelerations do not depend on the type of movement, or on the category of soil.

We have got: $PGA = 111 \text{ cm/s}^2$;

The predominant period was calculated by the formula (1) and is equal to $T = 0.17 \text{ s}$;

The duration of the oscillations τ in the far zone should be determined by the formula [1]:

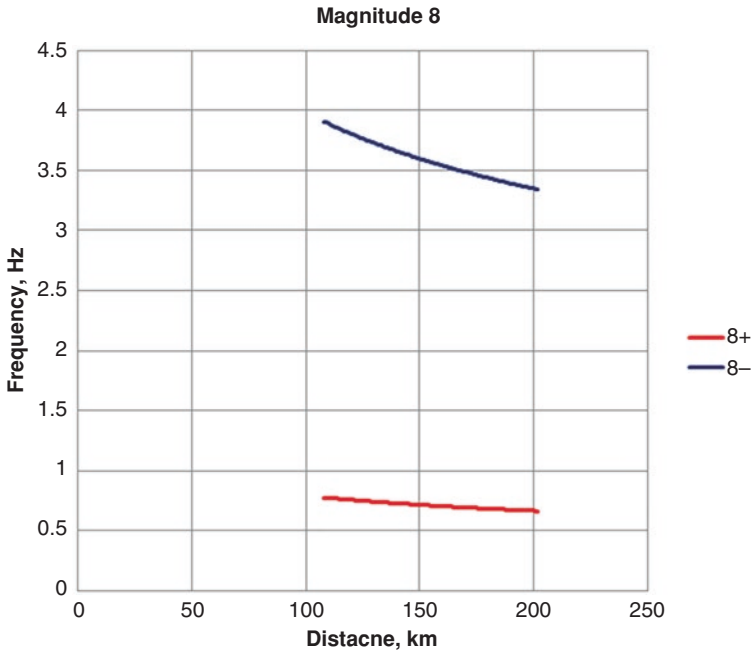


Fig. 5 The prevailing frequency range for an earthquake of magnitude 8

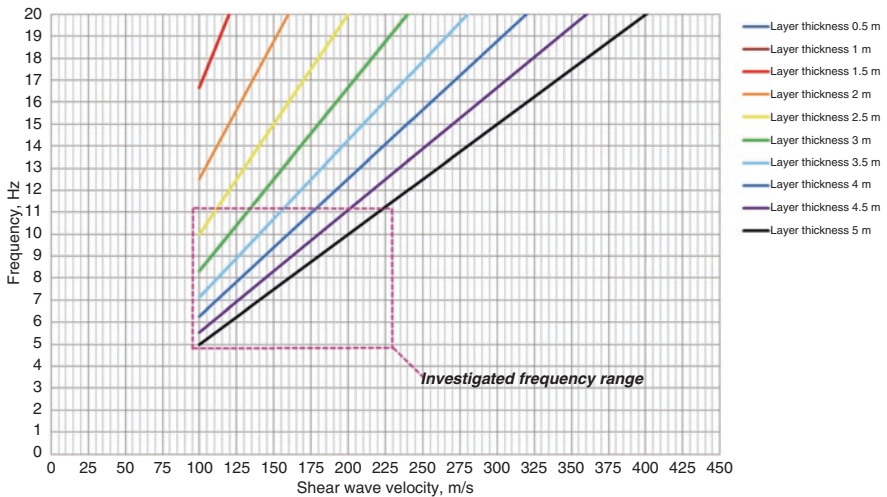


Fig. 6 A graph of the dependences of the natural frequencies of the small formations oscillations on the shear wave velocity in them

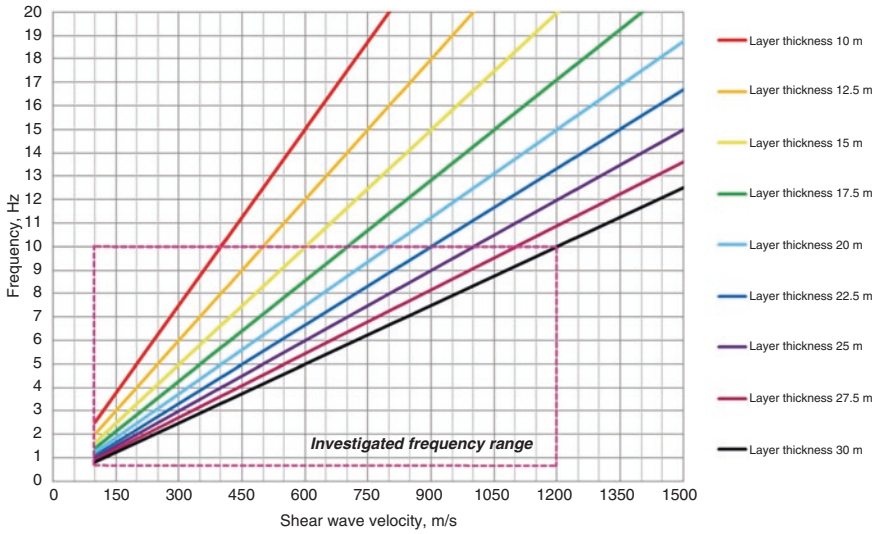


Fig. 7 A graph of the dependences of the natural frequencies of high-power layers (systems of several layers) on the shear wave velocity in them

Table 1 A seismic-geological model #1

			Fundamental period (s)	0.21			
			Average shear wave velocity (m/s)	467.40			
			Total number of sublayers	11			
	Layer number	Soil material type	Number of sublayers in layer	Thickness of layer (m)	Maximum shear modulus G_{max} (MPa)	Total unit weight (kN/m^3)	Shear wave velocity (m/s)
Surface	1	2		1.5	136.01	19.00	265
	2	2		1.5	136.01	19.00	265
	3	1		1.0	354.24	19.70	420
	4	1		3.0	354.24	19.70	420
	5	1		3.0	354.24	19.70	420
	6	1		3.0	502.04	19.70	500
	7	1		3.0	502.04	19.70	500
	8	1		3.0	616.72	20.00	550
	9	1		3.0	616.72	20.00	550
	10	1		3.0	616.72	20.00	550
Bedrock	11	0			2804.08	20.80	1150

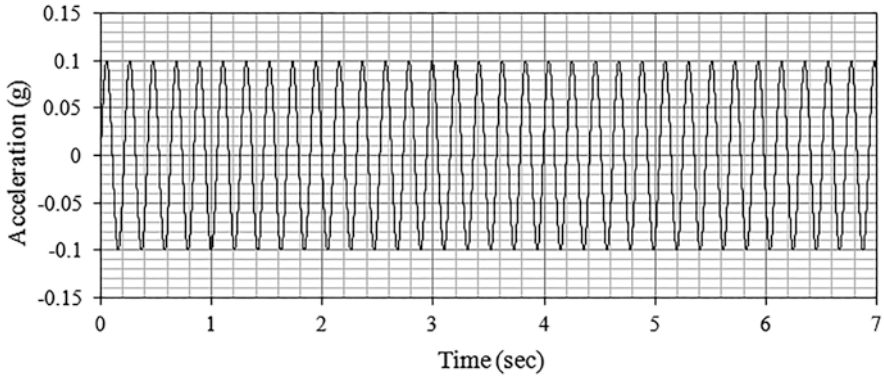


Fig. 8 The initial accelerogram

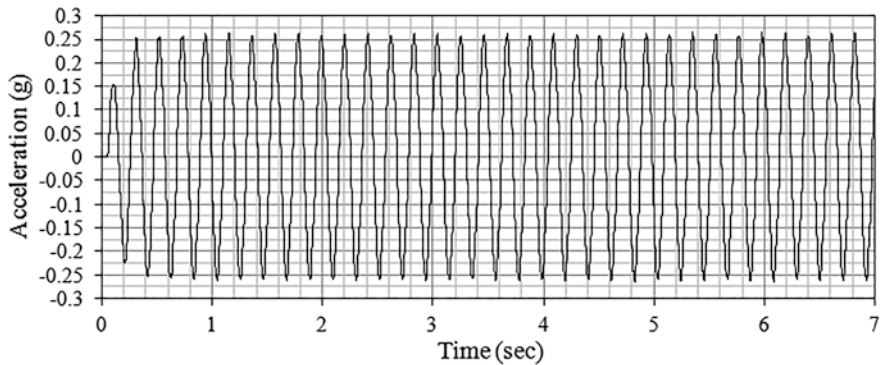


Fig. 9 The calculated accelerogram at the surface level of the seismic-geological model #1

$$lg\tau = 0.15M_s + 0.5lgR + C_1 + C_2 - 1.3 \tag{5}$$

where R – the distance at which there is the point from the source of the earthquake, the coefficient C_1 is 0.25 for faults, 0.00 for shifts and -0.25 for upthrows; C_2 is -0.15 for 1st category soils, 0.00 for 2nd category soils and 0.4 for 3rd category soils.

The duration of oscillations $\tau \approx 3$ s.

On the basis of the obtained initial parameters of the impacts given above, an accelerogram was synthesized on the surface of a conditional rock. The calculation of the synthesized accelerogram (Fig. 11) was carried out in a specialized program “PSEQGN” [10].

As a result, all necessary input data were obtained for performing calculations in the NERA program. The calculation results are shown in Figs. 12 and 13.

After analysis of the data obtained in the calculation results, the following conclusions could be drawn:

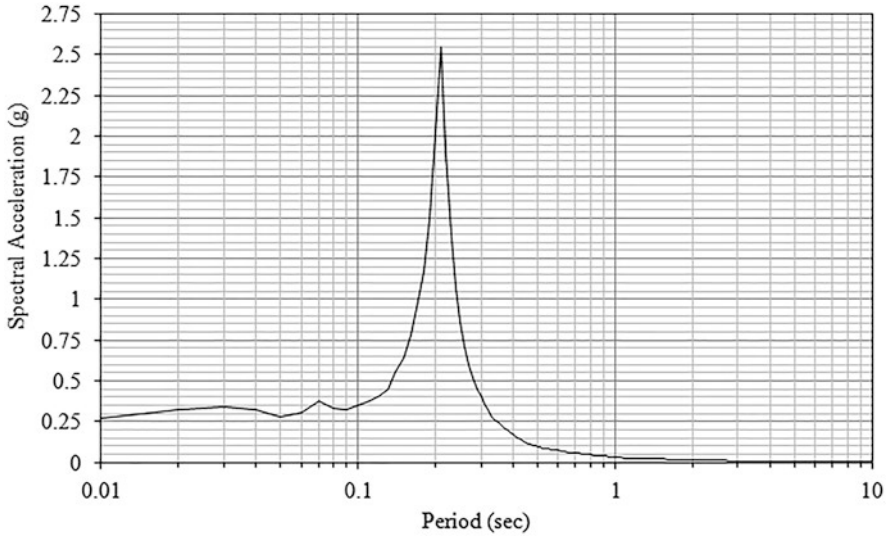


Fig. 10 The calculated spectrum of the reaction at the surface level of seismic-geological model # 1 (damping coefficient 5%)

Table 2 A seismic-geological model #2

	Layer number	Soil material type	Number of sublayers in layer	Thickness of layer (m)	Maximum shear modulus G_{max} (MPa)	Total unit weight (kN/m ³)	Shear wave velocity (m/s)
Surface	1	2		1.5	136.01	19	265
	2	2		1.5	136.01	19	265
	3	1		1	354.24	19.7	420
	4	1		3	354.24	19.7	420
	5	1		3	354.24	19.7	420
	6	1		3	502.04	19.7	500
	7	1		3	502.04	19.7	500
	8	1		3	616.72	20	550
	9	1		3	616.72	20	550
	10	1		3	616.72	20	550
Bedrock	11	0			2804.08	20.8	1150
Fundamental period (s)				0.21			
Average shear wave velocity (m/s)				467.4			
Total number of sublayers				11			

1. The value of PGA increased from 0.113 to 0.317 g, which in terms of the score corresponds to a change from 7.1 to 8.6 points (changed by 1.5 points);
2. On the calculated spectrum of the reaction, a peak is clearly distinguished in the period range 0.16–0.19 s, which corresponds to the predominant period of the initial accelerogram ($T = 0.17$ s);

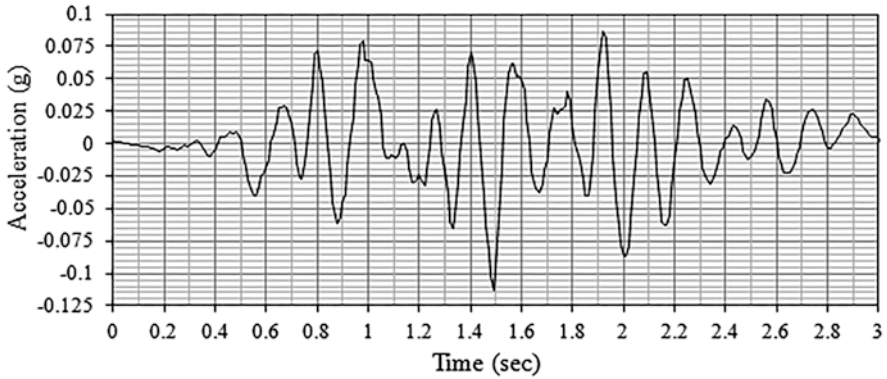


Fig. 11 The initial synthesized accelerogram in a program “PSEQGN”

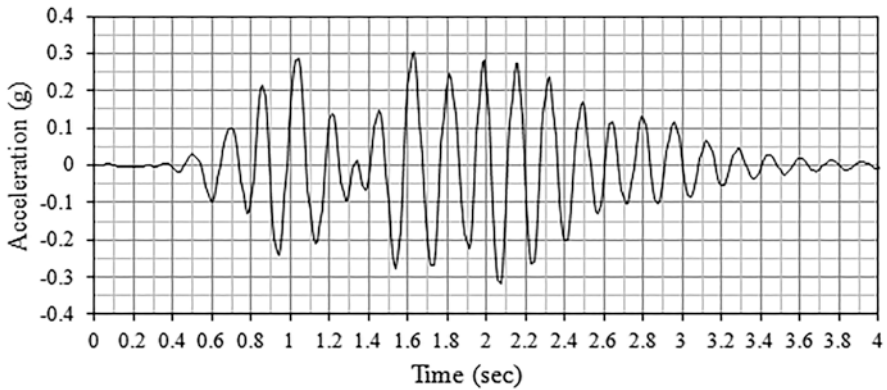


Fig. 12 The calculated accelerogram at the surface level of seismic-geological model #2

3. When comparing the initial accelerogram (Fig. 11) and the calculated one (Fig. 12), we can see that in addition to a significant increase in the amplitude, the shape of the accelerogram has also changed.

5 Conclusion

The main results of the work can be stated in the following paragraphs:

1. The main characteristics of the appearance of resonance effects in thin layers and massifs of high thickness rocks are given;
2. On an arbitrary seismo-geological model of soils and a simple initial seismic effect, the resonance effect was shown, which was clearly expressed on the calculated accelerogram and reaction spectrum;

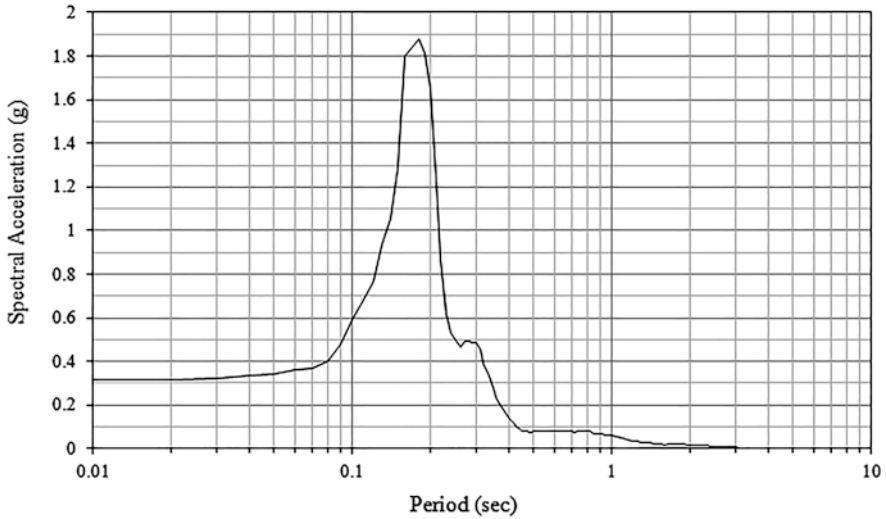


Fig. 13 The calculated spectrum of the reaction at the surface level of seismic-geological model # 1 (damping coefficient 5%)

3. In addition to an arbitrary model, calculations were carried out for the seismic-geological model, which is characteristic of many parts of the territory of the Russian Federation. It was shown how, due to resonance effects, a significant increase in seismic intensity occurs;
4. The results indicate the need to study and account for possible resonant effects in soils during seismic microzoning;
5. The values of the resonance frequencies (periods) of the soil mass are an important characteristic that must be taken into account when developing construction projects. It is necessary to avoid resonance between the natural frequency of oscillation of the structure and the thickness of the soil.

References

1. Aptikaev FF (2012) Seismic intensity tool scale. Science and Education, Moscow
2. Alyoshin AS (2010) Seismic microzoning of objects of increased responsibility. Svetoch plus, Moscow, 304 p
3. Alyoshin AS (2015) Continuum theory of seismic microzoning. Eng Surv 9:10–18
4. Kaurkin MD, Romanov VV (2017) Calculation of seismic effects in specialized programs NERA and EERA. Eng Surv 4:54–62. Geomarketing Publishing, Moscow
5. RCN 60-86 (1986) Engineering surveys for construction. Seismic microzoning. Construction norms. Moscow. State-13.code RSFSR, 17 p
6. SI-006-98 (1998) Determination of initial seismic impacts for project basis. Gosatomnadzor of the RF. Moscow, 72 p
7. DC 14.13330.2014 (2014) Construction in Seismic Areas. Ministry of Construction of the RF. Moscow, 125 p

8. DC 283.1325800.2016 (2017) Construction objects of increased responsibility. Rules for seismic microzoning. Moscow, 21 p
9. Bardet JP, Tobita T (2001) NERA: a computer program for nonlinear earthquake site response analyses of layered soil deposits. University of Southern California, Los Angeles, 44 p
10. Ruiz, Penzien J (1969) PSEQGN probabilistic study of the behavior of structures during earthquake. Earthquake engineering Earthquake Center, Report No. UCB/EERC-69/3, University of California, Berkley

Seismotectonic Model of the Western Margin of the South American Plate



Vladislav Morozov, Viktor Tatarinov, and Alexander Kagan

1 Introduction

This article [1] describes in detail the general concept of global tectogenesis based on the idea of a continuous crystallization of mantle melts, increasing the thickness of the global lithosphere in the process of the deep Earth slowly cooling down. The rate of crystallization of mantle melts at the «lithosphere – upper mantle» boundary depends on temperature. It is known that for the oceanic crust with a thickness of 50–100 km, the rate of crystallization is higher than for continents, where the thickness of the lithosphere exceeds 300 km. The determining factors are temperature, pressure, and the composition of melts in contact with the lithosphere.

The accelerated growth of the lithosphere thickness of oceans and margins of the lithospheric plates during the crystallization process as compared with the central territories of the continents leads to a planetary differentiation of the lifting forces (isostatic alignment forces), which, under the conditions of the Earth's consolidated but non-uniform lithosphere cause global deformation processes of the lithosphere explaining the periodic transgressions and regressions of seas and oceans and the formation of extended local stress concentrations responsible for orogenesis, for example, in areas of alpine folding (the Andes, Pamir, Himalayas), of modern seismicity, etc.

This article provides, based on this hypothesis, a seismotectonic model of the western margin of the South American Plate (the Chilean sector), assuming the rotational effect of the plate, caused by the forces of isostatic alignment. The authors analyzed the stress-strain state of the western margin of the South American Plate (the condition of plane strain) compared with the localization of the centers of strong earthquakes and their movements within the Chilean coastal area.

V. Morozov · V. Tatarinov (✉) · A. Kagan
GC RAS, Moscow, Russia
e-mail: v.tatarinov@gras.ru

© The Author(s), under exclusive license to Springer Nature
Switzerland AG 2021

V. Svalova (ed.), *Heat-Mass Transfer and Geodynamics of the Lithosphere*,
Innovation and Discovery in Russian Science and Engineering,
https://doi.org/10.1007/978-3-030-63571-8_28

469

2 Model of the South American Plate

As it is known, the South American Plate (SAP) has well-defined boundaries – in the west, the plate boundary is traced by the axis of the deep-water trench, in the east the border runs along the axis of the Mid-Atlantic Ridge. Within the continental part of the plate, an ancient platform lies, framed in the west by an alpine folded belt, including the extended chain of the Andes, and in the east a late Proterozoic folded belt stretches along the eastern coast of the South American continent.

The main volcanic provinces are localized within the Alpine folded belt: the Chilean-Argentinean, Chilean-Peruvian, and Ecuador-Colombian regions, traced by a colossal fault along the western edge of the plate.

Figure 1 shows a map of the foci of strong tectonic earthquakes $M > 7.0$ in the continent-ocean transition zone, including the Chilean sector. The epicenters of earthquakes and the area of subsequent aftershock activity, as a rule, are located east of the axis of a deep-water trench with hypocenters in the depth interval from 20 to 50 km. As a rule, after strong earthquakes, coastal areas of the western margin have a steady tendency to submerge. So, for example, after the May 22, 1960 earthquake at an area located north of the earthquake epicenter, the coast descended down to 1–5 m for more than 600 km [4]. We assume that the epicenters of the strongest earthquakes trace the resulting extended tectonic fault, repeating the contour of the western margin of the SAP. At the same time, the Pacific lithosphere of the western wing adjacent to the SAP has a tendency to rise, forming terraces at the intersection of the continental margins with a fault [3]. The eastern wing of the fault tends to submerge, and this tendency is clearly manifested in the co-seismic effects of strong earthquakes.

Determining the epicenters and depths of the foci of strong earthquakes within the Chilean sector over the past 100 years gives grounds for assuming a regular subsidence of the western margin relative to the oceanic lithosphere. Figure 2 shows the position of the epicenters of strong earthquakes of the Chilean sector in the time – south latitude coordinates ranging from 20° to 35° . From the above graph, it is possible to make an assumption that the Chilean sector of the SAP gradually subsides into the mantle, and this process is accompanied by strong tectonic earthquakes. The rate of accumulation of critical deformation followed by discharge in the form of an earthquake occurs from north to south and from south to north at a speed of about 50 km/year. This process (“the Chilean swing”) is caused by the dominant uplift of the eastern margin, creating a local concentration of stresses within the sinking western margin of the SAP.

Taking into account the data on the thickness of the lithosphere in this region [5, 6], Fig. 3 shows a hypothetical latitudinal section of the SAP lithosphere along a profile passing at 22° S approximately. On the western margin of SAP, the lithosphere thickness was 50 km with a dive in the east to a depth of 200 km and with a subsequent rise of the boundary (lithosphere – upper mantle) in the direction to the Atlantic Ocean up to 50 km. The assumed asymmetry of the lithosphere base section makes it possible to set the estimated ratio of the acting forces of isostatic

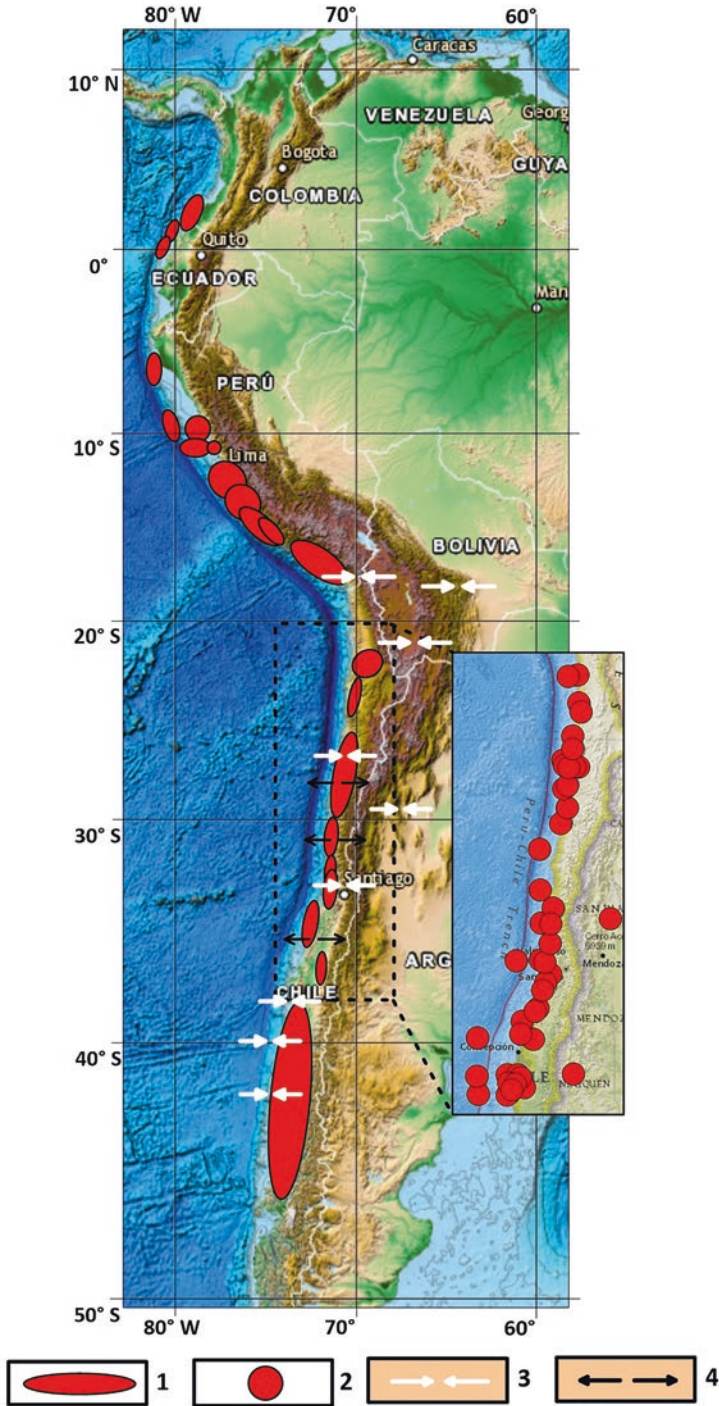


Fig. 1 South American Plate [2, 3]: 1 – areas of localization of aftershocks of strong earthquakes; 2 – earthquakes with $M > 7.0$ and depth of the hypocenter < 60 km; 3 – orientation of tectonic compression axes; 4 – orientation of tectonic tension axes

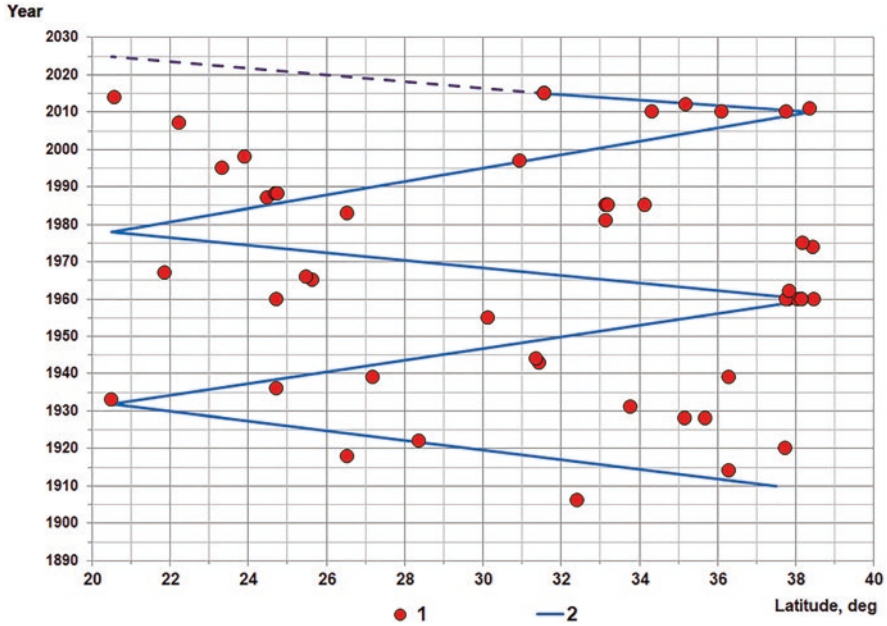


Fig. 2 The time path of the seismic process in the selected area in Fig. 1 (strong earthquakes with $M > 7.0$ and hypocenter depth < 60 km, according to [2]). 1 – earthquake epicenters; 2 – the expected course of the seismic process

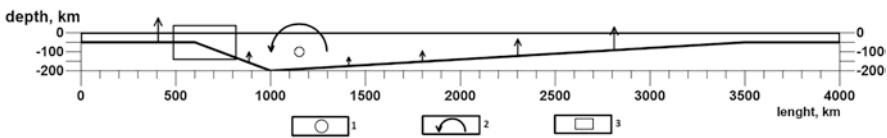


Fig. 3 The model of the latitudinal section of the Western margin of the South American Plate (22–23° South latitude): 1 – the center of rotation of the SALT; 2 – the direction of rotation; 3 – area of modeling the stress-strain state of the Western margin of the SAP

alignment. Conventionally, the value of a force acting on an elementary horizontal platform at a depth of 50 km and equal to zero at a depth of about 200 km is taken as a unit.

In the framework of a simplified model, we suggest that in the east the oceanic lithosphere floats isostatically and undergoes a rotation around a fixed center of gravity (indicated by the letter O) due to an imbalance of lift forces caused by the asymmetry of the elastic-isotropic lithosphere cross section in the latitudinal direction.

In this case we suppose that:

1. The center of gravity O is stationary in the YOX coordinate system, i.e. the lifting forces cause the plate mass to turn counterclockwise, and the weight of the plate prevents the center of gravity from moving;
2. In the area of DF (continental lithosphere) repulse of the mantle prevents the subsidence of the lithosphere;
3. The BD section under the trench has lower hardness values, i.e. the design scheme envisaged that the elastic modulus in this zone is an order of magnitude lower than outside its borders due to the processes of tectonic destruction preceding the present stage of tectogenesis.

This last point requires certain explanations. Assuming the possibility of the formation of a geosynclinal zone at an early stage of tectogenesis, the formation of an oceanic trench also should be allowed as a set of faults such as a transtensional fault (a strike-slip fault), that is, a zone of tectonic destruction separating the oceanic lithosphere from the continental lithosphere.

The axis of the deep-water trench traces the zone of fracture destruction formed prior to the Alpine folding period, which dampens the forces of the subsiding western edge of the plate. The consequence is the absence of earthquake foci to the west of the axis of the deepwater trench.

The authors analyzed the stress-strain state of the plate within its western margin and compared the existing stresses with the geomorphology of the transition zone, seismicity, volcanism and geodynamics within the Chilean sector of the western margin of the SAP.

The generally accepted point of view is the idea of a high rate of subsidence of the Chilean-Argentinean Andes and the formation of the Andean geosyncline [7, 8]. In the framework of the accepted model, the subsidence of the western margin of the plate and the formation of the geosyncline is associated with the elevation of its eastern part. The mechanism of application of forces and the estimated center of rotation of the plate are shown in Fig. 3.

3 Results of Modeling the Stress-Strain State

To calculate the stress-strain state (SSS) of an elastically deformed model, we used the finite element method, which is simultaneously a method for constructing a mathematical model and a method for studying it. The main idea of the method is that a continuous quantity, that is, a quantity defined by an infinite number of values, is approximated in the considered region by a discrete model. The latter is based on a set of piecewise continuous functions defined on a finite number of subsets. The mechanism of application of forces and the estimated center of rotation of the plate are shown in Fig. 3.

Figure 4c shows the simulation results of SSS, conventionally corresponding to the latitudinal section of the transition zone at 23° S. The stresses σ_{xx} and τ_{xy} are indicated in conventional units.

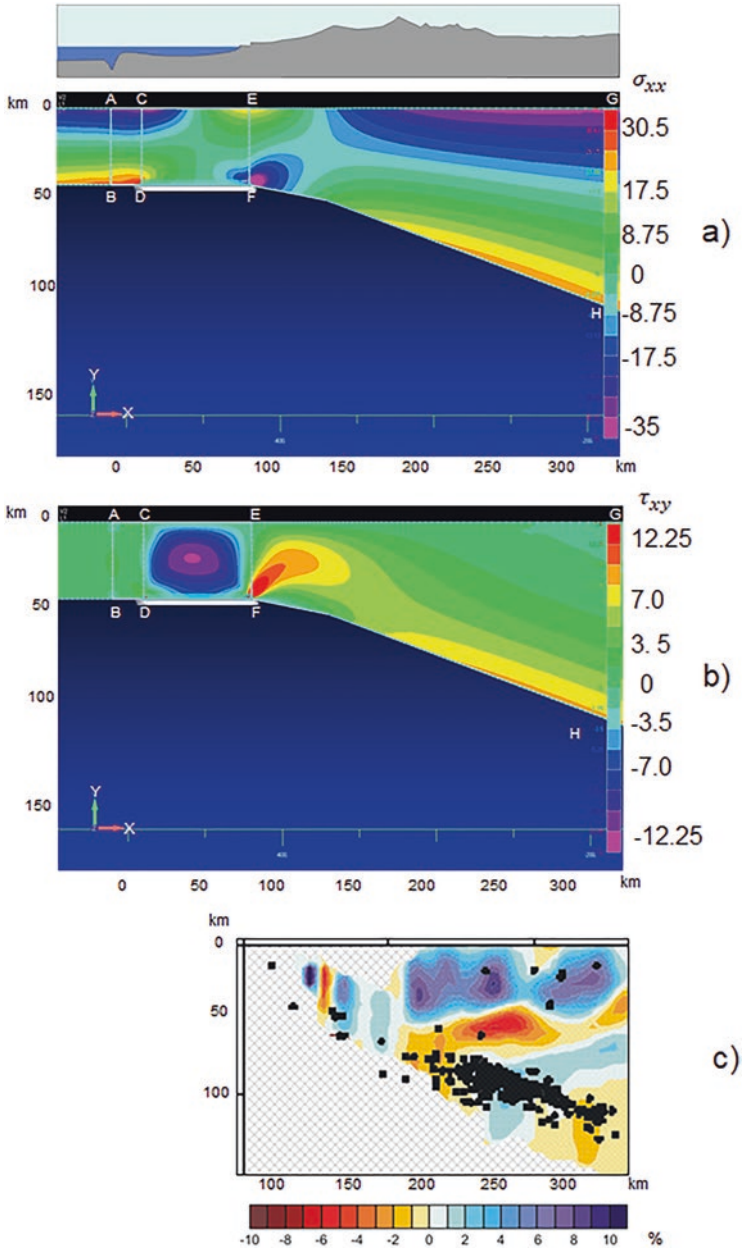


Fig. 4 Stresses σ_{xx} (a), stresses τ_{xy} (b) and velocities of longitudinal waves (c), western margin of the SAP [9]

Figure 4a, b shows the results of the calculation of SSS for the continent-ocean transition zone conventionally corresponding to the latitudinal section at 23° S. The stresses σ_{xx} and τ_{xy} are indicated in relative units of the given scales. It is interesting to compare local stress concentration zones with seismotectonic features of the western margin of the SAP. Let us pay attention to the formation of compression zones in Fig. 4a. In the upper part of the Earth's crust, within the framework of the adopted model, the zones of compression are localized in the AC section and in the longer continental EG section. And if within the AC section they capture depths of ~10–15 km, in the EG section they extend to depths of ~25 km, i.e. the model to some extent adequately reflects the data shown in Fig. 1 (white arrows indicate the direction of compressive stress axes). We suggest that the compressive stresses in the EG section of the western margin of the SAP are responsible for the formation of folding and the system of subsequent thrusts that form the Andes mountain system. It can also be assumed that the crust seismicity on the continent with a focal depth of up to 20 km is caused by compression stresses.

Anomalous compressive stresses are localized in the area of the supposed lithospheric bending in the vicinity of point F. As the boundaries of the lithosphere subside into the mantle, tensile stresses are formed (section FH). Tension stresses at a depth of 70–100 km contribute to the formation of tectonic fractures, which develop into tectonic faults, the formation of which is facilitated by penetrating magma solutions. Penetrating solutions formed the crystal body of the batholith, which determines volcanic activity. It can be assumed that as a result, a locally intermittent tectonic fault was formed and the position of volcanoes traced its exit to the surface.

The zone of localization of the foci of strong earthquakes shown in Fig. 1 is probably related to the stress concentration over point F, i.e. when the foot of the continental lithosphere subsided into the mantle. Figure 4b shows the distribution of shear stresses τ_{xy} in the DCEF segment, they are negative, and in the EFGH segment they change sign. We suggest that such a stress distribution explains the origin of the centers of strong earthquakes in this zone.

According to the used SSS model of the western margin of the SAP, we came to a conclusion that after an earthquake, i.e., a rupture, a weakened zone appears (shown in Fig. 5 by dotted lines with an elastic modulus an order of magnitude less than the surrounding lithosphere). This area significantly changes SSS in the transition zone (Fig. 5a, b), stimulating the development of aftershocks.

For comparison, Fig. 6a, b, c shows the areas of aftershock localization (within 2 weeks after the main shocks) of earthquakes of July 30, 1995, M 8.0, October 14, 2007, M 7.7 and July 30, 2010, M 8.8 [11–15].

The depths of earthquake foci are within up to 50 km, the spatial distribution of aftershocks, according to the real scale, is taken outside the section of the lithosphere used for SSS calculation model of the western margin of the SAP. It can be seen that the first aftershocks are localized in areas of abnormally high shear stresses.

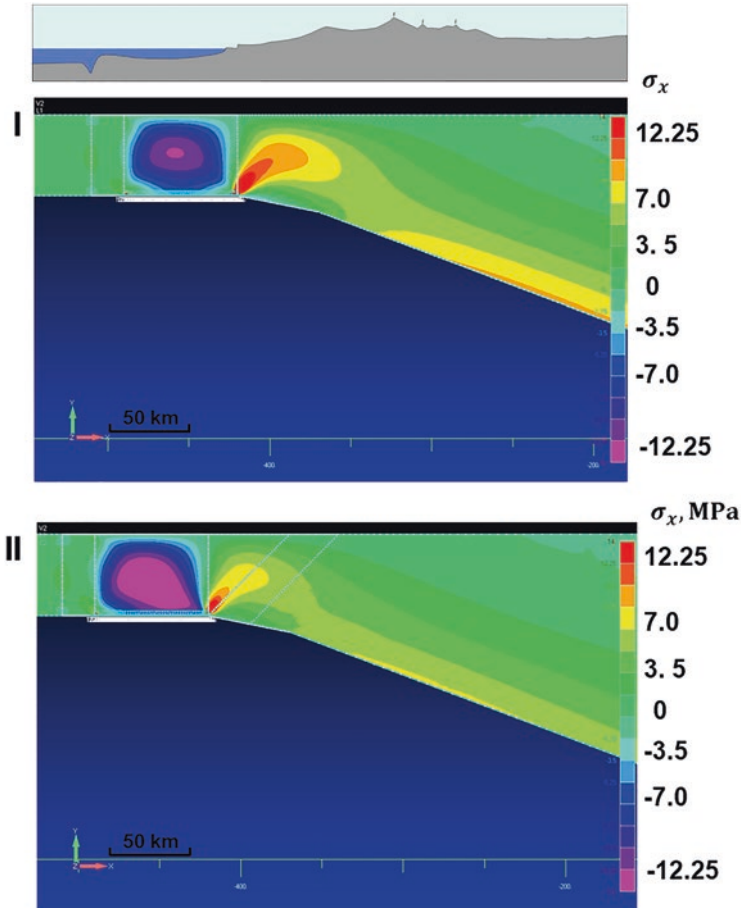


Fig. 5 Stresses σ_{xx} (a), stresses τ_{xy} (b) of the western margin of the SAP (the dotted line shows suppose a weakened zone after an earthquake)

4 Discussion of the Results

Being aware of the phenomenology of the used model of the lithosphere and the results of determining SSS based on the assumptions made, it is necessary to admit the expediency of further developing the model of the western margin of the SAP combining the seismotectonic aspects of this region based on ideas alternative to the concept of subduction of the oceanic crust under the continental lithosphere.

The model of the lithosphere of the western margin of the SAP and its SSS are in a certain correspondence with the available geological and geophysical data:

1. This proposed model assumes the rise of the oceanic crust and a fragment of the continental crust (DCEF), explaining the formation of terraces within the Chilean

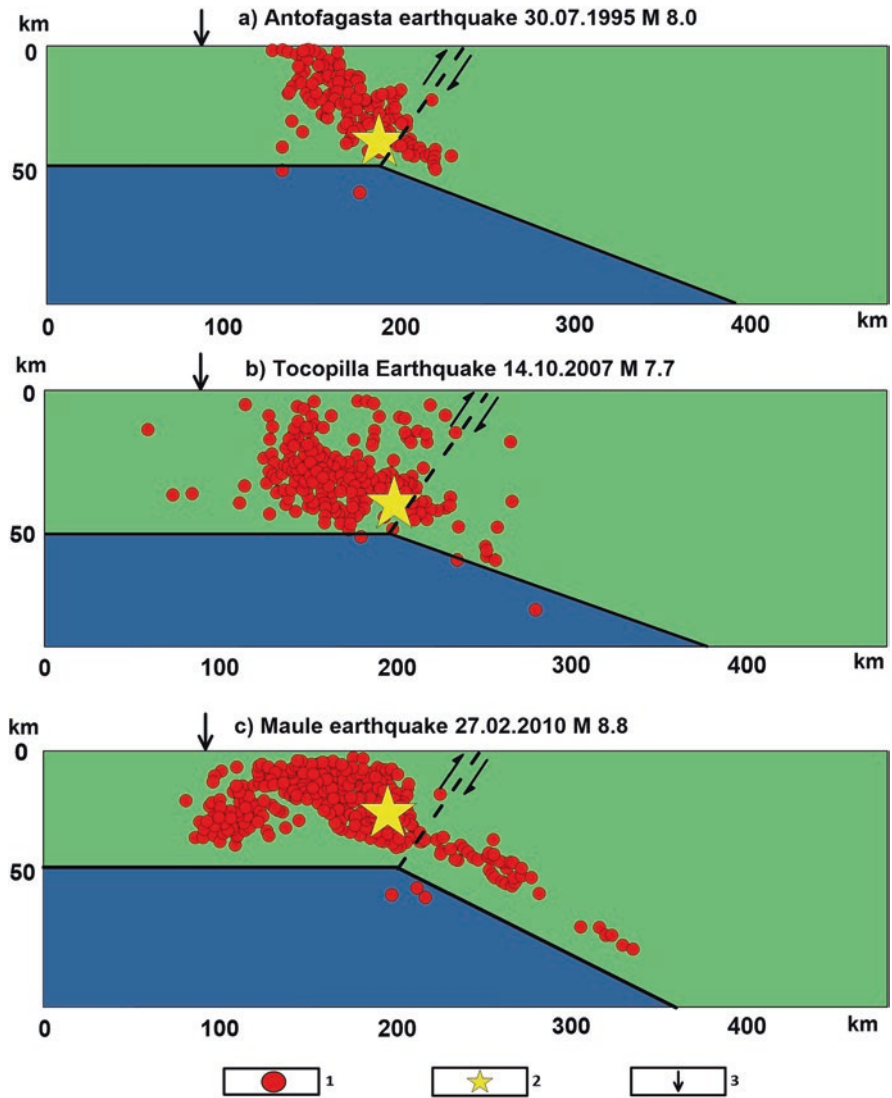


Fig. 6 Aftershock of strong earthquakes in Chile using data [10–13]: (a) – Antofagasta earthquake 07.30.1995 M 8.0; (b) – Tocopilla earthquake 10.14.2007; (c) – Maule earthquake 02.27.2010 M 8.8; 1 – aftershocks; 2 – the main push; 3 – the axis of the deepwater trench

sector [3], including the uplift of this zone according to GPS observations [16] and co-seismic effects accompanying strong earthquakes in this zone with a focal depth of 50 km.

2. The formation of compression crustal stresses in the FEGH sector explains the evolution of tectonic thrusts [17] that form the Andes mountain system and induce seismicity in the outer layer of the Earth’s crust.

3. The tensile stresses arising in the bottom of subsiding lithosphere FH explain the penetration of mantle melts to the surface due to the formation of tensile cracks forming tectonic faults, which are confirmed by seismic topography in this sector of the transition zone from the continental crust.
4. The concentration of shear stresses in the bottom of subsiding crust in combination with tensile stresses explain the seismic activity of the western margin of the SAP at depths above 50 km (in the Benioff-Zavaritsky zone).
5. The area of transition from west to east of the subsiding continental crust from the ocean-type crust with a thickness of up to 50 km, is an area of high stress concentration (σ_{xx} , τ_{xy}), responsible for the formation of foci of strong earthquakes within the coastline (Fig. 1).
6. It can be assumed that in the first days after the main shock of strong earthquakes, the CDEF area of aftershock process is associated with a change in the stress state and is an area where strong aftershocks occur.
7. The slow subsidence of the continental crust (Chilean sector) forms a fault zone west of the coast and is accompanied by strong earthquakes with a tendency of migration of foci along the coastline.

5 Conclusion

The proposed model of the western margin of the SAP does not claim to be complete. At the same time, the results obtained have some confirmation in other regions of the world: Japan, Russia (Kamchatka). The foci of strong tectonic earthquakes in these areas at depths of up to 50 km are located west of the axis of the deepwater trench and have spatial extension and manifestations of surface deformation during co-seismic processes similar to the SAP.

Acknowledgements The authors would like to express their gratitude to our colleagues for their help in writing this article: A.I. Manevich, T.A. Tatarinova, E.Yu. Firsova.

This work was conducted in the framework of budgetary funding of GC RAS, adopted by the Ministry of Science and Higher Education of the Russian Federation.

References

1. Morozov VN (1999) Global Tectonogenesis M. GEOS
2. Earthquake Catalog [USGS Earthquake Hazards Program]. URL: <https://earthquake.usgs.gov/earthquakes/search>. Accessed 15 Mar 2019
3. Moreno T, Gibbons W (2007) The geology of Chile. The Geological Society, London
4. Benioff H (1966) Movement along the largest faults. Drift of continents (horizontal movements of the Earth's Crust). Mir, Moscow
5. Bird P (2009) Long-term fault slip rates, distributed deformation rates, and forecast of seismicity in the western United States from joint fitting of community geologic, geodetic, and stress direction data sets. *J Geophys Res* 114:B11403. <https://doi.org/10.1029/2009JB006317>

6. Conrad CP, Lithgow-Bertelloni C (2006) Influence of continental roots and asthenosphere on plate-mantle coupling. *J Geophys Res* 33:L05312. <https://doi.org/10.1029/2005GL025621>
7. Lomize MG (1975) Tectonic development and volcanism of the Chilean-Argentine Andes. *Bull MOIP Geol* 50(3):48–69
8. Milanovsky EE (1975) Cenozoic orogenesis of the Central Andes. *Geodyn Stud M Sov. Radio* (2):76–161
9. Dobretsov NL, Kirdyashkin AG (1998) Deep-level geodynamics. A.A. Balkema, Rotterdam. 328 p
10. Fuenzalida A, Schurr B, Lancieri M, Sobiesiak M, Madariaga R (2013) High-resolution relocation and mechanism of aftershocks of the 2007 Tocopilla (Chile) earthquake. *Geophys J Int* 194(2):1216–1228. <https://doi.org/10.1093/gji/ggt163>
11. M 8.0-Antofagasta, Chile [USGS Earthquake Hazards Program]. URL: <https://earthquake.usgs.gov/earthquakes/eventpage/usp000714t/executive> Accessed 15 Mar 2019
12. M 8.8-Offshore Bio-Bio, Chile [USGS Earthquake Hazards Program]. URL: https://earthquake.usgs.gov/earthquakes/eventpage/official20100227063411530_30/executive Accessed 15 Mar 2019
13. Rietbrock A, Ryder I, Hayes G, Haberland C, Comte D, Roecker S, Lyon-Caen H (2012) Aftershock seismicity of the 2010 Maule Mw=8.8, Chile, earthquake: correlation between co-seismic slip models and aftershock distribution? *Geophys Res Lett* 39(8):L08310. <https://doi.org/10.1029/2012gl051308>
14. Delouis B, Monfret T, Dorbath L, Pardo M, Rivera L, Comte D, Haessler H, Caminade JP, Ponce L, Kausel E, Cisternas A (1997) The $M_w = 8.0$ Antofagasta (Northern Chile) earthquake of 30 July 1995: a precursor to the end of the large 1877 gap. *Bull Seismol Soc Am* 87(2):427–445
15. Delouis B, Pardo M, Legrand D, Monfret T (2009) The Mw 7.7 Tocopilla earthquake of 14 November 2007 at the southern edge of the Northern Chile seismic gap: rupture in the deep part of the coupled plate interface. *Bull Seismol Soc Am* 99(1):87–94. <https://doi.org/10.1785/0120080192>
16. Drewes H, Sánchez L (2017) Velocity model for SIRGAS 2017: VEMOS2017. Technische Universität München, Deutsches Geodätisches Forschungsinstitut (DGFI-TUM), IGS RNAAC SIRGAS
17. Costa HC, Vita-Finri C (1996) Late holocene faulting in the southeast Sierras Pampeanas of Argentina. *Geology* 24(12):1127–1130

Permeability of the Continental Crust –Possible High Values from Laboratory Measurements and Seismological Data



Mikhail V. Rodkin and Andrey V. Zharikov

1 Introduction

The data of superdeep drilling and deep geophysical studies indicate the mobile fluid occurrence at the depths that were previously considered inaccessible for them. Rock permeability is the main parameter that governs the flow dynamics of natural and technogenic fluids in the geological environment. Hence, it is very important not only to reveal the main trend of change of the permeability with the depth, but also to understand the mechanisms that cause these changes, and to obtain estimates both of the typical permeability values and, as well as their possible variations due to different depths, rock compositions, tectonic conditions and seismic regimes. The forecast of near-field rock permeability is very important for safe underground disposal of critical waste.

Permeability is the most variable of the physical properties of rocks: its changes, even in rocks of the same lithological type, can reach several orders of magnitude [3, 22]. The reasons of such high variability often are not clear. The very wide range of permeability change found from the geological data is also poorly understood. E. Roedder [21] wrote: «The mobility of metamorphic fluids presents us with a paradox, in that some metamorphic terranes provide abundant evidence of widespread and relatively rapid movement of fluids, whereas others provide equally con-

M. V. Rodkin (✉)
IEPT RAS, Moscow, Russia

OGRI RAS, Moscow, Russia
e-mail: rodkin@mitp.ru

A. V. Zharikov
IGEM,RAS, Moscow, Russia

vincing evidence of an almost complete lack of fluid migration, over millions of years».

Direct in situ permeability measurements using hydraulic tests are usually performed at depths of no more than 3–5 km, and only a few measurements were carried out in the superdeep wells SG-3 (Russia) and KTB (Germany) to the depth of about 10 km [5, 9].

However, fairly representative data on rock permeability at high temperatures and pressures corresponding to PT conditions of the deep Earth's crust were obtained in the laboratory on the samples. These estimations can be compared with other independent ones: from geological, geophysical and seismological data. Such a comparison for the first time presented in [7] revealed a strong discrepancy between the appropriate independent permeability estimations. The laboratory experiment data in the most cases give the lower values, but the geological data expect higher, and seismological ones - extremely high.

In this paper, we focus mainly on the analysis and comparison of laboratory and seismological data in order to examine the possible range of change of the permeability values in the Earth's crust. The possible mechanisms of the development of episodes of high permeability in the middle and the lower crust are discussed.

2 Laboratory Data

A research team, which included one of the authors, conducted a systematic experimental study of permeability of tight rocks at high temperature and pressure for many years – almost during four decades. A great amount of data were obtained due to original experimental methods and equipment developed. The main feature of the experimental technique was the use of inert gas – argon for filtration through the sample, which reduced the duration of measurements and, what was the mostly important, avoided any geochemical transformations caused by fluid-rock interaction at high temperatures. The technique of determination of water permeability by gas for both: steady state and transient methods with Klinkenberg's correction were developed and used; see [11, 25] for details. This approach, as well as, the use of specially designed apparatus [25, 31] made it possible to carry out experiments in a wide range of pressures (0.1–200 MPa) and temperatures (20–600 °C) and to obtain about of 40 permeability values at different PT-parameters during the single run on each sample (Fig. 1c)).

As a result, it became possible to obtain an appropriate amount of experimental data at high PT conditions (more than 50 samples of crystalline rocks were examined, and more than 2000 permeability values were obtained), which allow to found the general patterns, and in comparison with the results of microstructure studies - the causes and mechanisms of permeability changes at high temperatures and pressures.

It was found that permeability is strongly and in a complicated manner controlled by competitive effect of temperature and effective pressure. With an increase

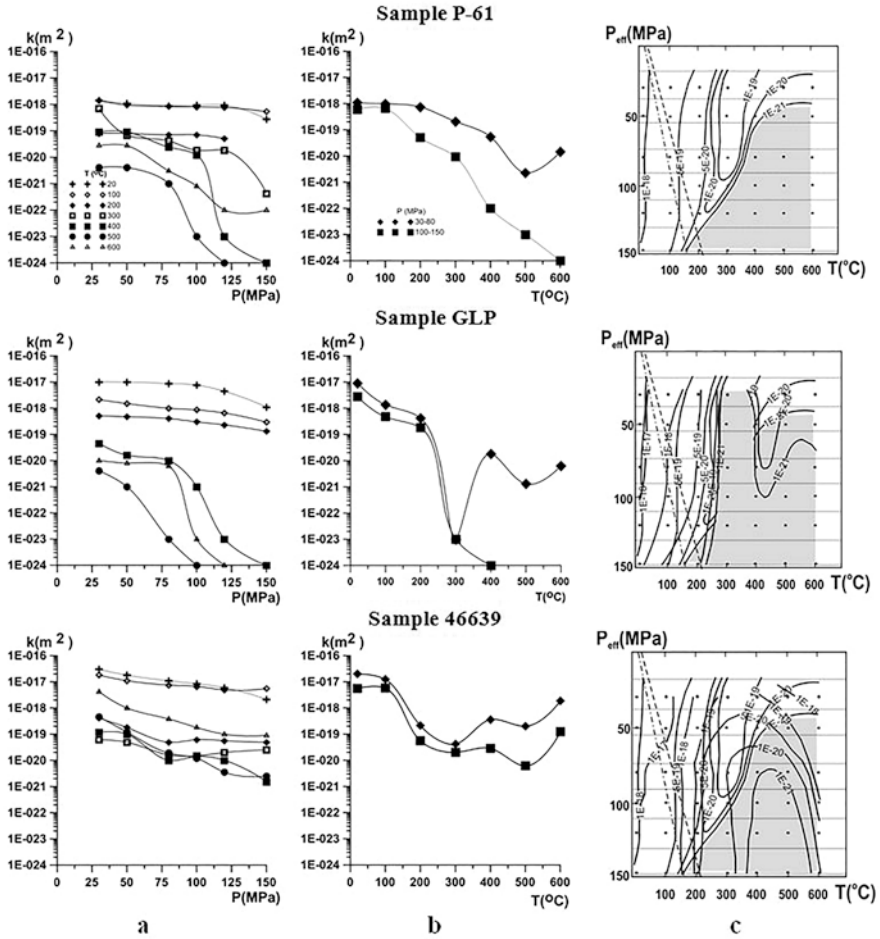


Fig. 1 Dependencies of permeability on effective pressure (a) and temperature (b), (c) – permeability maps in PT-coordinates (on the example of the amphibolite samples from the superdeep wells SG-3 (Russia) and KTB (Germany)). Dashed lines show changes of in situ PT-parameters for SG-3 and KTB, points – PT of measurements

in the effective pressure (at $T = const$) permeability, as a rule, decreases (Fig. 1a). The trend gradient has a tendency to increase with increasing of temperature and pressure. Temperature increase at constant effective pressure can lead to monotonous permeability increase or decrease within the entire temperature range, or to appearance of inversions in the trends (Fig. 1b). It is significant that in all cases the range of change in permeability values reaches several decimal orders of magnitude.

Such diverse permeability behavior is connected with the fact that in contrast to the other petrophysical properties, permeability does not depend mainly on the rock composition, but it is governed by the structure of the pore space - both on the size

and level of interconnectivity of pores and cracks. Studies under a scanning electron microscope show that rock microstructure can undergo strong and various transformations due to the effect of temperature and pressure. For example (see, Fig. 2), under heating long microcracks (with low aspect ratio), which cut many mineral grains, close, whereas at the same time short microcracks (with high aspect ratio), located at the mineral grain boundaries, on the contrary, open [31]. Local processes of microcrack closure and formation can take place simultaneously and their superposition leads to occurrence of inversions on the temperature trends in the permeability values (Figs. 1 and 2). Since the connectivity of fluid-conducting clusters is the main factor responsible for permeability of tight rocks, even minor changes in microcrack density, length, aperture and interconnectivity under high PT-parameters are able to cause dramatic changes in permeability. Therefore, the sharp, threshold transitions are rather typical of the permeability trends (Fig. 1).

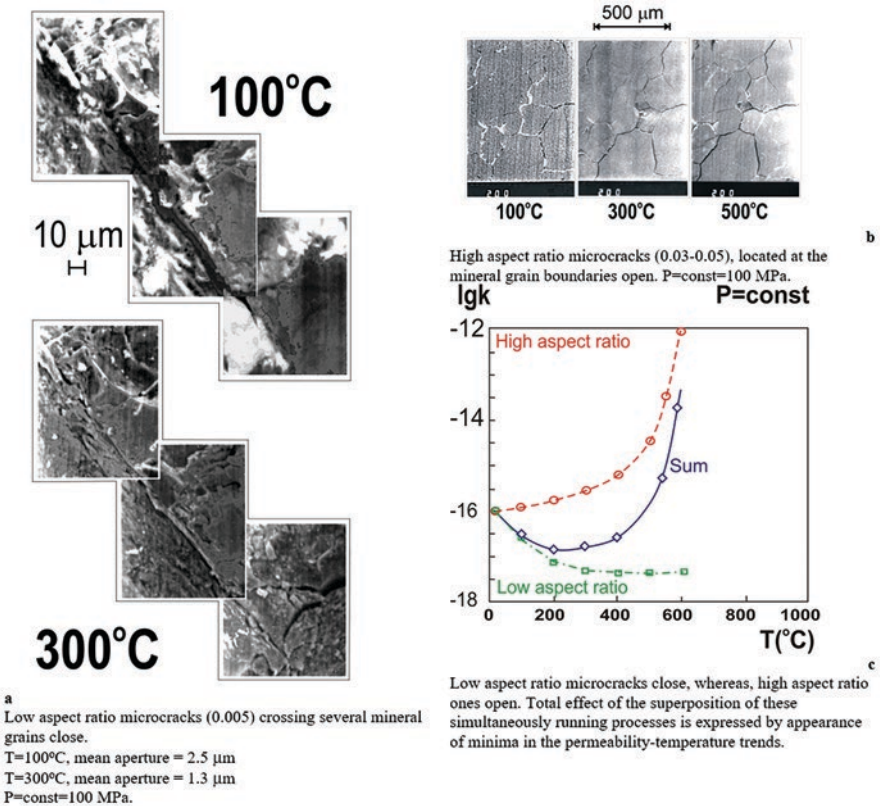


Fig. 2 Two families of microcracks with different behavior under heating due to their different aspect ratio. The data of SEM observations (a, b) and numerical simulation (c)

The trends of permeability for the samples of typical rocks of the continental crust obtained at simultaneous temperature and pressure elevation, simulating the *in situ* depth increase are presented in Fig. 3.

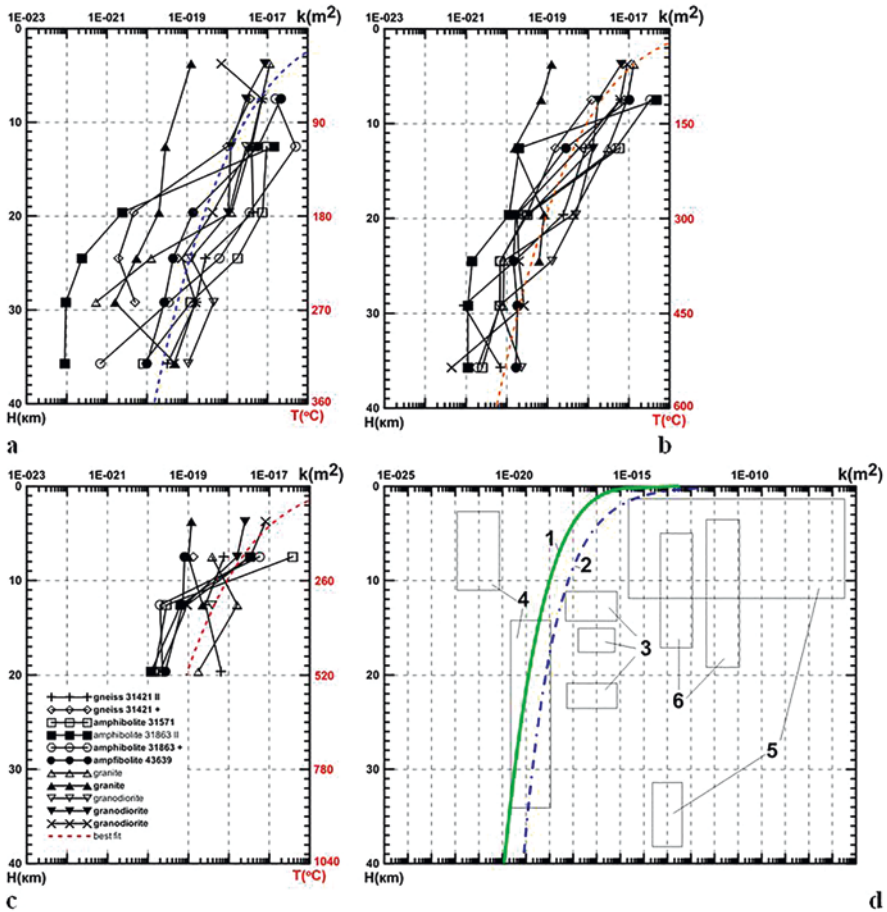


Fig. 3 The permeability dependencies obtained with simultaneous increase of temperature and pressure simulating *in situ* conditions of shields (with thermal gradient of 9 °C/km) – (a), platforms (with thermal gradient of 15 °C/km) – (b) and orogenic belts (with thermal gradient of 26 °C/km) – (c). (d) – 1 – generalized trend based on laboratory data [26], 2, 3 – estimations based on geothermal data and fluid flux during progressive metamorphism [7], 4 – estimations based on geophysical data (Vanyan, et al., 2001), 5, 6 – estimations from seismological data [7, 18]

The following assumptions were made: the thickness of the continental crust is 40 km and the areas with low (9 °C/km), medium (15 °C/km) and high (26 °C/km) thermal gradient were considered: shields, platforms and orogenic belts (Fig. 3a–c). The mean gradient of lithostatic pressure is 27 MPa/km [4]. The effective pressure was considered as

$$P_{eff} = P_{lit} - \alpha P_f, \quad (1)$$

where α values are assumed to be 0.85–0.95 according to [2]. Consequently, P_{eff} in the crust section varies from 0.54–1.62 MPa at the depth of 4 km to 54–162 MPa at the depth of 40 km.

With a depth increase the pressure effect prevails and, as a result, permeability decreases for all the studied samples. Hence, the generalized trend obtained on the basis of data processing (11 samples, 234 experimental points) shows monotonic permeability decrease (Fig. 3d) and can be described by the relation:

$$\lg K = -12.6 - 3.23H^{0.223}, \quad (2)$$

where K is permeability (m^2), and H is a depth (km) [26].

As it was mentioned above, there are no *in situ* permeability determinations at the depth more than 10 km. However, it seems reasonably to compare our laboratory estimations of the continental crust permeability with those obtained from the geological and geophysical data. In Fig. 3d curve 1 shows the trend based on experimental data [26]. The permeability, calculated from geothermal data and the fluid flow flux in metamorphic systems [6], also decreases with depth according to the power law (curve 2). Similar dependencies [10, 23] obtained from different methods appear to be in a suitable agreement. The values of “geothermal “permeability in the entire depth range are a decimal order higher than the values of “experimental” one, which corresponds to the stable craton condition. Thus, as noted in [7], the trends of permeability with depth are quite consistent. Much higher permeability values may be associated with fault-zone metamorphism. Some other evidences of high permeability are obtained, revising the time scale of regional metamorphism, which is considered to be one decimal order shorter (Fig. 3d, – 3) [7].

Permeability values estimated from magnetotelluric data are presented in [28]. For the depth interval of 15–35 km these values are close to ours, but in the upper crust they are significantly less (Fig. 3d, number 4).

The highest permeability values were obtained from some seismological data (Fig. 3d, number 5,6); these data and those discussed below appear to deviate sharply from the typical permeability estimates presented above.

Thus, an essential disagreement does take place between the valid estimations of the trend permeability values and much higher values revealed from some petrological and seismological data. In general, in the agreement with that mentioned above [6, 21] we can see a well grounded trend of a decrease in a permeability with the depth, whereas very high permeability values were revealed in some cases. The mechanisms of these increases are unclear.

As a preliminary suggestion, from the experimental data mentioned above (Figs. 1, 2, and 3) it can be noted that the effect of heating prevails under high temperature and low effective (high pore) pressure, and, as a result, at these specific conditions permeability increases and reaches much higher values (from 10^{-19} to 10^{-18} m²) that appear to agree with seismological data. Some other possible mechanisms of the permeability increases will be discussed below.

3 Seismological Data

As a rule, for permeability estimation a velocity of systematic displacements of earthquake foci, which are interpreted as a propagation of fronts of a high fluid pressure, are considered. The permeability estimates obtained this way show frequently the maximum values. Some examples of such estimates from the data collection [7] are presented in Fig. 3, where they are marked with the numbers 5,6. Naturally, this is not a full list of such type of behavior.

We will examine below the cases of foci displacements with a decrease in the mean depth values with time: this behavior seems to be the mostly expected for the cases of the propagation of the low-density fluid through the fractured crust. We firstly examined a few new examples of specific outbursts in aftershock activity that can be connected with the temporal epochs of an increase in permeability values in the continental crust. Then the typical patterns of seismicity of such type will be discussed using the results of examination of the seismic regime in the generalized vicinity of a major earthquake [16, 20]; in this method the volume of available statistics is strongly increased because the summing of data from a big number of vicinities of individual large earthquakes. Then some possible mechanisms of temporal increases in the permeability values will be discussed.

The first example is concerned with the examination of a change in depths of aftershock sequence of the Bhuj earthquake (Mw7.7, 2001, India). This earthquake is unique in its location away from the plate boundaries in the platform area and by the high activity and abnormally long duration of its aftershock sequence, which is studied in details because of installation of the local seismic network providing an exact determination of aftershock parameters [18]. The Bhuj earthquake took place in the ancient rift area, and the earthquake occurrence here is assumed to be associated with a release of the fluid from the lower crust [1, 13]; the fluid is assumed to be mostly of CO₂ content.

The changes of the magnitudes in the Bhuj earthquake aftershock sequence with time, and the mean current earthquake depth values $H(t)$ are shown in Fig. 4 for the 10 years time interval after the main shock occurrence. A few evident bursts in a number of aftershocks can be seen in Fig. 4a. The each point in Fig. 4b represents a mean depth value of 20 consecutive earthquakes at a step of 10 events. Aftershock foci are not concentrated along the causative fault of the Bhuj mainshock. Instead, they are dispersed in space, and the block adjacent to the causative fault from above is more seismically active than that adjacent to it from below [18]. Such pattern of

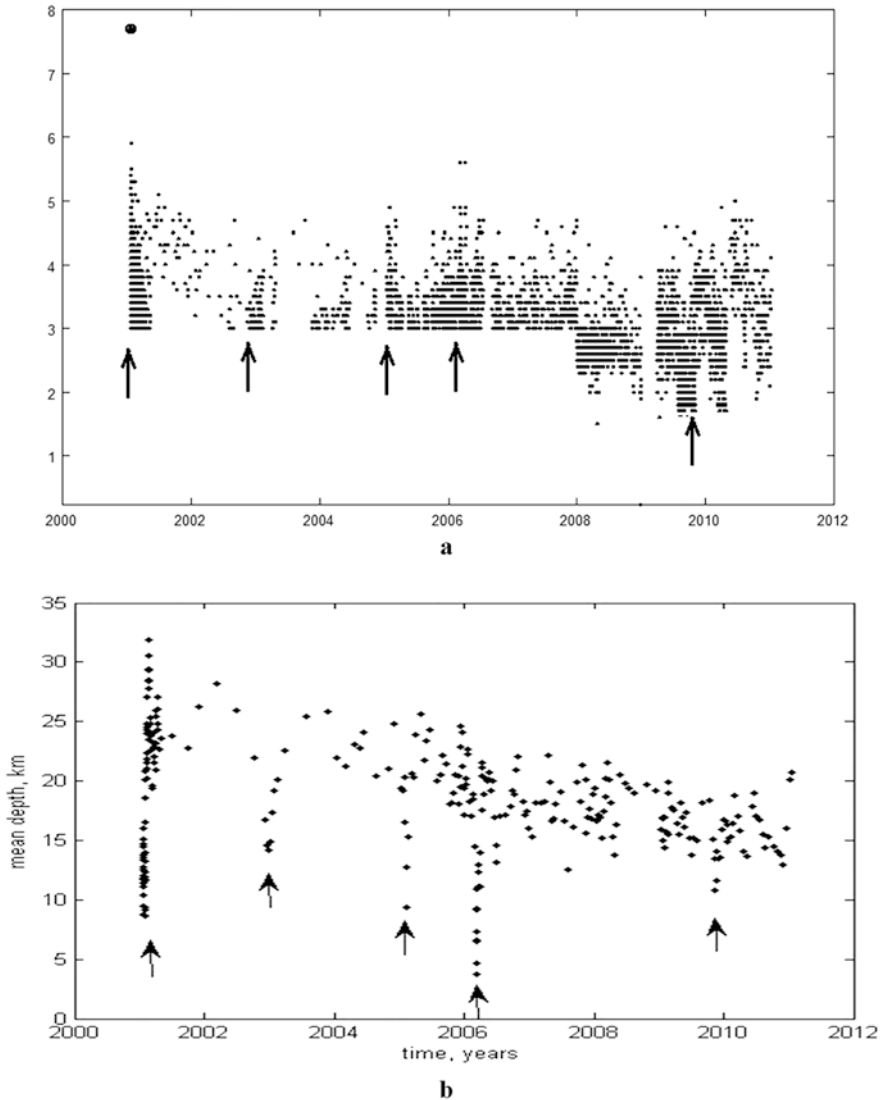


Fig. 4 Aftershock magnitudes vs. time in the 2001 Bhuj Mw7.7 aftershock sequence (a) and the mean depth values of groups of 20 consecutive aftershocks in this sequence (b). Arrows mark the moments of short episodes of increase in aftershocks number and decrease in the mean depth values. A large dot (4a) – Mw magnitude of the main shock

aftershock localization testifies in support of active diffusion of fluids through the entire aftershock zone and not only along the disrupted causative fault plane of the Bhuj mainshock.

Several short (less one-month in duration) episodes of a decrease in the mean depth values well coinciding with the bursts in the aftershock number can be seen in

Fig. 4. These episodes of decrease in the mean depth values took place in 2001, 2003, 2005, 2006 and 2009 years. Besides these episodes of a very rapid decrease in the mean earthquake depths, the general monotonous tendency of a decrease in the mean earthquake depths with time from about 25 to 15 km can be seen in Fig. 4b. The short episodes of decrease in the mean earthquakes depth values can be interpreted as episodes of a breakout of portions of the deep fluid through the crust to the surface. The episodes of breakout of the deep fluid to the Earth's surface can be expected to be associated with increases of a number of aftershocks due to a decrease in the rock friction. This expectations agree well with the real data (see Fig. 4).

During the episodes of the deep fluid breakout to the Earth's surface the decreases in b-values and in fractal dimension due to the concentration of aftershocks at the mechanically weakened fluid conducting structure of low dimensionality can be expected. These regularities were found factually in result of the examination of the Bhuj aftershock sequence [18]. Current b-values and correlation fractal dimension D_2 values do have a tendency to decrease when a number of aftershocks increases and the mean depth of the aftershocks decreases (Fig. 5). The events with magnitude $M > M_0$, where $M_0 = 3.0$ were used in the calculations. The each point in Fig. 5a represents a b-value obtained for 50 consecutive earthquakes at a step of 25 events, and each point in Fig. 5b represents a D_2 value obtained for 100 consecutive earthquakes at a step of 50 events.

The similar bursts in seismic activity with a tendency of a decrease in the mean earthquake depths and decreasing in b-value and correlation fractal D_2 values were noticed [17, 19] in the aftershock sequences of the Andaman mega-earthquake (December 26, 2004, $M_w = 9.3$) and Tohoku mega-earthquake (March 11, 2011, $M_w = 9.0$). In both these cases, a great number of aftershocks gives possibility for a suitable statistic examination. Similar features were found also in the aftershock sequence of two strong Simushir earthquakes (November 15, 2006, and January 13, 2007). In the majority of cases, the episodes of increases in aftershock number were accompanied by the decreases in the mean depth values, current b-values, and correlational fractal dimension D_2 values.

The model of a pulse wave-like fluid propagation with a velocity V through the porous media [12] gives a possibility to evaluate the effective rock permeability that could correspond to the discussed tendencies of a regular change in mean earthquake depths. This model was used in [12] for the examination of a possible pulse-like propagation of fluid that presumably had caused the earthquakes swarm occurred in the northern Italy in 1997. According to this model.

$$V = K \Delta\rho / \eta\phi \quad (3)$$

where K is the permeability, $\Delta\rho$ is the density difference between the rock and the fluid, η is the viscosity, and ϕ is the porosity.

Using this model, we had examined firstly the tendency of a monotonous decrease in the mean earthquake depths with time (see Fig. 4b) in the Bhuj aftershock sequence. The velocity of fluid high pressure front propagation V is evaluated from the clearly seen linear tendency of a decrease of mean depth values from 25 to

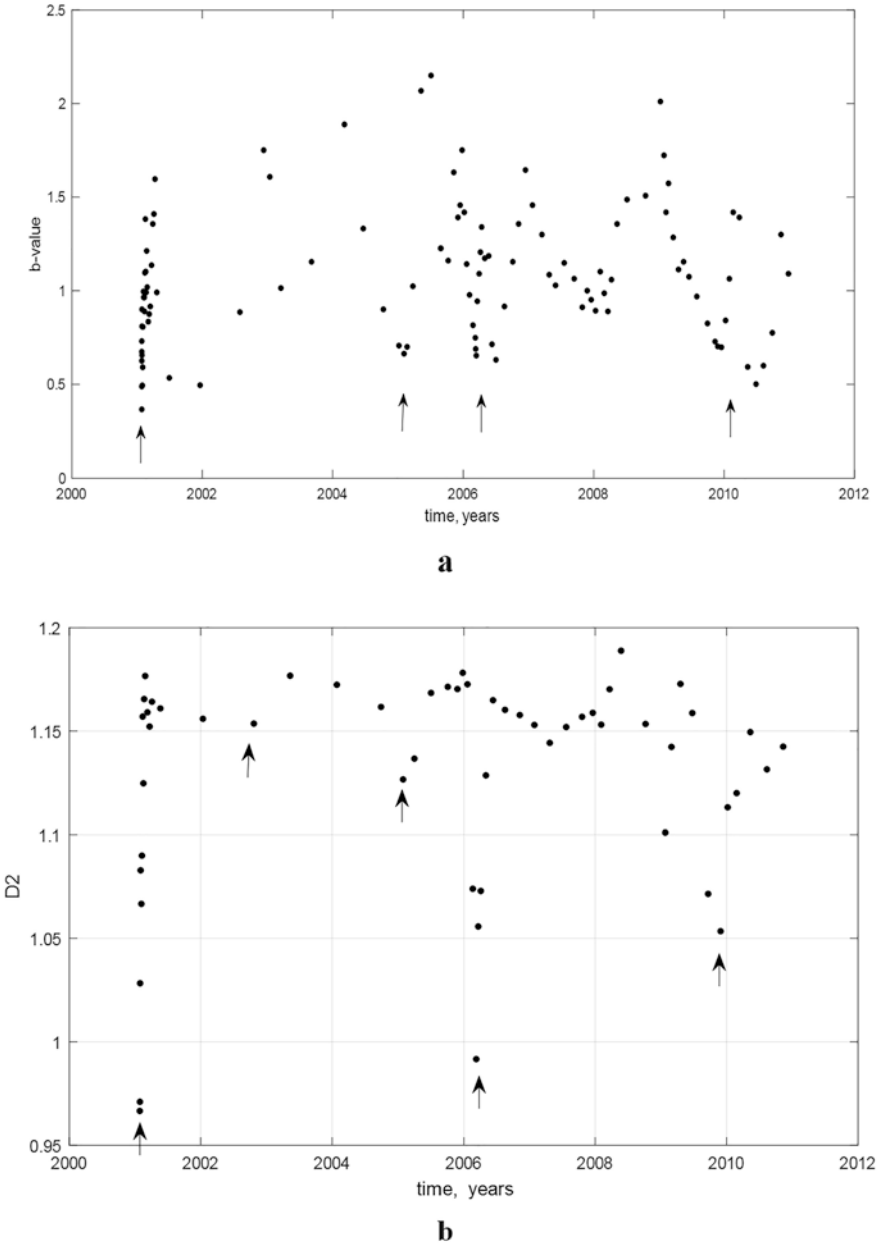


Fig. 5 The change in the current b-values (a) and in correlation dimension D2 values (b) in the Bhuj aftershock sequence. Arrows mark the decreases in b-values and D2 values, coinciding with those presented in Fig. 4

15 km during 2001–2010, which gives a V estimate as 3.5×10^{-5} m/s. From here we have estimated from (3) the permeability value $K = 10^{-13}$ m² using the typical γ , η , and ϕ values from Miller et al. [12]. The obtained permeability K value $K = 10^{-13}$ m² is high. It is in a disagreement with the typical permeability values in Fig. 3 (numbers 1 and 2), but it seems to agree with the permeability values obtained in a number of cases from seismological data sets and from some petrological terrains (Fig. 3d, numbers 3,5 and 6).

The permeability values associated with the short episodes of breakout of the deep fluid towards the Earth's surface appear to be even higher than 10^{-13} m². The change in the mean earthquake depth in these episodes can be crudely estimated as 15 km and it occurs during one month or even faster. Thus, the corresponding V velocities by analogy would be more than one hundred times higher than that associated with the discussed above monotonous change in the mean depth of aftershocks. Thus, the permeability values corresponding with the bursts can be evaluated as 10^{-11} – 10^{-10} m². These estimations are very high but nevertheless they agree with the maximum permeability values from the data collection presented in [7].

A number of bursts in the earthquake number and change in the mean depth values presumably associated with episodes of arising of high permeability values in the Earth's crust were presented above. These examples and those presented earlier in [7] have however are non-regular character and can be treated as rare non-typical cases. The typicality of such cases is convincingly supported below by the results of the examination of changes of a mean earthquake depth in the general vicinity of a major earthquake. The method of examination of the general vicinity of a major earthquake presented and realized in [15, 16, 20] gives a possibility to reveal a typical features of a seismic regime occurring in a vicinity of a major earthquake using data on a numerous (up to one thousand) individual strong earthquakes and their surroundings. The method strongly increases the available statistics summing up the data from vicinities of a large number of individual major earthquakes. This approach was shown to be useful in determination of the typical features in development of precursor and aftershock sequences of major earthquakes [15, 16, 20].

As it can be seen in Fig. 6, earthquakes seem to have a tendency to “float up” within the crust in the close general vicinity of a major earthquake. The solid and dotted lines in Fig. 6a show the tendency of change of the mean depth and its uncertainty as estimated by a bootstrap numerical modeling. The logarithmic time scale is used for the foreshock sequence (Fig. 6b) and for the aftershock sequence (Fig. 6c). The error of mean depth for clusters of subsequent 50 events can be estimated as a few kilometers. Thus, the decrease in the mean earthquake depth exceeding 10 km for the late foreshocks and for early aftershocks is reliable enough. This reliability is supported by closeness of results obtained from GCMT and ISC catalogs examination [15, 16]. In both these cases mean depth decrease appears to start about one hundred days before the main event (Fig. 6b). No distinct changes in the mean depth occur during the first day after the generalized mainshock (Fig. 6c); the compensating increase of the mean depth occurs during a few hundred days after the generalized mainshock.

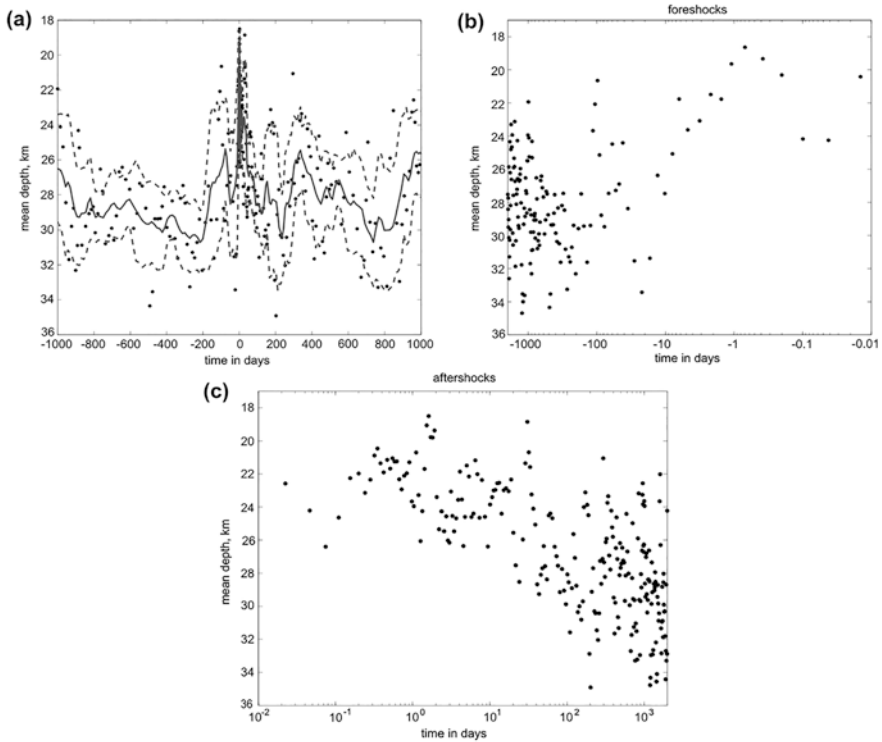


Fig. 6 Change in mean earthquake depth for a groups of 50 consecutive earthquakes at a step of 25 events, linear time scale (a); foreshock (b) and aftershock (c) sequences are given in logarithmic time scale. The tendency of a change in mean depth and of depth scatter obtained by numerical boot-strap method is shown (a), see [20] for the details

The decrease in b-value also takes place in the generalized vicinity of a major earthquake [15, 16, 20]. Thus, the character of anomalies typical of the generalized vicinity of a major earthquake appears to be similar with that found above in the aftershock sequences of a few carefully examined individual strong earthquakes.

The mentioned above features of the typical seismic regime in the vicinity of a generalized strong earthquake were interpreted in Rodkin & Tikhonov [20] as an evidence of the deep fluid involvement in the process of preparation and implementation of a major earthquake. Here we use the same results for an estimation of a temporal increase in permeability K values in the close vicinity of a major earthquake. As one can see, in the foreshock (Fig. 6b) and aftershock (Fig. 6c) sequences the mean depth variation reach 10 km and the duration of the anomaly up to about one hundred days. So, using the same approach as above, the mean permeability values in this temporal-spatial area can be roughly estimated as $K \sim 10^{-12}$ – 10^{-11} m². The maximum permeability value, near the very moment of the generalized major earthquake could be even higher, up to $K \sim 10^{-10}$ m², but it seems hardly possible to verify this high short-time transient permeability value.

We would like to emphasize that the presented estimates are obtained by the examination of the generalized vicinity of a major earthquake, and thus they are typical of a major earthquake occurrence. It should be noted also, that these estimations are in an agreement with that ones obtained above for the short pulses during the Bhuj's aftershock sequence and in a few other cases and with a few maximum permeability estimates of other authors, see data collection presented in [7].

Thus, it can be presumably concluded that the high permeability values do can origin in the Earth's crust rather regularly. These cases occur in connection with the strong earthquake occurrences and maybe in some other special temporal situations. However, the mechanism of origin of such high permeability values, especially in the foreshocks area before the mass mainshock fracturing and microfracturing, remains unclear.

4 Discussion

The data presented above display a possibility of rare but systematically repetitive developments of high permeability values in the middle and the lower crust. In the experiments [26, 31], the high permeability values were found to arise at high temperature and low effective pressure (Fig. 1, and [31]). The case of a high temperature and low pressure can correspond to the situation occurring during dehydration reactions when the effective pressure can be essentially decreased due to the pore pressure increase. However, it has to be emphasized that the extreme experimental values are essentially lesser than those obtained from some petrological data and especially from the earthquakes regime examinations. This difference can be connected with a few reasons.

Firstly, it should be noted, that the experimental results presented above were obtained in "dry" conditions due to the peculiarities of the experimental procedure. The gas permeability values were recalculated to water permeability [25]. The presence of water, which is the surface-active fluid, however can significantly reinforce thermal decompaction of rocks. Besides, a drastic increase of permeability can be caused by a positive feedback between microcracks formation under heating, that will cause the permeability increase and activating of the fluid flow, and in its turn accelerating microcrack initiation as it was supposed in [7]. Our experimental data give definite support to this assumption. The temperature dependences of porosity and permeability for dry amphibolite samples heated in nitrogen (that does not interact with the rock matrix) and saturated by distilled water were examined in [29, 30]. Both these properties - porosity and permeability - increase with heating. However, their values for water-saturated samples are higher than for gas-saturated ones in the entire temperature range (Fig. 7). Moreover, the prolongation of exposure time at higher temperature leads to a further increase of porosity and permeability in the water-saturated samples. This change occurs due to formation of microcracks located, as a rule, on mineral grain boundaries. Besides pore size distribution was shown to shift to the higher values at a water saturated conditions.

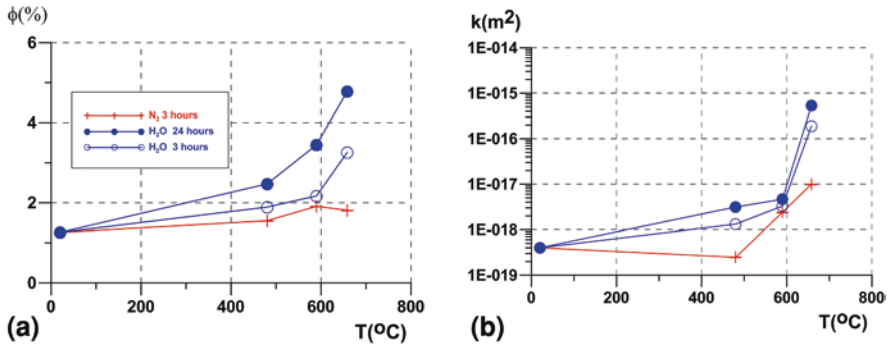


Fig. 7 Dependencies of porosity (a) and permeability (b) of amphibolite samples heated under gas pressure in dry conditions (in nitrogen) and under water pressure $P_{conf} = P_{fl} = 300$ MPa on quenching temperature

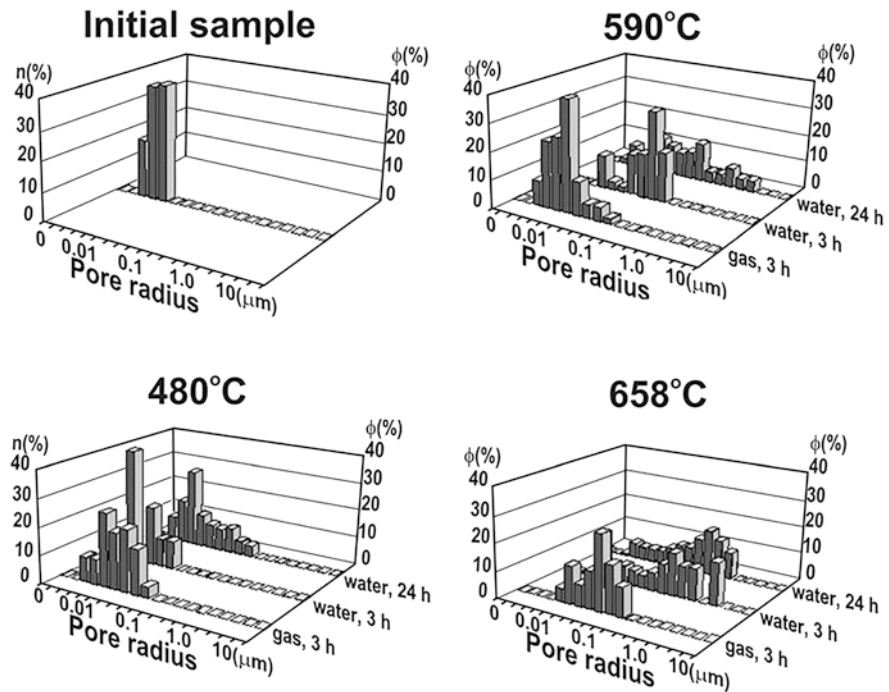


Fig. 8 Pore radius distributions for gas and water saturated amphibolite samples with different exposure time vs temperature

(Fig. 8). These experimental results testifies definitely for the importance of the fluid-rock interaction that can essentially influence the permeability values.

This effect has significance for the radioactive waste disposal and shows that water penetration into the hot rocks of the near field of the heat-generating waste

can lead to a sharp increase in their permeability and, consequently, to an increase in the risk of dangerous radionuclides escape in the biosphere.

Secondly, a scale effect should be taken into account. Correlating laboratory permeability data with *in situ* ones obtained in the shallow boreholes Brace [3] had found that the permeability of rock massif as a whole was usually three decimal orders higher than that measured on the samples taken from the massif [3]. However, it is not clear if this trend remains to be true for the greater depths, because the convincing data on fracture occurrence at great depth are not still available. Besides, it should be noted that similar scale effect was not found in comparison of the experimental and in most part of petrological and *in situ* measurements presented above (Fig. 3).

It should be noted also, that the results of the permeability measurements carried out in the superdeep wells are controversial. According to the results of the *in situ* hydraulic tests carried out in the Russian superdeep well SG-3 at depth of about 6.5 km [9] permeability value was found to be low in an agreement with our laboratory data at appropriate PT - about of $2 \cdot 10^{-19} \text{ m}^2$, see [31] for details. In contrast, the deep fracture zone with permeability as high as 10^{-15} was found in the German superdeep KTB [5]. Moreover, in KTB a hydraulic connection between the deep fracture zone at the depth of about 9.1 km with shallow one was found [5]. These factors are even more unclear for the deeper crust, where in contrast with the near-surface parts where the fractures are uniformly distributed, such aquifers can occur locally and temporally.

Thirdly, strong increases in permeability detected in some petrologic and seismological examinations are expected to have local and transitional character. They can be connected with microfracturing arising in the processes of earthquake preparation and occurrence and with impulses of metamorphic reactions. Note, that the stronger increases in permeability was found (see Figs. 1, 7, and 8) at temperatures 500–600 °C, at the conditions when reaction of dehydration in a number of rocks could occur.

In [8, 14, 24, 27] it was argued that the processes of earthquake preparation and occurrence are connected with metamorphic processes and phase transitions. Thus, it seems fairly plausible that similar drastic increases of permeability can occur in the Earth's crust rarely but systematically, and that these increases are connected with episodes of an increase in rates of metamorphic processes and earthquakes occurrence. Moreover, from the examination of the vicinity of strong earthquake it can be argued that the drastic increase in the permeability seems to be a necessary essential feature of the process of preparation and implementation of a strong earthquake.

It should be noted also, that a few types of characteristic anomalies were revealed presumably to occur in connection with the increase in permeability values. Besides the increase in an earthquake number and decrease in the mean depth of events there are the decreases in b-values and correlation fractal dimension values. These anomalies were found to occur systematically both in the aftershock sequences and in the generalized vicinity of a major earthquake; such anomalies can be expected to occur due to the concentration of aftershocks at the weakened fluid conducting structures of low dimensionality.

5 Conclusions

We had examined and compared a few independent estimates of permeability of the Earth's crust with emphasizing on the laboratory and seismological data. The permeability trends developed with use of laboratory data and calculated from geothermal data, the fluid flow in metamorphic systems and many other estimations obtained from different methods appear to be in a suitable agreement. However, some petrological data and the majority of seismological data testify for the possibility of much higher permeability values. Moreover, from the results of examination of the generalized vicinity of a major earthquake we can conclude that such high permeability values are typical of rare transitive but systematically repeated situations in the Earth's crust connected with the major earthquake occurrence.

Thus, the high permeability values appear to occur in non-equilibrium conditions, they are temporary and occur in transient situations.

We had found also a few characteristic anomalies in the seismic regime that appear accompany typically the epochs of increase in the permeability values. There are an increase in the number of weak earthquakes, and decrease in the mean depth of the events, and the decrease in the b-values and the fractal dimension values. Such anomalies are expected from the physical point of view to occur when the permeability increases due to the concentration of aftershocks at the weakened fluid conducting structures of low dimensionality.

However, the mechanism of increase of permeability of mid-crust is unclear. Moreover, we suggest that some episodes of the crust permeability increase could be related to the positive feedbacks between microcrack initiation due to rock metamorphic transformations, resulting in increase of permeability and active deep fluid infiltration, which in its turn accelerates the rate of metamorphic transformations. The experimental data presented above prove this suggestion.

We believe that the mentioned findings could answer the paradox from E. Roedder [21] cited above in the Introduction. These findings testify also in support of the close connection between a temporal drastic increase in permeability value and the earthquakes occurrences.

Acknowledgements The work was carried out within the framework of the IGEM RAS, IEPT RAS (taskno.AAAA-A19-119011490129-0) and ORGIRAS (taskno.AAAA-A19-119013190038-2, Section IX: "Earth Sciences". PFNI no. 132.) research plans, within the framework of the IGEM RAS project "Fundamental problems of the development of the mineral resource base of the high-tech industry and energy in Russia" and with the financial support of the RFBR (grant no.19-05-00466).

References

1. Abdul Azeez KK, Mohan K, Veeraswamy K, Rastogi BK, Gupta AK (2018) 3D crustal resistivity structure beneath the Wagad aftershock zone of the 2001 Bhuj earthquake, Kutch, India: heterogeneous resistivity structure controlled by widespread fluid infiltration and clues to aftershocks pattern. *Tectonophysics* 747–748:54–67

2. Bernabe Y (1987) The effective pressure law for permeability during pore pressure and confining pressure cycling of several crystalline rocks. *J Geophys Res* 92:649–657
3. Brace WF (1980) Permeability of crystalline and argillaceous rocks. *Int J Rock Mech Min Sci Geomech Abstr* 17:241–251
4. Christensen NI, Mooney WD (1995) Seismic velocity structure and composition of the continental crust: a global view. *J Geophys Res* 100:9761–9788
5. Huenges E, Erzinger J, Kuck J, Engeser B, Kessels W (1997) The permeable crust: Geohydraulic properties down to 9101 m depth. *J Geophys Res* 102:18255–18265
6. Ingebritsen SE, Manning CE (1999) Geological implications of a permeability-depth curve for the continental crust. *Geology* 27(1):107–110
7. Ingebritsen SE, Manning CE (2010) Permeability of the continental crust: dynamic variations inferred from seismicity and metamorphism. *Geofluids* 10:193–205
8. Kalinin VA, Tomashevskaja IS, Rodkin MV (1989) The effect of solid phase transformations on the deformation-strength properties of material and their part in seismotectonic processes in: high pressure investigations in geosciences. *Academie-Verlag, Berlin*, pp 205–212
9. Kozlovsky YA (ed) (1987) The superdeep well of the Kola peninsula. Springer, Berlin, 558 p
10. Kuang X, Jiao JJ (2014) An integrated permeability-depth model for Earth's crust. *Geophys Res Lett* 41:7539–7545. <https://doi.org/10.1002/2014GL061999>
11. Malkovsky V, Zharikov A, Shmonov V (2013) Use of argon for measurement of rock permeability. In: Sismanoglu BN, Maciel HS, Radmilovic-Radjenovic RS (eds) *Argon: production, characteristics and applications*. Pessoa Nova Science Publishers, New York, pp 17–36
12. Miller SA, Collettini C, Chiaraluce L, Cocco M, Barchi M, Kaus BJP (2004) Aftershocks driven by a high-pressure CO₂ source at depth. *Nature* 427:724–727
13. Mishra OP, Zhao D (2003) Crack density, saturation rate and porosity at the 2001 Bhuj, India, earthquake hypocenter: a fluid-driven earthquake? *Earth Planet Sci Lett* 212:393–405
14. Rodkin MV (1995) Crustal earthquakes induced by solid-state transformations: a model and characteristic precursors. *J Earthq Predict Res* 4(2):215–223
15. Rodkin MV (2008) Seismicity in the generalized vicinity of large earthquakes. *J Volcanol Seismol* 2:435–445
16. Rodkin MV (2012) Patterns of seismicity found in the generalized vicinity of a strong earthquake: agreement with common scenarios of instability development. In: Sharma AS et al (eds) *Extreme events and natural hazards: the complexity perspective*. Geophys. Monogr. Ser, vol 196. AGU, Washington, DC, pp 27–39. <https://doi.org/10.1029/2011GM001060>.
17. Rodkin MV, Tikhonov IN (2011) Megaequake of march 11, 2011, in Japan: the event magnitude and the character of the aftershock sequence. *Izv Atmos Ocean Phys* 46(8):941–950
18. Rodkin MV, Mandal P (2012) A possible physical mechanism for the unusually long sequence of seismic activity following the 2001 Bhuj Mw7.7 earthquake, Gujarat, India. *Tectonophysics* 536–537:101–109
19. Rodkin MV, Tikhonov IN (2014) Seismic regime in the vicinity of the 2011 Tohoku mega earthquake (Japan, M w = 9). *Pure Appl Geophys* 171(12):3241–3255
20. Rodkin MV, Tikhonov IN (2016) The typical seismic behavior in the vicinity of a large earthquake. *Phys Chem Earth* 95:73–84
21. Roedder E (1984) Fluid inclusions. *Rev Mineral* 12:338–358
22. Rojstaczer SA, Ingebritsen SE, Hayba DO (2008) Permeability of continental crust influenced by internal and external forcing. *Geofluids* 8:128–139
23. Saar MO, Manga M (2004) Depth dependence of permeability in the Oregon cascades inferred from hydrogeologic, thermal, seismic, and magmatic modeling constraints. *J Geophys Res* 109. <https://doi.org/10.1029/2003JB002855>
24. Sammis CG, Dein JL (1974) On the possibility of transformational superplasticity in the Earth's mantle. *J Geophys Res* 79:2961–2965
25. Shmonov VM, Votovtova VM, Zharikov AV (2002) Fluid permeability of rock of the Earth's crust. *Nauchnyi Mir, Moscow*, 232 p. (In Russian)

26. Shmonov VM, Vitovtova VM, Zharikov AV, Grafchikov AA (2003) Permeability of the continental crust: implications of experimental data. *J Geochem Explor* 78–79:697–699
27. Sornette D (1999) Earthquakes: from chemical alteration to mechanical rupture. *Phys Rep Rev Sect Phys Lett* 313:238–291
28. Vanyan LL, Berdichevski MN, Kuznetsov VA, Palshin NA, Kong XR, Yan Y, Zhao G (2001) Electromagnetic constraints on the East Tien Shan crust: analysis of the TM mode. *Izv Phys Solid Earth* 37(3):234–243
29. Zharikov AV, Pek AA, Lebedev EB, Dorfman AM, Zebrin SR (1993) The effect of water fluid at temperature up to 850 °C and pressure of 300 MPa on porosity and permeability of amphibolite. *Phys Earth Planet Inter* 76(3/4):219–227
30. Zharikov AV, Lebedev EB, Dorfman AM, Vitovtova VM (2000) Effect of saturating fluid composition on the rock microstructure, porosity, permeability and V_p under high pressure and temperature. *Phys Chem Earth* 25(2):215–218
31. Zharikov AV, Vitovtova VM, Shmonov VM, Grafchikov AA (2003) Permeability of the rocks from the Kola superdeep borehole at high temperature and pressure: implication to fluid dynamics in the continental crust. *Tectonophysics* 370(1–4):177–191

Endogenous and Exogenous Manifestations of Geodynamic Activity in the Central Caucasus



V. B. Zaalishvili, Kh. O. Chotchaev, M. G. Berger, O. G. Burdzieva,
B. V. Dzeranov, D. A. Melkov, A. S. Kanukov, V. B. Svalova,
and A. V. Nikolaev

1 Introduction

The Greater Caucasus, as a young geosynclinal structure of the Alpine orogenesis, continues the collision stage of its development in the contact zone of the Southern microplate from the south and the Scythian plate from the north. The geodynamic environment is characterized by intense destruction due to the uplift and uneven intracrustal movement of the separate individual blocks with a general drift of the entire mountain structure to the northeast under the influence of the continued advance of the Arabian Plate into the depths of the Eurasian continent. The Mamison-Kazbek relic scar is a geosuture, 550 km long from east to west with the typical tectonized terrigenous material containing different sized chunks and blocks of volcanogenic-sedimentary rocks and remobilized olistostromes of the ophiolite complex; it is also a zone of active endogenous and exogenous geodynamics.

The geosuture is controlled from the north by the Main thrust, alternating to the east by the Tsey and the Syrhubarzond thrusts of the northern fall and by Adaykom – Kazbek fault (passing along the ridge part of the Dzhimarai-Kazbek knot) from the south. The Syrhubarzond fault cuts in half the bed of the pulsating Kolkaglacier periodically discharged under the influence of a complex of geodynamic factors of an endogenous and exogenous nature.

V. B. Zaalishvili (✉) · K. O. Chotchaev · M. G. Berger · O. G. Burdzieva · B. V. Dzeranov
D. A. Melkov · A. S. Kanukov
Geophysical Institute – the Affiliate of Vladikavkaz Scientific Centre of the Russian Academy
of Sciences (GFI VSC RAS), Vladikavkaz, Russia

V. B. Svalova · A. V. Nikolaev
Sergeev Institute of Environmental Geoscience of the Russian Academy of Sciences (IEG
RAS), Moscow, Russia

According to the historical data of the catastrophic collapses of the Kolka and the Devdorak glaciers (since 1752–1776 respectively) five cases of multi-scale surges were recorded, the nature of which was considered to be glaciodynamic on the basis of the impact on the main glacier of ice masses breaking from above and a sharp change in its mass balance. Detailed analysis of the preparation process, the behaviour of catastrophic surges and continuing post-catastrophic phenomena at the site of the former glacier (fumaroles, “sand cone”, gas release) suggests that glaciodynamics itself, due to changes in mass balance or mechanical effects of breaking ice masses under the conditions of the glaciers of the Kazbek volcanic center, does not define critical conditions for a catastrophic glacier surge. Such situations can occur under certain geodynamic conditions, including seismic, tectonic and geothermal (due to postvolcanic processes or magmatic intrusions) factors [1, 2].

The presence of a tectonic factor for the considered territory of the eastern segment of the Central Caucasus (the region of the Republic of North Ossetia-Alania) is fundamental for the structural-tectonic zoning and separation of structural-material complexes. The intersections of sublatitudinal and submeridional tectonic violations of different ranks form the block structure of the mountainous part of the territory under consideration, isolated as structural-material complexes, characterized in some cases by hereditary features of isolated geodynamic environments. Endogenous activity under the conditions of intense tectonic fragmentation is determined by deep faults that pass into the upper mantle and serve as a transit of the crust and mantle magma. The intersections of such faults are dangerous primarily as zones of possible earthquake sources (PES). Such zones can also take place at the intersections of interblock faults of the first and second orders that have a continuation in the shell and the lower crust.

A seismic factor of endogenous nature, in addition to manifestation in the PES zones, may occur due to the magmatic intrusions of a discontinuous nature, interblock tectonic movements (intraplate tectonics), tectonics of lithosphere plates and deformation waves of discharging stresses. Seismicity can be induced due to the hydraulic structures (a load of reservoirs in seismically active zones), developed mining industry (intensive oil production, mine workings without filling, shale hydrocarbon production). The seismic factor may also occur from an exogenous source such as a rock slide, anthropogenic explosion or an industrial accident. The characterized segment of the Central Caucasus is a potential territory for the manifestation of most of the mentioned diversity of seismic factor occurrence.

The endogenous nature of the geothermal component of geodynamic activity in the territory manifests itself in the form of intrusions of crustal magma and the introduction of the mantle substrate, the indirect evidence of which are deep geophysical sections on the parameters of the earthquake converted-wave (ECWM) and specific electrical resistances obtained by the telluric current method (TCM), the confinement of thermal waters to the certain deep sections, data of bored wells for hydrogeological purposes, documented neo-intrusions with high petrothermal potentials (by the example of partially eroded Eldzhurt granitoid, where the geothermal gradient is almost two times higher than normal).

The assessment of the volcanic and postvolcanic activity of the Kazbek volcanic center in general and the Kazbek volcano, in particular, is extremely important for the development of the mountain areas for recreational purposes.

The data of the geophysical complex of aeromagnetic survey, ECWM, TCM, areal gravimagnetic survey suggest that the local minimum of the field of gravity over the Elbrus volcano corresponds to a roughly spherical object of a roughly spherical shape (diameter 10–15 km) with an extremely low density of $2.1 \cdot 10^3 \text{ kg/m}^3$, lying on the depth of the first kilometers. Local anomalies of lesser intensity are noted east of the Elbrus in the area of young volcanism development of the Chegem upland and the Eldzhurt granitoid in the valley of the river Baksan (density of the last $2.57 \cdot 10^3 \text{ kg/m}^3$). According to the magnetotelluric sounding along the Elbrus profile [3], the local anomaly of electrical conductivity at the depths of the “basalt” layer is associated with the site of rocks melting, which is a magmatic source of the Elbrus volcano. A local minimum of electrical resistance above it near the surface may correspond to the volcanic magma chamber. Their shape and approximate dimensions are underlined by the boundaries of the PS-waves exchange over the ECWM at depths of 3–5 km and 12–15 km. In the density section at depths up to 40 km, the concentration of the singular points of the gravity anomalies, outlined above by an aureole of the singular points of the magnetic anomalies, corresponds to the volcano.

Relatively positive values of the gravitational field of the Kazbek region, as the calculations show, are determined by the surface layer with an excess density of $0.15 \cdot 10^3 \text{ kg/m}^3$, the upper and lower boundaries of which are at the depths of about 0.5 and 4.5 km. This layer can be represented by a layer of deep-water Lower Jurassic sediments with products of basic magmatism (dikes, intrusions, sills of the Kazbek diabase belt) located on the crystalline basement. The Tepli and the Kazbek volcanoes are not accompanied by local gravitational anomalies. So, there are no grounds to assume here, by analogy with the Elbrus volcano, the presence of any “focal” objects, which, as a rule, are not compacted according to gravimetric data. The electrical survey also revealed no low-resistivity zones or areas of the earth’s crust, which could be identified with modern supply channels, foci or chambers of volcanic edifice, which is observed, for example, at the Elbrus volcano [4].

The last isotope-geochemical definitions [5] call into question even the very existence of an intermediate magmatic chamber in the given area, which is in complete agreement with geophysical data [6].

The absence of signs of a sleeping volcano in the stratovolcano Kazbek does not mean its postvolcanic passivity [7–12]. Its recent (according to geologic terms) eruption (6 thousand years ago according to radiocarbon analysis and confirmed by the tephrochronology [13], the data is listed in the Smithsonian Institution catalog) means a high temperature regime (800–900 °C), which is practically the upper temperature of the crystallization of basic composition magmas. Postvolcanic manifestations are the hot springs of the Karmadon group, both flowing and opened by wells at depths of 400–500 m, typically confined to the tectonic disturbances on the northern slopes of the Kazbek volcano, as well as occasional fumaroles and gas emissions during catastrophic surges of the glaciers of the Kazbek glaciers groups.

The impact of postvolcanic phenomena took place in the catastrophic collapse of the Kolka glacier on September 20, 2002, and as it is now becoming obvious, its periodic disastrous surges are a consequence of the manifestation of a complex of geodynamic factors [14–23], including the gas-hydrodynamic effect on the glacier of postvolcanic gases. Gas release up to concentrations of a gas cloud during the catastrophic collapse of the Devdorak glacier on May 17, 2014 [24] is also a manifestation of postvolcanic influence and the main cause of the sudden collapse of the glacier part sliding down from the rock bar.

Geodynamic impact of an endogenous nature (tectonic rupture with certain kinematics, focal or tectonic type earthquake, volcanic (postvolcanic) or magmatic nature, etc.) can provoke activation of exogenous processes (mudflows, landfalls, landslides, avalanches and collapses of glaciers, etc.) [15, 20, 23–37].

The exogenous geodynamic activity is partly determined by the degree of environmental impact of endogenous processes but depends largely on the landscape and climatic features and the degree of man-made interference.

Exogenous impacts are mainly observed in high mountainous areas, where orographic and climatic features are most pronounced; the interaction of factors manifests intensively; the number of interacting factors increases in proportion to the degree of intensification of the negative effects of exogenous nature on the environment.

2 Tectonic Features of Endogenous Geodynamic Activity

Before the collision of the main continents, the major tectonic events in the Caucasus region occurred due to the accretionary tectonics, i.e. due to the entry of allochthonous blocks of the earth's crust into the subduction zone of the active margin of Eurasia [38]. The differences in the geological structure of the structural-tectonic blocks determined to a certain extent the complexity of the tectonics of the Caucasian orogen, in the central part of which the fragments of the Pre-Caucasian, Bechasyansk and East-Caucasian microplates, attached to the East European Plate at the end of Paleozoic, are singled out [39–41].

The following structural and tectonic formations are distinguished within the territory of North Ossetia from north to south (Fig. 1):

Microplates – terrains: Pre-Caucasus, Bechasyansk, East Caucasian, Transcaucasian; Structural-tectonic zones: Mamison-Kazbek (relic zone), Vladikavkaz Basin, Northern monocline; the zone of the Glavnyi Range (Maker and Kassar subzones), Digor-Osetinsk, Ardon-Darial; the zone of the Southern slope, Chiaur.

The structural-material complexes of microplate-terrains, separated on the basis of block localization, form a system of uplifts and graben-synclines, delimited by tectonic discontinuities of various orders and activities.

Potentially active tectonic disturbances of the territory are shown in Fig. 2, and their geological interpretation is given in the regional section of the northeast strike

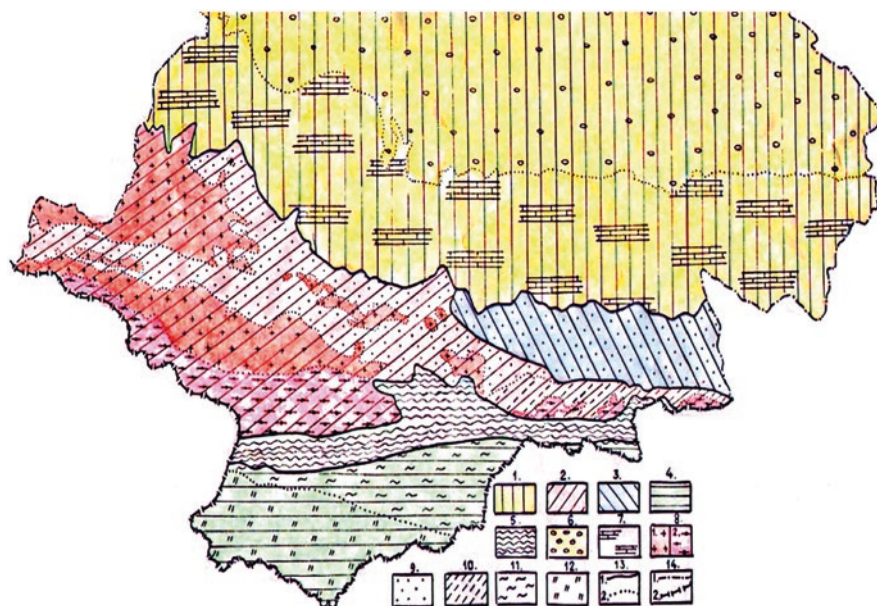


Fig. 1 The relationship of microplates and structural-tectonic zones of the Central part of the Greater Caucasus on the territory of North Ossetia Legend: Microplates – terrains: 1. Pre-Caucasus; 2. Bechasynsk; 3. East Caucasian; 4. Transcaucasian. Structural-tectonic zones: 5. Mamison-Kazbek (relic zone); 6. Vladikavkaz Basin; 7. Northern monocline; 8. Glavnyi Range (1-Makher and 2- Kassar subzones); 9. Digor-Osetinsk; 10. Ardon-Darial; 11. Southern slope; 12. Chiaur; 13. Contacts: (1-microplate – terrains, 2 – structural-tectonic zones); 14. Borders: (1- republics, 2-state)

in Fig. 3. The problem of localization of earthquake foci in some of them requires instrumental observations, but the presence of the PES active zone at the intersection of the Vladikavkaz and the Ardon deep faults is quite evident according to the current density of earthquakes in their intersection zone, which allows classifying events by an active geodynamic period. The frequent seismic events, starting from 2015, are not decreasing, but on the contrary, their number increases, covering the manifestation area across the entire width of the Vladikavkaz fault from Ingushetia to Kabardino-Balkaria, noticeably concentrating in the Ossetian sector of the fault. Three earthquakes during the day were noted near Alagir in 2015; seismic events in this territory were also recorded in 2016. On May 25, 2017, a seismic event with a magnitude of about 3.0 was recorded near Alagir. Two events were registered on October 18, 2018, at the distances of 58 and 36 km from Vladikavkaz. Then, on December 8, 2018, a seismic event with a magnitude of 3.3 occurred between Alagir and Ardon. Seismic events of April 12, 2018, and April 26, 2018, were also noted near Alagir. Two events with magnitudes 3.5 and 3.7 occurred on February 16, 2019, and two events with $M = 3.4$ on February 21, 2019. The majority of all these seismic events are united by the sublatitudinal band of their confinement, which coincides with the spatial position of the Vladikavkaz fault; it is sound evidence of

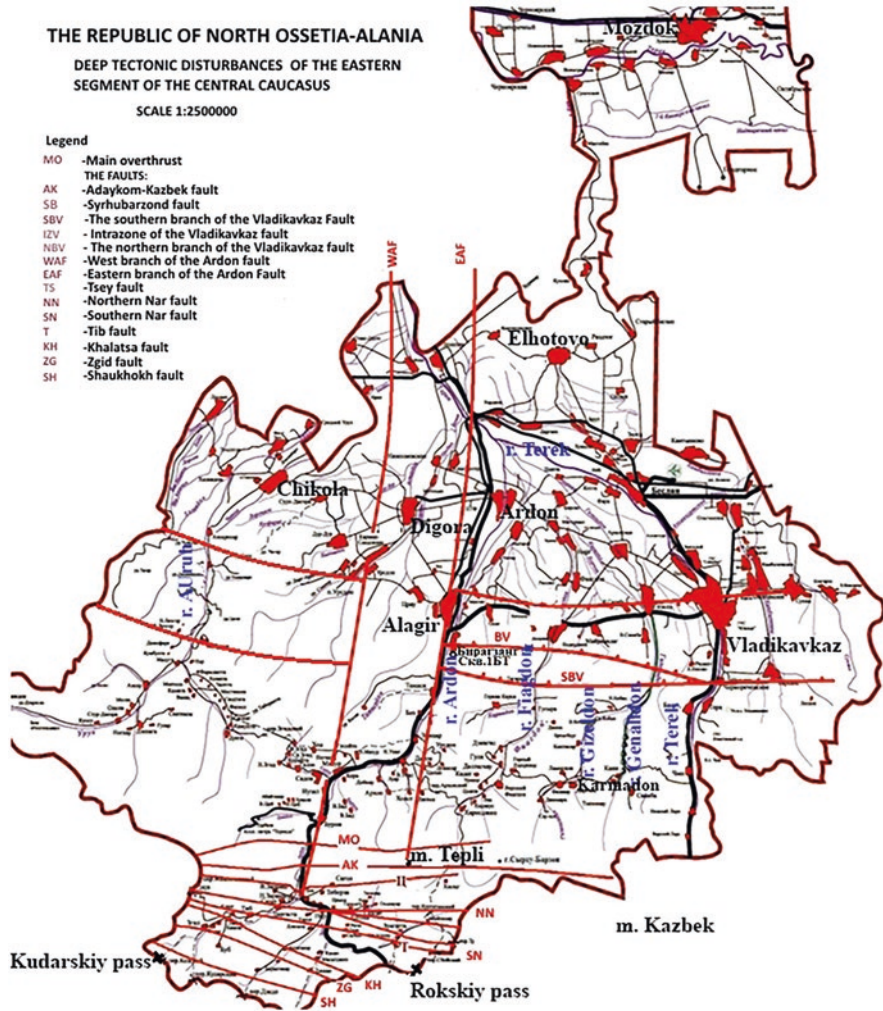


Fig. 2 Deep tectonic disturbances of the eastern segment of the Central Caucasus

the seismic activity of this territory caused, first of all, by the activity of the Vladikavkaz fault.

The territory where the epicenters of the above-mentioned earthquakes are concentrated is the intersection zone of the Vladikavkaz fault and the Ardon deep fault, which is an active interregional tectonic structure.

The Vladikavkaz fault delimitates from the south the Ossetian Basin of the Terek-Caspian foredeep, and the folded-block structure of the Central Caucasus from the north. In the field of horizontal gradients of gravity, the border between the Greater Caucasus and the Ossetian Basin is characterized by an anomalous regional

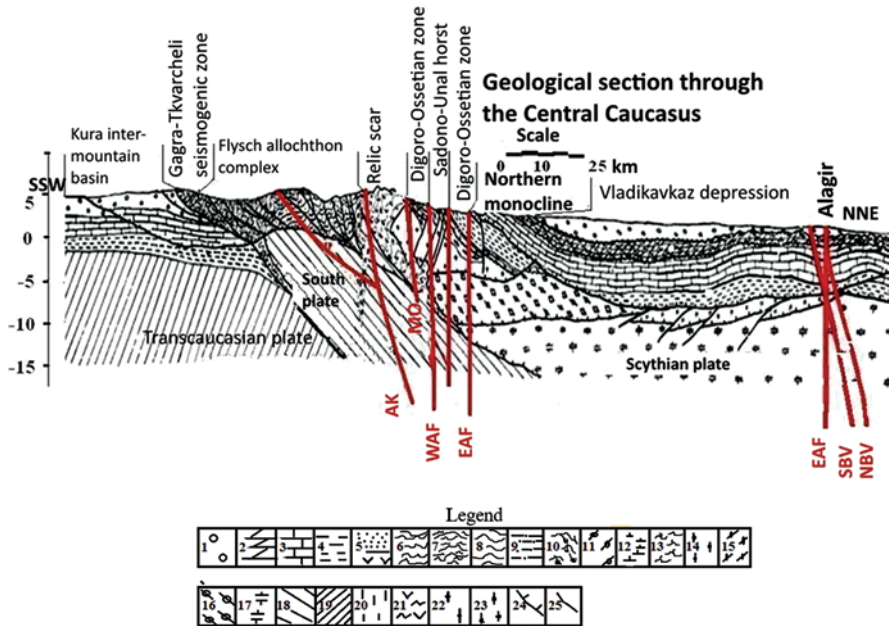


Fig. 3 The cross section of the Greater Caucasus Meganticlinorium along the conventional meridian of the river Ardon

Autochthon and para-autochthon complexes: 1- molasse formations ($N_1^3sm_3-Q$), 2- Oligocene-Miocene terrigenous-carbonate formation ($P_{g3}-N_1^3sr_2$), 3- limestone and sandy-clay-carbonate formation (J_3-Pg_2), 4- Lower-Middle Jurassic formation of shale (J_{1-2}), 5- Lower-Middle Lias marine terrigenous and andesidacite volcanogenic formation (J_{1-2})

Allochthonous complexes: 6- Malm-Eocene carbonate flysch formation (J_3-Pg_2), 7- Lower-Middle Jurassic sand-clay flyshidous formation (J_{1-2}), 8- Lower-Middle-Jurassic formation of shale (J_{1-2}), 9- Lower-Middle-Lias formation of metasandstones, quartzites, knotty and slate shales (J_{1-2}), 10- Triassic-Lias volcanogenic-sedimentary and ophiolitic formations and mixstites of the relic scar ($T?-J_1$)

Foundation complexes Scythian Plate: 11- Late Paleozoic-Triassic autochthonous and para-autochthonous complex (PZ_3-T), 12- Late-Proterozoic-Early-Paleozoic salic metamorphic formation ($smPR_2-PZ_1$), 13- the rocks of Maker and Atsgarinsk sheets (PR_2), 14- the rocks of Kyzylkolsk and Tokhanskysheets (PR_2), 15- Late-Proterozoic femic metamorphic formation (PR_2). 16- the rocks of Armovskiy and Shaukolsheets (PR_2), 17- undifferentiated substrate

Transcaucasian Plate: 18- South Microplate substrate, 19- Nakhchivan Terrain substrate

Other signs: 20- Pliocene diorite formation (dn_2), 21- Middle-Jurassic volcanic basalt, andesite formation (baJ_2), 22- Middle-Late Paleozoic granite and migmatite-granite formation (γPZ_{2-3}), 23- Middle-Paleozoic granite-gneiss formation ($ghPZ_2$), 24- main tectonic boundaries; 25- other faults

gravity step. The structure crosses the territory of the Republic of North Ossetia-Alania from west to east with a latitude of about 43° , continuing to the west in Kabardino-Balkaria and to the east in Ingushetia and the Chechen Republic [42].

The seismic character of the activation of the Vladikavkaz fault zone in the past is confirmed by displacement discontinuity of recent sediments, as well as colluvial

wedges and buried layers of fossil soils in lowered fracture wings, studied in specially driven mine workings. The amplitude of the one-act (probably, seismotectonic) vertical displacement along the northern branch of the Vladikavkaz fault zone reaches 40 cm. In the middle and southern branches, such displacements also do not exceed 40 cm. Using well-known statistical relationships between earthquake magnitude and the sizes of seismic dislocation zones, as well as a relationship between amplitudes of seismotectonic displacements and their kinematics [43], it can be assumed that the magnitude of seismic events caused the above-mentioned paleoseismic dislocation was 6.5–6.7 points.

The features of the deep structure of the Vladikavkaz fault [44, 45] are clearly noted on the sections of low-frequency microseismic sounding (MSS), instrumentally carried out along two submeridional profiles (Fig. 4) through Vladikavkaz and Alagir; the sections were constructed along two profiles, one of which passed through Vladikavkaz and continued further to the south along the Georgian Military Highway. The second profile passed along the Transcaucasian highway, crossing Alagir. The station interval was 420–450 m [46–49].

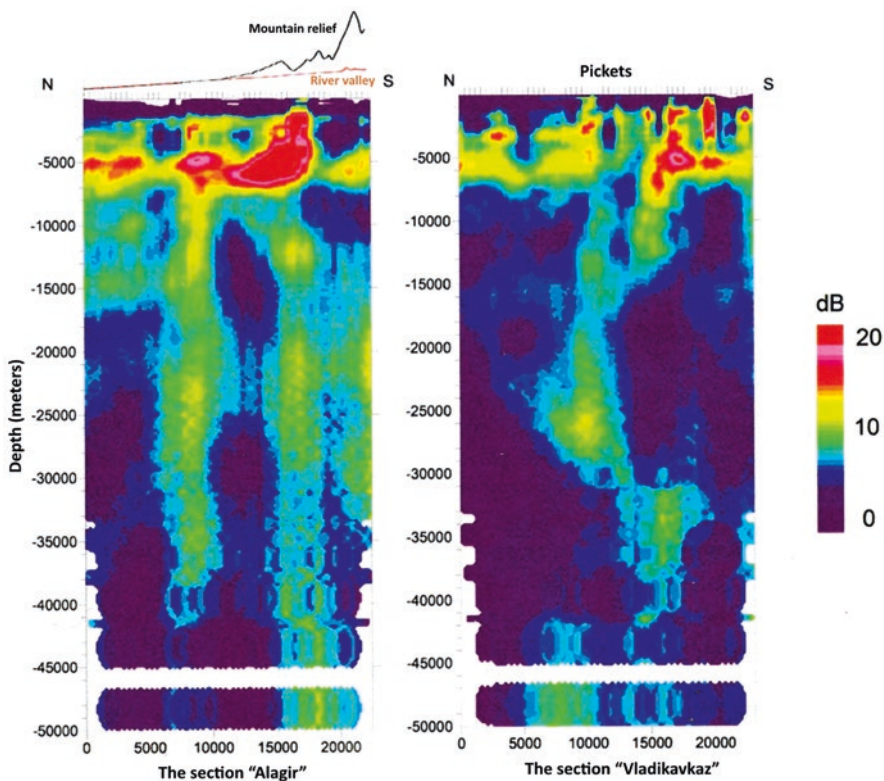


Fig. 4 Velocity model of the geological section in the interpretation of the method of microseismic sounding (MSS)

The sections were built in the parameters of the relative velocities of Rayleigh waves. The base station for both profiles was located in Vladikavkaz. The zones of high contrasts of velocities are zones of reduced strength of the medium. Subvertical zones of high contrasts of velocities are distinguished on both profiles within the boundaries of the Vladikavkaz fault. These zones are traced to the bottom of the earth's crust and below and go into the mantle. The subhorizontal inhomogeneities of microseismic sections sharply break and cannot be traced in the opposite blocks of the crustal section. At a depth of 7–8 km, several contrast zones are distinguished in the sections: two on the Alagir profile and three on the Vladikavkaz profile. These zones at a depth of 15 km are united into a single zone on the Vladikavkaz profile. And on the Alagir profile, these zones of high contrasts of velocities are traced scattered to the bottom of the earth's crust. The zone of the Vladikavkaz Fault is the most contrast in the area of Alagir. In terms of seismic events, the western flank of the Vladikavkaz fault, covering the territory of Alagir, is also the most active.

The Ardon fault controls the most part of the Ardon riverbed in Ossetia [50]; it has submeridional orientation and the length (instrumentally traceable, as well as controlled with the help of aerial and satellite images) of not less than 240 km, having a continuation in the Pre-Caucasian region.

The gravity step is interpreted [51] as the anomalous effect of the Ardon deep fault, by which the sialic (from the west) and femic (from the east) formations of the crystalline base are brought into contact. The strike azimuth of the zone is 30–40°.

A number of signs of the Ardon inter-block deep fault are given below:

Material signs (formational composition, intrusive, effusive, metamorphic rocks, etc.); the Paleozoic basement crops out to the west in the zone of the Glavnyi Range and to the east the Liasstrata is observed; the presence of granitoid neo-intrusions of the mountain Tepli; the confinement of the Sadon ore region (the main polymetallic deposits of the Mountainous Ossetia, i.e. Sadon, Zgid, Arkhon, Kholstinsk, Dzhimidon and others, are concentrated in the fault zone (Olkhovskiy G.P., Tibilov S.M. 1998); a province of hydrochloric-alkaline waters of deep-seated origin is located in the upstream of the river Ardon near the village of Zaramag; there are hydrosulfuric springs near the Tamisk settlement. The deep fault, passing the Tamisk resort area, can be interpreted as a PES zone. The relevant evidence base is considered below.

- The fact that after the earthquake of 1922, almost all deep hydrosulfuric springs previously recorded on the left bank of the river Ardon moved to its right bank serve as proof.
- Structural signs (folding, faults, stratification of rocks, distribution of intrusions, etc.); the transition from the monocline of the Central Caucasus to the folded zone of the Eastern Caucasus; wide tectonic crushing zones (limestone of the massif of the Kariu-Khokh mountain) in some places of the Scalisty Range; the same crushing zone near the Tamisk settlement; Sadon fault zone along the river Ardon, and to the north the foundation of the Terek-Sunzha anticlinorium, down going to the east from the fault, and blocks of the Prikumsk system of elevations in the Pre-Caucasus, gradually downgoing to the east.

- Geomorphological signs (ruggedness of the relief, the presence of depressions, etc.); the river Ardon with tributaries “notches” the Main Caucasian ridge; the valley of the river Ardon has knee-shaped bends, the beds of which are shifted three times to the east along the fracture system. Due to the open fractures, narrow plates are observed on the slopes of the massifs of the Adai-khokh and Tsmiakom-khokh [52].
- Geophysical signs (gravity steps, local anomalies, changes in the nature of the fields, etc.). Conjugation of gravitational anomalies of a different sign over the structure of the Glavnyi Range (a large minimum of the Elbrus block and the maximum of the Kazbek block); a similar situation of less intense anomalies in the foothill part of the territory is observed. To estimate the depth differentiability of the Ossetian Basin section, gravimetry data are used, which are reduced for three different densities of the intermediate layer: 2.0 g/cm³, 2.3 g/cm³ and 2.67 g/cm³.
- The density value of 2.67 g/cm³ for the intermediate layer makes it possible to estimate the influence of heterogeneities of the consolidated crust and to classify the Ardon fault as a deep one, which can be traced up to the depths of 40 km.
- The Ardon fault in the Terek-Sunzha depression is clearly distinguished in aerial and satellite images due to the behavior of the terraces; it crosses the western margin of the Sunzhenskaya and Terek anticlinal zones. The fault is identified by geophysical methods starting from a depth of 2–4 km and is confidently traced as the boundary of variously oriented deep structures. In the fault zone in the Pliocene-Anthropogene deposits, magmatic blocks with traces of brecciation and cataclasis (remnant) are observed, what is the evidence of its activity.
- The Ardon fault in the zones of intersection with faults of the Caucasian direction controls the magmatic activity from the Paleozoic to the Paleogene; hydrothermal mineralization, activation of hydrothermal processes and seismic hazard are associated with intersection zones. At the intersection of the Sunzha and Terek anticlinal zones with the Ardon fault, uplifts with the highest amplitudes and elevated headwaters of Mesozoic-Cenozoic age (Zamankul and Malgobek stress concentration centers) are observed.
- In the zone of the Ardon fault influence, the Tsey and Songuidon intrusive massifs, break fractures of the north-east orientation are located, in which the ore bodies of the Zgid and Sadonpolymetallic deposits are concentrated.
- The Ardon fault, being a regional submeridional fault that intersects tectonic zones of the Caucasian orientation, was seismically active in the past (the Late Jurassic and Late Cretaceous epochs) and continues to be active up to the present (it has numerous mineral springs associated with it) because it controls the PES zones, which in turn pose seismic hazard.
- In the rocks of the Terek-Caspian foredeep, the Ardon fault is reflected in abrupt changes in the thickness and facies of certain stratigraphic units of the sedimentary cover [53, 54].
- A blunt closing of positive and negative anomalies is observed in a magnetic field. According to the earthquake converted-wave method (ECWM) along the Yeisk – Caspian Sea profile between Budennovsk and Neftekumsk (on the

extension of the Ardon fault) in the area of the increased wave absorption, the displacement of the boundaries between the geological blocks in the earth's crust and in the mantle is recorded, which indicates a depth of the structure. According to the data of the method of magnetotelluric sounding (MMS), the Ardon fault zone is recorded on the same profile by a step-like type of electric fields and a sharp change in their characteristics. The place of the supposed intersection of the deep fault by the above-mentioned profile is located 250 km north of the village of Zaramag.

- The Ardon fault in the mountainous part of the Caucasus appears as the active (in tectonic-dynamical and magmatic respect) zone of conjugation of the Central and Eastern parts [55, 56].

Some authors believe that the Ardon deep fault is a component of the Kabardino-Sarpinsky submeridional suture zone and belongs to the ancient tectonic structures of the Paleozoic – Hercynian orogenic cycle and has a long development and deep embedding. According to the data of geological and geophysical studies, the Ardon deep fault zone, as a single structural zone, is traced from the neo-intrusive massif of the mountain Tepli, continues in the lower reaches of the river Ardon and further lies in the direction of Budennovsk through Elkhotovo.

The Ardon fault with a width of the zone of about 10 km consists of at least two branches; the Vladikavkaz fault zone has a width of about 5 km and has three branches. Since the active regional Vladikavkaz (sublatitudinal) and Ardon (submeridional) faults dissect the studied territory into equal segments, the degree of their geodynamic activity in seismic terms will affect the infrastructure of the most developed and densely populated areas.

It should be emphasized that a significant part of the social, transport, mining and developing tourist and recreational infrastructures of North Ossetia, including the area of the Dzuarikau-Tskhinval gas pipeline and the Zaramag hydropower plant (HPP), are located in the zone of the Ardon fault. It is characterized by repeated manifestation of geodynamic activation with the development of ore mineralization. Such structures, especially at the intersection with faults extending across them, are often characterized by PES zones. The most favorable conditions for the discharge of tectonic stresses (causing the development of modern endogenous and exogenous processes) are created in such structural nodes.

The brief characteristics of other large regional long-lived faults of the Caucasian sublatitudinal strike and a steep fall in southern and northern points are given below.

2.1 The Latest Tectonic Movements and Seismicity

The analysis of the nature of the latest tectonic movements was carried out on the basis of aerial visual observations and interpretation of large-scale materials (1:5000–1:25000) of planned and prospective aerial photography.

Particular attention is paid to the latest seismotectonic discontinuities, which are the direct signs of 8–10 point seismic events that took place in the Holocene. For the most part, they are located on the ridge and near-ridge areas and are expressed in the form of ditches, gutters, potholes up to 10 m wide and up to 3–4 km long. Often, there are the entire zones of en echelonditches, intermittently traced, as a rule, in the sublatitudinal direction. In some cases, there is a “splitting” of the ridges along their strike, as a result of the unloading of seismic energy concentrated in the near-ridge. Often, the modern forms of relief (ridges, buttresses, beams, gutters, etc.) are shifted along the latest seismic dislocations. So, a movement of the buttress of the meridional orientation by 50 meters in the plan and by 40 meters vertically is registered in the headwaters of the river Zakkaon the right side. As a rule, the latest seismic dislocations are attracted towards the main largest tectonic ruptures. Their maximum concentration is recorded along the Tib and the Nar faults.

In terms of the length and width of the development strip, the Nar zone of the newest seismotectonic discontinuities is unparalleled in the entire North Caucasus. The majority of landslide formations can be referred to seismogenic.

Analysis of geological information and the data from geophysical studies confirm that the area of Zaramag is one of the most active blocks of the earth’s crust in the Greater Caucasus. Variable movements along the vertical of individual blocks can reach 8–12 mm per year here.

According to the data of the Racha earthquake of 1991 in Georgia, the seismicity of the Central Caucasus was estimated at 9 points by the Institute of Physics of the Earth of the Russian Academy of Sciences in 1995.

In 2009–2010 for the first time for the territory of North Ossetia the map of detailed seismic zoning (DSZ) on a scale of 1: 200000 was compiled by Geophysical Institute VSC RAS, taking into account the fault map of E.A. Rogozhin (2007).

These are the main endogenous causes of the tectonic character of the increase in geodynamic activity, manifested in the form of seismic events.

3 Characteristic Exogenous Geodynamic Processes

For the development of methods and technologies for partial neutralization of manifestations of hazardous geological processes (HGP) at an early stage, forecasting scenarios of HGP development, at sites of projected economic development it is necessary to have a hazard, risk and HGP incidence maps taking into account their potential scales.

The statistics of the HGP types of exogenous nature within three separate valleys that have undergone anthropogenic impact on landscapes to varying degrees allows us to single out mining, transport and agricultural nodes.

The first is the Sadon-Unalecological node, which includes the main mining sites, the Mizurmining complex and the social and industrial infrastructure. The operation began in 1853 with the introduction of new and new deposits, the discovery and use of which was to a variable degree accompanied by environmental disturbance, which concerned mainly the engineering-geological environment and the places of primary rocks outcrop for laying the approach paths and roads, initiat-

ing the anthropogenic impact on the exogenous process. Dumps discharged, as a rule, down the slope to a lower part of the relief or to the river with corresponding consequences in heavy rains enhance to the negatives influence.

The gradual intensification of mining operations, an introduction of power-driven technologies for the sinking of mines and roads to new deposits and ore manifestations have led the environment of the Sadon-Unal ore field to the state that we have at the moment (Fig. 5).



River embankment. The river has not changed its course to the artificially created.



The building of the former office of Geological Exploration Crew (GEC). A third part of the building was destroyed and carried away by a mudflow.



Ruined wall of a residential building.



Residential mining houses destroyed by a mudflow.



Community Centre. Deep scour under the stairs.



One of the houses of Belgian construction. The ground floor is completely covered with debris flow deposits. The store sign is on the ground level.

Fig. 5 The effects of mudflow passage 2005 in the towns Sadon and Galon of Sadon Lead and Zinc integrated plant

The Transcaucasian Highway (Transkam, now the North Ossetian part of the highway “Caucasus”).

Negative interference into the loose-fragmental soils (already extremely unstable embedded on the steep slopes of the right bank of the river Nardon and the river Zakkadon) and into the rock outcrops of highly fractured Lower-Middle Jurassic rocks (represented mainly by the alternating flysch of clay slate, marl, sandstone) began in 1975. The main environmental nuisance is the construction of a road in the section of Nizhniy Zaramag – the Northern portal of the Rokskiytunnel and the workson road interval expansion from the settlement Buron to Nizhniy Zaramag, where all the features of dangerous exogenous destruction of various types that have not been localized before have appeared.

Until 2006, the river-valley of Mamison don did not undergo any significant negative environmental interference and was used as a residential area, free pastures and tourist routes.

A significant environmental intervention in the geology of the Quaternary formations was roughly organized ground power-driven works on laying the main line of the Dzuarikau-Tskhinval gas pipeline through the Kudarskiy pass.

A demonstrative example of the intensive exogenous destruction of the once stable slope is the pass area (2.5 km long) from the confluence of the rivers Zemegondon and Kozydon upwards to the pass through the valley talweg with a high vertical inset into moist loamy soils with fragmental filler material, which are subjected to gravitational gliding along the whole front, intensive drainage and unloading on the road, that leads to a sharp change in the hydrogeological regime of groundwater on the right slope of the river. Ecological damage to the landscape of the right slope would be significantly less if the engineering structures were laid much higher along the slope, where the power of the Quaternary formations in the hanging side could be chosen minimal, but the Project executors relied on technology, rather than on the conclusion of geologists and geophysicists.

For the intended use of the natural features of the Mamison node, in the application of the possible development of the Construction Project of a Year-Round Recreational and Tourist Complex, a high-altitude part of the valleys of the rivers Zug, Zemegondon and Kozydon is considered, within which dangerous exogenous geological processes (which are not yet additionally activated by anthropogenic interference) manifested by the already intensely characteristic for the Central Caucasus types [57].

The nodes under consideration are located in the Alpine tectonic-magmatic zone of the Greater Caucasus and are characterized by typical mountain-folded areas, complex engineering and geological conditions caused by the diversity of the lithological composition of rocks, their intense tectonic disturbance, active neotectonics and seismicity, a variety of geomorphological forms and a wide development of modern exogenous geological processes.

The analysis of the damage caused by exogenous geological processes using the example of a 25-year operation of the Transkam highway showed that the erosion processes make up 45%, mudflows – 30%, avalanches – 10–15%, landslide-talus – 8–10% and landslides – 1–2% in the total balance of HGP.

Known hazardous geological processes of exogenous nature that transform geology, endangering human life, life safety and the national economy can be divided into 2 groups: the first is associated with mass transfer or gravitational processes (landslides, collapses and debris, mudslides, avalanches); and the second group is characterized by the destruction or erosional processes (lateral river and deep ravine erosion, sheet erosion).

3.1 Dangerous Geological Processes in the Area of the Sadon-Unal Ore Field

Spontaneous anthropogenic interference into already unbalanced ecology of the geological environment leads to the massive development of man-made landslides and debris, formed during the cutting of slopes, destruction of vegetation, deforestation, weakening of the links at the level of lithostratigraphic or structural-textural elements of the mountain environment. The largest number of such manifestations is observed along the routes of mountain roads, on the industrial sites for the sinking of mines and during the open pit mining of mineral deposits [58].

On the geological plane, this node is characterized by high exposure of bedrock of a consolidated basement, destructed by intensive fracturing, the development of a dense network of tectonic disturbances and, as a result, by sharp relief forms with canyon-shaped valleys. The landscape and geological section to a depth in this area experienced the greatest anthropogenic load, which resulted in the predominance of landslide processes on the territory.

3.1.1 Landslides

In October 2005 one of the largest landslides occurred in the right bank of the river Arkhondon, along which the road to the high-mountain village of Arkhon passed. The landslide was formed in thick loose sediments represented by loams with a very small amount of fragmental material. These deposits have a high coherence in the dry condition, provide good stability of the slopes and stand with a large slope inclination up to a vertical cut. Their strength decreases sharply with the moisture increase and landslide-landslip phenomena initiate at the edges of the ledges.

The reason of the mountain slope collapse on the road was the gradual watering of the clay massif due to incessant rains, but the main factor contributing to the collapse was the undercutting of the slope base during the restoration of the road, which was destroyed by the flood in 2002. The volume of the collapsed soil was about 30 thousand m³. The road to the village of Archon was blocked by a rock formation up to 5 m high on the area 70 m long.

In 2005, a large landslide in the granite massif (3.5 thousand m³) occurred on the right side of the river Sadon; at the same time the road Turbina-Sadon was blocked

and the threat of failure of the district's power supply system arose. On the right side of the river Arkhon, the landslide of a volume of more than 30 thousand m³ blocked the only road in the village of Arkhon for 100 m. Development of landslide processes on the Mizur bypass tunnel was activated; the threat of collapse of large bedrock blocks to the western portal and the adjacent part of Transkam appeared.

In 2006, activation of the landslide block in the region of the river Gasai, where the threat of a large collapse right on the roadway of Transcamarose.

The landslide-landslip section on the 8th km of the road Turbina-Zgid remains active for several years. The integrity and the natural inclination of the rocky slope were severely disturbed while laying a roadway excavation in fractured granites. Now during its watering rock falls and collapses with volumes from tens to 200–300 m³, requiring clearance and causing traffic interruption for several hours, occur every year.

The main part of the active landslide-landslip phenomena is observed in man-made disturbed steep uphill slopes of mountain roads.

3.1.2 Failures

The first recorded failure from the surface to the exploration mine working, laid in the left bank of the river Tseydon in order to assess the ore occurrence in the area of the village of Khukali, formed in 70 m from the mouth of the mine adit. It was a sink with a 6–7 m diameter and the same depth. Its appearance in the loose soils of the left slope terrace of the river was caused by the delayed installation of the next lining link, but there was a precedent.

The failure of a larger scale (Fig. 6a) appeared in the second half of the eighties of the last century. Its occurrence was instantaneous. It is confirmed by the fact that two hours earlier one of the authors of this article and the truck driver pass the road in the mouth of the mine working and did not see the sink, but on the way back the base of the sink was already threatening the road. The diameter of the almost perfect cone did not exceed 28–30 m, the depth of the sink was commensurable with the diameter. The top of the cone did not yawn, perhaps by the time the witnesses arrived at the place of the event, the process of outflow of the collapsed material into the void space and the formation of the sink had stabilized.

During two months before the described event, the same author at the head of the seismic survey team conducted field observations on this area in order to chart the regional diagonal and local ore control faults and could not notice the failure of such a scale.

The rest of the failures on the site Zgid, as well as over the workings of the left-bank deposit near the village of Unal are somewhat late and obviously not the last (Fig. 6b).

Unfortunately, despite the threat to people and animals, these failures continue to be unfenced for so long time, without mentioning their recultivation.

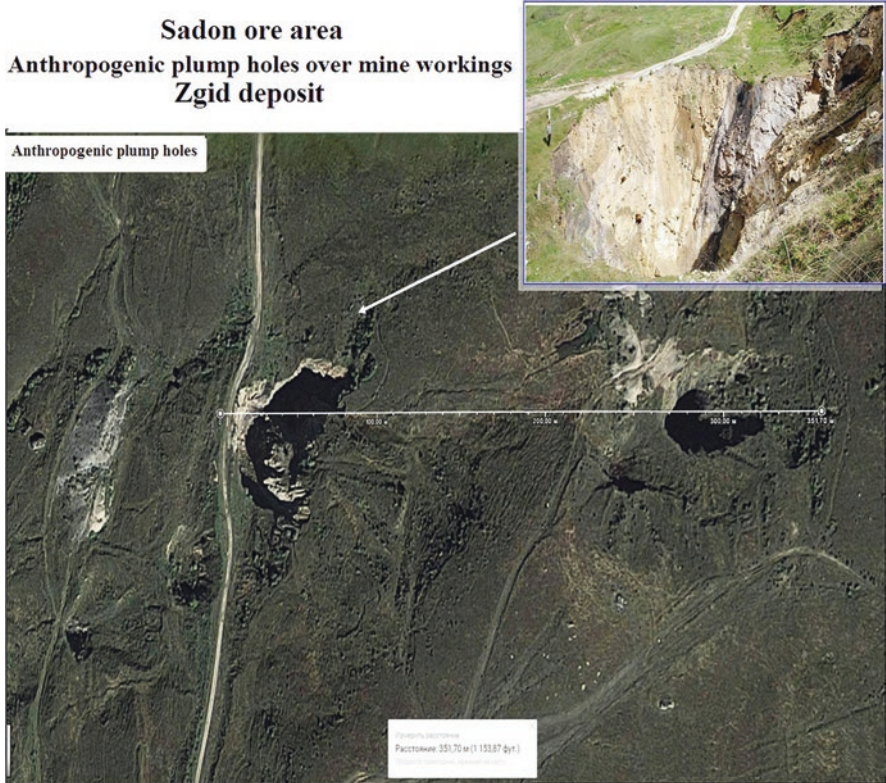


Fig. 6a Anthropogenic plump holes over mines of Zgid deposit (bottom – view from the orbital station)

3.1.3 Mudflows

Mudflows with rainwater feeding are formed in this area, and the main source of the formation of the solid component is a landslide- landslip deposits. The lack of sources of glacial feeding limits the water component of the mudflow focus due to snowmelt and precipitation in the form of rain.

Small areas of local sites for collecting snow and rainwater do not provide, with rare exceptions, a sufficient amount of water flow through the pipelines. In addition, the area is sufficiently forested, which contributes to partial water infiltration and slow melting of the snow cover.

Nevertheless, at the end of June 2002, the mudflow descended along the river Sadon and formed a powerful debris cone, blocking the Federal highway “Caucasus” and forming a dam of the river Ardon. Significant damage was caused to the infrastructure of life support and the inhabitants of the villages of Sadon and Galon which already were in a difficult situation.

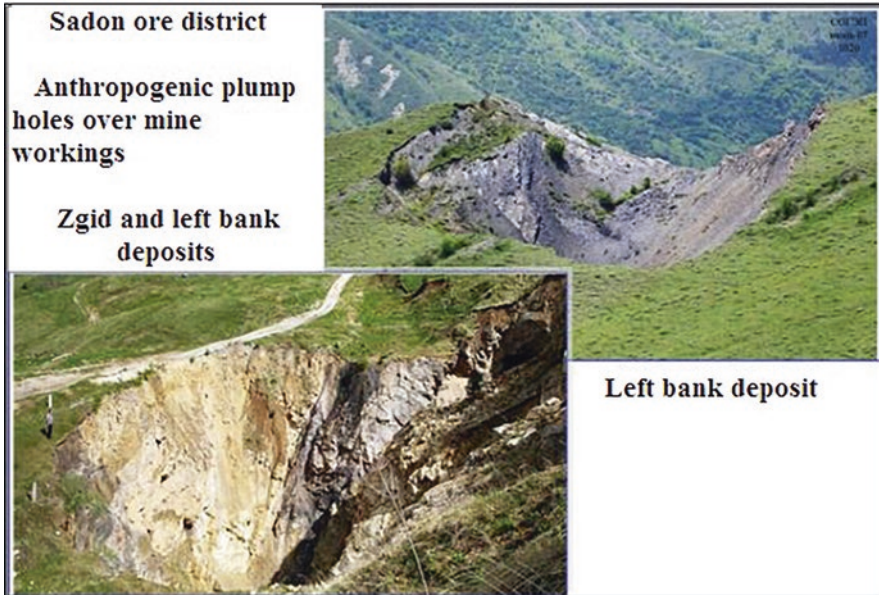


Fig. 6b Anthropogenic plump holes over mines of Zgid and Levoberezhnoe deposits

A real catastrophe for the same miners' villages was the spring flood of 2005 when the level on most of the rivers reached critical levels. The once prosperous-mining settlements were almost completely destroyed left without administrative supervision and economic care (Fig. 5). The road in the Turbina-Galon section was destroyed; the population of the villages of Galon and Zgid was cut off from the rest of the Republic for several days.

3.2 Typical Hazardous Geological Processes in the Area of the Caucasus Highway (Transkam) in the Interval from the Village. Buron – Roki Tunnel

The activation of the hazardous geological processes (HGP) in the area of the Caucasus highway is very often provoked and amplified by anthropogenic impact (cutting the slopes, hydraulic engineering, disruption of vegetation cover and rock structure during mass drilling and blasting operations).

3.2.1 Landslides

In total, more than 50 landslides were detected in the area of the Caucasus highway from the settlement of Bouron to the northern portal of the Roki tunnel. 15% of these landslides are large (up to 5–10 million m³), about the same amount of

medium-sized landslides (up to 100 thousand m³), most of the landslides (up to 70%) are small (up to 10 thousand m³). All landslides of the Zakka river basin in the range of km 86/11 to km 93 + 300 (from the “Gorbatyi” bridge to the northern portal of the Roki tunnel) are small in size [59].

According to the degree of activity among landslides there are stabilized ancient landslide bodies, stabilized landslides with minor (local) signs of activation in the frontal or rear part and modern landslide displacements on steep deluvial-proluvial slopes that occur during over-wetting of slopes and earthquake shocks.

The main damage to the road is caused by small landslides, land slumps and mud slides caused by anthropogenic factors and located along major tectonic dislocations. Along with the landslides located on the right slope of the river Zakka, the Caucasus highway is constantly at risk of landslides located on the opposite left slope of the valley. Their activation can cause ponding of the river, followed by a breakthrough and flood. In terms of damage inflicted in the general balance of losses caused by HGP and by the length of sections requiring engineering protection (180 m), landslide processes take the last place (1–2%).

3.2.2 Landslide-Scree Processes

Almost all large unvegetated outcrops (including anthropogenic) as well as upland slopes of roads are covered by these processes.

The main factor causing the activation of landslide-scree processes is the deep technogenic cutting of the slopes. The uphill slope of the road, which was not settled after drilling and blasting, serves as a constant source of landslides and rockfalls after and during atmospheric precipitation.

Active scree processes are caused mainly by natural factors: the steepness of the slope, the composition of rocks and their ability to weathering.

Scree is mostly developed in the high mountain zone in the upper reaches of the Zakka River. The size of the scree reaches 500 m in length. They are composed of large rock fragments, timber and rubble. Among the scree can be distinguished active and stabilized. A typical representative of active scree is a scree at the northern portal of the Roki tunnel on the left bank of the Zaka river in the headwaters of river Toy.

The landslide-scree processes are actively manifested in the entire interval of the Caucasus highway from the village of Buron to the Northern portal of the Roki tunnel, especially during periods of precipitation. On average, the volume of masses falling on the road during one-time precipitation can be taken as 1 m³/day. on meter of track. Naturally, the volumes of collapsing masses are unevenly distributed and depend on the degree of destruction of bedrock as a result of anthropogenic impact (mass explosions), on the position taken of the road in relation to the bedding elements of the bedrock, landforms (beam, buttress) and the state of friable fragmental complexes intersected by the road.

The negative effect of the technologically-cut rocky buttress is especially pronounced in the areas where the bedrock is intersected by road along the stretch or in

the conditions of the rocks falling into the slope. Technologically-cut buttresses, ridges with dislocated destructive ridge and sub- ridge parts of hard rocks up to 5 m in depth, are among the main sources of friable fragmental material moved onto the road bed.

Along the length of the areas affected by landslide-scree processes, periodically (12.5 km) and permanently (3.6 km), this type of HGP noticeably prevails over the others, but in terms of total annual damage it is in the penultimate place (8–10%) .

3.2.3 Mudflows

The location area of the highway “Caucasus” as well as the entire mountainous part of the Republic of RNO-A, is one of the most mudflow-prone areas in the Central Caucasus. Mudflows, like snow avalanches, are among the most destructive HGP.

According to the volume of mudflows, all basins are divided into 4 groups:

very powerful with a one-time release of over 100,000 m³ of solid material;

average power – from 10,000 to 100,000 m³;

weak – from 1000 to 10,000 m³;

micro-mudflows (slope) – less than 1000 m³ [60].

In the upper part of the Ardon river basin there are about 50 mudflow sites of various types and hazard levels. 18 mudflow sites out of 50 constitute direct hazard for highway “Caucasus”. There are 6 of them in Zakka site (Khuradag, Alkhatkom, Takhkadon, Small and Big Puriat, and Toy). The reserves of friable material in most mudflow sites do not exceed 10–30 thousand m³, however there are also those in which the volumes of friable material are classified as unlimited (Labagom, Vilsadon, Kasaykomdon, Alkhatkom).

According to the formation mechanism landslide and erosion mudflow sites are distinguished. In the first, mudrock flows [61] are formed with a laminar mode of motion and a maximum ejection of solid material of no more than 50 thousand m³ (Babiat).

In erosional sites with river channel slopes of more than 15°, the most hazardous high-density mudflows with a turbulent mode of movement and volumes of one-time ejection of solid material up to 300 thousand m³ (Kasaykomdon) can be formed.

The descent of mudflows directly on the road leads to the overlap and even destruction of the roadway in areas from 10 to 200 m. When the mudflow reaches a river flow, temporary stoppings and dammed lakes are formed with a water volume of up to 50–100 thousand m³, the breakthrough of which leads to strong destruction of downstream objects. Catastrophic mudflows occur, as a rule, in July–August with an interval of 10–15 years (the last mass activation of mudflows in the entire Mountainous Ossetia occurred in 2002).

Catastrophic mudflows occur, as a rule, in July–August with an interval of 10–15 years (the last mass activation of mudflows in the whole of Mountainous Ossetia occurred in 2002).

At the Zakka area of highway “Caucasus”, the mudflow site Khuradag, located on the right bank of the Zakka River, is distinguished. Until 1987, the site was active on average once every 5 years. After a catastrophic activation in 1987, the annual release of solid components onto the roadway was determined by the first tens of cubic meters. In the case of mudflow the semi-liquid mass spreads along the roadway, which leads to its destruction in certain areas. Ejections of maximum volume can partially impound Zakka river.

The mudflow site of Alkhatkom is also located on the right bank of the Zakka river and crosses the highway route. The site is associated with the accumulation of friable material in the channels of temporary and small streams with steep ($> 15^\circ$) thalwegs. The basin has several zones of intermediate discharge. The largest of them is the turning point of the main river channel from the longitudinal to the latitudinal direction. Here a ponding followed by a breakthrough can also occur. The discharge (disintegration) zone of the mudflow is located on the right side of the Zaka river and in the floodplain for 300 m length.

The mudflow site Takhkadon (Vodopadny) is located in the right side of the Zakka river and also crosses the highway. The maximum recorded ejection was in 1964 (about 20 thousand m^3 of solid phase). Small single ejection of a few hundred m^3 are observed almost annually.

The mudflow cite Small Puriat is located on the right side of the Zakka river in 650 m upstream from the bridge of the northern portal of the Roki tunnel. The basin has a complex structure and consists of 3 chambers. As a rule, the mudflow activation is manifested in one of the chambers, and in the periods of mass activation of the HGP – in all three chambers. The maximum fixed one-time ejection was 15 thousand m^3 of the solid phase (1987).

The mudflow basins of the Small and Big Puriat constitute hazard of the portal bridge demolition of the Roki tunnel or the destruction of a road part if a mudflow dam is formed and breakthrough.

The mudflow site Toy is located on the left side of the river Zakka on the northern portal site of the Roki tunnel, has a typical fan-like shape and is evenly inclined ($7-8^\circ$) to the river Zaka, surface. The grass-covered debris cone, composed of proluvial-deluvial sediments (pdQ_{IV}), reaches 350 m long and 250 m wide, its area is 0.087 km. As approaching river Zakka, the debris cone is broken by a steep ledge 20–25 m high.

In the process of economic development of the site during the Roki tunnel construction, the main mudflow cone of river Toy was terraced with construction in the frontal parts of the three main terraces of avalanche protection ditches. On the low-ermost terrace, the near-entrance structures are located.

The annual damage to the highway “Caucasus” by the mudflow processes amounts up to 30% of all HGP.

Not only the roadbed and engineering structures, but also high-voltage power lines, communication cables, industrial facilities and settlements adjacent to the road suffer due to mudflows and floods.

3.2.4 Snow Avalanches

The basin of river Ardon especially its headwaters by virtue of its geographic location is characterized by constant intense snowfall and it is the most avalanche-prone area in Mountain Ossetia. In total, 144 channeled avalanches were identified in the immediate vicinity of the highway from Buron to the northern portal of the Roki tunnel, 110 of which constitute hazard to the highway. Single volumes of avalanche ejections in some cases reach 300 thousand m^3 (Sidan, Gomkhat, Toy) [62].

A significant part of avalanches belongs to high-velocity (up to 150 km/h) having a powerful shock wave, the destruction front of which reaches 500–600 m (Gomkhat, Khalankus, Toy, etc.) [63, 64].

The total length of areas affected by avalanches, taking into account the shock wave is 7.8 km. At 13 sites, the length of which ranges from 200 to 900 m, the distance between adjacent avalanche trays does not exceed 90 m, i.e. there is a completely affected zone. The total length of snow drifts from the village Buron to Roki tunnel reaches 3 km.

The avalanching frequency is highest in the upper part of the region (PK215 – PK280) and can reach 8–9 times per season. Downstream of the river Zakka, the avalanching frequency decreases to 1–3 times.

The observation of the avalanche regime, their precautionary descent in the region, is carried out by a special AMS (avalanche monitoring service) of the Highland Geophysical Institute (HGI, Nalchik).

The most avalanche-prone area is the last 8 km interval in front of the Northern portal of the Roki tunnel, where individual sections fall into the affected area, followed by 25 avalanches from both sides of the Zakka river. All avalanches are high-velocity with powerful shock waves completely blocking the river bed with transfer of snow masses to the opposite side. The most effective type of engineering protection of the road in such areas are galleries and tunnels.

At this interval, the largest avalanches are Batin, Tomadzhin, Khuradag, Alkhatybynta-1, Alkhatkom, Shakhta, Zaladag, Dzuary-kulta-1, Khoshtykom, Takhkadon, Dallag-Puriat, Toy, left side of the Zakka river.

One-time emissions of snow masses of the listed avalanches often exceed 30–50 thousand m^3 , and Dzuary-Kulta-1 avalanches exceed 100 thousand m^3 with the roadway overlapping more than 100–150 m each.

Avalanche site of Toy with volumes of single discharge up to 300 thousand m^3 from the port side of the Zakka river covers the roadway for 200–250 m with a snow cone thickness up to 10 m. The front of the shock wave exceeds 1 km. In the indicated volumes, the Toy avalanche comes down 1 time in 15–25 years.

From time to time, avalanches from the left side of the Zakka and Dallagkom rivers descend snow masses onto the roadway. In the total balance of damage from the HGP avalanches account for 10–15%.

3.2.5 Erosion Processes

In this type of HGP, river lateral erosion (erosion of banks) and deep erosion of temporary streams dominate, leading to the development of ravines and erosion of the lower slope of the road shelf.

Causes of lateral erosion can be the bursts of mudflow dammed lakes or the suppression of the riverbed by the proluvial cones of the tributaries. The rate of side erosion varies on average from the first meters to 40 m/year, and in periods of floods it can reach 1–2 m/day.

Most often lateral river erosion is observed in areas of steep river bends, frontal parts of activated landslides and proluvial cones.

The Babiat site (km 85/12 – km 86/11) where the protection of the left bank with the help of 2 guide dams that proved to be inadequate, is referred to areas prone to both types of erosion (lateral and deep).

The nature of lateral erosion in the floodplain expansion areas is very variable, since after each large flood the river can significantly change the position of the channel.

Along with lateral and deep erosion, damage to individual objects can be caused by an extremely increased accumulation of erosion material, especially during mud-floods and bursts of mudflow dams.

It should be noted that most cases of erosion of the road, bridges and other objects are caused by the absence or insufficient effectiveness of protective engineering structures.

In the general balance of damage from HGP, erosion processes firmly occupy the leading place and constitute about 45%.

It should be noted that of the whole variety of natural and anthropogenic factors that determine the development of an HGP, the most intense consequences are caused by climatic extremes (an abnormally large amount of precipitations) that can cause a catastrophic activation of almost all types of HGP. Such catastrophic phenomena in Mountain Ossetia, including in the basins of Ardon and Zakkadon rivers were noted in 1953, 1967, 1986, 1990, 1996, 2002, 2005 and they were accompanied by great destruction of various economic objects.

3.3 *Hazardous Geological Processes at the Mamison Site*

3.3.1 Erosion Processes

These processes are widely developed throughout the territory, occur very often and cause significant damage to economic objects and especially to linear structures. Erosion processes include sheet flood, ravine erosion, lateral and deep erosion of rivers. The intensification of erosion processes on a regional scale is due to the fact that at present the orogen of the Greater Caucasus is captured by a tectonic uplift at a speed of 2 to 14 mm/year. Upward movements increase the overall energy of the

relief, which is already quite high. This is evidenced by the high erosional dissection of the relief [65] and a very large elevation difference to local erosion bases. In high-mountainous areas, the length of the erosion network is 2.5–3.4 km/km², and the depth of local erosion bases reaches 1000–1500 m. Under these conditions, water flows are characterized by high speed (up to 3 m/sec and more) and perform significant erosion work [66]. On the Mamison site, all types of erosion processes are noted: sheet flood, jet erosion, lateral erosion, and vertical (ravine).

3.3.1.1 Landslide-Scree Processes

About 80% of the entire observed area is covered by friable fragmental sediments, much of which is the product of landslide-scree processes.

The reasons for the landslides in the conditions of sharply dissected relief and intensively disturbed rocks are: active geodynamic processes characteristic for the territories located at the junctions of tectonic plates; seismic effects of intensity up to 7–9 points, the discharge of which gravitates toward the ridged and summit parts of the relief and leads to the collapse of large blocks of hard rock and friable ground; the mechanism of work of side impact cracks, especially effective in the high-altitude zone with sharp daily temperature differences. In this case, the main role is played by microcracks, in which the effect of freezing moisture is particularly strong.

On Mamison area the sites of powerful tectonic disturbances (Tsey thrust and a series of tectonic faults of the southern slope – North and Nar faults, Tib, Khalats, Zgil, Sauhokh), as well as areas of development of newest discontinuous seismic dislocations [65, 66] are the most landslide prone areas.

In the zone of the relic scar and the southern slope, individual tectonic blocks move relative to each other up to 12–15 mm per year against a background of 2–3 mm/year in the Greater Caucasus as a whole, which creates enormous stresses and causes not only earthquakes, but also landslides. There are cases when a long-term impact on the environment of the TransKAM with a cable-tool drilling method caused the collapse of bedrocks with a volume of up to 5000 m³ from the uphill road slope, despite the decline of the rocks back to the slope.

In May 1990, near the village Matsuta (RNO-Alania) seismic effect with an intensity of 4 points (“Tsey” seismic station) caused a landslide of 20 million m³.

3.3.1.2 Scree

Scree is a widespread type of landslide-scree processes, they are particularly intense on the slopes composed of shale and thin-bedded rocks of the terrigenous formation of the lower-middle Jurassic [67]. At the foot of such slopes with a steepness of more than 30°, almost everywhere there are plumes of active fine-grained screes, not grass-covered and almost without aggregate. The slope of scree plumes is 28–35°.

On the undercut ridge areas, creeps are actively formed, which are the main source of loose detrital material entering the zone of linear structures. On the contrary, beams and corridors with active deep erosion (floods, mudslides, avalanches), which have already lost the destructed part of the rock section, solid friable fragmental, properly scree, material supply a minimum. Landslide-scree processes affect up to 30% of the total area.

3.3.1.3 Mudflows

Prospective for use in recreational and tourist purposes, the territory of the Mamison site, as well as the entire mountainous part of North Ossetia-Alania, is a high level mudflow hazardous area. This is conditioned by the Karling profile of mountain peaks, composed of unstable flysch rocks, modern glaciation, high seismicity, huge reserves of friable fragmental material, high moisture content create favorable conditions for the formation of mudflows. The exposure of the territory to this type of exogenous geological processes is close to 50% and is on the border of the categories of highly hazardous and danger hazardous.

The following genetic soils of mudflow sites have been noted, associated with: the accumulation of friable fragmental material in the channels of temporary and small watercourses, with the ponding of rivers and with the activity of modern glaciers [68].

3.3.1.4 Sites Associated with the Ponding of Rivers

This type of mudflows is especially hazardous for its suddenness, short-term high costs, unpredictable consequences and the almost instantaneous creation of conditions for mudflow formation. Pondings of rivers can be landslide, creep, avalanche, mudflow and scree.

During heavy rains, discharges on major mudflow-forming tributaries reach 5 m³/sec and more. Under these conditions, even an insignificant and short-term damming can form a water storage tank of up to 10,000 m³ or more for 30 minutes.

Judging by the breakthrough terraces located below the dammed reservoirs, the discharge takes place in 2–3, and sometimes in 4 stages. The first wave with a flow rate of up to 100 m³/sec reduces the water storage volume by about 50% and lasts for a few minutes, and this is enough so that a downstream (about 1 km) is formed a full-fledged mudflow with an discharge of solid mass up to 40–50 thousand m³.

Sites of potential ponds are available practically in all watercourses, depending on the waterway gradient, they can reach 30–40 t.m³.

After a snowy winter and intense melting of 13.06.1987 from the right slope of the river Adaykomdon opposite to V. Zaramag, the collapse of friable clastic soils of 50 thousand m³ with the overlap of the river bed occurred. The volume of the water reservoir was 8.5 thousand m³.

3.3.2 Avalanches

The high-mountainous part of Mamison area, where one-time snowfall with a thickness of up to 1 m is an ordinary phenomenon, is characterized by a wide development of avalanches.

The sharply dissected relief, the presence of slopes of various angles, the steepness and treelessness of the slopes, the huge (up to 1000 m) relative elevations within the avalanche sites, significant differences in daily temperatures cause avalanches of all types and structures to occur at almost any time of day, starting with the last dates of October to mid-May inclusive.

The most common and large are channeled avalanches, which are permanently tied to lower forms of relief (beams, corridors, canyons), and smaller ones are snow land slumps, which descend from the slopes of a steepness of more than 15° .

The roxen effect of avalanches (vertical erosion) is insignificant, since a small part of the stone material is captured by the snow mass (up to 2–5% of the volume). Most avalanches belong to the category of velocity (more than 100–150 km/h) and they have powerful shock waves that can lift into the air almost any equipment (cars, bulldozers, etc.). The shock wave capture zone, as a rule, is 2–3 times more than the width of the area affected by snow masses; often, a snow mass is thrown to the opposite side (avalanches of the left side of the Zemegon and Mamisondon rivers in the area of the village Zgil).

Avalanches affect 30–35% of the territory, which corresponds to the category of “Hazardous”. The site for the possible construction of the future village of Lisri is almost completely, with rare exceptions, exposed to avalanches from both the right and left sides of the riverbed. The recorded volume of a single descend is 18 thousand m^3 with the intersection of the roadway over 70 m.

On the right side of the river. Mamisondon, in the Kamskho-Lisri village interval, there are three sites of chanel-type avalanches and a site of active avalanche formation.

Avalanche site opposite villages Nizhnyi Kamskho has a water-catchment area of 0.97 km^2 , the thalweg length is 1.61 km, the average slope is 0.47. The total snow cover is more than one million m^3 , the estimated potential of a single discharge is about 300 thousand m^3 , the noted volume of a single discharge about 60 thousand m^3 was accompanied by the overlapping of the Mamisondon riverbed and transfer of snow masses to the left side. The effect of avalanches is somewhat reduced by winding thalweg and partial forest coverage of the sides. The possible impact of a shock wave on the front is estimated at about 700 m.

The avalanche site No. 66 with a water-catchment area of 0.25 km^2 has a thalweg length of 1.16 km, an average slope is 0.26, the total snow cover is 250 thousand m^3 , the estimated one-time release is 80 thousand m^3 . There was a descend of 12 thousand m^3 with overlapping of the Mamisondon riverbed and transfer of part of the snow mass to the left side.

One of the largest avalanche collectors is Zgil site (Bebetykom), located on the right side of the river Zemegon opposite village Zgil. Its water-catchment area is 3.81 km^2 , thalweg length is 3.92 km, average slope is 0.36. The total volume of

snow cover is about 4 million m³. The site is multi-chamber, part of the slopes is forested. Estimated one-time discharge, taking into account the relief and the state of the slope, is determined at 700–800 thousand m³. The affection front is up to 300 m. The fixed single release according to long-term observations did not exceed 100 thousand m³. Upstream from the right side of river Zemegon regularly descends another 12 avalanches that reach the riverbed cross it and can reach the water intake area. Volumes of one-time release do not exceed 15–20 tons. m³.

The “Kozy-com” site, which is promising for possible construction, is exposed to a powerful avalanche impact. It is located in the discharge zone of the main avalanche and three feeding avalanches. The water-catchment area is 1.01 km², the thalweg length is 2.41 km, the average slope is 0.33. The amount of snow cover is more than 1 million m³. The estimated volume of a single discharge is determined at 300 thousand m³. The fixed volume of a single discharge amounted to 40 thousand m³ with a front of destruction along the road line 150 m. Snow masses can reach the riverbed of Kozydon.

3.3.3 Landslides

Landslide accumulations on the territory of Mamison are widely distributed. They are diagnosed quite confidently by the presence of landslide cirques in the upstream part of the slope, the morphology of the accumulation surface and are easily isolated in the relief of the slopes of the valleys. As a rule, these are consequent landslides (successive in time up the slope), often large, merged and forming landslide slopes.

Landslide accumulations reach their maximum development in the basin of the Ruchatdon and Lagatkom rivers. Both landslide processes affect the valleys with the formation of areas of potential ponding of the channel, creating conditions for the formation of breakthrough-type water accumulators during mudflow activation. The power of accumulations is the first tens of meters, everywhere in the upper parts of the landslide cirques sub-Quaternary formations are exposed. Most landslide accumulations are characterized by signs of a high degree of activation of slope processes [69].

Landslide accumulations are widely developed in the middle part of the Gibitandon valley. On its right side there are four large landslide cirques, forming a continuous landslide slope 1.5 km long. Landslides of the right side, are composed of marls, limestones, shale deposits of the Zgil suite [70, 71] and have a thickness of 20–30 m and contribute to the formation of landslide dams during flood in river Gibitandon.

In the middle part of the Kozydon valley, on its left side, two landslides were identified. They are located above the site of the possible construction of the village “Kozykom” on the slopes of the trough and composed of thin (5–10 m) cobble-debris and lateral moraine accumulations of late-Neo-Pleistocene age. Landslide accumulations on moraines of Middle Pleistocene age are present in the left mouth of Caiticomdon and, if the mudflows are activated, they can form a sub-reservoir.

On the left side of Mamisondon, three sliding landslide bodies are mapped on the rocks of the Tekhtinsk suite of the upper Jurassic.

For the road section between the villages Tib and Satat there are 5 landslides constituting hazard, among which the largest is Satat, with an estimated volume of 2.0–2.5 million m³. Its width along the line of the existing road reaches 420 m, the thickness of the loose-fragmental mass in the landslide body is up to 23 m on the western flank and up to 5.3 on the east.

3.4 Features of the Glacier Movement of the Kazbek Group

In addition to the so-called glacial mudflows associated with the modern glaciers, for the Kazbek group for the first time a scenario of gas-hydrodynamic impact on the glacier of post-volcanic gases was proposed. The basis for this scenario are the above-mentioned cases of the catastrophic collapse of the Kolka glacier, accompanied by fumaroles, gas emission, “ant” heaps of up to 1.0 m in the liberated bed. Gas release was also noted during the collapse of a part of the Devdorak glacier on May 17, 2014. The nature of the “ant” heaps of fine-grained rock particles from the position of a breakthrough of postvolcanic gases is easily explained by the action of ascending gas jets, in an amount equal to the number of “ant” heaps in the area of their distribution. The pressure of the gas jets at the time of “erection” of the structures did not exceed 300 Pascals (0.03 atm.). Identifying the area of spread of “ant” heaps and the discharge density of gas in the approaching space, we can expect, in the presence of heat warming factor, the release of the glacier from the bed and side moraines. But such pressure would hardly provide an instant explosive release of 110 million m³ of glacial rock mass of the glacier, especially far beyond the bed. Of course if the construction of “ant” heaps was not the final stage of gas discharge.

In one of the expeditions to the ice-stone dam in order to explore the future road route and the location of the bridge through the river Genaldon the researchers of the Geophysical Institute of the VSC RAS found two “ant heaps” with a height of 4–5 cm and the same diameter on the surface of the dam. At the site of their location (VES No. 4), when the supply electrodes were driven into the body of the dam, a characteristic hum of the void space was heard, and with the theoretical expectation of a low-resistance environment, a high resistivity of apparent resistivity was obtained under the observation point, which, when interpreted, was interpreted with voids in the ice-rock dam. Comparing these observations and the description of “ant heaps” in the glacier bed, it can be argued that they have the same nature of formation – air-gas. The structures have a conical shape, they are composed of fine-grained rock material, apparently contained in ice. Such a structure can be formed when insignificant pressure flows from the bottom of the ascending gas flow, transporting a certain amount of fine-grained material.

It is quite obvious that the impulse of such a force is greater in power than any collisions of a moving glacier with obstacles in the way of transit. Within a radius of about 250 km, all seismic stations clearly recorded such collisions in the form of

wavetrain with characteristics of the direction of impact, amplitude and frequency parameters. Meanwhile, none of the stations recorded not only an explosive seismic entry, but also a characteristic impulse entry.

The theoretical substantiation of the gas-hydro-geodynamic nature of the catastrophic collapse of the Kolka glacier, including the event of September 20, 2002, is based on the geodynamic (seismotectonic) and post-volcanic effects on the glacier. The geodynamic impact is caused by the activity of the Syrhubarzond fault, which, in relation to the main structure of the Central Caucasus – the relic scar, the healed oceanic trench during the subduction period of the geological situation in the history of the Caucasus, extends to the east of the Glavnyi thrust and cuts through the Kolka glacier from west to east. The rear part of the Kolka glacier and other glaciers of the northern exposure is limited by the active Adaykom-Kazbek fault, which runs along the ridge part of the Dzhimarai-Kazbek mountain node. The activity of these structures is evidenced by the periodic occurrence of earthquakes. Considering the last eruption of the Kazbek volcano (6000 years ago), the temperature of the volcanic substrate (950–1000°C) and the temperature gradient of the cooling intrusive massif 180 °C for two million years, we can be sure that there is a high-temperature environment in the chamber at a depth of about 5–7 km. Geodynamic activity caused by intrusions of crust-mantle magma, kinematics of blocks, deformation waves of interaction stress in the zone of plate collisions, elastic response of the medium to continental drift, etc., in the form of seismic effects on active tectonic structures in the zone of influence on the glacier, increases permeability due to displacement, cracking, disclosure of minor faulting, which contributes to gas-hydro mixtures breaking up, sometimes concentrating in certain traps such as the ice shell of the Kolka glacier [72–75].

4 Conclusions

The geodynamic activity of the region is determined by the tectonic structures of the territory that are classified as active. These include Vladikavkaz, Ardon, Glavnyi in the west and Syrhubarzond in the east, Adaykom-Kazbek fault group, separating the Folded-block construction and the southern microplate.

Sustained uplift and lateral drift of the structure of the Central Caucasus, accompanied by frequent short-focus earthquakes, anchored by the extensive development of self-flowing and artesian thermal springs, confined to tectonic disturbances, the “parasitic” fumaroles of Elbrus stratovolcano, the gas-hydrogeodynamic effect, the postvolcanic impact on the Kolka glacier of the “sleeping” or “extinct” Kazbek volcano are direct signs of the geodynamic activity of the Central Caucasus.

Frequently occurring shallow-focus earthquakes in the eastern segment of the Central Caucasus are confined to the belt of the active Vladikavkaz sub-latitudinal deep fault, concentrating in the zone of its intersection with the regional deep Ardon fault of meridional strike where possible seismic source zones are potentially possible. Both faults continue in the upper mantle. The geodynamic state is estimated

as the active phase of development, characterized as a whole by the state of compression due to the advance to the north of the Arabian plate. All of the above faults are confirmed by a complex of geophysical methods, a reflection in the form of a gravitational step and an area of increased wave absorption in earthquake converted-wave method.

Geodynamic activity contributes to the accelerated exogenous processes in the highland areas caused by the impact of a complex of weathering factors (widespread exposure of bedrock, a combination of subarctic at night and a sharply continental daytime climate, frosty weathering, avalanches, heavy rain and eddy winds, steep slopes favoring gravitational collapse and creeping, fracturing and pronounced multi-rank block tectonics). The article discusses the main geodynamic manifestations in the form of seismological events, their spatial localization, direct and indirect signs of seismogenic structures and potential zones of earthquakes. Types of exogenous processes characteristic for the Central Caucasus are given in a causal relationship with deep geodynamic activation and the climatic conditions of the region.

Acknowledgments The research was supported by Russian Science Foundation (Project No. 19-47-02010 RSF-DST(2018):“Natural hazards and monitoring for mountain territories in Russia and India”.

References

1. Shubik BM, Kiselevich VL, Nikolaev AV, Rykunov LN (1991) Microseismic activity in the hydrothermal region. Physical bases of seismic methods. Moscow, p 143–158 (in Russ.)
2. Belyakov AS, Lavrov VS, Muchamedov VA, Nikolaev AV (2016) Joint analysis of the seismic data and velocity gravity model. *Dokl Earth Sci* 467(1):293–294
3. Shempelev AG, Prutskiy NI, Kompaniets MA, Morozova AG, Kukhmazov SU, Pyankov VY (2011) The results of deep investigations along the Elbrus profile (Elbrus volcano – Caucasian Mineral Waters). In: Volcanism, biosphere and environmental problems. Proceedings of materials of the VI International Scientific Conference. Maikop – Tuapse, 2011. p 103–105 (in Russ.)
4. Shempelev AG (2008) The deep structure of the Kazbek megablock of the Greater Caucasus. In: Proceedings of the XLI Tectonic Meeting “General and Regional Problems of Tectonics and Geodynamics”. Moscow, 2008, p 463–467 (in Russ.)
5. Lavrushin VY, Polyak BG, Strizhov VP, Italiano F, Rizzo A (2007) Isotopic helium area of the Kazbek volcanic center. *Rep Acad Sci* 414(2):239–242. (in Russ.)
6. Shempelev AG (2007) Results of deep investigations along the Genaldon profile. In: Abstracts of reports of the international scientific and practical conference “Hazardous natural and anthropogenic geological processes in the mountainous and foothill territories of the North Caucasus”. September 20–22, 2007 Vladikavkaz, 2007. p 36–38 (in Russ.)
7. Fedotov SA, Utkin IS, Zaalishvili VB, Utkina LI (2011) Evaluation of the possibility of using the heat accumulated by the magmatic source of the Elbrus volcano in the enclosing rocks for the production of electricity. *Geol Geophys S Russ* 1(1):32–37. (in Russ.)
8. Zaalishvili VB, Nevskaya NI, Nevskii LN, Shempelev AG (2014) On the peculiarities of geophysical fields over Elbrus and Kazbek. *Geol Geophys S Russ* 4(4–2):27–33. (in Russ.)

9. Shempelev AG, Zaalishvili VB, Kukhmazov SU (2017) Deep structure of the western part of the Central Caucasus from geophysical data. *Geotectonics* 51(5):479–488
10. Zaalishvili VB, Nevskaya NI, Nevskii LN, Shempelev AG (2015) Geophysical fields above volcanic edifices in the North Caucasus. *J Volcanol Seismol* 9(5):333–338
11. Zaalishvili VB, Burdzieva OG, Dzhgamadze AK (2015) Geothermal waters of North Ossetia. *Ecol Environ Conserv* 21(S Dec):151–155
12. Zaalishvili VB, Melkov DA, Burdzieva OG (2015) Possibilities of geothermal energy use on the North Caucasus (a view on a problem from Azores example). *Ecol Environ Conserv* 21(S Dec):145–149
13. Gushchenko II (1979) Catalog “volcanic eruptions of the world”, Nauka Moscow (in Russ.)
14. Zaalishvili VB, Nevskaya NI, Melkov DA (2014) Instrumental geophysical monitoring in the territory of northern Caucasus. *Izv Phys Solid Earth* 50(2):263–272
15. Zaalishvili VB, Melkov DA (2014) Reconstructing the Kolka surge on September 20, 2002 from the instrumental seismic data. *Izv Phys Solid Earth* 50(5):707–718
16. Zaalishvili VB, Berger MG, Maliev IN, Melkov DA, Kanukov AS, Makiev VD (2016) Development of the instrumental monitoring system of the Kazbek volcanic center. *Geol Geophys S Russ* 6(4):44–51. (in Russ.)
17. Zaalishvili VB, Melkov DA, Dzeranov BV, Morozov FS, Tuaevev GE (2018) Integrated instrumental monitoring of hazardous geological processes under the Kazbek volcanic center. *Int J Geomate* 15(47):158–163
18. Zaalishvili VB, Chotchayev KO, Shempelev AG (2018) Signs of the geodynamic situation and elements of the structural-material complexes of the Central Caucasus in the deep section of the Genaldon profile. *Geol Geophys S Russ* 18(4):58–74. (in Russ.)
19. Berger MG (2016) Deposits of explosive directional gas-dynamic ejection of a glacier – a new genetic type of sedimentary formations. *Geol Geophys S Russ* 16(4):20–30. (in Russ.)
20. Berger MG (2017) On genetic types of catastrophic avalanche-like flows and dynamic types of dangerous glaciers according to their manifestation. *Geol Geophys S Russ* 17(3):13–26. (in Russ.)
21. Berger MG (2018) About the uniqueness of the case with the Kolka glacier. *Geol Geophys S Russ* 18(1):93–108. (in Russ.)
22. Berger MG (2018) On the inconsistency and groundlessness of glaciological ideas about the catastrophic pulsation of the Kolka glacier, its causes and analogues. *Geol Geophys S Russ* 18(2):83–90. (in Russ.)
23. Berger MG (2018) On the role of seismotectonics in the Kolka catastrophe of 2002. *Geol Geophys S Russ* 18(3):5–16. (in Russ.)
24. Zaalishvili VB, Melkov DA (2017) Features of the collapse process of the stone-ice avalanche in the area of the Devdorak glacier on May 17, 2014 according to instrumental data of the Karmadon parametric range. *Geol Geophys S Russ* 17(4):39–47. (in Russ.)
25. Zaalishvili VB, Nikolaev AV, Puzich IN (1996) On the question of the relationship between the ground conditions of a territory and the dynamic parameters of wave fields under seismic influence. *Development of methods and means of experimental geophysics, Vol. 2. OIHP RAS, Moscow*, pp 314–321. (in Russ.)
26. Nikolaev AV, Gusev GA, Gufeld IL (2004) Physics of the seismic process and earthquake source. In: *Research in the field of geophysics: to the 75th anniversary of the United Institute of Physics of the Earth. O. Yu. Schmidt. OIHP RAS, Moscow*, p 3–12 (in Russ.)
27. Mirzoev KM, Nikolaev AV, Lukk AA, Yunga SL (2009) Induced seismicity and the possibilities of controlled relaxation of tectonic stresses in the earth’s crust. *Izv Phys Solid Earth* 45(10):885–904
28. Smaglichenko TA, Nikolaev AV, Jacoby WR (2010) Separated determination of the velocity structure and earthquake hypocenter parameters on the basis of the differentiated approach. *Dokl Earth Sci* 433(2):1057–1061
29. Nikolaev AV, Trofimov VT, Zhigalin AD, Lavrov VS (2018) Natural and technogenic impact structures: ecological-geological aspect. *Geol Geophys S Russ* 18(4):117–125. (in Russ.)

30. Svalova VB (2014) Modeling and monitoring for landslide processes. In: Linwood K (ed) Natural disasters – typhoons and landslides – risk prediction, crisis management and environmental impacts. Nova Science Publishers, New York, pp 177–198
31. Svalova VB (2016) Monitoring and reducing the risk of landslides in Taiwan. *Monit Sci Technol* 3:13–25
32. Svalova VB (2016) Analysis of landslide risk in Taiwan. “Commonwealth” Russia-China Sci J 4:136–141
33. Svalova VB (2016) Analysis and management of risk of landslides. *Scientia Phys Math* 2:28–31
34. Svalova VB (2016). Reducing the risk of landslides. *Unif All Russ Sci Bull* 2(3): 79-83
35. Svalova VB (2016) Landslides modeling, monitoring, risk management and reduction. *EESJ* 7(11):43–52
36. Svalova VB (2016) Risk analysis, evaluation and management for landslide processes. *Sci Eur (Praha, Czech Republic)* 4(6):15–25
37. Svalova V (2017) Landslide risk: assessment, management and reduction. Nova Science Publishers, New York
38. Zonenshayn LP, Kuzmin MI, Natapov LM (1990) Tectonics of lithospheric plates on the territory of the USSR. In: 3 books. “Nedra”, Moscow (in Russ.)
39. Baranov GI, Grekov IN (1982) Geodynamic model of the Greater Caucasus. In: Proceedings of the 2nd seminar on geodynamics of the Caucasus in Tbilisi, Apr.1980. Nauka, Moscow. 51 p (in Russ.)
40. Baranov GI (1991) Tectonic investigations in the North Caucasus. In: Abstracts of the VII territorial conference on geology and deposits of the North Caucasus. Essentuki, 1991, p 91–93 (in Russ.)
41. Baranov GI et al (1995) Geodynamic development of the Greater Caucasus in the Paleozoic. The main problems of geological exploration and use of the subsoil of the North Caucasus. In: Proceedings of the VIII anniversary conference on geology and deposits of the North Caucasus. Essentuki, 1995, pp. 54–56 (in Russ.)
42. Averyanova VN, Baulin YI, Koff GL, Lutikov AI, Mindel IG, Nesmeyanov SA, Sevostyanov VV (1996) Comprehensive seismic hazard assessment of the territory of city Grozny. PNIIS, Moscow. p 6–18. (in Russ.)
43. Wells DL, Coppersmith KJ (1994) New empirical relationships among magnitude, rupture length, rupture width, rupture area, and surface displacement. *Bull Seis Soc Am* 84(4):974–1002
44. Gorbatiykov AV, Ovsyuchenko AM, Rogozhin EA (2011) The structure of the Vladikavkaz fault zone according to the results of research by a complex of geological and geophysical methods. *Geol Geophys S Russ* 11(2):28–31. (in Russ.)
45. Zaalishvili VB, Rogozhin EA (2011) Assessment of seismic hazard of territory on basis of modern methods of detailed zoning and seismic microzonation. *Open Constr Building Technol J* 5:30–40
46. Rogozhin EA, Gorbatiykov AV, Zaalishvili VB, Stepanova MY, Kharazova YV, Andreeva NV, Melkov DA, Dzeranov BV, Dzeboev BA, Gabaraev AF (2013) New ideas about the deep structure of the Ossetian sector of the Greater Caucasus. *Geol Geophys S Russ* 13(4):3–7. (in Russ.)
47. Zaalishvili VB, Chotchayev KO (2016) Comprehensive analysis of geological data and the velocity model of the microseism sounding method on the sections of the Central Caucasus. *Geol Geophys S Russ* 16(4):52–67. (in Russ.)
48. Gorbatiykov AV, Rogozhin EA, Stepanova MY, Kharazova YV, Andreeva NV, Perederin FV, Zaalishvili VB, Melkov DA, Dzeranov BV, Dzeboev BA, Gabaraev AF (2015) The pattern of deep structure and recent tectonics of the greater Caucasus in the Ossetian sector from the complex geophysical data. *Izv Phys Solid Earth* 51(1):26–37
49. Rogozhin E, Gorbatiykov A, Zaalishvili V, Stepanova M, Andreeva N, Kharazova Y (2015) New data on the deep structure, tectonics, and geodynamics of the greater Caucasus. *Dokl Earth Sci* 462(1):543–545

50. Zalishvili VB, Nevskaya NI, Nevskii LN, Trofimenko SN, Shempelev AG (2012) Deep geophysical investigations in the North Caucasus Federal District: problems of deep geology and geophysics in regional investigations about the zone of the alleged Ardon inter-block fault. *Geol Geophys S Russ* 12(2):11–20. (in Russ.)
51. Gazdanov AI (1994) Report on thematic work BI-4/313/397: “analysis of the state of exploration of the western part of mountain Ossetia within the Uruk, Shtulu-Khars and Buron-Sauhokh ore districts for 1986–1993”. *Vladikavkaz* (in Russ.)
52. Chotchayev KO, Zaalishvili VB, Nevskii LN, Shempelev AG (2016) Geomorphology as a sign of heredity of the structural features of the Earth’s crust. *Geol Geophys S Russ* 16(1):140–147. (in Russ.)
53. Krisyuk IM et al (1986) Report on the topic № 623/86 prognostication of hydrocarbon accumulations in deep-drenched zones of the Terek-Caspian trough due to their fault-block structure. Funds PGO “Sevkavgeologiya” (in Russ.)
54. Smirnova MN, Brazhnik VM (1980) Report on the topic: investigation of the deep structure of the Chechen, Ossetian and Kabardian depressions in connection with the prospects for oil-bearing. GNR, Grozny (in Russ.)
55. Enna NL (2004) Geology and minerageny of the conjugation zone of the Central and Eastern Caucasus (Interfluve Cherek Balkarsk – Terek): Disertation Cand. Geol.-Mineral. Sciences. RGB, Novocherkassk (in Russ.)
56. Krisyuk IM, Smirnova MN (1966) About the Ardon deep fault. *Proceedings GNI*, 29:28–30 (in Russ.)
57. Tavasiev RA (2010) Ice collapses and their impact on the safety of recreational areas of North Ossetia (Central Caucasus). In: proceedings of the international scientific conference “Sustainable development of mountain areas in the context of global change” [electronic resource] – Vladikavkaz: Publishing House “Terek” SKGMI (GTU), 2010, 19 p. (in Russ.)
58. Akoeva LA, Zalikhanov MCh (1987) Natural phenomena in the Caucasus and their intensification under the influence of economic activity. *Gydrometeoizdat, Moscow* (in Russ.)
59. Kulaev IG et al. (1991) Report “investigation of conditions for the development and activation of exogenous geological processes in the mountainous part of the North Ossetian SSR and Chechen-Ingush autonomous SSR 1986–1991”. *Vladikavkaz* (in Russ.)
60. Agibalova VV (1983) Mudflows in North Ossetia. *Ir, Ordzhonikidze* (in Russ.)
61. Kobayashi S, Izumi K (1991) A study on slush flow disaster. Japan-U.S. Workshop on Snow Avalanche. *Landslide, Debris Flow Prediction and Control*, p 197–205
62. Shreyder P (1989) The avalanche-hazard index. *Ann Glaciol* 13:241–247
63. Zalishvili VB, Melkov DA, Dzeranov BV, Kanukov AS, Gabaraev AF, Shepelev VD (2014) The collapse of the rock-ice avalanche in the area of the Devdorak glacier on May 17, 2014 according to instrumental data. *Geol Geophys S Russ* 14(4):122–128 (in Russ.)
64. Rastvorova VA (1973) The formation of the mountain relief on the example of North Ossetia. *Moscow* (in Russ.)
65. Goncharenko OA (2012) The report “Engineering and geological surveys on the object: The project of creating a tourism cluster in the North Caucasus Federal District, Krasnodar Territory and the Republic of Adygea”. All-Season Tourist and Recreational Complex “Mamison”, *Vladikavkaz* (in Russ.)
66. Rogozhin EA (2009) Seismotectonics of the central sector of the greater Caucasus as a basis for seismic monitoring and hazard assessment. *Bull Vladikavkaz Sci Cent* 9(4):16–22. (in Russ.)
67. Toshihisa A, Nobuyuki Y, Makoto K (1993) Stability of slopes in sedimentary soft rocks. *Res. Activ. Civ. Eng. and Relat, Fields Kyoto Univ.*, 1989–91. Kyoto, 79p
68. Sheko AI (1980) The main patterns of formation and prediction of mudflows. *Moscow* (in Russ.)
69. Baoping W (1996) The state of the art and trend of the landslide predictions. *Daxue qianyuan Earth Sci Front* 3(1):87–91

70. Kelsey HM et al (1996) Geomorphic analysis of streamside landslides in the Redwood Creec basin, northwestern California. *Int J Rock Mech Mining Sci Geomech* 33(7):292
71. Chotchaev KhO., Zalishvili VB, Nevskii LN, Shempelev AG (2016) Geomorphology as a sign of heredity of the structural features of the Earth's crust. *Geol Geophys S Russ* 16(1):141–158 (in Russ.)
72. Zalishvili VB, Nevskaya NI, Makiev VD, Melkov DA (2005) Interpretation of instrumental data of the Kolka glacier collapse process on September 20, 2002. *Bull Vladikavkaz Sci Cent Russ Acad Sci RNO-A* 5(3):43–54. (in Russ.)
73. Berger MG (2007) Three glaciodynamic motions and four gas-dynamic ejections of the Kolka glacier. Little-known pages and discussion questions of the history of the development of a pulsating glacier. *KomKniga/URSS, Moscow* (in Russ.)
74. Berger MG (2007) Kolka glacier: the catastrophe of September 20, 2002 – a sudden gas-dynamic ejection of a glacier. *Publisher LKI/URSS, Moscow* (in Russ.)
75. Chotchayev KhO (2007) Periodic gatherings of the Kolka glacier – a consequence of tectonic activity. In: Abstracts of the International Scientific and Practical Conference “Dangerous natural and anthropogenic geological processes in the mountainous and foothill territories of the North Caucasus”. September 20–22, 2007, Vladikavkaz. p 35–36 (in Russ.)

Index

A

Above-Jurassic aquifer, 203, 204, 206, 207, 217
Accelerograms, 459, 463–465
Accumulating reservoirs, 179
Acoustic noise, 101
Active scree processes, 517
Afro-Arabian mantle plume, 387, 388
Aftershock localization, 475
Aifantis's equations, 219, 223
Aifantis's theory, 220
Air temperature, 115, 116
Akhs kaya suite, 179
Alpine and Pacific belts
 geological-geophysical features, 402
 mechanical-mathematical models (*see* Mechanical-mathematical models)
Alpine-Himalayan belt, 393, 402
Alpine-Himalayan mountain-folded belt, 348
Alpine zone, 392
Amur basin, 128
Andaman mega-earthquake, 489
Andean geosyncline, 473
Andesite-dacite tuff-lava volcanogenic formation, 44
Angola-Brazil Geotraverse, 161
Angular velocity, 109, 173
Anomalous compressive stresses, 475
Anthropogenic activities, 203
Anthropogenic load, 194
Anti-Caucasian strike, 39
Anti-icing reagents (CaCl₂), 206
Antipayata gas emission crater (AntGEC), 88
A priori, 259

Arabian Plate, 348
ArcGIS Online account, 342
ArcGIS system, 341, 346
Archie formula, 66
Ardon deep fault, 53, 54, 57–59
Artificial channel, 259
Artificial hypothesis, 220
Asthenosphere upwelling, 32
Asthenospheric flows, 397
Asthenospheric reservoir, 174
Asymmetry
 geothermal, 160, 163, 167, 173, 175
 heat flow, 165, 171
 MOR (*see* Mid-oceanic ridge (MOR))
 structural, 166
 tectonic processes, 163
Atlantic Ocean
 northern Earth hemispheres, 159–175
 southern Earth hemispheres, 159–175
Authentic geological-geophysical material, 394
Avalanches, 393, 524, 525

B

Back-arc areas, 145
Back-arc basins, 140, 143–147, 151
Back-arc spreading, 152
Baikal, 346
Baikal rift zone (BRZ), 365, 373
Baltic geodynamic areas, 433
Barenblatt's particular medium model, 220
Barenblatt's theory, 223
Barrier algorithm, 443

- “Barrier-3” algorithm
 - Caucasus, 447–449
 - characteristics, 446
 - definition, 443
 - EPA problem, 450
 - EPA recognition procedure, 450
 - epicenters, 449
 - fuzzy set, 451
 - idea and construction, 450
 - joint recognition, 450
 - lineament intersections, 448
 - low seismicity class, 448
 - morphostructural lineaments, 444
 - recognition module, 446
 - Basaltoid magmatism, 49
 - Basalt volcanism, 402
 - Basement age, 144
 - Batholiths, 354
 - Bathymetric map, 166
 - Bathymetry data, 163
 - Bazhenov clay Formation (J_3-K_1), 346
 - Bazhenov formation, 181
 - Belorechensk complex, 49–51
 - Benioff-Zavaritsky zone, 478
 - Bhuj earthquake, 487
 - Bhuj mainshock, 488
 - Big Data, 337
 - Bioaccumulated limestones, 183
 - Biot equations, 236
 - Biot model, 219, 221–223, 260
 - Birazsang, 59
 - Bitlis-Zagros Fault (BZF), 381
 - Black and Caspian Seas, 393
 - Black sea, 28, 33
 - Blind Tanadon massif, 37
 - Borehole temperature measurements
 - applications, 101
 - FTC (*see* Free thermal convection (FTC))
 - infrared thermography, 106–108
 - numerical simulations, 102–105
 - Rayleigh numbers, 101
 - suppressing convection, 109–111
 - temperature noise estimation, 108–109
 - water-filled boreholes, 101
 - Bouguer gravity anomaly map, 75
 - Boussinesq approximation, 102
 - Brazilian wing, 163
- C**
- Calc-alkaline melts, 385
 - Calc-alkaline volcanics, 385
 - Canary-Bahamian Geotraverse, 167–169
 - Cape basin, 164
 - Carboniferous, 120, 200, 201
 - Carter leakage model, 266
 - Cartesian coordinate system, 236
 - Caspian geodynamic areas, 433
 - Catastrophic mudflows, 518
 - Caucasian-Arabian segment, 388, 389
 - Caucasian-Arabian Syntaxis (CAS)
 - arc-like tectonic domains, 381
 - deep-seated structure, region, 384
 - difffluence material, 383
 - geological features, 382, 383
 - geophysical data, 383, 387
 - location, 382, 388
 - mantle plume, 387
 - modern plume-related volcanism, 385, 386
 - modern volcanism, 385
 - Neogene-Quaternary volcanic belt, 388
 - NS-trending positive isostatic anomaly, 381, 388
 - seismic tomography data, 387
 - Caucasus region
 - geodynamics, 392
 - geological and geophysical data, 392
 - geothermy, 393
 - lithosphere, 398
 - mechanical-mathematical modelling, 398
 - modern vertical movements, 392
 - seismotomographic cross-section, 399
 - thermal field, 393
 - Cenozoic volcanic belts, 128
 - Central Caspian, 431
 - The Central Caucasus
 - Alpine orogenesis, 499
 - deep faults, 36
 - Devdorak glaciers, 500
 - eastern segment, 43, 45–47, 50
 - endogenous geodynamic activity (*see* Endogenous geodynamic activity, Central Caucasus)
 - exogenous geodynamic processes (*see* Exogenous geodynamic processes, Central Caucasus)
 - geodynamically active zones, 59
 - geodynamic environment, 499
 - geosuture, 499
 - glaciodynamics, 500
 - Kolka glaciers, 500, 502
 - Mamison-Kazbek relic scar, 499
 - seismicity, 500
 - southern syncline, 44
 - structure, 39
 - tectonic factor, 500
 - Western Caucasus, 47

- Central-Finland, 431
 - Central Hokkaido–Sakhalin narrow zone, 135
 - Central Russian geodynamic areas, 433
 - Chikoi basin, 373
 - Chilean–Argentinean Andes, 473
 - The Chilean swing, 470
 - Chilean type, 147
 - Chloride–hydrocarbonate groundwater, 204
 - Cimmerian folding zone, 43, 44
 - Clapeyron slope, 9
 - Classical EPA-dichotomy algorithms, 442
 - Climate factor, 115–119
 - Closest point (CP) projection, 269
 - Cluster Analysis Toolbox, 342
 - “Clustering.tbx” script toolkit, 342
 - Coal-mining regions of Russia, 197
 - Coarse-grained non-porphyry granites, 50
 - Cold descending convective flows, 20
 - Cold stone plates, 20
 - Collapsing masses, 517
 - Collision-folded systems, 123
 - Compensatory groundwater regime, 198
 - Compensatory hydrodynamic regime, 192
 - Continental collision, 383, 389
 - Continental crust permeability, 486
 - Continent–ocean transition, 123, 124, 127–130, 132, 134, 135
 - Convective cells, 102
 - Cora-3 algorithm
 - Caucasus, 450
 - EPA, 442, 450
 - epicenters, 449
 - fuzzy set, 451
 - high seismicity, 448
 - morphostructural zoning, 450
 - non-dynamic applied dichotomy problems, 450
 - subclasses, 442
 - training material, 446
 - training objects, 448
 - Coriolis force, 159, 173–175
 - Coupled problem, 219
 - Cramer–Welch criterion, 160, 161
 - Cretaceous rocks, 200
 - Crozet–Mozambique Basin, 161
 - Cryolithozone, 96, 97
 - Crystallization, 469
 - Cylindrical coordinate system, 226, 238
- D**
- Data integration, 338
 - Data reliability, 338
 - Data Science, 349
 - Deep faults
 - Ardon deep fault, 53, 54, 57–59
 - the Central Caucasus, 36
 - magmatism manifestation, 52
 - mantle sphere, 59
 - Deep heat flow, 36
 - calculation, 180, 181
 - density, 179, 180
 - hydrocarbon fields, 179
 - Ostaninskoe group of fields, 183–187
 - research, 179
 - Yamal, 181–183
 - Deep mantle plumes, 20
 - Deep reservoir, 67
 - Deep-sea trenches, 135
 - Dehydration, 149, 150, 152
 - Density, 180
 - Deryugin and Kuril basins, 417
 - Devonian–Lower Carboniferous, 183
 - Diabases, 48
 - Diapir, 25, 26, 33, 391
 - Dimensionless variables, 244–246
 - Dirichlet boundary condition, 263, 268
 - Discrepancy, 181
 - Discrete mathematical analysis (DMA), 342
 - Dislocation creep mechanism, 8
 - Dislocation viscosity, 9
 - DMA-based clustering algorithms, 342
 - Donskaya moraines, 201
 - Double porosity, 219–222, 224, 226, 228–230
 - Drainage elasticity modulus, 239
 - Drift, 499, 520, 527
 - Drinking water, 200, 201, 203, 217
 - Dry boiler, 38
 - Dynamic data, 339
 - Dynamic interface conditions, 265
 - Dynamometamorphic formations, 370
 - Dzhida–Uda rift, 367
 - Dzhimara–Godtanadag fault, 46
- E**
- Earth crust, 351–353, 355, 356, 361, 364, 367, 370, 371, 373, 374, 495
 - Earthquake converted-wave method (ECWM), 47, 500, 508
 - Earthquake-prone areas (EPA) recognition algorithm, 441
 - “Barrier-3” algorithm, 446, 450, 451
 - Caucasus (*see* EPA in Caucasus $M \geq 6.0$)
 - classification errors, 443
 - “Cora-3” algorithm, 442, 448

- Earthquake-prone areas (EPA) recognition (*cont.*)
 - dynamic, 449
 - geological and geophysical characteristics, 444
 - GIS-oriented database, 450
 - informativity, 444
 - limitary recognition problem, 442
 - morphostructural zoning, 442
 - pattern recognition block, 450
 - pattern recognition problem, 441
 - posteriori independent verification, 441
 - reliability, 443
 - rule, 442
 - seismic zoning, 441
 - seismicity morphostructural nodes, 442
 - vector representation, 444
- Earthquakes, 417, 418, 487, 491, 492, 502–504, 506, 507, 510, 517, 522, 527
 - foci, 475
 - distribution, 419
 - frequency composition, 456–461
- Earth's crust layers research
 - deep layers, 431, 434
 - deformations, 434, 435
 - geodynamic active areas
 - Baltic, 433
 - Caspian, 433
 - Central-Russian, 433
 - Pre-Dniester, 433
 - intermediate layer, 436
 - local structures, 431
 - Moho discontinuity, 432–433
 - near-surface neotectonic structures, 431
 - subvertical tectonic separability, 437
 - thickening and thinning, 431
- Earth's global tectonics theory, 20
- Earth's heat, 3
- Earth's lithosphere inhibits convection, 5
- Earth's mantle
 - convection features, 5
 - core-mantle boundary, 5
 - heat flux, 4
 - heat transfer, 3
 - internal heating rate, 5
 - mass, 4
 - radioactive heat, 4
 - secular cooling rate, 4
 - sphericity, 5
 - temperature gradient $gradT$, 5
 - thermal balance, 4
 - thermal convection, 4
- Earth's surface, 36, 180
- Eastern flanks, 163
- East European platform, 30, 392
- East Pacific Rise, 164, 165, 170
- EBA approximation, 6
- Effective viscosity, 10
- EGS Soultz site, 77
- Elastic components, 235, 241, 243, 244, 247–249, 253, 255
- Elastic deformations, 242
- Elastic equation, 228
- Elastic-isotropic lithosphere cross section, 472
- Elasticity theory, 227, 243
- Electrical conductance mechanisms, 66
- Electrical energy, 38
- Electrical resistivity, 65–67, 69, 75, 77, 78, 374
- Electromagnetic geothermometry, 66, 67
- Elementary volume boundary, 227
- Empirical/semi-empirical formulas, 65
- EM sensors, 67
- Endogenous geodynamic activity, Central Caucasus
 - allochthonous complexes, 505
 - Ardon deep fault, 503–505, 507–509
 - autochthon and para-autochthon complexes, 505
 - collision of the continents, 502
 - deep tectonic disturbances, 502, 504
 - ECWM, 500, 501
 - foundation complexes, 505
 - geomorphological signs, 508
 - geophysical signs, 508
 - Kazbek volcanic center, 501
 - latest tectonic movements, 509, 510
 - material signs, 507
 - MSS, 506
 - Ossetian Basin, 504
 - seismic events, 503
 - seismicity, 509, 510
 - structural-material complexes, microplate-terrains, 502
 - structural-tectonic zones, 502, 503
 - TCM, 500, 501
 - Terek-Caspian foredeep, 508
 - transcaucasian plate, 505
 - Vladikavkaz fault zone, 505–507
- Energy sources, 35
- Environmentally-friendly energy sources, 35
- EPA in Caucasus $M \geq 6.0$
 - “Barrier-3” algorithm, 445–447
 - comparative analysis, 448
 - “Cora-3” algorithm, 445, 448
 - desired high-seismicity, 448

- epicenters analysis, 449
 - geological and geophysical
 - characteristics, 446
 - high seismicity criteria, 449
 - high seismicity zones, 447
 - lineaments, 448
 - morphostructural lineaments, 445
 - Epibaikalian-Hercynian structural stage, 45
 - Erkuta gas emission crater (ErkGEC), 86, 87, 89, 90, 93
 - Erosion, 36, 521–523
 - Eurasia, 392
 - Eurasian, intercontinental regions, 123
 - Eurasia-Pacific transition zone
 - Cenozoic, 411
 - deep structure, 413
 - geodynamic models, 413
 - Okhotsk Sea region (*see* The Sea of Okhotsk)
 - region, 411, 412
 - Exogenous geodynamic processes, Central Caucasus
 - ecological damage, 512
 - gas-hydrodynamics, 526
 - gas-hydro-geodynamic, 527
 - glacial mudflows, 526
 - HGP (*see* Hazardous geological processes (HGP))
 - ice-stone dam, 526
 - Kolka glacier, 527
 - Mamison node, 512
 - Nizhniy Zaramag, 512
 - postvolcanic gases, 526
 - quaternary formations, 512
 - Transcaucasian highway, 512
 - Zemegondon and Kozydon, 512
 - Explosive processes
 - in permafrost, 83, 85, 93, 96 (*see also* Permafrost)
 - Extended Boussinesq approximation (EBA), 6
 - eXtended Finite Elements Method (X-FEM), 269
- F**
- Feedback, 393
 - Fiagdon complex, 49
 - Filtration components, 244, 249–253, 255, 256
 - Floating continents, 15, 17
 - Flood basalts, 385
 - Fluid circulation paths, 76–80
 - Fluid-conducting clusters, 484
 - Fluid content, 222
 - Fluid-dynamic geosystem, 96
 - Fluid permeability, 221
 - Fluid-rock interaction, 482
 - Fluid thermal conductivity, 102
 - Fluid transfer, 227
 - Fluid viscosity, 221, 236
 - Forecasting techniques, 192
 - Forecast uncertainties, 196
 - Fourier transform, 251
 - Fracture flow model, 260, 263–265
 - Fracture front boundary conditions, 267–269
 - Fracture/medium boundary, 265–267
 - Fracture mid-surface, 260
 - Fracture propagation, 234
 - Fracture space, 223
 - Fracture's vicinity, 243
 - Fracture viscosity, 238
 - Fracture flow model, 263–264
 - Free surface kinematic condition, 395
 - Free thermal convection (FTC)
 - acoustic noise, 101
 - characteristics, 104
 - development, 102
 - infrared thermography, 106–109
 - numerical modeling, 102–105
 - suppression devices, 109, 111
 - temperature noise, 101–103, 108–110
 - thermal effects, 102
 - water-filled boreholes, 101
- G**
- Gabbro-diabases, 48
 - Gabbroids, 48
 - Gas, 179–181, 183–187
 - Gas dynamic geosystem, 96
 - Gas emission crater (GEC), 91–94
 - ErkGEC (South Yamal), 86
 - GEC-1 (Central Yamal), 86, 87
 - GEC-2 (Central Yamal), 86, 87
 - GEC-3 (Central Yamal), 86–88
 - hypothesis, 91–94
 - Osokin's craters, 86
 - SeYKhGEC (North-eastern Yamal), 86, 90
 - in Yamal peninsula, 86
 - YeniGEC, 86, 87, 89
 - Gas emission crater genesis, 91–94
 - Gas-hydrodynamics, 526
 - Gas permeability values, 493
 - Genaldon profile, 58
 - Genetic-statistical method, 196
 - Geochemical transformations, 482
 - Geodynamic active zones (GdAZ), 430–431

- Geodynamic conditions, 140
- Geodynamic models, 413
- Geodynamic processes, 123
- Geoelectric, 374
- Geological-geophysical data, 391, 394
- Geological history, 343, 346
- Geological map of Russia 1:2500000 (VSEGEI), 342
- Geological modelling, 391
- Geological structures, 25
 - Caucasus region, 393
 - comparative analysis, 399
 - geodynamics, 399
 - mechanical-mathematical modelling, 397
 - origin and evolution, 391, 394, 396
 - plumes, 391
- Geology, 200–202
- Geomechanical effects, 260
- Geomechanics
 - Biot model, 260
 - HF (*see* Hydraulic fracture (HF))
 - reservoir state, 260
- Geometry model
 - media and fracture, 261
- Geophysical Center of the Russian Academy of Sciences, 450
- Geophysics, 394
- Geospatial database, 339
- Geosuture, 499
- Geosynclinals zone, 473
- Geotemperature field, 174
- Geotemperature gradient (DGG), 180
- Geothermal areas, 65–80
- Geothermal circulating system (GCS), 38
- Geothermal depressions, 30
- Geothermal energy, 36
 - production, 276
 - utilization devices, 303
- Geothermal exploration, 123
- Geothermal fluids, 67
 - aqueous NaCl solution, 305
 - density, 305
 - flow characteristics, 303
 - geothermal heat, 303
 - geothermal power plants, 303
 - high pressure measurements, 305
 - Izberbash and Ternair (*see* Izberbash and Ternair geothermal field)
 - Kayakent and Kizlyar (*see* Kayakent and Kizlyar geothermal field)
 - pure water, 304
 - Republic of Dagestan, 276
 - thermodynamic and transport properties, 303–305
 - viscosity, 305
- Geothermal gradient, 36, 37
- Geothermal lithosphere, 125–127, 131, 133, 134
- Geothermal measurements, 165
- Geothermal model, 30, 429
- Geothermal parameters, 135
- Geothermal permeability, 486
- Geothermal power industry, 303
- Geothermal power plants, 303
- Geothermal reservoirs, 67
- Geothermal resources, 276
- Geothermal sources, 36
- Geothermy, 101, 105
 - marginal sea (*see* Marginal sea)
 - Moho temperatures and thickness, 131–134
 - parameters
 - continental part of region, 127–130
 - marginal seas, 131, 132
 - structural-formation zones, 123
 - thermo physical models, 125, 126
- Geotraverses, 161, 175, 421
 - Angola-Brazil, 161, 162
 - Angolo-Brazilian, 162
 - arithmetic mean heat flow distribution, 171, 172
 - Canary-Bahamian, 167–169
 - Cape basin, 164
 - characterization, 165
 - geothermal asymmetry, 174, 175
 - geothermal data, 171
 - heat flow database, 159
 - latitude, 175
 - Indian Ocean, 161
 - location latitude, 174
 - Mid-Atlantic Ridge, 164
 - MOR, 160
 - morphostructure, 162
 - Northern hemisphere
 - Atlantic Ocean, 168, 170, 171
 - Pacific Ocean, 171
 - Southern hemisphere
 - Atlantic Ocean, 161
 - Indian Ocean, 167
 - Pacific Ocean, 165
 - statistical analysis, 175
 - in World Ocean, 160
- GIS-oriented database, 450
- GIS Project
 - comparative study, 346
 - deposits concentration, 344
 - giant provinces, 345
 - hydrocarbon resources, 345
 - narrow mature intervals, 345

- oil and gas deposits, 343
 - Persian Gulf oil and gas province, 348
 - sedimentary cover, 345
 - West Siberian oil and gas province, 346, 348
 - Glacial mudflows, 526
 - Global geodynamics, 3
 - Global thermochemical convection scheme, 21
 - Global thermo-chemical model, 17–21
 - Granitoids, 49–51, 353, 354, 370, 372
 - Gravity data, 75
 - Greater Caucasus (GC), 381, 382, 384, 385, 387, 388, 393
 - Greenhouse gases, 97
 - Green's function, 240
 - Grensdalur area, 72
 - Groundwater chemistry, 199, 200, 203–206, 210, 211, 216, 217
 - Groundwater contamination, 203
 - above-Jurassic aquifer, 206, 207
 - assessment, 203
 - hydrogeological windows, 199, 203
 - oil products, 204
 - Podol'sko-Myachkovskii aquifer, 207–210, 212–214
 - Groundwater infiltration nutrition, 192
 - Groundwater temperatures, 116, 117, 119, 120
 - Growth criterion, 267–269
 - Gydano-Yenisei Epibaikal basin, 348
- H**
- Hazardous geological processes (HGP)
 - Caucasus highway
 - erosion processes, 521
 - landslides, 516, 517
 - landslide-scrree processes, 517, 518
 - mudflows, 518, 519
 - snow avalanches, 520
 - exogenous nature, 510
 - Mamison site
 - avalanches, 524, 525
 - erosion processes, 521–523
 - landslides, 525, 526
 - Sadon-Unalecological node
 - failure, 514
 - landslides, 513, 514
 - man-made landslides and debris, 513
 - mining operations, 511
 - mining sites, 510
 - mudflows, 515, 516
 - Heat carrier, 36, 67
 - Heat energy, 38
 - Heat flow (HF), 355, 371, 414–416
 - asymmetry (*see* Asymmetry)
 - in axial zone, 143
 - distribution, 125, 139–145, 151
 - island-arc systems (*see* Island-arc) and marginal seas (*see* Marginal sea)
 - measurements, 125, 135, 139, 160
 - Ostaninskoe group of fields (Tomsk Region), 183–187
 - Yamal, 181–183
 - Heat flux
 - density, 5
 - regional average values, 140
 - Heat generation, 125
 - Heat sources, 70–76
 - Heat transfer mechanisms, 76–80, 135
 - Heavy metals, 195
 - Helix pitch, 107
 - Hellisheidi (He) area, 70
 - Hemming, 442
 - Hengill, 67, 70–75
 - H-horizon, 68, 69
 - High-temperature steam-water mixture, 37
 - Homogeneous areas, 203
 - Host medium, 261–263
 - Hromundartindur area, 72
 - Husmuli area, 72
 - Hveragerdi (Hv) area, 70
 - Hydraulic fracture (HF)
 - analytical investigation, 235
 - artificial, 257
 - boundary layer, 227–229
 - characterization, 237
 - chemical and physicochemical processes, 235
 - coupling scheme, 254
 - crack, 225–227
 - elastic components, 235, 253
 - external problem, 236–243
 - filtration components, 253
 - flow components, 235
 - hydro-driven cracks, 233
 - identical transformations and natural simplifications, 235
 - incomplete coupling, 235, 236
 - internal problem, 252
 - KGD model, 234
 - magmatic fracture, 233
 - mathematical model, 260
 - oil and gas production, 259
 - in oil reservoirs, 256
 - physical and mathematical description, 259
 - poroelastic environment, 233

- Hydraulic fracture (HF) (*cont.*)
 poroelastic medium, 234, 252
 quantity, 235
 self-consistent description, 233
 self-similar solution (*see* Self-similar solution)
 and simulation, 234
 software packages, 234
 specific features, 243
 structural features and dynamics, 256
 three-dimensional self-consistent formulations, 259
 toughness model, 234
 uncoupled components, 235
- Hydraulically coupled system, 194
- Hydrocarbon, 424
- Hydrochloric-alkaline waters, 507
- Hydrocarbon deposits, 345
- Hydrocarbon fields, 179
- Hydrocarbon generation, 179
- Hydrocarbon production technologies, 233
- Hydro-driven cracks, 233
- Hydrodynamic methods, 196
- Hydrodynamic regime
 flood indicator, 191
 forecast errors, 195–197
 forming factors and conditions, 192, 193
 mine water balance, 191
 patterns, 192–194
 undermining effects, 194, 195
- Hydrogeological forecast, 191, 192, 198
- Hydrogeological windows
 areas, 200
 filtration time, 199
 and geology, 200–202
 groundwater chemistry, 203–206
 groundwater contamination, 199, 203
 large-scale mapping, 199
 mapping, 199
 normal/lognormal distribution law, 203
 of II order (vertical filtration time is less than 1000 days), 212, 214
 of III order (vertical filtration time is less than 15 years), 212, 213, 215
 of IV order (vertical filtration time is less than 25 years), 214
 of V order (vertical filtration time is less than 50 years), 214, 215
 of VI order (vertical filtration time is less than 100 years), 215, 216
- Podol'sko-Myachkovskii aquifer (*see* Podol'sko-Myachkovskii aquifer)
- RFB, 200
- sites, 200
- SPSS® software, 203
- tectonic features, 201, 202
- territory, 216
- Hydrothermal activity, 140, 141, 143, 145, 151
- Hydrothermal processes, 65
- Hydrothermal reservoirs, 67
- Hydrothermal resources, 56–58
- Hydrothermal springs, 36
- Hypothetical, 37
- Hypsometric marks, 194
- I**
- Incomplete coupling, 219, 220, 230, 235, 236, 240, 256
- Incompletely coupled equations, 233–257
- Indian Ocean, Southern Earth
 hemispheres, 165–167
- Indirect electromagnetic geothermometer, 66, 67, 70, 76
- Indirect geothermometers, 65, 66
- Infrared thermography, 106–109
- In situ permeability measurements, 482, 495
- Intercontinental regions of Eurasian, 123
- Interface conditions, 265–267
- Internal region, 237
- Internal seismic boundaries, 394
- Intra-annual dynamics, 198
- Irwin condition, 246
- Irwin's criterion, 226, 227
- Island-arc
 back-arc basins, 140
 basement age, 144
 characteristics, 139
 geodynamic and thermomechanical processes, 145–152
 geological data, 140
 geothermal field, 144
 lithosphere, 144
 magmatic series, 149
 magmatism, 152
 Manus basin, 143
 plate tectonics, 140
 seafloor spreading, 140, 143
 sedimentation, 143
 subduction models, 144
 tectono-thermal regime, 152
 water circulation, 143
 young back-arc basins, 143
- Islands of heat, 115
- Isopachytes, 434

- Ivolga-Uda basin, 366, 367
- Izberbash and Ternair geothermal field
- adiabatic coefficient, bulk
 - compressibility, 326
 - carbon dioxide content, 313
 - chemical compositions, 310–312
 - components, geothermal samples, 311, 313
 - correlation models
 - density, 309, 319–321
 - speed of sound, 309, 319–321
 - viscosity, 309, 319–321
 - dissolved gases, 313
 - enthalpy difference, geothermal fluids, 329
 - geothermal brine samples, 313
 - high pressure prediction models
 - aqueous salt solutions, 321
 - density, 321–324
 - speed of sound, 321–324
 - viscosity, 321–325
 - ions, 318
 - location, 310
 - measurements
 - density, 306, 307, 309, 314, 317, 318, 325, 327–329
 - speed of sound, 309, 315, 317, 318, 325, 327–329
 - viscosity, 308, 309, 315, 317, 318
 - pure water, 306
 - salt concentrations, 317
 - salt ions, 305
 - systematic measurements, 307
 - temperatures, 306, 307, 318
 - thermal expansion coefficient, 326
 - thermal pressure coefficient, 326
 - thermodynamic properties, 307, 308, 310
 - wells characteristics, 310
- K**
- Karel-Finnish down lift, 431
- Kayakent and Kizlyar geothermal field
- aqueous salt, 278
 - chemical compositions, 279, 281–284
 - component, 277
 - correlation models
 - density, 280, 289–291, 293
 - speed of sound, 280, 289, 290, 293
 - viscosity, 278, 289–294
 - geographical location, 281
 - geothermal wells, 280
 - high pressure prediction models
 - densities, 295, 296
 - speed of sound, 294
 - thermodynamic and transport
 - properties, 294, 295
 - viscosity, 292, 294–296
 - location, 282
 - measurements, 278
 - density, 284–288
 - speed of sound, 285–288, 290
 - viscosity, 285–289
 - prediction models, 278
 - pure water, 279
 - sodium chloride solution, 279
 - systematic measurements, 279
 - thermodynamic and transport properties
 - density, 276, 277
 - enthalpy, 277
 - experimental study, 279
 - geothermal energy, 276
 - geothermal resources, 277
 - geothermal systems, 276
 - heat capacity, 276, 277
 - pure water, 277
 - temperature, 276, 279
 - viscosity, 277
 - viscosity, 280, 294
- Kazbek volcano, 56
- Khamar-Daban block, 365
- Ivolga-Uda basin, 366, 367
 - Khamar-Daban range, 366
- Khamar-Daban Range, 366
- Khilok-Chikoi basin, 371, 372
- K-horizon, 68
- Khristianovich-Zhel'tov-Geertsma-De Klerk (KGD) model, 234
- Kizelovsky coal basin, 195
- The Kolka glacier, 500, 502, 527
- Kolmogorov-Smirnov/chi-squared test, 203
- Kuril basin, 423–425
- L**
- Laboda-Karaugom fault, 45
- Laboda-Tsmiakom subzone, 45, 46
- Lag, 234
- Landslides, 513, 514, 516, 517, 525, 526
- Landslide-scree processes, 517, 518, 522
- Large Low Shear Velocity Provinces (LLSVP), 18
- Late Cenozoic mafic magmatism, 128
- Lateral erosion, 521
- Linear elastic fracture mechanics, 267
- Linearly elastic media models, 260
- Liquidated mines, 192
- Liquidation, 194

- Lithosphere cooling, 140, 141,
144–147, 149–151
- Lithospheric magnetic anomalies, 444
- Lithospheric plate tectonics theory, 14
- The local geodynamic active zones*
(secondary), 430–431
- Localization zone, 475
- Logarithmic time scale, 491
- Longitudinal coordinate, 250
- Long-term amplitude in groundwater
temperatures, 120
- Long-term shear deformation, 12
- Long-term temperature amplitudes, 118
- Long-term temperature fluctuations, 105
- Lower and Upper Cretaceous, 346
- Lower Karmadon, 59
- Lower-Karmadon mineralized thermal
waters, 56
- M**
- Magmatic fracture, 233
- Magmatic stream, 175
- Magmatism, 385
- Magnetic field, 416, 417
- Magnetotelluric sounding (MTS), 76, 509
- Barguzin igneous province, 359
- Chikoi basin, 373
- components, 357
- conductive layer roof depth vs. heat flow
 value, 352
- conductivity, 352
- deep electrical conductivity distribution
 features, 353
- deep geoelectric section, 364
- deep rift faults, 358
- Earth crust, 351, 352, 355, 356, 361
- ELAS program, 351
- geoelectric characteristic, Earth deep
 section, 351
- geoelectric inhomogeneities, 352
- geological setting, 353–355, 360
- heat flow, 352
- heterogeneity parameter, 358
- Khamar-Daban block, 365–367
- Khilok-Chikoi basin, 371, 372
- lithosphere, 352
- Malkhan block, 372
- MV, 361
- Phoenix Geophysics software, 357
- Selenga block, 362, 364, 365
- Selenga River Delta, Krasnyi Chikoi
 Village, 351, 353, 363
- semicharacteristic MT curves, 360
- Tsagan-Daban block, 367
- Tugnui block, 368–370
- Western Transbaikalia, 361, 362
- Zagan block, 370, 371
- Magnetovariational (MV) sounding, 66, 361
- Main Caucasian Fault (MCF), 381–383, 388
- Malkhan block, 372
- Malkhan ridge, 374
- Mamison-Kazbek relic scar, 47–49
- Mamison-Kazbek zone, 48
- Mantle convection
- equations, 6, 7
- floating continents, 15, 17
- Mantle-derived magmas, 385
- Mantle intrusions, 36, 57, 59
- Mantle lithosphere, 429
- Mantle parameters
- activation energy value, 8
- characteristic values, 7
- convection equations, 7
- dimensional coefficient, 7
- lithostatic pressure, 9
- power function, 9
- pressure and temperature, 8, 9
- viscosity, 7
- Mantle plume, 381, 384–389
- Manus basin, 143
- Map of the Boundaries of Hydrogeological
 Windows, 203
- Marginal seas, 131, 132
- basins, 140
- geothermics, 139
- heat flow and age, 140–142
- and island-arc systems (*see* Island-arc
 systems)
- mechanism of formation, 144
- Mariana type, 147
- Marine regime, 181
- Mass conservation equation, 262
- Mass flux, 269
- Mass transfer
- hydrogeological windows (*see*
 Hydrogeological windows)
- Massif
- crystallization, 38
- Darial, 47
- Shaikhokh, 46
- Material resources, 35
- Maximum paleothermometer, 181
- Mechanical boundary conditions, 263
- Mechanical coupling, 17
- Mechanical-mathematical modelling, 33
- asthenosphere diapir, 407
- balance of mass, 406, 407

- Caucasus region, 398
 - characteristic parameters, 405
 - crust and mantle lithosphere layers, 406, 407
 - deep depression formation, 408
 - discontinuity equation, 404
 - Frude number, 404
 - geological and geodynamic reconstruction, 398
 - geological-geophysical data, 397
 - geological region evolution, 401
 - geological structures, 401
 - lithosphere evolution, 408
 - lithospheric deformations, 403
 - Moho boundary, 404
 - Navier-Stocks equation, 404
 - numerous geological structures, 403
 - problems, 391
 - Reynolds number, 404
 - seismotomography, 398
 - Strukhal number, 405
 - velocity, 405–407
 - Mediterranean Sea, 145
 - Mega-anticlinorium, 43
 - Melt crystallization, 37
 - Mesopotamian Trough, 348
 - Mesozoic–Cenozoic belts, 128
 - Mesozoic–Cenozoic sedimentary, 181
 - Mesozoic–Cenozoic superimposed, 123
 - Mesozoic–Cenozoic waters, 54
 - Mesozoic orogenic belts, 127
 - Mesozoic riftogenic structures, 374
 - Metamorphic fluids, 481
 - Method of seismic sounding (MSS), 55
 - Microcracks, 12, 484, 493
 - Microfracturing, 495
 - Microseismic sounding (MSS), 506
 - Midagrabin, 37
 - Mid-Atlantic Ridge, 163, 167–170
 - Middle Jurassic oil and gas complex (OGC), 181
 - Middle Miocene–Early Pliocene, 181
 - Mid-oceanic ridge (MOR)
 - and abyssal basins, 159
 - and asymmetry, 159, 160
 - Coriolis force, 159
 - Cramer–Welch criterion, 160, 161
 - geological and geophysical models, 159
 - Geotraverse, 160, 161
 - Northern Earth hemispheres (*see* Northern Earth hemispheres)
 - Southern Earth hemispheres (*see* Southern Earth hemispheres)
 - Mine flooding forecasts, 191
 - Mining
 - coals, 194
 - deposits, 191
 - hydrogeological forecasts, 191
 - plans reliability, 197
 - technology, 197
 - underground, 196
 - water conductivity, 198
 - Mixed magmatism, 385
 - Modeling geothermal wells, 277, 304
 - Modern geographic information system, 341
 - Modern magmatism, 384
 - Modern volcanism, 385
 - Moho discontinuity, 432–433
 - Moho surface, 163
 - Moho temperatures and thickness, 131–134
 - Molten mantle diapir, 394
 - Morphostructural lineament intersections, 444, 445
 - Morphostructural zoning, 445
 - Morphostructures, 162
 - Moscow, 115–120
 - Moskovskaya moraines, 201
 - Moskva River, 201
 - Mudflows, 515, 516, 518, 519, 523
 - Multilayered continuous medium, 25
- N**
- Natural explosions, 84
 - Natural-technogenic system, 198
 - Navier-Stocks equations, 25, 394
 - Near-field rock permeability, 481
 - Near-surface neotectonic structures
 - deep structures, 437
 - deformations, 437
 - Fennoscandian shield, 437
 - geodynamic connection, 437
 - Pan-regional, 437
 - Neighborhood (NLC), 448
 - Neogene–Quaternary sediments, 348
 - Neo-intrusions, 37
 - Neo-intrusive massifs, 38, 54
 - Nesjavellir (Ne) area, 70
 - Neumann boundary conditions, 266
 - Neumann homogeneous, 263
 - Neutral layer, 120
 - Newtonian liquid, 220
 - Newtonian viscosity η_a , 8
 - Nondeep basins, 27
 - Non-deformable upper boundary, 13
 - Nondrainage and drainage volume moduli, 254
 - Non-drainage mode, 240, 241

- Non-isothermal flow effects, 264
 Nonlinear Earthquake site Response Analyzes
 (NERA) program
 acceleration values, 460
 accelerogram, 459, 460, 463, 464
 calculating seismic impacts, 458
 fundamental period, 458
 seismic-geological model, 458
 Nonlinear system, 17
 Non-observed values, 222
 Non-renewable energy resources, 35
 Non-uniform lithosphere, 469
 Normal/lognormal distribution law, 203
 North China sedimentary basin, 128
 Northern earth hemispheres
 Atlantic Ocean, 167–171
 Pacific Ocean, 170, 171
 Northern Mongolia-Western Transbaikalia
 (NMWT), 355
 North Sakhalin sedimentary basin, 424
 Numerical boot-strap method, 492
 Numerical modeling, FTC, 102–105
 Numerical simulations, 102–105
- O**
- Oceanic lithosphere floats, 472
 Oceanic lithospheric plates, 12
 Oil, 179–181, 183–187
 Oil and gas condensate field (OGCF), 85
 Oil and gas industry establishment, 339
 Oil-gas generation zones, 33
 Oka-Don lowland, 437
 Oligocene-Lower Miocene, 348
 Olistoblocks, 48
 Olistostrome, 48
 Olivine-wadsleyite transition, 9
 1D basin modelling, 180
 One-dimension boundary layer, 226
 Open pit mining, 191
 Ophiolite sections, 168
 Optimal consistency, 181
 Orogene under pressure, 397
 Orogene under stretching, 397
 Orogenic belts, 127
 Ostaninskoe group of fields, 183–187
- P**
- Pacific Ocean
 Northern Earth hemispheres, 170, 171
 Southern Earth hemispheres, 164, 165
 Paleoclimate factor, 180
 Paleogene tectonic processes, 411
 Paleogeography conditions, 346
 Paleozoic–Cenozoic accretion, 123
 Paleozoic section, 348
 Paleozoic sedimentary rocks, 200
 Paleozoic Selenga–Stanovoy orogenic
 belt, 127
 Paleozoic volcanic fields, 128
 Parabolic diffusion equation, 220
 Permafrost
 drilling operations, 85
 exploration and subsurface mining
 operations, 84
 gas emissions, 85
 gas permeable zones, 94
 KRIOS company, 85
 local heating, 95
 thickness, 85, 95
 from YeniGEC, 89
 Permeability
 continental crust
 characteristic anomalies, 495
 earthquake, 495
 experimental values, 493
 gas permeability values, 493
 geological data, 481
 in situ permeability measurements,
 482, 495
 laboratory data, 482, 483, 485–487
 measurements, 495
 metamorphic processes, 495
 microcracks, 493
 near-field rock, 481
 physical properties, rocks, 481
 pore radius distributions, 494
 radioactive waste disposal, 494
 rock permeability, 481, 482
 seismological data, 487, 489, 491, 493
 surface-active fluid, 493
 temperature dependences, porosity,
 493, 494
 behavior, 483
 dependencies, 483, 485
 values, 491
 Perovskite-postperovskite transition, 18
 Persian Gulf oil and gas province, 348
 Perturbations, 225, 238
 Petroleum Geology, 179
 Petrothermal resources
 Belorechensk complex, 49–51
 the Central Caucasus (*see* The Central
 Caucasus)
 Cimmerian folding zone, 43, 44
 feasibility, 37
 geological map, 43, 44

- Mamison-Kazbek relic scar, 47–49
 rift-related margin of the continent, 39
 Shaukhokh-Darial elevation, 46, 47
 structural and material complexes, 38, 39
 Taymazy-Labagom elevation, 45, 46
 tectonic localization of thermal
 medium, 52–56
 TLP, 38
 Ullukamsk complex, 51, 52
 volcanogenic formations, 49
 Phases continuity, 223
 Phase transition, 7
 Piezoconductivity, 239, 242, 245, 247, 249
 Piezoelectricity, 249
 Piles, 17
 Plane deformation equation, 238
 Planetary differentiation, 469
 Plane variant, 237
 Plate tectonics, 140
 Plumes, 10, 11, 20
 Podol'sko-Myachkovskii aquifers, 200, 201,
 203, 204, 206–210, 212–214, 217
 Poisson equation, 227, 240
 Poisson's ratio, 226, 238
 Pore pressure, 226
 Pore radius distributions, 494
 Poroelastic environment, 233
 Poroelasticity, 236, 240, 241, 243, 255
 Poroelastic medium, 234, 235, 239, 265, 266
 analogous system, 228
 artificial hypothesis, 220
 Barenblatt's theory, 223
 coefficients, 221
 and double porosity (*see* Double porosity)
 elementary volume deformations, 222
 fluid pressure, 224
 fracture space, 223
 and fracture systems, 220
 homogeneous, 224
 incomplete coupling principle, 219, 220
 mechanic equations, 221
 Newtonian liquid, 220
 non-observed values, 222
 one-dimension boundary layer, 226
 Rice's thermodynamic considerations, 223
 stress state, 224
 tensile fracture, 226
 and thermodynamics, 219
 Poroelastic model, host medium, 261–263
 Poroelastic processes, 236
 Poroelastic reservoir, 264
 Porphyroblastic granites, 50
 Possible Seismic Source (PSS) zones, 53
 Postperovskite phase, 18, 19
 Post-volcanic gases, 526
 Precambrian blocks, 127, 135
 Precambrian crystalline rocks, 200
 Precambrian platforms, 123
 Pre-Caspian Depression
 geological selection, 27
 geothermal zones, 29
 gravimetric model, 32
 heat flow, 29
 lithosphere structure, 31
 mantle diapir, 26
 multilayered medium, 30
 oil and gas deposits, 29
 sedimentary cover, 26
 subsalt deposits, 28
 temperature distribution, 30
 Predictive-mineragenic map of Russia
 1:2500000 (VSEGEI), 342
 Pre-Dniester geodynamic area, 433
 Primorye, 194
 Principal component analysis (PCA)
 groundwater chemistry, 211
 hydrogeological windows (*see*
 Hydrogeological windows)
 varimax method, 211
 Principal tectonic elements, 348
 Program "PSEQGN", 463, 465
 Proluvial-deluvial sediments, 519
 Pulsations, 11
 Pulse wave-like fluid propagation, 489
 γ PZ3 U, 51, 52

Q
 Quasi-equilibrium, 262
 Quasi-stationary plumes, 11
 Quasi-turbulent convection, 3
 Quaternary rocks (Q), 200, 448

R
 Radioactive isotopes, 3, 4
 Radioactive waste disposal, 494
 Radiogenic heat flux, 4
 Raw data, 337
 Rayleigh numbers, 7, 9, 101, 102, 104, 105,
 107–109, 111
 Real modern Earth, 17
 Regularization method, 394
 Relative content of fluid, 239
 Relic scar, Mamison-Kazbek, 47–49
 Renewable energy, 35, 37

- Renewable hydrothermal fluid, 57
- Renewable sources, thermal energy, 37
- Reservoir flow model, 260
- Reservoir state, 260
- Residual Bourger anomaly map, 76
- Resonance
 - extended waveguides, 455
 - NERA (*see* Nonlinear Earthquake site Response Analyzes (NERA) program)
 - soil properties, 455, 456
 - soil stratum effects, 456
- Reykjanes Peninsula Rift (RPR), 70
- Reynolds lubrication equation, 263
- Rheological behaviour, 25
- Rice-Cherepanov J-integral, 260
- Rice's thermodynamic considerations, 223
- Rift-related margin of the continent, 39
- Ringwood-perovskite phase transition, 13
- RNO-A, 37
- Rock microstructure, 484
- Rock permeability, 481, 482
- ROSA database
 - analytical studies, 338
 - ArcGIS, 341, 342, 344
 - attribute tables, 338
 - data collection, 338
 - data integration, 338
 - data reliability, 338
 - development stages, 339
 - dynamic unit parameters, 340
 - end-to-end parameters, 340, 341
 - general structure, 339
 - GIS Project (*see* GIS Project)
 - information levels, 339, 340
 - interaction levels, 339, 340
 - open Internet sources, 339
 - preliminary datasets, 341
 - principles, 339
 - scientific knowledge, 338
 - systematization model, 338
 - systems approach, 338
 - thematic maps, 342
 - unique and unified parameters, 340
- Russian and foreign bibliographic sources, 339
- Russian Federation, 455
- Russian Foundation for Basic Research (RFBR), 200

- S**
- Sakhalin Island, 422, 423
- Sakhalin seismicity, 418
- Salt diapirism, 348
- Salt domes, 30
- Sand-clay Quaternary deposits, 200
- Sandy-argillaceous soils, 118
- Saturated medium, 263
- Scree, 517, 522
- Seabed trenches, 135
- Seafloor spreading, 140, 143
- The Sea of Okhotsk, 144
 - basement rocks, 422
 - Cenozoic, 413
 - crust, 422
 - deep faults, 413
 - Eurasia-Pacific transition zone, 413
 - Geotraverse, 421
 - HF, 414–416
 - Kuril basin, 423
 - lithospheric plate, 413
 - location, 414
 - magnetic field, 416, 417
 - marginal trough, 423
 - northwest pacific basin, 424
 - Paleozoic–Mesozoic crystalline rocks, 413
 - plate structure, 413
 - Sakhalin Island, 422, 423
 - sedimentary basins, 413, 422
 - seismicity, 417, 418
 - structures, 413, 420
 - Tatar Strait, 422
 - upper mantle, 424, 425
 - volcanism, 418, 421
- Sea transgressions, 346
- Secular cooling rate, 4
- Sedimentary basins
 - geothermics
 - basement surface temperature, 27
 - basin evolution, 30
 - convective movements, 28
 - diapir upwelling, 29
 - heat conductivity, 30
 - mantle diapir, 28
 - mechanical equations, 26
 - oil-gas generation, 27
 - paleotemperatures reconstruction, 28
 - Pre-Caspian Depression, 28
 - salt diapirs, 30
 - salt domes, 30
 - temperature distribution, 28
 - three-layer sedimentary, 29
 - pressing surface conditions, 396
 - stretching surface conditions, 396
- Sedimentary cover
 - exogenic chemical reaction, 30
 - thickness, 27–29, 33
- Sedimentary layer, 164

- Sedimentation, 140, 143–145, 151, 180
 - history, 180
 - mass, 180
- Seismic focal zone, 146
- Seismic-geological model, 458, 459, 462–466
- Seismicity, 70–76, 151, 417, 418, 441, 487, 500
- Seismic microzoning, 455, 466
- Seismic velocities, 67
- Seismic waves propagation, 459
- Seismotectonic discontinuities, 510
- Seismotectonic model, *see* South American Plate (SAP)
- Seismotomography, 391, 393, 399
- Selenga block, 362, 364, 365, 374
- Self-consistent description, 233
- Self-consistent mathematical models, 259
- Self-developing gas-dynamic geosystems, 96
- Self-induced hydraulic fracturing, 260
- Self-similar solution
 - elastic components, 247–249
 - filtration components, 249–252
 - fluid flow, 246
 - second (filtration) component, 247
 - three-dimensional space, 248
 - three-dimensional version, 248
 - time and space variables, 246
 - transition to dimensionless variables, 244–246
- Semivariogram model, 208
- Sergeev Institute of Environmental Geoscience, Russian Academy of Sciences (IEG RAS), 199
- Serpentinization, 149, 150
- Serpentinous picrites, 47
- Seyakha crater (SeYkhGEC), 86, 87, 89, 93
- Shallow reservoir, 67, 70
- Shaukhokh-Darial elevation, 46, 47
- Shaukhokh-Darial SFZ, 46
- Shear stress, 5, 146
- Short-term temperature fluctuations, 105
- Silicate mantle, 4
- Simulation, 269–271
- Single pore system, 227
- Small-strain tensor, 236
- Smolensk-Dmitrov-Vetluzhsk zone, 437
- Smolensk-Orel active center, 433
- Snow avalanches, 520
- Society of Petroleum Engineers and Petroleum Resources Management System, respectively (SPE-PRMS), 338
- Soil freezing, 119
- Soil resonance properties
 - frequency-selective response, 456
 - natural high-power layers frequency, 462
 - natural oscillation frequency, 457, 461
 - natural vibration frequency, 457
 - seismic intensity, 457
 - uniform layer, 456
- Soil temperature, 117–119
- Solid-state phase transformations, 5
- Songutidon, 37
- Soultz-sous-Forêts, 67, 76–80
- South American Plate (SAP)
 - Chilean sector, 470
 - deep-water trench traces, 473
 - hypothetical latitudinal section, 470
 - isostatic alignment, 470
 - latitudinal section, 472
 - localization, 471
 - plate boundary, 470
 - Proterozoic folded belt stretches, 470
 - seismotectonic aspects, 476
 - SSS (*see* Stress-strain state (SSS)) stresses, 476
 - western margin, 470, 478
- South Caspian Depression, 28, 33
- Southern Earth hemispheres
 - Atlantic Ocean, 161–164
 - Indian Ocean, 165–167
 - Pacific Ocean, 164, 165
- Southern syncline, 44
- South Icelandic Seismic Zone (SISZ), 70
- South-West Indian Ridge, 165–167
- Spatial statistics, 342
- Speed equation, 268
- SPSS® software, 203
- Srednevasyuganskiy megaswell, 183
- Statistics
 - asymmetry of MOR, 167
 - average values, 168
 - Cramer-Whelch criterion, 163
 - geothermal characteristics, 169
 - Geotraverse (*see* Geotraverse)
 - global heat flow database, 159
 - mean heat flow values, 160
 - Mid-Atlantic Ridge axis, 170
 - sampling, 160
- Stokes momentum transfer equation, 6
- Strain tensor components, 238
- Stress intensity factor, 246
- Stress-strain state (SSS), 261
 - calculation model, 475
 - continent-ocean transition zone, 475
 - elastically deformed model, 473
 - phenomenology, 476
 - SAP western margin, 475, 476
 - simulation, 473

- Stress tensor, 242
- Structural-geodynamic zoning
 areas, 432–434, 436
 earth's crust layers research, 432–433
 geodynamic active centers, 429
 heterogeneous stresses, 429
 research (*see* Earth's crust layers research)
- Strukhal number, 395
- Subclasses, 442
- Subduction
 Black Sea, 145
 Chilean type characterizes, 147
 geological and geophysical parameters, 152
 Mariana type characterizes, 147
 processes, 144–146, 411
 thermal models, 146, 147, 149
 velocity, 147
 zone, 144, 147–149
- Submarine volcano Krylatka, 420
- Submerged plates, 14
- Sub-thrust sedimentary complexes
 distribution, 345
- Super plume, 391
- Supercritical fluids, 69, 70, 80
- Supercritical reservoir, 67–70
- Suppressing convection, 109–111
- Suppression devices, 109, 111
- Surface-active fluid, 493
- Surface heat loss, 3
- Symmetrical divergence mechanism, 171
- System analysis methods, 338
- Systematization model, 338
- Systems analysis, 338
- T**
- Tamisk sanatorium, 57
- Tanadon-Buron subzone, 45
- Tatar Strait, 422, 424
- Taymazy-Labagom elevation, 45, 46
- Technogenic conditions, 197
- Technogenic disturbance, 120
- Technogenic factors, 197
- Technogenic genesis, 194
- Tectonic disturbances, 196–198
- Tectonic earthquakes, 470
- Tectonic localization of thermal medium
 Ardon deep fault, 53, 54
 magmatism manifestation, 52
 PSS zones, 53
 seismological explorations, 52
 velocity model, geological section, 54, 55
 Vladikavkaz fault, 52, 53
- Tectonics of lithospheric plates (TLP), 38, 47
- Tectonic stresses, 36
- Tectonic zoning, 123, 124
- Tectono-magmatic activation, 352, 391, 426
- Tectonosphere, 411
- Telluric current method (TCM), 500
- Temperatures, 358, 359, 483
 dependency, 65
 effects, 105
 estimation, 65
 fluctuations, 105, 108, 110
 model, 70
 monitoring, 101, 106, 108
 noise estimation, 108–110
 profile, 66
 regime, 120
- Tensile fracture, 226
- Tensile stresses, 475, 478
- Tepli volcano, 37, 56
- Terzaghi model, 221
- Thematically oriented database, 337
- Thermal blanket effect, 16
- Thermal conductivity, 102, 125, 146, 180
- Thermal convection
 Earth's lithosphere, 12
 horizontal velocities distribution, 12, 13
 microcracks, 12
 oceanic lithospheric plates, 12, 14
 rigid plates, 12
 subduction, 13
- Thermal decompaction, rocks, 493
- Thermal diffusivity, 125, 172, 180
- Thermal energy, 35–37
- Thermal field, 135
- Thermal subduction models, 146
- Thermal waters, 57
- Thermistors, 102
- Thermobaric conditions, 69
- Thermo-compositional rather than thermo-chemical one, 5
- Thermodynamics, 219
- Thermo-gravimetric model
 asthenosphere upwelling, 32
 geological-geophysical parameters, 32
 heat transfer equation, 30
 lithosphere thickening, 32
 radioactive elements, 31
- Thermo mechanical modeling, 33
- Thermo physical model, 125–126, 180
- Thermostability, 285, 315
- 3D Analyst and Spatial Analyst, 342, 343
- 3-D electrical resistivity model, 73

- Three-dimensional problem, 248
 Three-dimensional space, 236, 248
 3-D temperature model, 70, 73
 Tocopilla earthquake, 477
 Tomsk region, 183–187
 Tomsk Region, 179
 Toughness model, 234
 Transition zone, 123, 131
 Travale, 67–70
 Travale geothermal area, 67, 68
 Tsagan-Daban block, 367
 Tsariit-Tsatadon fracture, 46
 Tsariit-Tsatadon uplift, 46
 Tugnuï block, 368–370
 Tula region, 194
 Tuzo in honor of T, 18
 2D conceptual model, 80
 2D electrical resistivity model, 69
 2D lubrication Reynolds layer equation, 260
 Two-dimensional model, 243
 Two-phase medium, 221, 236
- U**
- Ullukamsk complex, 51, 52
 Ultrabasic rocks, 423
 Uncertainty, 197
 Uplift, 499, 502, 508, 521, 527
- V**
- Varimax method, 211
 Velocities, 25
 Velocity distribution, 395, 396
 Vigorous thermal convection
 - hot spot chain eruptions, 11
 - mantle material and conditions, 9
 - plumes, 10, 11
 - pulsation, 11
 - Rayleigh number, 9, 10
 - viscosity, 10
 - volcanic eruptions, 11
- Viscoplastic rheology, 13, 17
 Viscosity, 7, 277
 Viscosity distribution, 8
 Vitrinite reflectance (VR), 180
 Vladikavkaz fault, 52, 53
 Vocabulary, 227
- Volcanic provinces, 470
 Volcanics, 385
 Volcanic-sedimentary rocks, 47
 Volcanism, 146, 147, 149
 - Kuril island arc, 418–420
 - submarine volcano Krylatka, 420
 - volcano Atsonupuri, 420, 421
- Volcano Atsonupuri, 420, 421
 Volcanogenic formations, 49
 Volcano plutonic belts, 123
- W**
- Warm landscape, 87
 Wastewater in agricultural greenhouse
 - facilities, 36
- Water-caring communications, 115
 Water circulation, 143
 Water-filled boreholes, FTC, 101–103, 111
 Water filtration 3D simulation, 192
 Waterflooding field pattern, 261
 Water freezing, 83
 Web service, 342, 347
 Western flanks, 163
 Western Siberia, 179–187
 Western Volcanic Zone (WVZ), 70
 West Siberian and Persian Gulf provinces, 346
 West Siberian oil and gas province, 346, 348
 West Siberian Plain, 347
 West Siberian Plate, 346
 World Dark Grey Canvas Base, 344
- X**
- X-FEM/ CPP method, 260
- Y**
- Yamal, 84–86, 91, 181–183
 Young back-arc basins, 143
- Z**
- Zagan block, 370, 371
 Zagansky ridge, 370, 371
 Zapolyarnoye OGCF, 85
 Zaramag hydropower plant (HPP), 509
 Zero fluid mass flow, 263